A field and petrological study of an intermediate composition fissure eruption on Ascension Island

REBECCA WINSTANLEY

WINSTANLEY, REBECCA (2025) A field and petrological study of an intermediate composition fissure eruption on Ascension Island. Doctoral thesis, Durham University.

A field and petrological study of an intermediate composition fissure eruption on Ascension Island. R. Winstanley

Ascension Island is a Holocene, intraplate volcanic island in the South Atlantic Ocean and exhibits a wide compositional range of magma from basalt to rhyolite, but intermediate products make up <5% of the surface deposits. I focus on the 1.3 km long, trachyandesite Devil's Ink Pot fissure (DIP), located in the south-east corner of the island, and one of the youngest and best-preserved intermediate composition eruption on the island. I present detailed field work, petrographic, geochemical, and textural data to reconstruct the evolution of the DIP trachyandesite eruption, understand the genesis of intermediate magmas and shallow-surface processes occurring at low-flux ocean island volcanoes, and provide insights to future eruption scenarios on Ascension Island. The fissure is composed of 18 cones, 3 lava flow fields and tephra fall deposits up to 2 m thick. Two contrasting eruption styles are evidenced in cone deposits along the fissure. Despite the morphological and lithological differences, whole rock major and trace element analyses show that the erupted magma is chemically uniform. However, petrological, and geochemical analysis of plagioclase and olivine crystals identified textural and chemical variations. MELT's modelling from the least evolved Ascension Island deposits is not able to reproduce the same intermediate composition of the DIP fissure, therefore demonstrates that additional processes must be involved in the generation of intermediate melts. Analysis of feldspar microlite textures and anorthite contents indicate variations in the time spent in the upper conduit for the tephra and lava/spatter samples and the conduit dynamics, which can heavily influence the style of eruption. Small volume eruptions may be missing from the geological record, leading to a potential underestimation of their frequency. However, even small-volume eruptions are significant on small islands with limited options for self-evacuation of local inhabitants, therefore planning for eruptions with shifts in eruption styles should be incorporated into eruption scenarios on Ascension Island.

A field and petrological study of an intermediate composition fissure eruption on Ascension Island.

Rebecca Winstanley

PhD by Research

Department of Earth Sciences

Durham University

2023

Table of Contents

List of Tables:

List of Figures:

Statement of Copyright

Acknowledgements

I would like to thank all of my supervisors for giving me the opportunity to work on this project. Rich and Charlotte (and Sebastian and Arianna) for making the past 4 years much more enjoyable and keeping me sane throughout the whole process. For being my 'bubble' during COVID and providing much needed support. Katy C for supporting me since my undergraduate, for introducing me to Ascension and for the valuable discussions we had along the road (especially those had on horse-back). Katie P for always being there for discussions about anything I was unsure on and helping me get to grip with new skills.

I also want to thank DDS for the scholarship to complete the research and to NERC for the Ion Probe Grant, as well as the Durham Volcanology group for lots of interesting discussions.

Bridie for being the best field assistant, co-pilot and top DJ on Ascension and only needing to eat the emergency chocolate once! Everyone on Ascension Island who made our field work so enjoyable. From games nights at the US base), Burns Night on top of Green Mountain and the weekly HASH. To all of those in the conservation department, especially Sophie and Laura for driving us down to Letterbox some days, Lucie, Will, Matt and James for making us pesto pasta. Dee for all the help. The volunteers who helped with data collection and Hugh and Becky!

A special thanks to my family and friends, and a special mention to my best 4-legged friend Simba for providing the best way to de-stress (most of the time).

Chapter 1: Introduction and Aims

1.1 Introduction

Volcanic activity at ocean island volcanoes is dominated by fissure eruptions, defined by Hawaiian lava fountaining or Strombolian explosions (Head and Wilson, 1989; Parfitt and Wilson, 1995; Parfitt, 2004; Houghton et al., 2016). However, volcanic activity can transition between two end members of effusive or explosive and result in different eruption styles and deposits (e.g., Pioli et al., 2009; Cassidy et al., 2018; Bonadonna et al., 2022), which in turn controls the type of volcanic hazards (Cassidy et al., 2018).

Many processes occur within the magma storage region and conduit and during magma ascent, leading to the creation of a wide range of geochemical compositions and textures in the magma and crystal phases (Pan et al., 2022). Understanding these processes and the conditions involved for the genesis, transportation and storage of any magma is crucial for understanding the styles and size of volcanic eruptions (Carichi and Blundy, 2015; Magee et al., 2018; Bellver-Baca et al., 2020; Pan et al., 2022).

Intermediate magmas on ocean islands are less common (e.g., Beier et al., 2006; Déruelle et al., 2007; Thordarson and Larsen, 2007; Jeffery and Gertisser, 2018) compared to those erupted in island arc settings (e.g., Mercalli and Silvestri, 1891; Stix et al., 1997; Morrissey and Mastin, 2000; Burgisser et al., 2010; Gaunt et al., 2020), and identifying the processes that control the evolution of eruptions of intermediate compositions is difficult due to the limited exposure. Intermediate deposits can vary from whole eruptive sequences to inclusions within deposits of different compositions. Intermediate inclusions show that intermediate magmas do form in the magma chamber and therefore leads to questions about the Daly Gap and why we don’t always see intermediate deposits on the surface.

Ascension Island is a British Overseas territory and an ocean island volcano active in the last 500 years (Preece et al., 2018). It has a resident population of ~800 people and is host to United Kingdom Royal Air Force (UK RAF) and United States Air Force (USAF) bases. It has critical infrastructure and is strategically important for world communication systems, GPS systems and intelligence services.

A wide variety of eruption styles indicate that, whilst many eruptions have a localised impact, others have been more widespread. Some studies (e.g., Chamberlain et al, 2020) have suggested that the magma is stored at depths that cannot be detected by most monitoring techniques, and rises quickly to the surface, in the order of hours, resulting in limited time for warning signs. Therefore, the understanding of previous volcanic activity on Ascension Island is paramount for developing a volcanic hazard assessment on the island. Currently, there are no obvious signs of unrest on the island, but what the ‘normal’ background levels are, are unknown, because there is no long-term monitoring in place.

Previous work on Ascension Island has led to building an island wide understanding of the stratigraphy and age relations of the different deposits (e.g. Neilson and Sibbett, 1996; Preece et al., 2018; Preece et al., 2021), understanding mafic and felsic magma genesis (Weaver et al, 1996; Kar et al., 1998; Jicha et al., 2013; Chamberlain et al., 2016; Chamberlain et al., 2019), understanding mafic and felsic eruptions, their products and associated hazards (e.g., Neilson and Sibbett, 1996; Weaver et al., 1996; Jicha et al., 2013; Chamberlain et al., 2019; Preece et al., 2021; Preece et al., 2021; Davies et al., 2021), and beginning to understand the hazards that will be associated with future eruptions on the island (e.g., Preece et al., 2021; Davies et al., 2021). This study will be the first attempt to reconstruct an intermediate eruption and assess the potential hazards and impacts, by focusing on a single eruption from the Devil's Ink Pot Fissure (DIP). DIP is located in the southeast of the island and was chosen as it is one of the most well-preserved, intermediate composition eruption and shows an interesting link between explosive and effusive eruption styles. The fissure has never been fully studied, with the exception of a few petrographic and geochemical analysis of the lava flows (e.g., Daly, 1925; Paulick et al., 2010; Chamberlain et al., 2019). It cuts through a series of older trachyte and rhyolite domes and rhyolite lava flows. Previous geochemical analysis (Daly, 1925; Paulick et al., 2010; Chamberlain et al, 2019) show that the lava from the fissure is of a trachyandesite composition. $^{40}Ar/^{39}Ar$ dating of the fissure provided two different dates that highly contradict each other and the apparent freshness of the lava flows (Preece, personal communication).

1.2 Aims

The aim of this project is to build a detailed volcanic history of the Devil's Ink Pot (DIP) fissure. The project combines detailed fieldwork with petrographic, geochemical and groundmass texture analysis to understand the eruption dynamics and processes that occurred prior, during and after the eruption. Specific aims include:

- Understand the eruption styles that occurred throughout the DIP fissure and identify any similarities or differences between trachyandesite fissure eruptions and basaltic fissure eruptions.
- Identify what intermediate eruptions look like from a volcanic hazard perspective and think about how a future eruption of this style and magnitude would affect the island.
- Understand the magma ascent dynamics and identify the conditions and processes that occurred as the magma ascended to the surface.
- Understand how the intermediate magmas are created.

The outcomes of the project will contribute to the wider study on Ascension Island and studies on other ocean islands, by aiding in the understanding of different eruption styles and how they are influenced by the deep magma storage processes and associated ascent rates, and therefore assist in the preparation of volcanic hazard assessment for future eruptions.

Chapter 2: Background Information

2.1 Ocean Island Volcanoes

Ocean island volcanoes are often the largest volume volcanoes on earth (Klügel et al., 2015) but can experience rapid changes in morphology due to processes such as eruptions, subsidence, or flank instability (Paris et al., 2018). These volcanoes can have multiple source parameters (table 2.1, Fig. 2.1), for example, Tristan da Cunha magmatism is attributed to a deep mantle plume (Le Roex et al., 1990; Hicks et al., 2012), whilst the Azores is fed by plume formed by the spreading ridge axis (Beier et al., 2006). However, not all ocean islands generate melt via a plume (Jefferey and Gertisser, 2018). Petrological and geochemical studies are used to understand the petrogenesis of ocean island basalts (OIB) and infer the origin of the melt (e.g., Niu et al., 2011; Tepp et al., 2013).

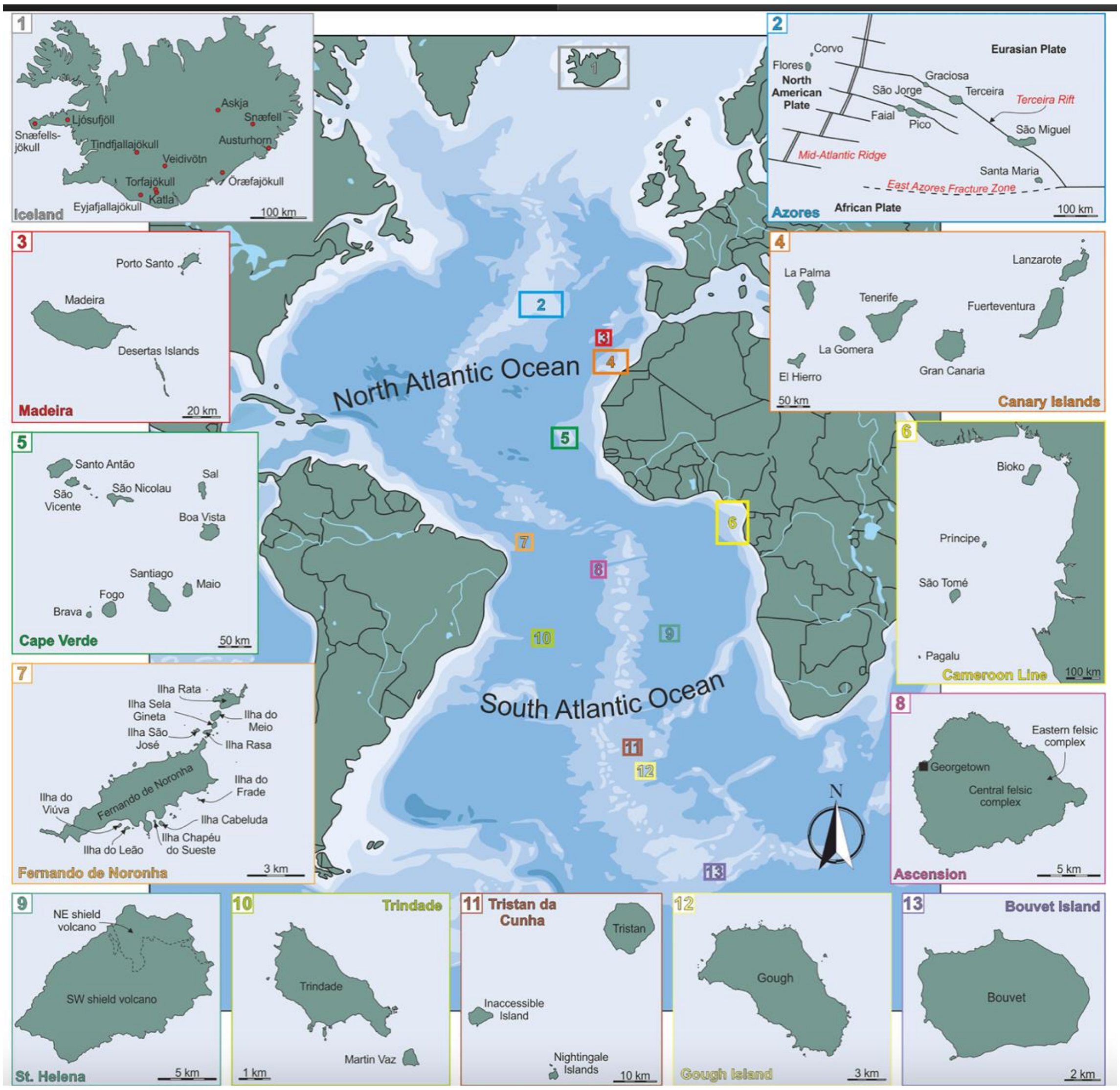

Figure 2.1: *Maps showing the ocean island volcanoes located in the Atlantic Ocean (1) Iceland, (2) the Azores archipelago, (3) the Maediera archipelago, (4) the Canary Islands, (5) the Cape Verde archipelago, (6) the oceanic sector of the Cameroon Line, (7) Fernando de Noronha, (8) Ascension Island, (9) St. Helena, (10) Trindade, (11) Tristan da Cunha, (12) Gough Island, and (13) Bouvet Island. Map from Jeffery and Gertisser (2018).*

The magmatic systems of ocean islands can reflect variations in both internal or external parameters, such as depth and degree of melting, the composition of source rocks, transport mechanisms and rainfall (Clague and Dixon, 2000), which interact in multiple ways to form different eruptions styles. Most ocean islands are often believed to have large similarities to Hawaii, which is in fact not typical of an ocean island system (Cas et al., 2022). This is because Hawaii erupts mostly an effusive, basaltic composition, whereas other ocean islands, such as Ascension Island, Tenerife, Azores, erupt both end members of mafic and effusive to felsic and explosive (e.g., Beier et al., 2006; Jicha et al., 2013; Cas et al., 2022).

Ocean Island volcanoes transfer magma to the surface through subvertical ascent through the oceanic crust from the mantle lithosphere and lateral movement via rift zones (Michon et al., 2015). Eruptions create scoria cones, pit craters and fissure eruptions, and the size of the eruptive structures can depend on the plumbing system, structure of the crust and degree of deformation of the volcanic edifice (Dieterich, 1988; Chaput et al., 2014; Michon et al., 2015).

2.2 Intermediate Magma Genesis

There is a wide debate about the origin of andesitic magmas at convergent boundaries and uncertainty regarding the processes that form them (Kent, 2014).

It is common to see a wide range in the erupted mafic lava and evolved lava compositions at ocean island volcanoes, but deposits of intermediate compositions are scarce and sometimes result in a Daly Gap, for example in the Azores and St Helena (table 2.1) (Mungall and Martin, 1995; White et al., 1979; Jicha et al., 2013; Jeffery and Gertisser, 2018). The Daly Gap is proposed for places where there are bimodal eruptive products with a lack of intermediate compositions (Jefferey and Gertisser, 2018). However, the presence of intermediate composition inclusions within mafic and felsic deposits (e.g., Bachmann et al., 2002; Ferla and Meli, 2006; Macdonald et al., 2008) is evidence that magma storage regions can host a complete range of compositions.

Intermediate magma on ocean islands commonly form from fractional crystallisation of mantle-derived basaltic liquid (Geist et al., 1995; Mungall and Martin, 1995; Weaver et al., 1996; Beier et al., 2006;), however they can also be produced by partial melting of basalt under water-saturated and undersaturated conditions (e.g., Helz, 1976; Bohrson and Reid, 1997), assimilation (e.g., Haase et al., 2005; Tegner et al., 2006; Freund et al., 2013), mixing or mingling of two different magma types (e.g., Hibbard, 1981; Martin and Sigmarsson 2007; Ray et al., 2011) that can form a new, hybrid magma (e.g., MacDonald et al., 2008) or a combination of these processes (Haase et al., 2005; Freund et al., 2013), for example fractional crystallisation of basaltic magmas, mixing between basaltic magmas and further fractional crystallisation along several liquid lines of descent (e.g., Greater

Location	Age	Magma Source	Type	Intermediate rocks
Iceland	24 Ma	Interaction between Mid-Atlantic Ridge and mantle plume.	Basalt – rhyolite, subalkaline tholeiitic trend; 79% mafic, 16% intermediate, 5% felsic.	Basaltic andesite, andesite, basaltic trachyandesite, trachyandesite.
Azores	20 – 7 Ma	Azores plateau, a morphologically complex area of thickened oceanic crust. Triple plate junction.	Alkali basalt – trachyte; Alkaline trend; Daly Gap; Mafic products fissure related; Intermediate products infrequent; Felsic products explosive and effusive.	Mugearite, trachyandesite.
Madeira Archipelago	5.6 Ma	Underlying mantle plume	SiO_2-overstaurated trend; Picrite and basanite – trachyte; Dominantly mafic; Rare intermediate and felsic.	Mugearite, trachyandesite.
Canary Islands	20.6 Ma	Underlying mantle plume	Multiple evolutionary trends: SiO_2-understaurated (basanite – phonolite); SiO_2-oversaturated (basalt – rhyolite); Tholeiitic trend; Mafic and intermediate. Abundance of felsic rocks is variable on each island.	Basaltic trachyandesite, trachyandesite, phonotephrite, tephriphonolite
Cape Verde	26 Ma	Two sub-marine chains from underlying plumes.	SiO_2-understaurated. Two magmatic series: picrite – peralkaline phonolite and picrobasalt – trachyte; Not all islands exhibit entire compositional range.	Phonotephrite, tephriphonolite.
Cameroon Line	52 Ma	Continental and oceanic sectors. Underlying plume.	Picrite and basalt – phonolite, trachyte, rhyolite; Uncommon intermediate; Oceanic felsics - phonolite and trachyte. Continental felsics – rhyolite and trachyte.	Mugearite, trachyandesite.
Fernando de Noronha	40 Ma	Underlying mantle plume	Three formations; Remédios Formation with two suits of rock: sodic series (basanite – phonolite), potassic series (alkali basalt – trachyte); Quixaba and São José Formations: nephelinites and basanites.	Phonotephrite, tephriphonolite, basaltic trachyandesite, trachyandesite.
Ascension Island	6 - 7 Ma	Complicated source	Sub-alkaline series. Basalt – trachyte; Mafic rocks located island wide, felsic rocks in two main areas; Lack of intermediate compositions (Daly Gap).	Mugearite, trachyandesite.
St Helena	14.3 – 11.4 Ma	Hot spot theory	Alkaline suite – alkali basalt – peralkaline trachyte and phonolite; 70 – 80 vol.% mafic, 15 – 25 vol.% trachybasalt, 4 vol.% trachyandesite, 1 vol.% felsic.	Basaltic trachyandesite, trachyandesite.
Trindade	3.6 Ma	Underlying mantle plume	Multiple formations. Nepheline - phonolite. Rare basanite.	Phonotephrite, tephriphonolite.
Tristan da Cunha	0.2 – 0.1 Ma	Underlying mantle plume	Mainly SiO_2-understaurated basanites (~ 80%); Intermediates (~15%); Tephriphonolites are most evolved composition (~5%)	Phonotephrite, tephriphonolite.
Gough Island	2.55 Ma	Underlying mantle plume	SiO_2-understaurated. Picrite basalt – aegirine-augite trachyte. Felsic rocks dominant in volume and are explosive and effusive.	Basaltic trachyandesite, trachyandesite.
Bouvet Island	<1.4 Ma	Underlying mantle plume.	Single, sodic SiO_2-overstaurated series. Alkali-basalts – peralkaline trachyte and rhyolite.	Mugearite, trachyandesite.

Table 2.1: Summarising the different ocean island volcanoes from the work of Jeffery and Gertisser (2018) and references therein.

Olkaria Volcanic Complex, Kenya (Macdonald et al., 2008), or fractional crystallisation and partial melting (e.g., Terceira island (Mungall and Martin, 1995).

Magma mixing is usually characterised by a range of mineral compositions with most phenocrysts either too evolved or too mafic to be in equilibrium with the whole rock composition and ranges in groundmass glass compositions that extend from more mafic to more felsic than the whole-rock compositions (e.g., Reubi and Nicholls, 2005).

Intermediate deposits formed from oceanic crust, often cannot solely be reproduced by fractional crystallisation (Haase et al, 2005). Instead, it is believed to be the product of combined fractional crystallisation and assimilation or partial melting of wall rock or hydrothermally altered material (e.g., Haase et al., 2005; Freund et al., 2013). Incorporation of wall rock by partial melting or assimilation can also modify the compositional and fractionation pathways of the initial magma (e.g., Haase et al., 2005; Freund et al., 2013).

2.3 Eruption Processes

Eruptions of intermediate composition magmas result in a wide variety of eruption styles ranging from explosions with lava fountaining, lava flows and pyroclastic flows (Naranjo et al., 1992; Yamagishi and Feebrey, 1994; Kimura et al., 2005; Pioli et al., 2008; Zobin et al., 2015; Bain et al., 2018; Nakada et al., 2019) to effusive dome building events and dome collapses (e.g., Sparks et al., 1998; Herd et al., 2005; Kimura et al., 2005). Fissure eruptions with deposits of intermediate composition are very rarely described in the literature (e.g., Belousov et al., 2015; Gansecki et al., 2019).

2.3.1 Lava Fountaining

Hawaiian style eruptions generate lava flows and lava fountains. Lava fountains are defined as sustained ejections of hot pyroclasts (Taddeucci et al., 2015; Snee et al., 2021). The eruptions result from a mixture of gas and magma that fragments before reaching the surface (Head and Wilson, 1989; Parfitt and Wilson, 1995; Parfitt, 2004). The exsolved magma-gas and volatile content, the volume flux and the vent geometry control the lava fountain temperature, heights, and accumulation rates (Head and Wilson, 1989; Calvari et al., 2021).

Hawaiian lava fountains can be sub-divided into high fountains (>100 m) or low fountains (<100 m) (Parcheta et al., 2012). High fountains have rapid discharge rates and are associated with single point sources, whereas low fountains have low mass eruption rates and are linked to fissure sources (Parcheta et al., 2012). High lava fountains generally have viscosity less than 10^6 Pa s and the difference between the gas and melt velocity is less than the melt velocity (La Spina et al., 2021). Lava fountains during Hawaiian style eruptions typically range between 100 – 500 m high (e.g., Brown et al., 2014 and references therein).

2.3.2 Eruption Mechanisms

Hawaiian lava fountain eruptions are primarily controlled by magma ascent rates. For a lava fountain to occur, magma must rise quickly (Parfitt and Wilson, 1995). The Rise Speed Dependent Model (RSD) demonstrates that if the rise speed is high, bubbles are unable to rise far enough through the overlying magma before it is erupted (Parfitt, 2004). The RSD model assumes that both magma and gas are present but act as a single (Fig. 2.2), combined gas-magma phase, where bubbles can grow and ascend until the bubble volume is great enough to initiate fragmentation (Sparks, 1978; Houghton and Gonnerman, 2008). After fragmentation, less friction is exerted on the conduit walls, allowing rapid acceleration for eruptions to occur (Blackburn et al., 1976; Parfitt, 2004). However, if the rise speed is low, the rising gas bubbles segregate due to a greater bubble coalescence depleting the gas-magma mixture, resulting in lower fountain heights (Parfitt and Wilson, 1995). Larger bubbles rise faster than smaller bubbles and either overtake smaller bubbles or form a gas slug (Parfitt, 2004). For Hawaiian style eruptions, the RSD model assumes a homogenous gas-magma flow with different driving gases, but the model only works if H_2O is the main driving gas (Parfitt, 2004).

The Collapsing Foam Model (CF) assumes that magma is stored in a magma chamber, at depths where gases can exsolve (Vergniolle and Jaupart, 1986; Parfitt, 2004). As the gas bubbles rise and accumulate at the top of the storage region, they are arranged into a foam layer (Fig. 2.2). When the foam layer reaches critical thickness, it becomes unstable and collapses, allowing the bubbles to coalesce and form gas slugs. The gas slugs migrate up an open vent system, moving faster than the surrounding magma, and are erupted (Parfitt, 2004; Burton et al., 2007). Hawaiian style eruptions would imply a rapid foam collapse and depend on CO_2 as the main driving gas (Parfitt, 2004).

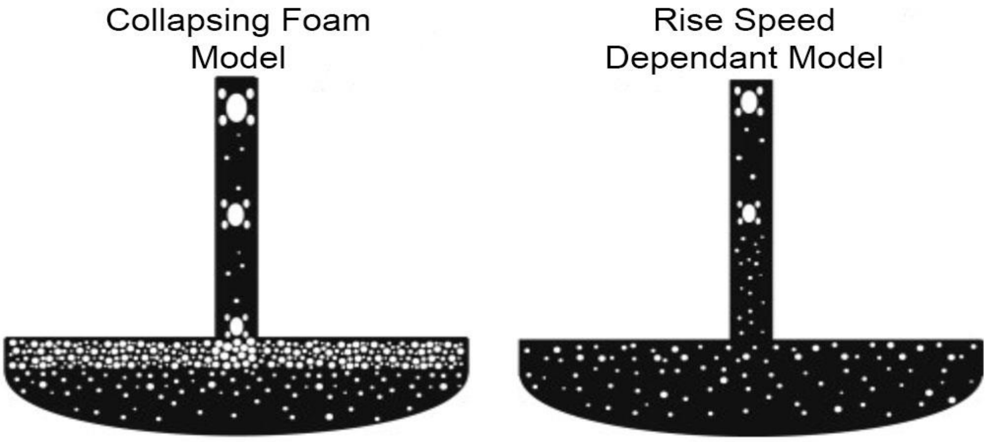

Figure 2.2: *Diagram showing the mechanisms of the collapsing foam model of Vergniolle and Jaupart (1986) and the Rise Speed Dependant Model of Parfitt (2004) (Houghton and Gonnerman, 2008).*

2.3.3 Paroxysmal Eruptions

Defined as a climatic phase of an eruption where lava fountaining and tephra plumes co-exist (Alparone et al., 2003; Calvari et al., 2018). However, paroxysmal eruptions can also have effusive phases (Bonaccorso and Calvari, 2017). During a paroxysmal phase, a mixture of gas and pyroclasts emerge from a vent as a single jet and expand vertically into an eruption column (Calvari et al., 2018). There are three main regions of an eruption column from a paroxysmal eruption: 1) gas-thrust region, is the lowest and contains the lava fountains. 2) convective region, where atmospheric mixing occurs, leading to the ascent velocity and lateral wind transport to decrease. 3) umbrella region, where the plume reaches the zone of natural buoyancy and spreads out laterally (Calvari et al., 2018). The periodicity of explosions has been related to magmatic composition, where mafic explosions have a greater frequency than intermediate or silicic explosions (Dominguez et al., 2016; Bonaccorso and Calvari, 2017). The unusually abrupt transitions in eruptive behaviour shown during paroxysmal eruptions can be attributed to: (1) the highly efficient draw-down of the fragmentation front; (2) large-scale eruption column instability initiated either by changes in the conduit shapes or phreatomagmatic activity; (3) volatile and rheological contrasts of the magma (Turbeville, 1992).

2.3.4 Fragmentation

Fragmentation transforms from a continuous liquid phase with gas bubbles and crystals to a gas phase with pyroclasts (Cashman and Scheu, 2015). Fragmentation is a result of decompression and gas exsolution and can occur when a fresh batch of magma enters the shallow magma chamber and changes the internal pressure. This leads to the nucleation of bubbles which forces the magma up towards the surface (Cashman and Scheu, 2015). As the amount of exsolved gas in the magma increases, fragmentation increases, and the clast size decreases (Head and Wilson, 1989).

Fragmentation can occur in four ways; 1) rapid magma ascent during explosive eruptions, 2) after rapid decompression caused by the collapse of lava domes or volcanic edifices, 3) shearing of magma along conduit walls, 4) impact-induced explosion of hot solid blocks during dome collapse (Cashman and Scheu, 2015). The low viscosity of basaltic magma prevents fragmentation and leads to effusive and lava fountaining activity (Arzilli et al., 2019). As magma rises rapidly to the surface, undercooling occurs and drives rapid crystallisation, which in turn prompts a change in the viscosity and triggers brittle fragmentation (Zimanowski et al., 1997; Moitra et al., 2018; Arzilli et al., 2019). If the criterion for brittle fragmentation is not met, than fragmentation occurs by inertial fragmentation or fluid dynamic breakup (La Spina et al., 2021). The criteria for inertial fragmentation and fluid dynamic breakup do not apply during ascent in the conduit, therefore lava fountaining can represent the process where magma arrives at the vent with significant overpressure and a high velocity but without fragmenting inside the conduit (La Spina et al., 2021). Instead, fragmentation occurs once the magma is erupted form the vent (La Spina et al., 2021). However, it is unlikely that either of the mechanisms can form large, fluidal pyroclasts and thus there must be an additional mechanism for spatter to form (La Spina et al., 2021).

2.4 Vulcanian Explosions

Vulcanian eruptions occur as the result of magma ascent in a conduit and a gas-rich accumulation region at the top of the magma column that causes the build-up of pressure beneath a dense magma plug (Yamagishi and Feebrey, 1994; Stix et al., 1997; Morrissey and Mastin, 2000; Burgisser et al., 2010; Bain et al., 2019; Gaunt et al., 2020). The intensity, duration and course of Vulcanian explosion are varied, depend on the amount of pressure that builds up beneath the pug and can transition between Sub-Plinian and Strombolian explosions (Maeno et al., 2013; Gaunt et al., 2020), however characteristically, eruptions only last seconds to minutes (Clarke, 2013). There are limited constraints on the processes that inflect the observed cyclic behaviour (Wright et al., 2007).

At the point of fragmentation, the vesicular magma is moved into a gas-pyroclast mixture, propelled upwards and ejected from the vent (Fig. 2.3) (Self et al., 1997; Clarke, 2013). The resulting eruption can produce buoyant plumes up to 20 km high (Nairn and Self, 1978) and pyroclastic flows (Clarke, 2013).

Vulcanian activity can be associated with ground water interaction followed by explosions caused by vesiculated magmas (Heiken and Wohletz, 1987). Many basaltic volcanoes are produced in part by water-magma interaction and produce phreatomagmatic features, including tuff rings and cones, maars (Walker, 1973; Wohletz and Sheridan, 1983; Houghton and Schmincke, 1989; Valentine and Gregg, 2008).

2.5 Type of Eruption Deposits

Hawaiian style eruptions can produce several different types of deposits, from scoria cones to spatter ramparts, lava flows and tephra fall deposits (Wood, 1980; Head and Wilson, 1981; Riedel et al., 2003; Valentine and Gregg, 2008; Taddeucci et al., 2015). Pyroclasts in the fountains range in grain size and are often coarse enough that they fall to the surface rather than be entrained into a convecting cloud over the vent (Wilson and Head, 1981; Valentine and Gregg, 2008; Bonaccorso and Calvari, 2017). Lava fountains can create scoria cones at point sources or spatter ramparts along fissures (Riedel et al., 2003; Valentine and Gregg, 2008; Taddeucci et al., 2015), and the spatter deposits have varying degrees of welding and agglutination. Fine lapilli and ash particles from the fountaining can be entrained into small wind-advected thermal plumes, carried short distances from the vents and deposited as tephra fall deposits (Valentine and Gregg, 2008; Taddeucci et al., 2015). The textures and chemical composition of juvenile clasts can record changes in the pre- and syn-eruptive magmatic conditions (D'Oriano et al., 2014).

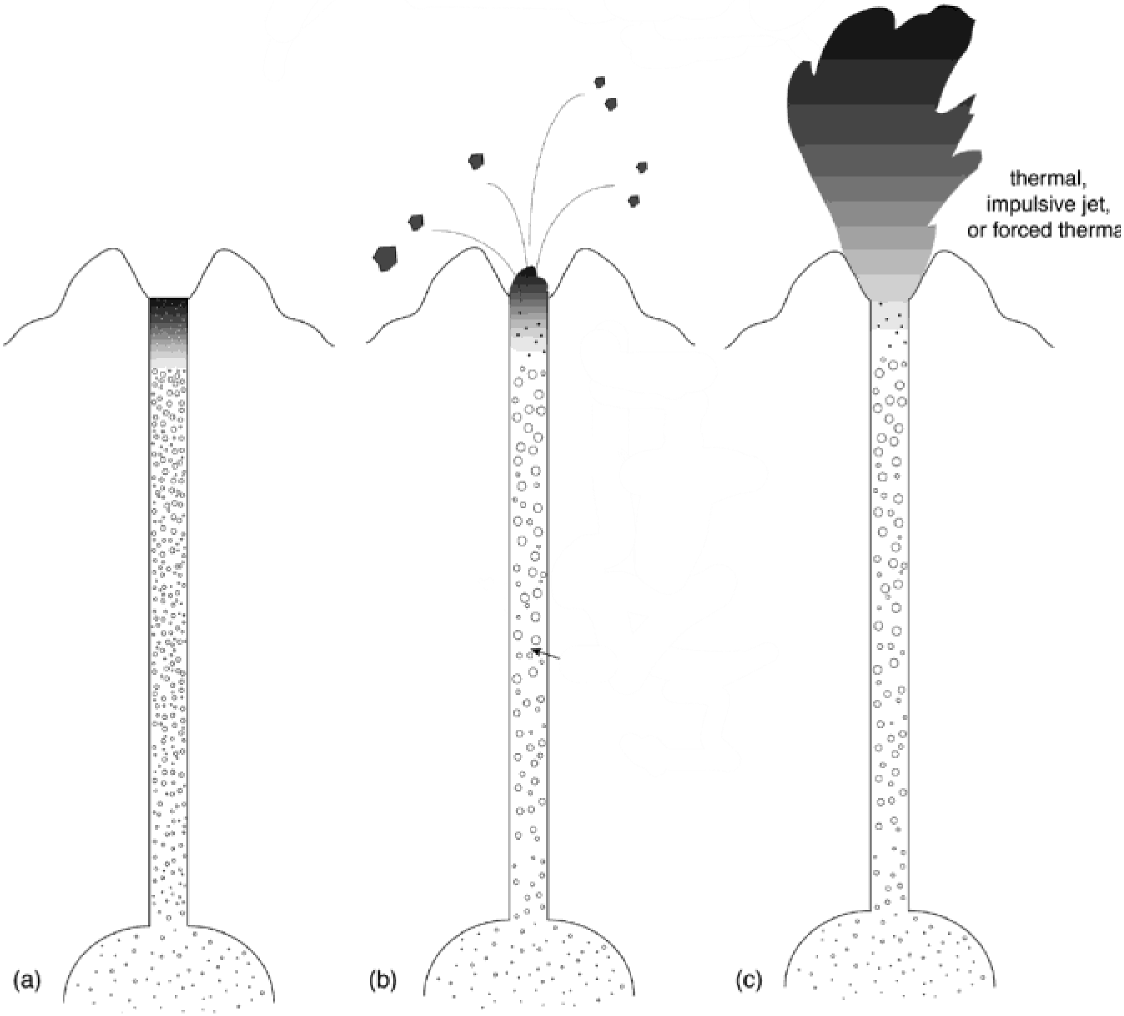

Figure 2.3: *Schematic of a Vulcanian explosion, modified from Clarke (2013).* ***A)*** *Pre-eruption: a vesicular magma underlies a dense plug.* ***B)*** *The Vulcanian explosion begins as the plug is moved and ballistic clasts are expelled into the air.* ***C)*** *A buoyant and/or unsteady jet of gas and fragmented magma mixture erupts into the atmosphere*.

2.5.1 Spatter Deposits

Spatter is defined by Radar and Geist (2015) as an accumulation of fluidal pyroclasts that agglutinate on landing. The following terminology will be used to describe the different spatter deposits (Sparks and Wright, 1979; Cas and Wright, 1987; Henry et al., 1989; Branney and Kokelaar, 1992; Quane and Russell, 2005; Russell and Quane, 2005; Sumner et al., 2005):

- Welding → the sticking together and point contacts and compaction of clasts under the influence of overburdening pressures in a hot deposit.

- Agglutination → the flattening, sticking and gradual cooling of hot, fluidal pyroclasts as they impact on an accumulation surface.
- Coalescence → the process where fluidal droplets form a homogenous liquid and remnant particle outlines are destroyed.

Multiple semi-quantitative schemes have been defined in order to classify degrees of welding based on petrographic traits (e.g., Smith 1960), estimated porosities (e.g., Smith and Bailey, 1966), bulk density measurements and pumice flattening ratios (e.g., Sheridan and Ragan, 1976; Peterson, 1979; Russell and Quane, 2005) and combinations all the above (e.g., Streck and Grunder, 1995; Wilson and Hildreth, 2003; Quane and Russell, 2005).

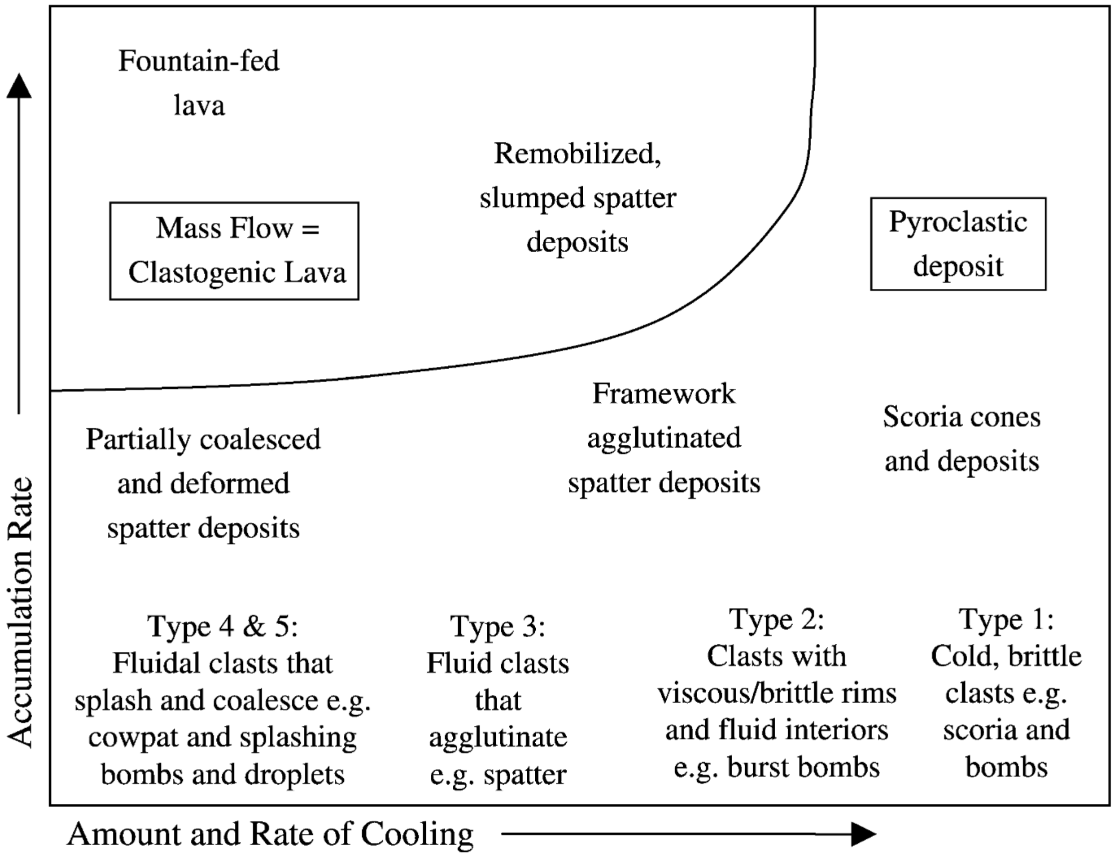

Figure 2.4: *Showing the different types of deposits that are produced by lava fountaining, depending on the accumulation rate and the amount and rate of cooling Sumner et al., 2005.*

Agglutination of the clasts only occurs when the exterior temperatures exceed the glass transition temperature (500 – 739 °C for basalts) (Radar and Geist, 2015). The extent of fusing of the clasts can aid in quantifying conditions such as accumulation and cooling rates of eruptions (Radar and Geist, 2015). The abundance of welding and lack of grain avalanching are typical characteristics of Hawaiian style eruptions (Walker, 1973; Reynolds et al., 2016). The rapid variations seen in pyroclast sizes and degrees of welding result from pulsing fountains and variations in the accumulation rates (Sparks and Wright, 1979; Head and Wilson, 1989; Reynolds et al., 2016). The degree of welding can change over short vertical intervals without showing any changes in grain size (Quane and Russell, 2005;

Carey et al., 2008a). Determining accumulation rates of spatter provides insight into eruptive flux, an essential parameter for understanding eruption behaviour (Sparks and Wright, 1979; Radar and Geist, 2015).

Sumner et al., (2005) defined five different spatter clast types by ranking them according to their increasing fluidity (Fig. 2.4). The first type are cold and brittle clasts (e.g., scoria clasts). The second are clasts with brittle rims and fluid interiors (e.g., cowpat bombs). The third are fluidal clasts that agglutinate. The fourth are fluidal clasts that splash on landing or coalesces to form lava flows. The fifth are clasts with a brittle core and fluid rim.

As the pyroclasts hit the ground several processes can occur. The clasts can deform in a brittle manner and fracture or deform plastically and flatten. They can also rupture with a brittle skin, fold or be disrupted by splashing (Sumner et al., 2005).

At higher temperatures, the clasts deform into elongate shapes either during flight by stretching from the force of the eruption, due to the gravitational impact on landing or after deposition when gas escapes and the clasts cool and contract (Rader et al., 2018).

The welding process involves sintering, compaction and flattening of hot pyroclastic material (Sparks and Wright, 1979; Quane and Russell, 2005). For welding of clasts to occur, there must be short durations of particle transport from fragmentation to deposition to prevent excessive cooling and high accumulation rates to quickly cover clasts and prevent overcooling (Sparks and Wright, 1979; Carey et al., 2008a; Carey et al., 2008b). The degree of welding increases with increasing clast size, as the coarser clasts lose less heat than smaller clasts within any period, and so have more residual heat available for welding (Sparks and Wright, 1979; Russell and Quane, 2005; Quane and Russell, 2005; Carey et al., 2008a). The degree of welding also increases with increasing deposit thickness, as the welding tephra can thermally equilibrate, maintaining the temperature for longer and allowing the deposit to cool as a single unit (Carey et al., 2008a). Finally, welding can occur due to the overburden of tephra compacting the underlying deposit (Carey et al., 2008a).

2.5.2 Lava Flows

Basaltic lava flows originate from vents as coherent flows from a small opening, overspills from an overflowing or breached lava lake, or from lava fountains where the spatter is re-established around the vent and flows away (Sumner, 1998). Lava flows can have durations ranging from weeks to years and can pose long lived hazards (Cashman et al., 2013). A’a lava flows have a brecciated surface and base and dense core (Harris et al., 2017). The auto-brecciated surface clasts are classified as clinkery if fresh looking and spiny or rubbly if they have undergone abrasion during transport (Harris et al., 2017). For magmas to erupt from sources with high volatile contents, the magma must degas to prevent pressure build up (Cas and Wright, 1988). This can be done by 1) direct escape of exsolving volatiles 2) an earlier phase of explosive activity (Cas and Wright, 1988).

Factors that increase lava flow advance include: 1) high flow velocity, 2) steep underlying slopes, 3) high lava temperatures, 4) low cooling rates, 5) low bulk viscosity, 6) high effusion rates (Hulme, 1974; Gregg, 2017), whilst factors that decrease lava flow advance include: 1) high bulk viscosity, 2) increased crystal content, 3) rigid vesicles, 4) low lava temperatures, 5) high cooling rates, 6) low flow velocity (Walker, 1967; Hulme, 1974; Gregg, 2017). Walker (1973) found that the distance travelled by a lava flow was directly proportional to the effusion rates (Cas and Wright, 1988). The higher the effusion rate, the further the lava flow will travel before cooling (Cas and Wright, 1988). Lava flows with high effusion rates form single flow units, whilst lava flows with low effusion rates form small, compound flows that pile up close to the vent (Cas and Wright, 1988). Levee heights are good indicators of flow depth and are proportional to the yield stress of the lava (Hulme, 1974; Naranjo et al., 1992). For levees to form, the flow depth, and hence yield strength, must decrease during the eruption (Hulme, 1974). The change in yield strength can be due to: 1) change in composition of lava, 2) change in lava temperature, 3) change in eruption rate (Hulme, 1974).

A’a lava flows have velocity profiles that increase towards the centre (Harris and Rowland, 2015). Lava channels form either as the lava at the flow margins is too thin and does not have enough force to flow or due to pre-existing topography confining the lava (Gregg, 2017). Once the channels are formed, an order of magnitude change in effusion rate or flow velocity is required to modify the channel morphology (Gregg, 2017). A’a lava flow fields form when lava is transported through open channels at high eruption rates (Macdonald, 1953; Pinkerton and Sparks, 1976; Blake, 2000). Flows generated from lava fountains can be clastogenic lavas and contain remnant clast outlines and spatter fragments (Cas and Wright, 1987; Sumner, 1998; Carracedo Sánchez et al., 2012). However, in most spatter fed eruptions the clasts completely coalesce and no textural evidence for clastic origin is preserved, therefore a clastic origin can only be inferred if the eruption is observed (Sumner, 1998; Carracedo Sanchez et al., 2012).

2.5.3 Pyroclasts

The morphology and shape of juvenile pyroclasts are heavily influenced by melt viscosity and vesicle content during fragmentation and transportation (Houghton and Gonnerman, 2008; Houghton and Carey, 2015). Angular and blocky pyroclasts with planar or curvi-planar surfaces imply brittle failure of a cooler and more viscous magma (Houghton and Carey, 2015) and a more explosive eruption, whilst elongate and fluidal surfaces imply the clasts were still molten after fragmentation (Jutzeler et al., 2016). The different clast characteristics suggest that different physical processes, including different fragmentation processes, are responsible for their formation (La Spina et al., 2021).

2.5.4 Ballistic Bombs

Air drag limits the transport distance of ballistic particles (Capaccioni and Cuccoli, 2005). The range of transport distance increases as the size and density of particles are increased (Capaccioni and Cuccoli, 2005). Ballistics can be ejected on almost parabolic trajectories (Breard et al., 2014) and the angle of the jet can reflect source depth (Maeno et al., 2013).

Ballistic clasts (defined as anything >64 mm) can be hazardous for areas within 1 – 2 km of a vent (Breard et al., 2014). Understanding the size, mass distribution and lithology of ballistics is vital for interpreting eruption dynamics and the hazards associated with them (Breard et al., 2017). Factors that can affect the dispersal of ballistics include: 1) explosion type (magmatic vs phreatomagmatic vs hydrothermal), 2) explosion depth, 3) mechanism of the explosive impulse, 4) crater morphology (Breard et al., 2017).

The original study of Vulcano (Walker 1969; Walker, 1982) defined three types of ballistics: 1) dense blocks that were hot on impact and didn't expand, 2) blocks with thick and quenched rinds that had limited expansion, 3) blocks with a thin glassy crust and broad shallow cracks that were highly expanded (Wright et al., 2007). The difference in ballistic morphology is related to differences in magma viscosity and clast cooling times (Wright et al., 2007).

Breadcrust bombs are the products of poorly vesiculated and degassed magma in an almost solid state (Clarke et al., 2015). The threshold for when dense or vesicular bombs with no rinds form depends on the initial bubble composition and conditions (Benage et al., 2014). Therefore, breadcrust bombs can reflect either quenching of magma by external water (Fisher and Schmincke, 1984; Wright et al., 2007) or delayed vesiculation of partially degassed magma (Yamagishi and Feebrey, 1994; Wright et al., 2007). There are variations explanations for the mechanisms that lead to bread crusting. The exterior cracking can occur due to interior expansions of a bomb with a quenched rind, in response to thermal contractions of the outer surface or from stresses applied during impact (Wright et al., 2007). Pre-eruptive magma degassing produces delays in syn-eruptive bubble nucleation and allows rinds to form (Hoblitt and Harmon, 1993; Yamagishi and Feebrey, 1994; Wright et al., 2007). Bread crusting of pumice clasts can be produced by locally high temperatures and low volatile contents (Polacci et al., 2001; Wright et al., 2007).

2.6 Crystal textures

Crystals in volcanic rocks give clues to processes and time scales of magma evolution (Bacon and Lowenstern, 2005). Crystal phases that are in textural equilibrium with the magma crystallised almost or fully in equilibrium and the residual magma likely segregated from the phenocrysts before the next stage of crystallisation occurred (Reubi and Nicholls, 2004). However, the dynamic environment within magma storage regions can lead to textural heterogeneities in crystal textures on phenocryst to microlite scales (Grogan and Reavy, 2002).

Disequilibrium textures in crystals have been widely observed and detailed in volcanic rocks (Hibbard, 1981; Umino & Horio, 1998; Perugini et al., 2003; Sumner and Wolf, 2003; Xing et al., 2017; Pan et al., 2022). The main factors that lead to the evolution of disequilibrium textures is the chemical and physical interaction between different batches of magma (Grogan and Reavy, 2002). The textures develop due to the processes that guide the crystallisation of a melt, i.e., rates of nucleation, diffusion, pressure and temperature variations and crystal growth, changing in response to changing conditions in the magma storage region, e.g., undercooling (Nixon, 1988; Grogan and Reavy, 2002; Perugini et al., 2003; Pan et al., 2022). Crystals in volcanic rocks can show a range of disequilibrium textures within short scales, which suggests that disequilibrium is not consistent throughout a magma body (e.g., Anderson, 1984; Perugini et al., 2003). Disequilibrium textures can provide evidence for processes such as magma mixing (e.g., Hibbard, 1981; MacDonald et al., 2008; Ray et al., 2011; Pan et al., 2022) or crustal assimilation (e.g., Meade et al., 2014).

2.7 Rates of magma ascent and groundmass textures

The style that a volcano erupts is dependent on magmas ascent rates and conduit geometry (Rutherford, 2008; Brugger and Hammer, 2010; Browne and Szramek, 2015; Befus and Andrews, 2018). The rate that magma ascends from a storage region can be estimated by using different techniques, such as: (1) seismicity during eruptive periods (e.g., Scandone and Malone, 1985; Brugger and Hammer, 2010), (2) plagioclase size distributions (e.g., Cashman, 1992; Brugger and Hammer, 2010), (3) reaction rim development on amphibole crystals (e.g., Rutherford and Hill, 1993; Nicholis and Rutherford, 2004; Browne and Gardner, 2006; Brugger and Hammer, 2010)

Factors that control the rate of magma ascent include temperature, composition, volatile budget and crystallinity, all of which also affect viscosity, density and permeability of the conduit walls (Browne and Gardner, 2006; Browne and Szramek, 2015) and hence the processes occurring within the conduit. Magma ascent cannot easily be tracked as it occurs in the subsurface, therefore the understanding of these processes and rates come from a combination of geophysical measurements, modelling, and comparing high temperature experiments with textures from past eruptions (Browne and Gardner, 2006; Befus and Andrews, 2018). Intermediate magmas generally are less buoyant and rise slowly to the surface, allowing more time for degassing and crystal growth from decompression (Bugrisser and Degrruyter, 2015).

As magma rises, decompression forces water to exsolve from the melt due to the increasing decompression causing the liquidus temperature of the magma to increase and changing the stability of anhydrous phases (Cashman and Blundy, 2000; Browne and

Szramek, 2015). The kinetics of magma crystallisation can be controlled by melt composition, mineral phase, pressure, degrees of undercooling, temperature, time, melt water concentration, oxygen fugacity, cooling and decompression rates (Cashman and Blundy, 2000; Cashman and McConnell, 2005; Brugger and Hammer, 2010; Arzilli et al., 2015 and refs in). Although these factors are not independent, they can strongly affect the nucleation and growth rates.

Groundmass crystal sizes, shapes and abundance control the extent to which increasing crystallisation affect the rheology of the magma (Cashman and Blundy, 2000). Change in magma rheology due to variations in volatile concentrations and crystallisation, can play a large role the changing rate, style and duration of an eruption (Cashman and Blundy, 2000). Isothermal decompression and degassing generate a driving force for crystallisation, particularly plagioclase, but the extent to which crystallisation occurs depends on the effective undercooling, created by the relative rates of decompression and degassing, and the time before quenching (Casman and Blundy, 2000). Feldspars are stable at varying temperatures and pressures. A more Ca Rich feldspar will form at high temperatures whilst a more Na-Rich feldspar will form at low pressures (Flood and Knapp, 1968).

Microlites are sensitive to the host melts degree of undercooling (Befus and Andrews, 2018). The extent of undercooling can be controlled by the decompression rate. Fast decompression rates lead to lower degrees of crystallisation and greater degrees of undercooling (Befus and Andrews, 2018). Microlite number density and size distribution represent shallow and deep magma conduit environments by provided insights into the rates that microlites nucleate and grow (Befus and Andrews, 2018).

Natural igneous rocks often contain crystal phases with disequilibrium textures, suggesting that magmas often follow non-equilibrium, time dependant pathways that are recorded in the petrological and geochemical characteristics of the rocks (Arzilli et al., 2015; Befus and Andrews, 2018).

Plagioclase crystallisation in basaltic magmas has been studied as a function of undercooling (e.g. Lofgren, 1974; Arzilli et al., 2015) but rarely through decompression experiments (Arzilli et al., 2015 and references therin), whereas intermediate and silicic composition eruptions are more commonly studied through decompression experiments (Arzilli et al., 2005; Blundy et al., 2006; Brugger and Hammer, 2010; Shea and Hammer, 2013; Arzilli et al., 2015, Arzilli et al., 2019; Bamber et al., 2020). The basaltic magma experiments generally show that the decrease in pressure causes water exsolution and an increase in plagioclase liquidus temperatures, with this undercooling providing the driving force for crystallisation (Arzilli et al., 2015). Decompression experiments done on intermediate and silicic systems show that feldspar abundance, composition and morphology depend on the decompression path, degree of undercooling and viscosity of the melt (Brugger and Hammer, 2010). These experiments replicate the pressure-temperature changes undergone by the magma during ascent (Befus and Andrews, 2018) and show that average nucleation rates decrease with decreasing decompression rates (Hammer, 2008; Befus and Andrews, 2018).

Crystal growth is crucial in systems that exhibit small deviations from equilibrium (Blake, 2000; Brugger and Hammer, 2010). Microlite textures record the effective undercooling generated during ascent and temporary storage (Cashman and Blundy, 2000; Blake, 2000; Arzilli et al., 2015) and the crystal shapes are related to growth rates and undercooling (Arzilli et al., 2015). Crystallisation can occur through nucleation of new crystals or by growth on existing nuclei (Blake, 2000). Nucleation process dominates when undercooling is high, and the textures are controlled by rates of crystal nucleation which vary depending on the decompression pathway the magma takes (Cashman and Blundy, 2000; Blake, 2000; Befus and Andrews, 2018). Experiments by Arzilli et al., (2015) show that nucleation rates in basaltic magmas are higher than those in basaltic andesites, but decrease with increasing time, suggesting that the main nucleation event occurs within the first stage of the process, and that the crystals reach equilibrium within 1-2 hours (Arzilli et al., 2015).

Plagioclase growth rates vary as a function of cooling rates (e.g., Cashman, 1993; Conte et al., 2006; Brugger and Hammer, 2010), with low amounts of undercooling favour conditions for growth on pre-existing crystals (Befus and Andrews, 2018; more refs). Crystal growth reduces supersaturation of the melt and pushes the system towards equilibrium. Undercooling also plays an important role in the morphology of plagioclase crystals (Arzilli et al., 2015). Plagioclase microlite sizes change with decompression rate. The microlites are larger and more tabular during slow decompression with average growth rate decreasing exponentially (Brugger and Hammer, 2010; Befus and Andrews, 2018) and more skeletal and acicular as decompression rates increase (Brugger and Hammer, 2010; Arzilli et al., 2015).

2.8 Ascension Island

2.8.1 Tectonic History

Ascension Island is situated in the South Atlantic Ocean, ~100 km west of the Mid-Atlantic Ridge (MAR) and ~50 km south of the Ascension Fracture Zone (AFZ) (Fig. 2.5) (Nielson and Stiger, 1996; Webster and Rebbert, 2001; Chamberlain et al., 2016). The subaerial edifice covers ~93 km^2, whilst the base, at 3000 m below sea level, covers more than 2000 km^2 (Brozena, 1986). The highest point on the island, Green Mountain, is 859 m asl. The island has four fundamental fault orientations on the island: northwest, northeast, north-south and east-west (Nielson and Sibbett, 1996). These faults developed from uplift by the intrusion of melt beneath the island and are one of the main restraints on the location of eruptions (Nielson and Sibbett, 1996).

The origin of the magmatic source for Ascension Island has been heavily debated, with two competing models proposed to explain the presence of magma underneath Ascension. The first proposes that the drift of the Mid-Atlantic Ridge axis away from the Ascension plume led to an asthenospheric flow towards the westward migrating ridge axis (Schilling et al., 1985; Brozena, 1986). If this model is correct there is no plume directly underneath Ascension Island now. The chemistry of the basalts provides supporting evidence for this model: The Pb isotope variations in MORB's indicate that the plume is currently underneath the Circe Seamount (Jicha et al., 2013).

The second model proposes that Ascension Island is the product of a flow of hot material that originates from an off-axis plume that is moving toward the spreading axis and ridge crest of the AFZ (Brozena, 1986). In this model, the older, thicker lithosphere acts as a barrier, diverting the flow and forming two seamounts. This means that no plate movement over a fixed hotspot occurred.

Evidence for a plume relation was suggested to explain the presence of magma underneath Ascension Island, due to the surface rocks exhibiting mildly alkaline affinities with typical ocean island basalt trace element systematics (e.g., Harris et al., 1983; Weaver et al., 1996; Kar et al., 1998), however there is no hotspot track and the alignment of Ascension Island to two sea mounts in the vicinity is inconsistent with plate motions (Paulick et al., 2010). Also, the crustal structure is inconsistent with a hotspot origin (Klingelhöfer et al., 2001; Paulick et al., 2010). The crustal thickness is 12 – 13 km and includes an overthickened layer at 7 km thick, which suggests that Ascension Island may have begun forming on-axis (Klingelhöfer et al., 2001; Evangelidis et al., 2004; Paulick et al., 2010). Therefore, Paulick et al., (2010) suggest that Ascension Island formed on or near the MAR ~5 – 6 Ma. The westward drift of the lithosphere caused the submarine edifice of Ascension Island to disconnect from its magma supply and cease erupting. The magma generation was restarted when an enriched mantle domain entered the zone of partial melting beneath the MAR and in the off-axis region (Paulick et al., 2010). There is an anomalous high velocity area within the mid-crustal region, which has been inferred to be plutonic regions (Klingelhoefer et al., 2001; Evangeledis et al., 2004; Chamberlain et al., 2019).

Radiometric dates show that Ascension Island has been undergoing growth at a rate of 0.4 km/My since 3.4 Ma (Minshull et al., 2010). Compared to a growth rate of 0.9 km/My from borehole samples from the Hawaii Scientific Drilling Project and 8.6 km/My from Mauna Kea during its shield building phase (Sharp and Renne, 2005), Minshull et al. (2010) suggest that Ascension Island is in a its 'Post Shield Alkalic' phase.

2.8.2 Volcanic History

The island is composed mainly of volcanic deposits and small quantities of beach deposits and guano (Daly, 1925; Harris, 1983; Nielson and Sibbet, 1996; Weaver et al., 1996; Preece et al., 2018; Chamberlain et al., 2019). The first geological observations were made by Charles Darwin 1836, when he arrived on the island via the H.M.S Beagle (Daly, 1925; Wilkinson, 2003). The volcanic deposits are made up of ~57% mafic and felsic lava flows and domes and 43% pyroclastic material (Daly, 1925; Harris, 1983; Weaver et al., 1996). The volcanic rocks exhibit a compositional range of basalt-trachybasalt-trachyandesite-trachyte-rhyolite (Nielson and Sibbett, 1996; Weaver et al., 1996; Kar et al., 1998; Ammon et al., 2009; Jicha et al., 2013; Chamberlain et al., 2016; Chamberlain et al., 2019).

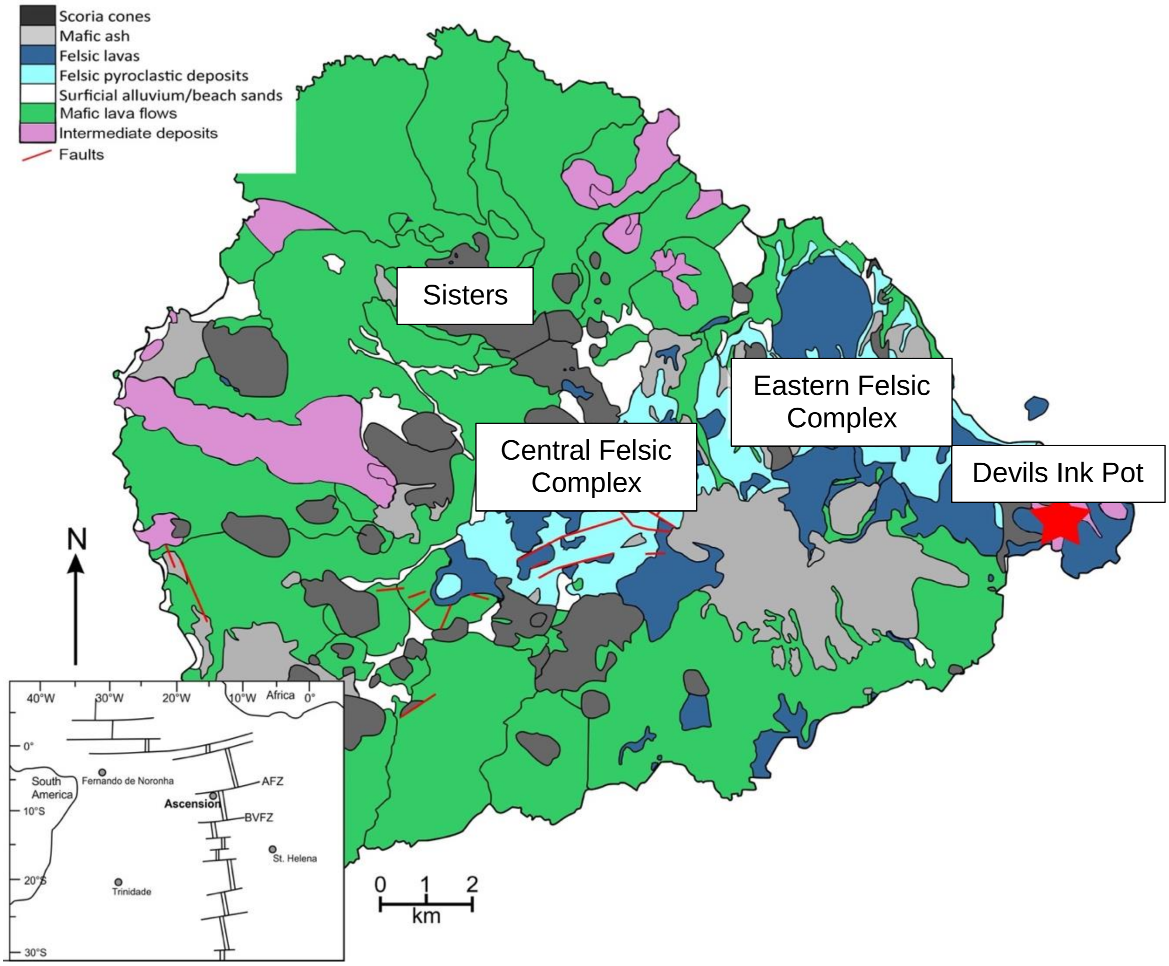

Figure 2.5: *Geological map of Ascension Island. The inset shows the location of Ascension Island relative to the MAR and the AFZ. (Modified from Chamberlain et al, 2016).*

Mafic, Strombolian eruptions were the dominant eruption style and were distributed in the north, northwest and south of the island (Fig. 2.5). Felsic volcanism was localised in two areas, the Central Felsic Complex and the Eastern Felsic Complex (Fig. 2.5) (Nielson and Stiger, 1996; Nielson and Sibbett, 1996; Kar et al., 1998; Preece et al; 2021). There have been more than 80 explosive eruptions during the last 1 Ma, throughout which, phreatomagmatic and sub-Plinian eruptions have been common, forming at least 12 pyroclastic density currents (Preece et al., 2021).

Submarine volcanism on Ascension Island began ~6 – 7 Ma (Harris, 1983; Klingelhöfer et al., 2001; Minshull et al., 2010; Paulick 2010?). Borehole data collected during a geothermal exploration programme activity by Nielson and Stiger (1989, 1996), records most of the island’s volcanic history down to 3126 m below sea level (bsl). The subsurface deposits are composed of basalts, hyloclastites, felsic tuffs interbedded with basalt and a series of felsic tephra overlain by a rhyolite flow and capped by felsic pyroclastic rocks that become more mafic upwards (Fisher and Schmincke, 1984; Nielson and Stiger, 1996). The range in eruptive deposits also show that there was 1.5 – 2 km of subsidence, with the more felsic deposits formed in the subaerial environment (Nielson and Stiger, 1996). In the borehole, the Middleton Ridge Rhyolite was seen between 56 – 75 m deep, with a trachyte flow below it (Nielson and Sibbett, 1996). Most of the felsic rocks sit above the uppermost hyaloclastite, showing that felsic volcanism is relatively recent in the history of the island. The lithological relationships also suggest that the felsic eruptions have become more voluminous with decreasing age. The relationships show that there was an important trachyte and rhyolite volcanic episode that preceded the formation of the Middleton Ridge (Nielson and Stiger, 1996).

Subaerial activity began ~1 Ma (Jicha et al., 2013) with felsic activity focused in the Central Felsic Complex (Middleton Ridge and Green Mountain). The Central Felsic Complex consists of trachyte, rhyolite and trachyandesite lavas and trachyte pyroclastic rocks that range from 1094 – 719 ka (Kar et al., 1998; Jicha et al., 2013; Preece et al., 2022). From 829 – 652 ka, felsic volcanism continued in the northern section of the island (Jicha et al., 2013), and the final stage of the first, ~500 ka silicic volcanism is seen at Ragged Hill and on the southwest slope of Green Mountain (Kar et al., 1998), with the trachytic lavas aged between 637 – 602 ka (Jicha et al., 2013). The eruptions of the first mafic lavas, located west of Devil’s Riding School and east of Cross Hill overlapped with the felsic volcanism from 758 – 705 ka (Jicha et al., 2013).

Mafic lavas in the southern section of the island, including South Gannett Hill and southeast of the Green Mountain Peak, were erupted after the Central Felsic Complex formation and have ages ranging from 589 – 298 ka (Harris, 1983; Jicha et al., 2013).

The Eastern Felsic Complex is the second, younger felsic complex. The trachyte and rhyolite lava and lava domes, and mafic scoria cones and lava deposits range in age between 169 – 52 ka (Nielson and Sibbett, 1996; Kar et al., 1998; Jicha et al., 2013).

Mafic deposits, aged between 38 – 0.51 ka prevail in the north-west of the island (Nielson and Sibbett, 1996; Jicha et al., 2013; Preece et al., 2018). The deposits include lavas with variable volumes and areal extent, up to 4 km long, and scoria cones up to 413 m high (Weaver et al., 1996; Kar et al., 1998; Nielson and Sibbett, 1996). The youngest known eruption on the island is located within the Sisters scoria cone complex and has erupted a series of trachybasalt lavas. The eruption has been dated at 0.51 +/- 0.18 ka (Preece et al., 2018) and thus classes Ascension Island as an active volcano.

2.8.3 Source and genesis of mafic magmas

Isotopic data from Ascension Island suggests that the source for melt genesis is an ancient, subducted slab that contained a large volume of sedimentary rocks (Faneros and Arnold, 2003). However, multiple trace element and isotope studies for on and off axis volcanism within close proximity to Ascension Island (e.g., Paulick et al., 2010; Hoernle et al., 2011) indicate that the mantle domain during submarine volcanism had a raised Hf signature, and therefore was not involved in the genesis of the sub-aerial edifice and magmas (Jicha et al., 2013). Instead, there is a single zone of melt extraction, derived by varying degrees of partially melting, which is the source for all Ascension Island volcanism. However, this melt is geochemically different from the mantle melt that is believed to be responsible for the larger volume submarine volcanism (Chamberlain et al., 2019).

The mafic magmas are be categorised into three groups based on their Zr/Nb ratios (Weaver et al., 1996; Kar et al., 1997). The low Zr/Nb lavas (ratio 4.1) are grouped in the southwest of the island and contain intermediate-aged trachybasalt lavas. The high Zr/Nb lavas (ratio 6.0) are located in the southeast of the island. The intermediate lavas (ratio 5.0) cover the rest of the island. This group contains some of the youngest mafic deposits on the island (Weaver et al., 1996; Kar et al., 1997).

These variations in Zr/Nb could be due to multiple factors: (1) crystal fractionation involving clinopyroxene and Fe-Ti oxide fractionation; (2) low degrees of partial melting of the mantle source of mafic magmas; (3) magma tapped from mantle sources that have different Zr/Nb ratios and undergoes source mixing; (4) a combination of all processes described above (Kar et al., 1998). However, Weaver et al. (1996) suggests that the low and high Zr/Nb magmas were not produced by different degrees of melting of a similar source because there is a contrast in isotopic compositions. The intermediate Zr/Nb lavas have been suggested to be a product of mixing of the high and low Zr/Nb magmas or their sources (Weaver et al., 1996; Jicha et al., 2013). The intermediate Zr/Nb lava flows were originally interpreted to be recent eruptions and the youngest type of mafic magmas, and therefore were highly unlike to represent early felsic volcanism (Weaver et al., 1996; Kar et al., 1998). However, further dating found that the eruptive history of these intermediate Zr/Nb lava flows date back to 705 ka, thus classing it as the second oldest erupted mafic magma type (Jicha et al., 2013).

2.8.4 Evolution of magmas

The changing compositions seen on Ascension Island have been inferred to be dominated fractional crystallisation (Harris et al., 1983; Kar et al., 1998; Jicha et al., 2013; Chamberlain et al., 2016; Chamberlain et al., 2019). Previous studies (e.g., Jicha et al., 2013; Chamberlain et al., 2019) show that trachyandesite results from crystal fractionation of the intermediate Zr/Nb magmas along a simple liquid line of descent at depths greater than 7 km, whilst the trachyte and rhyolites result from crystal fractionation of the high Zr/Nb magmas (Harris, 1983). This is evidenced by age data showing that the high Zr/Nb lavas preceded the felsic eruptions (Kar et al., 1998; Jicha et al., 2013). However, more recent dating of the intermediate Zr/Nb lavas show that they coexistent with the early periods of felsic volcanism (Jicha et al., 2013), and thus could be a suitable parent melt to the felsic deposits. The major and trace element trends within the rocks and plutonic xenoliths, exhibit continuous trends that show that the basaltic magmas evolved to intermediate and silicic compositions by low pressure fractional crystallisation of the intermediate Zr/Nb basalts in a closed system (Nielson and Sibbett, 1996; Weaver et al., 1996; Webster and Rebbert, 2001; Jicha et al., 2013; Chamberlain et al., 2016; Chamberlain et al., 2019).

Other trachyandesite flows on the island include flows from Broken Tooth, Hollow Tooth, the northwest flank of Bears Back and southwest of Lady Hill (Weaver et al., 1996; Nielson and Sibbet, 1996). These flows are smaller in volume than other flows on the island (Nielson and Sibbett, 1996). The flows are mainly restricted to the west and north of the island, with the exception of Letterbox in the east (Weaver et al., 1996).

A model for the magmatic plumbing system was suggested by Chamberlain et al., (2019) (Fig. 2.6). Within the central region of the island, it has been inferred that there are discrete plutonic bodies with differing compositions (discuss plutonic block evidence from past papers here). These bodies stall the rising magma, causing it to fractionate until the buoyancy has increased enough for them to continue to ascend. This means that felsic magma evolution can only occur in the lower crust and at pressures greater than 170 MPa. However, there is evidence for magmatic stalling of the melts at pressures less than this (Chamberlain et al., 2019). The magmas are all erupted as discrete batches (Chamberlain et al., 2019). To date, there is no evidence for any long-lived storage or recycling of crystals between eruptions in either a mushy or melt-dominant storage region, thus magma mixing cannot be suggested as an eruptive trigger (Chamberlain et al., 2019). The magmas that feed explosive or effusive felsic eruptions display differences in the presence or absence of low-pressure phases (Chamberlain et al., 2019). This proposes variations in the storage region locations and the ascent rates but, fractional crystallisation is still suggested as the main evolutionary trend (Chamberlain et al., 2019).

2.8.5 Devils Ink Pot and Letterbox region

The Devils Ink Pot fissure is located in the southeast of the island, in the area otherwise known as Letterbox. The fissure cuts through a series of trachyte and rhyolite domes and a rhyolite flow. The open fissure erupted lava flows and pyroclastic rocks of trachyandesite composition (Daly, 1925; Nielson and Sibbett, 1996; Paulick et al., 2010; Chamberlain et al., 2019). The Devils Ink Pot lavas contain feldspar phenocryst and rare clinopyroxene phenocrysts and are inferred to represent the more evolved end of the range of mineral composition within all the mafic lavas (Nielson and Sibbett, 1996; Chamberlain et al., 2019).

The first dome in the Letterbox region is White Horse, a trachyte dome that had an individual eruptive centre and exhibits multiple outflows up to 200 m thick (Daly, 1925). The second dome is the Little White Hill dome that reaches 168 m asl (Daly, 1925). It was first a rhyolite dome, with the most evolved rhyolite composition (Weaver et al., 1996), and produced flows to the south and west before a trachyte dome formed on top (Nielson and Sibbett, 1996). To the west, north and northeast of the dome is a curved ridge, inferred to be a basaltic crater through which the dome arose (Daly, 1925).

The third dome is Wig Hill dome another trachyte dome that reaches 145 m asl. The dome is inferred to be a remnant of a different, steep-sided dome that rose up in the southern section of the same wide crater as Little White Hill dome (Daly, 1925). The remnant dome is coated by basaltic scoria and driblet flows of vesicular, basaltic lava (Daly, 1925).

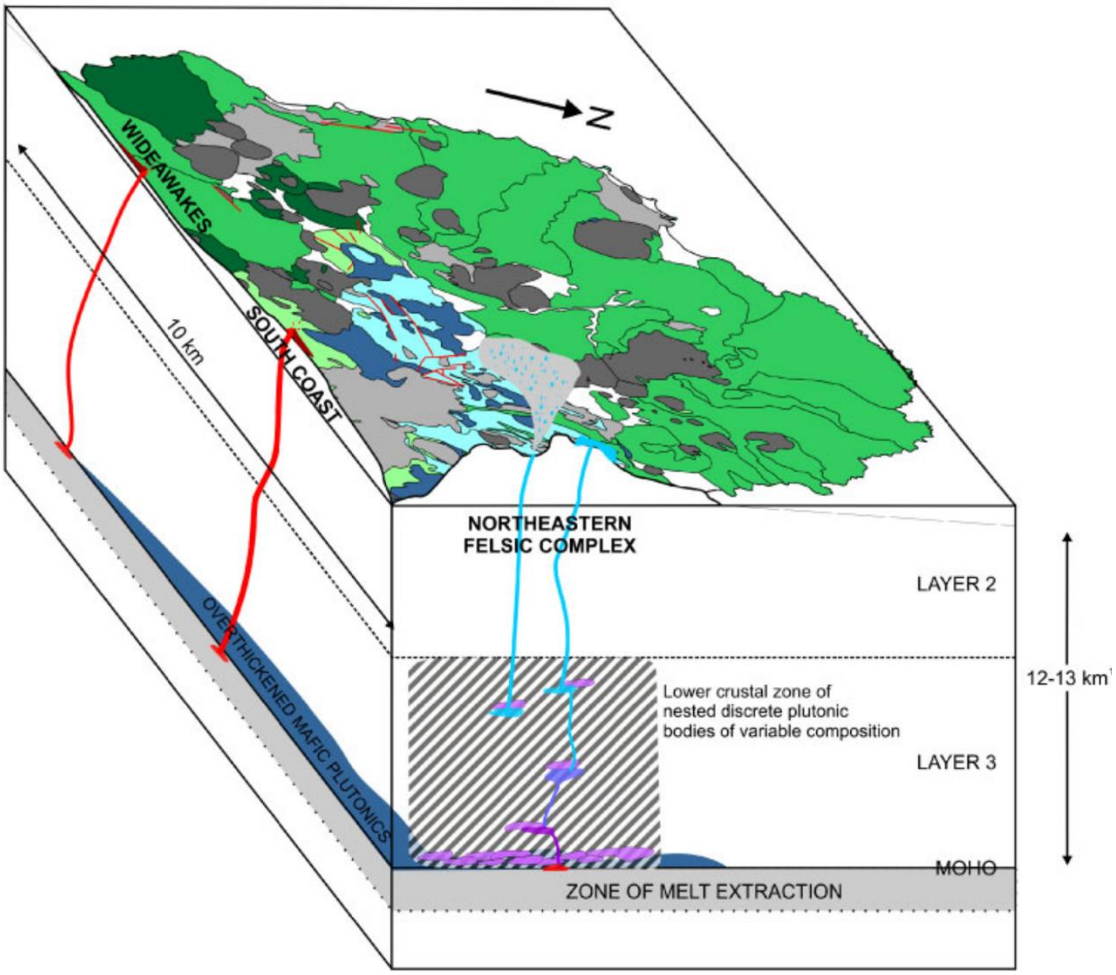

Figure 2.6: *The model for the magmatic plumbing system proposed by Chamberlain et al., (2019) and showing the geographical variation in plutonic body distribution within the crust and the magma ascent pathways. Mafic plutonic bodies are blue and mafic ascent pathways are red. Felsic plutonic bodies are purple or diagonal shading and felsic ascent pathways are purple and blue.*

It is assumed that the Wig Hill scoria cone represents basaltic activity through a series of cones that penetrated the dome (Daly, 1925).

The final dome in the area is South East Head dome which forms the Letterbox peninsula and hosts 6 of the DIP cones, running E-W through the summit of the dome (Daly, 1925). It has a flat top due to multiple overflows and is inferred to be unrelated to the other domes in the area (Daly, 1925).

Chapter 3: Contrasting eruption styles from the intermediate composition, Devil's Ink Pot fissure eruption.

3.1 Introduction

Volcanic activity can result in eruptions that have both effusive or more vigorous explosions, sometimes transitioning between the two end members within a single eruption, resulting in variable eruption styles and deposits (e.g., Pioli et al., 2009; Cassidy et al., 2018; Bonadonna et al., 2022). The style of an eruption controls the types of hazards produced by the volcano (Castro and Gardner, 2008; Cassidy et al., 2018). Eruptions can transition between eruption styles over time and so hazards can vary throughout the eruption. Therefore, reconstructing past eruptions in detail is important as classifying eruptions based on one predominant style can deter the ability to identify potential eruption scenarios and determine the likely future hazards from a similar eruption (Houghton et al., 2016).

Ocean island volcanoes are predominantly fed by basaltic magmas that erupt through fissures characterised by Hawaiian lava fountaining and Strombolian explosions (Head and Wilson, 1989; Parfitt and Wilson, 1995; Parfitt, 2004; Houghton et al., 2016). Such eruptions produce scoria cones, spatter ramparts, lava flows and weak plumes that disperse tephra short distances (Wood, 1980; Riedel et al., 2003; Valentine and Gregg, 2008; Taddeucci et al., 2015). Some ocean island volcanoes also erupt felsic magmas, which produce pumice fall deposits, ignimbrites, lava flows and lava domes (Shea and Owen, 2016; Jeffery and Gertisser, 2018; Pimentel et al., 2021; Preece et al., 2021). Intermediate composition magmas are less common on ocean islands (e.g., Beier et al., 2006; Déruelle et al., 2007; Thordarson and Larsen, 2007; Jeffery and Gertisser, 2018) and very few intermediate composition fissure eruptions have been described in the literature (e.g., Sumner et al., 1998; Belousov et al., 2015; Gansecki et al., 2019). Eruptions of intermediate composition at island arc settings are commonly described as having Vulcanian eruption styles (Mercalli and Silvestri, 1891; Burgisser et al., 2010; Morrissey and Mastin, 2000; Stix et al., 1997; Gaunt et al., 2020) and produce lava domes and/or tephra deposits (Sparks, 1997; Calder et al., 2015; Isgett et al., 2017; Nakada et al., 2019).

Ascension Island is a small, 98 km^2, island in the South Atlantic Ocean. The last eruption on Ascension Island was in the north of the island and produced basaltic lava flows dated at 0.51 ± 0.18 ka (Preece et al., 2018), The volcanic deposits on the island exhibit a compositional range from basalt to rhyolite. The basaltic activity on Ascension Island produces, scoria cones and lava flows (Daly, 1925; Harris, 1983; Weaver et al., 1996; Jicha et al., 2013; Chamberlain et al., 2016; Chamberlain et al., 2019), whilst the silicic eruptions have resulted in pumice fall deposits, rare pyroclastic flow deposits and lava domes preserved on the island (Nielson and Stiger, 1996; Nielson and Sibbett, 1996; Karr et al., 1998; Jicha et al., 2013; Chamberlain et al., 2019; Preece et al., 2021). Deposits of intermediate composition are randomly distributed around the island, covering ~ 6% of the island's surface (Fig 3.1), and consist of scoria cones, scoria falls and lava flows (Weaver et al., 1996; Nielson and Sibbett, 1996; Jicha et al., 2013). However, no intermediate composition deposits have been described in detail, and little is known about the character of the eruptions that produced these deposits.

Here we present the first detailed study to reconstruct the evolution of the Devil's Ink Pot (DIP) trachyandesite eruption. Detailed fieldwork highlights two contrasting eruption deposit that provide evidence for multiple eruption styles and resulting hazards along the eruptive fissure. These findings contribute an understanding of the intensity, style and duration of the DIP eruption and the diversity and complexity of the resulting volcanic hazards. The results provide insights to future eruption scenarios on Ascension Island which may be useful evidence for planning and preparedness activities on the island.

3.2 Geological Setting

Ascension Island sits on ~ 5 – 6 Ma old oceanic crust (Klingelhöfer et al, 2001; Paulick et al., 2010; Preece et al., 2021). The magmatic source for Ascension Island has been the subject of debate, with some studies linking Ascension Island to a mantle plume (Schilling et al, 1985; Brozena, 1986), while more recent geophysical research indicates that the crustal structure is inconsistent with a hotspot origin (Klingelhöfer et al, 2001; Paulick et al, 2010) and is instead consistent with an on-axis origin (Klingelhöfer et al, 2001; Evangelidis et al., 2004; Paulick et al, 2010). The 1 Mya sub-aerial section of the island was produced by off-axis volcanism, fed by partial melting of an enriched mantle source (Paulick et al., 2010; Preece et al., 2021) and evolved through fractional crystallisation (Weaver et al., 1996; Karr et al., 1998; Chamberlain et al., 2016; Chamberlain et al., 2019).

Volcanism on Ascension Island span the compositional range from basalt – hawaiite – Mugearite – benmoreite – trachyte – rhyolite, with ~ 75 vol.% mafic deposits, ~ 6 vol.% intermediate deposits and ~ 19 vol.% felsic deposits (Daly, 1925; Harris, 1983; Weaver et al, 1996; Nielson and Sibbett, 1996; Karr et al, 1998; Ammon et al, 2009, Chamberlain et al, 2016) (figure 3.1). Eruption styles have varied between effusive and explosive, with >75 explosive eruptions occurring within the last ~1 Myr (Preece et al, 2016, 2022). The mafic volcanic products include scoria cones, lava flows, and scoria fall deposits, occur all over Ascension Island and can be split into three categories based on their Zr/Nb ratios (Weaver et al, 1996; Kar, 1997; Chamberlain et al, 2016). The felsic volcanic products include pumice fall deposits, pyroclastic flow deposits, lava flows and lava domes and outcrop in two main areas of the island: the older, Central Felsic Complex (figure 3.1) and the younger Eastern Felsic Complex (figure 3.1) (Nielson and Sibbett, 1996; Weaver et al., 1996; Karr et al., 1998; Jicha et al., 2013).

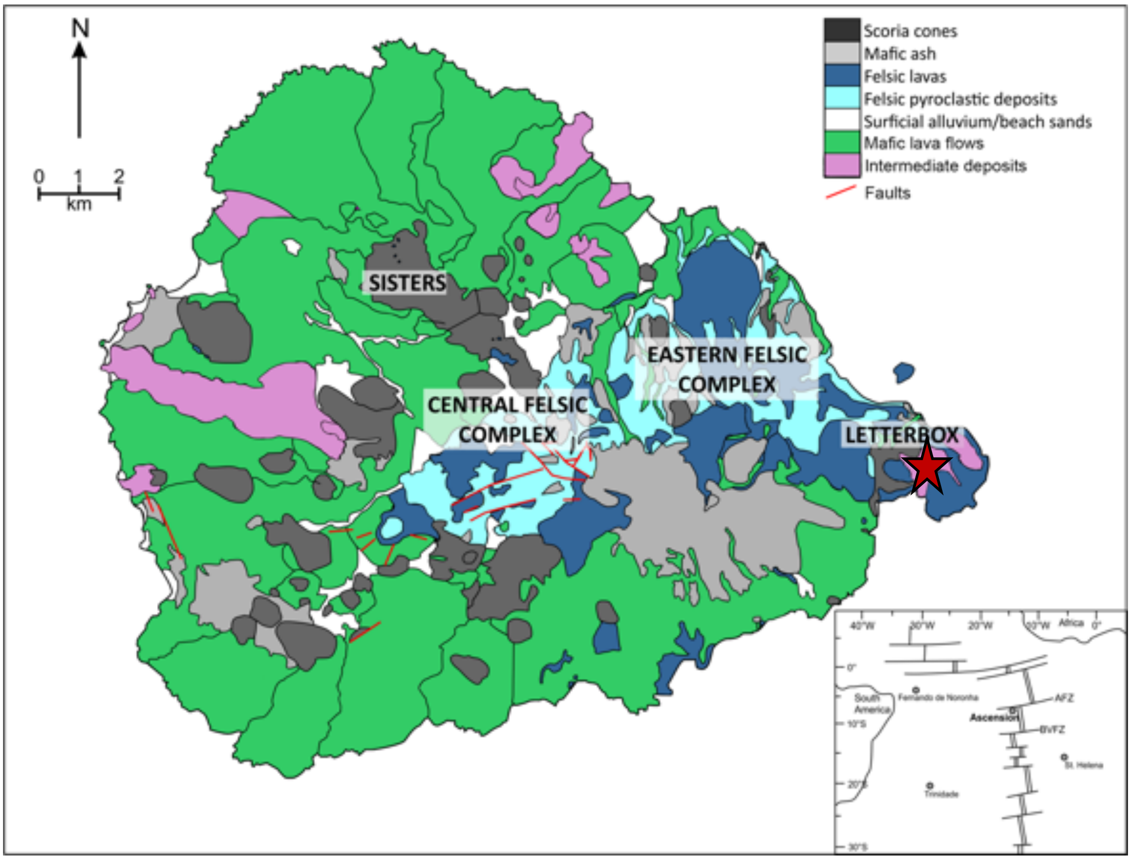

Figure 3.1: *Geological map, modified from Chamberlain et al (2016) to include the intermediate deposits shown in pink. The star represents the DIP fissure, located in the Letterbox region on the island.*

3.3 Devil's Ink Pot Fissure (DIP)

The 28 ka DIP fissure (Preece, pers. comms) represents the best preserved and youngest intermediate composition eruption products on Ascension Island. The 1.3 km long fissure, on the south-eastern corner of the island, is orientated along an average azimuth of 98° with minimal offset. The DIP fissure (Fig. 3.2a) consists of 18 cones, numbered from west to east, sixteen channelised lava flows that form three lava flow fields, pyroclastic fall deposits, and a ballistic bomb field extending up to 1.5 km north/northwest from the fissure.

The fissure is located on the Eastern Felsic Complex (fig. 3.1) and erupted through a series of trachyte lava flows and domes (Fig. 3.2b,c). The western-most cones (1 – 5) make up the first segment of the fissure and erupted through the 70 ± 3 ka (Preece, pers comms), White Horse trachyte dome (Fig. 3.2d), that is overlain by pumice-rich pyroclastic deposits. The middle segment of the fissure (cones 6 – 11) has erupted through a 488 ± 5 ka (Preece, pers comms), porphyritic trachyte lava, characterised by crystal-rich mafic inclusions. (Fig. 3.2f). This was probably erupted from the White Horse area. The southwest edge of the fissure, also classed as the middle segment, cut through the Wig Hill scoria cone (Fig. 3.2e). Remnants of an older trachyte dome (undifferentiated) outcrop below the Wig Hill scoria cone deposits on the south coast. The DIP South East Head lava flow field sits on top of this dome.

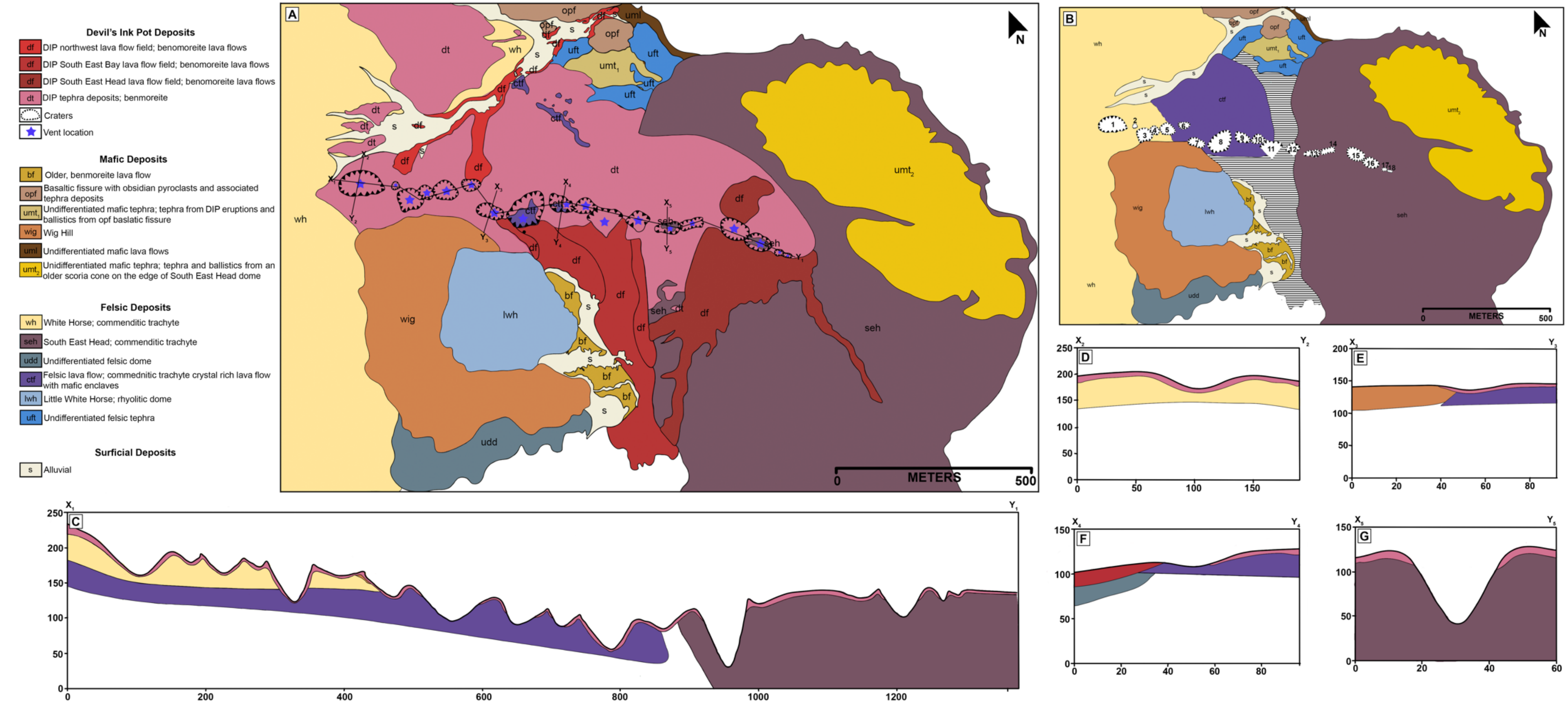

Figure 3.2: ***A)*** *Geological map and key of the Letterbox area. The DIP deposits are in pink/red. Lines show the locations of the cross sections.* ***B)*** *Underlying geological map of the letterbox area.* ***C)*** *Cross section (X$_1$-Y$_1$) through the whole fissure.* ***D)*** *Cross section (X$_2$-Y$_2$) through crater 1.* ***E)*** *Cross section (X$_3$-Y$_3$) through crater 7.* ***F)*** *Cross section (X$_4$-Y$_4$) through crater 9.* ***G)*** *Cross section (X$_5$-Y$_5$) through crater 18. Note that the thicknesses of the units are not true to scale, and the purpose of the cross section is to show how the underlying geology changes along the fissure.*

The third segment is the eastern half of the fissure, cones 13 – 18, and erupted through the South East Head (SEH) trachyte dome (age unknown) (Fig. 3.2g). In the north-eastern corner of the SEH trachyte dome there is a basaltic scoria cone that erupted through the side of the dome. The erupted material consists of red and brown scoria clasts and ropey bombs, easily distinguishable from the fresh, black DIP deposits. There are inactive areas between several of the cones **(Fig. 3.2a).** This is mostly observed between each of the segments. It is possible that these gaps represent regions within the crust where the magma could not propagate through.

Some of the deposits from the eruption have been eroded or are poorly exposed due to high erosion rates and on-going volcanic activity at the time of deposition. The proximal and medial deposits are relatively well preserved, but the distal deposits have been lost to sea.

There is very little work on the structure of the island (Ross et al., 1996; Nielson and Sibbett, 1996; Evangelidis et al., 2004**),** however the middle segment of the fissure sits directly above a trachyte lava flow *(ctf;* Fig. 3.2a)*,* both the first and middle segments run parallel to another small basaltic trachyandesite fissure (*opf;* Fig. 3.2a) (Foster, 2020**)** and an older scoria cone sits ~ 400 m from the end of the third segment of the DIP fissure (*umt*$_2$*;* Fig. 3.2a)**.**

3.4 Methods

3.4.1 Fieldwork

A 7-week field season was undertaken from December 2019 to February 2020 and included detailed logging and identification of lithofacies exposed in crater walls, mapping and sampling of erupted products, and analysis and sieving of tephra to identify key features that indicate the type of eruption processes occurring along the fissure. Mapping was only undertaken of the existing DIP deposits, including their structures, but did not consider faults or fractures in the DIP deposits or the underlying country rock.

Bulk samples of the fresh spatter were taken from each cone where access was possible. Bulk lava samples were taken from the tops and ends of the lava flows wherever possible. Where not possible, samples were taken from flow margins or from features along the flow.

To sample each individual layer of fall deposits, small, stepped profiles were made, each layer was scraped onto clean plastic tarp, and then further processed (described in Chapter 3.2.3). The top of each tephra unit is defined by a palaeosol horizon and reworked tephra material.

The eruption deposits were mapped, and geospatial data were recorded using a handheld global positioning system (GPS) with a ± 5 m horizontal accuracy. Where possible, the crater walls were logged. Where access was not possible, logs were created using photographs taken in the field. In cones where detailed examinations were possible, logs were created on a cm scale to identify and describe lithofacies. Lithofacies were determined based on grain size, shape and degree of welding or agglutination. Spatter aspect ratios were calculated by measuring the length and width of 50 spatter clasts at each cone. Lavas were mapped both in the field and remotely using field photographs and Google Earth. Measurements for spatter unit thicknesses and lava flow dimensions given are the best representation but should be seen as a minimum due to loss of deposits, e.g., lavas entering the sea. Viscosity of the lava flows was calculated based on the model of Giordano et al. (2008) and does not consider the effect of crystal populations.

The composition and abundances of lithic clasts were documented at each cone to provide insight into the underlying geology and to attempt to link the tephra fall deposits to individual cones. At each cone, sampling was conducted within two 5x5 m grids located on the ground at the cone rim and 100 clasts were described.

Volcanic bombs were mapped to understand the distribution of bomb types and size of bombs ejected from the cones. North-south transects, at ~100 m spacing were constructed along the fissure. Every 20 m the largest bomb within 5 m either side of the transect was measured, described, photographed, and located with a handheld GPS. Bombs reasonably attributed to neighbouring volcanoes were omitted.

3.4.2 Granulometry

Tephra fall deposits were sieved in the field down to 8 mm. The volume of material sieved was calculated by weighing the largest clast, and assuming this represents 5% of the total weight of tephra needed for analysis (Cas and Wright, 1987). The other 95% of the tephra weight required was collected, weighed, and passed through an 8 mm sieve. Clasts larger than 8 mm were measured on their longest axis and grouped into the 16 mm, 32 mm, and 64 mm size fractions. For these size fractions, lithic clasts were separated out and both the tephra clasts and lithic clasts were weighed. Tephra < 8 mm was weighed, poured into a cone shape, and quartered or halved, depending on the total weight. Where the beds were fine (<20 cm thick) 2 kg of material were bagged.

3.5 Results

3.5.1 Pyroclastic Cones

The DIP fissure consists of 18 well preserved, sub-spherical cones, numbered from west (cone 1) to east (cone 18). The terms used to describe the cones are given in Fig. 3.3. The morphology of the cones gained from field and satellite data reveals a range of sizes from 10 – 132 m in diameter and 5 – 80 m deep (table 3.1). Minimum areas and volumes range from 1.9×10^2 – 2.7×10^4 m^2 and 2.0×10^2 – 1.2×10^5 m^3, respectively. Descriptions are

Cone & type	Dimensions	Cone features	Spatter Lithofacies	Lithic Clasts	Ballistics	Lava flows
C1 *T3*	120 x 81 m diameter; 32 m deep; NC-A – 3 x 6 m; NC-B – 9 x 11 m (basal diameters); 23750 m^2 area; 121000 m^3 volume.	Two vents; 16 x 6.5 m septum creates two nested cones (NC-A, NC-B); Excavated down into White Horse Trachyte (lithic clasts whTr; table 3.1) substrate. **NC-A/septum:** fossil fumaroles reach 5 m in diameter; composed of vesicular scoria, sub-rounded trachyte clasts; anomalous orange, red, yellow discolouration; patches of green lichen.	Unit thickens towards SE; NC-B 4 – 14.2 m thick; NC-A 0 – 2 m thick. **NC-A:** sharp contact pre-eruption substrate; transitions laterally from unconsolidated, scoriaceous bomb-rich fall deposit (lithofacies LpB; table 3.2) to moderately agglutinated spatter, moderately welded spatter and densely welded spatter (lithofacies magSp, mwSp, dwSp). **NC-B:** base not seen; weakly stratified; alternating layers of oxidised red, moderately agglutinated spatter, moderately welded spatter, dark grey, densely welded spatter (lithofacies magSp, mwSp, dwSp); rare, black, vitreous glassy clasts, up to 4.5 cm in diameter, mixed in moderately agglutinated spatter (~10 m high).	NC-A: whTr lithic rich talus slope deposits on SE and E cone walls.	Tortoise shell bombs (bomb type tsB; table 3.5); up to 4 m in diameter; emplaced on top of spatter unit.	-
C2 *T1*	10 x 8 m diameter; 6 x 3 m basal diameter; 7.5 m deep; 220 m^2 area; 196 m^3 volume.	Single vent; Partially destroyed by construction of dirt road;	Densely welded spatter (lithofacies dwSp; table 3.2); lenses of moderately agglutinated spatter and weakly agglutinated lapilli and bombs (lithofacies magSp, wagLpB).	-	-	FF1; F1; ‘A’ā lava flow extends out cone towards NE.
C3 *T2*	75 x 72 m diameter; 20 m deep; 9425 m^2 area; 29452 m^3 volume.	Single vent; E cone wall borders C4.	**N cone wall:** layer of weakly agglutinated lapilli and bombs (lithofacies wagLpB; table 3.2); rare, <2 cm diameter whTr; moderately vesicular bombs; rare highly vesicular bombs. Ballistics and spatter occur in upper 11.5 m of cone walls. **NE cone wall:** 35 cm thick; densely welded spatter coated in moderately agglutinated spatter (lithofacies dwSp, magSp); black, glassy clasts (as in C1) occur in dwSp layer.	whTr, gTr lithic rich talus slope on S cone wall; rare juvenile clasts.	Composite bombs, vesicular bombs (bomb type cB, vB; table 3.5) and undifferentiated bombs sit on cone walls and rim.	-
C4 *T2*	37 x 47 m diameter; 8 m deep; 3568 m^2	Single vent; E and W walls border C5 and C3; 5 x 5.5 m nested cone; surrounded	**N cone wall:** upper 1.5 m; layer of weakly agglutinated lapilli and bombs (lithofacies wagLpB; table 3.2); up to 20 cm diameter whTr lithic clasts; up to 30 cm diameter	whTr lithic clasts; surround nested cone; within lithofacies.	On cone rim; upper 4 m S cone wall; tortoise shell	-

	area; 4627 m^3 volume.	by lithic and juvenile clasts (10 and 15 cm diameter).	bombs; moderately vesicular bombs; densely welded bombs (lithofacies dwSp); **S cone wall:** no spatter deposits.		bombs (bomb type tsB; table 3.5); clustered in W end of N cone wall; dwSp bombs; >1 m long.	
C5 *T3*	67 x 66 m diameter; variable depth; 53 m SW cone wall; 10 m W cone wall; 7205 m^2 area; 11752 m^3 volume.	Single vent; Fossil fumaroles on ridge separating C5 and C6; excavated down into edge of Wig Hill scoria cone (lithic clasts ardC).	**S/SW cone wall:** partially exposed, 3.7 m thick lapilli and bomb layer; not accessible but inferred to be weakly agglutinated lapilli and bombs (lithofacies wagLpB; table 3.2) based on other carter deposits, structure and strong alignment of larger bombs; bombs heavily cracked; infer some bombs fragmented on impact; grades into 2 m scree; densely welded spatter (lithofacies dwSp) with lenses of weakly agglutinated lapilli and bombs and minimal moderately welded spatter (lithofacies wagLpB, mwSp); 4.8 m thick on S/SW cone wall; occurs around whole cone, varies in thickness ~0.5 – 7 m.	S/SW cone wall: ardC rich talus slope.	S end of ridge has cluster of bombs up to 5 m diameter.	**NE cone wall:** fractured lava tongue; 17 x 14 m flowed into cone base; blocky ‘a’ā toe 1.5 m thick; ropey texture transitions into glassy, tortoise shell skin with aligned striations and scratch marks.
C6 *T1*	38 x 45 m diameter; ~ 6m deep; 3236 m^2 area; 3181 m^3 volume.	Single vent	**N, NW, SE cone wall:** no spatter deposits; loose, dense blocks of lava and scree; **SW cone wall:** minimal moderately welded spatter and moderately agglutinated spatter (lithofacies mwSp, magSp); horizontally graded; sharp contacts; magSp contains <1% whTr clasts (<2 cm diameter).	Scree <10% lithic clasts.	-	FF1; F2; ‘A’ā lava flow extends out cone towards NE; fractured lava tongue; 5 x

						3.5 m flowed back into cone; glassy tortoise shell skin; dense coherent core.
C7 *T3*	72 x 45 m diameter; variable depth; 15 m W cone wall; 2 m E cone wall; 8149 m^2 area; 2714 m^3 volume.	Single vent; Excavated down into edge of Wig Hill scoria cone.	Deposits vary 4 – 8 m thick; weakly agglutinated lapilli and bombs (lithofacies wagLpB); interbedded layers moderately welded spatter and densely welded spatter (lithofacies mwSp, dwSp); sharp contacts (mwSp – dwSp); gradational contacts (wagLpB – mwSp, dwSp).	NE cone wall: ardC rich talus slope; angular pmTr bomb; 2 m diameter.	-	FF3; F5; ‘A’ā lava flow extends out cone towards S.
C8 *T3*	132 x 75 m diameter; variable depth; 30 m N cone wall; 6 m S cone wall; 27426 m^2 area; 27370 m^3 volume.	Two vents; Excavated down ~ 30 m into porphyritic commendite lava flow (lithic clasts pmTr); thin covering of loose juvenile lapilli and block scree; nested cone; 50 cm high ridge with fossil fumaroles.	**S cone wall:** 1 m thick layer moderately agglutinated spatter (lithofacies magSp); lower 20 cm include 15% altered whTr; upper 80 cm include 10 – 15% gTr and pmTr.	Nested cone surrounded by whTr lithic clasts;	Sub-rounded, vesicular bombs (bomb type vB) clustered on SW cone wall	FF3; F6; Spiny ‘a’ā lava flow inferred to originate from cone; flows S.
C9 *T3*	66 x 41 m diameter; 9 – 23 m deep; 6967 m^2 area; 10264 m^3 volume.	Single vent; E cone wall borders C10; excavated down into pmTr lava flow; only exposed on half of S and N cone walls.	Deposits vary 2 – 3 m thick; sharp contact with pre-eruption substrate; thicken to E; rare layers weakly agglutinated lapilli and bombs; interbedded moderately agglutinated spatter, moderately welded spatter and rare densely welded spatter (lithofacies wagLpB, magSp, mwSp, dwSp); dwSp varying degrees if vesiculation.	-	Very rare bombs on top of spatter unit.	-
C10 *T1*	62 x 44 m diameter; 17 m deep; 6462 m^2	Two vents; E and W cone walls border C11 and C9; E cone wall has fossil fumaroles; yellow coating	Deposits vary 2 – 9 m thick; alternating layers altered red moderately agglutinated spatter and moderately welded spatter (up to 40 cm thick) and dark grey densely welded	-	-	-

	area; 17108 m^3 volume.	on surrounding spatter; nested cone surrounded by red spatter blocks.	spatter (up to 30 cm thick) (lithofacies magSp, mwSp, dwSp).			
C11 *T1*	N cone wall: 40 m deep, 90 m long.	Single vent; S cone wall lost during and/or after eruption; only N cone wall and small portion of E/W cone walls remain.	Deposit 18 m thick; lower spatter unit 5 m thick; undifferentiated spatter as degree of welding/agglutination not identified; upper spatter unit 13 m thick; interbedded layers rare moderately agglutinated spatter, moderately welded spatter, and densely welded spatter (lithofacies magSp, mwSp, dwSp); abundant small dwSp bombs; dense spatter crust covers sections of cone wall; sits on top of spatter unit.	-	-	FF3; F7; 'A'ā lava flow extends south.
C12 *T1*	50 x 56 m diameter; 5 m deep; 4965 m^2 area; 4105 m^3 volume.	Single vent; Large outcrop in centre of cone – central spatter mound (CSM); two, parallel, semi-circular spatter deposits – inner spatter walls (ISW) and outer spatter walls (OSW).	Deposits vary 1.5 – 3 m thick; outcrop in multiple places around cone. **CSM:** altered red moderately vesicular densely welded spatter, moderately welded spatter, and moderately agglutinated spatter (lithofacies dwSp, mwSp, magSp); magSp contains ~ 2% sehTr lithic clasts. **ISW/OSW:** as CSM but no sehTr lithic clasts; become less welded and agglutinated upwards; grades up from dwSp, to dwSp bombs and mwSp, to bomb rich wagLpB.	-	-	-
C13 *T3*	66 x 39 m diameter; 80 m deep; 12393 m^2 area; 91232 m^3 volume.	Single vent; First on Southeast Head dome; excavated down ~ 74 m into the trachyte dome (lithic clasts sehTr); has three cone walls; E cone wall borders C14.	Deposit 6 m thick; sharp contact with the pre-eruption substrate; interbedded moderately welded spatter, densely welded spatter, and rare moderately agglutinated spatter (lithofacies mwSp, dwSp, magSp); single, 1.4 m thick layer of dwSp at base of unit; spatter contours steeply dipping edge of trachyte dome.	-	-	FF2; 'A'ā lava flow field formed as lava flows flowed S.
C14 *T1*	56 x 20 m diameter; elongate cone; 2 – 10 m deep; 189 m^2 area; 1642 m^3 volume.	3 vents; 3 nested cones (NC A-C); **NC-A:** borders C13; 8.5 x 3 m diameter. **NC-B:** middle cone; 7 x 3 m diameter; **NC-C:** 5 x 3 m diameter. Fossil fumaroles between NC-B and NC-C.	Massive cone wall deposits at all NC's; loose lapilli and bombs (lithofacies LpB); densely welded spatter blocks (lithofacies dwSp) between NC-B and NC-C.	sehTr identified around all NC; most abundant around NC-C; up to 30 cm diameter.	Composite bombs (bomb types cB) seen but rare.	FF2; F4; 'A'ā lava flow field formed as lava flows flowed S.

C15 ***T1***	72 x 61 m diameter; 11 m deep; 8329 m^2 area; 14929 m^3 volume.	Single vent; E cone wall borders C16; 3 m high ridge with fossil fumaroles; excavated down ~ 6 m into trachyte dome (lithic clasts sehTr); spatter builds up ~ 3m above sehTr.	**N cone wall**: 2.5 m thick deposit; weakly stratified; oxidised red, moderately agglutinated spatter and moderately welded spatter (lithofacies magSp, mwSp) layers 22.5 – 37.5 cm thick; densely welded spatter bombs (lithofacies dwSp) layers 38 – 78 cm thick; dwSp bombs abundant in lower part of unit and rare in layers of magSp and mwSp. S cone wall: **62 cm thick densely welded spatter (lithofacies dwSp) deposit;** sharp contact with underlying, weakly stratified spatter unit (as N cone wall); **dwSp unit pinches to east**, 22 cm – 3 m thick; above dwSp unit 93 cm thick, interbedded magSp and mwSp. **E cone wall**: core of a lava flow contours cone topography; sharp contact with pre-eruption substrate (sehTr); gradational contact with N cone wall spatter deposit; patches of pāhoehoe texture.	-	Vesicular bombs (bomb type vB); up to 1.5 m diameter; emplaced on upper 1.7 m of cone wall.	FF2; F4; ‘A’ā lava flow field formed as lava flows flowed S.
C16 *T3*	73 x 40 m diameter; 40 m deep; 10395 m^2 area; 55805 m^3 volume.	Single vent; W cone wall borders C15; excavated down ~ 35 m into trachyte dome (lithic clasts sehTr); spatter builds up above trachyte dome.	Lava flow cores exposed on S, E, W cone walls; 2 m thick; sharp irregular contact with pre-eruption substrate (sehTr); contours cone topography. **S cone wall:** 1 m thick lava flow; dips N; sits above another lava flow core. N cone wall: lava flow core in NW corner; covered by moderately agglutinated spatter (lithofacies magSp); grades into loose lapilli and bombs (lithofacies LpB); bombs highly fragmented; lava flow core unit grades horizontally into 2.8 m thick, weakly stratified spatter deposit; alternating layers of densely welded spatter bombs (11 – 19 cm thick) and moderately agglutinated spatter (13 – 51 cm thick) (lithofacies dwSp, magSp); spatter unit grades horizontally into 2.1 m thick, weakly agglutinated lapilli and bombs (lithofacies wagLpB).	-	Glassy bombs and rubbly tortoise shell bombs (bomb types gB, rtB); emplaced on cone rim; up to 6.5 m diameter.	FF2; ‘A’ā lava flow field formed as lava flows flowed S.
C17 *T1*	29 x 22 m diameter; 15 m deep; 1611 m^2	Single vent; E cone wall borders C18.	**N cone wall:** 50 cm thick dwSp band; dwSp band sharp contact with underlying, blocky juvenile material and overlying scree; below dwSp band alternating dwSp and lava-like	-	Few glassy bombs and rubbly tortoise shell bombs	FF2; ‘A’ā lava flow field formed as

	area; 3303 m^3 volume.		spatter (lithofacies l-lSp); gradational contacts. S cone wall: massive, 11 m thick, densely welded spatter unit (lithofacies dwSp).		(bomb type gB, rtB); up to 90 cm diameter; emplaced on cone rim.	lava flows flowed S.
C18 *T1*	21 x 17 m diameter; 7 m deep; 763 m^2 area; 808 m^3 volume.	Single vent; W cone wall borders C17; excavated down ~ 1.5 m into trachyte dome (lithic clasts sehTr); spatter deposits build up ~ 11 m above trachyte dome.	N cone wall: sharp contact with pre-eruptive substrate (sehTr); 9 m thick, massive, lava-like body (lithofacies l-lSp); sehTr lithic clasts welded surface of lower 1.1 m; sub-spherical bulges within l-lSp; vertical and sub-horizontal cracks cut through bulges and spatter deposit; grades rapidly up to 2 m thick, weakly stratified moderately agglutinated spatter, up to 41 cm thick, and densely welded spatter, up to 68 cm thick, (lithofacies magSp, dwSp). S cone wall: 70 cm thick spatter deposit, lava-like spatter (l-lSp); contours cone topography; lobes partially dribble back into cone; surface of l-lSp is rubbly and blocky (as an ‘A’ā lava flow).	sehTr outcrops at base and middle of S cone wall; highly fractured.	Breadcrust bombs and vesicular bombs (bomb type bcB, vB) emplaced on cone rim.	FF2; ‘A’ā lava flow field formed as lava flows flowed S.

Table 3.1: *Descriptions of the cones, including cone features, spatter lithofacies, lithic clasts, surrounding ballistic bombs (separate to bombs in the lithofacies) and associated lava flows.*

provided below of pyroclastic and lithic components of each of the cones from which the cones have been subdivided into types to evaluate the evolution of the eruption (Fig 3.4a).

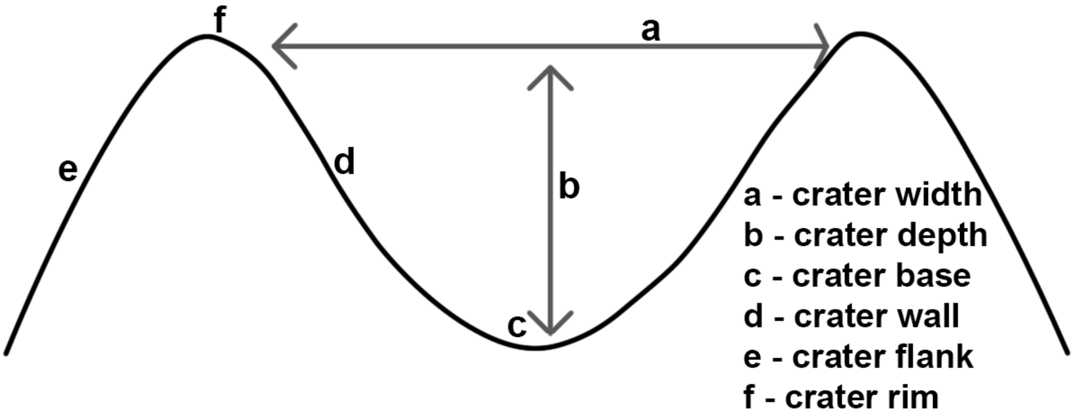

Figure 3.3: *Schematic drawing of a crater, where the terminology used throughout the thesis is labelled.*

3.5.2 Lithic Clasts

The lithic clasts in the pyroclastic deposits exposed in the crater walls of each cone are derived from the underlying geology (Fig. 3.4b) and are described in table 3.2.

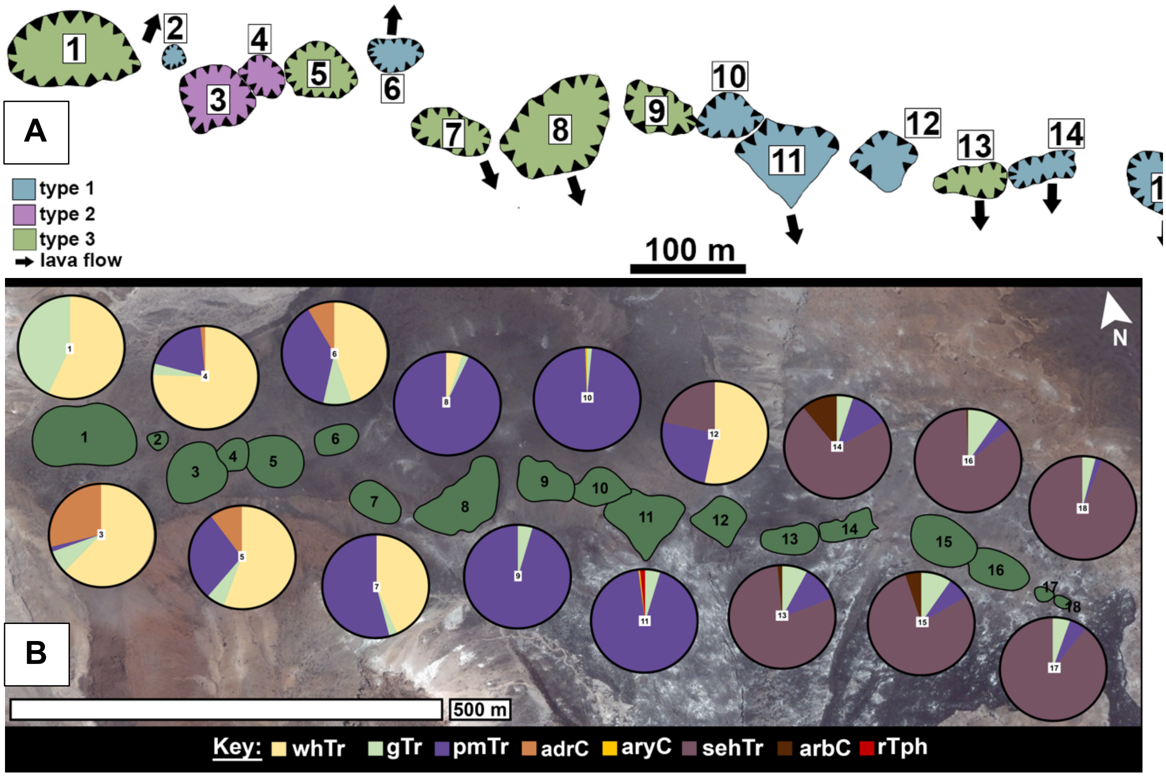

Figure 3.4: A) *Schematic map of the cones showing the distribution of the different cone types along the fissure*. **B)** A *map showing the distribution of vents along the fissure (filled in green). Pie charts show the total % of each type of lithic clast counted around the fissure. whTr – White Horse trachyte, gT – green trachyte, pmTr – trachyte with mafic enclaves, ardC – altered red dense clasts, aryC – altered red/yellow clasts, sehTr – South East Head trachyte, arbC – altered red/brown clasts, rTph – red tephra clasts. It should be noted that all lithic clast counts were taken north of the craters.*

Name	Abbrv.	Textures	Crystal Phases	Other features
White Horse trachyte	whTr	Light grey/yellow colour; some have grey flow bands; light bands, up to 7 mm thick, fine - medium grained, aphyric; dark bands, up to 1 cm thick, aphanitic and/or glassy; non-banded aphyric, fine grained and/or glassy; non-vesicular.	Essential: feld, cpx. Accessory: Fe-Ti ox Groundmass: feld, ox	Rare, dark purple, aphanitic inclusions; some have ~ 3 vol.% feldspar phenocrysts.
Green trachyte	gTr	Grey/green colour; weak bands of darker crystals; crystalline, fine grained phaneritic; non-vesicular.	Essential: feld Accessory: Fe-Ti ox Groundmass: feld, ox	Patches of red/orange alteration; single dark, porphyritic inclusion with black, 1.4 cm thick rims.
Trachyte with mafic enclaves	pmTr	Light grey colour; dark grey patches with weakly aligned crystals; crystalline, fine – medium grained phaneritic, weakly porphyritic; non-vesicular.	Essential: feld, cpx Accessory: Fe-Ti ox Groundmass: feld, ox	Rich in dark, porphyritic inclusions.
Altered dense clasts	ardC	Brown/red colour; microcrystalline, fine grained, aphanitic; incipiently/moderately vesicular.	Essential: feld, cpx. Accessory: n/a Groundmass: n/a	Heavily altered clasts.
Altered red/yellow clasts	aryC	Red/yellow surface; interior dark grey/black; microcrystalline, aphanitic; non-vesicular.	Essential: feld Accessory: n/a Groundmass: n/a	Surface is heavily altered.
SHE trachyte	sehTr	Pale grey/brown; fine grained, crystalline, aphanitic; non-vesicular.	Essential: feld, cpx, *hbl* Accessory: Fe-Ti oxides Groundmass: feld, ox,	Dark grey/brown inclusions. White alteration patches on the surface of some of the clasts.
Altered red/brown clasts	arbC	Red/brown; microcrystalline, fine grained, aphanitic; non-vesicular	Essential: feld Accessory: n/a Groundmass: n/a	Crumbly and can be platy.
Pumice	Pu	Pale grey; aphyric; microvesiuclar	Essential: feld, Accessory: n/a Groundmass: n/a	Contains altered orange specks.
Rounded dense clasts	rdC	Black/ dark grey; microcrystalline, fine grained, aphanitic; non-vesicular	Essential: feld Accessory: n/a Groundmass: n/a	Some clasts have weak platy surface.
Jagged dense clasts	jdC	As rdC	Essential: feld Accessory: n/a Groundmass: n/a	As rdC
Red tephra	rTph	Red; aphyric; moderately vesicular	Essential: n/a Accessory: n/a Groundmass: n/a	
Unidentified clasts	Unid'd	Clasts are either too small or are too weathered/altered to clearly identify a specific type.		

Table 3.2: *The different lithic clasts found in the field. Where possible, the crystal phases from microscopy work have been included. For samples where this was not possible, descriptions are based wholly on hand specimen descriptions and n/a is implied.*

White Horse trachyte lithic clasts (whTr) clasts are either pale yellow-cream or banded and are inferred to originate from a lobe of lava. Green trachyte lithic clasts (gT) do not outcrop on the surface and are inferred to be an older, now sub-surface, trachyte deposit, covered by more recent eruptions. Porphyritic trachyte lithic clasts (pmTr) with mafic inclusions are inferred to be the product of an older trachyte lava lobe that outcrops beneath cones 7 – 12. The altered, dense, red lithic clasts derive from the Wig Hill scoria cone, which cones 5 and 7 partially overlie. The altered red and yellow lithic clasts are inferred to have originated from cone 10 or cone 11. The SEH trachyte is from the underlying South East Head trachyte dome. The altered dark brown lithic clasts are too altered to identify original textures. Red tephra clasts are inferred to be not in situ and have been transported in a plume from a previous eruption.

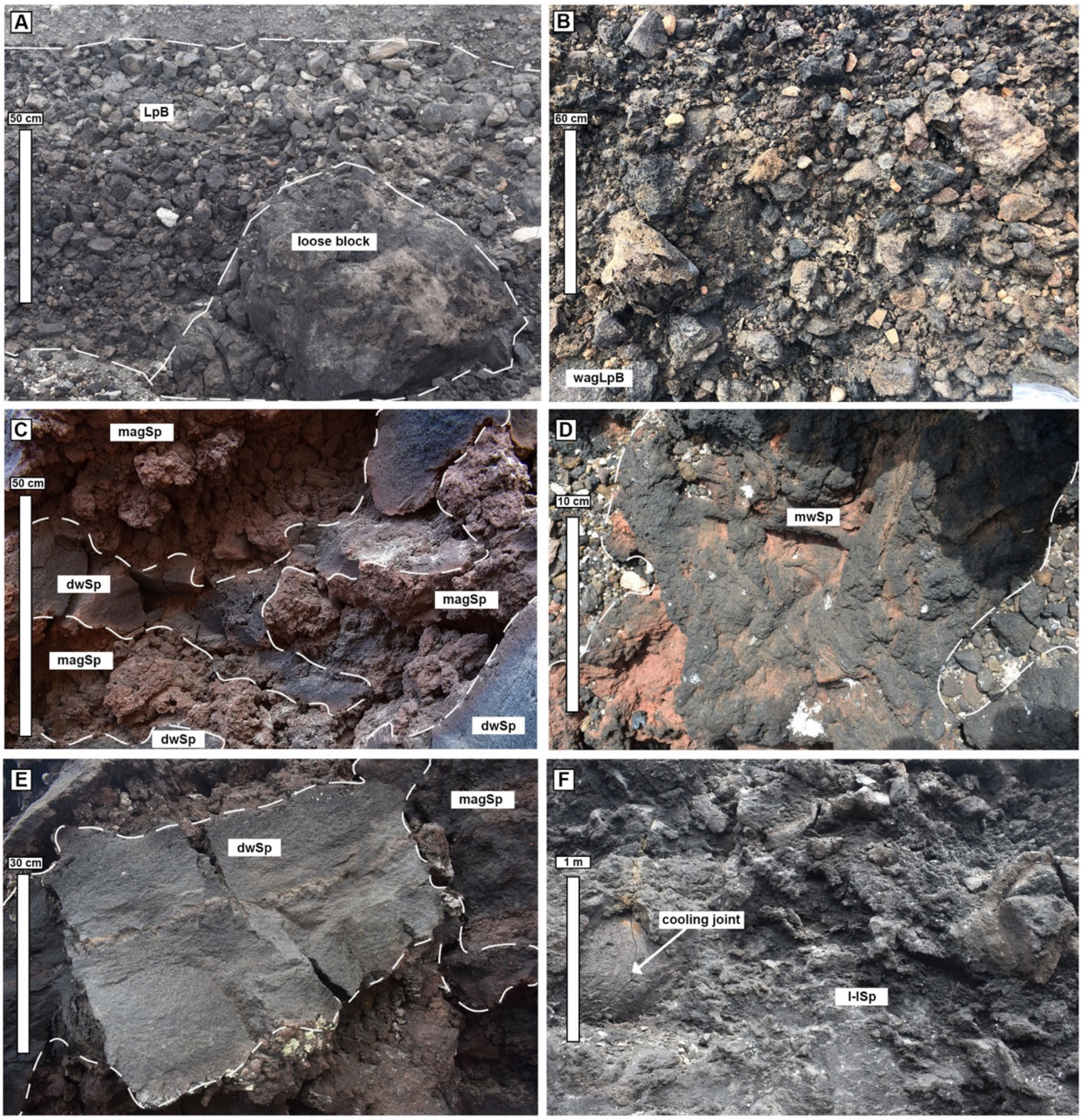

Figure 3.5: *Images of the different spatter lithofacies identified in the field.* ***A:*** *Loose lapilli and bombs (LpB)* ***B:*** *weakly agglutinated lapilli and bombs (wagLpB)* ***C:*** *moderately agglutinated spatter (magSp)* ***D:*** *moderately welded spatter (mwSp)* ***E:*** *densely welded spatter (dwSp)* ***F:*** *lava-like spatter (l-lSp).*

3.5.3 Pyroclastic Cone Lithofacies

Six different lithofacies (Fig. 3.5; table 3.1) were recognised in the cone walls based on degree of coalescence, agglutination and welding, and size of clasts (Cas and Wright, 1987; Henry et al., 1989; Branney and Kokelaar, 1992; Sumner et al., 2005). As the degree of welding and/or coalescence increases, the clasts become more deformed and outlines less visible, void space decreases and contacts between different lithofacies become sharper. Welded and moderately agglutinated lithofacies occur in crater walls, whilst weakly agglutinated and loose lapilli deposits occur in crater walls and up to 400 m from the cones. Clast aspect ratios increase with welding intensity (Fig. 3.6a) and there is a strong positive correlation between clast size and aspect ratio (Fig. 3.6b).

Three types of cones were identified in the field based on the lithofacies exposed in the crater walls. Type 1 (Fig. 3.7) consist of moderately agglutinated, moderately welded, and densely welded spatter deposits and some been the source of lava flows. Type 2 (Fig. 3.8) consist of weakly agglutinated and loose scoria? lapilli and bombs, lithic clast-rich talus slopes and ballistic bombs. Type 3 cones are composed of the spatter lithofacies seen in type 1 and the talus slopes and ballistic bombs seen in type 2. Some of the type 3 cones have evidence of a single eruption vent (Fig. 3.9), whilst others exhibit individual spatter characteristics around nested craters, which is evidence for more than one eruption vent. For example, at cone 1 (Fig. 3.10), a nested crater (NC-A) exhibits lithic clast rich talus slopes and non-welded fall deposits, whilst a second nested crater (NC-B) is surrounded by thick, moderately agglutinated, moderately welded, and densely welded spatter deposits. Of the cones, 10 are type 1, 2 are type 2 and 6 are type 3. No one cone type is larger than the other, however, the type 3 cones are always the deepest (up to 80 m deep).

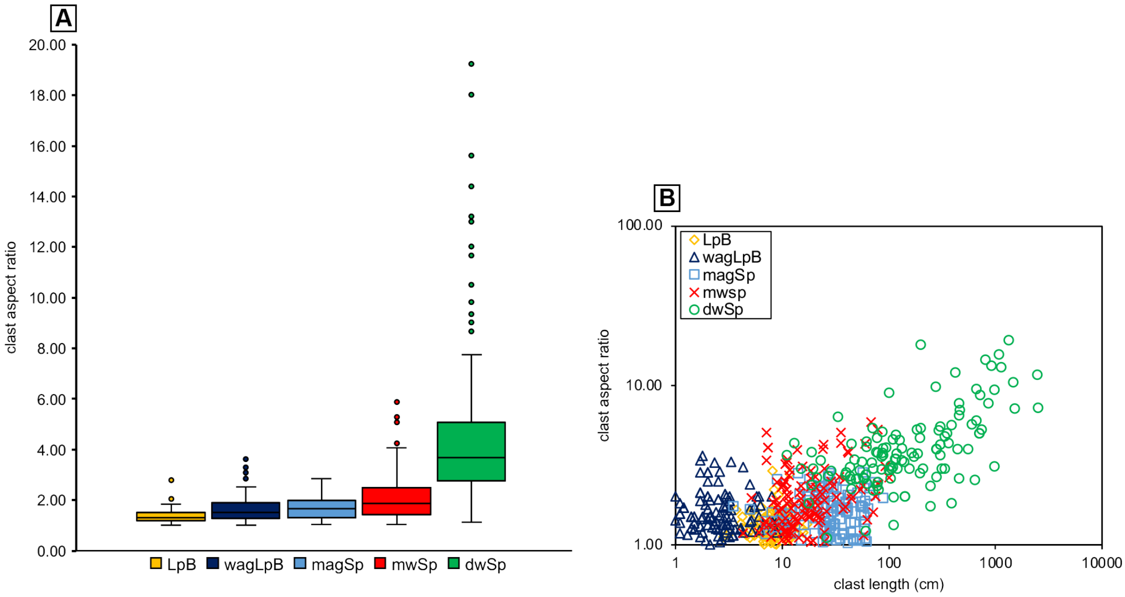

Figure 3.6: ***A)*** *Box and whisker plot showing the distribution of the aspect ratios of the spatter lithofacies. Circles represent outliers.* ***B)*** *Graph showing clast size vs aspect ratio of the different lithofacies. There is a weakly positive correlation between aspect ratio and clast size.*

NAME	ASPECT RATIO	COMPOSITION AND TEXTURE	STRUCTURE	OCCURRENCE	INTERPRETATION
Lapilli & bombs **(**_LpB_)	N/A	Black or golden-brown coarse ash – bombs, <1 - 128 cm; moderately - poorly sorted; clast supported; aphanitic; angular - sub-rounded shapes; moderate - highly vesicular; vesicles sub-rounded - elongate, up to 3 cm; variations in scoriaceous and pumice-like textures; angular lithic clasts, varying compositions.	Massive; unconsolidated; clasts undeformed and randomly orientated; abundant void space.	Up to 20 m from vent, on all outer cone walls/ top of all cones along whole fissure.	Fall deposits from an unsteady eruption plume above Hawaiian fire fountains. Pyroclasts too cool to sinter or agglutinate on deposition.
Weakly agglutinated lapilli and bombs (wagLpB)	1.25 – 2.00	Black or altered red/brown; fine lapilli – bombs, 5 – 120 cm long; poorly sorted; clast supported; clasts edges have point contacts; all clasts visible; aphanitic, scoriaceous texture; angular – sub-rounded shape; moderately - highly vesicular; vesicles irregular – elongate, up to 2 cm; angular lithic clasts, up to 20 cm, varying compositions.	Massive; lack of fines (< 2 mm) between clearly defined outlines of particles; clasts undeformed; random - weakly orientated; abundant void space.	< 10 m from vent in 39% of cone walls to the west of fissure.	As above. Accumulation of mostly solidified well fragmented clasts. Higher accumulation rates allow pyroclasts to sinter but maintain blocky shapes on deposition.
Moderately agglutinated spatter (_magSp_)	1.03 – 2.85	Dark grey or altered red; fine lapilli – bombs, 3.5 – 89 cm long; moderately sorted; clast supported; multiple point contacts; edges of some clasts visible; aphanitic; irregular - sub-rounded shape; moderately vesicular; vesicles sub-rounded – irregular, up to 2 mm.	Massive; lack of fines (<2 mm) between clearly defined outlines of particles; sharp contacts; clasts weakly deformed, no clast flattening; weakly orientated; moderate void space.	< 10 m from vent in ~ 67% of cone walls along whole fissure.	Fallout from the outer part of a fire fountain with increasing accumulation rates leading to agglutination on deposition.
Moderately welded spatter (_mwSp_)	1.05 – 2.59	Black or altered grey/brown; 7 – 45 cm long; few clast outlines visible; aphanitic; can have a scoriaceous texture and blue iridescence; poorly - moderately vesicular; vesicles irregular - elongate, up to 1.5 cm.	Massive; sharp contacts; clasts moderately deformed; some clast flattening; moderately orientated; voids rarely seen.	< 10 m from vent in ~ 61% of cone walls along whole fissure.	Fallout from the inner part of the fountain with rapid accumulation on deposition.
Densely welded spatter (_dwSp_)	2.18 – 9.82	Black/dark grey; spatter bombs with flattened and elongate shape; range from 13 - 450 cm long and 3 - 59 cm wide; no obvious pyroclast texture; clast outlines rarely visible, defined by varying zones of vesiculation; weakly vitrophyric; non – incipiently vesicular; vesicles irregular - sub-rounded, rarely up to 1.5 cm.	Massive; sharp contacts; clasts fully deformed; clasts strongly flattened; no void space.	< 10 m from vent in ~ 89% of cone walls along whole fissure.	Fallout of large clasts ejected from the inner part of the fountain.
Lava like spatter (_l-lSp_)	N/A	Black/dark grey; no obvious pyroclast structure; clast outlines not visible; weakly vitrophyric; non-vesicular; jagged and spiny or smooth surface.	Massive; vertical and horizontal cooling joints; bulges; clasts fully deformed; no void spaces.	< 5 m from vent in ~50% of cone walls along the South East Head dome.	Fallout of clasts from the inner fountain at highest accumulation and discharge rates. Hot, fluidal pyroclasts coalesce on deposition due to limited time for cooling between clasts landings.

Table 3.3: _Descriptions, interpretations and abbreviations of the different cone lithofacies seen in the field. Descriptions were aided by the classification scheme of **Quane and Russell (2005)**._

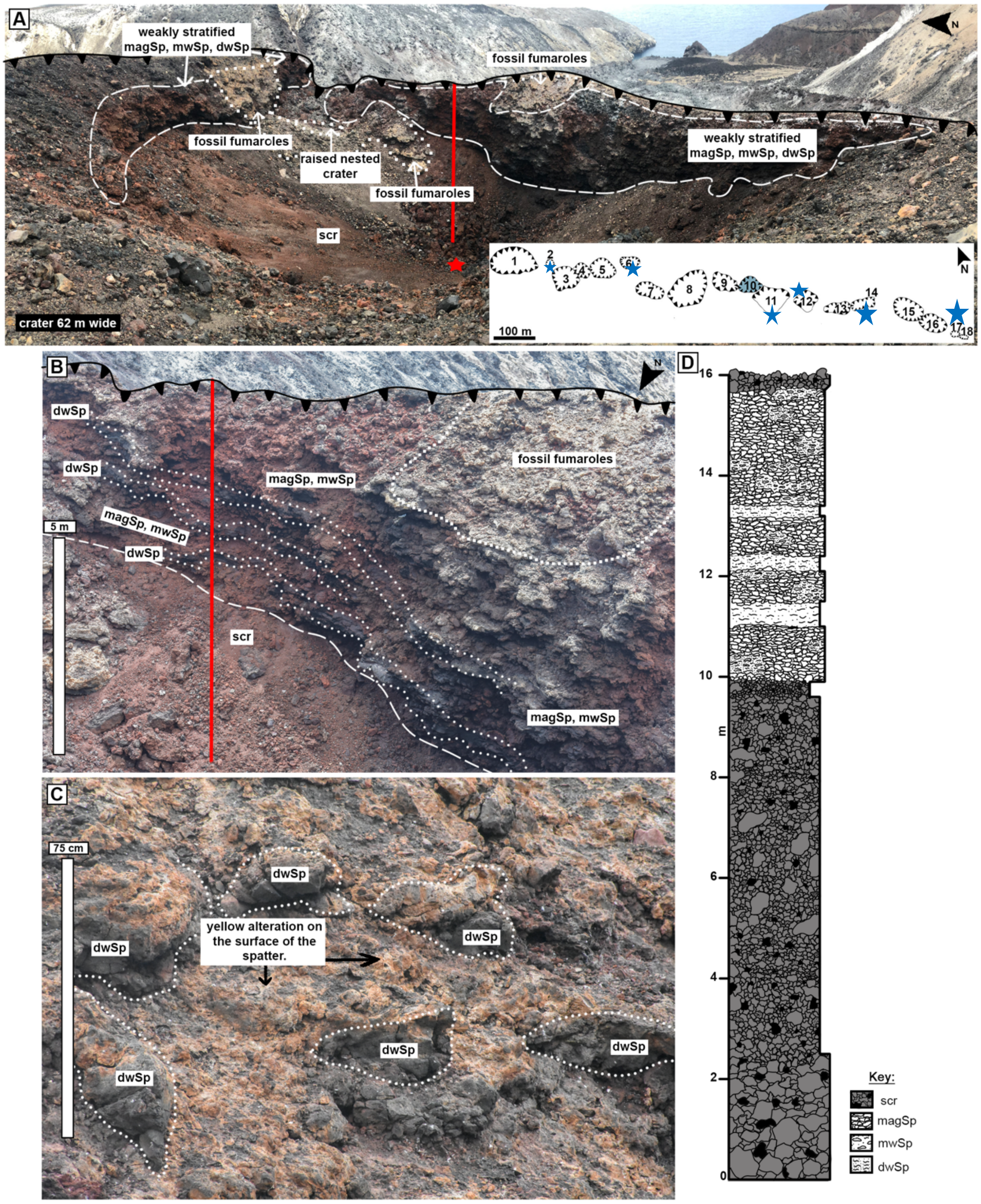

Figure 3.7: ***A)*** *Panoramic view of crater 10, an example of the type 1 cones, showing the weakly stratified spatter units on the northern and southern crater walls and the fossil fumaroles. Crater is 62 m wide. Inset: schematic map showing the position of the crater along the fissure and other type 1 cones (stars).* ***B)*** *A close up of the spatter unit, showing the alternating layers of densely welded spatter (lithofacies dwSp; table 3.1) and the moderately welded spatter and moderately agglutinated spatter (lithofacies mwSp, magSp).* ***C)*** *A close up of the yellow coating surrounding the fossil fumaroles and blocks of densely welded spatter (lithofacies dwSp).* ***D)*** *Log through the northern crater wall. Location of log marked by the red line in. Thickness of the units estimated from a distance. scr – scree, magSp – moderately agglutinated spatter, mwSp – moderately welded spatter, dwSp – densely welded spatter.*

3.5.4 Lavas

The DIP eruption produced at least 16 small, channelised lavas of variable surface morphology. They form three distinct flow fields: the northwest flow field (NWFF); South East Head flow field (SEHFF) and South East Bay flow field (SEBFF) (Fig. 3.11). All but one of the lavas are clinkery ‘a’ā lavas but can show transitions to and from a slabby pahoehoe crust, the other is spiny ‘a’ā lava. The lavas range in measured length from 145 - 630 m long and may exceed these lengths where the lava flows enter the sea. The volume of individual lavas have been calculated using the mapped extents and average lava flow thicknesses. Lava flow volumes range from ~1.4 x10^3 – 2.2 x10^5 m^3 (table 3.4). All measurements should be classed as minimum dimensions due to uncertainties of mapping boundaries and loss of material either into the sea, from weathering or burial during the eruption. Initial viscosities were calculated using the method of Giordano et al., (2008), without considering the effect of crystal populations. The viscosity of the lava ranges from $10^{3.0}$ – $10^{3.1}$ Pa S and consistency is seen for each lava flow field (table 3.4).

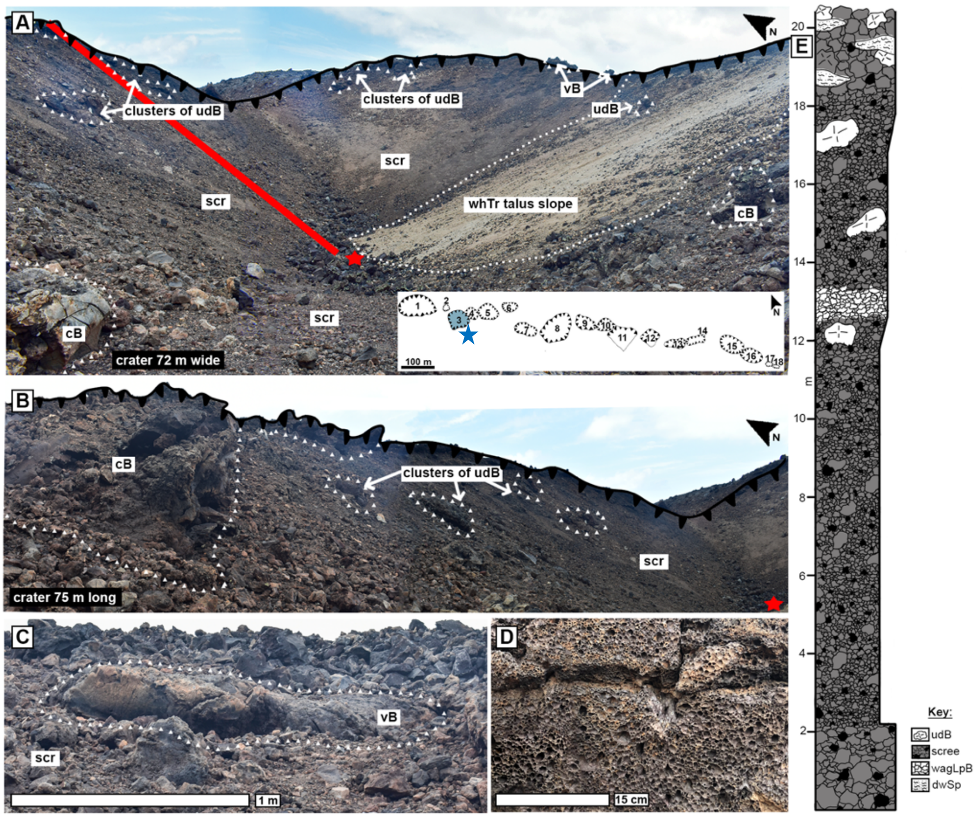

Figure 3.8: ***A)*** *Panoramic view of crater 3, an example of type 2 cones, showing the White Horse trachyte lithic clast (lithic clasts whTr; table 3.2) rich talus slope that makes up most of the southern crater wall. Ballistics are in clusters on the upper crater walls, (ballistics udB – undifferentiated bombs, vB – vesicular bombs, cB – composite bombs; table 3.5). Most of the crater walls are composed of scree (scr). Crater is 72 m wide. Inset: schematic map showing the position of the crater along the fissure aa and other type 2 cones (blue star).* ***B)*** *The northern crater wall showing the distribution of the different ballistics. Crater is 75 m long.* ***C)*** *An example of the vesicular bombs (ballistics vB) observed in the upper portion of the edifice walls.* ***D)*** *Close up view of the highly vesicular bombs seen in the weakly agglutinated spatter unit (lithofacies wagSp; table 3.1)* ***E)*** *Log through the edifice wall. Location marked by red line in* ***A****. udB – undifferentiated bomb, scr – scree, wagLpB – weakly agglutinated lapilli bomb, dwSp – densely welded spatter.*

3.5.4.1 Petrography of Lavas

The DIP lavas are dark grey, fine grained aphanitic and are incipiently to poorly vesicular (vesicle classification based on Houghton and Wilson, (1989)) with irregular shaped vesicles. They contain phenocrysts, and microphenocryst assemblages dominated by stumpy plagioclase crystals up to 2 mm in diameter (<3 vol.%), olivine, clinopyroxene and

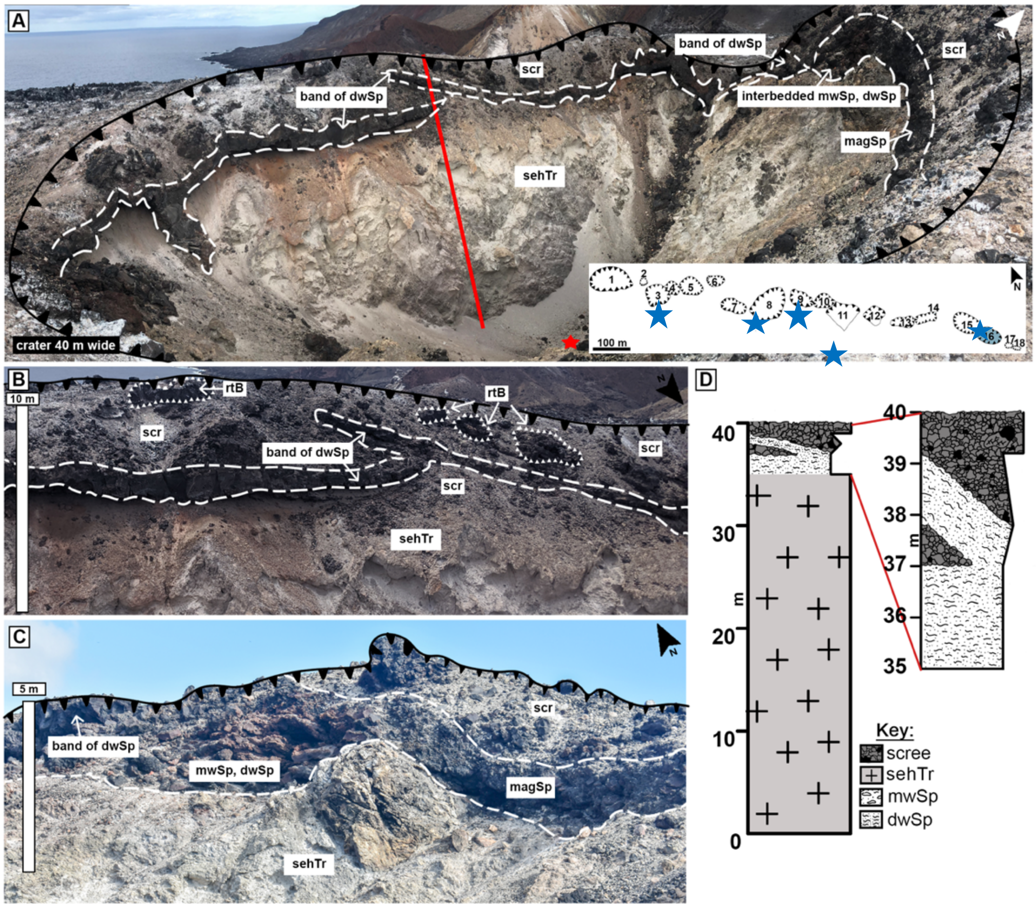

Figure 3.9: ***A)*** *Panoramic view of crater 13, an example of type 3 cones, showing the trachyte substrate (lithic clasts sehTr; table 3.2) and the overlying spatter unit composed of a combination of moderately agglutinated spatter, moderately welded spatter, and densely welded spatter (lithofacies magSp, mwSp, dwSp; table 3.1). The crater is 66 m wide. Inset: schematic map showing the position of the crater along the fissure and other type 3 cones.* ***B)*** *A close up of the spatter unit, where the sharp contact with the underlying substrate, the alternating layers of moderately agglutinated spatter, moderately welded spatter and densely welded spatter (lithofacies magSp, mwSp, dwSp) and the layer of densely welded spatter (lithofacies dwSp).* ***C)*** *A log through the crater wall. Location marked by the red line in* ***A****. Thickness of the units were estimated from a distance. sehTr – Southeast Head trachyte, magSp – moderately agglutinated spatter, mwSp – moderately welded spatter, dwSp – densely welded spatter.*

Lava Flow Field	Lava Flow	Length (m)	Cone No.	Width (m)	Thickness (m)	Area (m^2)	Total FF Area (m^2)	Volume (m^3)	Total FF Volume (m^3)	Viscosity (Pa S)
Flow Field 1	F1	260	2	55	2.5	1.4 x10^4	2.5 x10^4	3.4 x10^4	7.9 x10^4	10$^{3.1}$
	F2	180	6	50	4 ± 1	1.1 x10^4		4.5 x10^4		10$^{3.1}$
Flow Field 2	F3	90 - 570	13 - 18	30 - 120	1 ± 0.25 – 2 ± 0.5	1.1 x10^5	1.2 x10^5	2 x10^5	2.2 x10^5	10$^{3.0}$
	F4	115	15 - 16	70	2 ± 0.5	1.0 x10^4		2.1 x10^4		10$^{3.0}$
Flow Field 3	F8	150	unknown	25	5 ± 1.25	1.2 x10^3	9.3 x10^4	5.7 x10^3	1.9 x10^5	10$^{3.1}$
	F5	155	7	20	0.6 ± 0.15	2.4 x10^3		1.5 x10^3		10$^{3.1}$
	F7	630	11	75	1.5 ± 0.38	6.5 x10^4		9.8 x10^4		10$^{3.1}$
	F6	265	8	40	6 ± 1.5	1.4 x10^4		8.4 x10^4		10$^{3.1}$

Table 3.4: *Showing the main dimensions of the lava flows and lava flow fields. Each dimension is the minimum dimension.* FF = flow field.

amphibole (<1 vol.% each) (Fig. chapter 5). Fe-Ti oxides are also present. The groundmass is microcrystalline and consists of plagioclase, olivine, clinopyroxene and Fe-Ti oxides. Further details on the petrography of the lavas and the crystal assemblages are in Chapter 4 and 5.

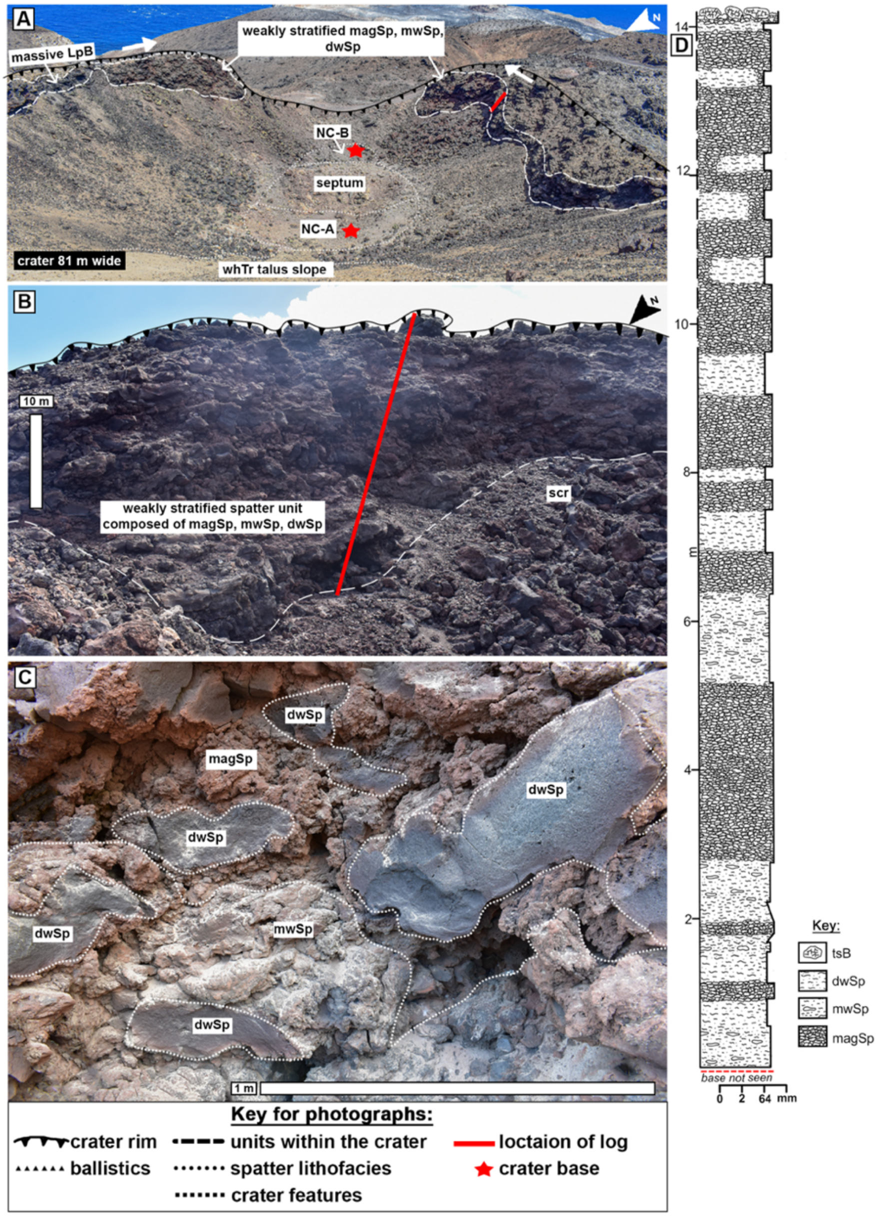

Figure 3.10: ***A)*** *Panoramic view of crater 1, an example of type 3 cones, showing the two nested craters (NC-A, NC-B) with the septum between them and the spatter units that build the crater up. The spatter units are composed of loose lapilli and bombs, moderately agglutinated spatter, moderately welded spatter and densely welded spatter (lithofacies LpB, magSp, mwSp, dwSp; table 3.1) and thicken in the direction of the white arrows. The White Horse trachyte (lithic clasts whTr; table 3.1) talus slopes represent the eruption cutting down into an underlying White Horse lava flow lobe.* ***B)*** *The spatter unit at nested crater B (NC-B), showing the weakly stratified appearance of moderately agglutinated spatter, moderately welded spatter and densely welded spatter (lithofacies magSp, mwSp, dwSp).* ***C)*** *Showing the distribution of the different spatter lithofacies within the unit.* ***D)*** *Log through the spatter unit at nested crater B (NC-B). Location shown by red line in* ***A*** *and* ***B****. tsB – tortoise shell bomb, dwSp – densely welded spatter, mwSp – moderately welded spatter, magSp – moderately agglutinated spatter.*

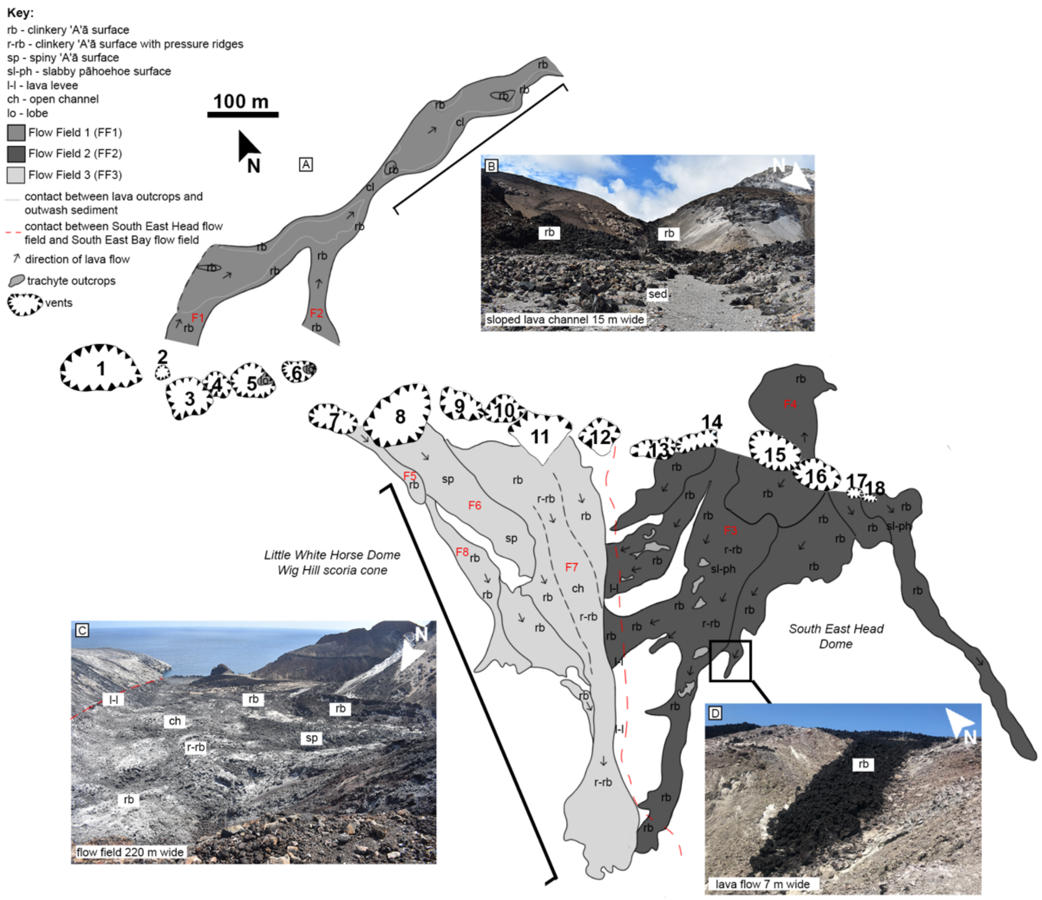

Figure 3.11: ***A)*** *Structure map of the lava flows at DIP with the main lava flows numbered.* ***B)*** *Image of the Northwest lava flow field.* ***C)*** *Image looking down onto the Southeast Bay lava flow field.* ***D)*** *Image of one of the lava lobes in the Southeast Head lava flow field. Areas described in detail below.*

3.5.4.2 Flow Field 1 (FF1)

FF1 has an area of 3.6 x10^4 m^2 and a volume of 2 x 10^5 m^3 and is composed up of two partially preserved, channelised rubbly ‘a’ā lavas, F1 and F2, and an outwash plain, where the lava has been eroded (Fig. 3.12c). Along the outwash plain, the remnant, 2.5 m high levee of the F1 lava intercept the levees of the F2 lava, which bank up on the margins of a pre-DIP trachyte lava (Fig. 3.12a). The lava flowed over a cliff and down a ~ 40° slope, into a lower outwash channel with 5.5 m high, rubbly levees (Fig. 3.12d). An inaccessible lava delta protrudes from the coastline, but its exact relation to the DIP lavas is unknown. Due to the lack of outcrop and textural similarities in the field, it was not possible to understand the original extent of the F1 lava.

Dark grey, highly vesicular, brittle, stretched glassy filaments infill cracks within the F1 lava (Fig. 3.13a-d). In places, the glassy material has a highly viscous appearance and is inferred to have been more ductile, with filaments protruding away from the surface (Fig. 3.13e).

The F2 lava channel is roughly symmetrical in appearance, looking up flow, with the largest blocks (15 – 110 cm in diameter) in the central channel, the smallest blocks (10

– 60 cm in diameter) either side of the central channel, and the medium sized clinker (10 – 100 cm in diameter) at the rubbly levees.

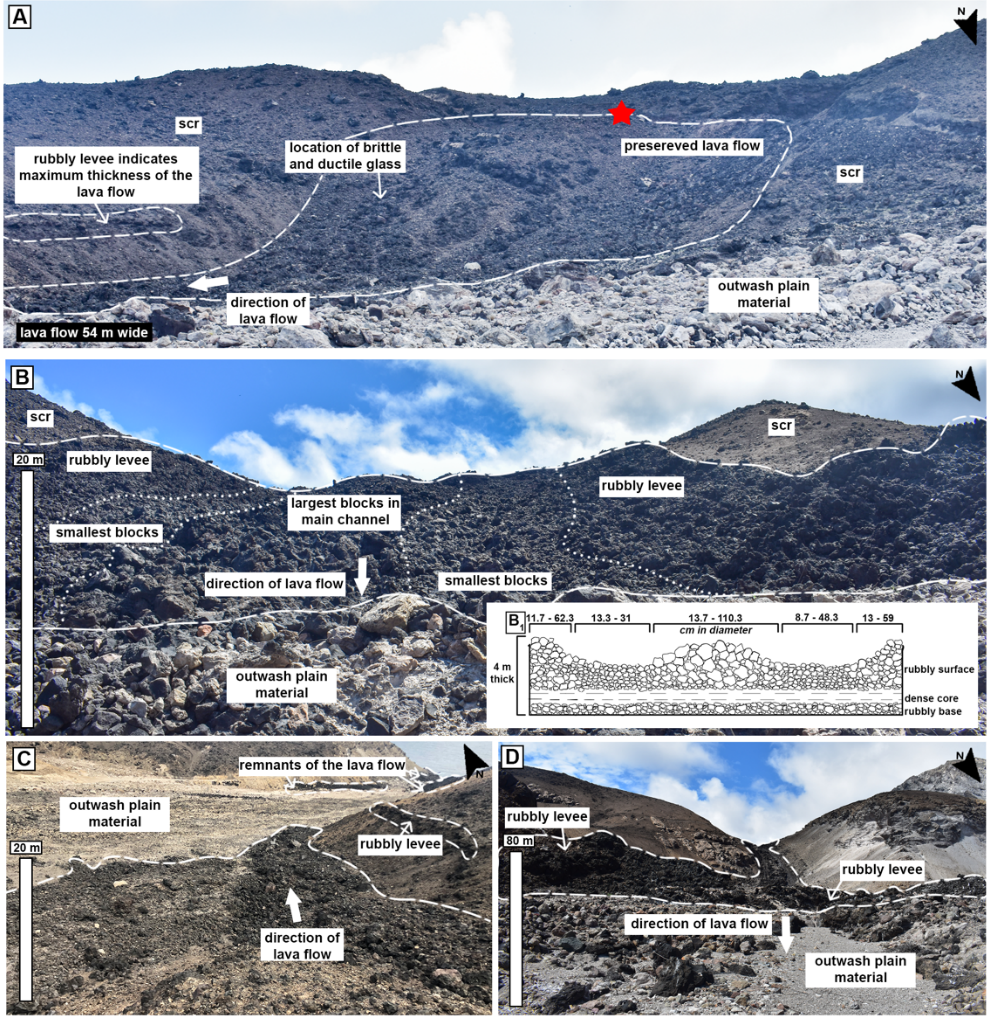

Figure 3.12: ***A)*** *Looking up at the F1 lava and rubbly levee showing the maximum thickness of the flow. Red star indicates vent location. Thick white arrow indicates direction of flow.* ***B)*** *Looking up at F2 lava and the rubbly levee. Dotted lines outline the sections of the channel based on block size. Inset – schematic diagram of the channel showing the different block sizes and the ranges measured in the field. Diagram not drawn to scale. Each measurement is average block size and are cm in diameter.* ***C)*** *Looking down from F1 lava and showing the outwash plain channel and the remnants of lava banked up along the channel sides.* ***D)*** *Looking back up towards the F1/F2 lava from the lower outwash channel.*

3.5.4.3 Flow field 2 (FF2)

FF2 is located on the South East Head dome. The lava flow field is made up of at least eight channelised, rubbly ‘a’ā lavas, of which seven of the lava flows flowed south (F3), following large joints and narrow valleys and one lava flow flowed north (F4) over a relatively flat terrain.

F3 lava flows followed valleys carved out of the trachyte dome. There is no evidence for hiatuses between the lava flows and I assume they were erupted close in time (Fig. 3.14a). Seven lava flows advanced down the side of the trachyte dome (Fig. 3.14b). Four of the lava lobes merge into the South East Bay flow field and three lobes cooled on the side of the dome. Large pāhoehoe slabs, up to 4 m in diameter, with ropey textures occur

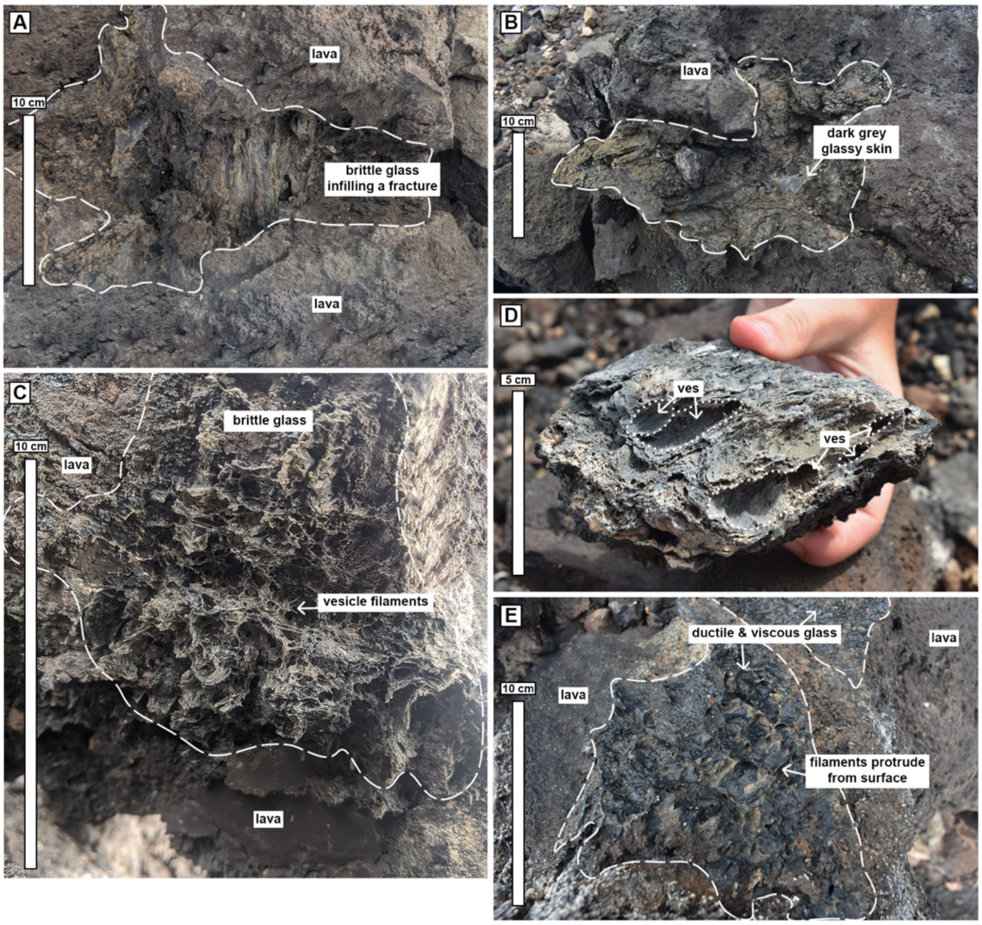

Figure 3.13: ***A, B)*** *Brittle glass with the dark grey/black skin infilling fractures within the lava flow.* ***C)*** *Brittle glass with the individual vesicles and filaments seen.* ***D)*** *Hand specimen of the glass showing the larger elongate vesicles.* ***E)*** *The black, ductile, and more viscous glass with the filaments protruding from the surface.*

in the upper part of the lava flows and at small break outs (Fig. 3.14c). The vent proximal parts of the lava flows are composed of equant ‘a’ā blocks ranging in size from 15 – 80 cm in diameter at the channel centre and 10 – 70 cm in diameter at the channel margins (Fig. 3.14d). The lower sections of the lava flow are composed of blocks of up to from 2 - 40 cm in diameter.

The F4 lava is a low-profile, simple lobe of rubbly pāhoehoe and flowed over a <5° slope. The low aspect ratio and syn-eruption/deposition of tephra/ ballistic deposits make the margins hard to define (Fig. 3.15a,b). The toe of the lava flow has a sub-spherical, ~ 3.5 m long, 3 m wide and 0.2 m thick tumulus (Fig. 3.15a,c) with a dense core and a crenulated upper surface.

3.5.4.4 Flow field 3 (FF3)

FF3 is made up of at least seven channelised, rubbly ‘a’ā (F5, F7) and spiny ‘a’ā (F6) lava flows (Fig. 3.16a) that follow a relatively flat terrain towards the coast. A ridge of lava (F8), assumed to be older than the DIP deposits based on field relationships (dip direction and a large variation in thickness compared to the DIP products), runs along the northwestern

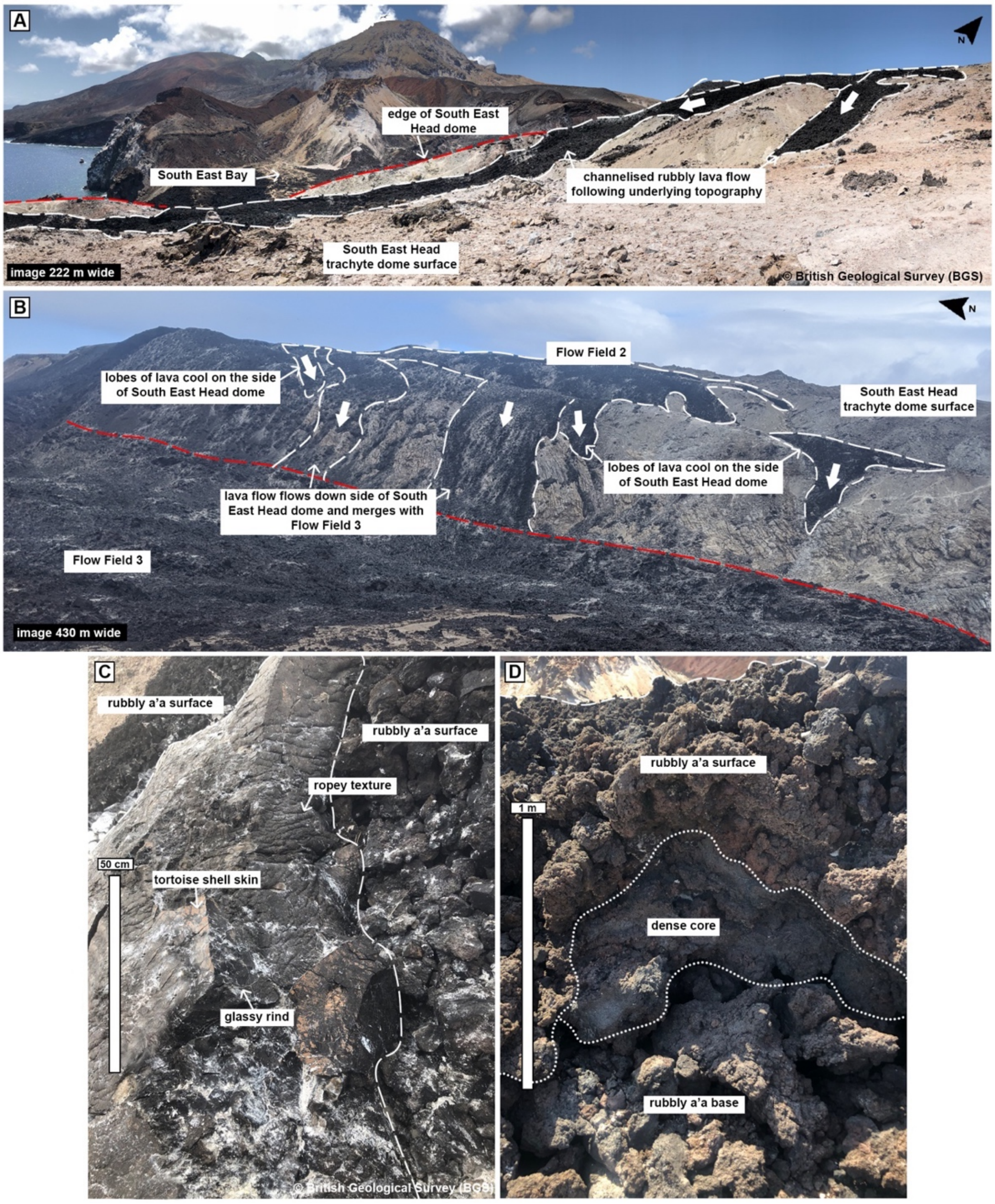

Figure 3.14: ***A)*** *The individual channelised lava flows of the FF2 lavas following the topography. Thick white arrows indicate direction of flow. Red dashed line indicates contact between FF2 and FF3.* ***B)*** *The channelised lava (F4) flow down the side of the trachyte dome. Two of the lavas meet the FF3 whilst three cooled before reaching the base.* ***C)*** *An example of the slabby pahoehoe seen in the upper section of the lava flows.* ***D)*** *A cross section through one of the channelised lava flows, showing the rubbly a'a base, dense core and rubbly a'a surface.*

margin of the lava flow field. The surface of the ridge is composed of large breadcrust bombs, spatter bombs with lapilli clasts up to 8 cm in diameter and abundant rhyolitic scree. Dense, coherent lava occurs at the upper end of the ridge.

The F5 lava flow follows a narrow channel between cone 7, cone 8 and Wig Hill scoria cone (Fig. 3.16c). The lava flow is the smallest along the fissure, with the toe stopping just before the older lava ridge.

F7 is confined at the mouth by the F6 lava flow and South East Head dome (Fig. 3.17a). As the F6 lava flow ends, the F7 lava flow fans out and forms a 170 m wide lava

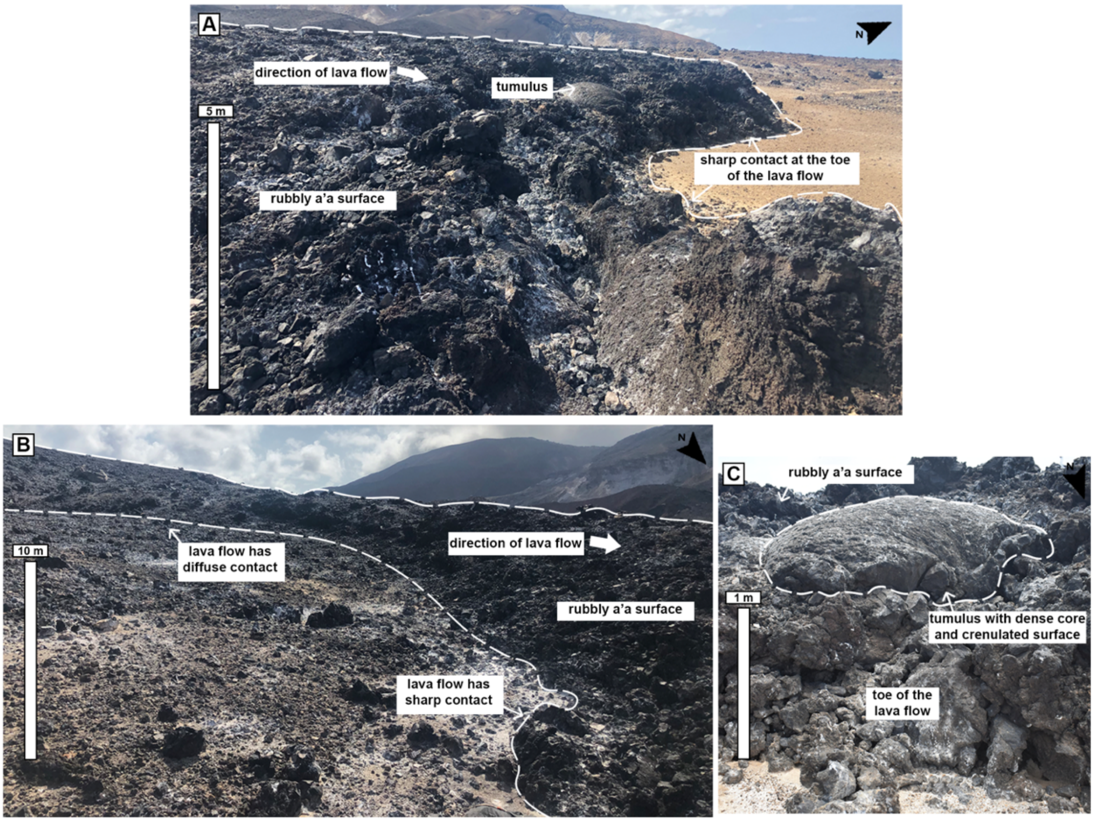

Figure 3.15: ***A)*** *The toe of the north FF2 lava (F4) with sharp contacts to the underlying substrate. Showing the rubbly a'a surface and location of a tumulus. Thick white arrow indicates direction of flow.* ***B)*** *Showing the gradational change from sharp to diffuse contact back towards the vent.* ***C)*** *The tumulus with a dense core and crenulated surface within the rubbly a'a surface.*

delta (Fig. 3.17c). The F7 lava flow is the largest channelised flow in the flow field. A rubbly levee, on the southern side of the lava flow, banked up 10 m onto the side of South East Head dome (Fig. 3.17b). A'ā blocks range in size from 10 – 90 cm in diameter at the start of the delta to 5 – 45 cm in diameter at the end of the delta.

The F6 lava flow runs alongside the F8 lava ridge and has a sharp contact with the F7 lava flow (Fig. 3.18a). The surface of the lava flow exhibits crenulations up to 8 cm high in a slightly stepped profile. A small, 5 m long and 50 cm wide, crenulated lava tube is exposed towards the toe of the flow (Fig. 3.18b). Spiny, angular blocks on the surface (Fig. 3.18c) of the lava flow are up to 125 cm in diameter, whilst rubbly 'a'ā blocks range from 5 – 90 cm in diameter.

3.5.5 Ballistic bombs

More than 200 ballistic bombs were documented at distances up to 600 m from the fissure. Seven different types (Fig. 3.19) were identified based on morphology, surface texture, rind thickness and presence and abundance of cracks (Wright et al, 2007) (table 3.4). These features all presented distinctly different ballistic bombs and therefore categorising them was done through visual observations. Tortoise shell bombs, rubbly tortoise shell bombs, breadcrust bombs, cowpat bombs, vesicular bombs, and glassy bombs (ballistic bombs tsB, rtB, bcB, cpB, vB, gB; table 3.5) occur along the whole fissure (Fig. 3.20a), whilst the

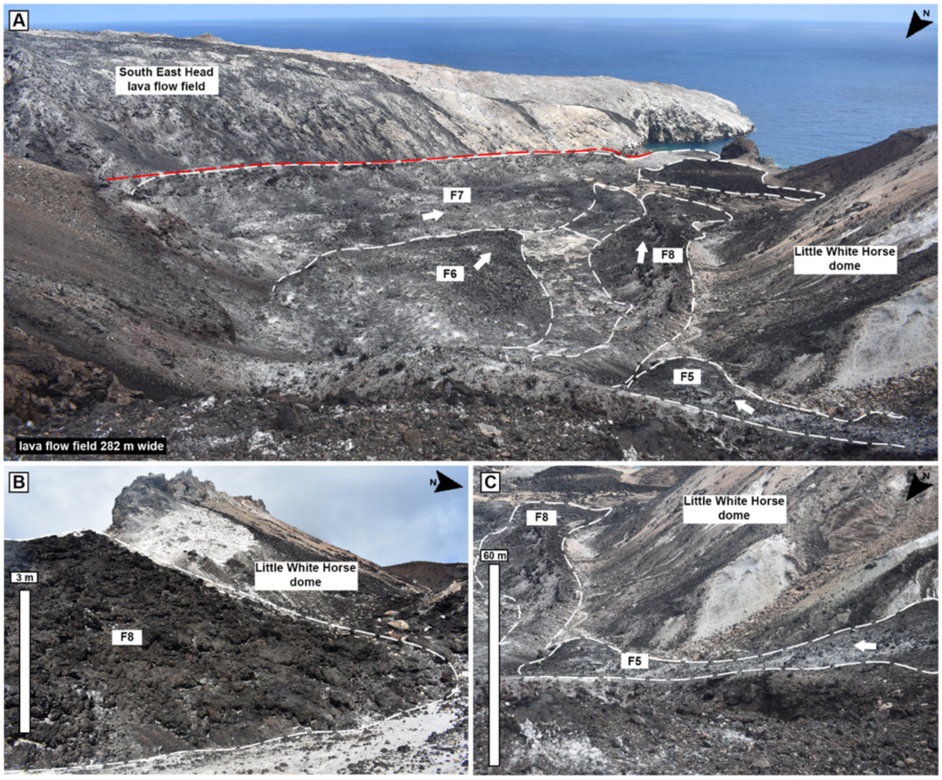

Figure 3.16: ***A)*** *Showing the FF3. The individual lava flows have been outlined. Thick white arrows indicate direction of flow. Red dashed line indicates contact between FF2 and FF3.* ***B)*** *Showing the upper end of F8.* ***C)*** *Looking down onto the toe of the small volume, F5 and F8.*

composite bombs (ballistic bombs cB; table 3.5) only occur within or on the rims of cones. Bomb reach 15 m in diameter (Fig. 3.20b). Only ballistic bombs larger than 40 cm were described to ensure exclusion of bombs fallen from eruption columns. There was no evidence of impact craters around the ballistic bombs. In some cases, the ballistic bombs had broken on impact, however this was only observed within 100 m of the fissure and predominantly in the vesicular bomb type.

Vesicular bombs and rubbly tortoise bombs (ballistic bombs vB, rtB; table 3.5) are the most common types along the fissure (35 vol.% and 30% vol.% respectively). Tortoise shell bombs (ballistic bombs tsB; table 3.5) are the least abundant (4 vol.%). Cowpat bombs (13 vol.%) and breadcrust bombs (11 vol.%) (ballistic bombs cpB, bcB; table 3.5) have similar abundances, whilst glassy bombs (ballistic bombs gB; table 3.5) account for 7 vol.% of bombs > 50 cm in diameter (Fig. 3.21a).

In section 1 of the fissure (cones 1 – 12), ballistic bombs were identified up to 160 m from the vents, excluding a single transect on Razer’s Edge that ran from 280 – 580 m from the fissure (refer to map). In section 2 of the fissure (cones 13 – 18), ballistic bombs were identified up to 460 m from the fissure.

Vesicular bombs (ballistic bombs vB; table 3.5) are most abundant in both sections (38 vol.% (section 1) and 34 vol.% (section 2) respectively) and tortoise shell bombs

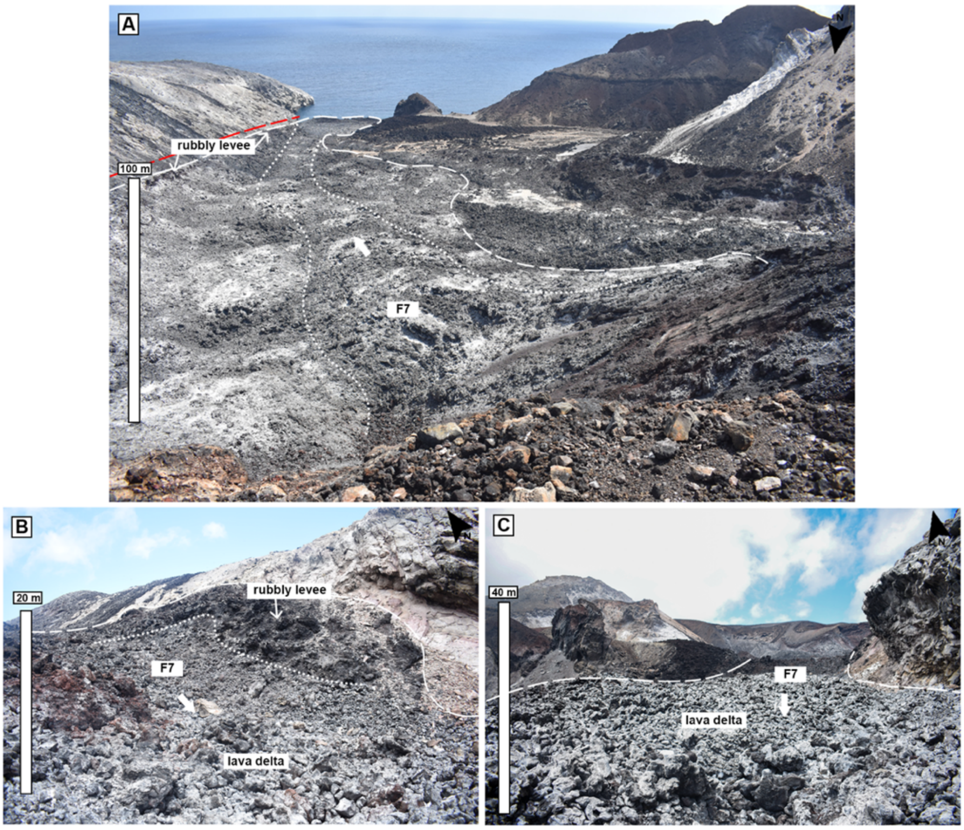

Figure 3.17: ***A)*** *Showing the F7 lava. The main channel is indicated by the white dotted lines. A rubbly levee is seen on the left-hand side of the lava flow. White thick arrow indicates direction of flow. Red dashed line indicates contact between FF2 and FF3.* ***B)*** *Looking up at the rubbly levee as it drops down onto the lava delta.* ***C)*** *The lava delta of the F7 lava with smaller rubbly blocks.*

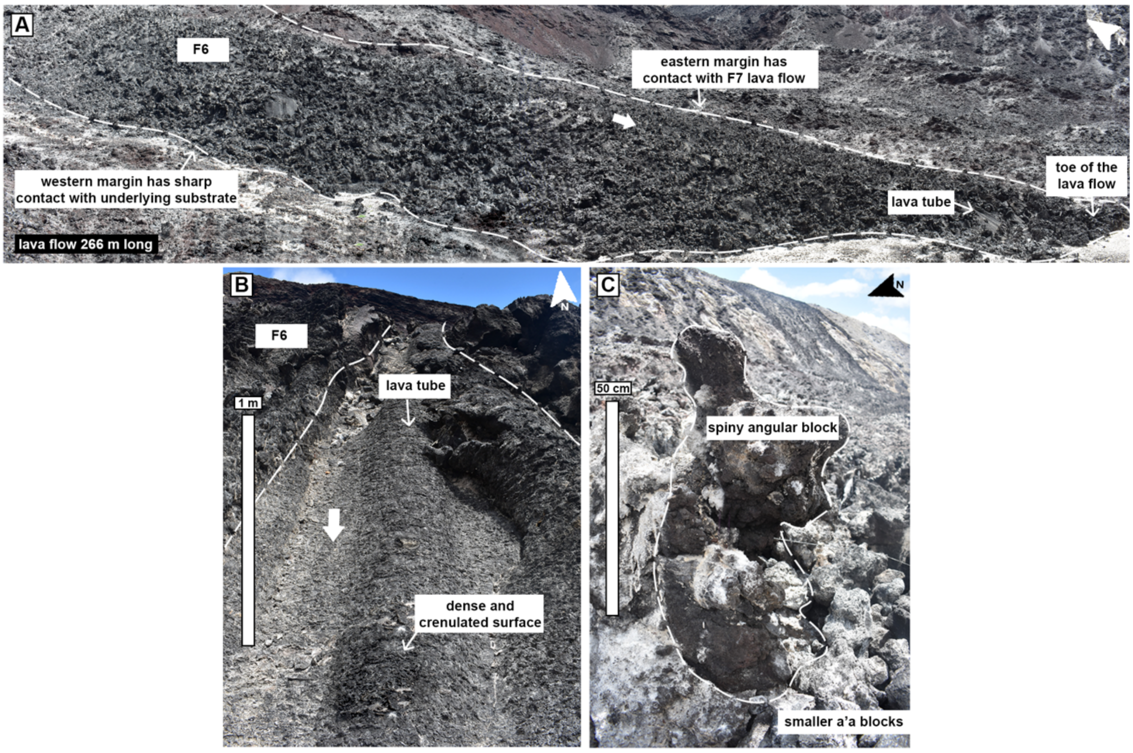

Figure 3.18: ***A)*** *The F6 lava with the toe and western margin showing sharp contacts with the underlying substrate. The eastern margin has a contact with the F7 lava.* ***B)*** *The lava tube with the crenulated surface surrounded by the spiny and rubbly a'a blocks.* ***C)*** *An example of the spiny a'a blocks and the smaller a'a blocks seen within the F6 lava.*

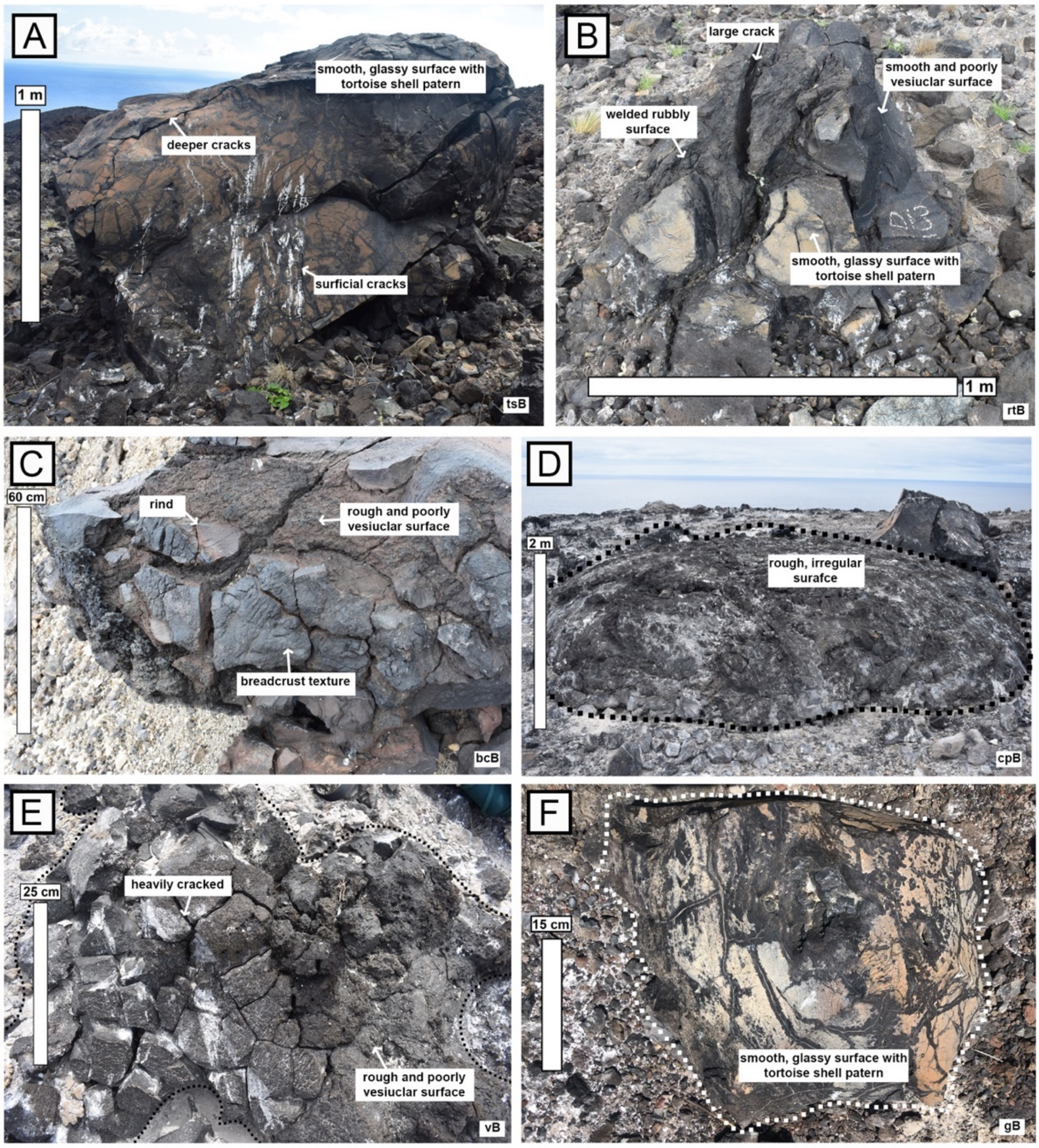

Figure 3.19: *Images of the 6 different ballistics identified along transects in the field.* ***A)*** *Tortoise shell bombs.* ***B)*** *Rubbly tortoise shell bombs.* ***C)*** *Breadcrust bombs.* ***D)*** *Cow-pat bombs.* ***E)*** *Vesicular bombs.* ***F)*** *Glassy bombs.*

(ballistic bombs tsB; table 3.5) are the least abundant in both sections (5 vol.% (section 1) and 4 vol.% (section 2) respectively), (Fig. 3.21b,c). Rubbly tortoise shell bombs (ballistic bombs rtB; table 3.5) have similar abundances in each section (28 vol.% section 1 and 31 vol.% section 2). Glassy bombs and breadcrust bombs (ballistic bombs gB, bcB; table 3.5) are more abundant in section 1 (9 vol.% and 12 vol.% respectively) compared to section 2 (7 vol.% and 10 vol.% respectively) whilst cow pat bombs (ballistic bombs cpB; table 3.5) are more abundant in section 2 (15 vol.%) compared to section 1 (9 vol.%).

Half of the measured ballistic bombs were 0.5 – 2 m in diameter (Fig. 3.22b) and almost one third of the measured ballistic bombs were 2 – 5 m in diameter. The ballistic bombs within these size factions are mainly rubbly tortoise bombs (ballistic bombs rtB; table 3.5) with very rare tortoise shell bombs and vesicular bombs (ballistic bombs tsB, vB; table 3.5). Ballistic bombs less than 0.5 m in diameter make up ~ 10 vol% and between 5 – 15 m in diameter make up less than 5 vol.%. Although these size groups are the least abundant,

Name	Exterior			Interior
	Textures	Rind	Cracks	
Tortoise shell bombs (tsB)	Rounded/sub-rounded shape; fluidal; glassy; aphanitic; smooth; polygonal joint pattern perpendicular to surface (like a tortoise shell); vesicular patches; tensional fractures.	Glassy; non-vesicular; 0.1 - 10 cm thick.	Moderately cracked; can cut through rind into core; 0.1 – 49 cm deep; 0.4 – 36 cm wide; some are surficial.	Poorly vesicular; highly vesicular zones with scoriaceous texture; aphanitic
Rubbly tortoise bombs (rtB)	Angular shaped; breadcrust texture; variations between welded rubbly, smooth, tortoise shell and smooth poorly vesicular textures; tortoise shell texture is glassy and incipiently vesicular; rubbly texture composed of juvenile and lithic clasts up to 10 cm; vesicular surface has sub-rounded vesicles up to 0.5 cm; all textures aphanitic; tensional fractures.	Glassy where tortoise shell is present; 0.5 – 5 cm thick; absent elsewhere.	Moderately cracked; cut through all textures; 0.3 – 26 cm wide; up to 12 cm deep; Surficial cracks radiate in similar orientations.	Aphanitic; poorly vesicular; irregular shaped vesicles up to 0.4 cm.
Breadcrust bomb (bcB)	Sub-angular shape; aphanitic; poorly vesicular; breadcrust texture; rind grades into a smooth poorly vesicular surface.	Aphanitic; poorly vesicular; 0.5 – 6 cm thick.	Moderately cracked; 0.3 - 7 cm wide.	Poorly vesicular; jagged and rough; scoriaceous texture; blue iridescent; aphanitic.
Cow pat bombs (cpB)	Rounded shape; rough, irregular surface; aphanitic; poorly vesicular; weak scoriaceous texture.	Thin rind; 0.5 – 3 cm thick; not well defined.	Mainly seen around edges; 1.5 – 4 cm deep; 0.4 – 5 cm wide; any on surface are <1 cm wide and infilled.	Black; aphanitic; poorly vesicular; spherical – elongate shaped vesicles – 2.5 cm.
Vesicular bombs (vB)	Sub-rounded to angular shape; can be fluidal shaped; aphanitic; poorly vesicular; very weak bread crusted texture; exhibits similar texture to ‘a’ā lava blocks.	No rind.	Highly cracked; normally defined by the weak breadcrust texture; 0.2 – 3.5 cm wide.	Poorly vesicular; vesicles irregular shaped, up to 2 cm; aphanitic; scoriaceous texture becomes more apparent towards core.
Glassy bombs (gB)	Rounded to angular shaped; fluidal; dense glassy exterior; aphanitic; tortoise shell pattern; patches of welded rubbly texture; patches of vesicles elongate in same direction; vesicles up to 0.2 cm.	No difference between rind and core.	Moderately cracked; 0.2 – 1.5 cm wide; up to 3 cm deep; surficial cracks; 1 mm wide.	Dense glassy interior; aphanitic; non – incipiently vesicular.
Composite bomb (cB)	Sub-angular shape; surface has agglutinated spatter clasts 2-5 cm – 35 cm or as tsB texture; moderately vesicular; aphanitic.	No rind.	Moderately cracked; 0.7 - 3 cm wide. Segregation vein 3 cm wide.	Black; moderately vesicular; aphanitic.

Table 3.5: *Descriptions and abbreviations of the different ballistic bombs seen in the field.*

it is important to understand that these eruptions were capable of erupting material of this size. The ballistic bombs generally decrease in size away from the vent, with the occasional larger ballistic bombs seen (Fig. 3.22a), for example a ballistic bomb with a maximum diameter of 6 m was seen ~ 360 m from the fissure, whilst the surrounding ballistic bombs had maximum diameters of between 0.3 – 0.8 m.

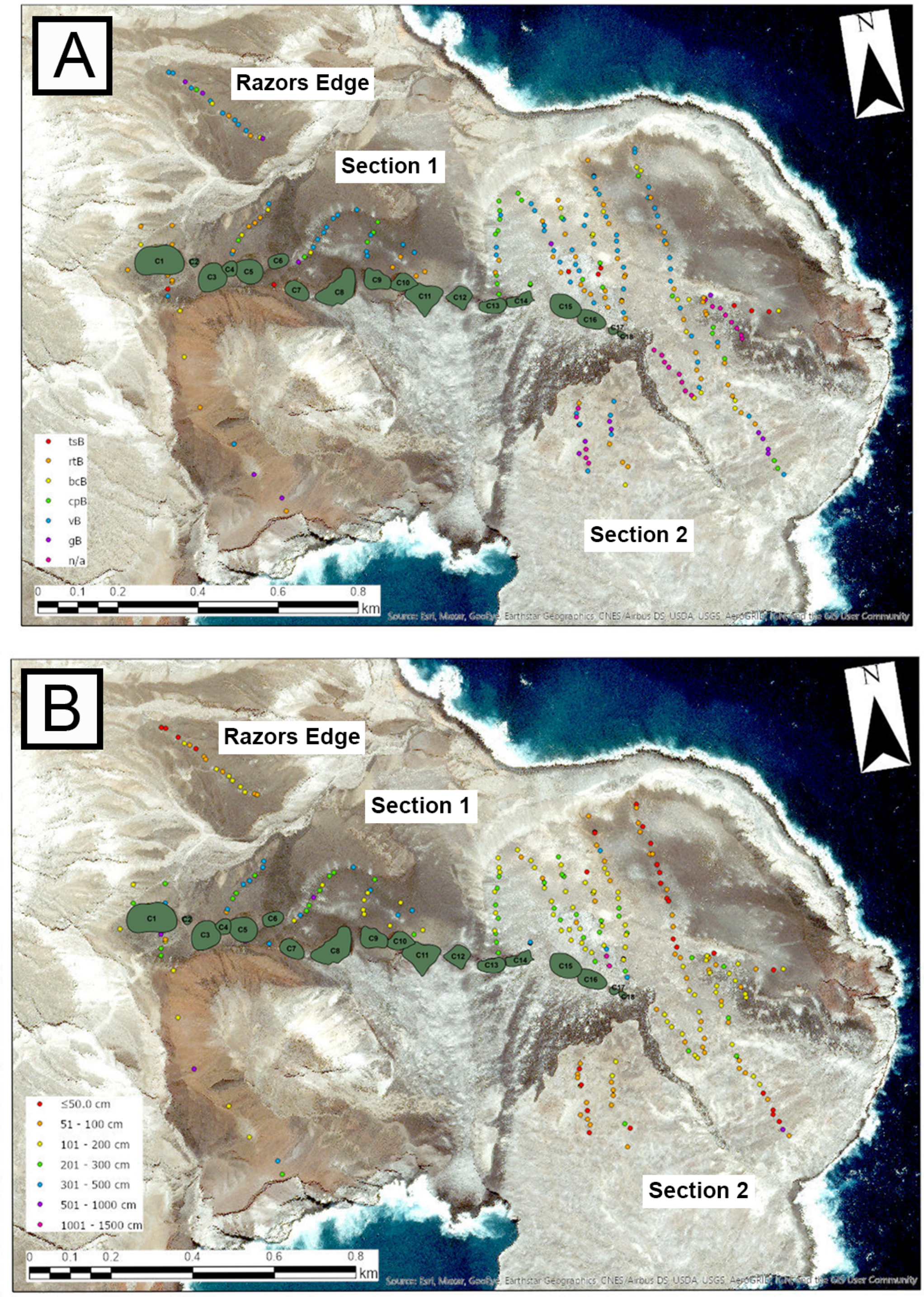

Figure 3.20: ***A)*** *Distribution map showing the different types of ballistics and their locations along the fissure. Craters filled in green. N/a is given for any ballistics that were unidentifiable or marked as lithic clasts.* ***B)*** *Distribution map showing the size ranges of the ballistics along the fissure. Craters filled in green. Both maps also indicate the locations of the transects.*

In section 1 and section 2, over one third of the measured ballistics were 1 – 2 m in diameter. Ballistic bombs with maximum diameter of <0.5 – 1 m are greater in section 2 (14

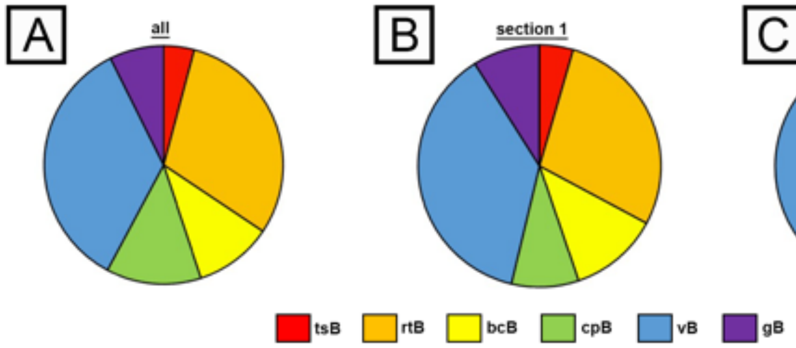

Figure 3.21: ***A)*** *Pie chart showing the different types of bombs along whole fissure****.*** ***B)*** *Pie chart showing the different types of bombs along section 1 of the fissure.* ***C)*** *Pie chart showing the different types of bombs along section 2 of the fissure.*

vol.% and 28 vol.% respectively) than section 1 (6 vol.% and 13 vol.% respectively), whereas ballistic bombs with a maximum diameter of 2 – 5 m are greater in section 1 (19 vol.% and 6 vol.% respectively) than section 2 (16 vol.% and 3 vol.% respectively). In both sections, ballistic bombs with a maximum diameter of 5 – 15 m are the least abundant (6 vol.% and 1 vol.%, respectively) (Fig. 3.22c,d). The 5 - 15 m ballistic bombs are found within 100 m of the vents and have the identical rubbly tortoise texture and fluidal shapes as the smaller sized ballistic bombs.

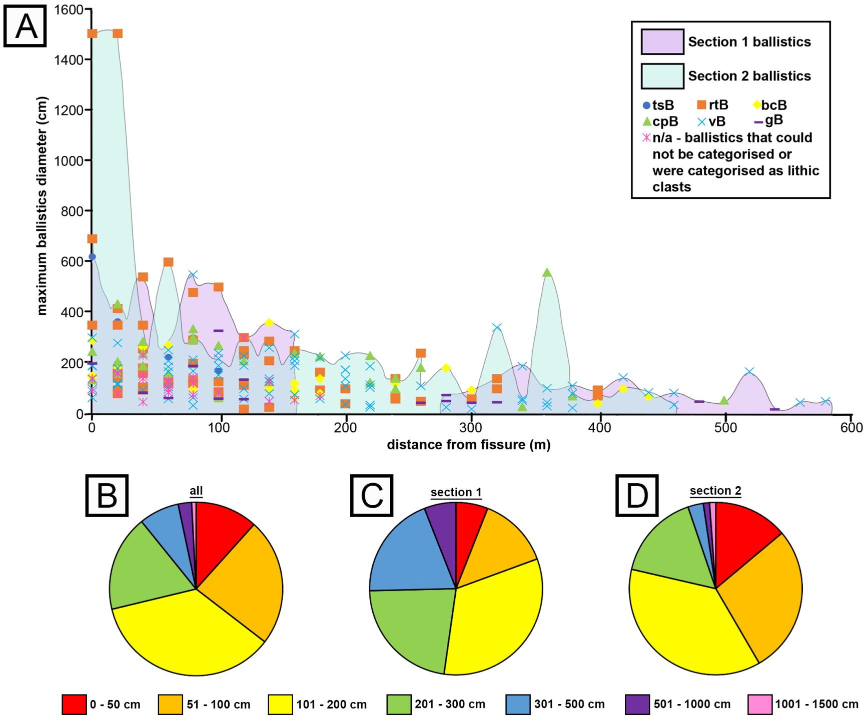

Figure 3.22: ***A)*** *Graph showing ballistics size vs distance from fissure. Purple field represents size range and distance from section 1 of the fissure. Blue field represents size range and distance from section 2 of the fissure. Symbols show the size and location of the individual types along the fissure. tsB – tortoise shell bomb, rtB – rubbly tortoise shell bomb, bcB – breadcrust bombs, cpB – cowpat bombs, vB – vesicular bombs, gB – glassy bombs, n/a – ballistics that could not be categorised in the field/from images or were categorised as lithic clasts.* ***B)*** *Pie chart showing the different sizes of bombs along whole fissure****.*** ***C)*** *Pie chart showing different sizes of bombs along section 1 of the fissure.* ***D)*** *Pie chart showing the different sizes of bombs along section 2 of the fissure.*

3.5.6 Tephra Deposits

Tephra deposits appear to have been dispersed to the north west of the fissure, based on the preserved deposits, and represent several components from multiple cones. The proximal locations (SC-1, SC-2, SC-3, SC-9, SC-10), within 200 m of the fissure (Fig. 3.23), are composed of scoria clasts, whilst the distal locations (SC-4, SC-5, SC-6, SC-7, SC-8, SC-11, SC-12, SC-13, SC-14), up to 600 m from the fissure (Fig. 3.24), are composed of scoria clasts, pumice clasts and lithic clasts. Eight distinct units (Unit I – VIII) were identified throughout the tephra deposits. Unit I is a pyroclastic flow deposit, whilst Unit II – VIII are fall deposits.

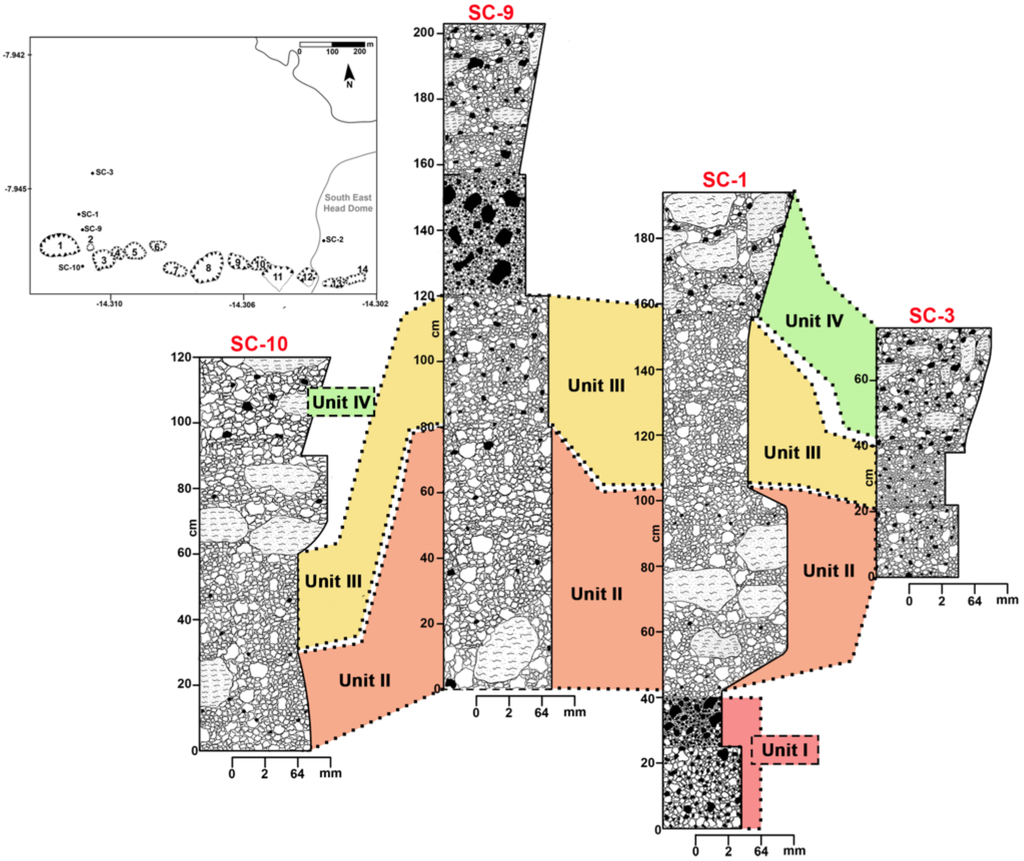

Figure 3.23: *Stratigraphic columns of the proximal tephra fall deposits. Identifiable units are linked where possible. Inset map showing location of the fall deposits in relation to the fissure.*

Unit I

Unit I is massive, 30 cm thick, and poorly sorted with a sorting coefficient (σφ) ranging from 2.35 – 2.95 σφ. The unit is composed of fine, sub-rounded and medium, sub-angular, dense, pumice and scoria lapilli to coarse ash, and up to 28 vol.% angular lithic clasts. The unit has a bimodal grain size distribution with a weak peak at -2φ, and a median grainsize (Mdφ) ranging from –0.9φ – -1.5φ. The PDC was deposited up to 80 m from the vent.

Unit II

Unit II is massive, 22 – 74 cm thick and poorly sorted (σφ 2.2 – 2.45) with coarse black scoriaceous blocks, sub-rounded medium to coarse scoria lapilli and up to 16 vol.% angular lithic clasts. The unit has a unimodal grain size distribution, with a modal peak at -4φ and Mdφ ranging from -3.4φ – -3.7φ.

Unit III

Unit III is massive, 15 – 41 cm thick, moderate to poorly sorted (1.85 – 2.25 φ) with fine, sub-rounded and medium, sub-angular, dense, pumice and scoria lapilli to coarse ash, an absence of coarse scoriaceous blocks and up to 10 vol.% angular lithic clasts. The unit has a unimodal grain size distribution with modal peaks decreasing from -5φ to -3φ with distance from the fissure, and Mdφ ranging from -3.2φ – -4.3φ.

Unit IV:

Unit IV is weakly reverse graded, 30 – 39 cm thick and poorly sorted (σφ 2.5 – 3.4) with sub-rounded medium to coarse scoria, rare dense and pumice lapilli clasts and up to 20 vol.% angular lithic clasts. The upper section of the unit is composed of sub-angular, medium to coarse scoriaceous blocks and the finer material is reworked. The unit has a unimodal grain size distribution with modal peaks decreasing from -6φ to -4φ with distance from the fissure, and Mdφ ranging from -4.2φ – -4.4φ

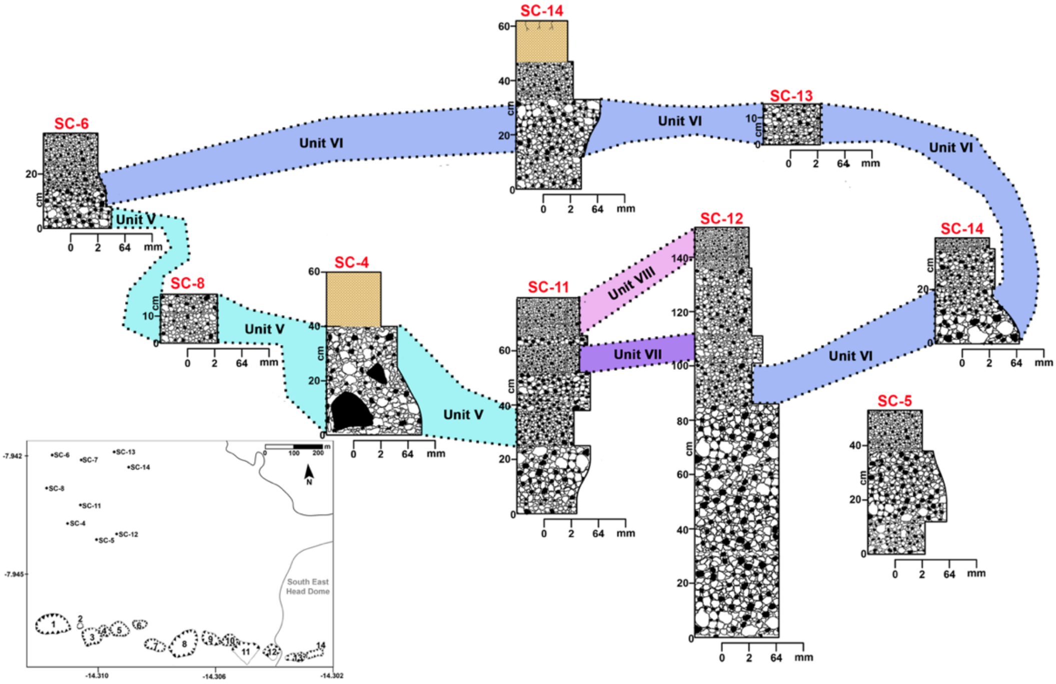

Figure 3.24: *Stratigraphic columns of the distal tephra fall deposits. Identifiable units are linked where possible. Inset map showing location of the fall deposits in relation to the fissure.*

Unit V:

Unit V is a massive, 9 – 40 cm thick, moderate to poorly sorted (1.3 – 1.9 σφ) with sub-angular coarse ash, fine to medium pumice lapilli, medium pumice and scoriaceous blocks and lapilli, and up to 21 vol.% angular lithic clasts. The unit has a broadly unimodal grain size distribution with modal peaks decreasing from -3φ to -1φ with distance from the fissure, however SC-8 is weakly bimodal with a second, minor peak at 3φ. Mdφ ranges from -1.6φ – -3.6φ.

Unit VI:

Unit VI is massive, 13 – 21 cm thick, moderately sorted (0.9 – 1.7 σφ) with denser, sub-rounded medium pumice and dense and rare scoria lapilli, rare coarse ash, and up to 22 vol.% angular lithic clasts. The unit has a unimodal grain size distribution with modal peaks ranging from -3φ to -1φ, and Mdφ ranging from -1.6φ – -3.3φ.

Unit VII:

Unit VII is massive, 10 cm thick and moderately sorted (1.3 – 1.4 σφ), with sub-rounded fine pumice and dense lapilli, rare fine scoria lapilli and up to 21 vol.% angular lithic clasts. The unit has a unimodal grain size distribution with modal peaks at -1φ and 0φ, and Mdφ ranging from -1.2φ – -1.4φ.

Unit VIII:

Unit VIII is massive, 14 – 15 cm thick and moderate to poorly sorted (1.75 – 2.35 σφ) with sub-rounded fine to medium pumice and dense lapilli, rare fine scoria lapilli, medium to coarse ash and up to 14 vol.% angular lithic clasts. The unit has a broadly unimodal grain size distribution with modal peaks at -1φ, however SC-11.6 is weakly bimodal with a second, minor peak at 3φ. Mdφ ranges from -0.9φ – -1.3φ.

When Mdφ is plotted against σϕ (Inman, 1952) the samples plot within a range of fields defined by Walker and Croasdale (1972) and Houghton and Carey, (2015) (Fig. 3.25). The proximal units (Units I, II and III) are coarse grained and poorly sorted. They mostly sit above the Strombolian field (Walker and Croasdale, 1972) and overlap of the Hawaiian, Strombolian and weakly Phreatomagmatic fields (Houghton and Carey, 2015). Both samples from Unit I plot within the Surtseyan field (Walker and Croasdale, 1972) and one sample sits within the PDC field (Houghton and Carey, 2015). The distal deposits (Units IV, V, VI, VII and VIII) are relatively coarse grained but more well sorted. All of the units sit within the Strombolian field (Walker and Croasdale, 1972) and either in the weakly

Phreatomagmatic or Hawaiian fields with some overlap into the Strombolian field (Houghton and Carey, 2015).

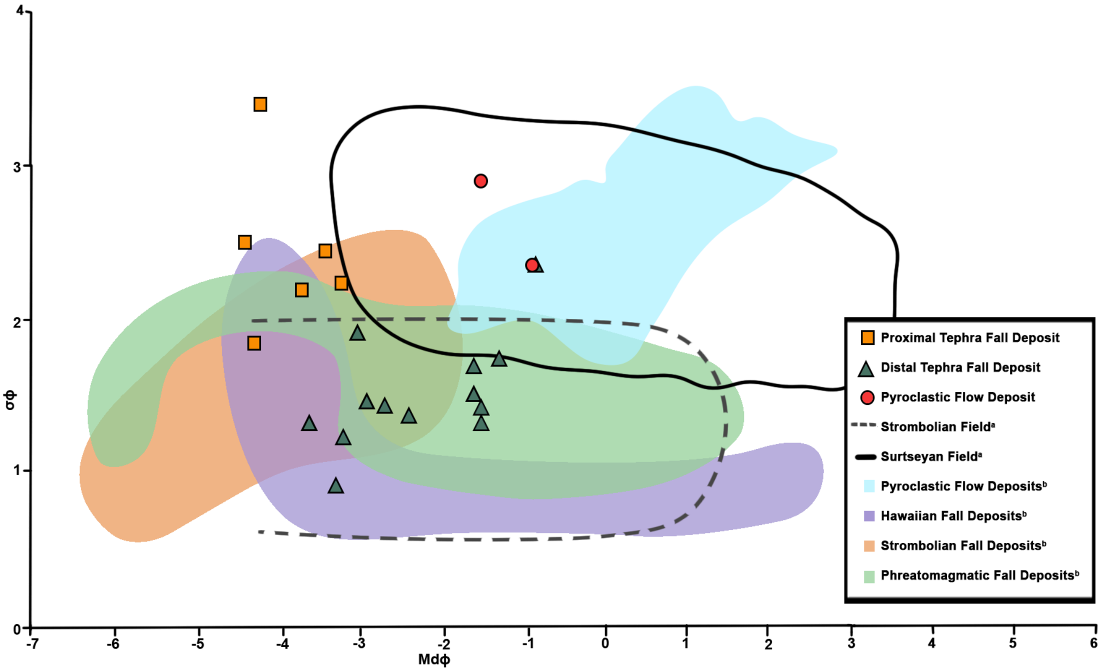

Figure 3.25: *Mdϕ vs σϕ for the different tephra units; Squares represent proximal fall deposits; triangles are distal fall deposits and circles are pyroclastic flow deposits. Strombolian field and Surtseyan field (straight and dashed lines) are from* ***Walker and Croasdale (1971)****, whilst the Hawaiian, Strombolian, phreatomagmatic, and Pyroclastic flow deposit fields are from* ***Houghton and Carey (2015)****.*

3.5.7 Summary of results

Three contrasting cone types were identified in the field, based on spatter lithofacies, lithic clast and ballistic bomb distribution (table 3.6). Although monogenetic, the cones do not exhibit characteristics of a typical scoria cone or spatter rampart expected along a fissure (e.g., Fedotov et al., 1980; Wood, 1980; Parcheta et al., 2012). For example, the cones are up to 80 m high, generally <80 m wide (with the exception of two cones), and the flanks dip <5°. There is no significant difference between the mean dimensions (table 3.4), however type 3 cones are always the deepest cones and type 2 cones occur next to each in the first section of the fissure.

3.6 Interpretation of deposits and surface features.

3.6.1 Type 1 Cones (T1)

Type 1 cones are characterised by weakly interbedded, moderately agglutinated to densely welded spatter, indicative of open vent, pulsating lava fountaining, with variations in accumulation and discharge rate affecting spatter build up phases and effusive lava flow phases (Fig. 3.26a) (e.g., Allen, 2004; Carracedo Sanchez et al., 2012). Two of the spatter cones have been breached by lava flows, suggesting that lava fountaining coexisted with

	Type 1 (T1)	Type 2 (T2)	Type 3 (T3)
Lithofacies	magSp; mwSp; dwSp	LpB; wagLpB	magSp; mwSp; dwSp; sits on top of exposed country rock.
Lava flows	yes	no	Some produce lava flows, others do not.
Lithic clast distribution	No lithic clast-rich talus slopes. Visually seen fewer lithic clasts on the ground around the cones.	Lithic clast rich talus slopes. Abundant lithic clasts on the ground around the cones.	Lithic clast rich talus slopes at some cones; Abundant lithic clasts on the ground around the cones.
Ballistic bombs	Rare ballistic bombs. Spatter bombs more abundant.	Abundant around cone rims and on cone slopes.	Moderately abundant around cone rims but not on cone slopes.
Tephra deposits	Abundant scoria clasts. Rare pumice, dense and lithic clasts. Seen up to 100 m from fissure.	Abundant pumice, dense and lithic clasts. Pumice clasts can have breadcrust texture Rare scoria clasts Seen up to 0.7 km from fissure.	Abundant pumice, dense and lithic clasts. Pumice clasts can have breadcrust texture Rare scoria clasts Seen up to 0.7 km from fissure. Weak PDC seen up to 80 m from cone 1.

Table 3.6: *Summary of the differences between the three cone types. Lithofacies codes from table 3.3.*

lava effusion. The moderately agglutinated spatter (magSp; lithofacies table 3.3) is composed of clasts that fell from the outer section of a lava fountain, where high accumulation rates lead to agglutination on deposition (e.g. Head and Wilson, 1989; Andronico et al., 2008; Brown et al., 2014; Reynolds et al., 2016). The moderately welded and densely welded lithofacies (mwSp, dwSp; lithofacies table 3.3) are larger clasts ejected from the inner section of the lava fountains (e.g. Head and Wilson, 1989; Sumner et al., 2005; Carey et al., 2008(L); Cabrera and Caffe, 2009; Brown et al., 2014; Reynolds et al., 2016). Retention of heat on deposition, coupled with rapid accumulation and deposition rates led to the development of weakly stratified welded deposits (e.g., Thomas and Sparks, 1992; Allen, 2004; Russell and Quane, 2005; Cabrera and Caffe, 2009). The positive correlation between spatter clast size and aspect ratio (Fig. 3.5a) is typical of basaltic pyroclast deposits, as larger clasts retain heat for longer and are more likely to be fluid as they land (Sumner et al., 2005; Brown et al., 2014).

Gradual to sharp variations in welding intensity, laterally and vertically, within the deposits of the cone walls record spatial and temporal variation in accumulation rates and grain size, probably resulting from unsteady and non-uniform fountaining. Gradual transitions between the mwSp and magSp imply a gradual change in magma discharge rate (e.g., Head and Wilson, 1989; Carey et al., 2008R; Carracedo Sanchez et al., 2012).

Uniform beds of dwSp in the lower regions of the deposit imply a high accumulation rate in the early stages of the eruption.

3.6.2 Type 2 Cones (T2)

Type 2 cones are characterised by a general absence of non-welded and non-agglutinated deposits (Fig. 3.8), suggesting accumulation rates were lower (e.g., Head and Wilson, 1989; Sumner et al., 2005; Valentine and Gregg, 2008), therefore lava fountaining was unlikely to be the dominant process. Loose lapilli and bombs and weakly agglutinated lapilli and bombs (lithofacies LpB, wagLpB; table 3.3) represent mostly solidified and well fragmented clast-rich fall deposits from an unsteady eruption plume (Valentine and Gregg, 2008). The preservation of whole clasts and surface textures suggests that the LpB pyroclasts were too cool to sinter or agglutinate on deposition (e.g., Allen, 2004; Quane and Russell, 2005), whereas the wagLpB clasts are inferred to have fallen out under slightly higher accumulation rates, allowing the pyroclasts to sinter but maintain their blocky shape on deposition (e.g., Allen, 2004; Russell and Quane, 2005; Sumner et al., 2005; Cabrera and Caffe, 2009; Brown et al., 2014).

Angular ballistic bombs, abundant lithic clast rich talus slopes on the cone walls and rims, and outcrops of underlying substrate suggest a more explosive eruption (Fig. 3.26b) (e.g., Naranjo and Lara, 2004), with a higher eruption column, allowing more time for the erupted material to cool before deposition.

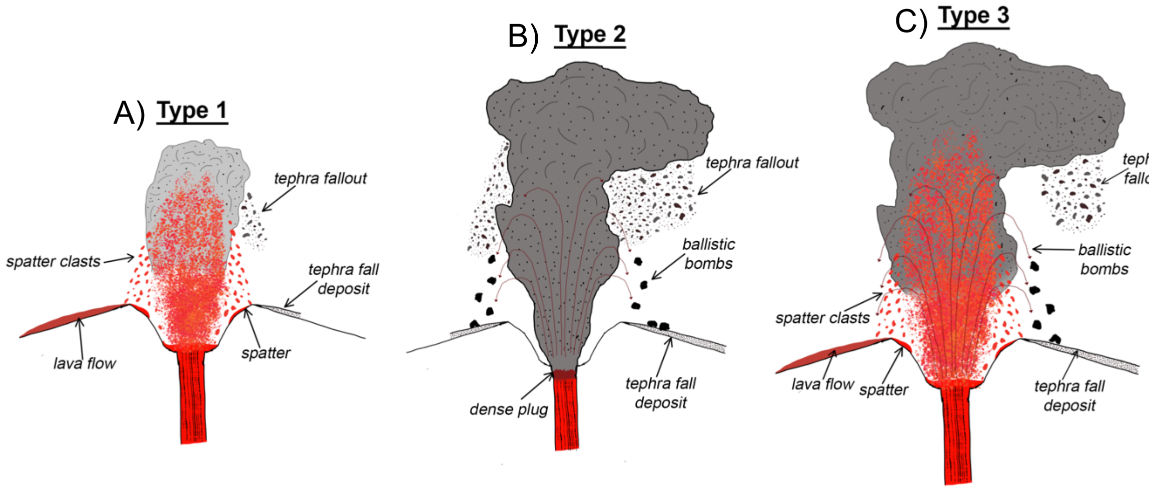

Figure 3.26: *Schematics showing the different eruption styles.* ***A)*** *Eruption style from type 1 cones, with lava fountaining leading to spatter build up, lava effusion and a small plume and weak tephra fallout.* ***B)*** *Eruption style from type 2 cones, with an eruption related to the breakup of a shallow, dense plug that generated larger plumes, tephra fallout and ejected ballistic bombs.* ***C)*** *Eruption style from type 3 cones, which started as a paroxysmal eruption (similar to cone type 2) and then transitioned to lava fountaining (similar to cone type 2).*

3.6.3 Type 3 (T3) Cones

The type 3 cones are hybrids of both type 1 and type 2. Some of the cones, for example cone 8 and cone 13, exhibit outcrops of country rock (T2), up to 40 m thick, overlain by spatter deposits (T1) up to 5 m thick, and abundant ballistic bombs (T2) focused on a single vent (Fig. 3.9) which indicates eruptions from these cones transitioned from more explosive explosions to lava fountaining and possibly fed lava flows. I suggest that these cones initially formed during paroxysmal explosions (Fig. 3.26c). Other cones, such as cone 1 and cone 9, exhibit the same characteristics as above, but around separate vents within the main cone, which indicates that both explosive eruptions and lava fountaining occurred simultaneously (Fig. 3.26c).

3.6.4 Tephra Deposits

Unit I has been interpreted as a small volume, lithic rich pyroclastic flow deposit around the base of cone 1, identified by the presence of rounded clasts and poor sorting (Fig. 3.25). The pyroclastic flow deposit has a greater abundance of scoria clasts and lithic clasts, which isn't a combination of components seen together in the fall deposits. The eruption at cone 1 occurred through a lithic rich debris fan that resulted in a dense eruption jet containing a lot of cold lithic clasts. I infer that this collapsed to form a short-lived pyroclastic flow that travelled <100 m from the cone (e.g., Di Roberto et al., 2014).

Two different types of tephra fall deposits were recognised extending away from the cones. The first type is a scoria fall deposit, with abundant scoria clasts with few pumice clasts, dense juvenile clasts and lithic clasts, and the second is a pumice fall deposit, with abundant pumice clasts, dense juvenile clasts and lithic clasts and rare scoria clasts.

Unit II – V are coarse-grained, poorly sorted, scoria rich deposits that outcrop within 200 m of the fissure and represent episodes of open-vent Hawaiian fountaining and fallout from eruption plumes created above the fountains (e.g., Head and Wilson, 1989; Houghton and Gonnerman, 2008; Calvari et al., 2021; Namiki et al., 2021). The lack of fine ash in the proximal fall deposits and spatter deposits suggests that the lava fountaining events underwent a more fluidal fragmentation rather than brittle fragmentation (Turbeville, 1992; Self et al., 1993; Head and Wilson, 1987; La Spina et al., 2021). The increase in grain size for Unit IV is suggested to be due to a degree of reworking.

Unit VI – VIII are finer grained, moderately well sorted deposits, pumice, dense and lithic clast rich deposits are found more distal to the fissure and are implied to represent more explosive episodes that generated larger, more sustained plumes (e.g., Fiske et al., 2009). The lack of these outcrops in the proximal region is due to the lack of exposure and covering by larger and younger clasts. The presence of ash in the unit VI – VIII deposits implies elevated fragmentation efficiencies which is commonly described during water-magma interactions (Sheridan and Wohletz, 1893; Houghton and Hackett, 1984; Liu et al., 2017), whilst the abundance of lithic clasts and dense clasts throughout these deposits implies the onset of more explosive activity, which I infer to be due to the role of a plug of partly solidified magma in the upper part of the magma column (e.g., Burgisser et al., 2011; Bain et al., 2019; Thivet et al., 2020). The lack of stratification within the units shows that there was no transition to a more unsteady eruption dynamic and could suggest that phreatomagmatic activity was not the driver for the change in eruption style (e.g., Houghton et al., 2015).

These two contrasting types of fall deposits result from two different eruption styles. Evidence for changing eruption styles can be identified in the changing stratigraphy and clast types away from the fissure. Further investigation into the componentry and textures of the clasts will be presented in Chapter 5. Due to lack of distal deposits, no deposit volumes could be reasonably calculated.

3.6.4.1 Lithic Clasts

The bulk of the lithic clasts at each cone derive from the shallowest older lava, for example the White Horse lava, the trachyte with mafic enclaves and the South East head lava. This shows that they are derived from the shallow widening of conduits (e.g., Reynolds et al., 2016), therefore the conduits themselves must be shallow. The lack of other lithic clasts shows that there was little erosion at greater depths, therefore the conduits likely narrowed rapidly to a dike at depths of more than a few tens of meters. The shallow nature of the conduit also suggests that the eruptions were short-lived.

3.6.5 Ballistic Clasts

The textural variations of ballistic bombs infer contrasting degrees of magmatic vesiculation at the point of fragmentation. This, combined with the systematic variation and distribution of the different types of ballistic bombs clasts on both sections of the fissure (Fig. 3.21), suggests that each type of ballistic bomb represents a region of a plug of semi-solidified magma within the conduit (e.g., Yamagishi and Feebrey, 1994; Bain et al., 2018). The tortoise shell ballistic bombs and dense glass bombs are inferred to be from the coolest, solidifying, upper section of the magma column or dense plug, whilst the cowpat and vesicular bombs are inferred to form from hotter, less viscous magma in the lower section of the magma column (e.g., Yamagishi and Feebrey, 1994; Gaunt et al., 2020). The largest ballistic bombs (5 – 15 m in diameter) have the same tortoise shell ballistic bomb texture and are inferred to be larger sections of the upper, cooling magma column. Similar sized blocks have been identified in other Vulcanian explosions but have been ejected greater distances (e.g., Nairn and Self, 1978; Yamagishi and Feebry, 1994), which suggests that the explosive energy of the DIP eruption was smaller than other Vulcanian explosions (e.g., Melson and Saenz, 1973; Nairn and Self, 1978; Yamagishi and Feebry, 1994).

Blocks of almost identical texture have been identified in block and ash flow deposits (e.g., Hoblitt et al., 1980) however, they formed by collapse of lava domes rather than Vulcanian explosions (Yamagishi and Feebry, 1994).

Dense glass ballistic bombs, related to plug formation, were erupted during Vulcanian explosions at both Soufrière Hills Volcano, Montserrat (Druitt et al., 2002; Formenti et al., 2003) and Galeras volcano, Columbia (Bain et al., 2018). Variation in the textures of the cowpat and vesicular bombs suggest that the magma was zoned in respect to the degree of vesiculation and degassing (Yamagishi and Feebrey, 1994; Wright et al., 2007; Isgett et al., 2017; Bain et al., 2018). Breadcrust textures could have formed by either quenching of magma by an external water source, inflation by internal degassing or vesiculation along impact fractures, caused by a pressure decrease when the fracture opened (e.g., Yamagishi and Feebrey, 1994; Wright et al., 2007). Breadcrust textures have also been produced during many Vulcanian explosions e.g., Eboko volcano, Guagua Pichincha, Galeras volcano, (Morissey and Mastin, 2000; Wright et al., 2007; Bain et al., 2018; Belousov et al., 2021).

3.6.6 Lavas

Lava flows were emitted from 11 cones during the DIP eruption however, lava flows from other cones may have been resurfaced and be underrepresented beneath the later lavas. Most were erupted from either T1 or T3 cones (Fig. 3.27).

FF1 is composed of two ‘a’ā lavas, inferred to have been fed from a combination of lava fountaining and effusion from the vent at cone 2 and cone 6. The levee described at the F1/F2 intercept (Fig. 3.12) suggests that the two synchronous lavas merged into one main channel. The F1 levee is higher than the main lava body (Fig. 3.12a,c), inferring that the lava was once at least 2.5 m thick, before the eruption rate declined and the channel drained (e.g., Magnall et al., 2017). Extensive erosion since the emplacement of the lava (Fig. 3.12c,d) is due to alluvial processes and suggests that the lava flows were rubbly, incoherent, and relatively young (e.g., Macdonald, 1953).

FF2 is composed of ‘a’ā lavas, implied to have been fed by multiple lava fountaining events. Individual lavas have been emplaced as thin (1 – 2 m thick) lobes that coalesced as they advanced away from the vent area. However, there is little evidence of time relations between lava flows within the flow fields. Coalescence of the lavas at the start of the lava flow field, and the rubbly morphology of the lava away from the fissure are suggested to be related to the changing terrain, from relatively flat to steeper slopes with predefined channels. Blocks of slabby pāhoehoe lava (Fig. 3.14c) within the lava indicate that the flow rate was too great for the crust to accommodate shear strain plastically and that there were

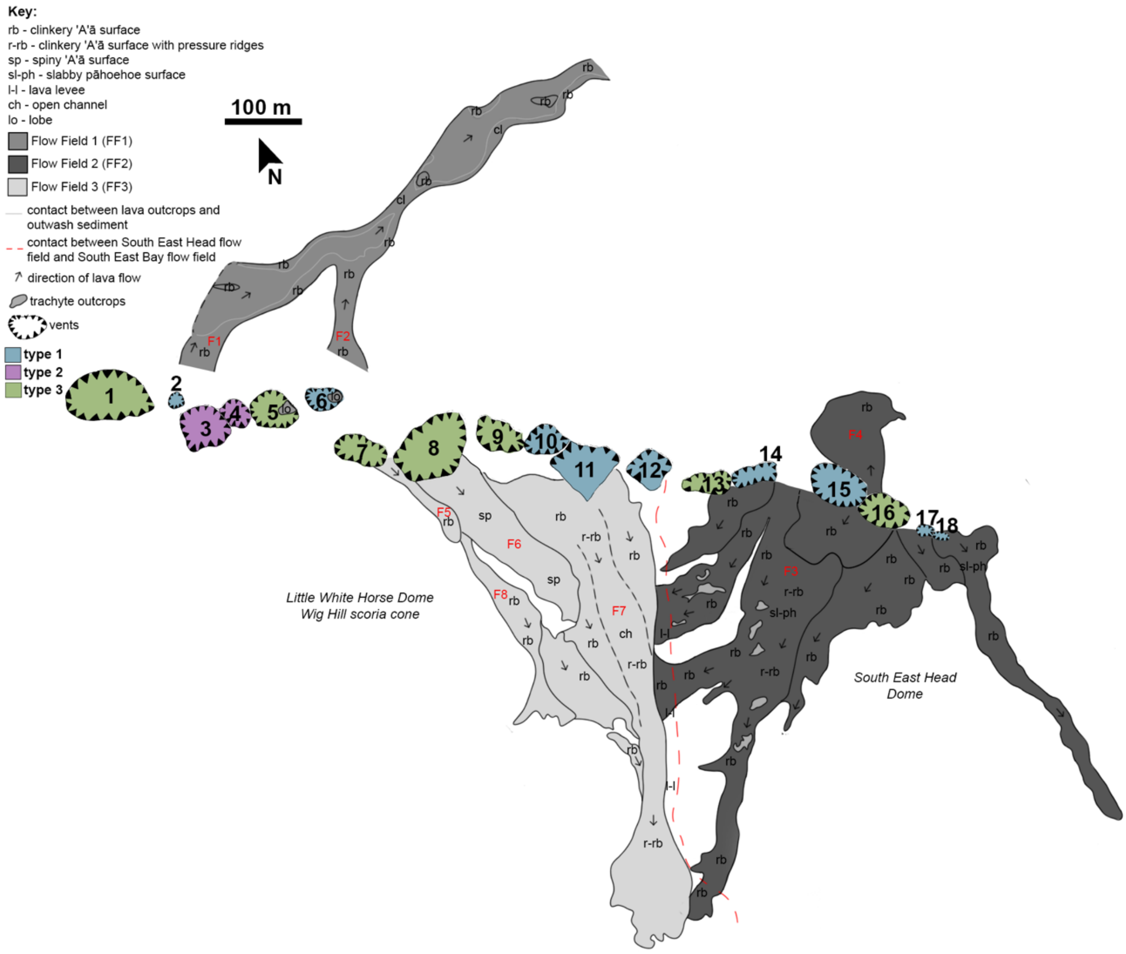

Figure 3.27: *Map showing the different cone types and linking them to the different lava flow fields.*

variations on the rate of lava supply along the second half of the fissure (e.g., Walker, 1991; Guilbard and Self, 2005; Lakroud et al., 2019).

The gradual boundaries of the F4 lava (Fig. 3.15) suggests that the lava flowed slightly uphill rather than downhill. Tumuli seen in the lava imply an increase in flow rate, related to an increase in head pressure (e.g., Guildbard and Self, 2005; Lakroud et al., 2019), however inflation features such as tumuli are rarely seen in ‘a’ā lavas (Gregg, 2017).

In FF3, the F5, F6 and F7 lavas are implied to have formed from a combination of lava fountaining and effusion directly out of the main vents (e.g., Valentine and Gregg, 2008) at individual cones (cone 7, cone 8, carter 10 and cone 11, respectively). F7 lava is confined at the mouth by F6 lava (Fig. 3.16a), before fanning out into the lava delta, and therefore is younger than F6 lava. F7 lava is too small to make any assumptions on time relations (Fig. 3.16c). The raised rubbly levee at the contact of the F7 lava and South East Head dome (Fig. 3.17 suggests that the lava ponded in the channel (e.g., Harris et al., 2009), however, the lack of a stepped profile in the levees suggest that the lava was not stagnated (e.g., Naranjo et al., 1992). It can be assumed that the sea front was higher up and cooled the toe of the lava quickly. Over time, cracks and cooling fractures weakened the toe and caused the lava to spill out into the sea, forming the lava delta. A blockage within the channel can cause flow rates to temporarily increase, hence increasing flow depths (e.g., Naranjo et al., 1992).

The F6 lava is implied to have been fed by a lava fountain with an increase in magma discharge rates and fountain heights that produced a largely degassed lava (e.g., Head and Wilson, 1989; Guilbard and Self, 2005), allowing it to effuse from the main vent. The viscosity of the F6 lava is no different to the viscosity of the other lava deposits from the DIP fissure, which suggests that the different morphology of the flow (Fig. 3.18a) is not related to viscosity. The small-scale lava tubes (Fig. 3.18b) suggest that, although the surface solidified, the effusion rate remained steady (e.g., Gregg, 2017). The absence of secondary levees within all the lava channels suggest that the channels remained stable for the duration of the flow (e.g., Harris et al., 2009).

3.7 Comparison with basaltic fissure eruptions and other intermediate eruption deposits

The DIP eruption is a rare example of a trachyandesitic, intermediate composition fissure eruption. Intermediate composition eruptions are common in arc-related zones but less common in ocean island settings (e.g., Jeffery and Gertisser, 2018). Intermediate-composition volcanic centres erupt through a range of styles including Violent Strombolian (e.g., Naranjo et al., 1992; Pioli et al., 2008) and Vulcanian (e.g., Yamagishi and Feebrey, 1994; Kimura et al., 2005; Zobin et al., 2015; Bain et al., 2018; Nakada et al., 2019), and often lead to the production of lava domes, (e.g., Sparks et al., 1998; Herd et al., 2005; Kimura et al., 2005). Such eruptions can produce eruption columns up to 20 km high (Cas and Wright, 1987) and lava flows with viscosities up to 10^5 PaS (e.g., Naranjo et al., 1992).

Few fissure eruptions with a basaltic trachyandesite or trachyandesite composition have been described in the literature (e.g., Belousov et al., 2015; Gansecki et al., 2019). The 2012-2013 basaltic trachyandesite fissure eruption at Tolbachik had Hawaiian, Strombolian and Phreatomagmatic phases (Edwards et al., 2013; Belousov et al., 2015; Volynets et al., 2015). Unlike the DIP, the Tolbachik fissure was ~ 8 km long and the cones were up to 100 m wide (Belousov et al., 2015). Lava flows reached 10 km long from the vents and had an erupted volume of 0.53 km^3 (non-DRE) (Kubanek et al., 2015) and eruption columns attained heights of 6 km (Edwards et al., 2013; Belousov et al., 2015). The Lower East Rift Zone eruption at Kilauea in 2018 produced a fissure, offset from the main fissure, that erupted andesitic magma (55 – 60 wt.% SiO_2). The fissure produced lava fountains, viscous lava flows and explosions (Gansecki et al., 2019). Although rare, other intermediate composition eruptions on Ascension Island have produced lava flows and scoria cones, however, there has been little work on the morphology of the deposits and associated landforms.

In general, as the silica content of the magma increases, eruptions become more complex. Although small in size and length compared to other fissure eruptions (e.g., Belousov et al., 2015; Pederson et al., 2017; Houghton et al., 2019) the DIP shares some similarities with basaltic fissure eruptions, such as spatter deposits and spatter bombs in the cone walls (Fig. 3.7), lava flow fields (Fig. 3.11), scoria-rich proximal tephra fall deposits, and a small plume, evidenced by the dispersal of scoria clasts away from the vent. However, the proximal scoria clasts are blocky, but not fluidal, and the lavas show no evidence of being spatter-fed and clastogenic (e.g., Sumner, 1998). The lava flow fields produced from both the T1 and T3 cones range in volume from 1.9 x10^5 – 2.2 x10^5 m^3 (non-DRE) (table 3.4) which are smaller than flow fields from fissure eruptions at Holuhraun, Iceland, 1.4 x 10^9 m^3 (Pederson et al., 2017) and Mt Etna, Sicily (18.5 x10^6 m^3 (Guest et al., 1987). Two of the lava flow fields at DIP flowed into the sea, and therefore the calculated total erupted volume of 8.9 x 10^5 m^3 is a minimum estimate. The viscosity of the DIP lavas (10^3 PaS) sits within the range expected for basaltic lavas (10^2 – 10^3 PaS (Harris and Rowland, 2015)).

There were also explosive phases during the DIP eruption (Fig. 3.8, 3.9, 3.10). Until recently, explosive eruptions at basaltic/intermediate volcanoes have received relatively little attention (Allen, 2004). The well recorded fissure eruption of Volcan de Tajogaite, La Palma, demonstrates that multiple, contrasting eruption styles can occur at a single time, with vents less than 100 m apart producing contrasting eruption styles (e.g., Carracedo et al., 2022; Pankhurst et al., 2022; Bonadonna et al., 2022). This has implications for the anticipated impacts of future eruptions, such as evacuations on a small island, impacts on infrastructure and roof collapse (e.g., Osman et al., 2022).

Various terminology is used in the literature to describe small-scale explosive activity, some of which include Violent Strombolian (MacDonald, 1973) and Vulcanian (Mercalli and Silvestri, 1891). Small scale Vulcanian explosions produce light grey ash-poor plumes up to 3 km high with minimal ash and ballistic bombs (e.g., Karymsky, Colima and Semeru (Cassidy et al., 2015; Clarke et al., 2015) and are often linked to the failure of a shallow magmatic plug within the conduit (Diller et al., 2006; Clarke et al., 2015). However, the best studied Vulcanian eruptions are those that involve intervals of explosive activity during dome building events (e.g., Isgett et al., 2017 and references therein). The morphology of the ballistic bombs ejected produced during the DIP eruption (Fig. 3.19) are also similar to those from Vulcanian explosions (e.g., Mercalli and Silvestri, 1981; Diller et al., 2006; Bain et al., 2018).

Vulcanian explosions that do not involve magma-water interaction rarely contain lithic clast fragments whereas those that do contain abundant country rock fragments (Heiken and Wohletz, 1987; Clarke et al., 2015). Vulcanian explosions within the Nevados de Chillán Volcanic Complex contained 5 – 10 vol.% lithic clasts and has been linked to phreatomagmatic activity (Naranjo and Lara, 2004), whereas Vulcanian explosions with purely magmatic phases at Sakurajima volcano contained 3 – 5 vol.% lithic clasts (Gabellini et al., 2022). Therefore, small-scale, intermittent phreatomagmatic activity cannot be ruled out as the driver behind the explosive activity at the T2 cones, as water in the aquifer will most likely intermittently interact with the rising magma.

Phreatomagmatic eruptions are common at some point during many eruptions (e.g., Houghton and Schmincke, 1986; Houghton and Schmincke, 1989; Bertagnini and Landi, 1996; Belousov and Belousova, 2001; Kosik et al., 2016), with phreatomagmatic eruptions on ocean islands common (e.g., White and Schmincke, 1999; Pallister et al., 2005; Clarke et al., 2009;). Previous studies on Ascension have identified a range of stratigraphical units, from tuff rings that indicate substantial water-magma interaction (e.g., Preece et al., 2021), to thin 'wet' ash layers that show more intermittent water magma interaction (e.g., Winstanley, 2020; Preece et al., 2021). The increased lithic clasts and presence of finer ash in the distal deposits show that the DIP eruption sits within the range of phreatomagmatic activity identified in Ascension.

The movement of water through faults is a common occurrence (e.g., Gevrek and Kazanci, 2000; Nemeth et al., 2001; Lara and Moreno, 2008; Son et al., 2012; Kosik et al., 2016). Given the suspected reactivation of a fissure along a fault line in the DIP region, the interaction of water and magma along the faults to aid the more explosive eruptions cannot be ruled out.

3.8 Eruption Reconstruction

At the DIP fissure, magma rose through the crust in dikes. The DIP fissure runs parallel to another fissure, sits directly above a trachyte lava flows and is aligned with an older, basaltic scoria cone, therefore, it is likely that there was a pre-existing feeder system that reactivated, with dikes propagating along faults (e.g., Valentine and Krogh, 2006; Thiele et al., 2021) before localising as sheet dykes (e.g., Valentine and Krogh, 2006; Burchardt et al., 2011; Tibaldi et al., 2013; Tibaldi, 2015; Reynolds et al., 2016; Burchardt et al., 2018) and allowing the magma to reach the surface. The presence of inactive areas between the cones (Fig. 3.2b) also suggests that the magma followed specific routes to the surface.

The DIP fissure eruption was characterised by predominantly lava fountaining, which constructed small spatter cones and dispersed scoria lapilli and ash away from the vents (Fig. 3.26a). Seven of the cones produced paroxysmal explosions (Fig. 3.26c,d), excavating down into the underlying country rock and ejecting ballistic bombs up to 600 m from the fissure. The proximity of cones and shared crater walls showed that multiple cones erupted simultaneously. A single paroxysmal explosion through a debris fan generated a short-lived pyroclastic flow that travelled less than 80 m away from the vent.

Lava flows at 11 cones were syn-erupted with the lava fountaining and produced a minimum total erupted volume of 8.9×10^5 m^3. The complex lava flow fields indicate that multiple lava flows were effusing at the same time (Fig. 3.11) and occupy paleotopographic depressions in the country rock (e.g., Fig. 3.14). Lava flows from FF3 flowed into the sea and created a lava delta (Fig. 3.16). Two cones underwent more explosive activity (Fig. 3.26b), related to the breakup of a shallow plug, ejected ballistic bombs and lithic clasts and generated higher plumes that deposited pumice and dense clasts up to 600 m from the fissure. The plugs formed as either the magma stagnates in different areas, or the conduit becomes clogged, and material accretes onto the sides. The pressure from the ascending magma caused the plugs to break, creating more explosive and wider cones, evidenced by the range in lithic clasts.

Due to limited preservation and proximity to the coast, there is little indication of the plume height and more widespread distribution of the fall deposits. The deposits described, are those seen on the surface of the fissure and can be said to represent the end members of the eruption. The DIP eruption was one single eruption, evidenced by the lack of soils. There is a lack of chronological links between the deposits, however, the detailed morphology and deposit characterisation allows gaps to be filled by modern observations.

The DIP eruption was short-lived. The absence of a single, built-up edifice, the minimal spatter deposits and the small, low angled cones, and small lava flows shows that activity along the fissure was short lived and declined rapidly. The lack of infill in adjacent craters is evidence that the activity in the adjacent cones was not sustained for long periods of time. Turbeville (1992) showed that the eruption of Pitagoliano, Latera Caldera, built up ~15 – 20 m of spatter proximal to the vent in 5 – 6 hours, based on the minimum accumulation rates needed for efficient agglutination (Sparks and Wright, 1979).

DIP cones built up to 20 m above the underlying country rock (e.g., Fig. 3.9, 3.10 and produced a minimum total erupted volume of 8.9 x 10^5 m^3. Lava flows range in length from 0.12 – 0.63 km and the lava flow fields cover areas ranging from 0.03 – 0.12 km^2 (Fig. 3.11). In comparison, the main cone from the Tajogaite eruption, La Palma grew to 130 m high in 4 days (Carracedo et al., 2022; Romero et al., 2022), lava flows advanced up to 3.7 km per day and 5.75 km in 9 days (Pankhurst et al, 2022; Romero et al., 2022), and covered an area of 12 km^2 by the end of the eruption (Carracedo et al., 2022; Romero et al., 2022). The first phase of the Fagradalsfjall eruption, Iceland, lasted 9 days and during that time, the lava flows reached lengths of ~0.6 km and covered an area of 0.33 km^2 (Pedersen et al., 2022). Activity during this time changed from multiple eruptive vents to focusing on two vents (Eibl et al., 2022), but no heights of the two cones could be found in the literature. After 2 months, eruptive activity was confined to a single vent and the cone built up to more than 100 m above the pre-eruption surface (Bindeman et al., 2022; Eibl et al., 2022). Therefore, it can be assumed that the DIP eruption likely lasted no more than a week. However, without knowing effusion rates, this time frame should be only weakly considered.

The DIP eruption was a hybrid eruption, that emitted effusive products (e.g., lava flows) and explosive products (e.g., tephra blankets, PDC's, scoria cone) that resulted from changing eruption styles (Bonadonna et al., 2022 and references therein). Hybrid eruptions are common in long-lived eruptions where eruption dynamics vary depending on magma supply rates and fragmentation mechanisms (e.g., Valentine and Gregg, 2008; Pioli et al., 2008; Cioni et al., 2008; Bonadonna et al., 2022). Shifts in eruption styles and activity occurring at multiple vents during hybrid eruptions makes it difficult to classify based on traditional strategies, e.g., VEI (Newhall and Self, 1982) and erupted products (Walker, 1973; Valentine and Gregg, 2008; Bonadonna et al., 2022).

3.9 Conclusions

The Devil's Ink Pot fissure eruption is a small volume fissure eruption that demonstrated three different eruption styles:

a) Lava fountaining, evidenced by moderately agglutinated to densely welded spatter deposits, scoria clast-rich fall deposits and the generation of lava flows.

b) Explosive activity, evidenced by loose to weakly agglutinated lapilli and bomb clasts, ballistic bombs, lithic clast rich talus slopes and pumice and lithic clast rich fall deposits. Although minimal evidence, water-magma interaction cannot be ruled out as a driver for this more explosive activity.

c) Paroxysmal explosions followed by lava fountaining, evidenced by deep rooted cones, exposing up to 40 m of underlying country rock, ballistic bombs, moderately agglutinated to densely welded spatter deposits and in some places, the generation of small volume lava flows.

The range of eruption styles produced in the DIP eruption bridge those typical of both basaltic and silicic eruptions which presents a much wider range of hazards, including lava flows, ballistic bomb ejecta, pyroclastic flow deposits and pyroclastic fall deposits of different components. Intermediate composition fissure eruptions are rarely seen or described and therefore are most likely underrepresented in the geological record. However, the fact that the DIP eruption mostly presents like a basaltic fissure eruption, with spatter deposits and spatter bombs in the cone walls, lava flow fields with viscosities within the expected range of basaltic lavas (e.g. Harris and Rowland, 2015), scoria-rich proximal tephra fall deposits, and a small plume, evidenced by the dispersal of scoria clasts away from the vent, suggests that planning on Ascension Island for a basaltic eruption scenario could be applied to a future DIP style eruption, but geochemical and petrological analysis integrated within is needed to identify the eruption scenario for effective response.

Chapter 4: Quantitative textural analysis and shallow magma processes

4.1 Introduction

For unwitnessed volcanic eruptions, pyroclastic deposits play a key role in reconstructing eruption styles, modes of transport and deposition, fragmentation mechanisms and dispersal (e.g., Ross et al., 2022), but they can also provide insight into eruption dynamics such as magma ascent and vesiculation (Ross et al., 2022). Ascent rates are an important parameter that influence eruption scenarios (Martel and Schmidt, 2003; Lormand et al., 2021). The style of magma ascent and syn-eruptive degassing during ascent plays a large role in determining the style of eruption (Preece et al., 2013; Preece et al., 2023) and understanding the processes and timescales of magmatic storage and ascent processes is vital for understanding eruption triggers and for volcano monitoring (Kilgour et al., 2014; Lormand et al., 2021). Within the conduit there are multiple parameters that interact in order for the magma to rise to the surface. Some of these include volatile solubility, water and carbon dioxide contents, bubble coalescence, permeable outgassing and crystal nucleation and growth (e.g., Wallace, 2005; Zhang et al., 2007; Gonnerman and Manga, 2013; Ripepe et al., 2021). Conduit dynamics also play a large role in controlling the ascent rates, with conduit widening causing magma acceleration (Vitturi et al., 2008).

During ascent, groundmass crystallisation occurs due to decompression-induced degassing, and microlite textures can record snapshots of magmatic processes in time (Frey et al., 2024). Textural and compositional analysis of the microlites provide an ideal way to gain a better understanding of the magma ascent and the degassing processes (Cashman and McConnell, 2005; Preece et al., 2013; Preece et al., 2016; Frey et al., 2024). Crystal size distribution (CSD) analyses can be used to identify any changes in crystallisation conditions prior to eruption (Cashman, 1992; Higgins, 1996; Hammer et al., 1999; Lormand et al., 2021; Mangler et al., 2022; Frey et al., 2024). Crystallisation can occur through nucleation of new crystals or by growth of existing crystals (Blake, 2000). Nucleation is dominant when the degree of undercooling (ΔT) is high. Undercooling is defined as the difference between the temperature of the liquidus and the temperature of the magma (Preece et al., 2023) whereas the growth of pre-existing crystals occurs when the degree of undercooling is low (Hammer, 2004; Befus and Andrews, 2018), but the observed textures depend on the amount and rate of decompression (Cashman and Blundy, 2000; Blake, 2000; Befus and Andrews, 2018). Larger, tabular microlites form during slow decompression with average growth rate decreasing exponentially (Brugger and Hammer, 2010; Befus and Andrews, 2018), whilst skeletal and/or acicular microlites form as decompression rates increase (Brugger and Hammer, 2010; Arzilli et al., 2015).

In this chapter, I combine analysis of microlite abundances, textures, and compositions in a range of deposits from the trachyandesite DIP magma. By combining 2D and 3D feldspar microlite textures and chemical compositions, in addition to and amphibole textures, I elucidate the shallow magma storage and ascent conditions. These findings contribute to an understanding of the magmatic processes that led to the variation in eruption styles identified in chapter 3 and the evolution of the DIP system during a single eruption.

4.2 Methods

4.2.1 Componentry

Componentry analysis of the individual layers of the tephra fall deposits was undertaken to identify differences in the tephra fall deposits, described in chapter 3, in order to link them to eruption styles. For each layer, 400 juvenile clasts (or the whole sample where there was not 400 clasts) were randomly picked from the -3ϕ and -2ϕ size fractions. They were then grouped based on their physical characteristics: colour, shape and vesicularity (Eychenne and Le Pennec, 2012). 100 lithic clasts (or the whole sample where there was not 100 clasts) were randomly picked from the -6ϕ - -2ϕ size fractions. The larger size fractions were included for the lithic clasts as they were easily identifiable and important for linking individual units.

4.2.2 Petrology & Geochemistry

Thin sections of 25 spatter and lava samples were made at Durham University. Nine tephra samples were also made into thin sections by mounting the clasts into resin. The nine tephra samples represented the initial components (1) golden scoria, (2) transitional scoria, (3) black scoria, (4) black pumice, (5) transitional pumice, (6) pumice, (7) breadcrust textures (8) dense clasts, (9) banded clasts. Further analysis, including visual inspection and petrography allowed for the grouping of these components into the three main groups described below (1) scoria, (2) pumice, (3) dense clasts. Only one of each type was mounted onto a thin section and therefore no comparisons can be made to textures based on distance from vent.

Images were taken using a Zeiss microscope in the Durham University microscopy lab and the Hitachi SU-70 Scanning Electron Microscope (SEM) in the Durham University Physics Department.

Analysis of feldspar microlite chemical compositions was undertaken using EPMA. Full methods for the geochemical and petrological analysis, including standards and accuracy/precision is in chapter 5.

4.2.3 2D and 3D Textural Analysis of Crystals

4.2.3.1 Samples and Image Collection

Data acquisition for the microlite textural analysis was done following the method of Preece et al., 2013. Seven samples were selected for the textural study (table 4.1, Fig. 4.1). On visual inspection, groundmass textures for the spatter and lava were relatively uniform, with the exception of lava samples with dark and light bands (normal lava), therefore the chosen samples were representative of the textural variations. From here in, the term normal lava is given to the typical and common textures seen within the lava samples. Dark lava bands is the term given to the thinner, less common, darker bands seen within some of the lava samples. Groundmass montages were created on the Hitachi SU-70 SEM by using the automation feature on Aztec 2.0. The SEM was used with a voltage of 15.0 kV and a working distance of 15.00 mm. Images were taken using the backscatter detector. The magnification was set to x400 and the grid sizes between 1.0 x 1.0 mm to 2.0 x 2.0 mm depending on the vesicularity and phenocryst content of the sample, to ensure enough groundmass crystals were captured (n = >700).

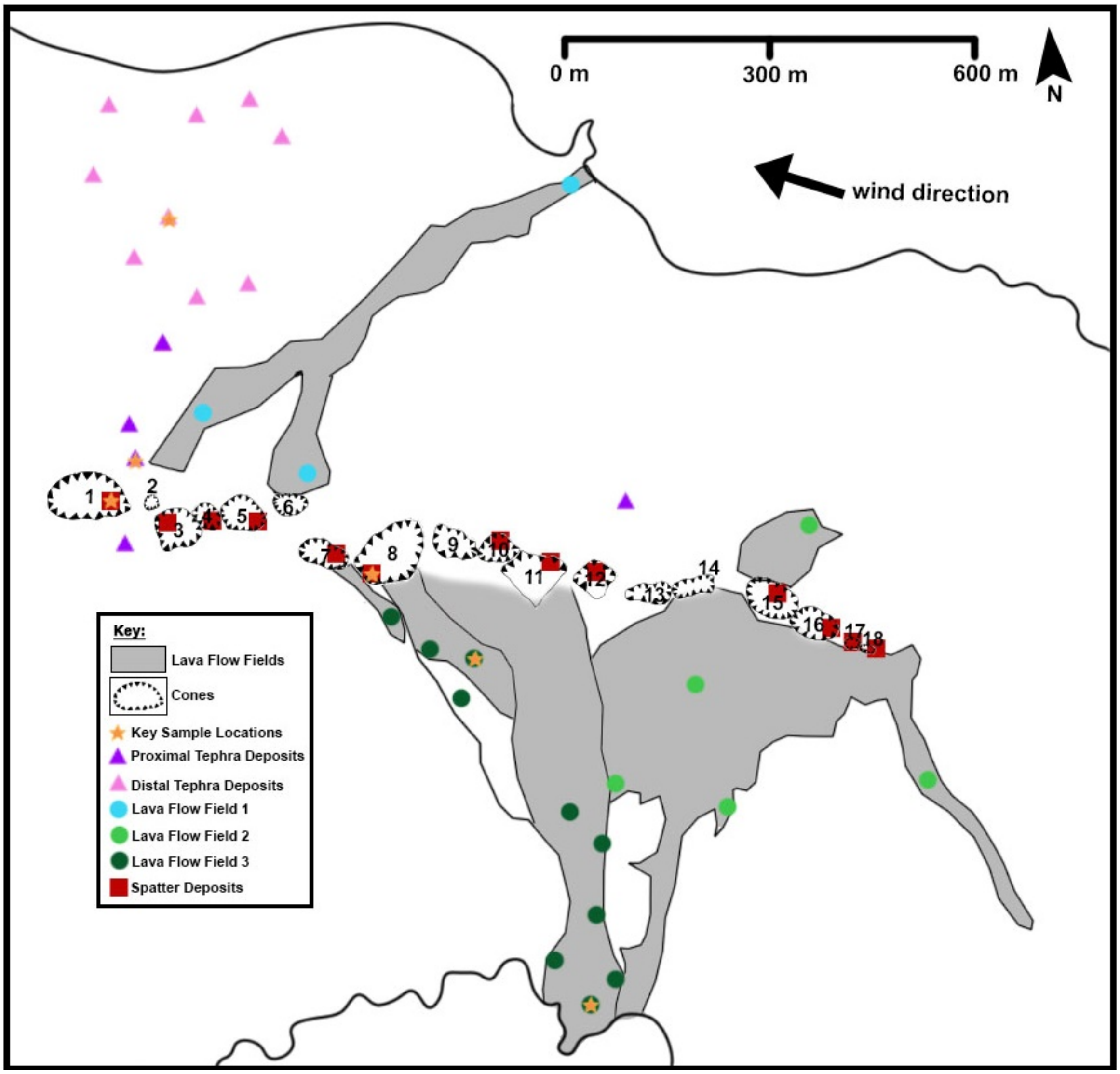

Figure 4.1: *Map showing the sample locations from the study. The stars represent the key sample locations, and the eight deposits used in the textural study.* The coloured symbols represent the deposits.

Sample No.	***Loc.***	***Sample Type***	***Analysis***	***Grid Ref.***
AI-19-008	Cone 1	*Spatter*	EPMA; CSD	*0575924, 9121450*
AI-19-121	Cone 8	*Spatter*	EPMA; CSD	*0576339, 9121425*
AI-10-026	F6; FF3	*Lava*	EPMA; CSD	*0576508, 9121239*
AI-19-028	F7; FF3	*Lava*	EPMA; CSD	*0576513, 9121149*
AI-19-028	F7; FF3	*Lava – dark bands*	EPMA; CSD	*0576513, 9121149*
DIP-3	Proximal fall deposit	Scoria Clasts	EPMA; CSD	*0575955, 9121622*
DIP-5	Distal fall deposit	Pumice Clasts	EPMA; CSD	*0575995, 9121929*
DIP-8	Distal fall deposit	Dense Clasts	EPMA; CSD	*0575995, 9121929*

Table 4.1: Table *showing the samples selected for analysis and description of each sample, including type of sample, location and type of analysis conducted. Loc. – location, F – lava flow, FF – lava flow field, EPMA – electron microprobe analysis, CSD – crystal size distribution. Proximal deposits are less than 100 m from the fissure. Distal deposits are more than 100 m from the fissure. Map showing the locations of each sample can be seen in* ***Fig. 4.1.***

4.2.3.2 Digitising Process

SEM images were imported into Adobe Fresco in order to digitise them. Plagioclase microlites were outlined and filled using an iPad, Apple Pencil, and the Adobe Fresco (Fig. 4.2). Past studies suggested that in order to gain accurate 3D shapes of the crystal population, where the true shape is unknown, the number of measured crystals must be greater than 200 (Mock and Jerram, 2005) or 250 (Morgan and Jerram, 2006). However, a study by Preece et al., (2013) found that at least 600 crystals should be analysed, and therefore in this study the number of crystals range from 750 – 3800.

4.2.3.3 2D Shape Analysis

ImageJ was used to calculate crystal dimensions, individual crystal area, mean crystal area, % area occupied by the feldspars, vesicles, and mafic phases (olivine, pyroxene, and Fe-Ti oxides), and total area. Crystal dimensions were measured using the best fit ellipsoid method. The digitised crystal outline images were opened in ImageJ and the image was converted to an 8-bit greyscale image and a threshold was set to include all the crystals and make a binary image. The scale and area to be measured (excluding the scale bar) were identified and the measurements to be made were defined by selecting the commands: Area, Fit Ellipse, Centroid, Limit threshold to 2 decimals. The crystals were then analysed by selecting the commands: Show outlines, display results, Clear results, Summarize, Exclude on edges and Record starts. Excluding edges ensured that no partially included crystals were analysed. ImageJ then output a results table with the major and minor crystal axis, which was exported as a .csv file for CSDSlice (Morgan and Jerram, 2006) and ShapeCalc (Mangler et al., 2022) and a .csd file for CSDCorrections, using the CSD Output plugin.

4.2.3.4 2D to 3D conversion

CSD's convert the 2D crystal measurements into 3D and therefore the 2D length and width must be converted into 3D long (L), intermediate (I), and short (S) axis. CSDSlice

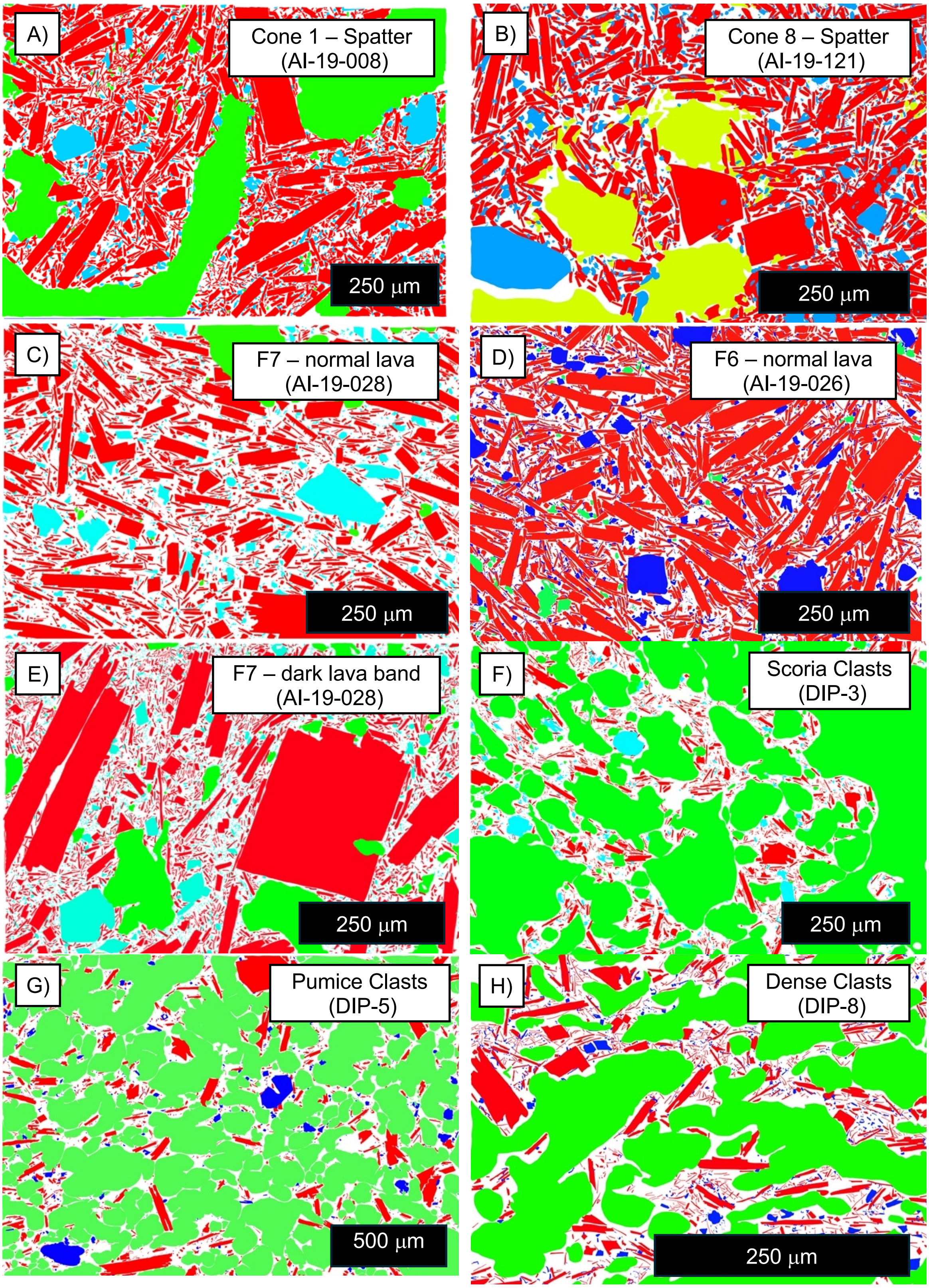

Fig. 4.2: *Representative images of the different groundmass microlites used in the CSD study. Images are digitised from back scattered electron images. Red represents feldspar microlites, shades of blue represent olivine, clinopyroxene and Fe-Ti oxides, shades of green represent vesicles and white areas indicate groundmass glass.*

(Morgan and Jerram, 2006) and ShapeCalc (Mangler et al., 2022) are both models that can do this. CSDSlice compares the measured 2D w/l dimensions to a database of 703 model w/l dimensions for 3D shapes, from 1:1:1: to 1:10:10 and identifies the five best S:I:L estimates based on a best fit test on the mode of the distribution (Morgan and Jerram, 2006; Mangler et al., 2022). The best fit should produce an R^2 value of >0.8.

ShapeCalc uses 2D width-length data to estimate 3D crystal shapes. The model compares the measured dimensions with 2618 model w/l dimensions from 1:1:1 to 1:20:20 and identifies the best match by maximising the cumulative measure of the goodness of fit (Mangler et al., 2022). The best fit should produce an R_c^2 value of >0.975, and lower values show poor model fits (Mangler et al., 2022). For ShapeCalc, the length-width datasets were grouped into bins based on crystal length with $L = 0 – 4.9$ μm, 5 – 9.9 μm, 10 – 29.9 μm, 30 – 99.9 μm and >100 μm. These bins ensure sufficient crystal intersection data for 3D shape modelling and allows for direct comparisons between samples (Mangler et al., 2022).

4.2.3.5 3D Shape Analysis

The crystal size distribution (CSD) is described as “the number of crystals of a mineral per unit volume within a series of defined size intervals” (Higgins, 2006). A CSD plots the population density against crystal size, with many systems plotting on straight lines, and therefore, the slope of the line can be used to calculate growth rate (G) or crystal residence time (τ) (Higgins, 2006).

$$slope\ (\alpha) = -1/G\tau \qquad (1)$$

CSDCorrections (Higgins, 2000) was used to perform stereological calculations on the 2D crystal data from each image and calculate the 3D crystal size distribution (CSD). The crystal shape is the crystal habit calculated using ShapeCalc and the rock fabric is massive. The 3D data was binned into 5 groups, based on the recommendations of Higgins, (2000) and any bins with less than 5 data points were removed to reduce the intersection probability effect (Brugger and Hammer, 2010a; Miwa et al., 2013; Preece et al., 2013; Bain et al., 2019).

4.3 Results

4.3.1 Componentry of Tephra Deposits

Componentry analysis led to the identification of 3 different types of juvenile tephra clasts. These are grouped as scoria, pumice, and dense clasts. Lithic clasts were also identified throughout the fall deposits and have been linked back to the lithic clasts and underlying geology described in table 3.2.

The scoria clasts (Fig. 4.3a) are a pale brown to black in colour and up to 64 mm in diameter. The pyroclasts range from jagged to sub-angular, elongate, and blocky shaped, with the black end member also exhibiting weakly fluidal shapes. The surfaces of the black scoria clasts are characterised by a thin, fluidal glassy skin that covers the vesicular interior, whereas the pale brown scoria clasts have no skin. Elongate ridges and surface mounds cover the vesicles and individual vesicle filaments can be seen. The surfaces of the clasts

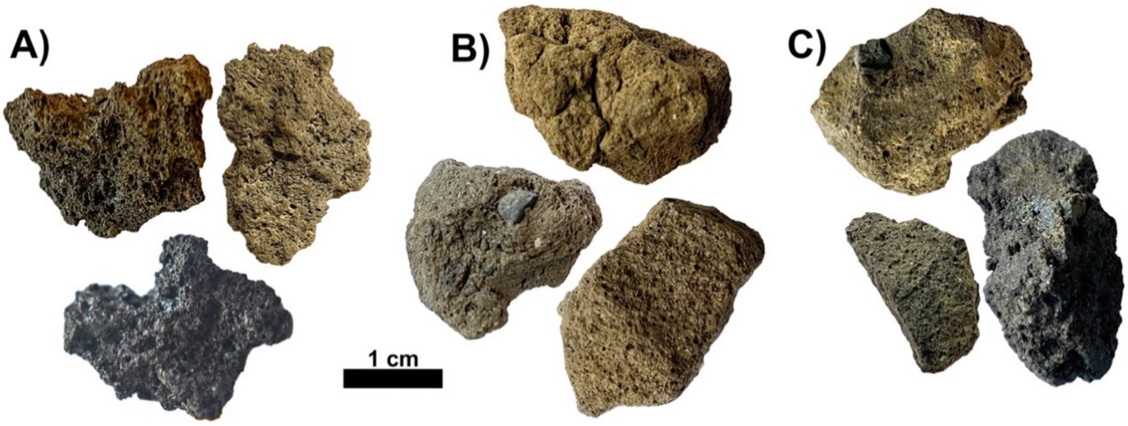

Figure 4.3: *Close up images of the different pyroclast morphologies.* ***A)*** *Black and brown scoria clasts* ***B)*** *Pumice clasts, exhibiting breadcrust texture and adhered lithic clasts.* ***C)*** *Dense clasts.*

are lightly covered in fine, <10 μm in diameter, spherical to elongate precipitates and rare fragments up to 50 μm in diameter, that protrude out from the surface. These clasts are both moderately to highly vesicular (terminology from Houghton and Wilson, 1989), with vesicularity ranging from 60 – 83%. Vesicles are up to 2000 μm in diameter and are mostly randomly distributed, sub-rounded and irregular shaped. There are also some bands of weakly aligned, elongate, irregular shaped vesicles. Individual vesical filaments can sometimes be seen, more so in the black pyroclasts than the brown.

The pumice clasts (Fig. 4.3b) are pale brown colour, up to 64 mm in diameter and sub-angular, elongate, or blocky. The surfaces of the pumice clasts can either exhibit a weak, wrinkly breadcrust texture, covering a vesicular interior or a microvesiuclar texture. The surfaces of both textures are characterised by a smooth exterior, with a honeycomb texture and a complex network of vesicles that are surficial or extrude deeper into the samples. Surface vesicles are smaller than 80 μm in the breadcrust texture and 500 μm in the microvesiuclar texture. The breadcrust texture also exhibits surface cracks up to 500 μm wide. In both textures, the surfaces are heavily covered fine (<10 m in diameter), spherical or blocky precipitates and angular ash fragments. Lithic clasts can be seen adhered onto the surface of a number of the breadcrust textured clasts. The pumice pyroclasts are moderately vesicular, with vesicularity ranging between 60 – 70%. Vesicles are up to 1500 μm in diameter and range from randomly distributed, sub-rounded and irregular shaped, to elongate, irregular shaped and weakly aligned. The larger, elongate vesicles formed by coalescence of multiple, smaller vesicles and individual vesicle filaments can sometimes be identified.

The dense clasts (Fig. 4.3c) are aphyric, dark grey/black colour, range in shape from angular to sub-rounded and equant and are up to 64 mm in diameter. The surfaces of the dense clasts are smooth with surficial, rounded vesicles up to 300 m in diameter. The surfaces are heavily covered with fine (<10 m in diameter), spherical or blocky precipitates and angular ash fragments. The dense clasts are poorly vesicular, with vesicularity ranging between 10 – 50%. Vesicles are up to 700 μm in diameter and are elongate, irregular shaped or sub-rounded and weakly aligned.

The abundance of the different pyroclasts varies throughout the deposits, based on proximity to the vents. The three described components are seen throughout all the size fractions within each unit. Scoria clasts are most abundant in the proximal deposits and rare in the medial/distal deposits. Pumice clasts and dense clasts are most abundant in the medial/distal deposits and rare in the proximal deposits.

4.3.1.1 Proximal Deposits

The proximal deposits are defined as any deposit within 200 m of the fissure and include Unit's I-IV (Fig. 4.4). Unit I is a pyroclastic flow deposit, whilst Unit's II – IV are pyroclastic fall deposits. In the pyroclastic fall deposits and the pyroclastic flow deposit scoria clasts are most abundant, ranging from 38 – 85 vol.%. Pumice clasts, dense clasts and lithic clasts ash are generally less abundant and range from 0 – 21 vol.% and 4 – 19 vol.%, respectively. However, pumice clasts, dense clasts and lithic clasts are more abundant in the pyroclastic flow deposits (7 – 21 vol.%, 15 – 17 vol.% and 26 – 28 vol.% respectively), compared to the pyroclastic fall deposits (0 – 13 vol.%, 4 – 19 vol.% and 1 – 20 vol.%, respectively). The abundance of scoria clasts and dense clasts decreases away from the fissure, whilst the abundance of pumice clasts and lithic clasts increases.

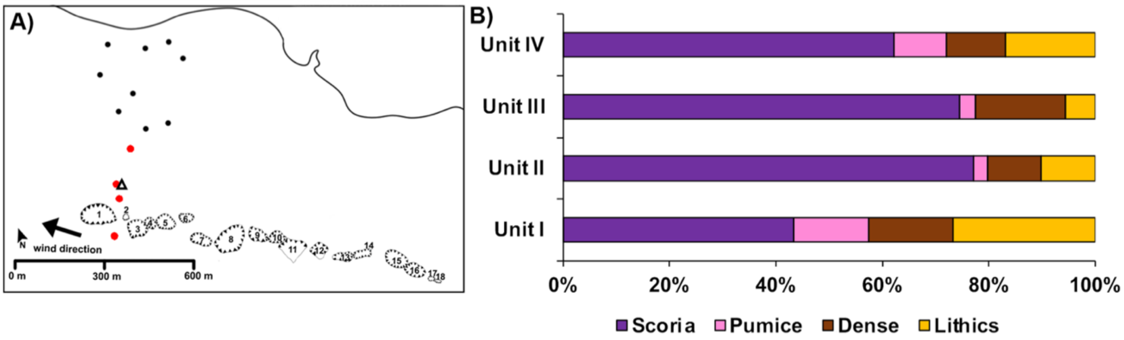

Figure 4.4: ***A)*** *Map showing the location of the proximal tephra deposits (red dots). The black triangle shows the location of the pyroclastic flow deposit (Unit I).* ***B)*** *Total componentry distribution for the Unit's I – IV found within the proximal deposits. The graph shows scoria clasts are most abundant, whilst pumice clasts, dense clasts and lithic clasts are less abundant.*

Unit I

Unit I is only identified at one locality and has been interpreted as a pyroclastic flow. The unit is made up of two beds of fine grained, sub-rounded and medium grained, sub-angular, dense, pumice and scoria lapilli to coarse ash and sub-angular lithic clasts up to 16 mm in diameter. Scoria clasts and pumice clasts have a relatively wide range in abundance from 38 – 48 vol.% and 7 – 21 vol.%, respectively (Fig. 4.5). Whilst, dense clasts and lithic clasts exhibit a narrower range, from 15 – 17 vol.% and 26 – 28 vol.%, respectively (Fig. 4.5). The lower bed (1.1) is composed of more pumice clasts, whilst the upper bed (1.2) is composed of more scoria clasts, dense clasts, and lithic clasts (Fig. 4.4).

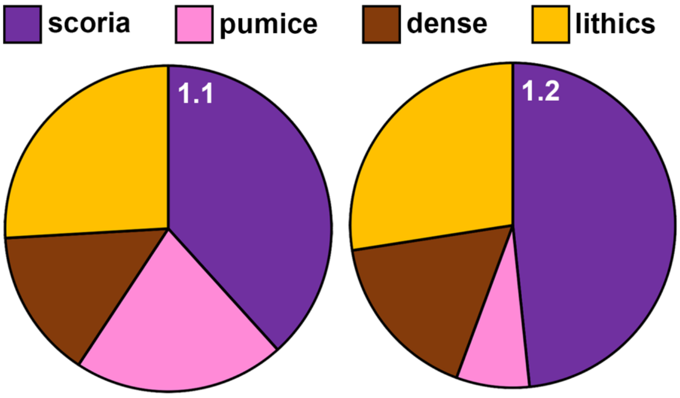

Figure 4.5: *Pie charts show the total percentage of the different clast types for Unit I, the pyroclastic flow deposit. Scoria clasts are most abundant with varying abundances of pumice, dense and lithic clasts.*

Unit II

Unit II is composed of coarse scoriaceous blocks, sub-rounded medium to coarse scoria lapilli and rare pumice and dense clasts, and angular lithic clasts up to 16 mm in diameter. Scoria clasts are the most abundant, ranging from 69 – 85 vol.% and decrease away from the fissure (Fig. 4.6). Pumice clasts are not seen in the most proximal deposits but are up to 5 vol.% away from the fissure (Fig. 4.6). Dense clasts show a narrow range, from 9 – 11 vol.%, but decrease slightly in abundance away from the fissure (Fig. 4.6). Lithic clasts show a similar pattern, ranging from 4 vol.% in the most proximal deposit and up to 16 vol.% away from the fissure (Fig. 4.6).

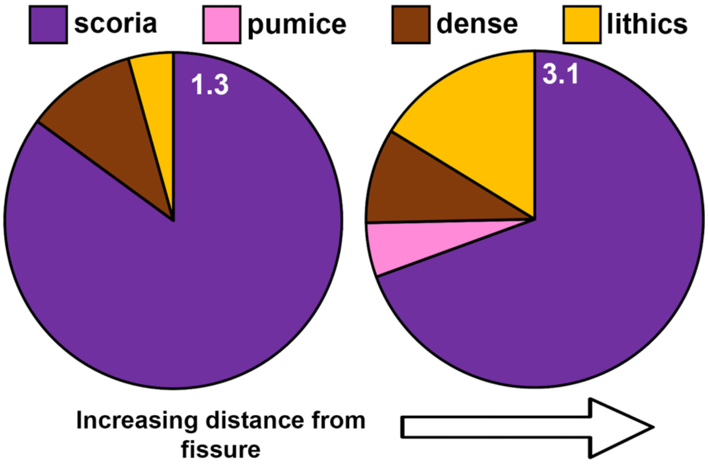

Figure 4.6: *Pie charts show the total percentage of the different clast types identified in Unit II at different localities. Scoria clasts are the most abundant with pumice clasts, dense clasts and lithic clasts abundances increasing away from the fissure.*

Unit III

Unit III and is composed of fine, sub-rounded and medium, sub-angular, dense, pumice and scoria lapilli to coarse ash and angular lithic clasts up to 16 mm in diameter. Unit III exhibits a similar componentry distribution to Unit II (Fig. 4.7). Scoria clasts are the most abundant, ranging from 68 – 82 vol.% and decrease away from the fissure (Fig. 4.7). Pumice clasts are not seen in the most proximal deposits but are up to 6 vol.% away from the fissure (Fig. 4.7). Dense clasts exhibit a narrow range, from 17 – 17 vol.% but decrease in abundance away from the fissure, whereas lithic clasts range from 1 – 10 vol.% and increase away from the fissure (Fig. 4.7).

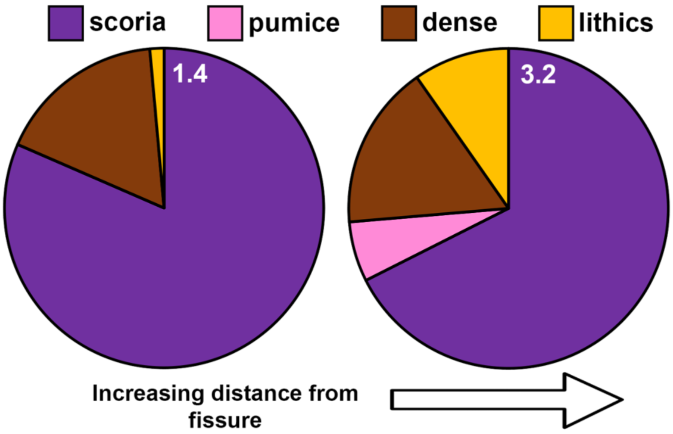

Figure 4.7: *Pie charts show the total percentage of the different clast types identified in Unit III at different localities. Scoria clasts are the most abundant with pumice clasts, dense clasts and lithic clasts abundances increasing away from the fissure.*

Unit IV

Unit IV is composed of sub-rounded medium to coarse scoria, rare dense and pumice lapilli clasts and angular lithic clasts up to 16 mm in diameter. Scoria clasts are still the most abundant, ranging from 54 – 70 vol.%, however, the abundance increases away from the fissure (Fig. 4.8). Pumice clasts range in abundance from 7 – 13 vol.% and increase away from the fissure (Fig. 4.8). Dense clasts and lithic clasts range from 4 – 19 vol.% and 14 – 20 vol.%, respectively, and decrease away from the fissure (Fig. 4.8).

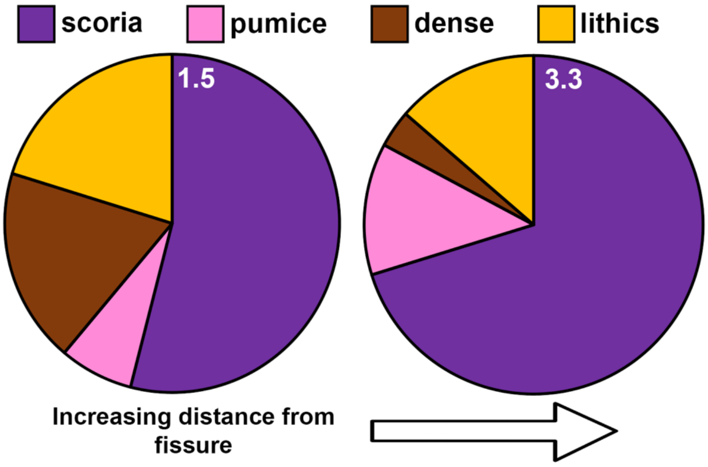

Figure 4.8: *Pie charts show the total percentage of the different clast types identified in Unit IV at different localities. Scoria clasts are most abundant with pumice clasts increasing and dense and lithic clasts decreasing away from the fissure.*

4.3.1.2 Distal Deposits

The distal deposits are defined as any deposit between >200 – 600 m from the fissure and include Unit's V – VIII (Fig. 4.9). All of the distal deposits are pyroclastic fall deposits. Pumice and dense clasts are most abundant throughout the units, ranging from 25 – 75 vol.% and 9 – 42 vol.%, respectively, whereas scoria clasts range from 0 – 26 vol.%. There is a negative correlation between pumice clasts and scoria clasts. As the abundance of scoria clasts decreases, the abundance of pumice clasts increases and the distance from the fissure has no influence on this correlation. Scoria clasts are more abundant in the deposits closest and furthest from the fissure. The abundance of dense clasts decreases away from the fissure. Lithic clasts abundances range from 10 – 22 vol.% and increase away from the fissure.

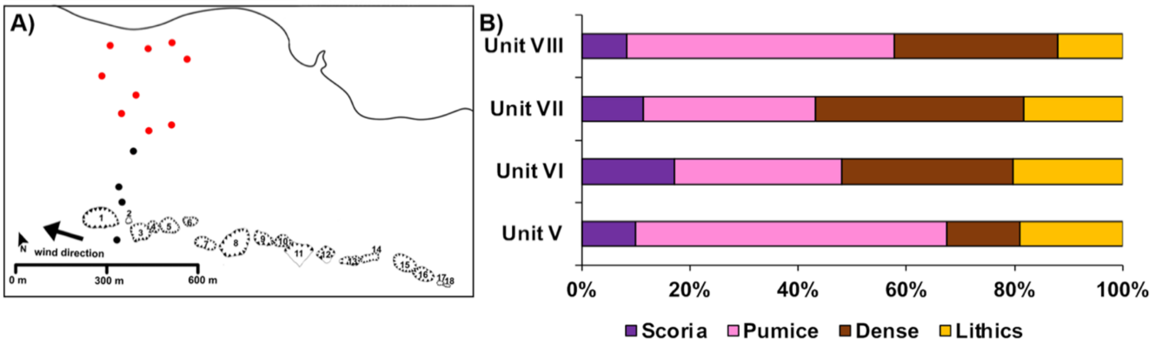

Figure 4.9: A) *Map showing the location of the distal tephra deposits (red dots).* ***B)*** *Total componentry distribution for the Unit's V – VIII found within the distal deposits. The graph shows pumice clasts, dense clasts and lithic clasts are most abundant, whilst scoria clasts are less abundant.*

Unit V

Unit V is composed of sub-angular coarse ash, fine to medium pumice lapilli, medium pumice and scoriaceous blocks and lapilli, and angular lithic clasts up to 16 mm in diameter. Scoria clast abundances range from 0 – 22 vol.%, with the abundance generally decreasing away from the fissure, but with a slight increase from 0 – 7 vol.% at the furthest point from the fissure (Fig. 4.10). Pumice clast abundances range from 41 – 75 vol.% and generally increase away from the fissure, but with a slight decrease from 75 – 49 vol.% at the furthest point from the fissure (Fig. 4.10). Dense clast abundances range from 9 – 20 vol.% and decrease in abundance away from the fissure (Fig. 4.10). Lithic clasts abundances show minimal range, from 18 – 21 vol.% and fluctuate away from the fissure (Fig. 4.10).

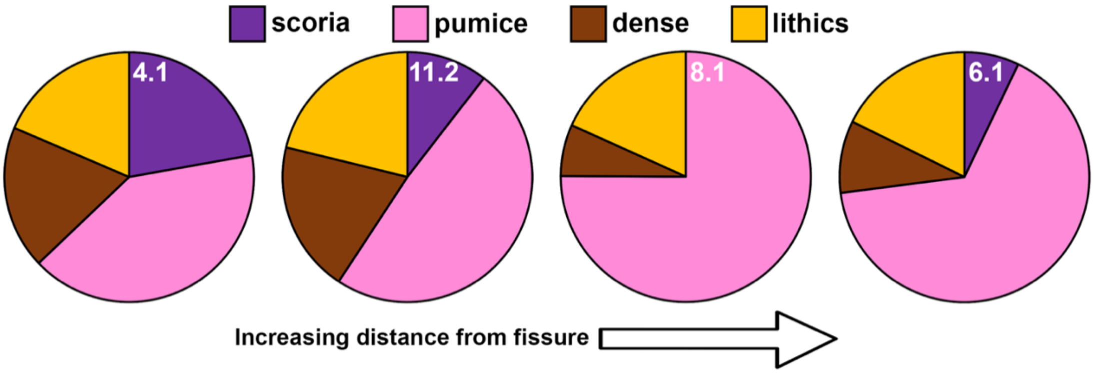

Figure 4.10: *Pie charts show the total percentage of the different clast identified in Unit V at different localities. Pumice clasts increase away from the fissure whilst dense clasts, lithic clasts and scoria clasts decrease.*

Unit VI

Unit VI is composed of denser, sub-rounded medium pumice, dense, and rare scoria lapilli, rare coarse ash, and angular lithic clasts up to 16 mm in diameter. Scoria clast abundances range from 9 – 26 vol.% (Fig. 4.11). The abundance is consistent at 13 vol.% and then increases up to 26 vol.% away from the fissure. Pumice clast abundances range from 25 – 36 vol.%. The abundance of pumice clasts fluctuates, with the greatest vol.% (35 – 36 vol.%) closest to the fissure and a slightly lower vol.% away from the fissure (25 – 31 vol.%) (Fig. 4.11). Dense clast abundances range from 21 – 42 vol.% and generally decrease in abundance away from the fissure (Fig. 4.11). Lithic clast abundances exhibit a narrow range, from 17 – 22 vol.% and increase away from the fissure (Fig. 4.11).

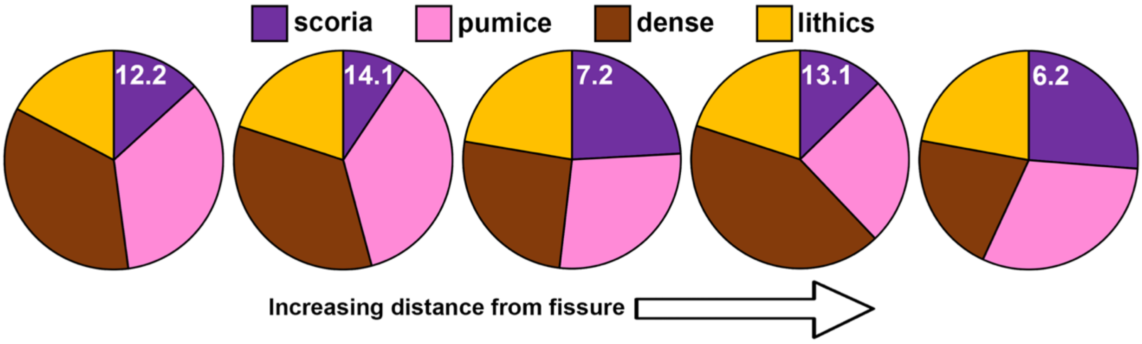

Figure 4.11: *Pie charts show the total percentage of the different clast types identified in Unit VI at different localities. Pumice clasts generally decrease, and scoria clasts increase away from the fissure. Lithic clasts remain consistent throughout and dense clasts fluctuate in abundance.*

Unit VII

Unit VII is composed of sub-rounded fine pumice and dense lapilli, rare fine scoria lapilli and angular lithic clasts up to 16 mm in diameter. Scoria clast abundances range from 10 – 13 vol.% and exhibit a weak increase away from the fissure (Fig. 4.12). Pumice clast and dense clast abundances range from 29 – 34 vol.% and 37 – 41 vol.%, respectively, and exhibit a weak decrease away from the fissure (Fig. 4.12). Lithic clast abundances range from 16 – 21 vol.% and increase away from the fissure (Fig. 4.12).

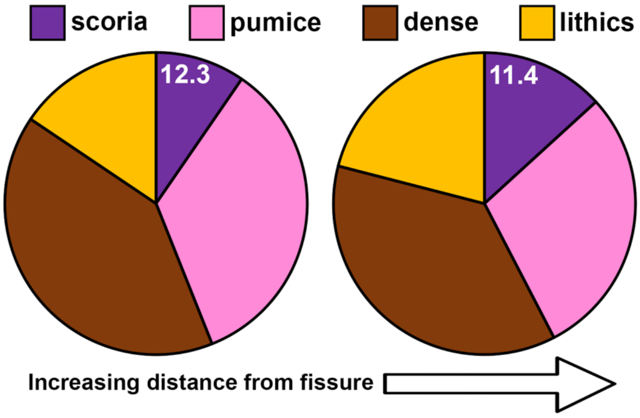

Figure 4.12: *Pie charts show the total percentage of the different clast types identified in Unit VII at different localities. Pumice and dense clasts show similar abundances away from the fissure with increasing scoria and lithic clasts.*

Unit VIII

Unit VIII is composed of sub-rounded fine to medium pumice and dense lapilli, rare fine scoria lapilli and medium to coarse ash, and angular lithic casts up to 8 mm in diameter. Scoria clast abundances range from 0 – 17 vol.% and increases away from the fissure (Fig. 4.13). Pumice clasts range in abundance, from 37 – 63 vol.% and decreases away from the vent (Fig. 4.13). Dense clasts and lithic clasts range in abundance from 28 – 33 vol.% and 10 – 14 vol.%, respectively. Both the vol.% of dense clasts and lithic clasts increases away from the fissure (Fig. 4.13).

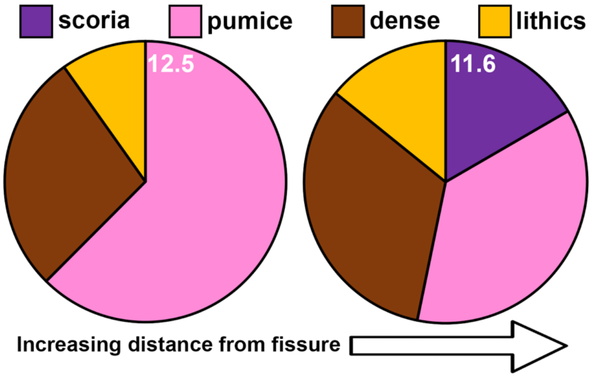

Figure 4.13: *Pie charts show the total percentage of the different clast identified in Unit VIII at different localities. Pumice clasts decrease away from the fissure and dense clasts show similar abundances. Scoria and lithic clasts increase away from the fissure.*

4.3.2 Tephra Petrography

4.3.2.1 Scoria

The scoria clasts (golden-scoria and black scoria) are composed of <1% tabular plagioclase phenocrysts up to 800 μm in diameter, and ~2% tabular and acicular plagioclase microphenocrysts, up to 500 μm in diameter, with ~85% exhibiting internal sieve texture and ~20% exhibiting weak swallow tail textures (Fig. 4.14a,b). Other microphenocryst phases include ~1% subhedral, sub-rounded or tabular olivine crystals, up to 350 μm in diameter,

<1% subhedral, sub-rounded clinopyroxene crystals, up to 300 μm in diameter, <1% elongate amphibole crystals, up to 350 μm in diameter, with no opaque rim and <1% blocky Fe-Ti oxides (Fig. 4.14a,b).

Groundmass textures

The scoria groundmass is hypocrystalline, pale brown, sideromelane glass and composed of plagioclase and rare olivine microlites <100 μm in diameter (Fig. 4.14a,b). Plagioclase microlites are acicular, elongate and ~20% exhibit weak swallow tail texture. Olivine microlites are subhedral, fragmental, or tabular, or anhedral with external resorption with varying degrees of hopper textures. Clinopyroxene microlites are not present in the groundmass.

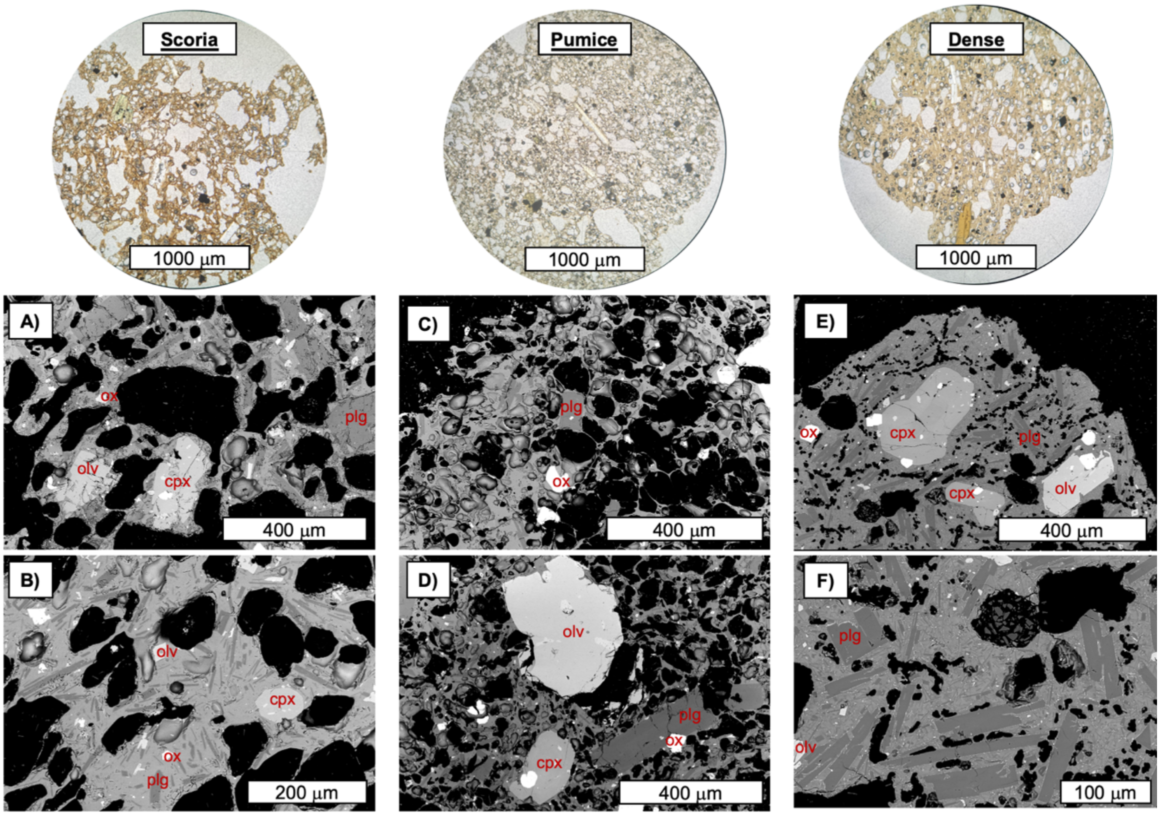

Figure 4.14: *Textural images of the DIP tephra deposits, showing the groundmass textures and the crystal phases Plg – plagioclase, cpx – clinopyroxene, olv – olivine, ox – Fe-Ti oxides. Circles show plane-polarised light (PPL) images of the different tephra deposits.* ***A,B)*** *Back scatter electron (BSE) images of the scoria clasts.* ***C,D)*** *BSE of the pumice clasts* ***E,F)*** *BSE of the dense clasts.*

4.3.2.2 Pumice

The pumice clasts are composed of <1% tabular, plagioclase phenocrysts, up to 800 μm in diameter with ~60-70% exhibiting internal sieve textures and ~2% tabular, plagioclase microphenocrysts, up to 400 μm in diameter, with ~40% exhibiting internal sieve textures and ~45% exhibiting weak swallow tail textures (Fig. 4.14c,d). Other microphenocryst phases include ~1% subhedral or tabular olivine crystals, up to 400 μm in diameter, <1% subhedral clinopyroxene crystals, up to 300 μm in diameter, <1% euhedral amphibole crystals, up to 300 μm in diameter, with no opaque rims, and <1% blocky Fe-Ti oxides (Fig. 4.14c,d).

Groundmass textures

The groundmass is hypocrystalline, pale brown, sideromelane glass and with plagioclase microlites and Fe-Ti oxides up to 100 μm in diameter (Fig. 4.14c,d). Plagioclase microlites are acicular or tabular, with ~40 – 50% exhibiting swallow tail textures. No olivine or clinopyroxene is present in the groundmass.

4.3.2.3 Dense Clasts

The dense clasts are composed of <1% tabular plagioclase phenocrysts up to 1000 μm in diameter with ~90% exhibiting internal sieve textures and ~2 – 3% tabular microphenocrysts, up to 550 μm in diameter, with ~30% exhibiting internal sieve textures and ~75% exhibiting swallow tail textures (Fig. 4.14e,f). Other microphenocryst phases include ~1 – 2% subhedral, sub-rounded and elongate olivine crystals, up to 450 μm in diameter, <1% subhedral clinopyroxene crystals, up to 400 μm in diameter, <1% euhedral, tabular amphibole crystals, up to 900 μm in diameter, with no opaque rims and blocky Fe-Ti oxides (Fig. 4.14e,f).

Groundmass textures

The groundmass is hypocrystalline, pale brown, sideromelane glass which contains plagioclase, olivine, and Fe-Ti oxides up to 100 μm in diameter (Fig. 4.14e,f). The plagioclase microlites have a weak trachytic texture and are acicular or tabular, with ~20% exhibiting swallow tail textures. The olivine microlites and Fe-Ti oxides range from subhedral and blocky or tabular to anhedral with varying degrees of resorption and hopper textures. No clinopyroxene crystals were identified in the groundmass.

4.3.3 Lava and Spatter Petrography

4.3.3.1 Lava Flow Field 1

The lavas in lava flow field 1 are black to dark, hypocrystalline, and fine-grained aphanitic (Fig. 4.15a,b). The lavas are non- to incipiently vesicular with elongate and aligned vesicles up 5 mm in diameter and <1 mm in diameter sub-spherical vesicles.

The lavas contain up to 2% euhedral, tabular, and acicular phenocrysts up to 7 mm in diameter, with internal sieve textures. Microphenocryst assemblages include 2 – 5% tabular plagioclase crystals, up to 600 μm in diameter, with 30-50% exhibiting internal sieve textures or normal zoning, ~2% subhedral, prismatic and anhedral, heavily resorbed olivine crystals, up to 500 μm in diameter, <1% subhedral, sub-rounded or tabular clinopyroxene crystals, up to 450 μm in diameter, and <1% elongate amphibole crystals, up to 600 μm in diameter, with opaque rims. Rare, <1%, subhedral, feldspar antecrysts up to 12 mm in diameter, are seen in few of the samples. Further details on the crystal phases and their associated textures for all the erupted products are described in detail in Chapter 5.

Groundmass textures

The groundmass is microcrystalline and consists of plagioclase, olivine, very rare clinopyroxene and Fe-Ti oxides up to 100 μm in diameter (Fig. 4.15a,b). Three distinct textures (light, dark and transitional) are identified within the lava flow deposits (Fig. 4.16). The lighter bands (normal lava) are the typical groundmass textures observed throughout each sample. They are hypocrystalline and contain abundant acicular plagioclase microlites up to 100 μm in diameter, with ~20% exhibiting weak swallow tail textures. In addition, subhedral, tabular and fragmented olivine microlites and few blocky or irregular shaped Fe-Ti oxides are present. The darker bands (dark lava bands) are also hypocrystalline and contain abundant tabular feldspar microlites, up to ~ 90 μm in diameter, with ~10% exhibiting weak swallow tail textures, and a visually high abundance of subhedral to anhedral olivine microlites and blocky and sub-rounded Fe-Ti oxides that are <10 μm in

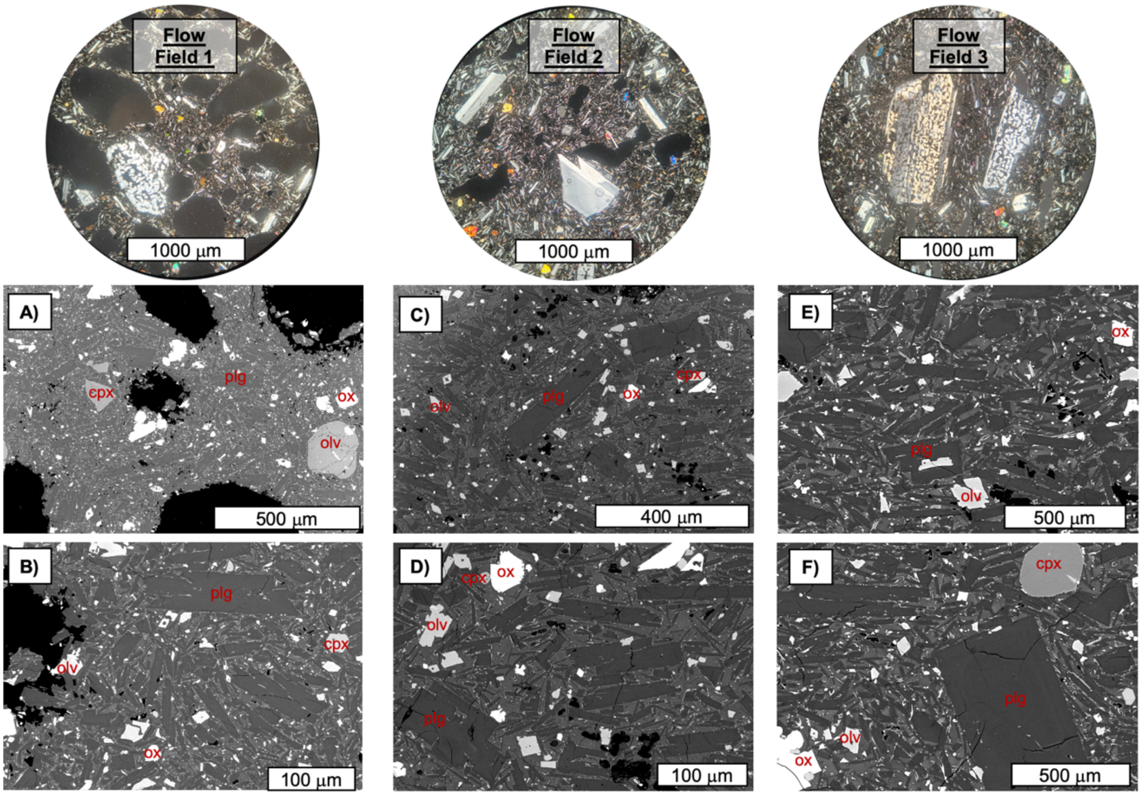

Figure 4.15: *Textural images of the DIP lava deposits, showing the groundmass textures and the crystal phases. Plg – plagioclase, cpx – clinopyroxene, olv – olivine, ox – Fe-Ti oxides. Circles show cross-polarised light (XPL) images of the different lava deposits.* ***A,B)*** *Back scatter electron (BSE) images of lava from flow field 1 (FF1).* ***C,D)*** *BSE of the lava from flow field 2 (FF2).* ***E,F)*** *BSE of the lava from flow field 3 (FF3).*

diameter. The transitional bands are very rare but are as the normal lava bands but with a greater abundance of oxides.

4.3.3.2 Lava Flow Field 2

The lavas in lava flow field 2 are black to dark grey, hypocrystalline and aphyric to fine-grained aphanitic (Fig. 4.15c,d). Two lavas from FF2 were used in the textural study – AI-9-026 (F6) and AI-19-028 (F7). The lavas are non-vesicular vesicular with weakly aligned, elongate vesicles up to 8mm in diameter and sub-spherical vesicles up to 2 mm in diameter.

The lavas contain up to 1%, tabular plagioclase phenocrysts, up to 3 mm in diameter, with ~95% exhibiting internal sieve textures. The microphenocryst assemblage consists of ~3 – 4 % plagioclase microphenocrysts, up to 600 μm in diameter, with ~80% exhibiting internal sieve textures or normal zoning, 1 – 2%, subhedral and tabular or heavily resorbed olivine microphenocrysts, up to 400 μm in diameter, <1% subhedral and sub-rounded clinopyroxene microhenocrysts, up to 400 μm in diameter, and <1% elongate amphibole microphenocrysts, up to 650 μm in diameter, with opaque rims.

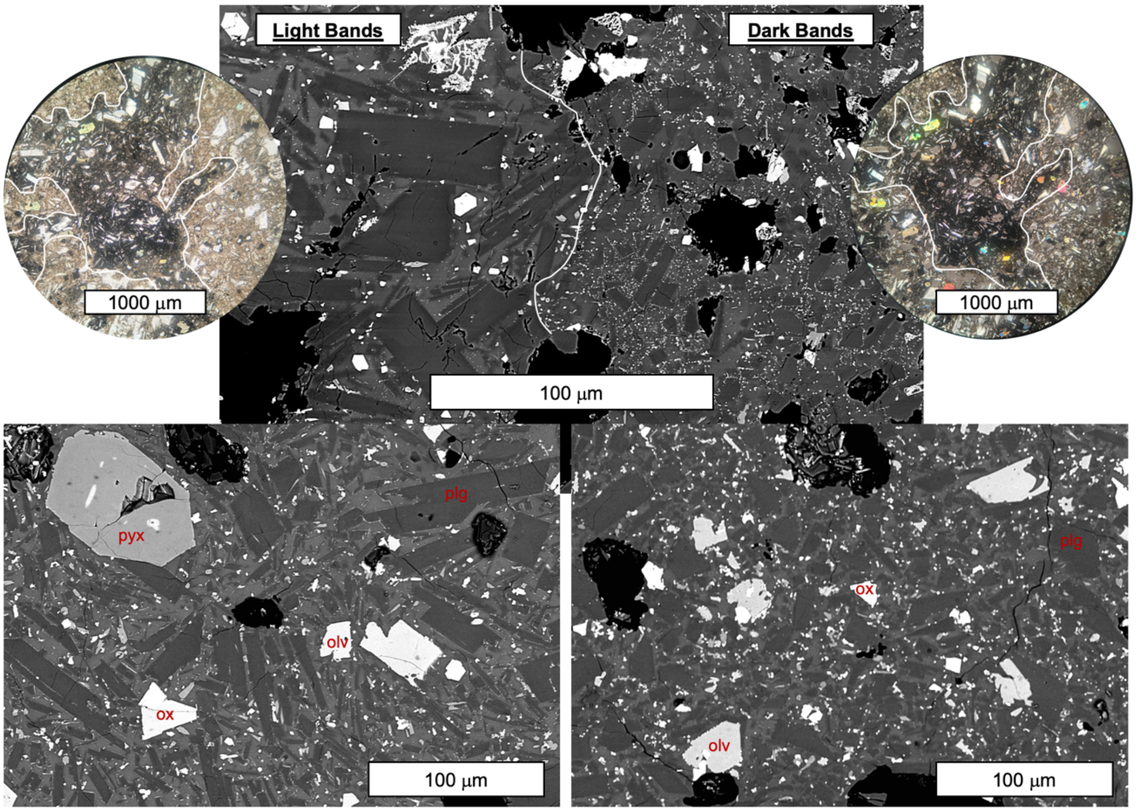

Figure 4.16: *Cross-polarised light (XPL) and plane-polarised light (PPL) images of the light and dark bands in the lava. BSE images show the contact between the two groundmass types and single BSE images of the different types, characterised by the morphology of the feldspar microlites.*

Groundmass textures

The groundmass is microcrystalline and consists of plagioclase, olivine, very rare clinopyroxene and Fe-Ti oxides up to 100 μm in diameter (Fig. 4.15c,d). Black, mafic-rich bands (dark lava bands) are common throughout the samples. Plagioclase microlites are acicular or tabular, and ~30% exhibit weak swallow tail textures. Olivine microlites are subhedral, sub-rounded or blocky. Clinopyroxene microlites are euhedral to subhedral, elongate or sub-rounded. Fe-Ti oxides ae tabular, blocky, or sub-rounded.

4.3.3.3 Lava Flow Field 3

The lavas in lava flow field 3 are black to dark grey, hypocrystalline and aphyric to fine-grained aphanitic (Fig. 4.15e,f). The lavas are non-vesicular with weakly aligned elongate vesicles up to 3 mm in diameter and sub-spherical vesicles up to 2 mm in diameter.

The lavas contain up to 3% tabular and elongate plagioclase phenocrysts up to 5 mm in diameter, with ~80% exhibiting sieve textures or normal zoning. Microphenocryst assemblage includes ~5% tabular plagioclase crystals, up to 600 μm in diameter, with ~40 – 80% exhibiting internal sieve textures or normal zoning, 2 – 3% euhedral, prismatic, or tabular and anhedral, heavily resorbed olivine crystals, up to 400 μm in diameter, ~1% subhedral, sub-rounded or tabular clinopyroxene crystals, up to 400 μm in diameter, and <1% subhedral amphibole crystals, up to 600 μm in diameter, with opaque rims. Rare, <1% anhedral feldspar antecrysts up to 11 mm in diameter are seen in a number of samples.

Groundmass textures

The groundmass is microcrystalline and consists of plagioclase, olivine, very rare clinopyroxene and Fe-Ti oxides up to 100 μm in diameter (Fig. 4.15e,f). Dark, mafic-rich bands (dark lava bands) are seen in at least two of the samples. Plagioclase microlites are acicular or tabular and <1 mm in diameter. ~30% of the plagioclase microlites exhibit weak swallow tail textures. Olivine microlites are euhedral to subhedral, tabular or fragmental. Clinopyroxene microlites are euhedral to subhedral, elongate or sub-rounded. Fe-Ti oxides are blocky, sub-rounded or irregular shaped with some weak resorption.

4.3.3.4 Type 1 Cones

The moderately to densely welded spatter clasts at the type 1 cones are black to dark grey, hypocrystalline, and fine-grained aphanitic (Fig. 4.17a,b). The spatter is non- to incipiently vesicular with varying regions of vesicularity. Spherical vesicles are usually <5 mm in diameter, whilst sub-spherical vesicles are usually up to 9 mm in diameter. Elongate and irregular shaped vesicles range from <1 mm – 8 mm in diameter.

The T1 cone spatter contains ~1% tabular plagioclase phenocrysts, up to 7 mm in diameter, with ~95% exhibiting internal sieve textures, and <1% sub-rounded clinopyroxene phenocrysts (Fig. 4.17a,b). Microphenocryst assemblages include ~ 3 – 5% tabular plagioclase crystals, up to 600 μm in diameter, with 50 – 60% exhibiting internal sieve textures or normal zoning, ~2% subhedral to anhedral, heavily resorbed olivine crystals, up to 500 μm in diameter, ~ 1% sub-spherical or tabular clinopyroxene crystals, up to 450 μm in diameter, and <1% subhedral amphibole crystals, up to 550 μm in diameter, with opaque rims. Rare, <1%, subhedral and tabular or anhedral feldspars antecrysts up to 20 mm in diameter and black subhedral and tabular clinopyroxenes up to 5 mm in diameter are seen in few deposits.

Groundmass textures

The groundmass is microcrystalline and consists of plagioclase, olivine, rare clinopyroxene and Fe-Ti oxides up to ~100 μm in diameter (Fig. 4.17a,b). The dark lava bands are seen in two samples from cones 11 and 12. Plagioclase microlites are acicular or tabular, <1 mm in diameter and can exhibit a weak trachytic texture. ~25 – 30% exhibit a weak swallow tail texture. Olivine microlites are subhedral and blocky or anhedral with varying degrees of internal and external resorption, hopper textures and spherical and elongate opaque inclusions. Clinopyroxene microlites are very rarely seen but are subhedral. Fe-Ti oxides are blocky and tabular.

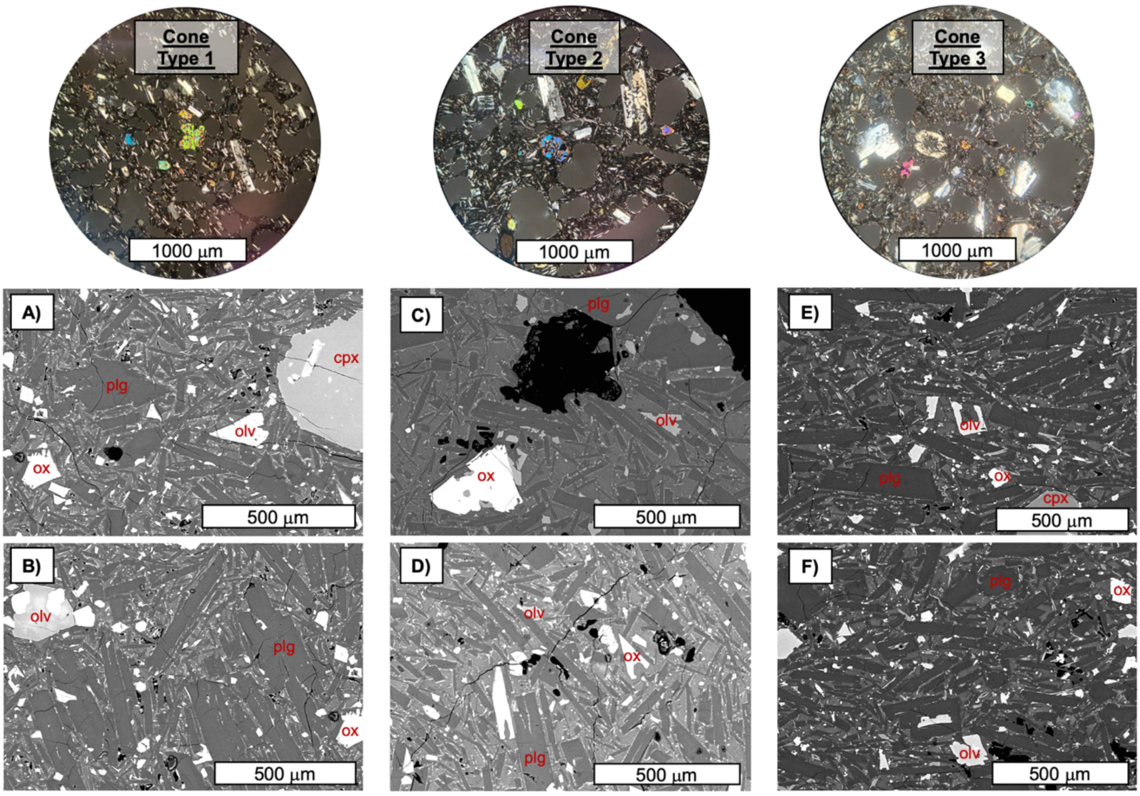

Figure 4.17: *Textural images of the DIP spatter deposits, showing the groundmass textures and the crystal phases. Plg – plagioclase, cpx – clinopyroxene, olv – olivine, ox – Fe-Ti oxides. Circles show cross-polarised light (XPL) images of the different spatter deposits.* ***A,B)*** *Back scatter electron (BSE) images of spatter from cone type 1.* ***C,D)*** *BSE of spatter from cone type 2.* ***E,F)*** *BSE of the spatter from cone type 3.*

4.3.3.5 Type 2 Cones

The weakly agglutinated spatter clasts at the type 2 cones are dark grey or black, hypocrystalline and fine-grained aphanitic (Fig. 4.17c,d). The spatter is incipiently vesicular with irregular shaped vesicles up to 15 mm in diameter, which in some places show weak alignment, and sub-spherical vesicles up to 5 mm in diameter. The largest vesicles exhibit broken filaments.

The T2 cone spatter contains <1% tabular plagioclase phenocrysts, up to 5 mm in diameter, with all the phenocrysts exhibiting internal sieve textures, and <1% subhedral olivine phenocrysts up to 1 mm in diameter. Microphenocryst assemblages include ~2% of tabular plagioclase crystals, up to 600 μm in diameter, with ~80% exhibiting internal sieve textures or normal zoning, ~1-2% subhedral and anhedral, prismatic, or heavily resorbed olivine crystals, up to 500 μm in diameter, ~1% euhedral to subhedral clinopyroxene crystals up to 600 μm in diameter, and <1% amphibole microphenocrysts up to 600 μm in diameter, with opaque rims.

Groundmass textures

The groundmass is microcrystalline and consists of plagioclase, olivine, clinopyroxene and Fe-Ti oxides up to ~100 μm in diameter (Fig. 4.17c,d). Plagioclase microlites are euhedral, elongate, and acicular or tabular with ~25% exhibiting weak swallow tail textures. Olivine and clinopyroxene microlites are euhedral to subhedral and elongate or prismatic. Olivine microlites contain spherical to elongate opaque inclusions. Fe-Ti oxides are euhedral to subhedral, sub-rounded or sub-elongate.

4.3.3.6 Type 3 Cones

The moderately to densely welded spatter clasts at the type 3 cones are dark grey, hypocrystalline, and fine-grained aphanitic (Fig. 4.17e,f). Two samples from type 3 cones were used in the textural study – AI-9-008 (cone 1) and AI-19-121 (cone 8). The spatter is non- to incipiently vesicular with varying regions of vesicularity. Sub-spherical vesicles are up to 2 mm in diameter, whilst elongate vesicles are up to 9 mm in diameter.

The T3 cone spatter contains ~2% of tabular plagioclase phenocrysts up to 8 mm in diameter, with ~90% exhibiting internal sieve textures, and <1% sub-rounded clinopyroxene phenocrysts. Microphenocryst assemblages include ~ 1 – 5% tabular plagioclase crystals, up to 550 μm in diameter, with ~40-60% exhibiting internal sieve textures or normal zoning, ~2% subhedral to anhedral, heavily resorbed olivine crystals, up to 450 μm in diameter, ~ 1% sub-spherical or tabular clinopyroxene crystals, up to 450 μm in diameter, and <1% subhedral amphibole crystals, up to 500 μm in diameter, with opaque rims. Rare, <1% subhedral and tabular or anhedral feldspar antecrysts up to 6 mm in diameter are seen in few deposits.

Groundmass textures

The groundmass is microcrystalline and consists of plagioclase, olivine, rare clinopyroxene and Fe-Ti oxides up to ~100 μm in diameter (Fig. 4.17e,f). Plagioclase microlites are acicular or tabular, <1 mm in diameter and can exhibit a weak trachytic texture. ~25 – 30% of plagioclase microlites exhibit a weak swallow tail texture. Black, mafic-rich bands (dark lava bands) are seen in a single sample from cone 7. Olivine microlites are subhedral and blocky or anhedral with varying degrees of internal and external resorption, hopper textures and spherical to elongate opaque inclusions. Clinopyroxene microlites are rarely seen but are subhedral. Fe-Ti oxides are blocky and tabular or sub-rounded with spherical opaque inclusions.

4.3.4 Amphibole Textures

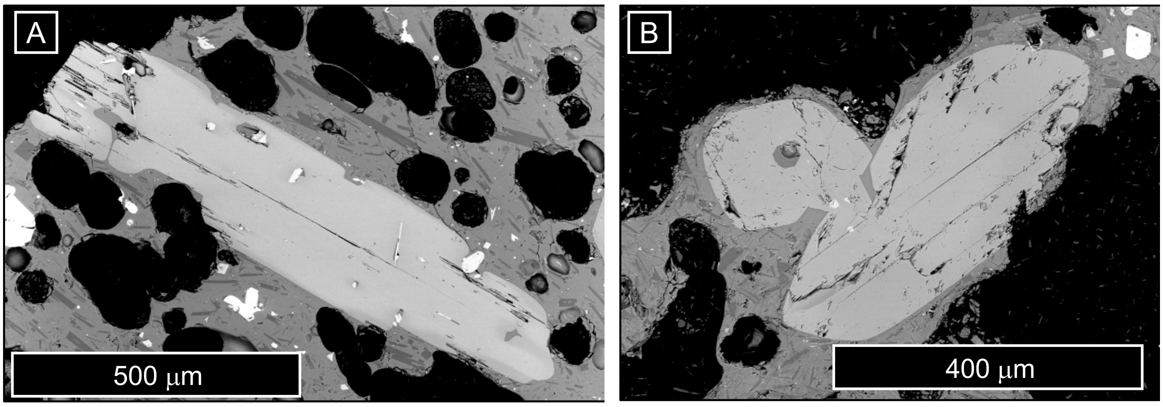

Figure 4.18: *BSE images showing amphibole with euhedral rims in the tephra samples.*

Amphiboles phenocrysts and microphenocrysts in the spatter, lava and tephra deposits exhibit different degrees of breakdown textures. The amphiboles in the tephra deposits (type ii) are euhedral and have no breakdown rims (Fig. 4.18), whereas the amphiboles in the spatter and lava (type i) have reaction rims that vary in thickness from 5 – 50 μm and exhibit varying textures. Symplectitc rims (Fig. 4.19a,b) are most common in the spatter and lava samples and are made up of crystals that are perpendicular to the crystal face and have sharp contacts with the amphibole phase. Granular rims (Fig. 4.19c,d) are less common but observed in spatter and lava samples with crystals that have thicker reaction rims (30 – 50 μm) or have completely broken down. Due to the size of the grains and accuracy of the electron probe beam, identification of the crystal compositions was not possible, however petrographic analysis suggests they are composed of feldspar, pyroxene and Fe-Ti oxides. Some amphibole crystals in the spatter and lava exhibit multiple breakdown rims with gradual transitions through from symplectitc to granular. The amphibole crystals in the spatter and lava also exhibit irregular volumetric decomposition, where the crystal is almost fully replaced by the breakdown rim (Fig. 4.20a,b) or aligned volumetric decomposition, with the crystals in the breakdown rims following fractures and cleavage planes within the amphibole crystal (Fig. 4.20c).

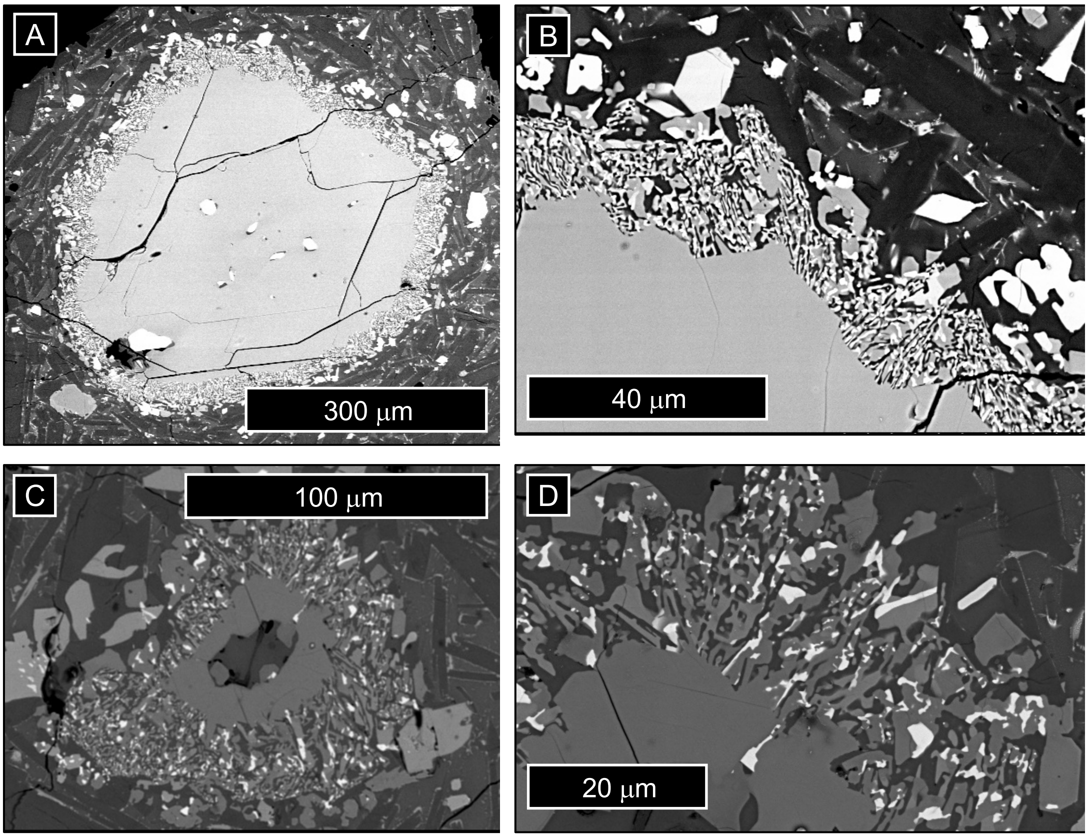

Figure 4.19: *Showing the different reaction rims seen in the type i amphibole crystals.* ***A,B)*** *Symplectic rims.* ***C,D)*** *Granular rims.*

Sample Type	**Al_19_034** Spatter	**Al_19_034** Spatter	**Al_19_008** Spatter	**Al_19_008** Spatter	**Al_19-_121** Spatter	**Al_19-_121** Spatter	**Al_19-_028** Lava	**Al_19-_028** Lava	**Al_19-_028** Lava DB
SiO_2	59.57	59.13	58.18	58.33	57.97	58.35	59.55	57.66	57.08
TiO_2	0.12	0.11	0.15	0.10	0.09	0.06	0.10	0.10	0.10
Al_2O_3	24.60	24.66	25.80	25.48	25.86	26.10	24.87	26.09	26.19
FeO	0.65	0.63	0.79	0.72	0.66	0.35	0.72	0.56	0.57
MnO	0.00	0.01	0.01	0.01	0.00	0.01	0.01	-0.01	0.01
MgO	0.06	0.05	0.08	0.05	0.04	0.00	0.05	0.01	0.04
CaO	7.31	7.62	8.11	7.83	8.27	7.81	7.34	8.47	8.69
Na_2O	7.05	6.94	6.68	6.89	6.63	6.80	6.98	6.48	6.40
K_2O	0.69	0.57	0.56	0.61	0.46	0.47	0.57	0.39	0.43
SrO	0.08	0.09	0.11	0.10	0.07	0.13	0.11	0.26	0.25
Total	100.13	99.82	100.46	100.13	100.04	100.47	100.29	100.02	99.94
An	35	37	39	37	40	38	36	41	42
Or	4	3	3	3	3	3	3	2	2
Ab	61	60	58	59	58	60	61	57	56

	Al_19-_028 Lava DB	**Al_19-_026** Lava	**Al_19-_026** Lava	**DIP-3** Scoria	**DIP-3** Scoria	**DIP-6** Pumice	**DIP-6** Pumice	**DIP-8** Dense	**DIP-8** Dense
SiO_2	56.67	59.16	57.80	57.58	59.36	58.35	58.16	58.05	56.96
TiO_2	0.11	0.16	0.10	0.15	0.15	0.13	0.10	0.09	0.08
Al_2O_3	26.17	24.68	26.42	25.80	24.71	25.47	25.52	25.07	26.04
FeO	0.65	0.75	0.66	0.86	0.78	0.85	0.70	0.78	0.66
MnO	0.03	0.02	0.02	0.02	0.01	0.02	0.01	0.02	0.01
MgO	0.10	0.05	0.07	0.10	0.07	0.09	0.06	0.06	0.07
CaO	8.55	6.98	8.42	8.40	7.24	7.79	7.84	7.64	9.01
Na_2O	6.49	7.06	6.54	6.38	7.11	6.80	7.10	6.97	6.41
K_2O	0.41	0.90	0.49	0.45	0.60	0.53	0.54	0.47	0.37
SrO	0.32	0.25	0.15	0.12	0.10	0.11	0.08	0.17	0.17
Total	99.95	100.02	100.67	99.84	100.15	100.12	100.11	99.32	99.79
An	41	34	40	41	35	38	37	37	43
Or	2	5	3	3	3	3	3	3	2
Ab	56	61	57	56	62	59	60	61	55

Table 4.2: *Table showing representative values of groundmass feldspar chemistry. For full data set see appendices 2. DB = dark band.*

4.3.5 Groundmass Feldspar Compositions

The composition of feldspar microlites were analysed (table 4.2) to understand the range of crystallisation conditions. Microlite compositions are mostly andesine (Fig. 4.21a-c), with rare anorthoclase in the transitional lava samples (Fig. 4.21b) and single oligoclase in the spatter samples (Fig. 4.21c). There is no clear change in microlite composition depending on the type of deposit and the texture of the lava deposits.

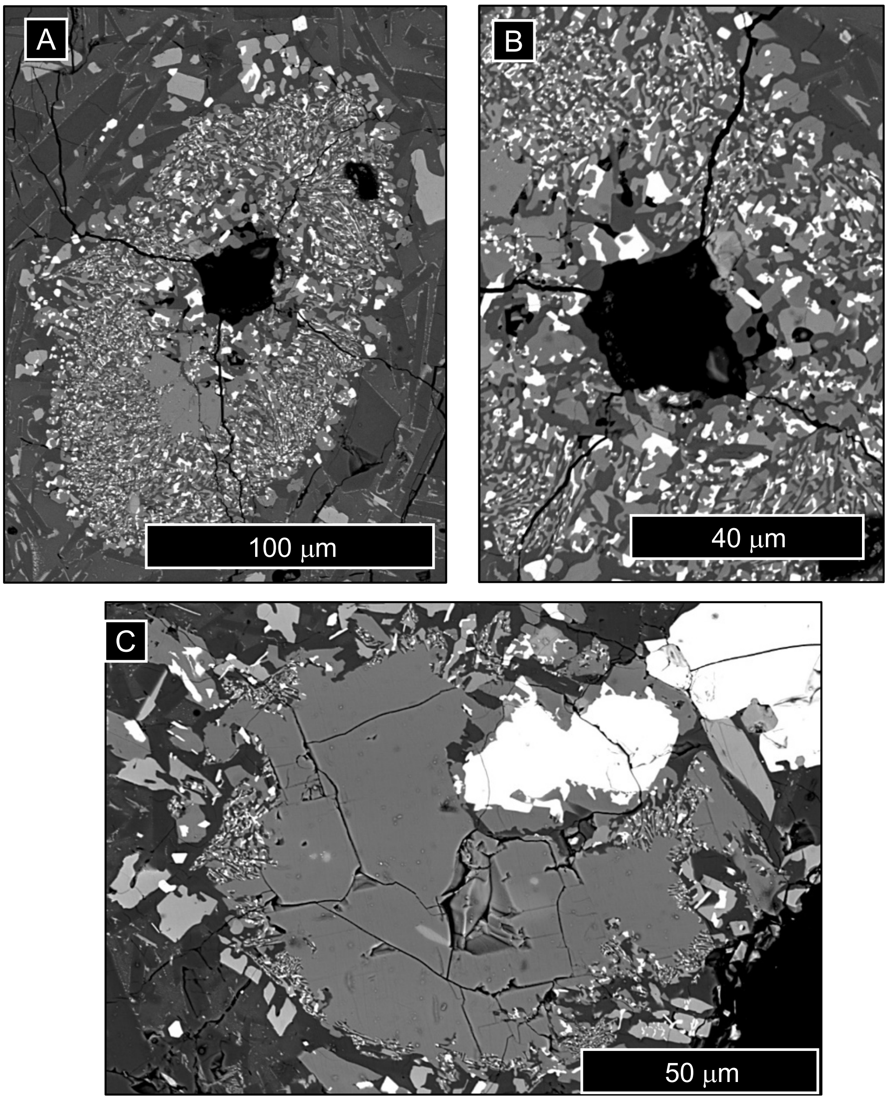

Figure 4.20: ***A, B*** *Irregular volumetric decomposition with an almost fully replaced amphibole crystal.* ***C)*** *Aligned volumetric decomposition with the crystals following fractures and cleavage planes.*

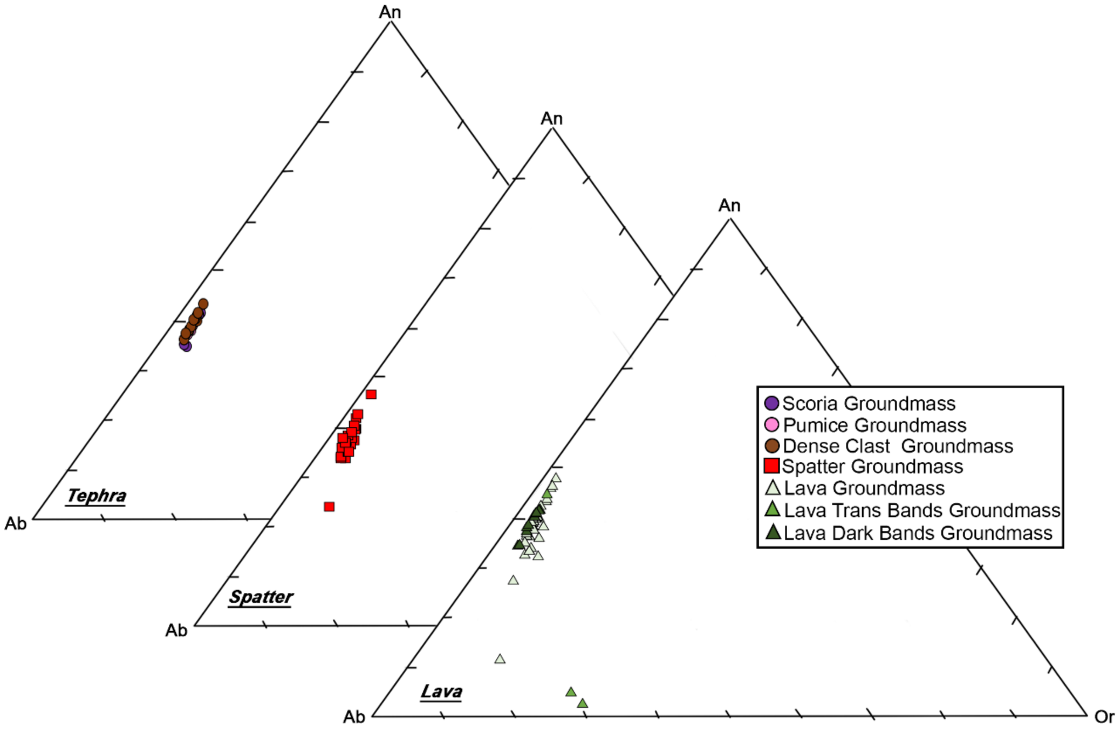

Figure 4.21: *Ternary feldspar plots for the feldspar microlites in the tephra, spatter and lava deposits. The lava plot shows the different microlite compositions based on the textures of the lavas.*

Anorthite (An) contents of the microlites range from $An_3Ab_{69}Or_{28}$ – $An_{48}Ab_{50}Or_2$ and a histogram is unimodal with a modal peak at An_{38} (Fig. 4.22a). There is very little variation in An contents between the spatter and tephra clasts. Groundmass crystals in the spatter range from $An_{23}Ab_{69}Or_7$ – $An_{46}Ab_{52}Or_2$, with a mode at An_{38} (Fig. 4.22b), and those in the scoria, pumice and dense clasts range from $An_{34}Ab_{61}Or_4$ – $An_{41}Ab_{57}Or_2$, $An_{37}Ab_{60}Or_3$ – $An_{39}Ab_{58}Or_3$, $An_{36}Ab_{60}Or_4$ – $An_{43}Ab_{55}Or_2$, respectively (Fig. 4.22c). The scoria and pumice clasts have a uniform distribution and no mode, whilst the microlites in the dense clasts have two modes at $An_{38}Ab_{60}Or_3$ and $An_{40}Ab_{58}Or_2$.

The results from the tephra should be treated with caution as not many data points were collected due to time constraints. Feldspar microlites in the lava show a wider range, from $An_3Ab_{69}Or_{28}$ – $An_{48}Ab_{50}Or_2$ and have a main mode at $An_{42}Ab_{56}Or_2$ (Fig. 4.22d). When the lava deposits are broken down into textures, the normal lava samples have $An_{12}Ab_{76}Or_{12}$ – $An_{46}Ab_{52}Or_2$.

The normal lava and dark bands have very similar An contents, ranging from $An_{35}Ab_{62}Or_3$ – $An_{48}Ab_{50}Or_2$, whilst the transitional bands show a larger range with two distinct populations at $An_3Ab_{69}Or_{28}$ – $An_5Ab_{70}Or_{25}$ and $An_{37}Ab_{60}Or_3$ – $An_{45}Ab_{53}Or_2$. However, the populations at $An_3Ab_{69}Or_{28}$ – $An_5Ab_{70}Or_{25}$ are not in equilibrium with the whole-rock magma and are evidence of microlite growth at a later stage, likely from a more degassed magma. All the other groundmass feldspars in each deposit type are with the whole rock composition. The tephra components are not in equilibrium with the glass compositions.

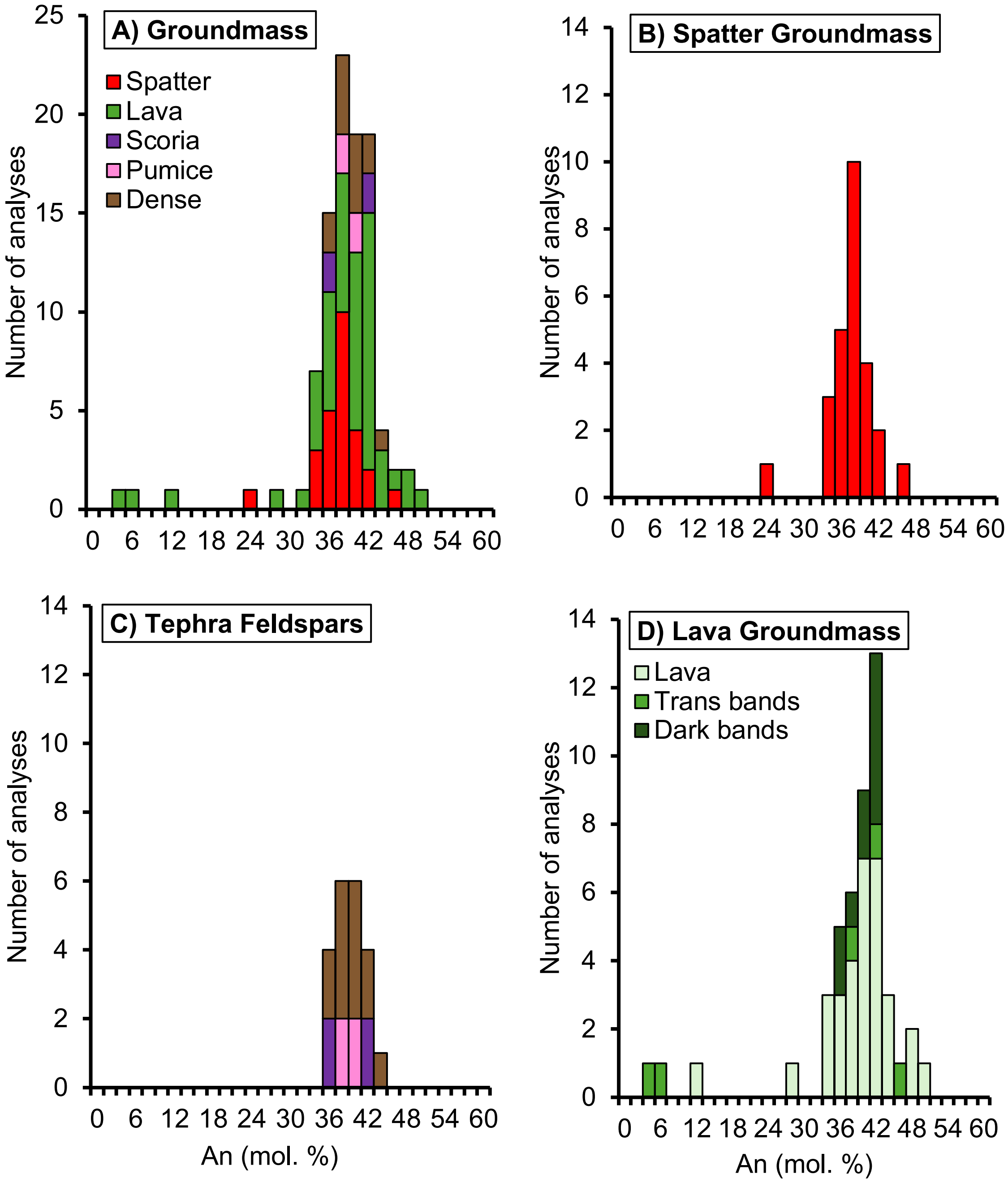

Figure 4.22 ***A)*** *A unimodal compositional histogram for all the eruption deposits (lava, spatter, and tephra clasts). Show the An range and the main mode at An_{38}.* ***B)*** *Unimodal compositional histogram for the spatter deposits, showing the main mode at An_{38}.* ***C)*** *Compositional histogram for the tephra deposits. The scoria and pumice clasts have a uniform distribution, and the dense clasts have two modes at An_{38} and An_{40}.* ***D)*** *Unimodal compositional histogram for the lava deposits and split based on the textures, showing a wider An range and the main mode at An_{42}.*

4.3.6 Intensive Variables

The feldspar-liquid thermometer (Putirka, 2005) was used to establish which crystal phases are in equilibrium with the melt (Fig. 5.29). Equilibrium was determined by comparing the An-Ab exchange (Putirka, 2005). For temperatures <1050 °C, the An-Ab exchange value should be 0.1 ± 0.05, and for temperatures >1050 °C the An-Ab exchange value should be 0.28 ± 0.11 (Putirka, 2005) (Fig. 5.29a). The thermometer require pressure as an input and so the sensitivity of the pressure input was tested.

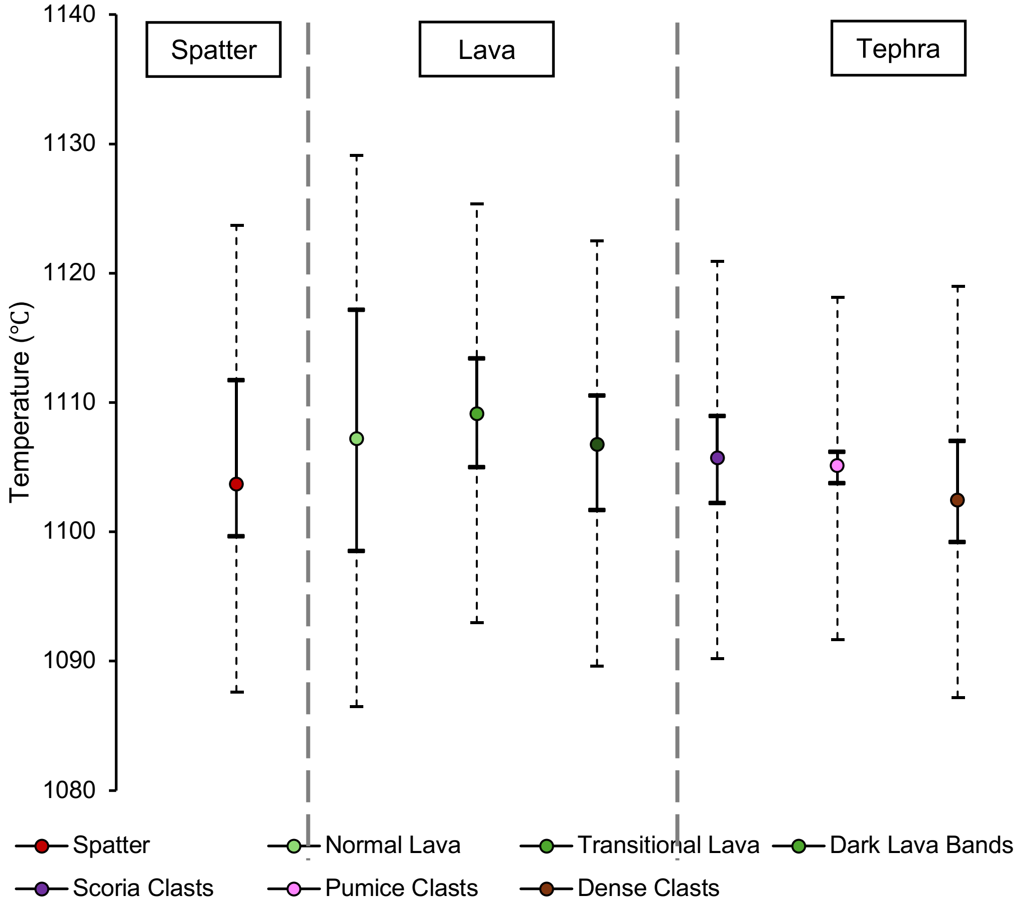

Figure 4.23: *Graph showing the temperatures from the feldspar microlites in the different deposits. The circles show the average temperature, and the lines show the range. The dashed lines show the estimated error depending on the pressure input.*

The initial pressure was started at 330 Kbar, as that marks the base of the lithosphere (refs). The testing confirmed that a difference of 1000 bars had only 6 °C difference on temperature, however, the microlites likely formed at lower pressures and therefore until further data is acquired, the temperatures should be treated with caution. Feldspar microlites in the erupted deposits have average temperatures ranging from 1102 – 1109 ± 12 °C. These temperatures are potentially too high for intermediate composition magma microlites, however narrow range is the point to be made. The lava and spatter have the widest range, from 1099 – 1117 °C (Fig. 4.23). When broken down, the normal lava texture shows the whole range (1099 – 1117 °C) (Fig. 4.23), whilst the transitional lava bands range from 1105 – 1113 °C, and the dark lava bands range from 1102 – 1111 °C (Fig. 4.23). The pumice clasts show the narrowest range, from 1104 – 1106 °C (Fig. 4.23), whilst the scoria and dense clasts show a slightly wider range, from 1102 – 1109 °C and 1099 – 1107 °C, (Fig. 4.23) respectively.

4.3.7 2D Feldspar microlite textures

The feldspar number density (N_A) ranges from 126 – 9812 mm^{-2} (table 4.3), with the highest densities in the dense tephra clasts and the lowest in one of the spatter samples. N_A for the lava and spatter samples range from 1525 – 4732 mm^{-2} and 126 – 2387 mm^{-2}, respectively. N_A for the normal lava textures is within a similar range (1525 – 1779). The tephra samples show the largest range with N_A of 2761, 1170 and 9812 for scoria clasts, pumice clasts and dense clasts.

Table 4.3: *The textural parameters obtained from the [a]ImageJ analysis, [b]ShapeCalc (Mangler et al., 2022) analysis and [c]CSD Corrections analysis (Higgins, 2000).*

Sample	Spatter	Spatter	Lava	Lava	Dark lava band	Scoria Clasts	Pumice Clasts	Dense Clasts
Type	AI-19-008	AI-19-121	AI-19-026	AI-19-028	AI-19-028	DIP3	DIP5	DIP8
No. of crystals [a]	1548	750	1110	2887	2556	3890	2059	2078
Area analysed (mm^2) [a]	0.36	0.33	0.30	0.24	1.91	0.26	0.48	0.04
N_A [a]	2378	230	1779	4723	1525	2761	1170	9812
Crystallinity [a]	0.604	0.103	0.496	0.440	0.523	0.201	0.288	0.263
Mean crystal area [a]	231	438	274	85	748	68	232	20
S/L [b]	0.18	0.18	0.19	0.15	0.14	0.11	0.16	0.11
S [b]	1	1	1	1	1	1	1	1
I [b]	2.7	2.8	3.5	3.6	3.9	6.2	4	6.2
L [b]	5.6	5.6	5.2	6.8	7.2	8.8	6.4	8.8
R_c^2	0.982	0.982	0.961	0.931	0.993	0.968	0.956	0.971
S/I [b]	0.37	0.36	0.29	0.28	0.26	0.16	0.25	0.16
I/L [b]	0.48	0.50	0.67	0.53	0.54	0.7	0.63	0.70
CSD slope α [c]	-20.33	-23.53	-27.89	-25.29	-19.98	-45.37	-26.03	-83.16
N° [c]	-13.95	-15.63	-13.25	-12.35	-14.66	-13.15	-14.73	-9.56

The groundmass feldspar crystallinity ϕ ranges from 0.103 – 0.604 (table 4.3), with the highest crystallinity in the one of the spatter deposits, and the lowest in the scoria clasts. ϕ for the lava samples range from 0.488 – 1.488, however there is little variation between the two 'normal' lava samples (0.488 and 0.496) and the dark bands (0.523). The spatter and tephra samples also show little variation in ϕ, from 0.604 – 0.614 and 0.201 – 0.288, respectively.

Mean crystal areas have a wide range from 20.41 – 748 μm^2 (table 4.3), with the lowest mean crystal area in the dense clasts and the highest in one of the spatter samples. Mean crystal areas exhibit wide ranges within the different deposit types; in the lava it ranges from 85 – 748, with no similarities between the normal samples, whilst in the spatter it ranges from 231 – 438. The tephra clasts range from 20 – 232, with the dense clasts exhibiting the lowest mean crystal area and the pumice clasts exhibiting the highest.

Crystal aspect ratios *S/L* have a narrower range from 0.11 – 0.19 (table 4.3), with the lowest *S/L* in the scoria and dense clasts, and the highest in a lava sample. *S/L* ranges from 0.14 – 0.19 in the lava samples, with no similarities in the normal lava textures. *S/L* is constant in the spatter samples (0.19). *S/L* in the tephra samples is consistent at 0.11 for scoria and dense clasts, but higher at 0.16 for the pumice clasts.

As N_A decreases, the mean crystal area slightly increases (Fig. 4.24). An exception to this is the dark lava bands, where the mean crystal area increases with increasing N_A. N_A also generally increases with increasing ϕ. The dense clasts have a higher ϕ than the other samples. Although very similar, N_A slightly decreases with increasing *S/L* (Fig. 4.24). The low *S/L* values represent more elongate, prismatic crystal shapes and correlate with a lower N_A. Higher *S/L* values represent tabular or equant crystal shapes. As *S/L* increases, the mean crystal area also increases. However, the dark lava bands have a low *S/L* but much higher mean crystal area (Fig. 4.24).

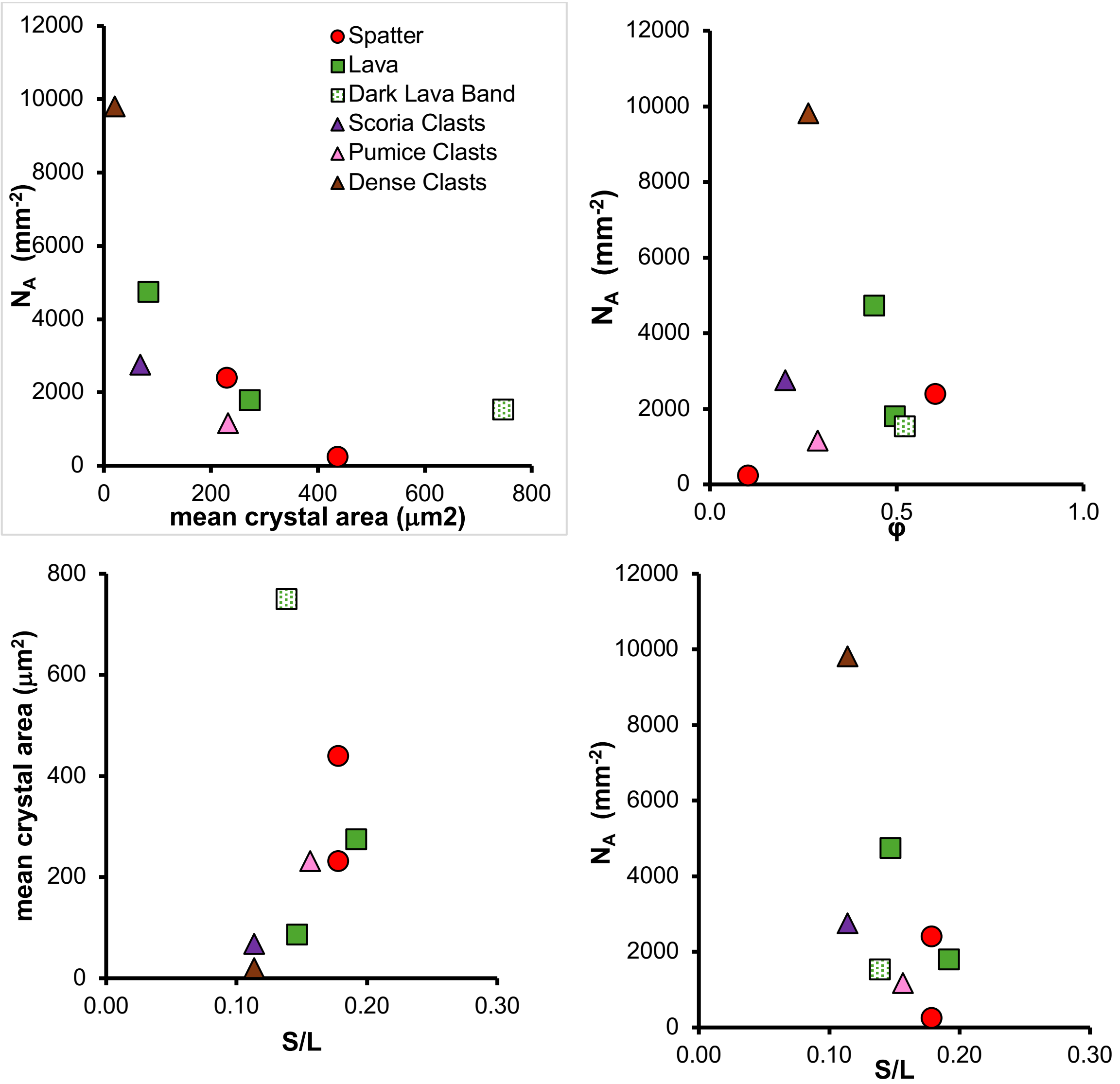

Figure 4.24: *Graphs showing the 2D feldspar parameters for the different deposits.*

Figure 4.25: *Zingg plots for the different samples, shown together on one graph and individually. In many cases, the error bars are smaller than the symbols.*

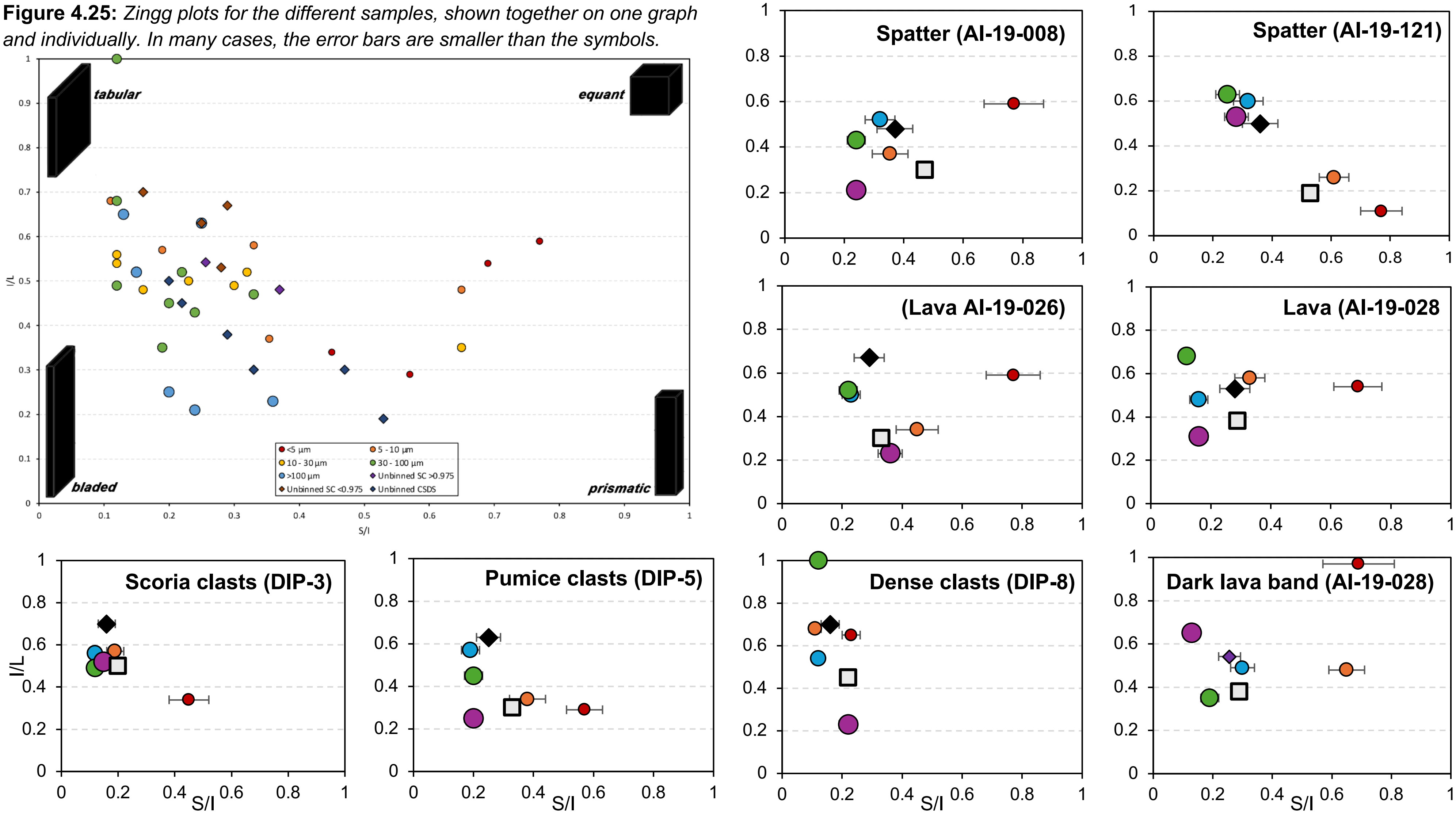

In summary, the textural parameters show that the groundmass textures range from glassy to more crystalline with variations between many small, prismatic microlites and fewer, larger prismatic microlites. The lava samples are more crystalline than the rest of the DIP deposits, with small, prismatic microlites, whilst the dark bands have a similar crystallinity but with fewer, larger, prismatic microlites. The spatter samples show some variation and either exhibit a low crystallinity with fewer, larger, prismatic microlites or a higher crystallinity with more, smaller prismatic microlites. The scoria and pumice clasts are glassy with fewer, small, prismatic microlites, whilst the dense clasts are glassy but with many small, prismatic microlites.

4.3.8 3D Crystal Populations

Higgins (1994) showed that the 2D length of a crystal shape is closer to the 3D intermediate dimension and that the 2D width is more likely the 3D short dimension. The 2D – 3D stereological conversion models, CSDSlice (Morgan and Jerram, 2006) and ShapeCalc (Mangler et al., 2022) provide the best S:I:L estimates based on a best fit test on the mode of the distribution of the crystal shapes and dimensions. The best fit values for CSDSlice should produce an R^2 value of >0.8, whereas the best fit value for ShapeCalc should produce an R_c^2 value of > 0.975, and lower values show poor model fits. Estimates for the best fit values for the DIP samples tend to produce much poorer fit models (table 4.3) with R_c values ranging from 0.5243 – 0.8686 (only two samples > 0.8), and R_c^2 values ranging from 0.931 – 0.993 (only 3 samples > 0.975). However, when binned on crystal length, shape estimates with acceptable fits are more common. The binned data sets produced R_c^2 between 0.825 – 0.999, with over 75% having R_c^2 values > 0.975.

When the best 3D estimates were plotted on a Zingg diagram for the spatter and lava, there are a few patterns identified between crystal size and shape (Fig. 4.25). In the spatter and lava samples, the largest crystals (> 100 µm bin) are typically bladed shapes, whilst crystals in bins 5 – 100 µm are either bladed or tabular shapes and the crystals in the < 5 µm faction are equant shapes. An exception to the above is a single spatter sample, where the > 100 µm faction has tabular shapes and the crystals in the 30 – 100 µm faction are bladed shapes. Crystals in the 5 – 10 µm and < 5 µm faction of the spatter and lava samples are prismatic shapes. In the dark lava bands, the crystals in the > 100 µm faction have tabular shapes, whilst the 10 – 30 and 30 – 100 µm crystal factions have bladed shapes. Crystals in the 5 – 10 µm faction of the dark lava bands are prismatic and those in the < 5 µm faction are equant shaped. The variation in crystal size and shape in the spatter and lava samples may also be a factor of syn-emplacement crystallisation.

Figure 4.26: *CSD's for the different samples. Each one is labelled. Error bars are smaller than the symbols. Dashed lines are regression lines using the 3 steepst segments of the CSD.*

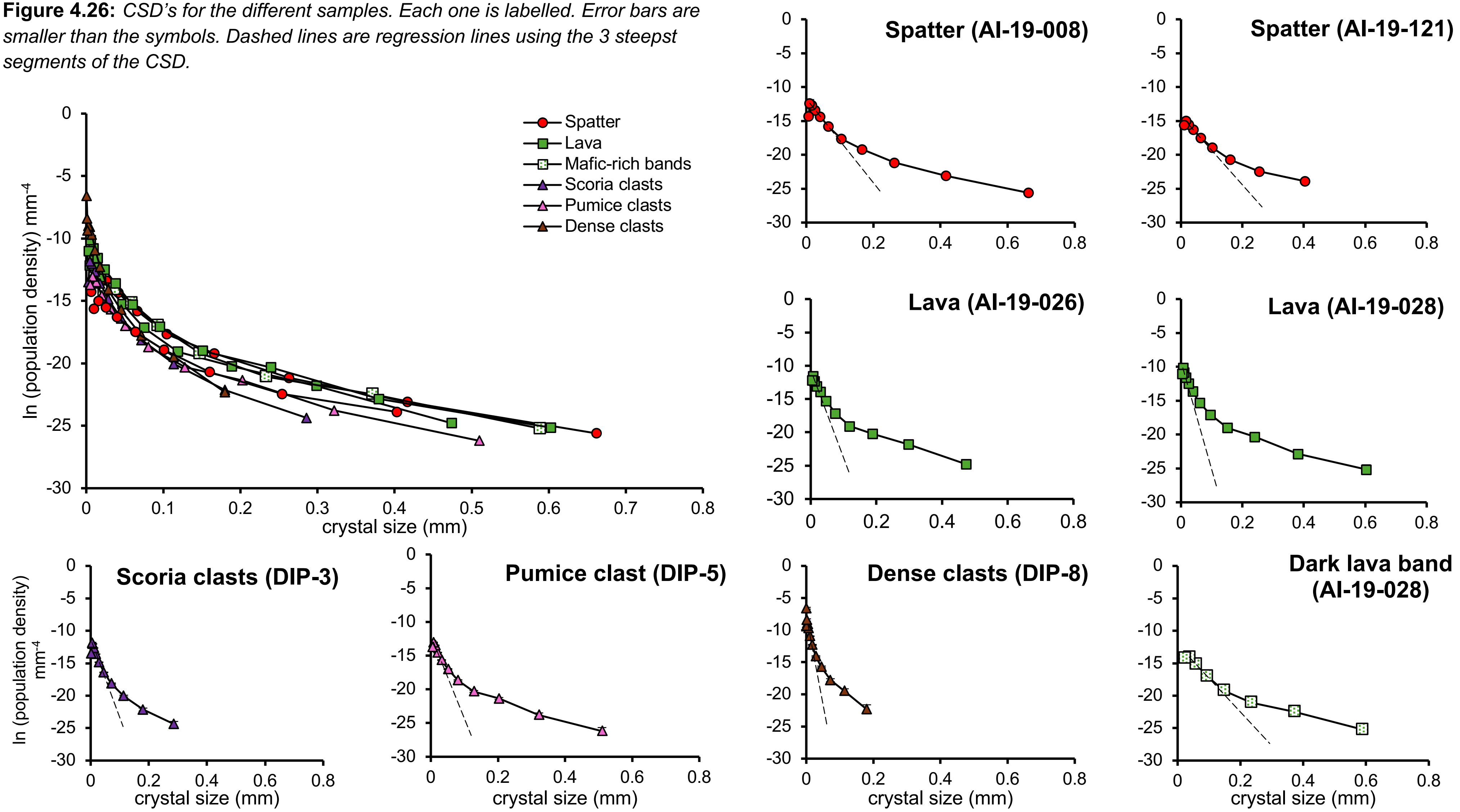

The pumice clasts and dense clasts have a wider range in crystal shapes (Fig. 4.25). In the pumice samples, the largest crystals (30 – 100 and >100 μm bins) and the smaller crystals (5 – 10 μm bin) have bladed shapes, whilst the crystals in the 10 – 30 μm bin have tabular shapes. The smallest crystals in the < 5 μm bin have prismatic shapes. In the dense clasts, the two largest crystal factions (> 100 μm and 30 – 100 μm bins) have bladed and tabular shapes, respectively. The smaller crystal factions (10 – 30, 5 – 10 and < 5 μm bins) in the dense clasts are tabular shaped. For the scoria clasts, all of the crystal sizes, with the exception of the smallest crystal faction (<5 μm bin) cluster with tabular shapes (Fig. 4.25). Crystals in the <5 μm faction have bladed shapes. The combined ShapeCalc data sets for all samples (Fig. 4.25) (although not all had R_c^2 > 0.975 or R_c > 0.8) are skewed towards higher I/L with more tabular shapes, whilst the CSDSlice data sets are skewed towards lower I/L with bladed shapes (Fig. 4.25).

4.3.9 Crystal Size Distributions (CSD)

The CSD of a rock can be defined as the number of crystals of a mineral per unit volume within a series of defined size intervals (Marsh, 1988). The CSD's calculated for the feldspar microlites in the spatter, lava and tephra samples are concave-up (Fig. 4.26) and reflect progressive changes in crystal growth and nucleation rates as a function of changing undercooling (ΔT). The CSD's can be grouped into two types. The first group consists of the spatter, lava, scoria, and pumice clasts and has y-axis intercept (n°) values of -12.35 – -15.63 with gradual slopes (α), -19.98 – -45.37 (table 4.3), that extend into the larger crystal sizes. The second group consists of the dense tephra clasts and has a lower n° of -9.56 and a steeper α (-83.16) that does not extend into the larger crystal sizes (Fig. 4.26).

The negative change of slope in the smallest crystal populations has been inferred to be related to the intersection probability effect (Brugger and Hammer, 2010a; Miwa et al., 2013; Preece et al., 2013; Bain et al., 2019) and are discounted from further analysis.

4.4 Discussion

Combining textural, and chemical measurements is crucial to characterize, understand, and monitor eruptive activity. Crystallisation can occur through nucleation of new crystals or by growth on existing nuclei (Blake, 2000), depending on the degree of undercooling. The erupted deposits from the DIP exhibit a range of textures, which are evidence for variations in the shallow storage and ascent conditions.

4.4.1 Componentry

Scoria clasts represent lava fountaining activity. The abundance of scoria clasts in the proximal fall deposits are further evidence that they are associated to lava fountaining activity. The golden-brown scoria clasts formed in the middle of the lava fountains, whilst the black scoria clasts formed in the lower sections and margins of the lava fountains. The morphologies of the scoria clasts (e.g., Fig. 4.3) represent ductile deformation within the fountain (e.g., Lautze and Houghton, 2005; Di Traglia et al., 2009; Winstanley, 2020; Thivet et al., 2020) and the stretched filaments and weak alignment of vesicles represent shearing at the margins of the conduit (e.g., Romero et al., 2018).

The abundance of pumice clasts and dense clasts in the distal deposits represent periods of more explosive activity where fragmentation efficiencies were different. The pumice textures suggest that the magma experienced significant pre-eruptive nucleation (e.g., Thivet et al., 2020)

The high vesicularity of the scoria and pumice clasts (> 60%) shows that the magma underwent rapid expansion and bubble nucleation (e.g., Polacci et al., 2006; Stovall et al., 2011; Parcheta et al., 2013; Winstanley, 2020; Thivet et al., 2020) and the glassy skins on the scoria clasts show rapid quenching. The vesicularity of the scoria clasts sits within range of Hawaiian lava fountain tephra fall deposits (e.g., Houghton and Wilson, 1989; Di Traglia et al., 2009), however, the relatively narrow range exhibited by the DIP scoria shows fountaining events were moderate to high intensity and the rapid ascent rates prevented the bubbles from migrating through the magma (e.g., Houghton and Wilson, 1989; Parcheta et al., 2013).

The dense, tachylite clasts are inferred to represent fragments of a magmatic plug within the upper section of the conduit. The higher content of small microlites and the poor- to non-vesicularity in the clasts suggests the magma had longer residence times within the conduit (e.g., Taddeucci et al., 2004). The evolution of conduit geometry controls the magmas ascent pathways at shallow levels (e.g., Pioli and Harris, 2017; Thivet et al., 2020), and therefore, the presence of dense clasts suggests that the magmatic flux decreased, allowing the magma to start degassing and crystalising to either form a plug before fragmenting prior to the explosion (e.g., Thivet et al., 2020) or allowing material to accrete onto the sides of a shallow and widening conduit. For this discussion, the term plug is used to describe a build-up of material that prevented the magma from initially reaching the surface, whether that be a cooling body of magma that stalled due to a decrease in magmatic flux (e.g., Thivet et al., 2020) or a blockage from the accretion of material along the conduit wall (e.g., Vitturi et al., 2008; Viccaro et al., 2021).

4.4.2 2D Textural Variations in the DIP deposits

The different eruptive deposits (lava, spatter, scoria, pumice and dense clasts) have the same bulk composition and therefore are inferred to have originated from the same magmatic source prior to microlite crystallisation. The alignment of the DIP, in relation to other volcanic structures such as an older fissure, a lava dome and a scoria cone, suggests that the DIP was influenced by the reactivation of pre-existing feeder system and therefore magma will have reached the surface through a series of dikes that propagated along faults before forming sheet dikes and reaching the surface. The explosive nature of a number of the cones (type 2 and type 3) and the associated deposits, in particular the lithic clasts being derived from the shallowest older lava, (chapter 3) has been linked to the shallow widening of the conduit and limited erosion at depth and shallow conduit clogging (e.g. Vitturi et al., 2008).

The composition of the feldspar microlites in the DIP deposits exhibit very little variation in An content (e.g., Fig. 4.21) and temperature (e.g., Fig. 4.23) which shows that the microlites all crystallised in similar conditions and so there is no correlation between microlite composition and the type of sample it was found in. For example, feldspar microlites in the dense tephra clasts, have been inferred to represent plug material and would be assumed to have undergone the most degassing, but have the same An contents as the feldspar microlites in all the other deposits (e.g., Fig. 4.21). Therefore, the lack of correlation between microlite composition and deposit type shows that crystallisation likely occurred due to degassing-driven crystallisation during ascent and under similar conditions (e.g., Bain et al., 2019; Thivet et al., 2020). For the more explosive eruptions, this crystallisation also likely occurred prior to plug emplacement or accretion along the widening conduit walls. The few lower An content microlites in the transitional lava bands (e.g., Fig. 4.21) are not in equilibrium with the host magma and represent either antecrysts or minimal evolution.

N_A and mean crystal area are 2D parameters. $\mathrm{N_A}$ varies as a function of crystal size due to the intersection probability effect, therefore must be treated with discretion (Royet, 1991; Bain et al., 2019). The inverse relationship between N_A and mean crystal area (e.g., Fig. 4.24) shows that the samples either have a high number of small microlites or a lower number of large microlites, whilst the positive correlation between N_A and ϕ means that samples with a higher N_A are more crystalline. The weak negative correlation between N_A and *S/L* (e.g., Fig. 4.24) shows that samples with higher N_A have more prismatic microlites and those with lower N_A have more tabular microlites. However, the <0.1 difference between the *S/L* suggests that all the microlites are prismatic, independent of N_A.

The higher N_A, smaller mean crystal sizes and lower ϕ of the dense clasts compared to the scoria and pumice clasts and the spatter and lava samples, shows that there must have been spatial variation in ΔT during crystallisation on ascent, associated with the widening of the conduits due to the more explosive nature of the type 2 and 3 cones. These textural observations show that the ΔT in the magma that erupted as dense clasts was higher compared to the magma that erupted as scoria, pumice, spatter and lava samples, and that the dense clasts underwent faster degassing. The higher mean crystal area in the dark lava band suggests that it had been crystallising at depth for a longer period of time, whilst the increase in crystallinity for the lavas and spatter suggests that the magma **stalled.** The lower crystallinity for the second spatter (AI-19-008) sample could indicate that it was one of the first explosions and therefore had no time to stall and crystallise. The higher number of smaller crystals in the spatter and normal lava (at least one normal lava) suggest that there was higher undercooling taking place. The DIP microlites have prismatic morphologies and show very little variation irrespective of N_A and average size. The similarity in textures of the lava, spatter, scoria and pumice samples (e.g., Fig. 4.24) suggests that they shared a similar storage history and therefore the eruptive style must be determined by processes happening in the shallow magma system (e.g., Preece et al., 2023).

The 2D dimensions for crystal shape suggest that the crystals are all prismatic, whereas the 3D calculations for crystal shape suggest that there are differences in crystal shape (e.g., Fig. 4.25), with many of the larger crystals exhibiting more tabular morphologies and the smaller crystals more prismatic morphologies. The presence of different shaped crystals within all the DIP samples, suggests that crystal growth was a common process, as different growth rates and stages led to the variation in crystal sizes and shapes**.**

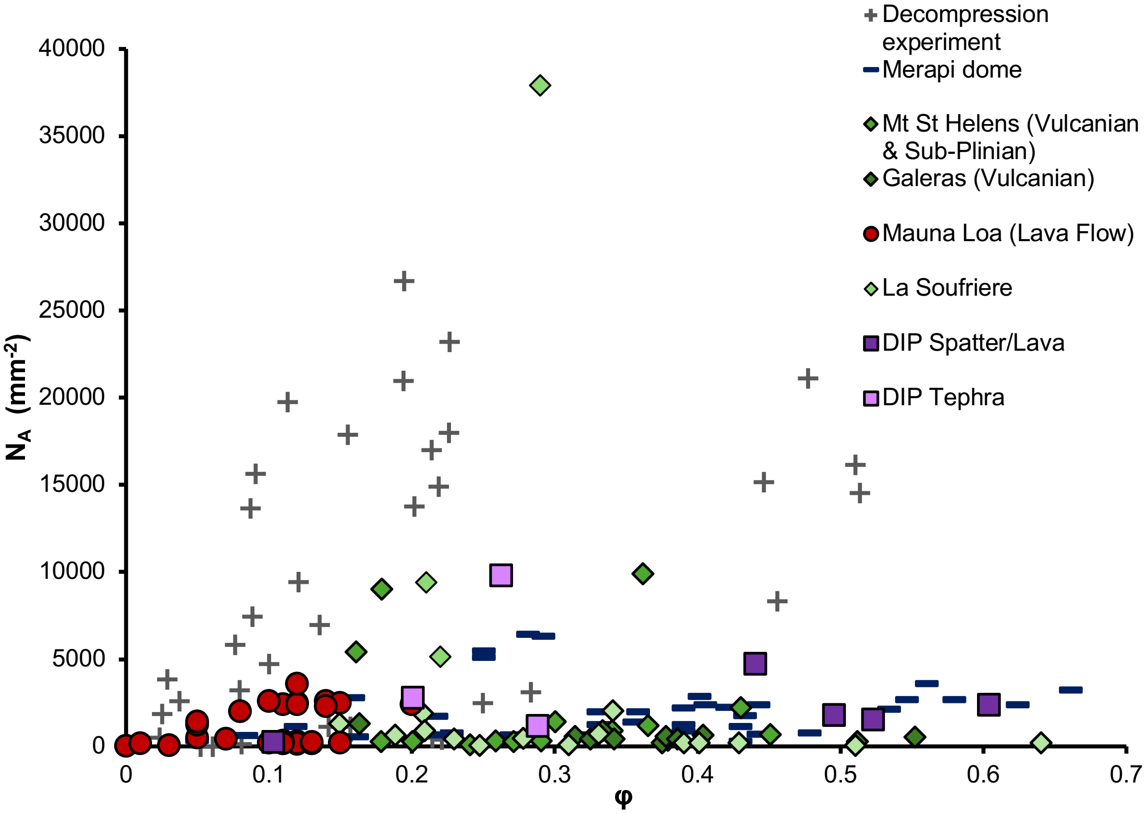

Figure 4.27: *Graph comparing the* N_A *and φ from a range of eruption styles to the DIP deposits, including the decompression experiments of Brugger and Hammer (2010), effusive lava flows from Mauna Loa (Riker et al., 2009), dome eruptions from Merapi (Hammer et al., 2000; Preece et al., 2013; Preece et al., 2016) and explosive Vulcanian eruptions from La Soufriere (Frey et al., 2024), Mt St Helens (Cashman and McConnell, 2005) and Galeras (Bain et al., 2019). A single point from Mt St Helens also shows a sub-Plinian style explosion.*

When compared to a range of eruption styles at other volcanoes, the DIP data show various overlaps (Fig. 4.27). The low N_A and higher ϕ of the spatter and lava samples is indicative of crystal growth dominated crystallisation and lower degrees of undercooling (lower ΔT)

and is more common in lower intensity eruptions, similar to values recorded for dome-forming eruptions (e.g., Hammer et al., 2000; Riker et al., 2009; Brugger and Hammer, 2010a; Preece et al., 2016; Bain et al., 2019). Vulcanian explosions at Montserrat, Galeras and La Soufriere show similar textural characteristics to low intensity eruptions, likely due to rapid shallow ascent (Clarke et al., 2007; Bain et al., 2019; Preece et al., 2023; Frey et al., 2024). However, the high N_A and low ϕ of the dense tephra samples is indicative of nucleation dominated crystallisation and higher degrees of undercooling (higher ΔT) and is more common in higher intensity eruptions, such as those seen at Mt St Helens (e.g., Cashman and McConnell, 2005; Brugger and Hammer, 2010a; Bain et al., 2019; Preece et al., 2023).

Following on from the 2D textural data, most studies would conduct or compare decompression experiments to understand the kinetics of crystallisation during ascent (Brugger and Hammer, 2010a). However, to the best of my knowledge, there has been no decompression experiments undertaken on material similar to the DIP deposits. For comparison, the decompressed samples from Brugger and Hammer (2010a) were plotted against the DIP samples, but do not overlap (Fig. 4.27).

4.4.3 Crystal Size Distribution Analysis

The curved CSD's reflect changes in the rates of growth and nucleation of the microlites during magma ascent and suggests progressive changes in ΔT during ascent and not individual episodes of growth or nucleation (e.g., Preece et al., 2013; Bain et al., 2019). The CSD analysis identifies two groups within the DIP samples. The first group consists of the spatter, lava, scoria, and pumice clasts, and have shallow gradients, lower y-axis intercepts (n^o) and larger crystal sizes (e.g., Fig. 4.26), which suggests that microlites grew under are growth-dominated conditions rather than nucleation dominated (e.g., Thivet et al., 2020). The second group consists of the dense tephra clasts and has a steeper gradient, higher n^o, and smaller crystal sizes (e.g., Fig. 4.26 which suggests microlites grew under nucleation-dominated conditions and supports the idea that ΔT was higher for the eruption of these deposits (e.g., Preece et al., 2013; Bain et al., 2019;).

Crystallisation times can be calculated from a CSD slope, as long as the crystal growth rate is known, using the equation from Marsh (1988): $Slope = -1/G\tau$, where G is growth rate and τ is crystallisation time. For example, using the slope of the 3 steepest segments represents the smallest crystals and the most recent crystallisation events (Zieg and Marsh, 2002; Preece et al., 2013). Nucleation rate (J) is calculated using the y-axis intercept (n^o) and the known growth rate (G), using the equation from Marsh (1988): $J = n^oG$.

Growth rates can differ with changing undercooling (Kirkpatrick, 1977; Preece et al., 2013). This factor, combined with the absence of known growth rates or crystallisation time for the DIP and island-wide deposits, and to the best of my knowledge, no decompression experiments undertaken on deposits of a similar composition, means that the calculated crystallisation rates and nucleation rates shown should be treated with caution. Due to this, I compare a range of growth rates for crystallisation times and nucleation rates.

Decompression experiments in basaltic systems found feldspar microlite growth rates ranged between 10^{-4} and 10^{-5} mm s^{-1} (Arzilli et al., 2015, Arzilli et al., 2019; Bamber et al., 2020), whilst those using basaltic andesites produced growth rates of 10^{-6} mm s^{-1} (Shea and Hammer, 2013; Bamber et al., 2020). On the other hand, growth rates reported in the literature for Etna magmas range from 10^{-7} and 10^{-11} mm s^{-1} (Pompilio et al., 2017). In contrast, experiments for andesitic and more silicic compositions produced feldspar microlite growth rates ranging from 10^{-6} and 10^{-9} mm s^{-1} (Hammer & Rutherford, 2002; Couch et al., 2003; Brugger and Hammer, 2010a). Due to the trachyandesite composition of the DIP deposits, but the more alkaline nature of the magma and the basaltic nature of the eruption style, including magma viscosity, crystallisation times are compared using the minimum growth rate of 10^{-5} mm s^{-1} and the maximum growth rate of 10^{-7} mm s^{-1}. Using these growth rates, the estimated crystallisation times range over three orders of magnitude for each sample (table 4.4). The shortest crystallisation time is ~ 20 minutes and the longest is ~ 5.69 days. Brugger and Hammer (2010a) suggested that the most accurate growth rate for decompression-induced crystallisation of plagioclase is 10^{-8} mm s^{-1}, however when that growth rate is applied to the DIP samples, crystallisation times of range from ~ 13.92 – 57.93 days. The shorter timescales suggest crystallisation was more likely to occur due to degassing-induced crystallisation on ascent or deep within the conduit (e.g., Bain et al., 2019; Thivet et al., 2020).

Basaltic paroxysmal eruptions in Stromboli, Kilauea and Mt Etna have crystallisation times ranging from 3 – 8 minutes (Moschini et al., 2023), whilst basaltic sub-Plinian eruptions are able to crystallise hopper and skeletal microlites within 1 – 5 minutes, and tabular microlites crystalise within 13 – 15 hours, with the range in growth rates 10^{-4} – 10^{-5} mm s^{-1} and 10^{-7} mm s^{-1}, respectively (Bamber et al., 2020). These crystallisation times are faster than those suggested to have occurred at the DIP, however, the rapid crystallisation seen here is distinctive for basaltic sub-Plinian eruptions (Arzilli et al., 2019; Bamber et al., 2020). On the other hand, more intermediate composition eruptions produce crystallisation times of ranging between 9 – 40 days (e.g., Cashman and McConnell, 2005). This shows that the composition of the magma, and likely viscosity can affect the crystallisation and growth rates (Thivet et al., 2020).

Nucleation rates are also compared using the maximum growth rate of 10^{-5} mm s^{-1} and the minimum growth rate of 10^{-7} mm s^{-1}. Using these growth rates, the estimated nucleation rates also range over three orders of magnitude for each sample. The estimated nucleation rates are based on y-axis intercept from the steepest section of the CSD which represents the smallest and last crystals to form (Preece et al., 2013).

Using a range of decompression experiments to identify growth rate and nucleation rates can give a very small insight into the shallow magma processes, but the reliability of the results is questionable due to the large assumptions made. For example, in the case of growth rates for the DIP deposits, the range varies from hours to days which, in terms of future volcano monitoring would be crucial.

	Crystallisation Time (mm^{-s})				
Growth Rate	10^{-5}		10^{-6}	10^{-7}	
	Minutes	Hours	Hours	Hours	Days
Lava (Norm)		1.00	9.96	99.59	4.15
Lava (Norm)		1.10	10.98	109.84	4.58
Lava (Dark)		1.39	13.90	139.03	5.79
Spatter		1.18	11.81	118.05	4.92
Spatter		1.37	13.66	136.63	5.69
Scoria Clasts	36.7	0.61	6.12	61.22	2.55
Pumice Clasts		1.07	10.67	206.71	4.45
Dense Clasts	20	0.33	3.34	33.4	1.39

Table 4.4: *Showing the range in crystallisation times for the different samples depending on the growth rates used.*

4.4.4 Amphiboles

Two types of amphiboles have been identified within the DIP deposits. Amphiboles with reaction rims (type i) are only present in the spatter and lava samples. The reaction rims show that the crystals left the stability field for >4 days and became unstable due to the pressure and the concentration of water in the melt decreasing on ascent to the surface (e.g., Rutherford and Hill, 1993; Browne and Gardner, 2006; Preece et al., 2023). However, Experiments by De Angelis et al., (2015) found that reaction rims can form over a 3 – 48-hour timescale with heating to 10 – 50 °C over their stability limit. The reaction rims identified in the DIP deposits are similar to those seen in dome forming eruptions, explosive eruptions, and effusive eruptions, and in compositions ranging from basalt to trachyandesite and andesite (e.g., Rutherford and Hill, 1993; Devine et al., 1997; Browne and Gardner, 2006; D’Mello et al., 2021; Pontesilli et al., 2022).

The symplectitc and granular rims in the lava and spatter (e.g., Fig. 4.19) formed due to the reaction of unstable amphibole with the host magma (e.g., D’Mello et al., 2021), with the gradual transitions between the two suggesting there was local regions of lower undercooling favouring crystal growth, likely linked to formation of melt pockets around the crystals (D’Mello et al., 2021). Irregular volumetric decomposition (e.g., Fig. 4.20) shows that there was a reaction between interstitial melt trapped within the amphibole and the amphibole during decompression induced degassing (D’Mello et al., 2021), whilst aligned volumetric decomposition (Fig. 4.20) shows that the breakdown crystals formed when the amphibole was heated past it’s stability limit (De Angelis et al., 2015; D’Mello et al., 2021). The finer grained, and acicular shape of the crystals within the reaction rims suggests that they formed from slow ascent rates and possible stalling at shallow depths (e.g., Browne and Gardener, 2006). The variations of the breakdown textures alone suggests that the rims cannot be characterised by single processes such as heating or decompression as seen in experimental decompression studies (e.g., Rutherford and Hill, 1993; De Angelis et al., 2015, D'Mello et al., 2021).

The type ii amphiboles are only found in the tephra deposits and have no reaction rims (e.g., Fig. 4.18), which initially suggests that the magma rose rapidly to the surface, likely during a more explosive episode (e.g., Rutherford and Hill, 1993; Nicholosi and Rutherford, 2004; Cashman and McConnell, 2005; Browne and Gardner, 2006). Amphiboles with no rims but rounded crystal edges have been observed in experimental and natural amphibole samples of hawaiite and basalts to trachyandesites (e.g., Nicholosi and Rutherford, 2004; Brown and Gardener, 2006; D'Mello et al., 2021). The studies suggest that for these crystals to form, amphibole dissolution rates are lower than the transport rate of material away from the crystal-melt boundary, and therefore no reaction rim can occur. However, if this processes occurred, it would be expected to see an increase in modal abundance of plagioclase, orthopyroxene, and Fe-Ti oxides (Browne and Gardener, 2006), which for the DIP deposits is not the case. The amphibole data fits with the textural data, which shows that the dense tephra clasts ascended faster than the spatter and lava samples. The scoria and pumice clasts have similar textures to the spatter and lava samples, but the lack of amphibole reaction rims suggests that this magma also ascended slightly faster.

Ascent rates based on the thickness of amphibole rims can be done if the amphibole stability field is known (Rutherford and Hill, 1993; Devine et al., 1998; Preece et al., 2023), however no work on this has been undertaken on Ascension Island and, to the best of my knowledge similar volcanic systems. In this study, the significance of the amphibole rim texture is not to provide accurate estimates of ascent rates but rather to show that there were changes in the ascent rates and degrees of decompression and heating for the different components throughout the eruption.

Although it is not possible in this study to gauge accurate ascent rates using the amphiboles and the textural data, a previous study of a mingled fall deposit on Ascension Island was able to use entrapment pressures from melt inclusions to identify storage depths and combined with the mingled textures, estimate an ascent rate of 0.13 m s^{-1}, from 11 km depth (Chamberlain et al., 2020). This ascent rate fits within published values of Vulcanian explosions, similar in style to the inferred eruption styles, (e.g., Miwa et al., 2009; Cassidy et al., 2015; Cassidy, 2018) and is at least one to two orders of magnitude higher than those in Strombolian explosions (e.g., Szramek et al., 2006), mildly explosive Vulcanian explosions (e.g., Cassidy et al., 2015; Cassidy, 2018) and effusive eruptions (e.g., Rutherford and Hill, 1993; Rutherford and Devine, 2003; Cassidy et al., 2015). However, paroxysmal eruptions on Mt Etna, Stromboli and Kilauea can produce ascent rates ranging from 4 – 10 m s^{-1} (Cassidy 2018; Moschini et al., 2023).

4.5 Conclusions and constraints on ascent rates and shallow surface processes

Textural studies like this are mainly completed for dome forming eruptions or well documented eruptions and often combine a number of data sets, such as seismic data and observational data (e.g., Preece et al., 2013; La Spina et al., 2016; Frey et al., 2024). Textural interpretations are also reliant on decompression experiments to be able to determine growth rates and conditions for formation (Cashman, 2020). The results from these can then be applied to natural samples to gain a more accurate understanding of storage and ascent processes. Without access to decompression experiments from the same, or very similar compositions, further assumptions have to be made, and it is not possible to accurately quantify ascent rates, growth rates and nucleation rates. However, this study has shown that by combining textural and compositional data, it is possible to quantitatively identify variations in the shallow surface processes.

The similarities between the phenocryst textures of the lava, spatter and tephra deposits suggest that the erupted products had shared storage conditions and so the variation in eruptive styles must have been controlled by shallow magma system processes. Microlites for the different eruptive products show some variation in, number density, shape, and size. Microlites within the dense clasts are small and prismatic with a high N_A but a relatively low ϕ, and therefore crystallised in nucleation-dominated conditions at a higher ΔT, which is suggested to be related to faster degassing and higher ascent rates. These dense clasts are associated with the more explosive, type 2 and type 3 cones (chapter 3). The presence of abundant lithic clasts (chapter 3) within these deposits shows that at the more explosive cones, the rapid ascent and more explosive nature of the explosions caused the conduit walls to erode, widening the conduit further (e.g., Vitturi et al., 2008).

On the other hand, microlites in the spatter and lava samples are also prismatic but are larger, with a lower N_A and relatively high ϕ, and therefore crystallised in growth-dominated conditions at a lower ΔT with higher crystallisation times, which is suggested to be related to slower ascent rates and slower degrees of decompression. Slower ascent rates in the lava and spatter samples, as the magma migrated through a pre-existing feeder system, are also evidenced by the presence of amphibole reaction rims. Microlites in the scoria and pumice clasts exhibit similar textures to the spatter and lava samples, however the amphiboles exhibit no break down rims which suggests that the magma rose more rapidly to the surface. Although very similar, the feldspar microlites in the spatter and lava samples exhibit a slightly wider compositional range compared to the tephra samples.

I suggest that the explosive activity, results from sub-surface cooling and degassing of a magma body due to decreases in the local magmatic flux resulting in the formation of a dense plug or accreted material along the conduit walls, represented by the dense clasts.

As the magma continued to ascend, it caused an increase in the pressure, and the plug to crack, which enhanced volatile exsolution and the growth of crystals so fragmentation could occur (e.g., La Spina et al., 2019; Thivet et al., 2020), as well as causing the shallow conduit walls to erode and become wider, allowing for a more explosive eruption to occur.

Very few textural studies have been completed on Ascension Island (e.g., Davies, 2023), and although lacking some desirable data, the study has provided valuable insights into the different processes occurring within the magma chamber. The similarities in the textures of the spatter, lava, scoria and pumice clasts suggests that even though the eruption styles were different (lava fountaining vs more explosive explosions) all the events were relatively small explosions from low intensity eruptions. As the textural and compositional differences are very minimal, it suggests that there was little variation in the average ascent rates, however differences between effusive and explosive activity can be linked to very small changes in ascent rates, regardless of the composition of magma erupting (Szramek et al., 2006). Variations in ascent rates will cause implications for monitoring and heightens the need for a dense seismic network to be installed on the island (e.g., Chamberlain et al., 2020). Such slight changes within ascent rates can be difficult to forecast during monitoring (e.g., Cassidy et al., 2018).

Chapter 5: Intermediate magma evolution

5.1 Introduction

In oceanic environments, intermediate magmas are less abundant than basalt or trachyte (Baker, 1968 The absence of eruptive deposits in this compositional range has been described as the 'Daly Gap'. The cause of these gaps has been linked to crystal fractionation crystallisation (Dufek and Bachman, 2010; Waters et al., 2021), magma chamber stratification (Bonnefoi et al., 1995; Waters et al., 2021), magma mixing (Kent 2014; Waters et al., 2021) or combinations of all.

Intermediate magmas can be generated in multiple ways: fractional crystallisation, magma mixing, partial melting, assimilation, and magma mush remobilisation (Anderson, 1976; Helz, 1976; Bohrson and Reid, 1997; Huppert and Sparks, 1988; Grove et al., 1992; Bachmann and Bergantz, 2003; Deruelle et al., 2007; Pan et al., 2022). The understanding of the processes and conditions involved in genesis, transportation, and storage of intermediate magmas in crucial for understanding the styles and size of volcanic eruptions (Caricchi and Blundy, 2015; Magee et al., 2018; Bellver-Baca et al., 2019; Pan et al., 2022).

Eruptions of (trachy)andesite magmas are mostly found in arc settings (e.g., Yamagishi and Feebrey, 1994; Sparks et al., 1998; Herd et al., 2005; Kimura et al., 2005; Zobin et al., 2016; Bain et al., 2019; Nakada et al., 2019), whilst the erupted products of intermediate magmas on ocean islands are much less common, with some examples including up to ~4 % on St Helena and up to ~16% on Iceland (Jeffery and Gertisser, 2018). Crystal phases within these volcanic rocks can give key information on the generation, evolution and storage of these intermediate melts, by studying the abundance, texture, and composition of mineral phases (e.g., Bachman et al., 2002; Reubi et al., 2003; Reubi and Nicholls, 2004; Ray et al., 2011;). Studies of intermediate magmas erupted from ocean islands have shown their generation through a range of process: magma mixing (e.g., Deruelle et al., 2007), high- or low-pressure fractionation (e.g., Mungall and Martin, 1995) partial melting of crust (e.g., Sigmarsson et al., 1991; Martin and Sigmarsson, 2007), or a combination of different processes (e.g., Mungall and Martin, 1995; Macdonald et al., 2008; Pontesilli et al., 2022). Thus, there is no single process through which intermediate magmas are generated in ocean islands settings.

The volcanic deposits on Ascension Island exhibit a compositional range from transitional basalt to trachy basalt through to rhyolite (Nielson and Sibbett, 1996; Weaver et al., 1996; Kar et al., 1998; Ammon et al., 2009; Jicha et al., 2013; Chamberlain et al., 2016; Chamberlain et al., 2019). Deposits of intermediate composition are mainly restricted to the north and west of the island (Fig. 5.1), cover ~6% of the islands surface and include scoria cones, scoria falls and lava flows (Weaver et al., 1996; Nielson and Sibbett, 1996; Jicha et al., 2013).

Previous studies on Ascension have shown that the wide compositional range is due to fractional crystallisation (Harris et al., 1983; Kar et al., 1997; Jicha et al., 2013; Chamberlain et al., 2016; Chamberlain et al., 2019). The trachyandesite deposits are believed to be the products of fractional crystallisation of intermediate Zr/Nb magmas at depths greater than 7 km (Weaver et al., 1996; Jicha et al., 2013). The whole rock major and trace element trends within the volcanic rocks and plutonic xenoliths, exhibit continuous trends that show that the basaltic magmas evolved to intermediate and silicic compositions by fractional crystallisation of the intermediate Zr/Nb basalts in a closed system (Nielson and Sibbett, 1996; Weaver et al., 1996). Whilst fractional crystallisation has been inferred to be the dominant process for magma evolution, some studies of individual eruptions have highlighted a role for magma mixing (Chamberlain et al., 2020). This suggests that there may be additional complexity within individual eruptions, not evident when studying the entire island's volcanic history.

Here I present the first detailed petrological study of the products from a purely intermediate composition magma on Ascension Island, erupted from the Devil's Ink Pot (DIP) fissure, located in the Letterbox region (Fig. 5.1) as a series of effusive and explosive events. By collecting whole rock major and trace element data, alongside textural and chemical characterisation of the crystal cargo I can elucidate how intermediate magma is generated and erupted. These findings contribute an understanding to the magma chamber dynamics and the styles and magnitude of volcanic eruptions in low-flux ocean island.

5.2 Geological Setting

Volcanic activity on Ascension Island was dominated by mafic, Strombolian eruptions in the north, northwest and south of the island (Fig. 5.1a), whilst felsic volcanism was localised to two areas, the Central Felsic Complex and the Eastern Felsic Complex (Fig. 5.1) (Nielson and Stiger, 1996; Nielson and Sibbett, 1996; Kar et al., 1998; Preece et al; 2021).

The mafic magmas on Ascension are categorised into three groups based on their Zr/Nb ratios (Weaver et al., 1996; Kar et al., 1997), however later studies have found that these groups have no significance (e.g., Chamberlain et al., 2019). Previous studies (e.g., Jicha et al., 2013) show that the trachyandesite results from crystal fractionation of intermediate Zr/Nb (ratio 5.0) mafic magmas along a simple liquid line of descent at depths greater than 7 km, whilst the trachyte and rhyolites formed by crystal fractionation of high Zr/Nb magmas (ratio 6.0) (Harris, 1983). This is evidenced by age data showing that the high Zr/Nb lavas preceded the felsic eruptions (Kar et al., 1997; Jicha et al., 2013). The major and trace element trends within the rocks and plutonic xenoliths, exhibit continuous trends that show that the basaltic magmas evolved to intermediate and silicic compositions by low pressure fractional crystallisation in a closed system (Nielson and Sibbett, 1996; Weaver et al., 1996;

Webster and Rebbert, 2001; Jicha et al., 2013; Chamberlain et al., 2016; Chamberlain et al., 2019).

Magma mixing is evident in at least one of the deposits on the island (Chamberlain et al., 2020) and is a possible cause for intermediate compositions. However, the non-linear variations seen in the island-wide studies of major and trace elements and the crystal phases show that this is unlikely (e.g., Weaver et al., 1996; Kar et al., 1997; Jicha et al., 2013; Chamberlain et al., 2019).

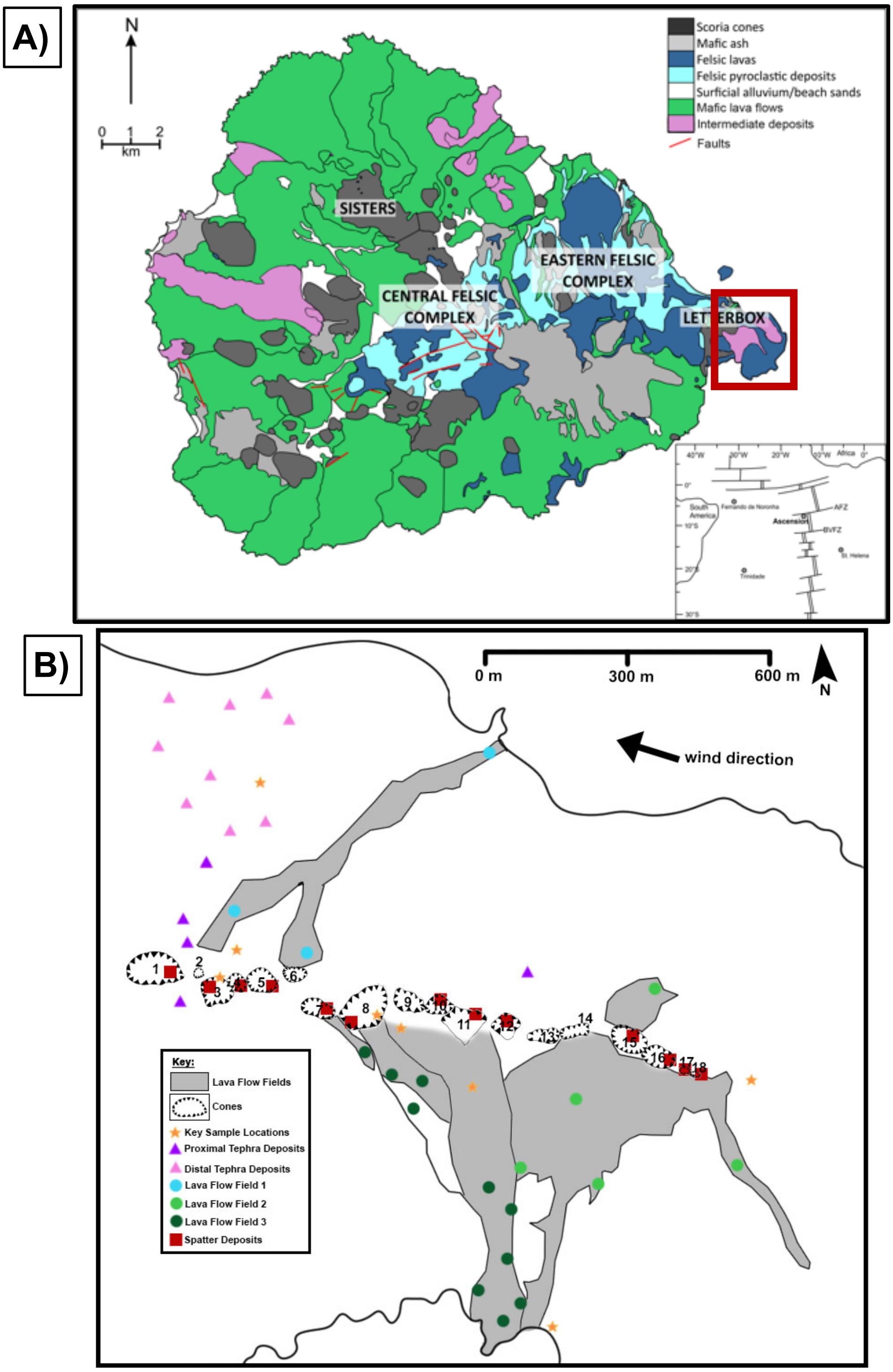

Figure 5.1: ***A)*** *Location map of Ascension Island. DIP located in the red square, in the Letterbox region.* ***B)*** *Schematic map showing the sample locations from the study (triangles – tephra deposits, circles – lava deposits, squares – spatter deposits) with the key sample locations marked by stars.*

5.3 Methods

Samples were collected during a 7-week field season (detailed in Chapter 3.2). The type of samples, locations and type of analysis conducted are summarised in Table 5.1 and Fig. 5.1.

Sample No.	Loc.	Sample Type	Analysis	Grid Ref.	Sample No.	Loc.	Sample Type	Analysis	Grid Ref.
AI-19-008	C1	Spatter	XRF; EPMA; CSD	0575924, 9121450	AI-19-030	F3; FF2	Lava	XRF	0576761, 9120979
AI-19-106	C3	Spatter	XRF	0576011, 9121487	AI-19-032	F8; FF3	Lava	XRF	0576472, 9121029
AI-19-134	C4	Spatter	XRF	0576086, 9121518	AI-19-039	F1/F2; FF1	Lava	XRF	0576563, 9121982
AI-19-145	C5	Spatter	XRF	0576156, 9121512	AI-19-046	F1; FF1	Lava	XRF	0576043, 9121491
AI-19-127	C7	Spatter	XRF; EPMA	0575980, 9121531	AI-19-049	F2; FF1	Lava	XRF	0576218, 9121561
AI-19-121	C8	Spatter	XRF; EPMA; CSD	0576339, 9121425	AI-19-126	F5; FF3	Lava	XRF	0576303, 9121407
AI-19-154	C10	Spatter	XRF	0576477, 9121474	AI-19-148	C5 lava	Lava	XRF	0576156, 9121512
AI-19-155	C11	Spatter	XRF	0576617, 9121438	AI-19-161	F4; FF2	Lava	XRF	0576958, 9121482
AI-19-156	C12	Spatter	XRF	0576635, 9121434	DIP1	Proximal	Light brown Scoria	XRF	0575955, 9121622
AI-19-159	C15	Spatter	XRF	0576901, 9121400	DIP2	Proximal	Scoria	XRF	0575955, 9121622
AI-19-071	C16	Spatter	XRF	0577037, 9121332	DIP3	Proximal	Scoria	XRF; EPMA; CSD	0575955, 9121622
AI-19-157	C17	Spatter	XRF	0577041, 9121361	DIP4	Distal	Pumice	XRF	0575995, 9121929
AI-19-034	C19	Spatter	XRF; EPMA	0577037, 9121332	DIP5	Distal	Pumice	XRF; CSD	0575995, 9121929
AI-19-025	F8; FF3	Lava	XRF	0576427, 9121266	DIP6	Distal	Pumice	XRF; EPMA	0575995, 9121929
AI-19-026	F6; FF3	Lava	XRF; EPMA; CSD	0576508, 9121239	DIP7	Distal	Pumice	XRF	0575995, 9121929
AI-19-027	F7; FF3	Lava	XRF	0576661, 9120943	DIP8	Distal	Dense	XRF; EPMA; CSD	0575995, 9121929
AI-19-028	F7; FF3	Lava	XRF; EPMA; CSD	0576513, 9121149	DIP9	Distal	Banded	XRF	0575995, 9121929

Table 5.1: *showing the samples selected for analysis and description of each sample, including type of sample, location and type of analysis conducted. Loc. – location, C – crater, F – lava flow, FF – lava flow field, XRF – x-ray fluorescence, EPMA – electron microprobe analysis, CSD – crystal size distribution. Proximal samples are less than 100 m from the fissure. Distal samples are more than 100 m from the fissure. Map showing the locations of each sample can be seen in Fig. 5.1.*

5.3.1 Cleaning and crushing

Samples were scrubbed in tap water and cleaned in an ultrasonic bath for 5 minutes to remove excess ash adhering to the surface before being soaked in milli-RO water for 48 hours. After soaking, the samples were lightly scrubbed and placed in the ultrasonic bath for 5 minutes. This process was repeated a minimum of three times or until the water appeared visually clear after the ultrasonic bath. Once clean, the samples were dried in an oven for 72 hours at 70°C.

Tephra samples had previously been sieved (chapter 3) to 5ϕ (32 μm) and samples selected for crushing were from 0 – -1ϕ (1 – 2 mm) size fraction. The samples were crushed further using a hammer, pestle and mortar before milling to powder in an agate swing mill for 15 minutes at Durham University. Spatter and lava samples were sent to the British Geological Survey (BGS) for crushing and milling.

5.3.2 XRF major and trace element analysis of whole rock

Thirty-six lava, spatter and tephra samples were selected for x-ray fluorescence (XRF) analysis. Analyses of major and trace elements were undertaken using the PANalytical Axios Advanced spectrometer at University of Leicester. Major elements were determined on fused glass beads prepared from ignited powders, with a sample to flux ratio of 1:7.5, 80% Li metaborate: 20% Li tetraborate flux. Results are quoted as component oxide weight percent and re-calculated to 100% to remove LOI. Trace elements were analysed on 32 mm diameter pressed powder briquettes. 7.5g sample was mixed with 15-20 drops of 7% PVA solution as a binding agent and pressed at 10 tons per sq. inch. Calibrated standards were run throughout the XRF analysis, at the start and end of each run to monitor for drift and assess precision and accuracy. Tables 5.2 – 5.4 show the calibrating values for three of the standards used (BH-1, WS-1 and MRG-1).

	SiO_2	TiO_2	Al_2O_3	Fe_2O_3	MnO	MgO	CaO	Na_2O	K_2O	P_2O_5
Average	67.36	0.41	15.22	5.72	0.13	2.48	3.50	3.93	0.84	0.08
Minimum	68.31	0.40	15.34	5.74	0.14	2.45	3.52	3.98	0.82	0.09
Maximum	68.42	0.41	15.55	5.80	0.14	2.58	3.58	5.06	0.83	0.09
2σ (wt.%)	0.112	0.003	0.216	0.060	0.00	0.133	0.062	0.082	0.007	0.002
2σ (%)	0.16	0.66	1.49	1.04	0.19	5.29	1.74	2.04	0.90	1.75
Reference	66.35	0.42	13.99	5.66	0.13	2.44	3.44	3.84	0.85	0.07
Offset (wt.%)	2.01	0.02	0.45	0.11	0.01	0.08	0.11	0.18	-0.02	0.02

Table 5.2: *Precision and accuracy of XRF analyses for BH-1 standard (Haslip, no year). N=5*

	SiO_2	TiO_2	Al_2O_3	Fe_2O_3	MnO	MgO	CaO	Na_2O	K_2O	P_2O_5
Average	51.30	2.51	13.94	13.46	0.18	5.30	8.72	3.04	1.34	0.30
Minimum	51.53	2.50	13.90	13.36	0.17	5.04	8.57	2.94	1.29	0.30
Maximum	51.69	2.52	15.00	13.48	0.17	5.27	8.75	3.04	1.29	0.30
2σ (wt.%)	0.16	0.02	0.10	0.12	0.00	0.22	0.18	0.10	0.01	0.00
2σ (%)	0.31	0.79	0.73	0.91	0.24	5.14	2.13	3.30	0.68	0.87
Reference	50.99	2.52	13.95	13.43	0.18	5.28	8.81	3.08	1.36	0.30
Offset (wt.%)	0.63	0.03	0.03	0.07	0.01	0.04	0.19	0.07	0.04	0.00

Table 5.3: *Precision and accuracy of XRF analyses for WS-1 standard (Potts et al., 1994) N=5*

	SiO_2	TiO_2	Al_2O_3	Fe_2O_3	MnO	MgO	CaO	Na_2O	K_2O	P_2O_5
Average	39.49	3.83	8.51	18.12	0.16	13.72	15.77	0.77	0.18	0.07
Minimum	39.87	3.89	8.51	18.16	0.15	13.65	15.83	0.74	0.17	0.06
Maximum	40.01	3.93	8.54	18.32	0.16	13.86	15.12	0.80	0.18	0.06
2σ (wt.%)	0.13	0.05	0.03	0.17	0.00	0.21	0.30	0.06	0.00	0.00
2σ (%)	0.33	1.16	0.34	0.91	1.32	1.54	1.99	7.99	2.75	5.54
Reference	39.09	3.77	8.46	17.93	0.17	13.55	15.71	0.74	0.18	0.08
Offset (wt.%)	0.80	0.11	0.11	0.38	0.01	0.34	0.11	0.05	0.00	0.02

Table 5.4: Precision and accuracy of XRF analyses for MRG-1 standard (Abbey, 1975). N=5

5.3.3 Petrography

All thirty-four samples in table 5.1 were made into thin sections. Lava and spatter samples were made into glass slides, whilst the tephra samples were impregnated with resin prior to being cut and mounted onto glass slides. The sections were studied under a petrographic microscope and a Hitachi SU-70 Scanning Electron Microscope (SEM) at Durham University. To prepare the samples for the SEM they were coated in up to 30 nm of carbon. The SEM was used with a voltage of 15.0 kV and a working distance of 15.00 mm. Images were taken using the backscatter detector for mineral identification and to look for changes in textures. Images under the petrographic microscope were taken in both plane polarised light and cross polarised light.

5.3.4 EPMA major element analysis of minerals and glass

Six spatter and lava samples and four tephra samples for analysis were selected to represent the range in textures and mineral abundances observed in thin sections. The selected samples were made into thin sections at Durham University. Spatter and lava samples were mounted on to glass slides, whilst tephra samples were mounted into resin and polished down by the Thin Section Lab team. The first set of analyses were undertaken using the CAMECA SX100 electron microprobe (EPMA) at the University of Edinburgh. Analytical conditions varied depending on the material being analysed (Table 5.5) and follow the analytical techniques dictated by the lab technician. For all samples, an accelerating voltage of 15 kV was used for analyses. For each set of analysis, two column conditions with varying currents were used for different elements (Table 5.6) Major element concentrations were calibrated using standard allocations (Table 5.7) and the results are presented as weight percent (wt.%) oxide concentration, with Fe calculated as total FeO.

Sample Type	Material	Current (nA)		Beam Size (μm)	Acceleration Potential (kV)
		Cond 1	Cond 2		
Spatter; Lava; Dense tephra clasts	Feldspar	6	100	2.2	15
	Pyroxene	6	100	2.2	15
	Olivine	6	100	2.2	15
	Amphibole	6	100	2.2	15
	Glass	6	100	2.2	15
Scoria tephra clasts; Pumice tephra clasts	Feldspar	2	80	8.8	15
	Pyroxene	2	80	8.8	15
	Olivine	2	80	8.8	15
	Amphibole	2	80	8.8	15
	Glass	2	80	8.8	15

Table 5.5: *Analytical conditions for the EPMA at University of Edinburgh. Following analytical procedures dictated by the lab technician.*

Secondary standards were run throughout the EMPA analysis at the start and end of each run to monitor precision and accuracy (Table 5.8 – 5.12). Access to the published standard values was not possible and therefore only the precision is shown.

Sample Type	Column Condition	Elements
Spatter; Lava, Dense tephra clasts	Condition 1	Na, Si, Fe, Mg, Ca, Al
	Condition 2	Fe, Mg, Ca, K, Ti, Mn, Cr, Al, Sr, Ni, P
Scoria tephra clasts; Pumice tephra clasts	Condition 1	Na, Mg, Al, Si, K, Ca, Fe
	Condition 2	Cl, S, P, Ti, Mn, F, Cr

Table 5.6: *Table showing the different elements measured under the different columns at University of Edinburgh.*

The second set of analyses were undertaken using the JEOL JXA8230 EPMA at the Leeds Electron Microscope and Spectroscopy Centre (LEMAS), University of Leeds. Analytical conditions varied depending on the material being analysed (Table 5.13). Major element concentrations were calibrated using standard allocations and the results are presented as weight percent (wt.%) oxide concentration, with Fe calculated as total FeO.

Standard	Wollastonite	Spinel	Jadeite	PuMn	Fayalite	Orthoclase
Elements	Si, Ca	Mg, Al	Na	Mn	Fe	K
Standard	Celestite	Rutile	Quartz	PuNi	Forsterite	
Elements	Sr	Ti	Si	Ni	Mg, Si	

Table 5.7: *Showing the EPMA primary standards at Edinburgh University. Some elements varied and were measured using different standards. There is no link between the standards used and the type of material analysed.*

	SiO_2	TiO_2	Al_2O_3	FeO	MgO	MnO	CaO	NiO
Average	49.966	0.003	0.603	16.445	7.897	0.485	22.813	0.002
Minimum	49.538	-0.002	0.593	16.345	7.814	0.469	22.564	49.538
Maximum	50.536	0.008	0.615	16.564	8.026	0.497	23.040	50.536
2σ (wt.%)	0.804	0.007	0.018	0.182	0.141	0.020	0.326	0.009
2σ (%)	1.610	213.04	3.07	1.11	1.79	5.11	1.43	421.04

Table 5.8: *Precision of EPMA analyses of local reference material Cpx Block 7 used for a combination of olivine, clinopyroxene and amphibole analysis. N=5*

	SiO_2	FeO	MgO	MnO	NiO
Average	40.070	9.730	49.600	0.130	0.320
Minimum	39.881	9.593	49.552	0.115	0.300
Maximum	40.310	9.916	49.637	0.138	0.340
2σ (wt.%)	0.360	0.273	0.0740	0.018	0.033
2σ (%)	0.900	2.810	0.150	15.480	10.320

Table 5.9: *Precision of EPMA analyses of local reference material Olv Block used for a olivine, clinopyroxene and amphibole analysis. N=3*

	SiO_2	TiO_2	Al_2O_3	FeO	MgO	MnO	CaO	Na_2O	K_2O	Cr_2O_3	P_2O_5	Cl
Average	55.346	2.262	13.125	12.454	3.581	0.187	7.052	3.296	1.854	0.002	0.343	0.010
Minimum	53.631	2.256	12.891	12.247	3.501	0.183	7.025	3.209	1.832	-0.001	0.322	0.008
Maximum	55.793	2.266	13.400	12.570	3.650	0.191	7.089	3.361	1.892	0.004	0.354	0.012
2σ (wt.%)	1.022	0.006	0.419	0.293	0.122	0.007	0.055	0.127	0.054	0.005	0.029	0.004
2σ (%)	1.88	0.25	3.20	2.35	3.41	3.81	0.77	3.87	2.92	207.61	8.33	38.65

	SO_2	F
Average	0.002	0.016
Minimum	0.000	0.014
Maximum	0.005	0.02
2σ (wt.%)	0.004	0.005
2σ (%)	181.99	33.46

Table 5.10: *Precision of EPMA analyses of BCR-2 (Wilson, 1997) used for a combination of plagioclase, olivine, clinopyroxene, amphibole and glass analysis. N=3*

	SiO_2	TiO_2	Al_2O_3	FeO	MgO	MnO	CaO	Na_2O	K_2O	Cr_2O_3	P_2O_5	Cl
Average	75.240	0.080	12.902	1.514	0.034	0.063	0.760	5.106	5.198	-0.004	0.016	0.369
Minimum	75.004	0.074	12.658	1.415	0.031	0.053	0.705	5.061	5.137	-0.006	0.010	0.364
Maximum	75.502	0.085	13.043	1.578	0.038	0.071	0.833	5.129	5.258	-0.002	0.020	0.376
2σ (wt.%)	0.409	0.009	0.346	0.141	0.006	0.015	0.107	0.064	0.098	0.003	0.008	0.010
2σ (%)	0.55	10.98	2.68	9.34	18.83	23.26	15.11	1.55	1.89	-73.46	52.51	2.78

	SO_2	F
Average	0.002	0.068
Minimum	0.002	0.062
Maximum	0.003	0.078
2σ (wt.%)	0.001	0.014
2σ (%)	55.24	20.14

Table 5.11: *Precision of EPMA analyses of local reference material Lipari used for a combination of plagioclase, olivine, clinopyroxene, amphibole and glass analysis. N=3*

	SiO_2	TiO_2	Al_2O_3	FeO	MgO	MnO	CaO	Na_2O	K_2O	SrO
Average	51.181	0.038	29.931	0.409	0.138	0.003	13.442	3.842	0.119	0.059
Minimum	50.186	0.035	29.467	0.393	0.134	-0.011	13.128	3.728	0.115	0.035
Maximum	51.958	0.045	30.624	0.435	0.143	0.011	13.639	5.005	0.123	0.092
2σ (wt.%)	0.896	0.005	0.497	0.025	0.004	0.014	0.335	0.129	0.005	0.030
2σ (%)	1.75	13.96	1.66	6.17	3.03	566.64	2.49	3.36	5.22	52.01

Table 5.12: *Precision of EPMA analyses of local reference material Labradorite used for plagioclase analysis. N=20*

Material	**Current (nA)**	**Beam Size (μm)**	**Acceleration Potential (kV)**
Feldspar	10	5	20
Pyroxene	30	0	20
Olivine	30	0	20

Table 5.13: *Showing the EPMA analytical conditions from Leeds.*

Secondary standards were run throughout the EMPA analysis, including at the start and end of each run to monitor precision and accuracy. Tables 5.14 – 5.21 show the values for each secondary standard.

	SiO_2	TiO_2	Al_2O_3	FeO	MnO	CaO	Na_2O	K_2O	SrO
Average	52.836	0.067	29.337	0.342	0.004	12.154	5.520	0.285	0.125
Minimum	52.298	0.047	29.116	0.317	-0.010	11.979	5.364	0.248	0.020
Maximum	53.193	0.097	29.482	0.367	0.022	12.299	5.666	0.333	0.245
2σ (wt.%)	0.407	0.027	0.242	0.028	0.017	0.178	0.189	0.057	0.153
2σ (%)	0.8	40	0.8	8.1	408	1.5	5.2	20	122
Reference	53.000	0.065	29.580	0.353	0.008	12.261	5.440	0.273	0.125
Offset (wt.%)	0.164	0.002	0.243	0.011	0.004	0.107	0.080	0.012	0.000

Table 5.14: *Precision and accuracy of EPMA analyses of SPH Labradorite (Kearns, no year) used for plagioclase analysis. N=4*

	SiO_2	Al_2O_3	FeO	MgO	CaO	Na_2O	K_2O	SrO
Average	52.884	29.440	0.434	0.074	12.063	5.458	0.366	0.156
Minimum	52.534	29.222	0.412	0.049	11.976	5.267	0.331	0.024
Maximum	53.213	29.722	0.467	0.113	12.215	5.662	0.424	0.224
2σ (wt.%)	0.438	0.298	0.031	0.039	0.114	0.222	0.060	0.114
2σ (%)	0.8	1.0	7.2	52.0	0.9	5.0	16.5	72.9
Reference	52.865	29.250	0.457	0.089	12.383	5.304	0.337	0.132
Offset (wt.%)	0.019	0.190	0.023	0.015	0.320	0.154	0.029	0.024

Table 5.15: *Precision and accuracy of EPMA analyses of SKL1 Labradorite (Kearns, no year) used for plagioclase analysis. N=4*

	SiO_2	Al_2O_3	Na_2O	K_2O
Average	65.813	18.714	1.375	15.485
Minimum	65.482	18.556	1.289	15.570
Maximum	66.244	18.972	1.523	17.457
2σ (wt.%)	0.422	0.192	0.108	2.067
2σ (%)	0.6	1.0	7.9	13.3
Reference	65.036	18.536	1.361	15.672
Offset (wt.%)	0.777	0.178	0.014	0.813

Table 5.16: *Precision and accuracy of EPMA analyses of GEO2 KSPAR (ref unknown) used for plagioclase analysis. N=4*

	SiO_2	Al_2O_3	FeO	MgO	CaO	Na_2O	K_2O	SrO
Average	51.277	30.575	0.410	0.128	13.522	3.723	0.120	0.090
Minimum	50.963	30.363	0.385	0.101	13.364	3.661	0.103	0.038
Maximum	51.474	30.801	0.430	0.163	13.720	3.822	0.145	0.188
2σ (wt.%)	0.296	0.247	0.029	0.035	0.230	0.096	0.026	0.104
2σ (%)	0.6	0.8	7.1	26.9	1.7	2.6	21.3	115.3
Reference	51.299	30.179	0.424	0.138	13.770	3.688	0.114	0.067
Offset (wt.%)	0.022	0.396	0.014	0.010	0.248	0.035	0.006	0.023

Table 5.17: *Precision and accuracy of EPMA analyses of SKBy1 Bytownite (Kearns, no year) used for plagioclase analysis. N=3*

	SiO_2	Al_2O_3	CaO	Na_2O	K_2O
Average	67.291	20.324	0.934	10.974	0.410
Minimum	67.010	20.141	0.888	10.705	0.347
Maximum	67.673	20.430	0.966	11.190	0.493
2σ (wt.%)	15.140	9.697	11.842	6.906	0.250
2σ (%)	22.5	47.7	1267.7	62.9	60.8
Reference	67.350	20.540	0.960	11.010	0.340
Offset (wt.%)	0.059	0.216	0.026	0.036	0.070

Table 5.18: *Precision and accuracy of EPMA analyses of local reference material WRS1485 Plag used for plagioclase analysis. N=3*

	SiO_2	FeO	MnO	MgO	CaO	NiO
Average	40.084	9.560	0.138	48.340	0.091	0.374
Minimum	39.693	9.499	0.130	48.118	0.087	0.363
Maximum	40.289	9.603	0.150	48.545	0.095	0.392
2σ (wt.%)	0.362	0.070	0.011	0.240	0.006	0.018
2σ (%)	0.9	0.7	8.2	0.5	7.0	5.9
Reference	40.810	9.550	0.139	49.421	0.050	0.370
Offset (wt.%)	0.726	0.010	0.001	1.081	0.041	0.004

Table 5.19: *Precision and accuracy of EPMA analyses of San Carlos Olivine used for olivine and clinopyroxene analysis. N=2*

	SiO_2	Al_2O_3	FeO	MnO	MgO	CaO	Na_2O
Average	55.170	0.049	0.197	0.037	18.496	25.906	0.053
Minimum	53.089	0.041	0.182	0.029	18.429	25.777	0.035
Maximum	55.908	0.060	0.214	0.043	18.563	25.961	0.068
2σ (wt.%)	1.319	0.010	0.020	0.009	0.086	0.112	0.022
2σ (%)	2.4	21.0	9.9	25.6	0.5	0.4	41.9
Reference	55.872	0.110	0.241	0.040	18.301	25.631	0.340
Offset (wt.%)	-0.702	-0.061	-0.044	-0.003	0.195	0.275	-0.287

Table 5.20: *Precision and accuracy of EPMA analyses of NY Diopside (Jarosewich, 1980) used for olivine and clinopyroxene analysis. N=2*

	SiO_2	FeO	MgO	CaO
Average	55.679	0.729	18.446	25.576
Minimum	55.201	0.697	18.336	25.432
Maximum	55.035	0.767	18.510	25.738
2σ (wt.%)	0.472	0.049	0.100	0.172
2σ (%)	0.9	6.8	0.5	0.7
Reference	55.360	0.900	18.130	25.720
Offset (wt.%)	0.681	0.171	0.316	0.144

Table 5.21: *Precision and accuracy of EPMA analyses of GEO2 Diopside (Jarosewich, 1980) used for olivine and clinopyroxene analysis. N=2*

5.4 Results

5.4.1 Whole rock geochemistry

The whole-rock compositions of all DIP products are trachyandesite with limited variations in major element concentrations (Fig. 5.2, Table 5.22). Whole-rock SiO_2 and Mg# ((MgO/40.3)/[(MgO/40.3) + (FeO*2/159.69)]) (Putirka et al., 2007) show minimal variation from 56.28 – 57.80 wt.% and 33 – 36. Total alkalis range from 7.89 – 8.48 wt.%.

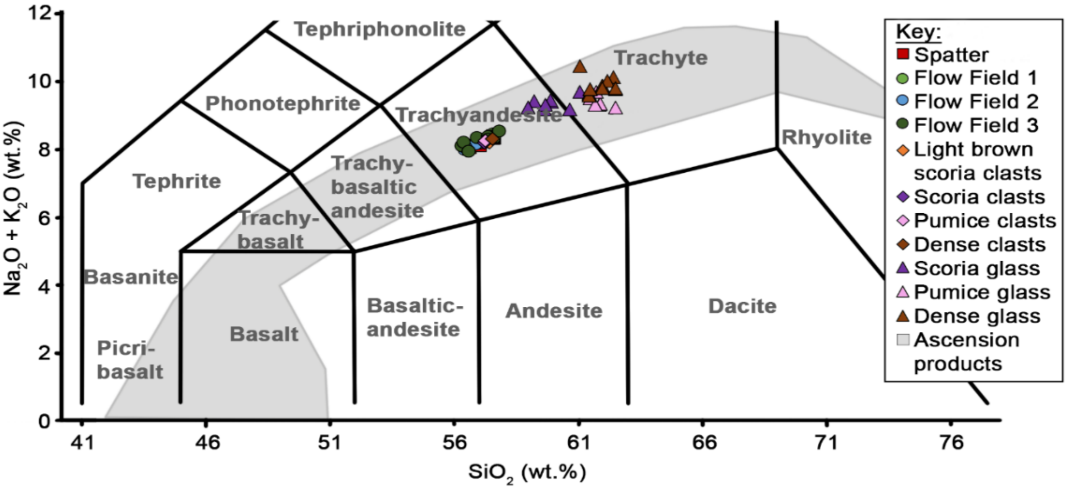

Figure 5.2: *TAS diagram with both whole-rock major and glass data for the DIP samples. Squares, circles, and diamonds show the whole-rock compositions of the spatter, lava and tephra samples. Triangles represent the glass compositions of the tephra samples (scoria, pumice, and dense clasts). Grey field shows all known Ascension Island whole rock data (Data from Weaver et al, 1996; Kar et al., 1998).*

The spatter samples range between 2.1 – 2.4 wt.% MgO (Fig. 5.3) and show no significant variations in major element concentrations. Samples from craters 3 and 18, craters 15 and 16 and crater 11, cluster at 2.2 wt.% MgO, 2.3 wt.% MgO, and 2.4 wt.% MgO, respectively, however they are all within the 2σ error range. As the spatter samples increase in MgO concentration, they also increase in TiO_2, Fe_2O_3 and CaO concentrations

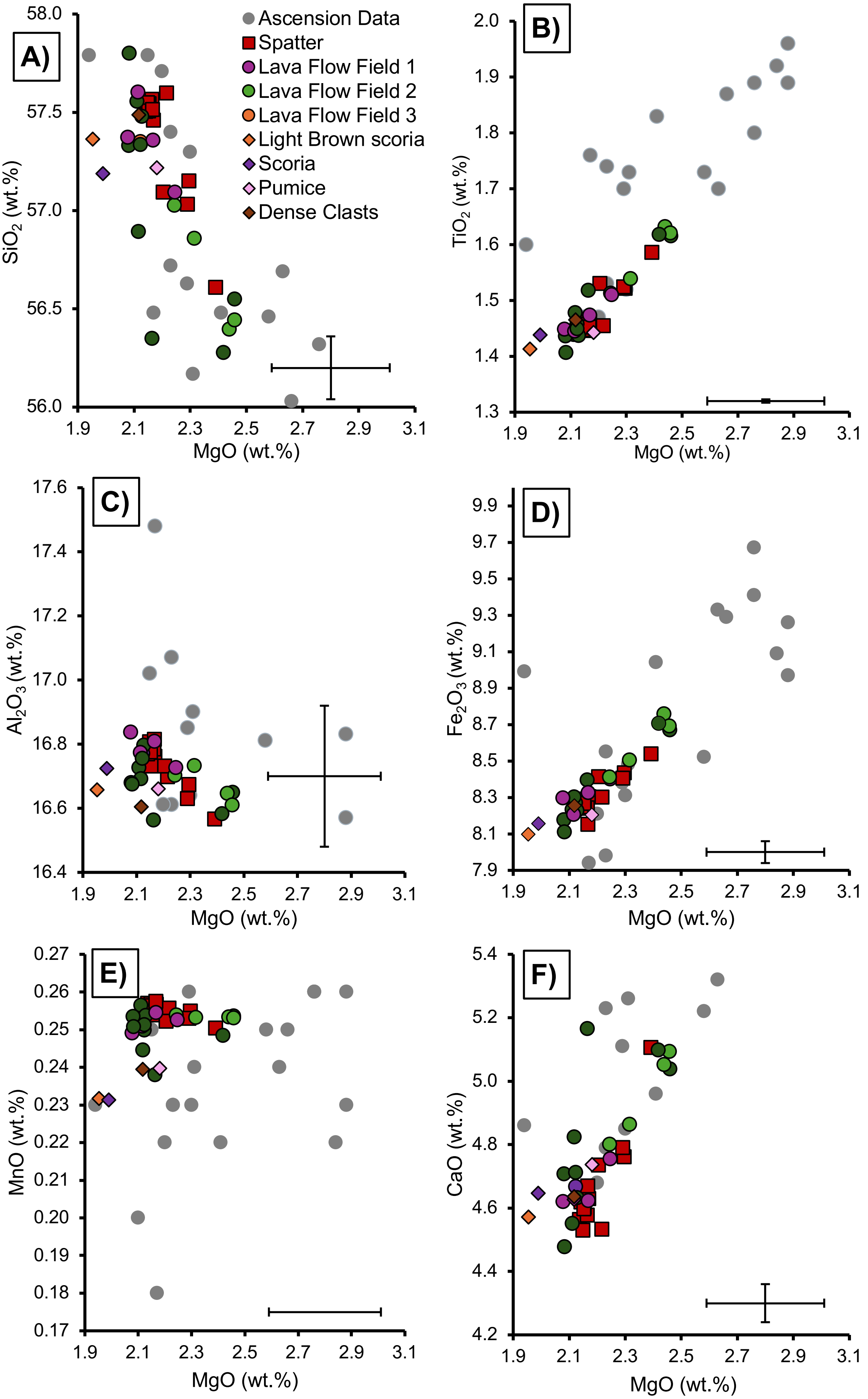
A)
SiO$_2$ (wt.%)
58.0
57.5
57.0
56.5
56.0
MgO (wt.%)
1.9
2.1
2.3
2.5
2.7
2.9
3.1
Ascension Data
Spatter
Lava Flow Field 1
Lava Flow Field 2
Lava Flow Field 3
Light Brown scoria
Scoria
Pumice
Dense Clasts
B)
TiO$_2$ (wt.%)
2.0
1.9
1.8
1.7
1.6
1.5
1.4
1.3
MgO (wt.%)
C)
Al$_2$O$_3$ (wt.%)
17.6
17.4
17.2
17.0
16.8
16.6
16.4
MgO (wt.%)
D)
Fe$_2$O$_3$ (wt.%)
9.9
9.7
9.5
9.3
9.1
8.9
8.7
8.5
8.3
8.1
7.9
MgO (wt.%)
E)
MnO (wt.%)
0.27
0.26
0.25
0.24
0.23
0.22
0.21
0.20
0.19
0.18
0.17
MgO (wt.%)
F)
CaO (wt.%)
5.4
5.2
5.0
4.8
4.6
4.4
4.2
MgO (wt.%)

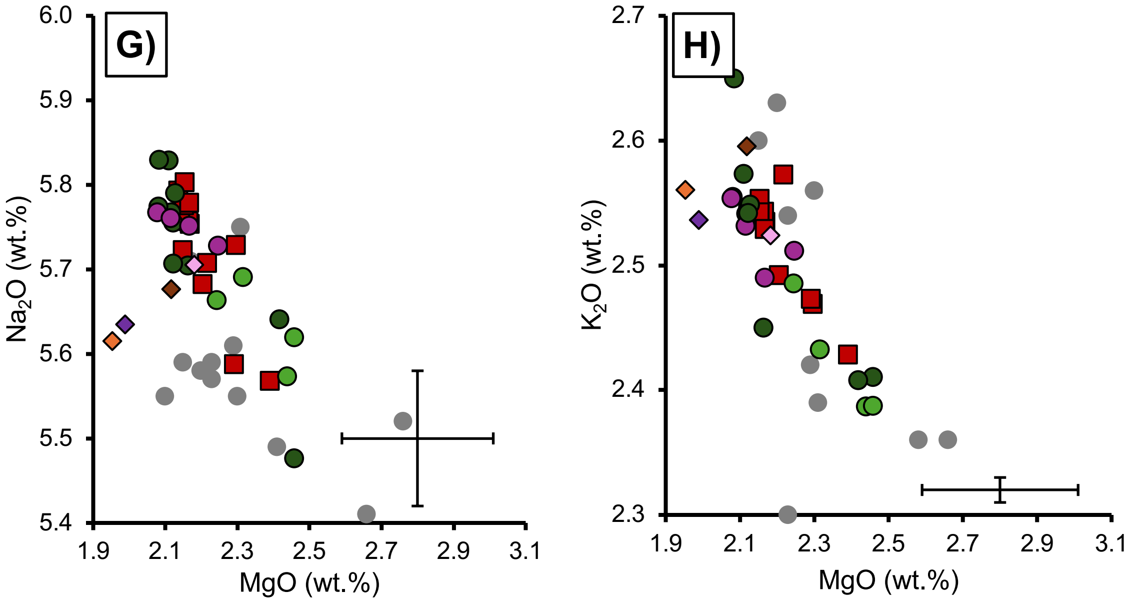

Figure 5.3: *Whole-rock variation for the DIP spatter (red squares), lava (green and blue circles) and tephra (orange, purple, pink and brown diamonds). Full data set shown in Table 5.23. Grey circles represent other trachyandesite deposits on Ascension Island (Weaver et al., 1996; Kar et al., 1998). Error bars show 2σ uncertainty.*

and decrease in SiO_2, Al_2O_3, MnO, Na_2O and K_2O concentrations. There is no correlation between the changes in major elements and spatial location along the fissure.

Lava samples range between 2.1 – 2.5 wt.% MgO, however they are all within the 2-sigma error range (Fig. 5.3). Samples from flow field 1 cluster within the 2.1 – 2.2 wt.% MgO, whilst lava samples from flow field 2 cluster between 2.4 – 2.5 wt.% MgO and lava samples from flow field 3 also cluster between 2.1 – 2.2 wt.% MgO, with two samples within the 2.4 – 2.5 wt.% MgO. Scoria components have the lowest MgO concentrations (1.9 – 2.0 wt.% MgO), whilst the dense clasts and pumice clasts range within the 2.1 – 2.2 wt.% MgO. Lava samples from flow field 2 is more enriched in MgO than all lavas samples in flow field 1 and all but one of the lavas in flow field 3. Lava from the top of the ridge (F8 – Fig. in Ch.3) in flow field 3 is enriched in SiO_2, Al_2O_3, MnO and K_2O wt.% for any given concentration of MgO wt.%. Lava from the base of the ridge sits within the cluster of the flow field 3 samples. Single lava flows also show minimal changes along the flow, with <0.04 difference in MgO concentrations. Minimal variation is also observed in flow field 2. Samples from one of the central channels has lower MgO concentrations than samples from the channel margins (2.3 and 2.4 wt.% MgO, respectively) but slightly higher MgO concentrations (2.2 wt.% MgO) than a lobe that broke out from the central channel.

Some differences were identified from the whole rock data for the different tephra components (Fig. 5.3). The scoria clasts are slightly depleted in MgO, MnO and Fe_2O_3 compared to both the dense clasts and the pumice clasts. The pumice clasts are more depleted in SiO_2, TiO_2, Fe_2O_3 and K_2O and enriched in Na_2O, CaO and Al_2O_3 compared to the dense clasts.

The compositions of the DIP samples overlap with those reported in previous studies of Ascension Island (e.g., Weaver et al., 1996; Kar et al., 1998; Chamberlain et al., 2019). However, the DIP samples are slightly depleted in TiO_2 and enriched in Na_2O in comparison (Fig. 5.3).

5.4.2 Trace Elements

Trace element concentrations also show limited variations (Fig. 5.4) and, although all follow a similar trend to OIB in REE space, are more enriched in all trace elements than a classic OIB (Sun & McDonough, 1995). The DIP products are more enriched than classic OIB (McDonough and Sun, 1995). The DIP products sit within the same range as the other trachyandesite samples on the island, however, U and Pb concentrations show the widest range, with some samples more enriched and others more depleted. High Zr/Nb basalts (Fig. 5.4)). The Low Zr/Nb basalt is more enriched in U and sits within the range of the DIP products, whilst the Sr concentrations sit just above the DIP products. On the other hand, the Ascension trachyte products are generally more enriched in incompatible trace elements than the DIP products (Fig. 5.4), with the exceptions of U, La, Ce and Nd which are within the same range, and Sr and Y which are more depleted.

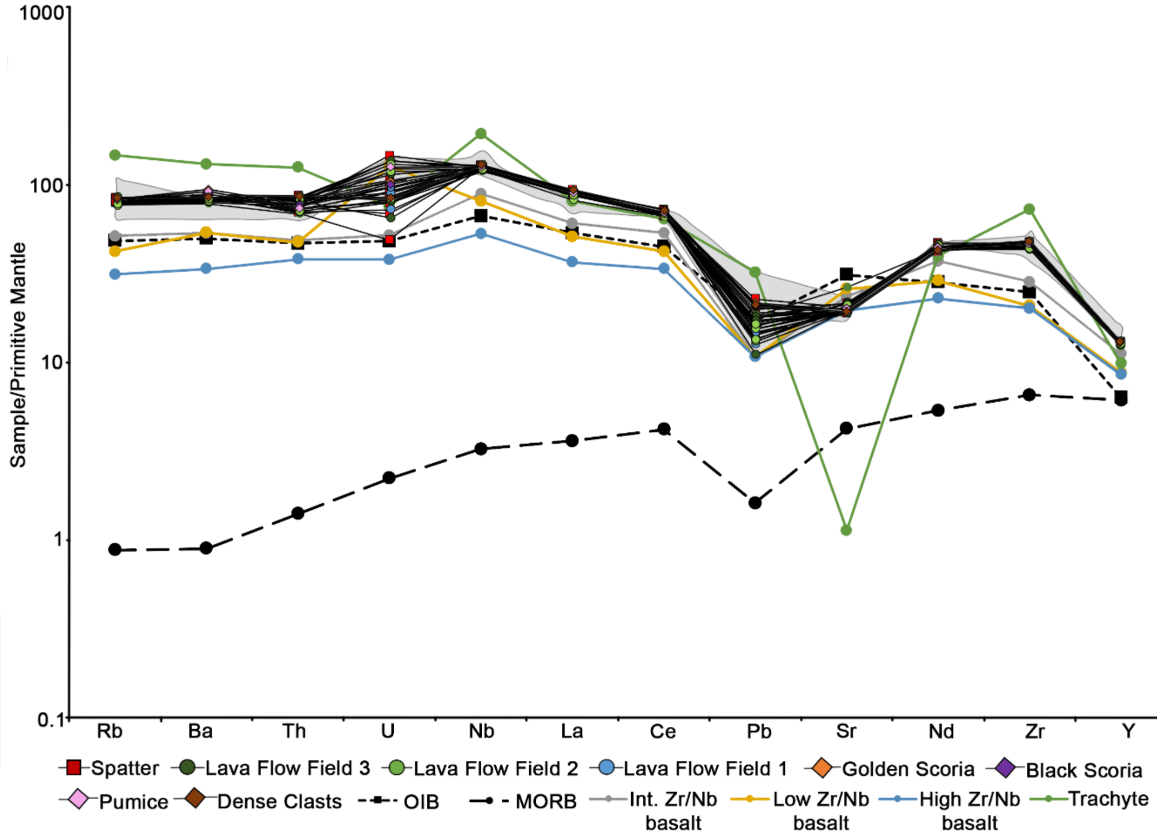

Figure 5.4: *Primitive mantle normalised trace elements from the DIP deposits. The grey field represents the trace elements of all the intermediate deposits on the island. Solid lines (grey, blue, yellow and green) show trace element compositions of basaltic and trachytic samples on Ascension Island. OIB (McDonough and Sun, 1995) and MORB (McDonough and Sun, 1995) also included.*

Sample:	**AI-19-008**	**AI-19-106**	**AI-19-134**	**AI-19-145**	**AI-19-127**	**AI-19-121**	**AI-19-154**	**AI-19-155**	**AI-19-156**	**AI-19-157**	**AI-19-159**	**AI-19-034**	**AI-19-071**	**AI-19-024**
Type:	*Spatter*	*Spatter*	*Spatter*	*Spatter*	*Spatter*	*Spatter*	*Spatter*	*Spatter*	*Spatter*	*Spatter*	*Spatter*	*Spatter*	*Spatter*	*Lava*
SiO_2	57.31	57.66	57.58	57.68	57.63	57.61	57.52	57.01	57.31	57.44	57.24	57.03	56.73	55.95
TiO_2	1.46	1.46	1.45	1.45	1.46	1.45	1.46	1.60	1.44	1.45	1.52	1.53	1.52	1.51
Al_2O_3	16.72	16.71	16.78	16.82	16.76	16.80	16.80	16.68	16.72	16.79	16.70	16.71	16.54	16.44
Fe_2O_3	8.28	8.31	8.26	8.26	8.25	8.26	8.29	8.60	8.24	8.14	8.45	8.40	8.36	8.34
MnO	0.26	0.26	0.26	0.26	0.25	0.26	0.26	0.25	0.26	0.26	0.26	0.25	0.25	0.24
MgO	2.16	2.22	2.14	2.17	2.16	2.15	2.15	2.41	2.15	2.17	2.30	2.20	2.28	2.15
CaO	5.62	5.54	5.56	5.58	5.61	5.63	5.53	5.14	5.58	5.66	5.77	5.73	5.76	5.13
Na_2O	5.74	5.71	5.79	5.77	5.81	5.77	5.72	5.61	5.76	5.77	5.74	5.68	5.56	5.66
K_2O	2.53	2.58	2.54	2.55	2.56	2.54	2.54	2.45	2.53	2.53	2.47	2.49	2.46	2.43
P_2O_5	0.67	0.67	0.67	0.67	0.66	0.71	0.70	0.96	0.68	0.67	0.71	0.89	1.01	1.45
SO_3	0.00	0.00	0.00	0.00	0.00	0.00	0.00	0.00	0.00	0.00	0.00	0.00	0.00	0.00
LOI	0.26	0.28	0.29	0.20	0.17	0.16	0.41	0.24	0.12	0.22	0.16	0.30	0.44	0.61
Total	100.00	100.39	100.31	100.39	100.32	100.35	100.35	100.95	99.78	100.10	100.31	100.19	99.90	99.91
As	1.5	0.8	<0.6	<0.7	1.4	1.1	0.7	1.1	1.0	0.9	1.0	2.9	1.0	3.3
Ba	620.1	602.5	620.8	606.6	623.2	620.0	621.5	589.9	622.8	623.0	605.2	592.6	598.1	585.8
Ce	122.4	120.6	127.6	127.7	125.5	127.8	129.5	127.6	128.9	121.0	119.3	125.6	128.5	125.2
Co	6.6	8.6	6.5	9.1	8.2	9.0	7.9	7.9	8.0	6.6	8.6	8.3	10.4	8.0
Cr	<0.7	<0.7	<0.7	<0.7	<0.7	<0.7	<0.7	<0.7	<0.7	<0.7	<0.7	<0.7	<0.7	<0.7
Cs	<1.8	2.5	2.4	<1.7	1.9	<1.8	2.1	<1.8	<1.9	2.6	<1.8	<1.8	2.7	<1.8
Cu	55.6	6.5	15.3	9.9	15.3	7.9	33.6	29.1	19.3	6.6	33.2	13.1	6.4	140.2
Ga	27.3	25.1	27.0	26.6	26.9	27.1	26.8	26.0	27.1	28.1	26.5	25.8	26.6	26.2
La	63.5	63.5	62.4	63.2	63.9	62.2	65.0	61.1	63.3	61.9	60.3	60.7	61.0	60.4
Mo	5.7	5.2	5.6	5.3	5.4	5.2	5.4	5.3	5.7	5.7	5.5	6.2	5.0	5.5
Nb	90.6	89.8	92.1	89.9	91.8	91.6	92.1	89.1	91.7	91.2	90.2	89.7	89.8	88.1
Nd	61.6	57.6	61.8	59.3	65.1	60.3	63.0	62.8	62.0	59.4	59.8	62.9	60.2	60.2
Ni	<0.7	<0.7	<0.7	<0.7	<0.7	<0.7	<0.7	<0.7	<0.7	<0.7	<0.7	<0.7	<0.7	<0.7
Pb	3.4	2.7	3.4	3.6	2.6	2.7	2.9	3.7	3.4	3.1	3.1	5.3	3.4	3.0
Rb	53.1	52.7	53.0	52.4	53.8	53.1	53.5	50.5	53.8	52.9	52.2	51.4	50.9	50.7
Sb	<1.1	<1.1	<1.1	<1.1	<1.1	<1.1	<1.1	<1.1	<1.1	<1.1	<1.1	<1.1	<1.1	<1.1
Sc	12.2	11.6	13.3	13.1	13.0	11.9	12.1	12.2	11.5	13.1	13.6	11.9	15.3	12.8
Se	<0.7	<0.7	<0.7	<0.7	<0.7	<0.7	<0.7	<0.7	<0.7	<0.7	<0.7	<0.7	<0.7	<0.7
Sn	15.0	2.9	6.0	2.7	5.1	2.6	10.4	8.2	7.0	2.2	9.1	3.8	3.6	42.2
Sr	415.4	399.9	415.4	405.0	419.3	421.4	416.6	457.1	420.4	425.5	428.0	436.1	443.5	456.3
Th	7.4	5.9	6.3	7.4	6.8	6.9	6.2	6.2	7.3	7.2	6.4	6.5	6.2	7.1
U	2.2	1.0	1.7	1.8	2.1	1.8	1.7	1.9	1.7	2.0	1.5	3.1	1.9	2.6
V	49.1	49.0	49.2	46.2	46.8	48.4	49.5	58.8	47.6	48.6	51.2	52.7	56.9	55.2
W	2.5	1.3	1.6	<1.2	1.3	2.4	2.6	0.2	<1.2	2.7	<1.2	2.2	<1.2	1.8
Y	59.1	58.8	60.2	58.5	59.6	59.7	59.8	59.0	60.0	59.3	59.2	59.1	59.7	58.2
Zn	142.7	132.9	135.9	135.7	135.5	132.6	135.6	138.9	133.0	136.1	137.4	136.8	136.1	137.6

Sample:	**AI-19-025**	**AI-19_026**	**AI-19-027**	**AI-19-028**	**AI-19-029**	**AI-19-30**	**AI-19-125**	**AI-19-126**	**AI-19-148**	**AI-19-032**	**AI-19-031**	**AI-19-033**	**AI-19-013**	**AI-19-161**
Type:	*Lava*	*Lava*	*Lava*	*Lava*	*Lava*	*Lava*	*Lava*	*Lava*	*Lava*	*Lava*	*Lava*	*Lava*	*Lava*	*Lava*
SiO_2	57.49	57.33	57.63	56.73	57.21	56.22	57.15	57.92	57.21	56.67	56.66	57.04	56.35	56.68
TiO_2	1.44	1.46	1.44	1.47	1.43	1.62	1.44	1.41	1.51	1.62	1.53	1.51	1.63	1.63
Al_2O_3	16.71	16.76	16.84	16.64	16.64	16.56	16.70	16.71	16.76	16.68	16.67	16.70	16.63	16.68
Fe_2O_3	8.22	8.27	8.25	8.28	8.16	8.69	8.22	8.13	8.42	8.69	8.47	8.41	8.75	8.73
MnO	0.26	0.25	0.25	0.24	0.25	0.25	0.25	0.25	0.25	0.25	0.25	0.25	0.25	0.25
MgO	2.11	2.12	2.13	2.11	2.08	2.42	2.12	2.09	2.25	2.46	2.31	2.25	2.44	2.47
CaO	5.54	5.66	5.64	5.81	5.70	5.09	5.69	5.49	5.76	5.05	5.85	5.80	5.05	5.11
Na_2O	5.82	5.75	5.81	5.75	5.76	5.63	5.69	5.84	5.74	5.49	5.67	5.66	5.57	5.64
K_2O	2.57	2.55	2.56	2.53	2.55	2.41	2.53	2.66	2.52	2.42	2.42	2.49	2.39	2.40
P_2O_5	0.73	0.81	0.71	1.14	1.01	1.00	0.86	0.72	0.78	0.88	0.81	0.90	0.86	0.81
SO_3	0.00	0.00	0.00	0.00	0.00	0.01	0.02	0.00	0.00	0.00	0.00	0.00	0.00	0.02
LOI	0.25	0.36	0.10	0.38	0.30	0.22	0.48	0.18	0.24	0.21	0.57	0.31	0.24	0.26
Total	100.13	100.32	100.37	100.09	100.08	100.12	100.16	100.39	100.44	100.42	100.21	100.33	100.15	100.67
As	2.2	1.2	0.7	2.2	1.6	1.5	0.7	<0.6	1.6	1.4	0.8	1.2	1.2	1.8
Ba	615.7	601.1	613.6	601.3	591.7	582.1	612.6	605.6	595.8	565.6	596.1	606.2	572.7	590.7
Ce	127.0	122.5	125.9	125.0	121.5	120.2	123.3	125.9	119.9	123.4	125.3	123.5	119.4	126.1
Co	10.2	7.6	7.8	7.8	8.8	8.2	7.6	7.8	7.9	9.1	8.6	7.7	8.5	10.5
Cr	<0.7	<0.7	<0.7	<0.7	<0.7	<0.7	<0.7	<0.7	<0.7	<0.7	<0.7	<0.7	<0.7	<0.7
Cs	<1.8	<1.8	<1.8	<1.8	2.2	<1.8	1.9	5.5	2.4	<1.8	<1.8	2.0	<1.8	<1.8
Cu	15.3	11.4	11.2	13.8	15.3	10.1	22.2	12.4	5.8	72.5	16.7	17.3	18.0	10.7
Ga	26.6	26.1	26.5	26.6	26.8	26.5	26.5	26.9	25.5	25.2	26.4	26.3	26.0	26.4
La	63.3	63.0	61.4	61.7	62.8	61.2	62.3	61.4	62.1	61.0	65.1	60.6	57.2	60.7
Mo	6.0	5.7	5.5	5.5	5.5	5.8	5.2	5.4	5.0	5.5	5.2	6.0	5.1	6.0
Nb	92.4	89.4	91.2	91.4	90.4	88.5	90.6	93.7	88.7	86.8	89.2	90.8	87.3	88.2
Nd	61.4	61.1	63.9	61.2	59.9	60.8	60.9	61.7	59.6	59.6	60.2	60.0	60.3	62.5
Ni	<0.7	<0.7	<0.7	<0.7	<0.7	<0.7	<0.7	<0.7	<0.7	<0.7	<0.7	<0.7	<0.7	<0.7
Pb	3.8	3.1	3.9	3.4	2.9	3.0	2.1	3.2	2.4	3.1	2.9	3.1	2.5	2.5
Rb	55.8	52.5	53.7	52.4	53.0	49.7	52.4	55.0	51.0	49.8	51.3	52.0	49.3	50.0
Sb	<1.1	<1.1	<1.1	<1.1	<1.1	<1.1	<1.1	<1.1	<1.1	<1.1	<1.1	<1.1	<1.1	1.1
Sc	13.4	12.0	12.4	12.6	13.1	15.2	13.8	13.2	13.3	12.6	12.5	13.2	13.5	15.2
Se	<0.7	<0.7	<0.7	<0.7	<0.7	<0.7	<0.7	<0.7	<0.7	<0.7	1.0	0.7	<0.7	<0.7
Sn	5.9	1.9	3.1	3.5	5.5	3.6	9.1	5.9	2.1	21.0	3.8	6.2	5.4	2.8
Sr	411.4	418.7	421.7	465.9	423.9	459.3	422.8	406.9	419.8	439.5	441.4	438.8	440.6	448.1
Th	7.3	6.5	7.3	7.4	7.2	7.0	6.4	7.0	6.0	6.5	7.1	6.6	6.8	6.1
U	2.9	2.0	2.4	2.9	1.8	2.9	1.7	1.4	1.5	2.2	2.8	2.2	2.5	1.8
V	48.0	47.4	48.0	50.4	45.9	60.5	46.1	47.4	55.1	59.5	55.0	50.0	61.9	61.6
W	2.4	1.8	2.0	<1.2	2.3	2.6	<1.2	<1.2	<1.2	1.9	1.3	3.6	2.3	2.7
Y	60.1	58.4	60.0	59.6	59.0	59.1	58.6	60.7	58.2	58.0	59.5	59.8	58.8	58.8
Zn	137.8	137.0	136.1	143.7	139.2	141.8	132.0	136.8	137.4	145.6	137.9	141.0	142.1	140.0

Sample:	**AI-19-039**	**AI-19-046**	**AI-19-049**	**AI-19-023**	**DIP3**	**DPI3**	**DIP6**	**DIP8**
Type:	*Lava*	*Lava*	*Lava*	*Lava*	*Scoria*	*Scoria*	*Pumice*	*Dense*
SiO_2	57.33	57.93	57.21	52.57	57.79	57.77	57.75	57.99
TiO_2	1.45	1.45	1.47	1.43	1.42	1.45	1.46	1.48
Al_2O_3	16.82	16.87	16.76	15.43	16.78	16.89	16.81	16.75
Fe_2O_3	8.29	8.25	8.30	7.80	8.16	8.24	8.28	8.33
MnO	0.25	0.25	0.25	0.22	0.23	0.23	0.24	0.24
MgO	2.08	2.13	2.16	2.17	1.97	2.01	2.20	2.14
CaO	5.61	5.65	5.61	6.78	5.61	5.69	5.78	5.68
Na_2O	5.76	5.79	5.74	5.51	5.66	5.69	5.76	5.73
K_2O	2.55	2.55	2.48	2.34	2.58	2.56	2.55	2.62
P_2O_5	0.78	0.69	0.75	3.48	0.87	0.87	0.66	0.75
SO_3	0.00	0.00	0.00	0.15	0.00	0.00	0.00	0.00
LOI	0.35	0.19	0.37	1.10	0.67	0.60	0.44	0.18
Total	100.27	100.75	100.11	98.96	100.73	101.02	100.93	100.88
As	1.4	0.7	1.2	3.4	2.3	2.0	1.4	2.1
Ba	611.6	618.1	620.4	555.7	662.0	622.5	645.1	597.9
Ce	123.7	121.6	125.4	120.3	128.5	129.8	125.9	128.8
Co	8.9	7.9	7.4	8.3	6.7	8.1	6.6	8.3
Cr	<0.7	<0.7	<0.7	<0.7	<0.6	<0.6	<0.6	<0.7
Cs	<1.8	<1.8	2.0	<1.9	<1.7	<1.7	<1.7	<1.7
Cu	5.4	5.1	15.8	90.6	8.1	10.1	8.7	11.1
Ga	27.6	25.8	26.9	25.5	26.9	26.5	26.4	25.7
La	61.3	61.1	62.2	61.4	63.7	63.5	62.6	65.8
Mo	5.6	5.3	6.0	5.2	5.3	5.2	5.4	5.0
Nb	90.7	90.1	91.6	86.3	91.7	91.5	90.5	93.2
Nd	58.7	60.4	59.2	59.3	60.7	61.4	60.5	58.4
Ni	<0.7	<0.7	<0.7	<0.7	<0.7	<0.7	<0.7	<0.7
Pb	2.6	2.8	2.7	3.4	5.0	3.9	3.9	3.9
Rb	53.1	52.6	52.1	49.8	53.5	53.1	52.9	55.2
Sb	<1.1	<1.1	1.6	<1.1	7.5	1.7	8.1	<1.1
Sc	13.1	12.7	11.6	11.2	15.3	12.6	15.0	15.8
Se	<0.7	<0.7	<0.7	1.0	<0.7	<0.7	<0.7	<0.7
Sn	2.2	2.7	5.7	32.1	2.7	2.2	2.5	1.5
Sr	421.9	412.2	422.5	568.0	419.4	426.0	427.1	410.1
Th	7.1	7.1	6.9	5.9	6.6	6.6	6.4	7.4
U	2.2	1.9	2.0	1.7	2.2	2.1	2.7	1.8
V	48.7	47.5	49.5	51.4	45.3	47.9	50.9	52.2
W	2.7	1.4	1.6	<1.2	2.7	2.5	2.7	3.5
Y	59.1	59.0	59.5	57.1	60.1	59.8	59.1	60.2
Zn	133.3	131.7	152.0	135.8	147.5	131.2	153.6	133.9
Zr	525.8	522.8	528.2	489.4	538.7	535.8	526.1	541.8

Table 5.22: The whole rock data for spatter, lava and tephra samples

5.4.3 Petrography

Following the definition of D'Mello et al., (2021) I consider macrocrysts as any single grain >300 μm in diameter, microphenocrysts are 300 – 30 μm in diameter and microlites are <30 μm in diameter. Macrocryst and microphenocryst phases, in order of abundance, consist of feldspar, rare olivine, pyroxene, amphibole and Fe-Ti oxides. Groundmass textures are described and discussed in chapter 4/5.

5.4.3.1 Plagioclase Feldspar

Plagioclase feldspar macrocrysts and microphenocrysts are the most abundant mineral phase in all samples. The plagioclases in the spatter and lava are similar sizes, ranging from 100 – 4000 μm in diameter, whilst the plagioclase in the tephras is smaller and range from 100 – 1000 μm in diameter. Three different textures were identified in back scatter electron (BSE) imagery. Type 1 feldspars only occur in spatter, lava and dense clast tephra samples. Type 2 feldspars occur in all the DIP samples and Type 3 feldspars are only present in the lava and spatter samples.

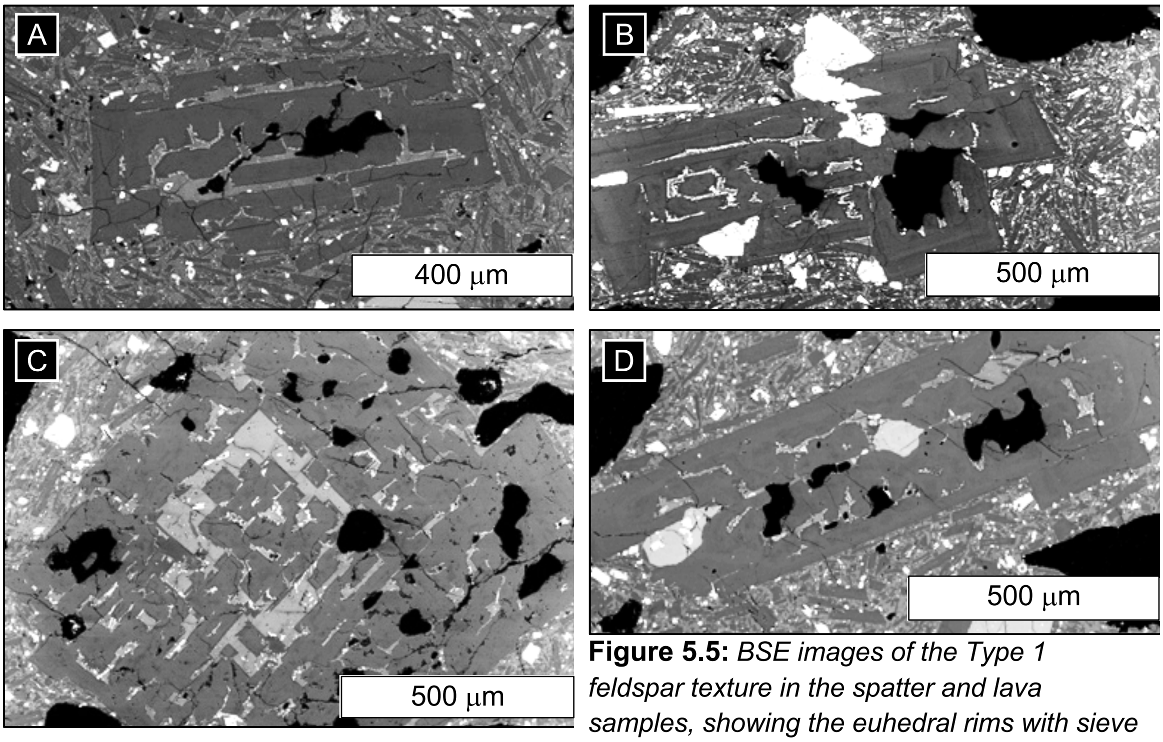

Figure 5.5: *BSE images of the Type 1 feldspar texture in the spatter and lava samples, showing the euhedral rims with sieve textures.* ***B, D)*** *exhibt weak oscillitary zoning.*

Type 1 feldspars (Fig. 5.5) make up ~ 45% of the feldspar population in the samples and occur as macrocrysts and occasionally microphenocrysts. They are euhedral to subhedral, tabular and can be both elongate and stumpy. Type 1 are characterised by sieve textures. Approximately 1% of the feldspars exhibit oscillatory zoning, however this is difficult to identify due to the sieve textures.

Type 2 feldspars (Fig. 5.6) are the most common and make up ~55% of the feldspar population. Macrocrysts are euhedral or subhedral, tabular and vary between elongate and

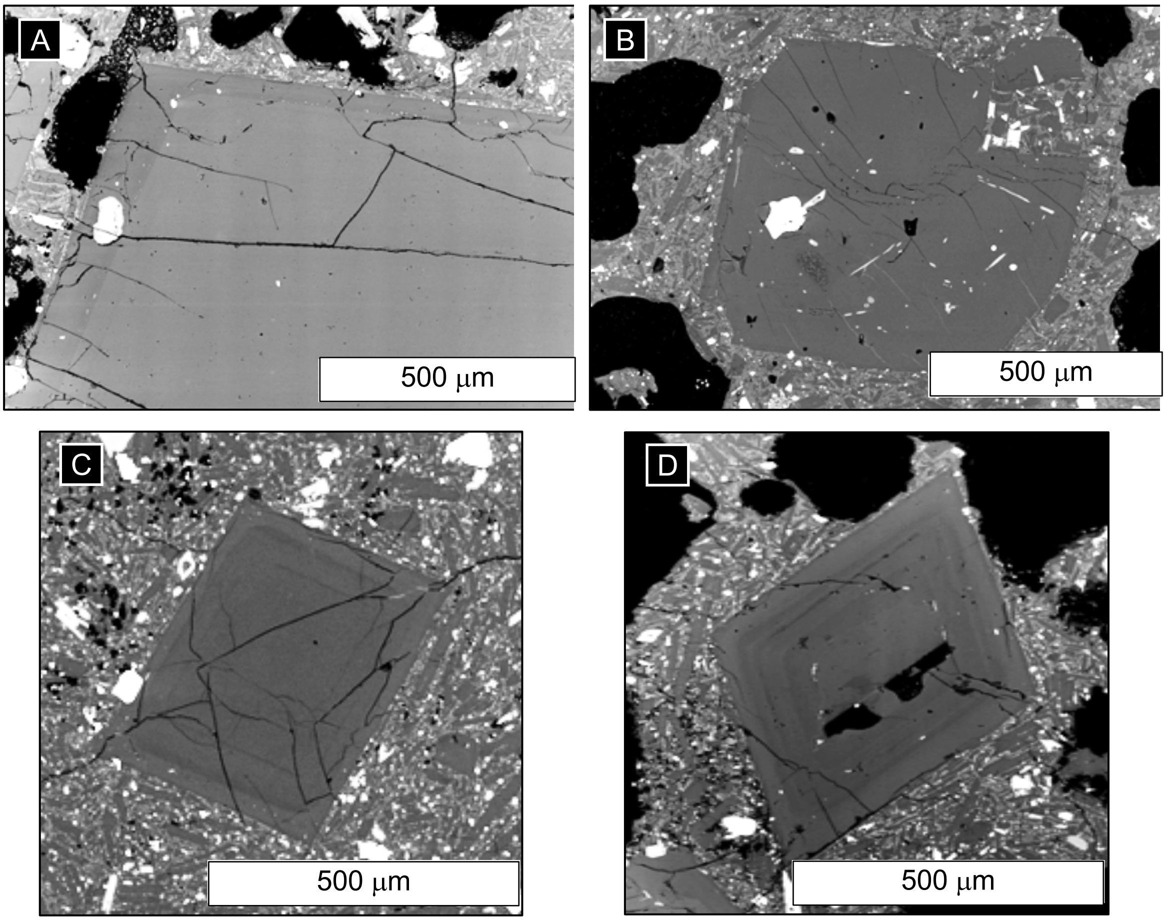

Figure 5.6: *BSE images of the Type 2 feldspar texture. A) Euhedral crystal with normal zoning. B) Euhedral crystal with no zoning. C, D) Euhedral crystal with weak oscillitary zoning.*

stumpy. In the spatter and lava samples, ~50 – 60% of the stumpy crystals exhibit normal, reverse, or oscillatory zoning and ~5% of the macrocrysts exhibit weak, external embayment. Zoning is rarely seen in the tephra feldspars (<1%), whereas ~30% of the macrocrysts exhibit varying degrees of external embayment. Microphenocrysts and microlites are subhedral, elongate, tabular or skeletal, with no evidence for internal resorption. Approximately 70% of the microphenocrysts throughout the samples exhibit either weak embayment or a hopper texture.

Type 3 feldspars (Fig. 5.7) occur as macrocrysts and make up ~1% of the crystal population in each sample. They are subhedral to anhedral. The crystal cores and inner rims are resorbed and exhibit sieve textures. Crystal rims show between weak to strong external resorption, and a number of feldspars have an overgrowth of feldspar microlites to form a new, outer rim. The crystals show varying degrees of reverse zoning but is distinguish due to the strong resorption. Approximately 60% of the crystals exhibit a breakdown texture between the core and the rim.

5.4.3.2 Olivine

Olivine crystals are similar sizes in the lava, spatter and tephra samples (up to 500 μm) and account for up ~1-2 vol % of the erupted products. Three different types were identified throughout. Type A is the most common and found in the spatter, lava and tephra samples,

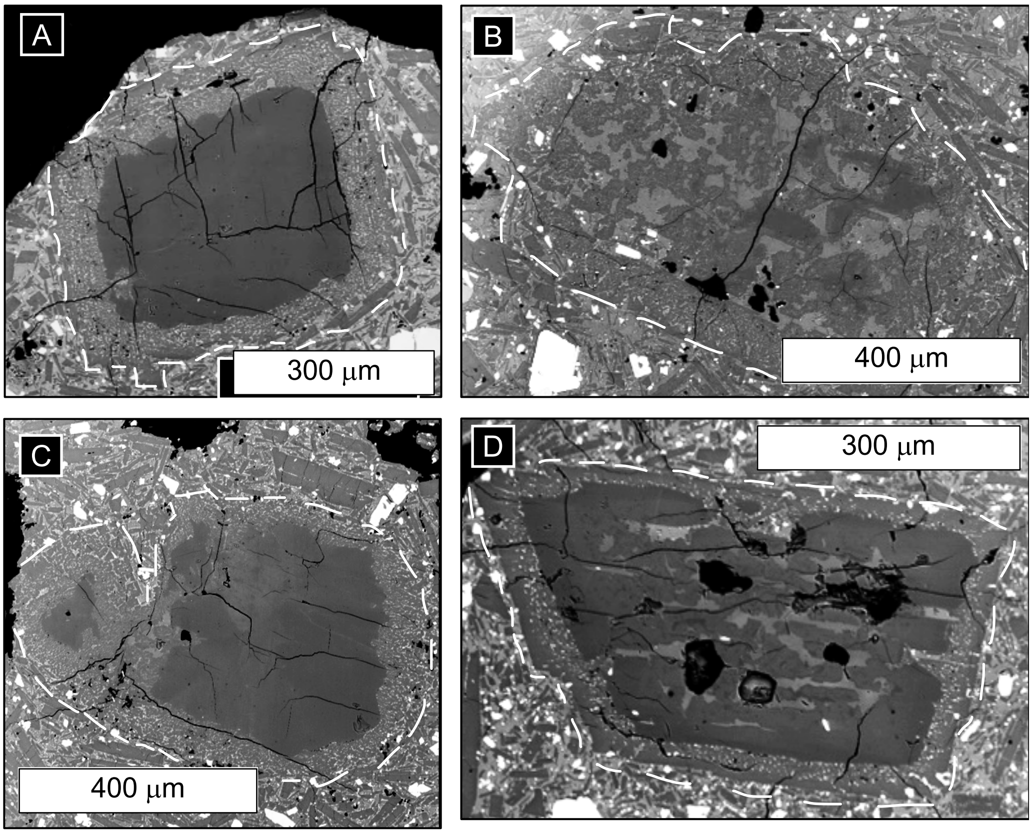

Figure 5.7: *BSE images of the Type 3 feldspar texture.* ***A,C)*** *Rims with whole cores.* ***B)*** *shows rims and resorbed cores. D) Whole rims with an inner, resorbed band and a partially resorbed core.*

whilst type B and C are rarer and only found in spatter and lava samples. Type A olivine grains (Fig. 5.8) are present from microphenocrysts to microlites in all of the DIP samples. The microphenocrysts are subhedral and equant, whilst the microlites range between euhedral to subhedral, equant, tabular and fragmental. Approximately 5 – 10% of the Type A microlites are embayed and ~2 – 5% exhibit hopper textures.

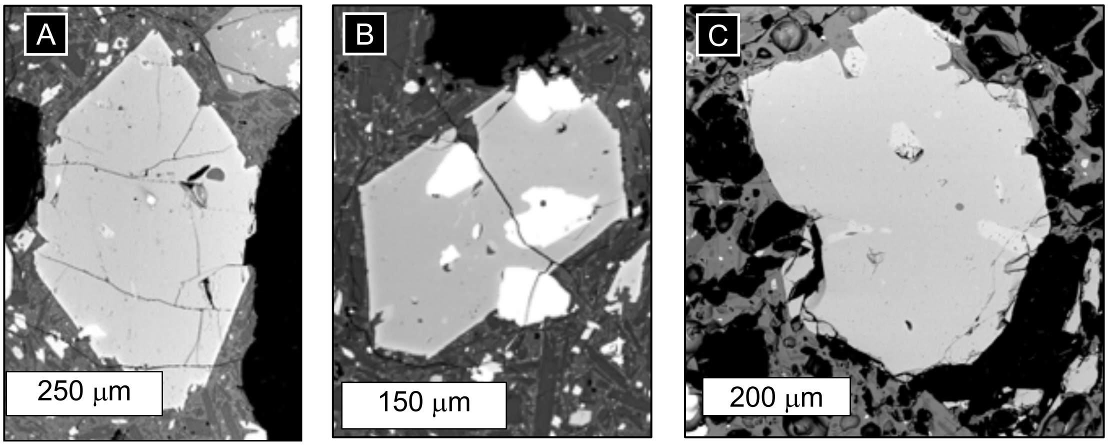

Figure 5.8: *BSE images showing the type A olivine crystals.*

Type B (Fig. 5.9) are present solely as microphenocrysts in the spatter and lava samples only. They are anhedral and have heavily resorbed rims. The crystals often exhibit Fe-Ti oxide overgrowths and amoeboid melt inclusions.

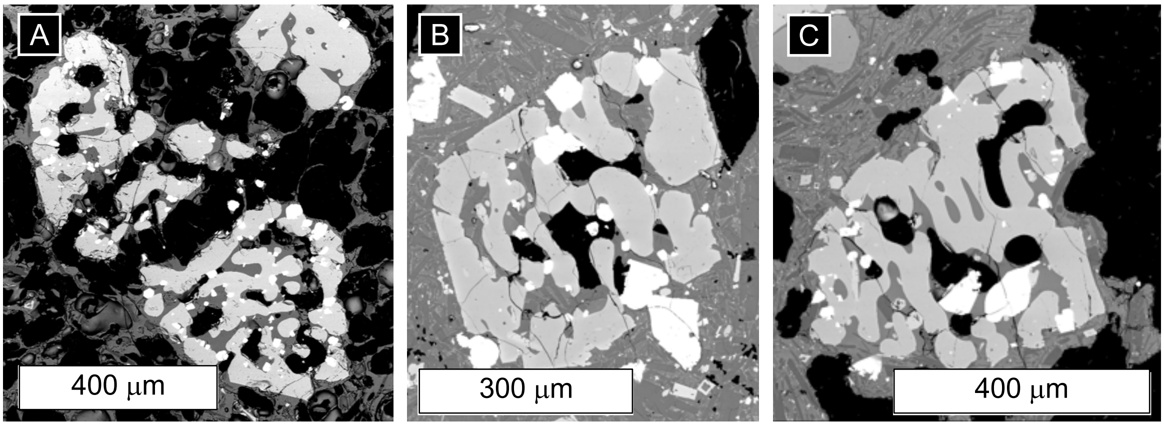

Figure 5.9: *BSE images showing the type B olivine crystals.*

Type C (Fig. 5.10) are restricted to microphenocrysts in the spatter and lava samples only and are anhedral. They exhibit sieve textures, which vary between fine to coarse (Fig. 5.10a) internal sieve texturing and finer sieve textures around the rims. The finer sieve texture is symplectitc (Fig. 5.10b,c) and forms near-perpendicular to the crystal rims. Fe-Ti oxides grow over the crystals.

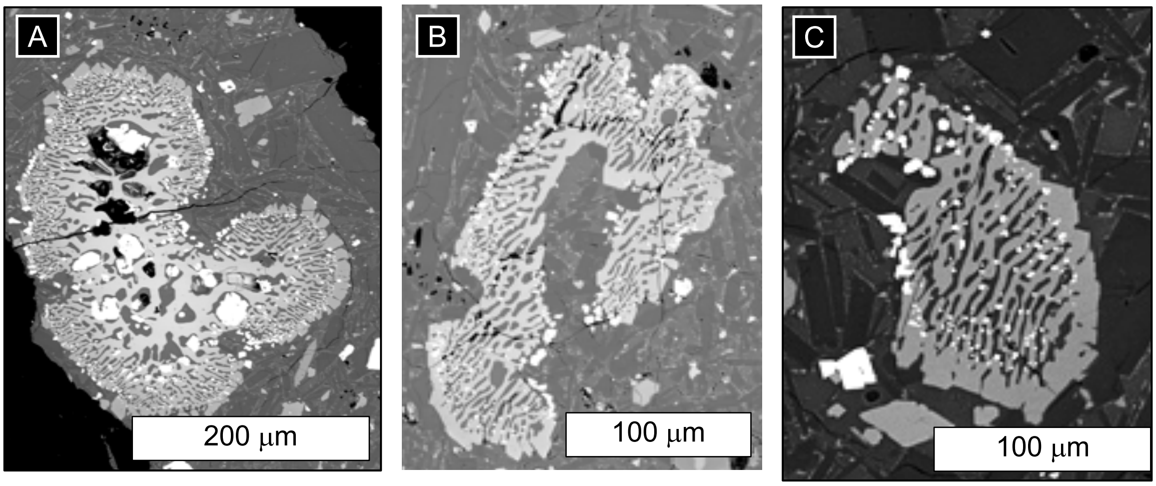

Figure 5.10: *BSE images showing the type C olivine crystals.*

5.4.3.3 Clinopyroxene

Macrocrysts and microphenocrysts of clinopyroxene crystals are up to 600 μm in diameter (Fig. 5.11) and make up <1% of the crystals in all the samples. They are subhedral and equant. Approximately 15 – 20% of the microphenocrysts exhibit normal zoning to Fe-rich rims. The crystals commonly exhibit oxide, apatite, and olivine overgrowths.

5.4.3.4 Amphibole

Amphibole crystals as rare (<1%), subhedral to anhedral macrocrysts to microphenocrysts, with rounded edges, and reach ~ 900 μm in diameter. Type i amphiboles are found in the spatter and lava samples and exhibit breakdown textures (Fig. 5.12a). Further details on the amphibole rim textures have been described in chapter 5. Type ii amphiboles are only

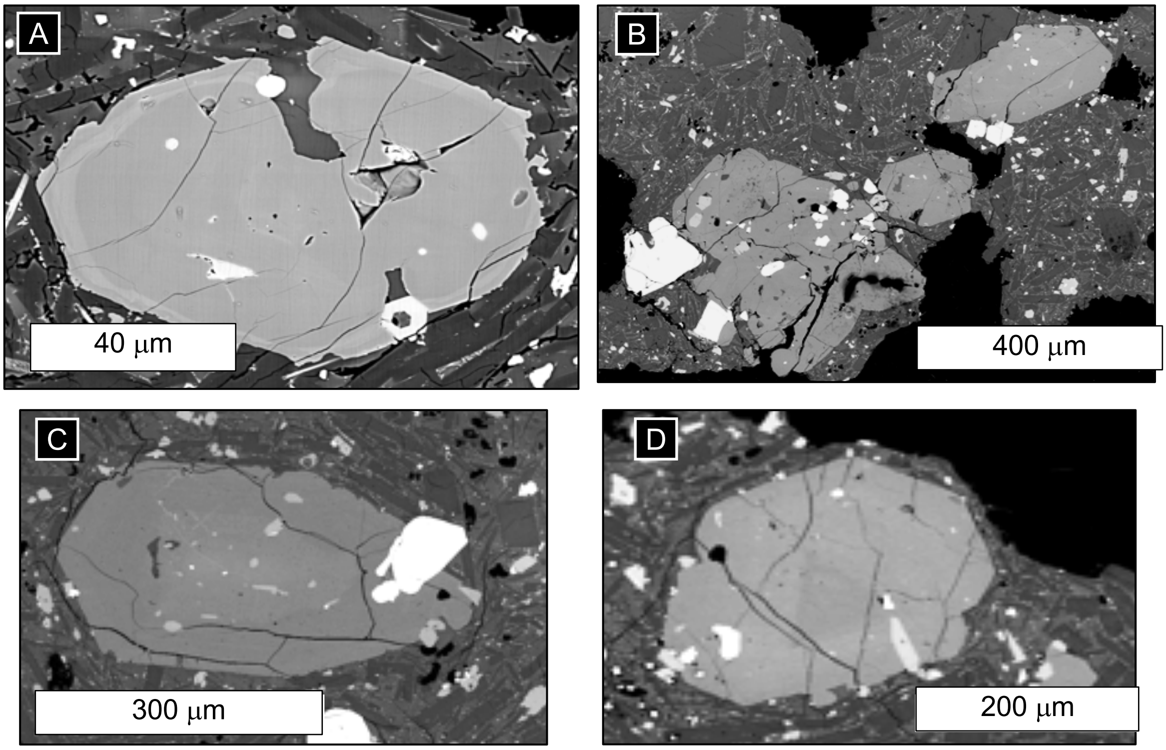

Figure 5.11: *BSE images of the euhedral and subhedral pyroxene crystals.*

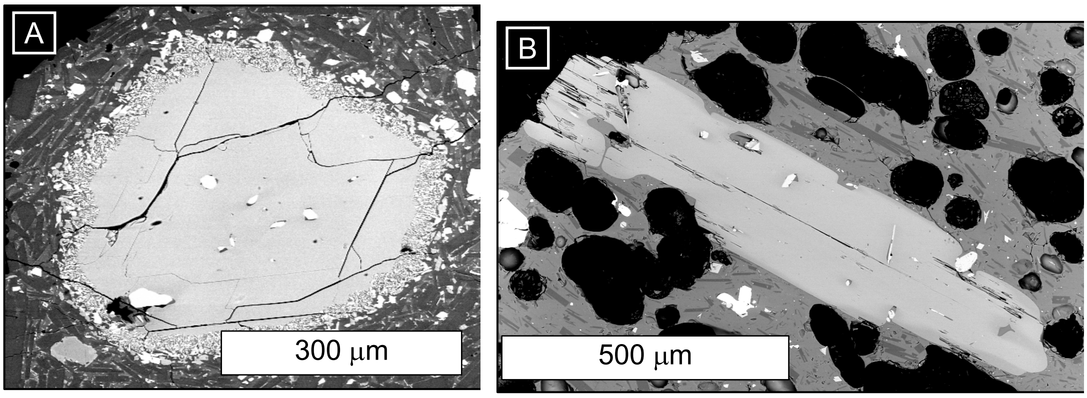

Figure 5.12: *BSE images showing the different amphibole types.* ***A)*** *Type i exhibiting breakdown rims and found in lava and spatter samples.* ***B)*** *Type ii with euhedral rims and found in the tephra samples.*

seen in tephra samples. These crystals are mainly macrocrysts, up to ~ 900 µm long and euhedral to subhedral with no breakdown rims (Fig. 5.12a).

5.4.4 Crystal Chemistry

5.4.4.1 Plagioclase Feldspar

Andesine ($Ab_{48}An_{50}Or_2$ – $Ab_{63}An_{30}Or_7$) is the most abundant feldspar composition for cores and rims in the DIP products (Table 5.23), with rare labradorite ($Ab_{47}An_{51}Or_2$ – $Ab_{48}An_{50}Or_2$), oligoclase ($Ab_{66}An_{29}Or_5$ – $Ab_{76}An_{12}Or_{12}$) and anorthoclase ($Ab_{67}An_2Or_{30}$ – $Ab_{72}An_8Or_{20}$) (Fig. 5.13, 5.15). Compositional histograms show the main modes at An_{46} for crystal cores, An_{44} for crystal rims and An_{38} for groundmass feldspars (Fig. 5.14a). Cores and rims are

Sample number	**AI-19-034**	**AI-19-034**	**AI-19-008**	**AI-19-008**	**AI-19-121**	**AI-19-121**	**AI-19-028**	**AI-19-028**	**AI-19-028**	**AI-19-028**	**AI-19-026**	**AI-19-026**	**DIP-8**	**DIP-8**
Spot	T1 C	T1 R	T1 C	T1 R	T1 C	T1 R	T1 C	T1 R	T1 C	T1 R	T1 C	T1 R	T1 C	T1 R
Description	Spatter	Spatter	Spatter	Spatter	Spatter	Spatter	Lava	Lava	Lava	Lava	Lava	Lava	Dense	Dense
SiO_2	55.80	57.57	57.59	58.13	56.42	56.46	57.89	57.85	45.20	56.18	56.53	58.42	56.54	56.53
TiO_2	0.04	0.07	0.05	0.07	0.06	0.06	0.05	0.06	0.05	0.07	0.07	0.04	0.05	0.07
$Al2O_2$	26.87	25.77	25.53	25.37	26.93	26.70	26.05	25.85	21.29	27.17	27.21	26.00	26.61	26.23
FeO	0.45	0.58	0.38	0.52	0.40	0.40	0.38	0.37	0.43	0.41	0.48	0.40	0.43	0.52
MnO	0.01	0.00	0.01	0.01	0.01	0.01	0.01	0.00	0.01	0.01	0.02	0.03	0.01	0.01
MgO	0.06	0.06	0.04	0.05	0.03	-0.01	0.04	0.02	0.01	0.04	0.04	0.03	0.05	0.05
CaO	9.88	8.47	8.51	8.09	9.06	8.92	8.12	8.36	9.41	9.51	9.39	7.91	9.24	8.83
Na_2O	5.85	6.37	6.56	6.73	6.14	6.34	6.67	6.54	5.91	6.05	6.03	6.80	6.08	6.11
K_2O	0.32	0.39	0.40	0.46	0.36	0.37	0.43	0.40	0.33	0.32	0.41	0.47	0.33	0.34
SrO	0.11	0.13	0.11	0.13	0.19	0.07	-0.12	0.08	0.11	0.21	0.18	0.20	0.14	0.15
Total	99.38	99.43	99.16	99.55	99.31	99.37	100.61	100.95	100.02	99.54	100.23	100.29	99.47	98.85
An	47	41	41	39	44	43	39	40	46	46	45	38	45	43
Or	2	2	2	3	2	2	2	2	2	2	2	3	2	2
Ab	51	56	57	58	54	55	58	57	52	53	52	59	53	54

Sample number	**DIP-8**	**DIP-8**	**AI-19-034**	**AI-19-034**	**AI-19-008**	**AI-19-008**	**AI-19-121**	**AI-19-121**	**AI-19-028**	**AI-19-028**	**AI-19-028**	**AI-19-028**	**AI-19-026**	**AI-19-026**
Spot	T1 C	T1 R	T2 C	T2 R	T2 C	T2 R	T2 C	T2 R	T2 C	T2 R	T2 C	T2 R	T2 C	T2 R
Description	Dense	Dense	Spatter	Spatter	Spatter	Spatter	Spatter	Spatter	Lava	Lava	Lava	Lava	Lava	Lava
SiO_2	57.40	57.03	57.92	58.46	57.00	57.72	55.94	57.85	56.94	56.70	57.08	57.62	58.52	57.32
TiO_2	0.04	0.06	0.06	0.07	0.05	0.07	0.06	0.06	0.07	0.07	0.08	0.07	0.05	0.08
$Al2O_2$	25.55	26.32	26.38	25.99	27.17	26.03	27.29	25.95	26.61	27.19	26.52	26.32	26.01	27.16
FeO	0.41	0.50	0.40	0.53	0.41	0.54	0.40	0.38	0.47	0.45	0.49	0.50	0.33	0.46
MnO	0.00	0.01	0.01	0.00	0.01	0.01	0.00	0.00	0.00	0.01	-0.01	0.02	0.00	0.01
MgO	0.04	0.05	0.05	0.06	0.05	0.05	0.02	0.04	0.05	0.04	0.09	0.03	0.00	0.05
CaO	8.32	8.76	8.81	7.87	9.35	8.54	9.57	8.01	8.91	9.10	8.83	8.45	8.06	9.20
Na_2O	6.44	6.30	6.48	6.85	6.04	6.56	6.06	6.95	6.13	6.30	6.31	6.51	6.75	6.30
K_2O	0.38	0.35	0.36	0.49	0.36	0.39	0.30	0.43	0.39	0.34	0.35	0.40	0.49	0.40
SrO	0.15	0.15	0.11	0.13	0.11	0.14	0.15	0.12	0.31	0.14	0.02	0.19	0.21	0.26
Total	98.72	99.53	100.58	99.45	100.54	100.06	99.33	99.05	99.82	99.47	100.08	100.07	100.43	101.24
An	41	43	42	38	45	41	46	38	44	44	43	41	39	44
Or	2	2	2	3	2	2	2	2	2	2	2	2	3	2
Ab	57	55	56	59	53	57	52	60	54	55	55	57	59	54

Sample number	**DIP-3**	**DIP-3**	**DIP-3**	**DIP-3**	**DIP-6**	**DIP-6**	**DIP-6**	**DIP-6**	**DIP-8**	**DIP-8**	**DIP-8**	**DIP-8**	**AI-19-121**	**AI-19-121**
Spot	T2 C	T2 R	T2 C	T2 R	T2 C	T2 R	T2 C	T2 R	T2 C	T2 R	T2 C	T2 R	T3 C	T3 R
Description	Scoria	Scoria	Scoria	Scoria	Pumice	Pumice	Pumice	Pumice	Dense	Dense	Dense	Dense	Spatter	Spatter
SiO_2	57.89	57.72	56.87	58.26	57.64	58.15	58.14	58.78	58.89	56.61	57.29	57.85	56.39	59.34
TiO_2	0.03	0.27	0.04	0.56	0.06	0.10	0.07	0.09	0.04	0.07	0.05	0.09	0.07	0.03
$Al2O_2$	25.30	25.16	26.30	25.66	25.58	25.38	25.91	25.25	25.31	26.20	26.49	25.28	27.56	25.58
FeO	0.37	1.13	0.40	2.40	0.59	0.77	0.58	0.67	0.36	0.48	0.40	0.56	0.31	0.26
MnO	0.01	0.03	0.01	0.07	0.00	0.01	0.01	0.01	0.00	0.00	0.00	0.01	0.00	0.02
MgO	0.04	0.18	0.05	0.45	0.05	0.06	0.06	0.06	0.03	0.05	0.04	0.06	-0.01	0.00
CaO	8.03	7.66	8.74	8.05	8.19	7.27	7.95	7.66	7.59	9.14	8.97	7.85	9.34	7.18
Na_2O	6.83	6.76	6.37	6.43	6.60	6.93	6.79	6.86	6.99	6.20	6.28	6.84	6.26	7.45
K_2O	0.42	0.81	0.37	1.29	0.42	0.54	0.46	0.56	0.51	0.34	0.33	0.44	0.30	0.50
SrO	0.11	0.07	0.12	0.09	0.14	0.12	0.14	0.15	0.11	0.15	0.16	0.14	0.17	0.12
Total	99.02	99.77	99.26	102.25	99.27	99.32	100.11	100.09	99.82	99.24	100.01	99.11	100.01	99.86
An	38	37	42	38	40	36	38	37	36	44	43	38	44	34
Or	2	5	2	7	2	3	3	3	3	2	2	3	2	3
Ab	59	59	56	55	58	61	59	60	61	54	55	60	54	63

Sample number	**AI-19-121**	**AI-19-121**	**AI-19-127**	**AI-19-127**	**AI-10-028**	**AI-19-028**	**AI-19-028**	**AI-19-026**	**AI-19-026**	**AI-19-026**	**AI-19-026**	**AI-19-026**
Spot	T3 Point	T3 Point	T3 Point	T3 Point	T3 C	T3 IR	T3 R	T3 C	T3 IR	T3 R	T3 Point	T3 Point
Description	Spatter	Spatter	Spatter	Spatter	Lava	Lava	Lava	Lava	Lava	Lava	Lava	Lava
SiO_2	61.69	61.24	61.77	61.31	62.48	57.81	61.34	65.72	65.10	59.02	67.63	68.53
TiO_2	0.24	0.22	0.36	0.28	0.01	0.04	0.00	0.01	0.02	0.12	0.01	0.06
$Al2O_2$	22.72	22.67	22.14	22.97	22.82	25.83	23.58	21.88	22.29	25.62	19.52	18.23
FeO	0.93	0.90	0.97	0.74	0.18	0.28	0.28	0.21	0.18	0.68	0.50	1.20
MnO	0.01	0.01	0.02	-0.01	-0.01	0.01	0.01	0.00	0.00	0.00	0.00	0.02
MgO	0.11	0.03	0.16	0.05	0.02	0.01	0.00	0.01	0.00	0.03	0.01	-0.02
CaO	5.15	5.05	5.31	5.44	5.23	7.99	5.49	2.92	3.50	7.52	0.80	0.69
Na_2O	7.65	7.73	8.07	7.79	8.57	6.85	7.99	9.32	9.19	6.72	8.51	8.05
K_2O	1.44	1.76	1.81	1.43	0.88	0.39	0.79	1.65	1.35	0.91	5.57	5.68
SrO	0.05	0.04	0.03	0.06	0.34	0.14	0.14	0.06	0.13	0.24	-0.02	0.00
Total	100.00	99.67	99.64	100.06	100.26	100.25	100.01	100.78	100.77	100.88	101.53	101.44
An	25	24	20	26	20	38	26	13	16	36	4	3
Or	8	10	10	8	5	2	5	9	7	5	25	27
Ab	67	66	69	66	75	59	69	78	76	59	71	70

Table 5.23: *Table showing the representative values of feldspar chemistry. For full data set see appendices 2. T1 = type 1, T2 = type 2, T3 = type 3, C = core, R = rim, IR = inner rim.*

predominantly andesine (An_{31-48} and An_{39-50}, respectively) with rare oligoclase ($Ab_{69}An_{26}Or_5$ – $Ab_{78}An_{13}Or_9$, $Ab_{66}An_{29}Or_5$ – $Ab_{65}An_{25}Or_{11}$), labradorite ($Ab_{48}An_{50}Or_2$, $Ab_{47}An_{51}Or_2$) and anorthoclase ($Ab_{72}An_8Or_{20}$, $Ab_{67}An_{30}Or_2$ – $Ab_{72}An_8Or_{20}$), respectively. Groundmass compositions are also predominantly andesine ($Ab_{50}An_{48}Or_2$ – $Ab_{63}An_{30}Or_7$) with rare oligoclase ($Ab_{67}An_{27}Or_6$ – $Ab_{76}An_{12}Or_{12}$) and anorthoclase ($Ab_{69}An_3Or_{28}$ – $Ab_{70}An_5Or_{25}$).

Feldspar crystals in the spatter are predominantly andesine ($Ab_{49}An_{49}Or_2$ – $Ab_{65}An_{32}Or_3$), with rare labradorite ($Ab_{47}An_{51}Or_1$), oligoclase ($Ab_{66}An_{29}Or_5$ – $Ab_{69}An_{19}Or_{12}$) and anorthoclase ($Ab_{67}An_6Or_{27}$ – $Ab_{72}An_8Or_{20}$). Compositional histograms show the main modes at An_{46} for crystal cores and rims, and An_{38} for groundmass crystals (Fig. 5.14b). Feldspar crystals in the lava show very similar compositions to the spatter, with the main composition being andesine ($Ab_{49}An_{49}Or_2$ – $Ab_{65}An_{31}Or_3$), and rare labradorite ($Ab_{47}An_{51}Or_2$

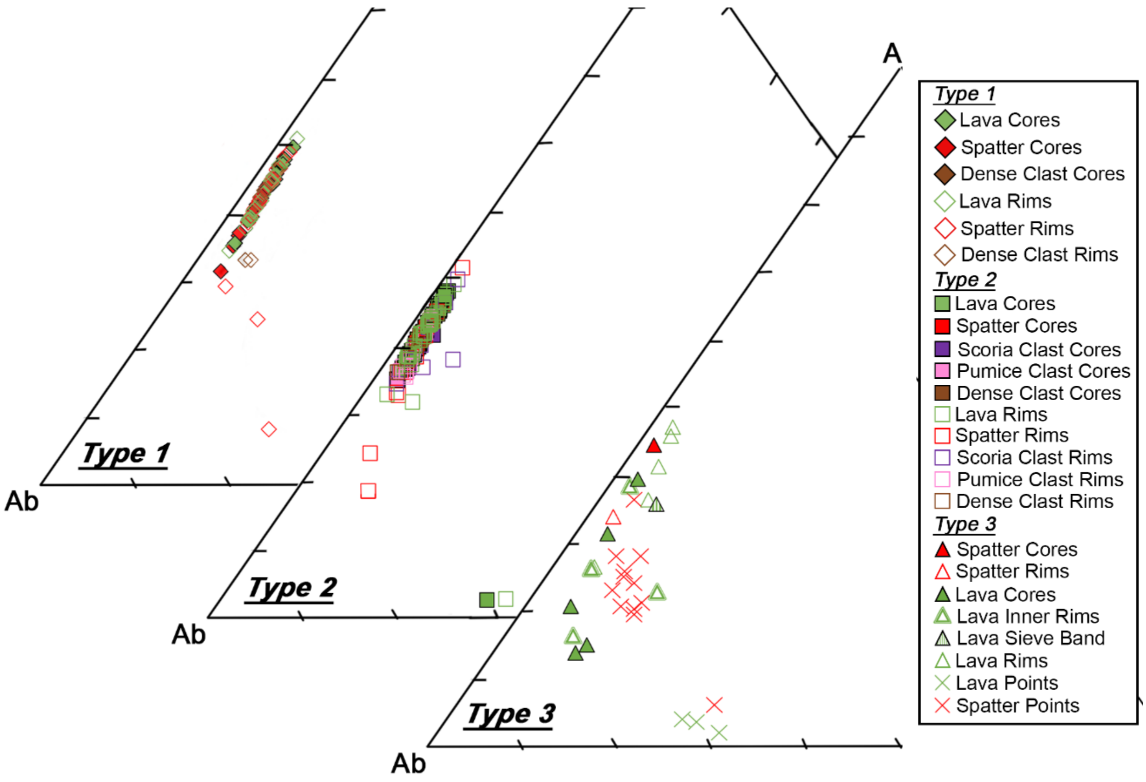

Figure 5.13: *Feldspar ternary plots for the three types of feldspar crystals. The majority of the feldspars sit within the anorthoclase range, with few type 1 and 2 within the labradorite range. All three types show rare oligoclase and anorthoclase compositions.*

– $Ab_{48}An_{50}Or_2$), oligoclase ($Ab_{69}An_{26}Or_5$ – $Ab_{76}An_{12}Or_{12}$) and anorthoclase ($Ab_{67}An_2Or_{30}$ – $Ab_{71}An_4Or_{25}$). Compositional histograms show the main modes at An_{40} for crystal cores, An_{44} for crystal rims, and An_{42} for groundmass crystals (Fig. 5.14c).

Feldspar crystals in the tephra clasts are solely andesine ($Ab_{48}An_{50}Or_2$ – $Ab_{61}An_{33}Or_6$). There is very little difference between cores ($Ab_{52}An_{46}Or_2$ – $Ab_{62}An_{35}Or_3$) and rims ($Ab_{48}An_{50}Or_2$ – $Ab_{61}An_{33}Or_6$). Groundmass compositions range from $Ab_{55}An_{43}Or_2$ to $Ab_{62}An_{34}Or_5$. Compositional histograms show the main modes at An_{42} for crystal cores, An_{44} for crystal rims, and An_{38} and An_{40} for groundmass crystals (Fig. 5.14d).

Within the DIP products, three groups of plagioclase (type 1, type 2 and type 3) were identified based on textural and compositional properties (Fig. 5.5 - 5.7). Type 1 (T1) feldspar crystals are dominantly andesine with rare labradorite, oligoclase and anorthoclase (Fig. 5.13). Compositional histograms show the two main modes at An_{46} for cores and An_{44} for rims (Fig. 5.14e). Type 2 (T2) feldspar crystals, similar to type 1, are dominantly andesine with rare oligoclase, anorthoclase and labradorite (Fig. 5.1, 5.153). Compositional histograms show that the two main modes for the cores are lower than the type 1 feldspars, at An_{40} and An_{42}, whilst the two modes for the rims are lower at An_{42} but also the same at An_{44} (Fig. 5.14f). Type 3 (T3) feldspar crystals are different to type 1 and type 2 and have the most evolved compositions of andesine, oligoclase and anorthoclase ($An_{2\text{-}47}$) (Fig. 5.13, 5.15). The outer rims of the T3 feldspars are dominantly andesine, whilst the inner rims and cores are less calcic and mainly have oligoclase compositions (Fig. 5.13, 5.15). The points vary in composition from oligoclase to anorthoclase (Fig. 5.13).

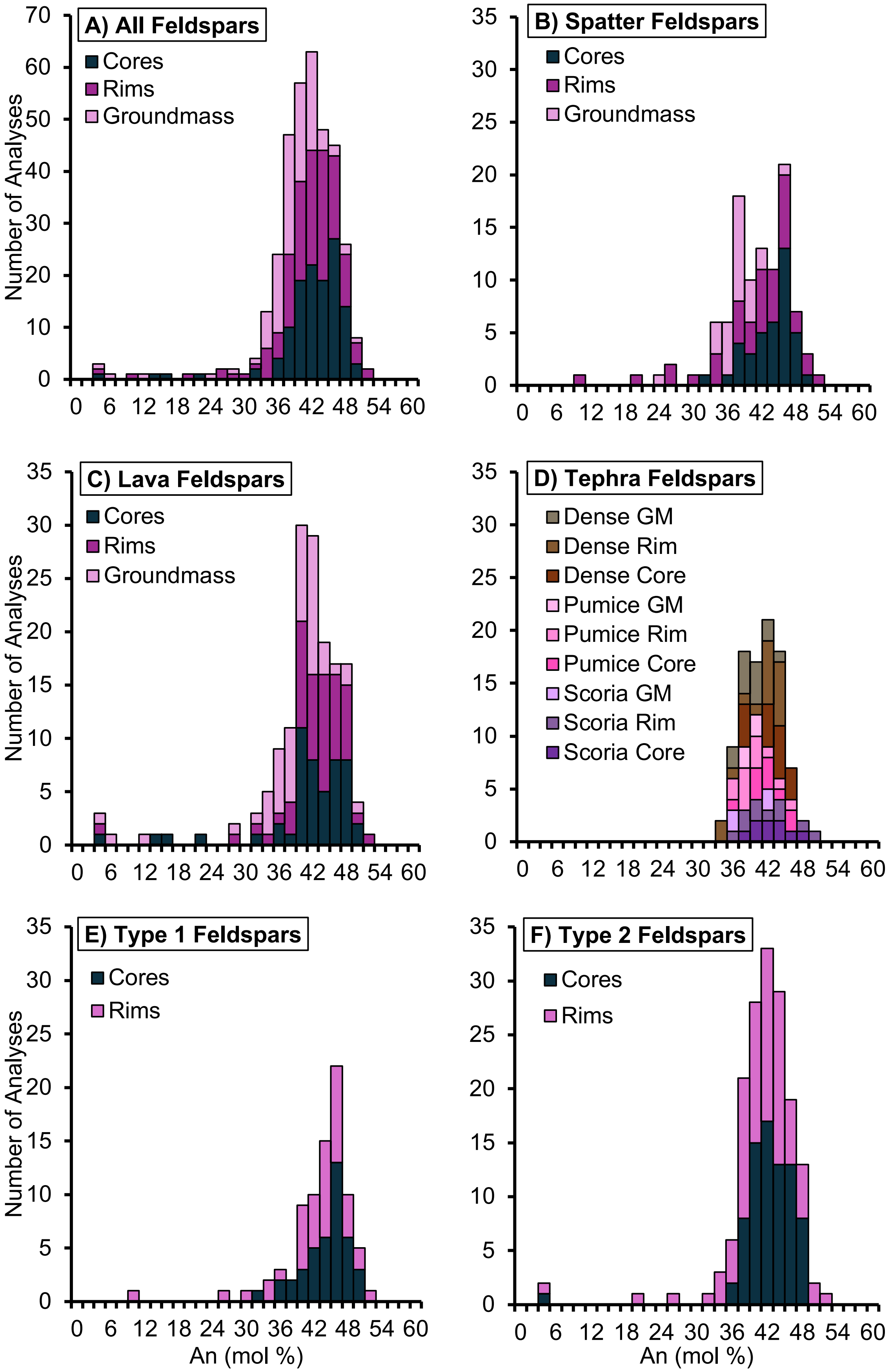

Figure 5.14: *Compositional histograms of the An content in cores, rims and groundmass (GM) feldspar crystals in* ***A)*** *All feldspars,* ***B)*** *Spatter feldspars,* ***C)*** *Lava feldspars,* ***D)*** *Tephra feldspars, grouped into scoria, pumice and dense clasts,* ***E)*** *type 1 feldspars,* ***F)*** *Type 2 feldspars.*

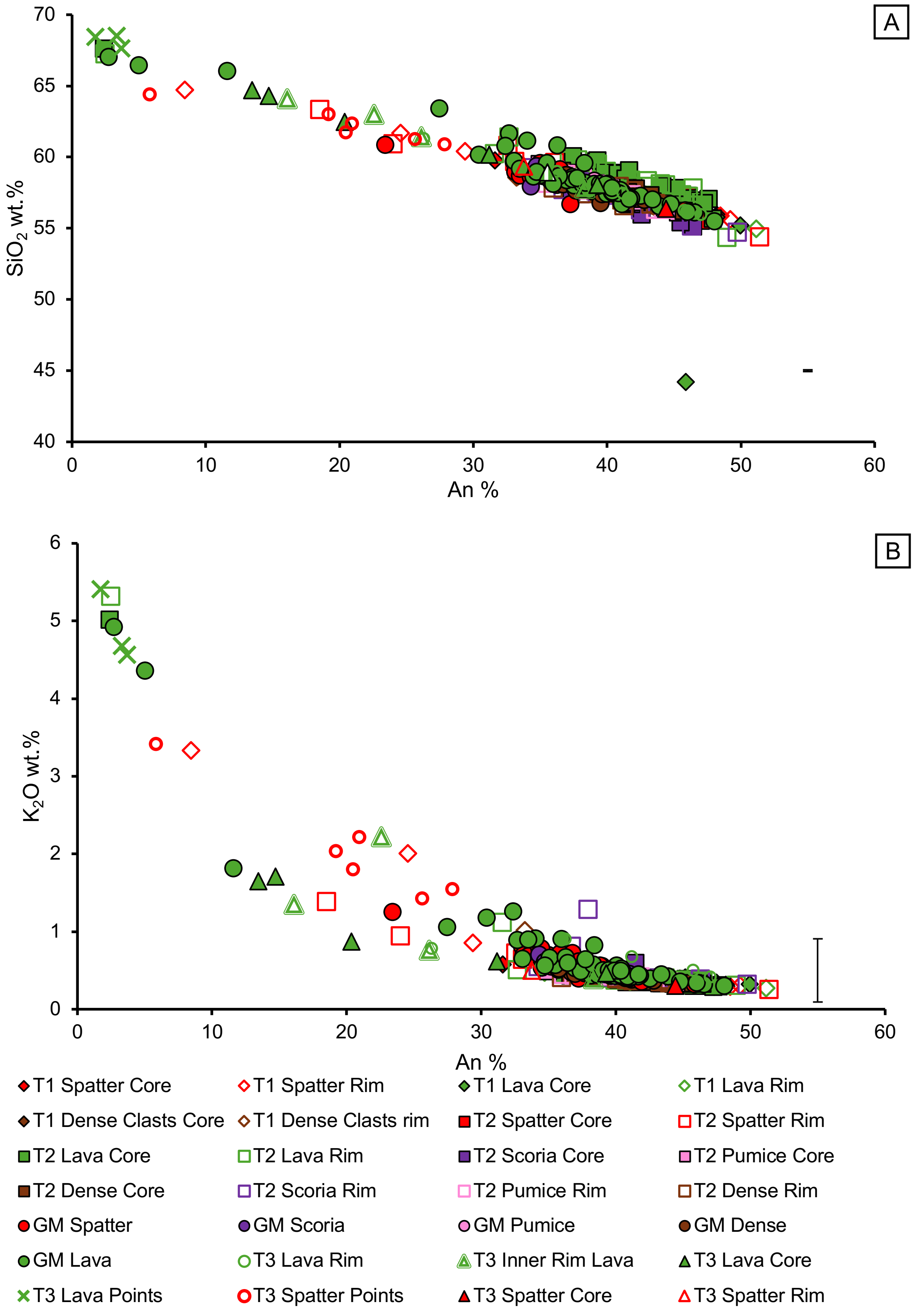

Figure 5.15: *Composition of feldspars in spatter, lava, and tephra (scoria, pumice and dense clasts), grouped by type and showing cores, rims and groundmass. Error bars show 2σ uncertainty.*

5.4.4.2 Olivine

Olivine crystals occur in all the DIP samples and range from Fo_{41-67} (Fig. 5.16; Table 5.24). Overall, crystal cores range from Fo_{60-66}, whilst rims have a wider range from Fo_{46-66}.

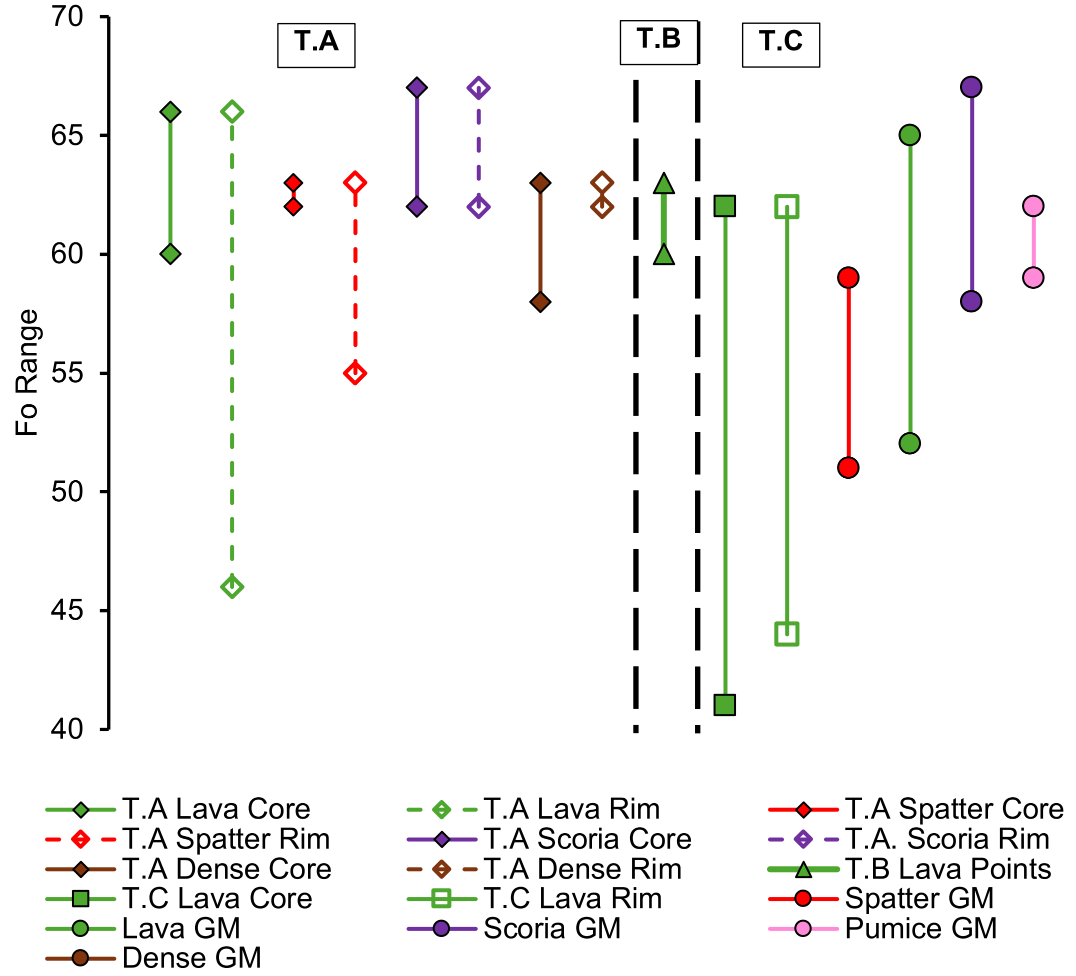

Figure 5.16: *Showing the ranges in Fo content for the different types of olivine crystals in each deposit type. T.A – type A olivines, T.B – type B olivines, T.C – type C olivines.*

Sample number	**AI-19-008**	**AI-19-008**	**AI-19-121**	**AI-19-121**	**AI-19-028**	**AI-19-028**	**AI-19-026**	**AI-19-026**	**DIP3**	**DIP3**	**DIP3**	**DIP3**	**DIP 8**
Spot	TA C	TA R	TA C	TA R	TA C	TA R	TA C	TA R	TA C	TA R	TA C	TA R	TA C
Type	Spatter	Spatter	Spatter	Spatter	Lava	Lava	Lava	Lava	Scoria	Scoria	Scoria	Scoria	Dense
SiO_2	36.31	36.38	36.41	35.96	35.91	36.19	35.54	35.17	37.44	37.29	36.74	36.87	36.33
TiO_2	0.04	0.03	0.05	0.04	0.04	0.04	0.27	0.08	0.04	0.05	0.04	0.04	0.03
Al_2O_3	0.02	0.04	0.02	0.02	0.01	0.01	0.03	0.02	0.00	0.00	-0.01	-0.01	0.01
FeO	31.80	31.97	31.77	35.85	31.56	31.77	33.41	36.70	29.47	29.34	31.05	31.07	31.47
MnO	1.07	1.08	1.09	1.19	1.11	1.08	1.20	1.51	1.00	0.99	1.14	1.13	1.08
MgO	30.49	30.62	30.65	28.46	31.14	31.01	29.70	26.48	31.68	31.57	30.08	30.10	30.96
CaO	0.18	0.18	0.18	0.20	0.17	0.19	0.20	0.26	0.18	0.18	0.18	0.18	0.17
Cr_2O_3	0.01	0.00	0.00	0.00	0.01	0.01	0.00	0.00	0.00	0.00	-0.01	-0.01	0.00
NiO	-0.01	-0.01	0.01	0.00	0.00	-0.01	0.00	0.00	-0.01	-0.01	-0.01	0.00	0.00
Total	99.95	100.32	100.20	100.74	99.99	100.32	100.36	100.29	99.79	99.40	99.21	99.37	100.11
Fo	63	63	63	59	64	64	61	56	66	66	63	63	64
Fa	37	37	37	41	36	36	39	44	34	34	37	37	37

Sample number	**DIP 8**	**DIP 8**	**DIP 8**	**AI-19-026**	**AI-19-026**	**AI-19-026**	**AI-19-026**	**AI-19-026**	**AI-19-026**	**AI-19-026**	**AI-19-026**	**AI-19-026**	**AI-19-026**
Spot	TA R	TA C	TA R	TB Point	TB Point	TB Point	TB Point	TB Point	TB Point	TC C	TC R	TC C	TC R
Type	Dense	Dense	Dense	Lava	Lava	Lava	Lava	Lava	Lava	Lava	Lava	Lava	Lava
SiO_2	37.01	36.65	36.90	36.00	35.82	36.57	36.43	36.34	36.32	33.94	36.14	35.23	36.16
TiO_2	0.03	0.02	0.04	0.06	0.05	0.04	0.06	0.03	0.05	0.11	0.06	0.16	0.04
Al_2O_3	0.02	0.02	0.02	-0.01	0.00	0.00	-0.01	0.00	-0.01	-0.02	-0.01	-0.01	-0.01
FeO	30.97	31.43	31.47	32.59	32.74	31.42	31.27	31.31	31.32	45.62	31.58	43.14	31.71
MnO	1.12	1.09	1.09	1.23	1.25	1.15	1.15	1.12	1.15	2.35	1.15	2.27	1.18
MgO	30.66	31.03	30.73	29.10	29.19	30.46	29.91	30.04	30.05	18.48	29.92	19.65	29.87
CaO	0.19	0.18	0.19	0.18	0.18	0.17	0.32	0.18	0.18	0.17	0.18	0.21	0.17
Cr_2O_3	-0.01	0.00	-0.01	0.00	-0.01	0.00	-0.01	0.01	0.00	0.00	0.00	0.00	-0.01
NiO	0.01	-0.01	0.00	-0.01	-0.02	0.01	-0.01	-0.01	0.00	-0.02	-0.01	0.00	-0.01
Total	100.04	100.47	100.45	99.14	99.19	99.82	99.11	99.03	99.05	99.63	99.00	99.65	99.11
Fo	64	64	64	62	61	64	63	63	63	42	63	45	63
Fa	36	36	36	38	39	36	37	37	37	58	37	55	37

Table 5.24: *Table showing the representative values of olivine crystal chemistry. For full data set see appendices 2. TA = type A, TB = type B, TC = type C, C = core, R = rim. Define Fo Fa*

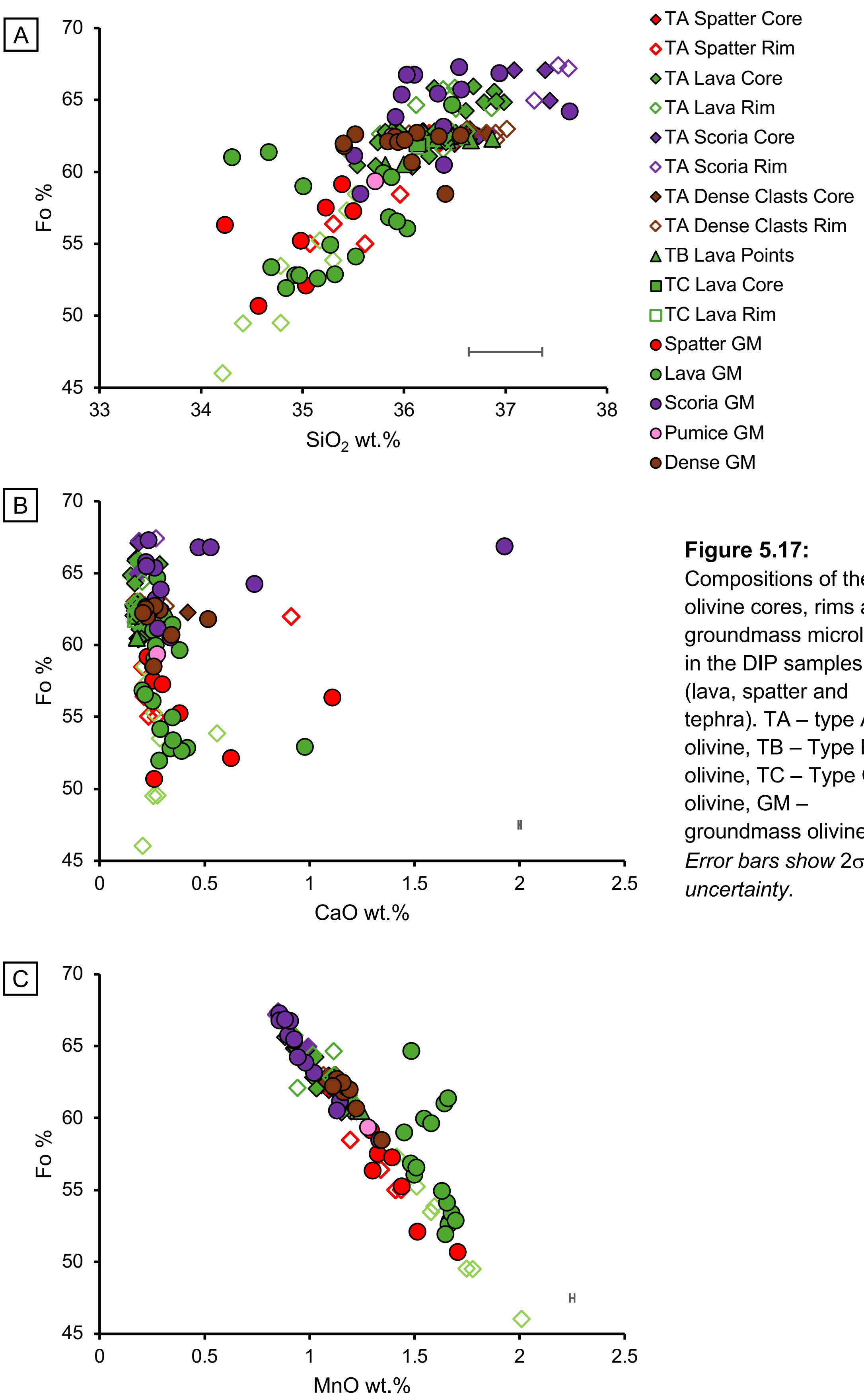

Figure 5.17: Compositions of the olivine cores, rims and groundmass microlites in the DIP samples (lava, spatter and tephra). TA – type A olivine, TB – Type B olivine, TC – Type C olivine, GM – groundmass olivine. *Error bars show 2σ uncertainty.*

Crystal rims are higher in MnO wt.% and lower in SiO_2 wt.% compared to the cores (Fig. 5.17a,c). CaO concentrations are low and range from 0.15 – 1.93 wt.% (Fig. 5.17b). Groundmass crystal compositions range from Fo_{41-67}. Compositional histograms (Fig. 5.18) show a main mode at Fo_{65}. Crystal cores and rims exhibit the same modes at Fo_{64} for spatter, lava and dense clasts and Fo_{68} for scoria clasts. In all crystals, NiO wt.% and Cr_2O_3 wt.% concentrations were below the detection limit.

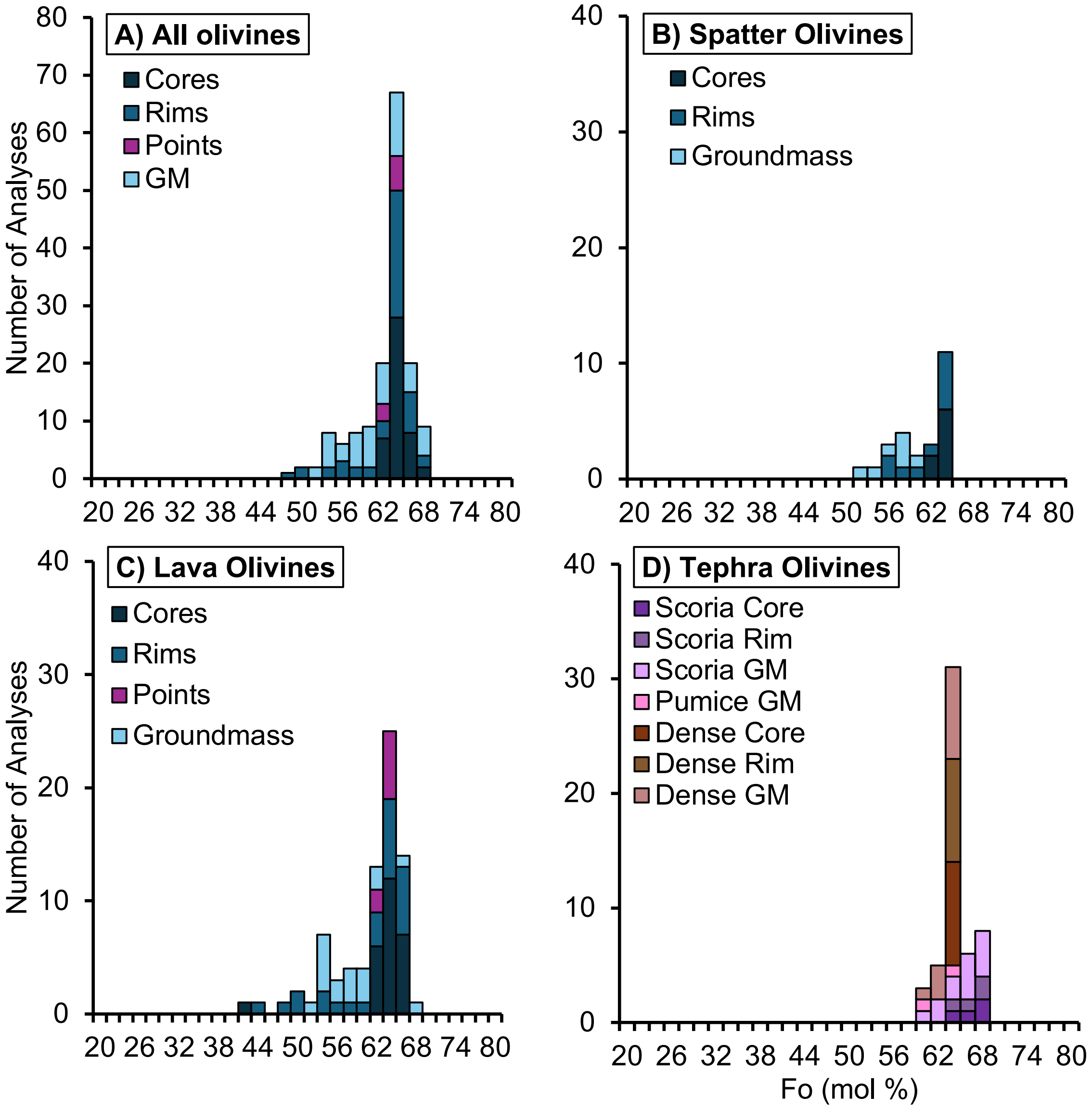

Figure 5.18: *Compositional histograms of the Fo content in cores, rims, and groundmass (GM) olivine crystals in* ***A)*** *All olivines,* ***B)*** *Spatter olivine,* ***C)*** *Lava olivines,* ***D)*** *Tephra olivine, grouped into scoria, pumice and dense clasts.*

Three types of olivine crystals were identified in the samples. Type A crystals are the most abundant. In the spatter they have Fo_{47-63} (Fig. 5.16), with crystal cores showing a very minimal range (Fo_{62-63}) and rims showing a greater range (Fo_{47-63}). Whereas, in the lava the crystals have a similar range (Fo_{46-66}) (Fig. 5.16), but the cores and rims exhibit wider ranges (Fo_{60-66} and Fo_{46-66}, respectively). Olivine crystals in the scoria clasts have the same core and rim ranges (Fo_{62-67}) (Fig. 5.16). Dense clasts olivines range from Fo_{58-63}, with cores and rims showing a minimal range of Fo_{62-63} (Fig. 5.16).

Compared to type A, type B crystals have a very narrow range (Fo_{60-63}) (Fig. 5.16). Due to the resorbed shapes, no core and rim data could be collected. The type C crystals

Sample number	**AI-19-034**	**AI-19-034**	**AI-19-008**	**AI-19-008**	**AI-19-127**	**AI-19-127**	**AI-19-026**	**AI-19-026**	**AI-19-026**	**AI-19-026**	**AI-19-026**	**AI-19-026**	**DIP-3**	**DIP-3**
Spot	C	R	C	R	C	R	C	R	C	R	Point	Point	C	R
Description	Spatter	Spatter	Spatter	Spatter	Spatter	Spatter	Lava	Lava	Lava	Lava	Lava	Lava	Scoria	Scoria
SiO_2	51.36	51.04	50.84	51.19	49.56	50.98	51.69	50.86	51.14	50.61	51.18	50.85	49.78	48.27
TiO_2	0.63	0.88	0.87	0.85	1.04	0.76	0.54	0.87	0.81	0.93	0.66	0.69	0.94	1.39
$Al2O_3$	1.97	2.49	2.71	2.53	2.62	2.21	1.45	2.47	2.47	2.65	1.61	1.82	2.69	5.16
FeO	10.32	9.39	11.14	9.42	11.36	9.28	11.49	9.33	11.15	9.62	10.02	9.29	10.29	9.85
MnO	0.67	0.51	0.71	0.54	0.76	0.53	0.77	0.52	0.65	0.54	0.67	0.58	0.69	0.48
MgO	15.11	15.39	13.47	15.24	13.65	15.58	15.43	15.37	13.51	15.18	15.07	15.88	13.69	13.86
CaO	19.01	20.55	19.77	20.58	19.02	20.45	18.87	20.04	19.53	19.42	19.17	19.98	19.97	19.38
Na_2O	0.47	0.49	0.50	0.51	0.53	0.47	0.37	0.50	0.43	0.48	0.35	0.42	0.53	0.58
K_2O	0.00	0.01	0.00	0.02	0.00	0.01	0.00	0.01	0.00	0.02	0.00	0.01	0.00	0.00
Cr_2O_3	0.00	0.01	0.00	0.00	0.01	0.00	-0.01	0.00	0.00	0.01	-0.01	-0.01	0.01	-0.01
Total	99.54	99.75	100.03	99.89	98.55	99.27	99.59	98.98	99.68	98.45	98.70	98.52	98.57	97.97
Wo	40	43	42	43	41	43	39	42	42	42	40	42	42	42
Fs	17	15	18	15	19	15	19	15	19	16	16	15	17	17
En	44	42	40	41	41	42	42	42	40	42	44	43	40	42
Mg#	72	73	68	73	68	74	75	72	64	73	73	74	70	71

Sample number	**DIP-3**	**DIP-3**	**DIP-6**	**DIP-6**	**DIP-6**	**DIP-6**	**DIP-8**	**DIP-8**	**DIP-8**	**DIP-8**
Spot	C	R	C	R	C	R	C	R	C	R
Description	Scoria	Scoria	Pumice	Pumice	Pumice	Pumice	Dense	Dense	Dense	Dense
SiO_2	49.90	50.92	50.21	50.64	50.61	50.70	51.68	50.56	50.28	50.45
TiO_2	0.81	0.55	1.05	1.07	0.89	0.95	0.83	0.97	1.47	1.20
$Al2O_3$	2.43	1.49	3.00	3.10	2.84	2.81	2.31	2.77	5.00	3.95
FeO	11.16	10.96	11.27	9.83	10.44	9.84	9.21	9.76	9.84	10.30
MnO	0.73	0.79	0.70	0.53	0.62	0.58	0.44	0.55	0.49	0.57
MgO	13.23	15.51	13.70	13.92	13.50	15.11	15.37	15.19	13.92	15.07
CaO	19.74	18.95	19.26	20.32	20.28	20.05	19.38	19.70	19.09	19.37
Na_2O	0.46	0.38	0.54	0.49	0.52	0.49	0.45	0.49	0.55	0.44
K_2O	0.00	0.00	0.00	0.02	0.00	0.01	0.00	0.01	0.00	0.18
Cr_2O_3	0.00	0.00	0.00	0.00	-0.01	0.00	0.00	0.00	0.00	0.00
Total	98.47	98.55	99.73	99.91	99.70	99.53	99.66	98.99	99.65	100.52
Wo	42	40	41	43	43	42	40	42	41	41
Fs	19	18	19	16	17	16	15	16	17	17
En	39	42	40	41	40	41	45	42	42	42
Mg#	68	70	70	73	70	72	72	72	70	71

Table 5.25: *Table showing the representative values of pyroxene crystal chemistry. For full data set see appendices 2. C = core, R = rim.*

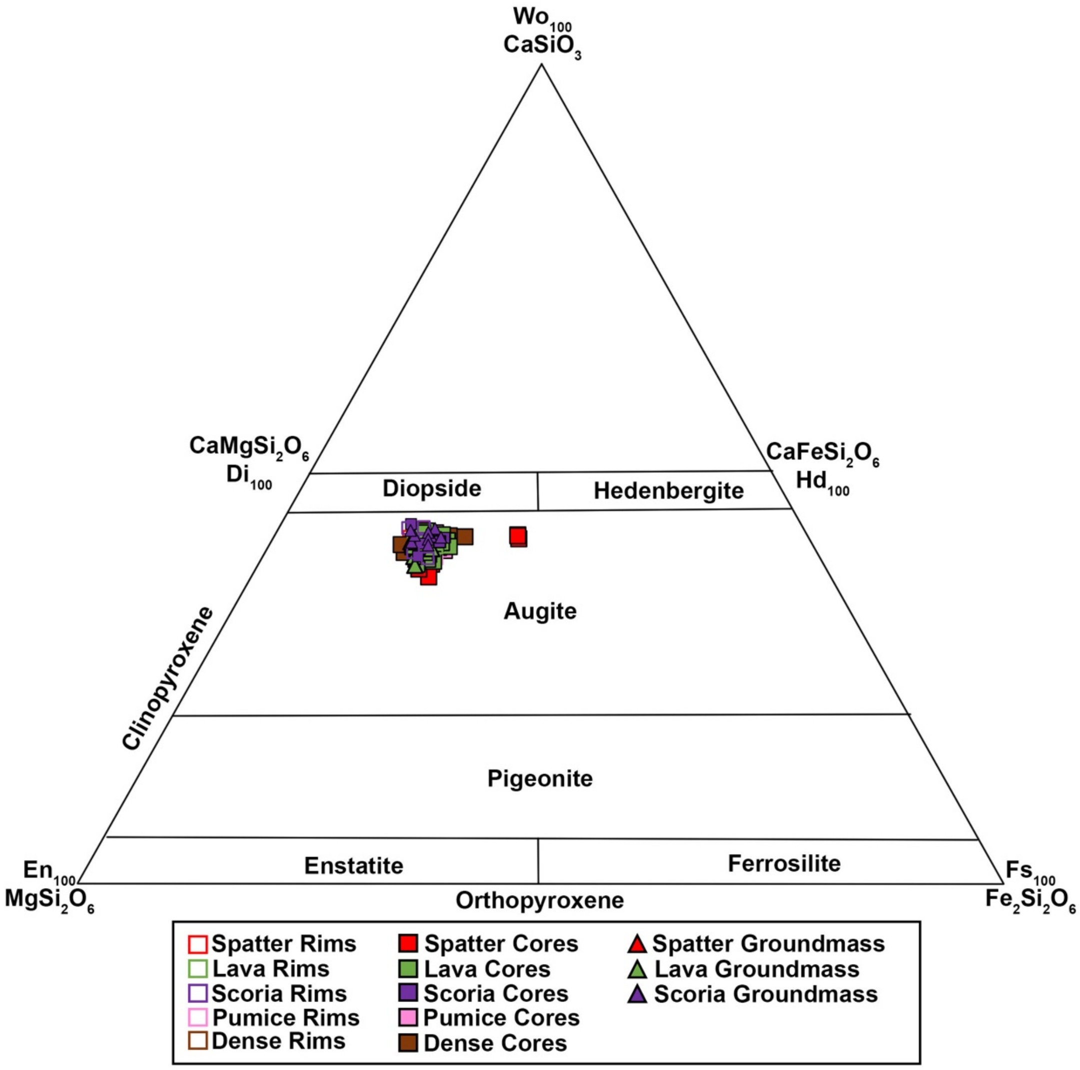

Figure 5.19: *Pyroxene classification diagram. Composition of the pyroxene cores, rims and groundmass in all the samples are clustered together, with the exception of few spatter cores. Modified from Deer et al., (1992).*

have a similar range to the type A crystals (Fo_{41-62}), however, the type C crystal cores wider ranges than type A (Fo_{41-62}) and the rims have similar ranges (Fo_{44-62}) (Fig. 5.16).

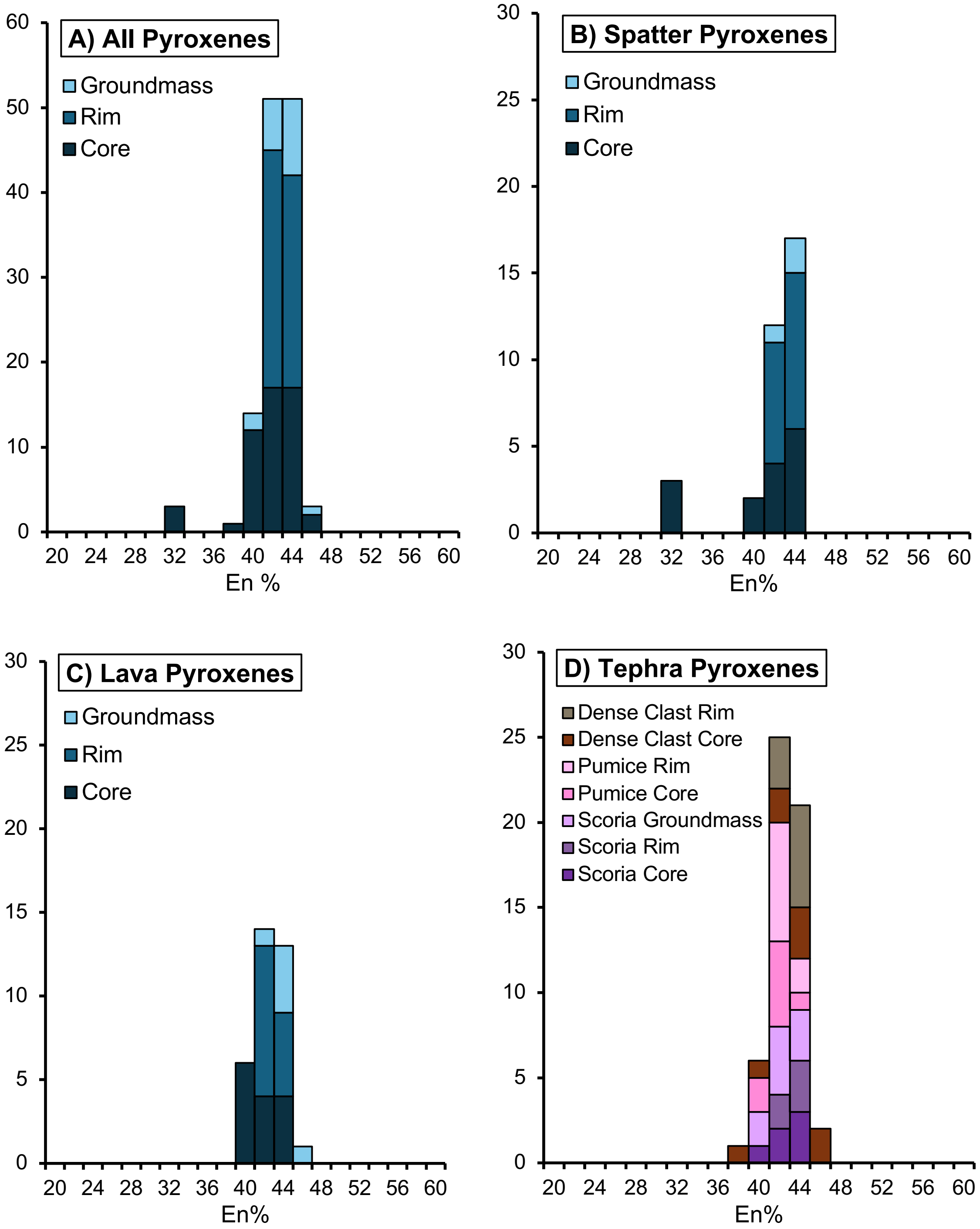

Figure 5.20: *Compositional histograms of the En content in cores, rims and groundmass (GM) feldspar crystals in* ***A)*** *All pyroxenes,* ***B)*** *Spatter pyroxenes,* ***C)*** *Lava pyroxenes,* ***D)*** *Tephra pyroxenes, grouped into scoria, pumice and dense clasts.*

5.4.4.3 Clinopyroxene

Clinopyroxene in the DIP samples are augitic (Fig. 5.19; table 5.25) with Mg# of 54 – 76 (Wo_{37-44}, En_{31-45}, Fs_{14-27}). Crystal cores range from Wo_{37-44}, En_{31-45}, Fs_{14-27}, whilst rims have smaller ranges, from Wo_{40-43}, En_{41-44}, Fs_{14-19} (fig. 5.19). Groundmass microlite compositions are more restrictive and range from Wo$_{39-43}$, En$_{40-44}$, Fs$_{14-18.}$ Compositional histograms (Fig. 5.20) show a strong mode at two identical modes at En$_{42}$ and En$_{45.}$ Crystal cores and rims.

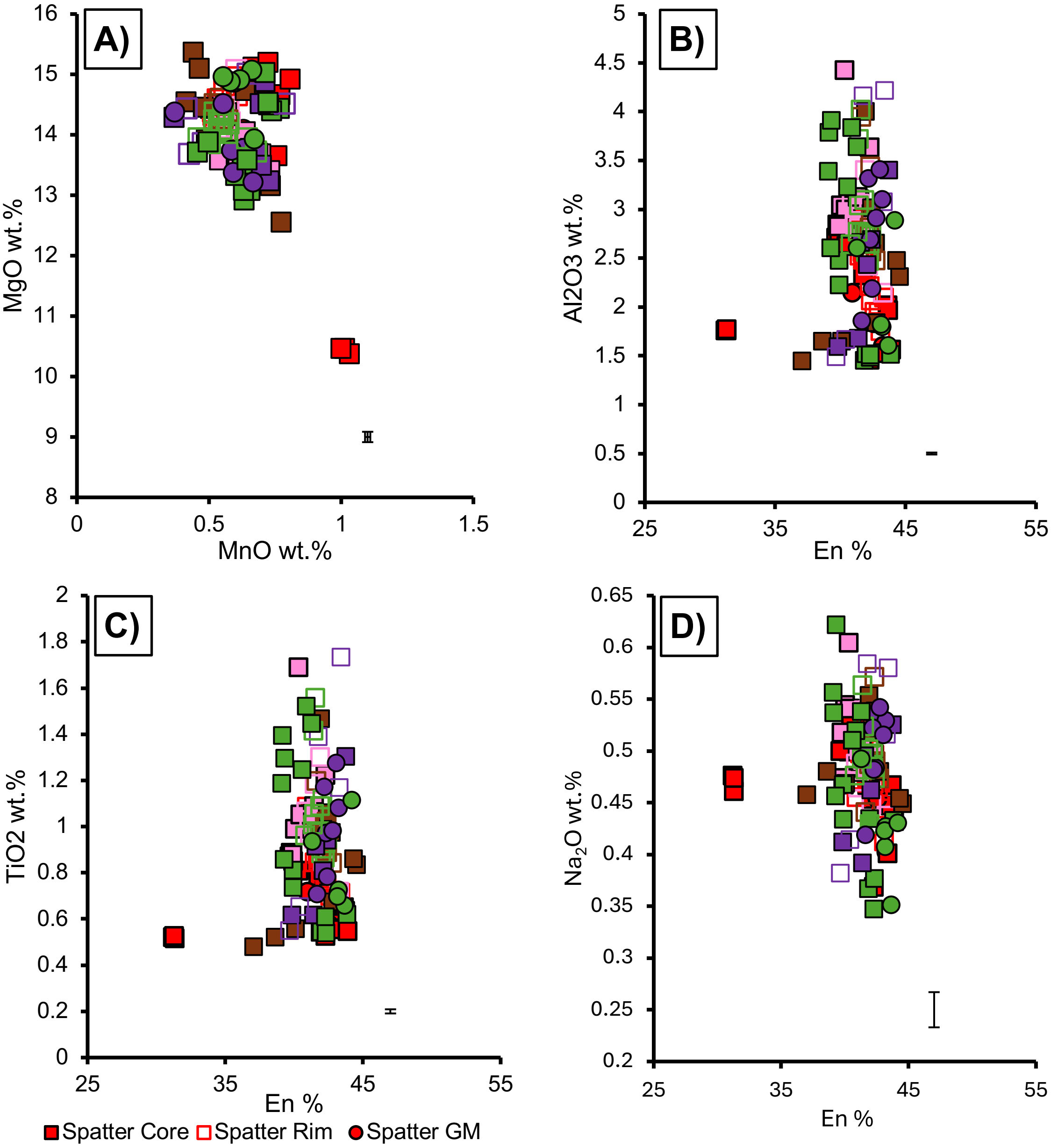

Figure 5.21: *Compositons of pyroxenes cores, rims and groundmass microlites in the DIP samples (lava, spatter and tephra). GM – groundmass olivine. Error bars show 2σ uncertainty.*

exhibit main modes at En$_{40}$ for lavas, En$_{42}$ for pumice clasts, En$_{44}$ for dense clasts and scoria clasts and En$_{44}$ for spatter, with rims at En$_{42}$. The crystals show minimal variation in chemical composition, with the exception of a number of crystal cores in the spatter samples have lower MgO wt.% and higher FeO wt.%. There is no obvious increase in Al_2O_3 or TiO2 with increasing En, and Na_2O doesn't increase with decreasing En (Fig. 5.21).

Clinopyroxene crystals in the spatter encompass almost the entire compositional range of all DIP clinopyroxenes: with Mg# 54 – 74 (Wo$_{37-43}$, En$_{31-44}$, Fs$_{15-27}$). Crystal cores exhibit a range from En_{31-44}, whilst rims and groundmass microlites exhibit a narrow range from En_{41-43}. Crystals in the lava have a narrower range than the spatter with Mg# 64 - 76 (Wo_{37-43}, En_{39-44}, Fs_{14-20}). Crystal cores range from En_{39-44}, whilst crystal rims and groundmass microlites have narrow ranges, En_{41-42} and En_{41-44}, respectively, similar to those in the spatter.

Clinopyroxene crystals in the three tephra samples show similar ranges to the spatter and lava, but are more restricted, in Mg# and composition to the spatter and lava sourced clinopyroxene (Mg# 67 - 75 (Wo_{40-44}, En_{37-45}, Fs_{14-21})). As in the spatter and lava, the crystal cores show a wider range in the cores (En_{37-45}) and a narrow range in the rims (En_{41-44}). Groundmass crystals were seen in the scoria clasts and also have a narrow range (En_{40-43}). No groundmass crystals were seen in the pumice clasts and dense clasts.

5.4.4.4 Amphibole

Two types of amphibole were identified based on rim textures. The first, type i, exhibit breakdown rims, whilst the second, type ii, have euhedral rims. Both types are rich in CaO (7 – 11 wt.%). The amphiboles show weak variations in FeO, MgO, MnO, and TiO_2 wt.% (Fig. 5.22; Table 5.26).

Sample number	**AI-19-034**	**AI-19-034**	**AI-19-121**	**AI-19-121**	**AI-19-127**	**AI-19-127**	**AI-19-026**	**AI-19-026**	**AI-19-026**	**AI-19-026**
Spot	C	R	C	R	C	R	C	R	C	R
Description	Spatter	Spatter	Spatter	Spatter	Spatter	Spatter	Lava	Lava	Lava	Lava
SiO_2	43.05	42.23	42.32	41.99	43.49	42.49	41.46	41.72	41.98	42.38
TiO_2	3.78	3.79	5.46	5.42	3.89	3.60	5.69	5.45	5.57	5.43
Al_2O_3	10.34	10.32	10.68	10.64	10.31	10.21	10.35	10.41	10.13	10.09
FeO	15.74	15.79	15.87	15.81	15.70	15.86	13.42	15.03	13.10	13.33
MnO	0.48	0.51	0.41	0.39	0.46	0.51	0.38	0.41	0.38	0.39
MgO	12.39	11.68	11.96	12.11	12.62	11.85	12.77	12.34	12.81	12.47
CaO	11.03	10.83	10.99	10.96	10.92	10.69	10.71	10.67	10.72	10.71
Na_2O	2.92	2.91	2.89	2.89	2.97	2.97	2.96	2.77	2.83	2.90
K_2O	0.69	0.71	0.63	0.66	0.68	0.71	0.61	0.62	0.60	0.63
Cr_2O_3	0.01	-0.01	0.00	0.01	0.00	-0.01	0.00	0.00	0.01	0.01
Cl	0.05	0.06	0.04	0.04	0.05	0.06	0.03	0.03	0.04	0.04
F	0.26	0.25	0.17	0.17	0.24	0.23	0.47	0.44	0.46	0.44
Total	99.73	99.08	99.41	99.08	100.34	99.18	97.87	97.91	97.63	97.82
Mg#	60	57	59	59	60	57	63	61	64	63

Sample number	**DIP8**	**DIP8**	**DIP8**	**DIP8**
Spot	C	R	C	R
Description	Dense	Dense	Dense	Dense
SiO_2	41.23	41.69	40.92	41.21
TiO_2	5.30	5.17	3.93	5.12
Al_2O_3	10.18	10.11	10.32	10.03
FeO	16.58	17.26	17.29	17.44
MnO	0.50	0.52	0.52	0.51
MgO	10.73	10.31	10.65	10.30
CaO	10.36	10.28	10.28	10.34
Na_2O	2.90	2.76	2.89	2.77
K_2O	0.63	0.67	0.61	0.67
Cr_2O_3	0.00	-0.01	0.00	0.00
Cl	0.04	0.05	0.04	0.04
F	0.37	0.39	0.39	0.35
Total	97.82	98.21	97.85	97.78
Mg#	54	52	52	51

Table 5.26: *Table showing the representative values of amphibole crystal chemistry. For full data set see appendices 2. C = core, R = rim.*

Core and rim compositions in the spatter type i amphiboles overlap with MnO ranging from 0.34 – 0.55 wt.%, TiO_2 from 3.55 – 5.79 wt.% and FeO from 12.12 – 17.92 wt.%. The Mg# also overlaps (50 – 64). Rims have more variable CaO and MgO concentrations (7.45 – 11.29 wt.% and 6.90 – 13.01 wt.%), than the cores (10.72 – 11.22 wt.% and 10.21 – 13.07 wt.%) (Fig. 5.22). Core and rim compositions in the lava type i amphiboles overlap, with MnO ranging from 0.37 – 0.56 wt.% and TiO_2 from 5.29 – 5.69

wt.%. Unlike the spatter, the CaO compositions also overlap from 10.58 – 10.96 wt.% and the FeO and MgO compositions and Mg# show more variation with cores from 12.78 – 17.46 wt.%, 9.67 – 12.88 wt.% and 50 – 64, and rims from 13.33 – 15.03 wt.%, 12.34 - 12.47 wt.% and 61 – 63 (Fig. 5.22). Type i amphiboles in the lava have slightly higher TiO_2

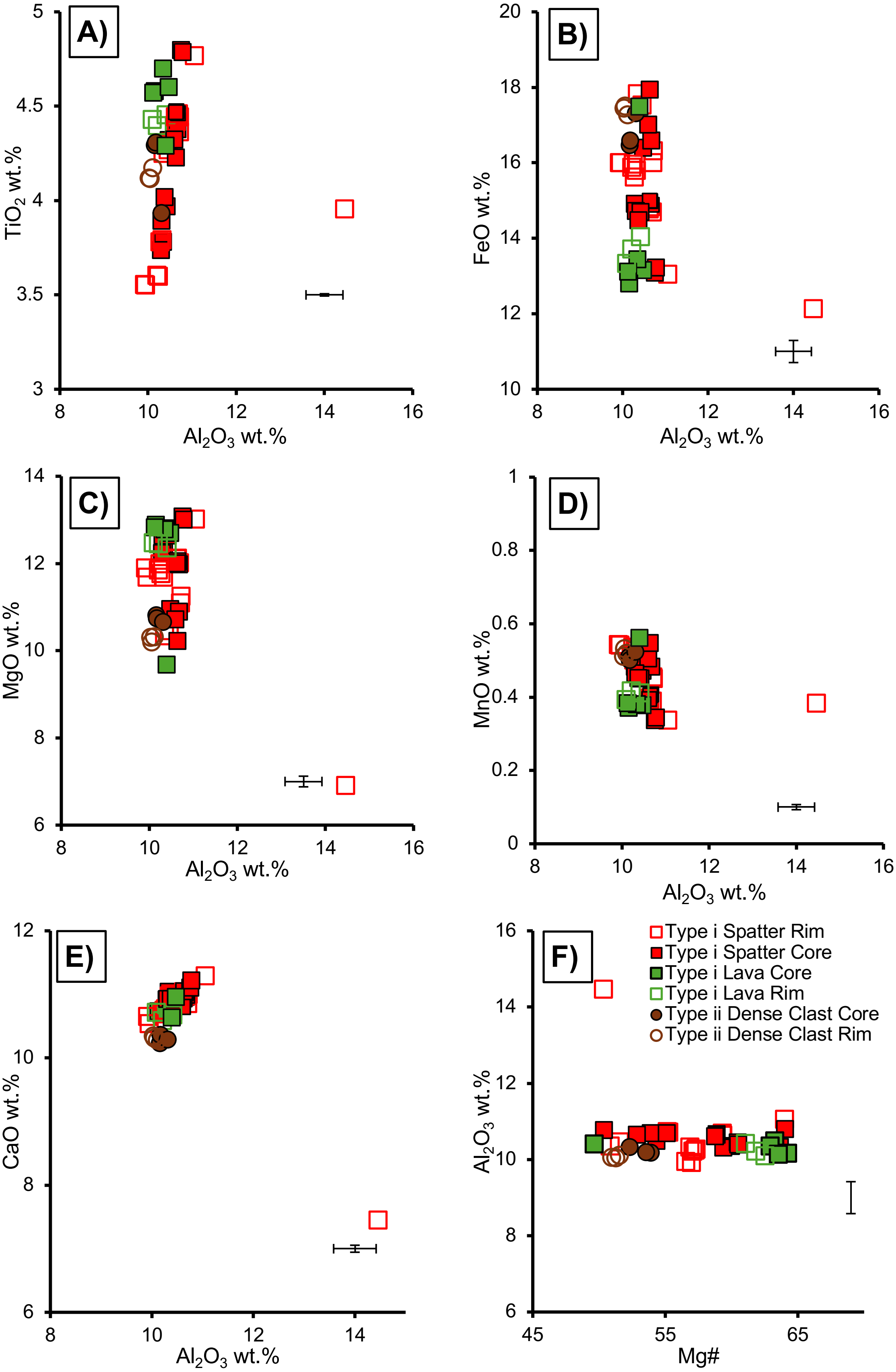

Figure 5.22: *Compositions of the type i and type ii amphibole cores and rims in the DIP samples (lava, spatter and dense tephra clasts). Error bars show 2σ uncertainty.*

and MgO wt.% compared to the type i amphiboles in the spatter, but lower MnO, FeO wt.% and Mg#.

Core and rim compositions in the tephra type ii all overlap. MnO ranges from 0.50 – 0.53 wt.%, CaO from 10.23 – 10.36 wt.%, TiO_2 from 3.93 – 5.30 wt.%, MgO from 10.19 – 10.80 wt.%, FeO from 16.45 – 17.49 wt.%, and Mg# from 51 – 54 (Fig. 5.22). The type ii amphiboles have higher FeO and MnO wt.% and lower MgO, CaO and TiO_2 wt.% than the type i spatter amphiboles but are within the ranges of the type i lava amphiboles. For both types, there is very little increase in Al_2O_3 with increasing Mg# (Fig. 5.22f).

5.4.5 Glass Chemistry

Matrix glass compositions for the tephra clasts range from trachyandesitic scoria clasts (59 – 61 wt.% SiO_2) to trachytic pumice and dense clasts (61 – 62 wt.% SiO_2) (Fig. 5.1; table 5.27). Total alkali contents for the tephra clasts range from 9.1 – 10.4 wt.%. Dense clasts have the highest total alkali contents (9.5 – 10.4 wt.%) and scoria clasts and pumice clasts have lower (9.1 – 9.6 wt.% and 9.2 – 9.7 wt.%, respectively). The major element compositions of the glasses show similar trends observed in the whole rock data. Pumice and dense clasts have lower MgO concentrations (1 – 1.5 wt.%) than the scoria (1.6 – 1.9 wt.%) (Fig. 5.23).

Sample number Description	Scoria Clasts **DIP3**	Scoria Clasts **DIP3**	Scoria Clasts **DIP3**	Pumice Clasts **DIP6**	Pumice Clasts **DIP6**	Pumice Clasts **DIP6**	Dense Clasts **DIP8**	Dense Clasts **DIP8**	Dense Clasts **DIP8**
SiO_2	60.60	59.19	61.04	61.44	62.46	61.39	62.35	62.43	61.40
TiO_2	1.84	1.93	1.67	1.25	1.30	1.29	1.49	1.34	1.37
$Al2O_2$	15.90	15.91	15.15	16.21	16.17	15.84	15.88	15.40	16.02
FeO	7.17	7.96	6.89	6.07	6.24	6.13	6.32	6.42	6.23
MnO	0.27	0.28	0.27	0.23	0.24	0.26	0.26	0.25	0.27
MgO	1.57	1.79	1.57	1.49	1.34	1.37	1.33	1.47	1.37
CaO	3.63	3.76	3.14	3.18	3.02	3.03	2.42	2.76	2.98
Na_2O	5.71	5.74	5.87	6.05	5.96	6.08	5.95	6.11	5.95
K_2O	3.44	3.63	3.77	3.41	3.23	3.52	5.13	3.61	3.60
Cr_2O_3	0.01	-0.01	0.01	0.00	0.00	0.01	0.00	0.00	0.00
Cl	0.18	0.17	0.20	0.19	0.20	0.19	0.16	0.19	0.21
F	0.10	0.10	0.09	0.08	0.08	0.07	0.22	0.22	0.22
P_2O_5	0.73	0.72	0.55	0.44	0.46	0.43	0.52	0.46	0.49
Total	100.17	100.17	100.22	100.05	100.70	99.61	100.04	100.67	100.11

Table 5.27: *Table showing the representative values of tephra glass chemistry. For full data set see appendices 2.*

The pumice has higher SiO_2 and Al_2O_3 concentrations and lower TiO_2, FeO and CaO concentrations than the scoria (Fig. 5.23). Dense clasts follow the same trends but have a slightly greater range in Al_2O_3 wt.% (15.88 – 17.01 wt.%) (Fig. 5.23c). For Na_2O concentrations pumice and dense clasts (5.78 – 6.37 wt.%) are generally higher than scoria clasts (5.63 – 6.08 wt.%) (Fig. 5.23g), whilst K_2O show a similar range in both pumice and scoria clasts (3.19 – 3.77 wt.%) but dense clasts have a slightly higher concentration (3.57 – 5.19 wt.%) (Fig. 5.23h).

5.4.6 MELTS modelling

Previous studies on Ascension Island have shown that the intermediate magmas were formed through closed system fractional crystallisation (e.g., Chamberlain et al., 2019). MELTs modelling (Gualda et al., 2012) was undertaken on the DIP products to test the

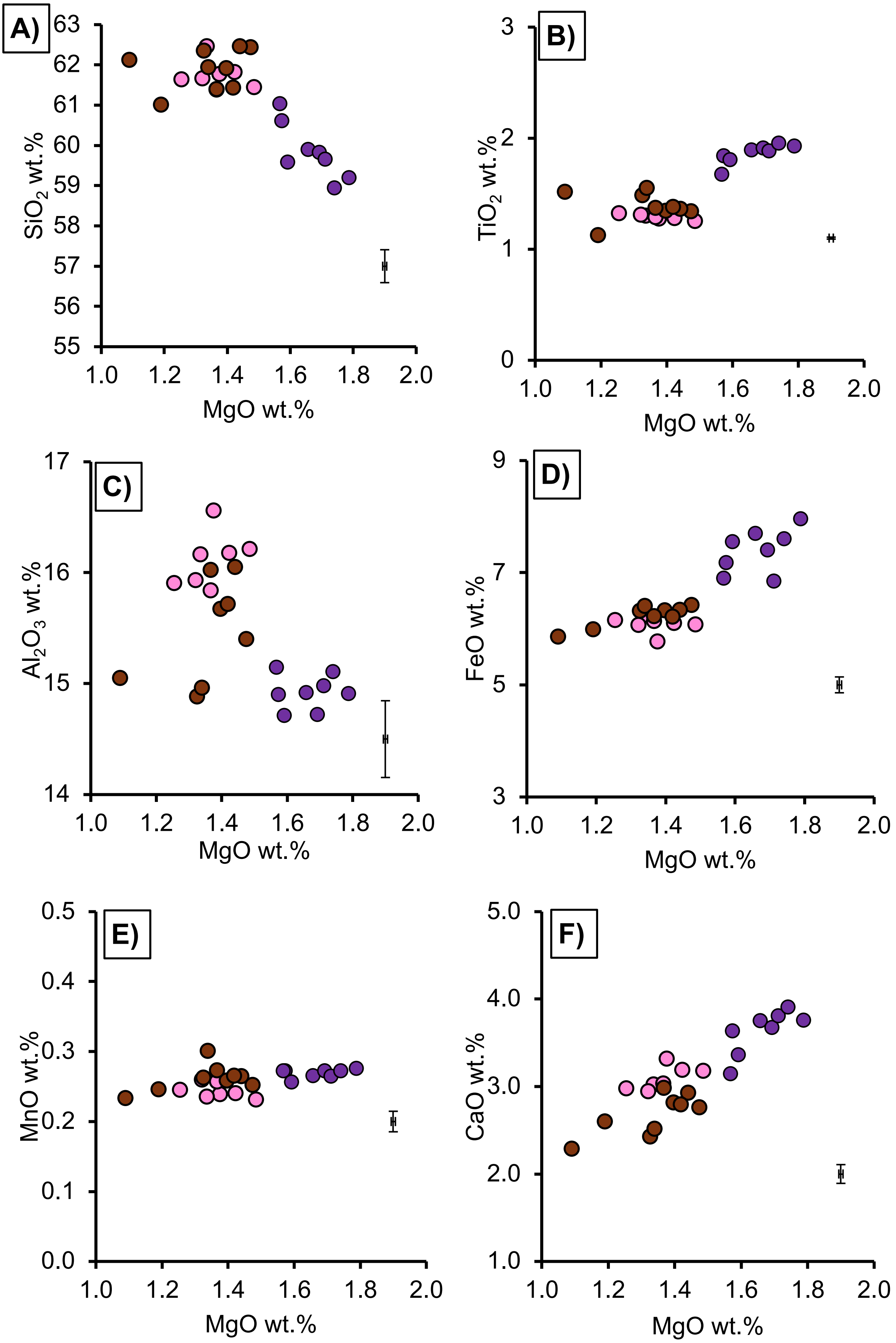

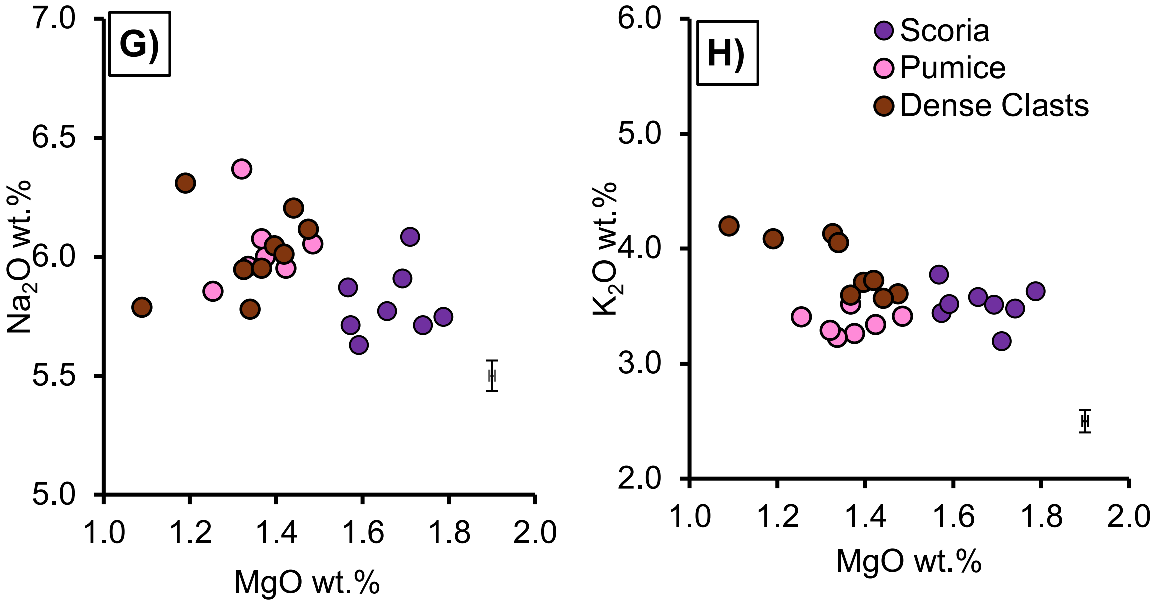

Figure 5.23: *Major element composition graphs for the glass of the three tephra components. Error bars show 2σ uncertainty.*

fractional crystallisation hypothesis. Modelling was initially done using the Cricket Valley lava flow as the starting composition (Weaver et al., 1996; Kar et al., 1998) due to its relatively high MgO concentration (5.23 wt.%), relatively low SiO_2 concentration (50.58 wt.%) and close proximity to the fissure. The Cricket Valley lava also sits within the High Zr/Nb grouping of Weaver et al., (1996) and Kar et al., (1998). Isobaric modelling was undertaken at a range of pressures, from 300 MPa to 100 MPa, at 50 MPa intervals, to simulate a range of depths from just above the base of the lithosphere under Ascension (Evangelidis et al., 2004) and in line with entrapment pressures inferred from melt inclusion analyses (Chamberlain et al., 2016, 2020). Initial water concentration was varied, with models run at 0.2, 0.5 and 1 wt.% H_2O (Fig. 5.24) based on the initial water concentrations from the feldspar hygrometry and water concentrations at other ocean island systems (e.g., Beier et al., 2006; Chamberlain et al., 2019). Models attempted to run at higher than 1 wt.% initial H_2O failed to find thermodynamic solutions. Both the QFM and the Nickel-Nickel Oxide (NNO) fO_2 buffers were used, however, a better fit was generated for the QFM buffer (Fig. 5.25). Evolution of the melt through a closed system fractional crystallisation does not reproduce the major elements of the whole rock data for the DIP, in particular Al_2O_3, CaO and Na_2O (Fig. 5.24). TiO_2 whole rock trends best match high pressure, 1 wt.% initial H_2O conditions, whilst MgO whole rock trends best match high pressure, 0.2 wt.% initial H_2O conditions (Fig. 5.24).

Modelling was also run using the same criterion as above but with higher MgO (6.65 wt.%) and lower SiO_2 (47.53 wt.%) initial concentrations, taken from the Command Hill lava flow (Weaver et al., 1996; Kar et al., 1998). The Command Hill lava sits within the Intermediate Zr/Nb grouping (Weaver et al., 1996; Kar et al., 1998). The modelled data produced very similar liquid lines of descent to the Cricket Valley lava flow (Fig. 5.26). Runs that suppressed olivine and feldspar phases, independently, were undertaken for

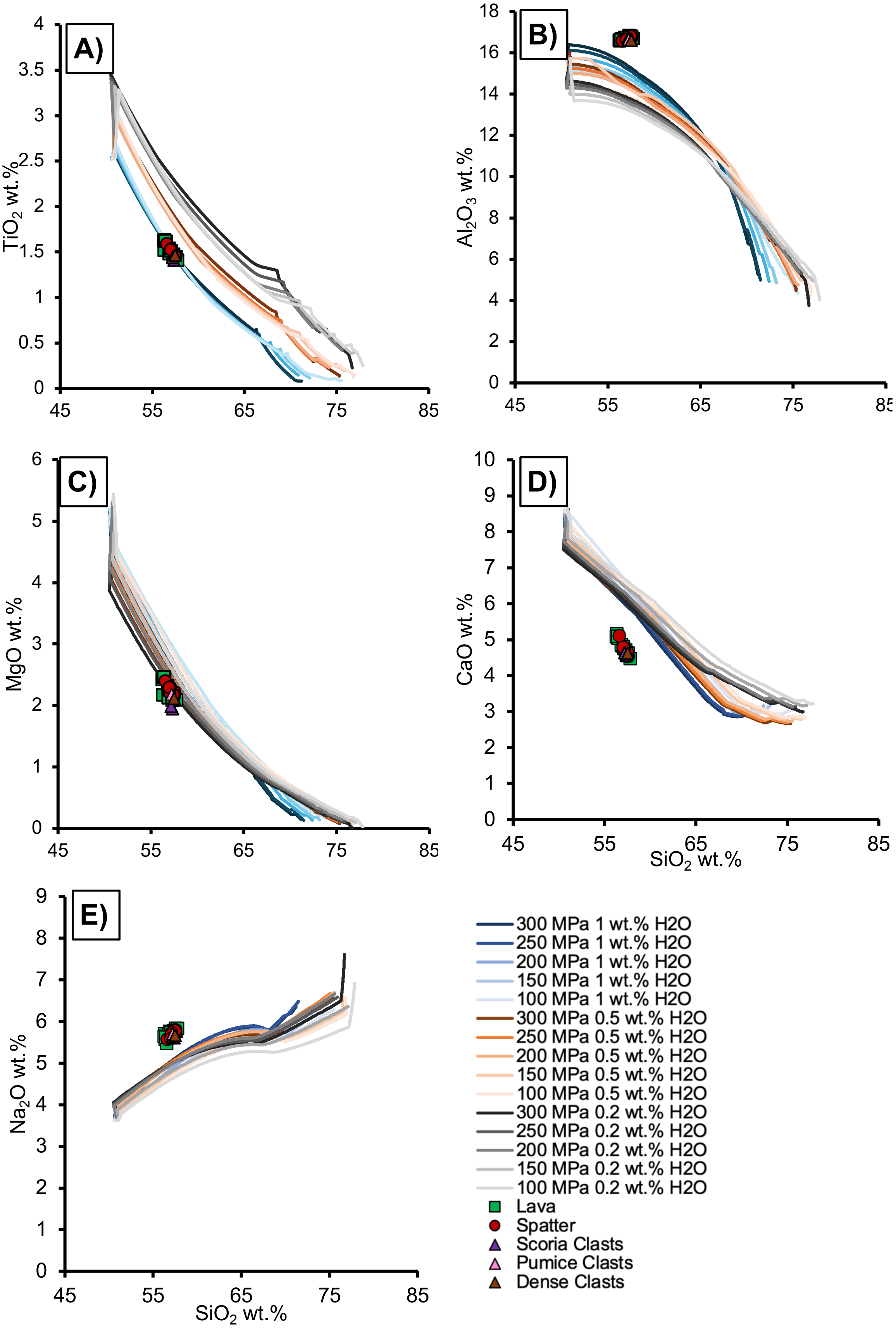

Figure 5.24: *MELTs modelling from Cricket Valley starting member at different water concentrations (1 wt.% - blues, 0.5 wt.% oranges, 0.2 wt.% greys) and a QFM buffer. Symbols show the DIP data. TiO_2 and MgO show the best fits at 1 wt.% and 0.2 wt.% H_2O respectively.*

Command Hill using the same inputs but 2 wt.% initial H_2O but also could not reproduce the same liquid line of descent curves (Fig. 5.27). Modelling run from the least evolved DIP product was also not able to reproduce the more evolved compositional range identified on Ascension Island (Fig. 5.28). The MELTs data shows that the Zr/Nb ratio has no significant impact on the evolution of the magma and that closed system fractional crystallisation hypothesis is not the sole driver for the intermediate magma composition of the DIP. .5

5.5 Intensive Variables

Temperature and water content were modelled for the erupted products (Table 5.1), using the feldspar-liquid thermometer (Putirka, 2005), olivine-liquid thermometer (Putirka et al., 2007), clinopyroxene-liquid thermometer (Neave and Putirka, 2017), amphibole-liquid thermometer (Putrika, 2016) and the plagioclase-liquid hygrometer (Waters and Lange, 2015). A maximum pressure of 330 MPa was assumed, as that marks the base of the lithosphere at Ascension (Evangelidis et al., 2004) and is in line with those inferred from melt inclusion analyses (Chamberlain et al., 2016, 2020). The thermometers were also used to establish which crystal phases are in chemical equilibrium with the melt. For all samples whole rock compositions are used as the liquid composition. The use of glass compositions resulted in no crystal phases in equilibrium.

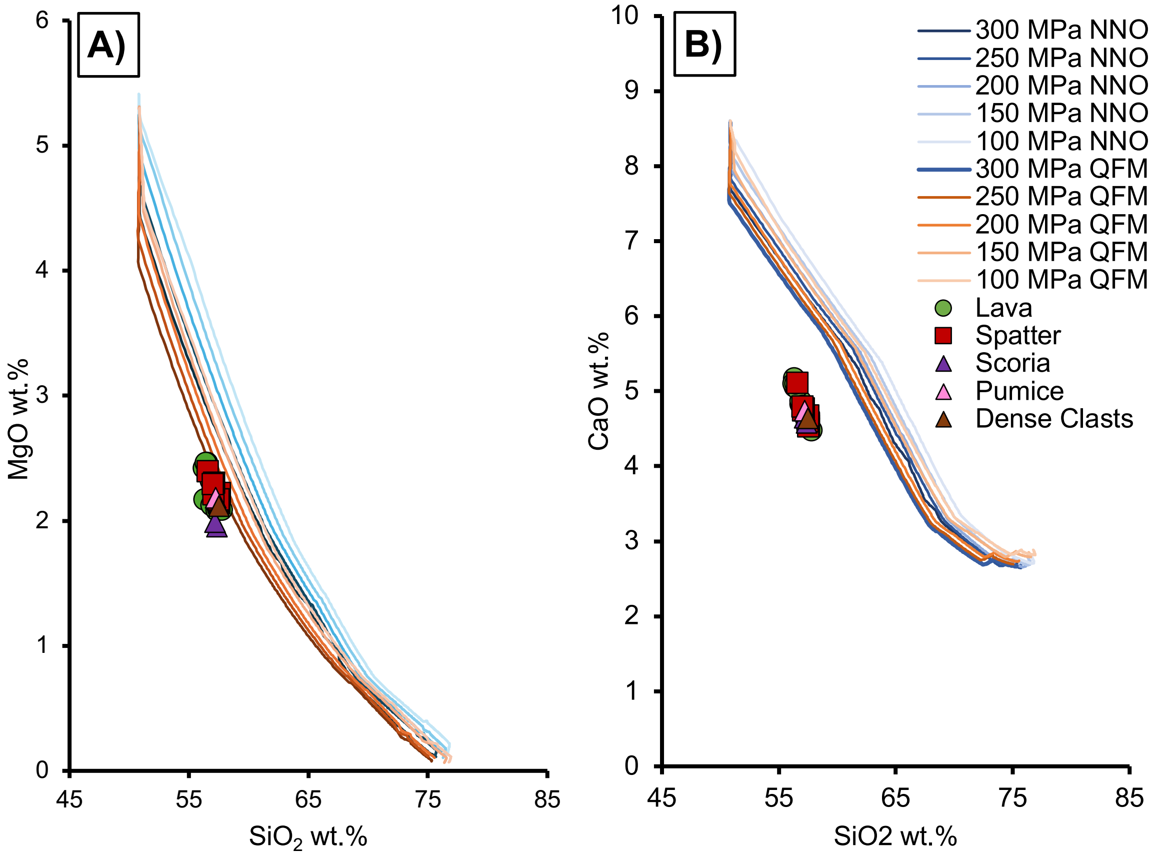

Figure 5.25: *Two representative Cricket Valley runs showing the two different buffers (NNO – blue, QFM – orange). Ran using 0.5 wt.% H_2O and pressures from 3000 – 1000 bars at 500 bar intervals.*

For the plagioclase-liquid thermometer, equilibrium was assessed by comparing the An-Ab exchange (Putirka, 2005). For temperatures <1050 °C, the An-Ab exchange value should be 0.1 ± 0.05, and for temperatures >1050 °C the An-Ab exchange value should be

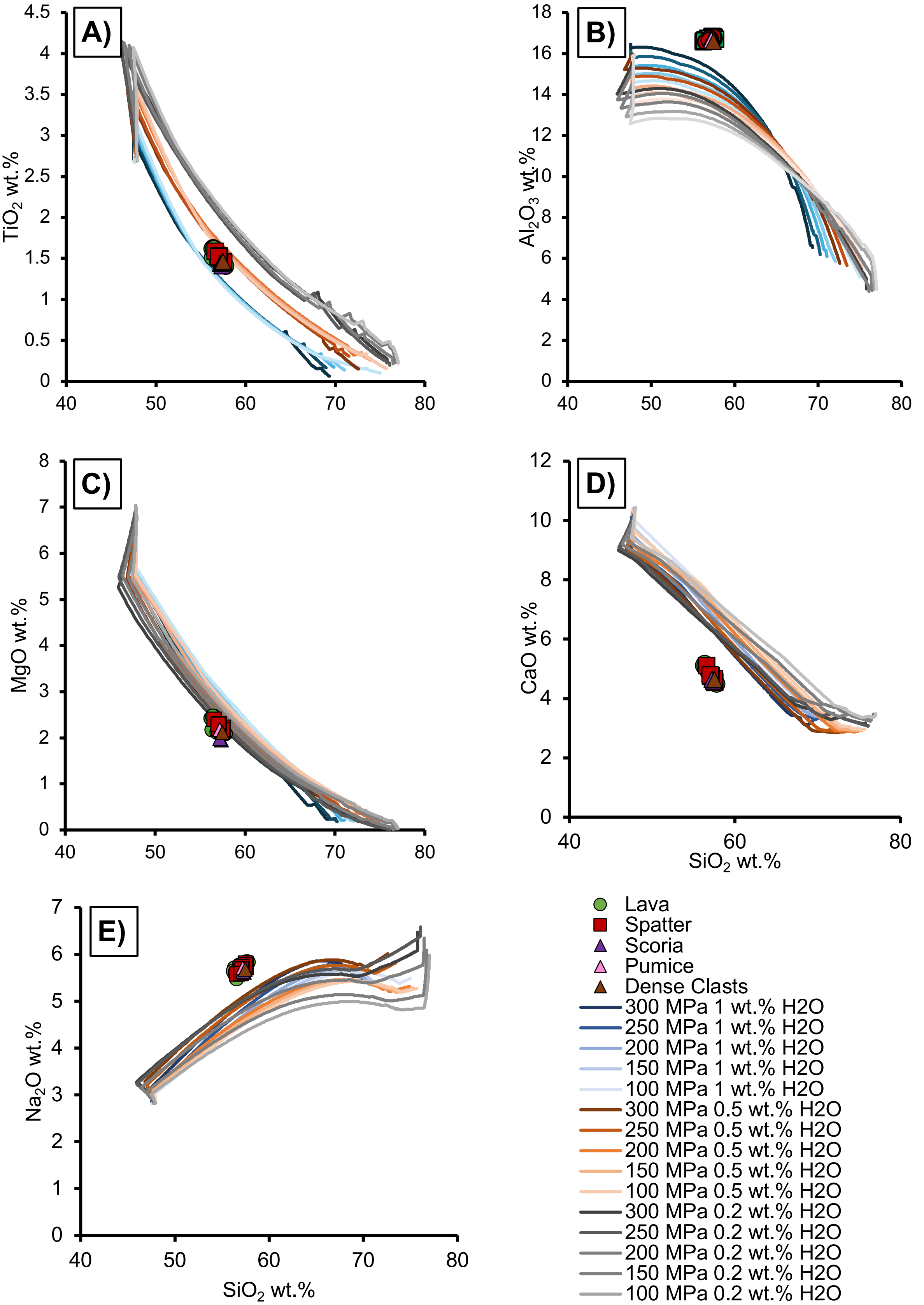

Figure 5.26: *MELTs modelling from Command Hill starting member at different water concentrations (1 wt.% - blues, 0.5 wt.% oranges, 0.2 wt.% greys) and a QFM buffer. Symbols show the DIP data. MgO shows the best fits at 0.2 – 0.5 wt.%* H_2O.

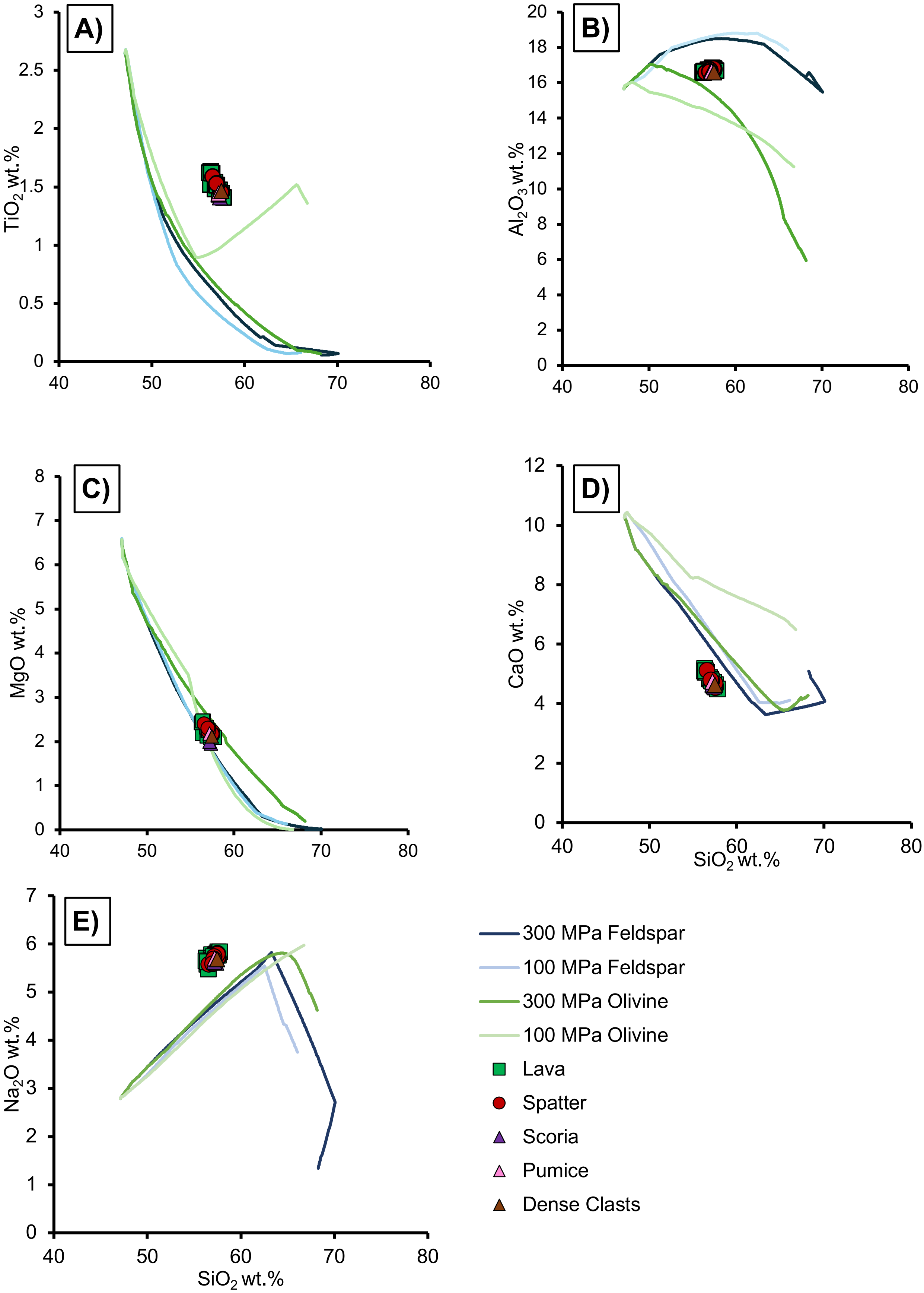

Figure 5.27: *MELTs modelling showing the liquid lines of descent when feldspars and olivines are suppressed at 2 wt.% H_2O.*

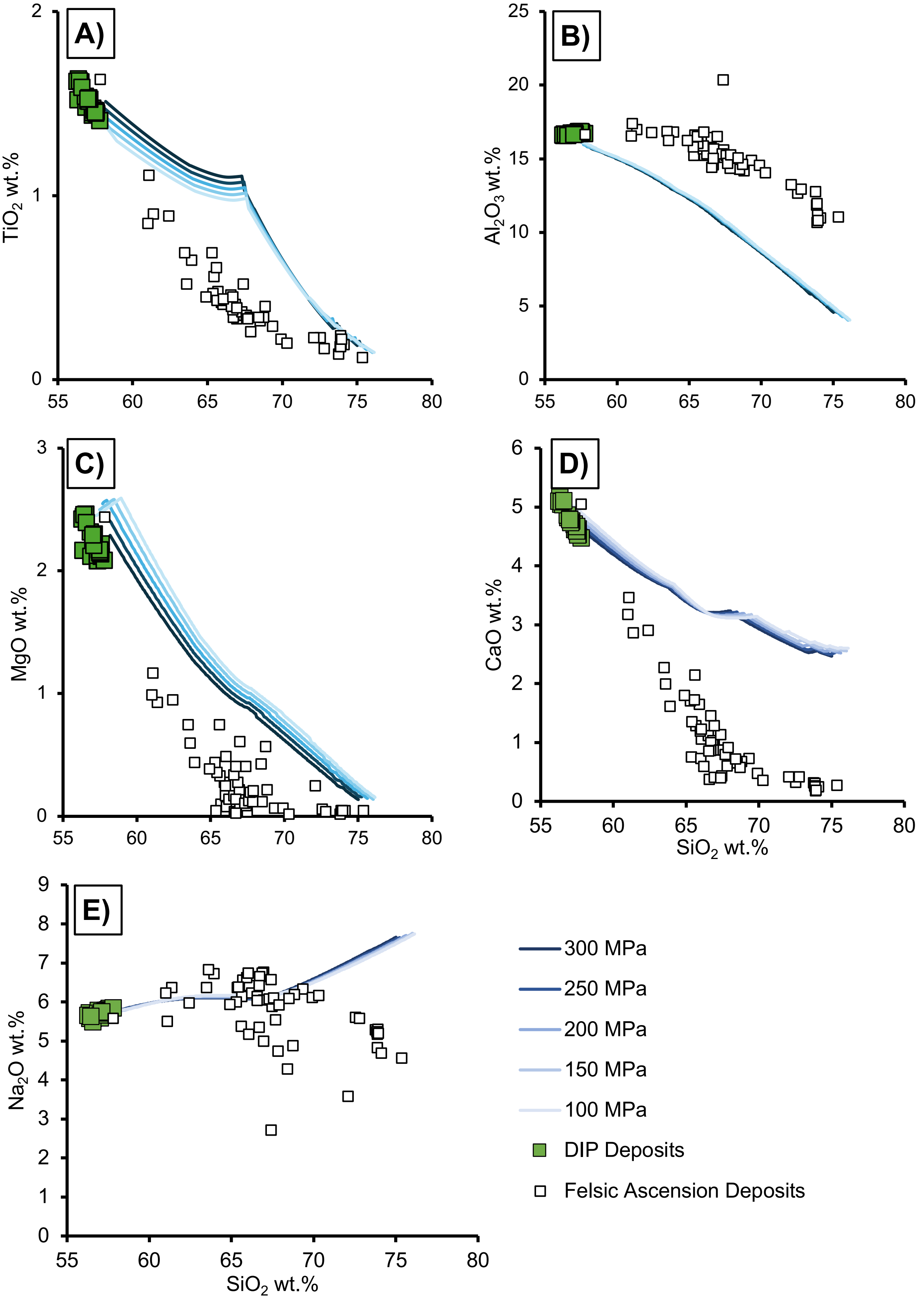

Figure 5.28: *MELTs modelled from the least evolved DIP deposit. White squares represent the more evolved compositional range on Ascension. Modelled from 56.35 wt.% SiO_2, 2.44 wt.% MgO and 0.6 wt.% H_2O.*

0.28 ± 0.11 (Putirka, 2005) (Fig. 5.29a). Both the feldspar hygrometer and thermometer require pressure as an input and so the sensitivity of the pressure input was tested. The testing confirmed that a difference of 100 MPa had only 6 °C difference on temperature and 0.02 wt.% difference on water concentrations.

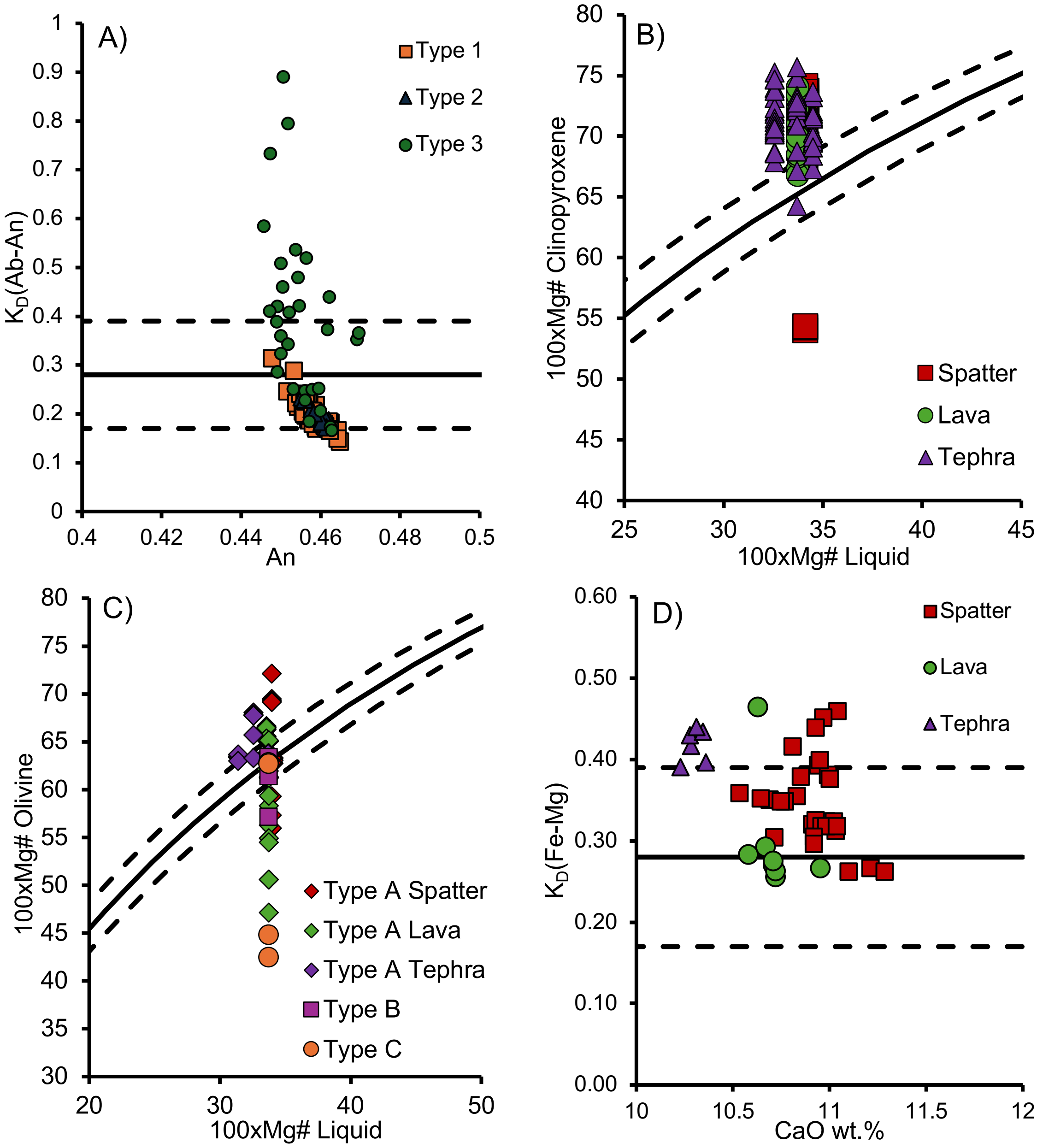

Figure 5.29: *Equilibrium graphs for the different crystal phases. For all graphs, the solid line represents the point of equilibrium at a certain value and the dashed lines represent the range. Any samples within the dashed lines are in equilibrium, whilst those outside are not in equilibrium.* ***A)*** *Equilibrium graph for the three different feldspar textures (****Putirka, 2005****).* ***B)*** *Rhodes diagram for the clinopyroxene crystals (Neave and Putirka, 2017).* ***C)*** *Rhodes diagram for the three different olivine textures (Putirka et al., 2007).* ***D)*** *Equilibrium graph for the amphibole crystals (Putrika, 2016).*

To test for equilibrium in the clinopyroxene-liquid thermometer, olivine-liquid thermometer and amphibole liquid thermometer, the K_D(Fe-Mg) value was used. For the clinopyroxene-liquid thermometer, the $K_D(\text{Fe-Mg})^{\text{cpx-liq}}$ value should be close to 0.27 ± 0.03 (Neave and Putirka, 2017), for the olivine-liquid thermometer, the $K_D(\text{Fe-Mg})^{\text{olv-liq}}$ should be close to 0.30 ± 0.03 (Putirka et al., 2007) and for the amphibole liquid thermometer, the $K_D(\text{Fe-Mg})^{\text{amph-liq}}$ should be close to 0.28 ± 0.11 (Putrika, 2016) (Fig. 5.29d). Both $K_D(\text{Fe-Mg})^{\text{cpx-liq}}$ and $K_D(\text{Fe-Mg})^{\text{olv-liq}}$ equilibrium tests can also be shown visually on a Rhodes

Diagram (Fig. 5.29b-c) (Roeder and Emslie, 1970; Putirka et al., 2007; Neave and Putirka, 2017).

Results from the feldspar-liquid thermometer yield temperatures ranging from 1095 – 1126 °C (Table 5.24) and an average temperature of 1107 °C (Table 5.25) for all the crystals in equilibrium (Fig. 5.30). There is no difference in the modelled temperatures between the samples studied or the textural classification of the feldspar. However, the T3 feldspars cores and inner cores are not in equilibrium with the whole rock composition.

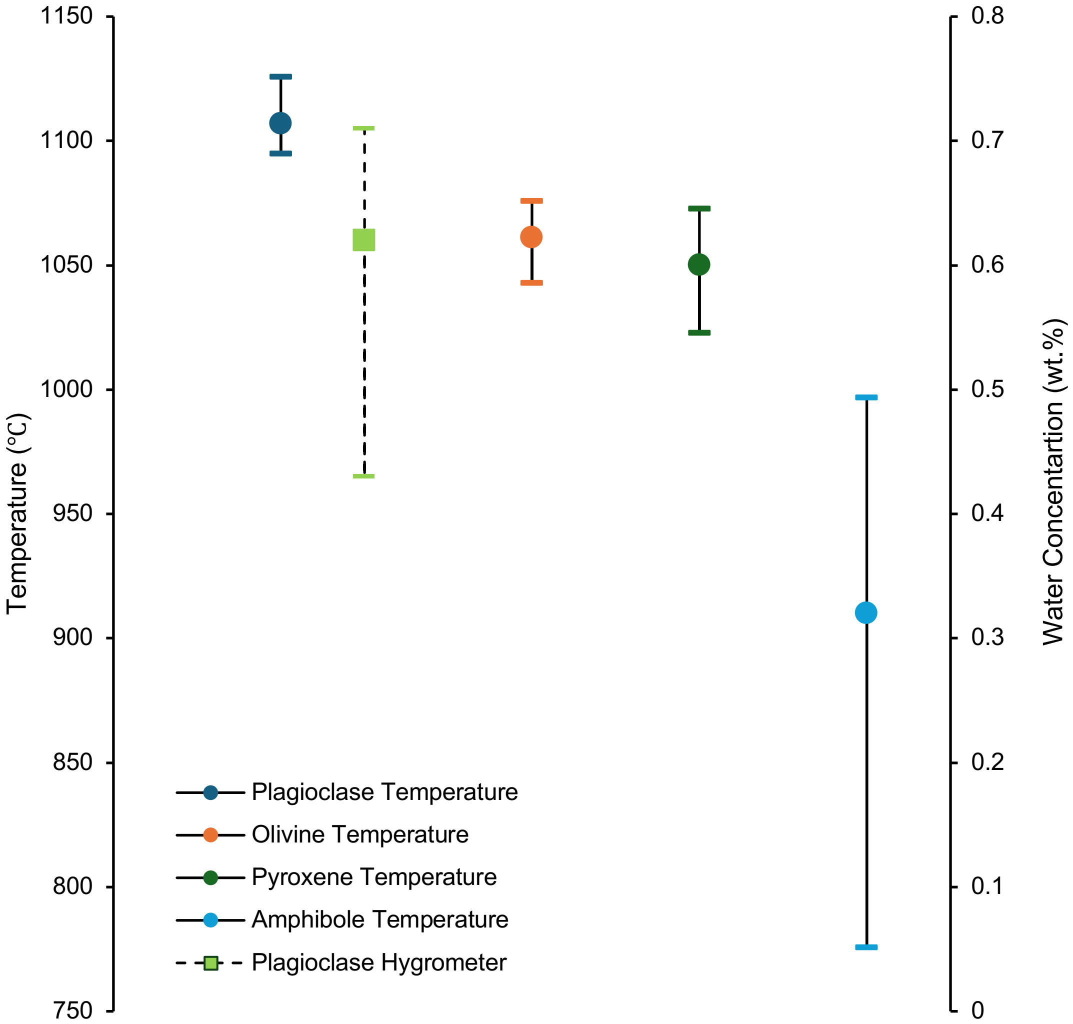

Figure 5.30: *Graph showing the average (circle for temperature or square for water) and range in temperature of the different crystal phases and water concentration of the feldspars.*

The olivine-liquid thermometer yields temperatures ranging from 1043 – 1076 °C (Table 5.24) and an average temperature of 1061 °C (Table 5.25) for all crystals in equilibrium (Fig. 5.30). The olivine crystals in the lava have the widest range (1046 – 1076 °C). The olivine crystals in the spatter and dense clasts are hotter, ranging from 1067 – 1075 °C, whilst the olivines in the scoria clasts are cooler at 1043 °C. There is no difference in the modelled temperatures between the textural classification of the olivine.

The pre-eruptive temperatures produced by the feldspar and olivine phases are unusually hot for trachyandesite magmas. They are similar to those from the andesitic fissure at Kilauea in 2018 (1030 – 1080 °C) and to andesitic magmas from the southern Taupō Volcanic Zone (1010 – 1130 °C) (Lormand et al., 2020). However, the Pavin trachyandesite (Massif Central, France), which has a near- identical composition to the DIP trachyandesite yielded temperatures of 950 – 975 °C (Rondet et al., 2019), while trachyandesites from Gran Canaria yielded lower temperatures still (850 – 900 °C) (Freundt and Schmincke, 1995).

Pyroxene crystals are rarely in equilibrium with whole rock and glass compositions. The few that are yield temperatures ranging from 1023 – 1073 °C (table 5.24) and an average of 1050 °C (table 5.25) (Fig. 5.30). Pyroxenes in the pumice samples show the widest range (1039 – 1071 °C) and overlap with both the spatter samples (1025 – 1055 °C) and lava (1054 – 1073 °C). However, the clinopyroxenes in the lava samples are hotter than the spatter samples, and the clinopyroxenes in the dense clasts are cooler (1023 – 1028 °C) than the spatter, lava, and pumice clasts. The lack of pyroxenes in equilibrium do mean that these temperatures should be treated with more caution. Amphiboles are not in chemical equilibrium in the spatter and lava samples but have much lower temperatures (Fig. 5.30). The similarity in amphibole composition (Fig. ch.4) shows that the amphiboles all have similar growth histories, and the majority are in chemical equilibrium with the surrounding magma which suggests that they are do not have a xenocryst origin and so the thermobarometers may be useful.

The temperatures range from 776 – 997 ± 25 °C and 969 – 989 ± 25 °C (table 5.24) and yield average temperatures of 977 ± 25 °C and 939 ± 25 °C, respectively (table 5.25). Amphiboles in the dense clasts are not in equilibrium. No amphibole data is recorded from the pumice or scoria clasts. The presence of amphibole suggests that the magma did not achieve water saturation below the stability limit of amphibole (e.g., Gardner et al., 1995; Reubi and Nicolls 2004).

Pressures calculated from the amphibole-liquid thermometer (Ridolfi, 2021) have an average of 262 and 270 MPa (~8 – 9 km deep) for the spatter and lava samples, and 253 MPa (~8.6 km deep) (table 5.26) for the dense tephra clasts, which is slightly lower than entrapment pressures, from melt inclusions from the Mingled Fall deposit 330 MPa (~ 11 km deep) (Chamberlain et al., 2020), but within range of the pressures from the Zoned Fall deposit (250 MPa, ~ 8.5 km) (Chamberlain et al., 2016).

Results from the plagioclase-liquid hygrometer yield water concentrations ranging from 0.43 – 0.71 wt.% H_2O (Table 5.27) and an average of 0.62 wt.% H_2O (Table 5.27) for all the crystals in apparent chemical equilibrium (Fig. 5.30). For the feldspar crystals in the spatter, modelled water contents range from 0.43 – 0.66 wt.% H_2O with an average of 0.61 wt.% H_2O and for the feldspar crystals in the lava, the water contents range from 0.54 – 0.67 wt.% H_2O with an average of 0.62 wt.% H_2O. The feldspars in the tephra range from

0.51 – 0.71 wt.% H_2O, with feldspars in the scoria, pumice and dense clasts ranging from 0.55 – 0.71 wt.% H_2O, 0.60 – 0.63 wt.% H_2O and 0.51 – 0.62 wt.% H_2O, respectively. Average feldspar water contents for the scoria clasts, pumice clasts and dense clasts are 0.68 wt.% H_2O, 0.61 wt.% H_2O and 0.59 wt.% H_2O. There is no systematic difference in the modelled H_2O contents based on textural types (Table 5.27). Water concentrations are lower in the DIP samples than in other intermediate composition eruptions from both arc settings e.g., Soufriere Hills; 2.8 – 3.1 wt.% H_2O (Frey et al., 2024), Sakurajima; 2.0 – 3.5 wt.% H_2O (Okumura, 2011; Miwa et al., 2013), and ocean island e.g., Eyjafjallajökull; 1.3 – 1.8 wt.% H_2O (Keiding and Sigmarsson, 2012; Cioni et al., 2014).

5.6 Discussion

The trachyandesite magma erupted from the DIP fissure exhibits very little compositional variation in both whole rock major and trace elements and in crystal phase compositions. However, crystal phases exhibit disequilibrium textures which provide insights into the processes that occurred in the magma chamber to generate the intermediate magma. On ocean islands, deposits of intermediate compositions have been found to form through magma mixing (e.g., Deruelle et al., 2007), high- or low-pressure fractionation (e.g., Mungall and Martin, 1995) or partial melting (e.g., Sigmarsson et al., 1991; Martin and Sigmarsson, 2007). In some locations, intermediate composition material is only erupted as inclusions, (e.g., Bachmann et al., 2002; Ferla and Meli, 2006; Macdonald et al., 2008), however the inclusion of intermediate compositions is still evidence that magma storage regions host a complete range of compositions in many locations.

5.6.1 Intermediate magma genesis at the Devil's Ink Pot fissure

Whole rock major and trace element data, crystal compositions and macrocryst phases show little variation between the different types of deposits which suggests that the mode of intermediate magma genesis was consistent throughout the eruption.

Isobaric MELTs modelling from an intermediate Zr/Nb basalt, a high Zr/Nb basalt and from the least evolved DIP sample were unable to fully reproduce the same intermediate composition of the DIP fissure and the more evolved compositions on the island. Polybaric MELTs models were not evaluated as MELTs was not able to provide solutions for the inputs used. The MELT's modelling showed that the Zr/Nb ratio of the basalt has no importance on the degree of fractional crystallisation. Fractional crystallisation at higher pressures (>250 MPa, corresponding to depths greater than 7 km, can account for the compositional variation in the MgO and TiO_2 but cannot account for any other oxides such as CaO, Na_2O and Al_2O_3 (e.g., Fig. 5.24, 5.25). This means that simple fractionation is unable to solely reproduce the compositional variation of the DIP magma through liquid lines of descent and therefore challenges previous island-wide studies that show that evolved magmas on Ascension have been derived by simple closed-system fractional crystallisation with parental magmas from either the intermediate Zr/Nb basalts (e.g., Weaver et al., 1996; Chamberlain et al., 2019) or high Zr/Nb basalts (e.g., Kar et al.,1998). Evidence of this is also seen in the 2018 Kilauea fissure eruption. An offset fissure erupted an andesite magma that could not be reproduced in MELTs using local magma sources within the Lower East Rift Zone, whilst additional modelling suggested the andesite was also not produced from two component magma mixing (Gansecki et al., 2019). As there are very few examples where individual, intermediate composition eruptive sequences are pulled apart in detail, the possibility that this is more common than once thought, cannot be dismissed.

Further evidence for fractional crystallisation on Ascension can be seen in deposits from a zoned magma storage region (e.g., Chamberlain et al., 2016), whereby the closed-system fractional crystallisation created a continuous gradation in the composition, with trachyte at the top of the magma storage region and trachy-basaltic andesite at the base (Chamberlain et al., 2016). However, mingled deposits have also been identified in multiple locations around the island (e.g., Chamberlain et al., 2020) so it is known that fractional crystallisation is not the sole process occurring and that there is a mix of open and closed system events.

Instead, the higher concentration of the CaO, Na_2O and Al_2O_3 in the DIP samples compared to the modelled MELTs trends, could have resulted from the accumulation of feldspar antecrysts. However, simple accumulation calculations show that more than 50% feldspars would need to be accumulated to get the DIP composition from basaltic Ascension magmas with different compositions, and therefore accumulation of feldspars alone is also not able to reproduce the observed composition.

Magma mixing is not an obvious candidate for intermediate magma genesis for the DIP eruption, due to the restricted range of both macrocryst and matrix glass compositions (e.g., Fig. 5.15, 5.17, 5.23) (e.g., Reubi and Nicholls, 2004). However, the diversity in the textures of the DIP feldspar (e.g., Fig. 5.5 – 5.7) and olivine crystals (e.g., Fig. 5.8 – 5.10) represent different growth conditions and, combined with the disequilibrium textures, could indicate that there was an initial degree of mixing early on in the magma evolution rather than in the final stages when the growth of new rims and microlites occurred (e.g., Tepley et al., 1999; Reubi et al., 2002; Reubi and Nicholls, 2004; Pal et al., 2007; Martin and Sigmarsson 2007; Loewen et al., 2021). Magma mixing linked to zoned and resorbed feldspar crystals has also been inferred on other ocean islands such as Iceland and Stromboli (Landi et al., 2004; Martin and Sigmarsson, 2007). The mixing of two magma bodies may have created a hybrid magma that became fully homogenised during or after the mixing event (e.g., Wyers and Barton, 1986). In this scenario, new crystals form in equilibrium with the new magma and crystals not in equilibrium are fully or partially resorbed (e.g., Wyers and Barton, 1986). However, for a magma to mix and become fully hybrid, it requires a relatively long time within a storage region (Macdonald et al., 2008). The generation of a potential early, hybrid magma could be the reason why fractional crystallisation trends cannot be successfully modelled in MELTs (e.g., Longpré et al., 2014; Gansecki et al., 2019).

It is more likely that the evolution of intermediate magma at the DIP is partly due to the accumulation of crystals, with varying compositions, from multiple sources, such as mush zones and plutonic bodies (e.g., Chamberlain et al., 2019), and that the disequilibrium textures are evidence that the crystals have been incorporated into new magma.

Partial melting of intrusive material can lead to intermediate magma genesis (Lanzafame et al., 2021). No evidence is found at Ascension to support this hypothesis: the lack of cumulates and glomerocrysts in the samples and the co-linearity of the island wide trace elements suggests that partial melting was not the main driver for intermediate magma genesis at the DIP (e.g., Kar et al., 1997; Bohrson and Reid, 1997; Jicha et al., 2013; Chamberlain et al., 2019). Due to the lack of data on xenoliths and crustal end members in this study, it was not possible to test the effect of assimilation with any accuracy, however simple assimilation calculations show that 50% crustal assimilation is needed to reach the DIP composition. A study on magma evolution by Wyers and Barton, (1986) found that K_2O concentrations become enriched relative to Na_2O concentrations during assimilation: a trend not observed in the DIP samples. Recent studies on Ascension Island have shown that whilst fractional crystallisation is responsible for the compositional range seen on the island, it cannot produce the water-rich rhyolite magmas (Chamberlain et al., 2020). Instead, these more evolved magmas formed from partial melting of gabbroic cumulates, a rare process in low-flux islands like Ascension, due to the lower input rates of crustal basalt into the lower crustal melting regions (Chamberlain et al., 2020).

The lack of evidence for a single evolutionary process (e.g., simple fractional crystallisation evidenced along a single liquid line of descent or magma mixing evidenced through distinct crystal populations suggests that more than one process was involved in the generation of the DIP magma. This has been proposed for other volcanic systems (e.g., Greater Olkaria Volcanic Complex, Kenya (Macdonald et al., 2008)) undergoing fractional crystallisation of basaltic magmas, mixing between basaltic magmas and further fractional crystallisation along several liquid lines of descent (e.g., Macdonald et al., 2008), and others (e.g., the Azores) undergoing fractional crystallisation and partial melting of dry or hydrated basaltic material within the mid or lower crust (e.g., Mungall and Martin, 1995).

Island-wide studies of ocean island volcanoes can show closed system fractionation trends (e.g., Sete Cidades (Beier et al., 2006)), but on further investigation, intermediate compositions do not always fit within the trends which suggests that they formed through different or multiple processes (e.g., Legendre et al., 2005; Lanzafame et al., 2021). This has been proposed for Nuku Hiva island, where the mafic and felsic magma evolved through closed system fractionation but the trachyandesites formed through partial melting (Legendre et al., 2005), and on Tenerife, where the deposits of intermediate composition provide evidence of magma mixing (e.g., Cas et al., 2022).

5.6.2 Crystal phases and disequilibrium textures

The majority of the feldspar and olivine microphenocrysts appear to have had at least one phase of disequilibrium with the surrounding magma as evidenced by the sieve and resorption textures and the normal, reverse, and oscillatory zoning patterns in the type 1 and 2 feldspars (T1 and T2) (e.g., Fig. 5.5 – 5.6) and type B and C olivines (TB and TC) (e.g., Fig. 5.9 – 5.10). Disequilibrium textures observed in the TB and TC olivines are similar to the olivine textures described in metamorphic rocks, which result from increasing heat and pressure (e.g., Peltonen, 1990), but they appear to be underrepresented and rarely described in the igneous petrology literature.

The resorbed textures of the olivines and feldspars suggest that the crystals were taken out of their stability domains during the evolution of the magma and the resulting chemical disequilibrium led the crystals to be partially dissolved by the magma. Where new rims were able to form (e.g., type 1 and type 3 feldspars), the crystals must have reached a composition where growth could continue. The dissolution rates of the feldspars are controlled by the degree of disequilibrium between the feldspar and the melt (Wark and Stimac, 1992). Olivines in trachyandesites can be resorbed over a period of 8 – 375 hours depending on the degree of super heating of the magma and the extent of chemical disequilibrium (Wyers and Barton, 1986).

Although many of the feldspar and olivine crystals exhibit obvious signs of disequilibrium, the compositions of the majority of the feldspar and olivine crystals are in apparent chemical equilibrium (e.g., Fig. 5.29a, c). T1 and T2 feldspars have similar compositions (e.g., Fig. 5.13) and show little difference in composition between core and rim, which shows that they formed in the same magma source rather than being incorporated as antecrysts. The type 3 feldspar textures (T3) represents either rapid growth from a liquid in an undercooled environment (e.g., Hibbard, 1981; Anderson, 1984; Ray et al., 2011) or the transformation of sodic to calcic by dissolution of the sodic component, during heating (e.g., Anderson, 1976; Ray et al 2011). The compositional relationships of the crystals, where the resorbed inner rim is more calcic than the core and less calcic than the outer rim, suggest the T3 crystals formed from the transformation of sodic to calcic plagioclase. This process that forms the T3 textures does not necessarily result from mixing of two magma bodies but could solely represent the accumulation of more sodic feldspar into a less evolved magma. Instead, the destabilisation of the feldspar could be related to shifts within the feldspar stability field, influenced by the concentration of volatiles (e.g., Tepley et al., 2000) or the pressure and melt water concentration within the magma (e.g., Freise et al., 2003; Ray et al., 2011)

The TA olivines and groundmass olivines in the spatter and lava have lower Fo% than the TA olivines and groundmass olivines in the tephra clasts and the TB and TC olivines (e.g., Fig. 5.16) which suggests that the olivines in the spatter and lava grew on ascent. The TB and TC olivines have varying degrees of equilibrium with the whole rock composition (e.g., Fig. 5.29), and those not in equilibrium have higher average temperatures (~1149 °C compared to 1061 °C) and are also inferred to have been incorporated as antecrysts.

The calcic composition of the plagioclase and the presence of clinopyroxene suggest the crystals grew from more mafic melts (e.g., Bachmann et al., 2002). However, the T1 feldspars with a resorbed cores overgrowths and euhedral rims are typical following the entrainment of plagioclase from a more felsic magma into a more mafic magma (e.g., Bellver-Baca et al., 2020). The lower MgO compositions of the glass compared to the whole rock shows that the accumulation of mafic phases modified the whole rock composition (e.g., Beier et al., 2006). The olivine crystals are mostly in chemical equilibrium with the whole rock compositions, whilst the pyroxenes are not. Therefore, it is probable that the whole rock composition was partially modified by clinopyroxene crystals derived from a more mafic magma. The closeness to equilibrium of the plagioclase and olivine crystals also suggests that, if mixing did occur, the difference in composition of the two mixed magmas was minimal or that only a small volume of mafic magma was involved (e.g., Reubi and Nicholls, 2005).

The co-existence of calcic plagioclase and olivine with limited variation in compositions and the weak oscillatory zoning seen in some of the feldspars could suggest a combination of weak magma mingling and crystal accumulation (e.g., Tepley et al., 1999; Ray et al., 2011). However, the T3 feldspars and the heavily resorbed olivines suggest substantial mixing prior to cooling (Pal et al., 2007; Ray et al., 2011). The olivines likely resorbed during or after mixing if the hybrid magma didn't sit on the olivine saturation surface (e.g., Wyers and Barton, 1986).

The onset of these disequilibrium textures could be due to multiple factors, such as a large oversaturation via addition of volatiles, repeated recharge and mixing processes, decompression, or rapid crystal growth by extreme undercooling, all of which can occur alongside fractional crystallisation (e.g., Reubi and Nicholls, 2005; Shaw and Dingwell, 2008; Ray et al., 2011; Freund et al., 2013; Bellver-Baca et al., 2020). A large oversaturation of volatiles can be ruled out, as although fractional crystallisation at depth can release volatiles, it is less likely in this case given the melts low water concentration (0.43 – 0.71 wt.%) and the failure pf MELTS models ran at higher than 1 wt.% H_2O. Decompression can Finally, magma mixing can be ruled out due to the absence of distinct crystal populations and lack of variation in glass composition for individual samples.

The erupted minerals hosted in the DIP samples are texturally different to other erupted minerals on the island (e.g., Harris, 1983; Chamberlain et al., 2019; Winstanley,

2020) due to the abundance of sieve textures and overgrowths compared to simple, euhedral to subhedral crystals. The DIP deposits were erupted between the Central Felsic Complex and the Eastern Felsic Complex and have likely accumulated crystals from more evolved felsic or plutonic bodies that have sat in evolving magmas and re-equilibrated over a range of time frames. The mafic deposits on the rest of the island have been shown to have risen to the surface with limited evidence for stalling or crystal accumulation (e.g., Harris, 1983; Weaver et al., 1996; Chamberlain et al., 2019; Winstanley, 2020). There are no petrological observations on other trachyandesite composition deposits on the island.

5.6.3 Island model for evolved magma genesis

The magmatic plumbing system model of Chamberlain et al., (2019) requires that antecrysts are incorporated shortly before eruption and during ascent. However, the reaction rim textures in the DIP samples suggest that the antecrysts must have been incorporated within the storage region for long enough periods of time for the formation of new rims in chemical equilibrium with the host magma. The TB and TC olivines are inferred to have accumulated as the magma ascended, but prior to the period of stalling, which allowed for varying degrees of resorption as the magma evolved. The incorporation of these antecrysts, particularly the feldspars, can shift the whole rock composition and is the reason why the composition cannot be remodelled in MELTs. Although not described in the results, rare plutonic lithic clasts were identified within a number of the DIP samples in the field, which agrees with the model in that mafic magmas ascend and then stall and fractionate due to overlying felsic bodies. Therefore, combined with the textural evidence and the more evolved composition, I propose that the T3 feldspar antecrysts were incorporated from the felsic plutonic bodies into a stalled magma undergoing fractional crystallisation (represented in dark purple; Fig. 5.31).

The Ascension model, combined with modelled entrapment pressures from melt inclusions in a zoned fall deposit (Chamberlain et al., 2016) shows that felsic magma evolution occurs at pressures between 200 – 300 MPa (6.8 – 10.2 km depth). Pressures obtained from amphibole barometers also sit within this region and average at 229 MPa which corresponds to a depth of ~7.8 km (assuming a crustal density of 3000 kg m^{-3} (Webster and Rebbert, 2001). However, the addition of entrapment pressures from melt inclusions within the DIP samples will be more beneficial in identifying storage depths.

The DIP magma is compositionally homogenous in terms of major element and trace element compositions, which suggests that there was not an influx of fresh magma into the shallow storage region prior to eruption, and therefore mixing was not an initial eruption trigger. Also, the lack of at least two compositionally distinct crystal phases and glass compositions also suggests that late-stage magma mixing or mingling did not occur and also cannot be the eruptive trigger.

Intermediate magmas are usually not buoyant enough to continue to rise and erupt (Mungall and Martin, 1995), however, alkaline melts are less viscous than tholeiitic melts

(Romano et al., 2003) and therefore, it is possible that the lower viscosity of the melt allowed it to rise to the surface. On the other hand, it is possible that the magma body became a convective, self-mixing layer (Couch et al., 2001; Reubi et al., 2005; Bachmann and Bergantz, 2006) and become buoyant enough to begin to ascend. The lack of macrocrysts within the trachyandesite magma would allow this process to occur much easier. This self-mixing can also explain the occurrence of both resorbed and euhedral phenocrysts and the slight range in crystal composition (e.g., Reubi and Nicholls, 2005). Other studies have shown that a combination of self-mixing and degrees of fractional crystallisation have generated intermediate magma compositions (e.g., Lascar Volcano, Chile (Matthews et al., 1999), Montserrat (Couch et al., 2001), Batur Volcano, Bali (Reubi and Nicholls, 2004; Reubi and Nicholls, 2005), Daisen Volcano, Japan (Tamura et al., 2003)). An increase magma volatile content would be expected if the hot mafic body accumulates at the base and cools. Volatile exsolution during the crystallisation of the lower mafic magma would be transferred to the trachyandesite magma (Reubi and Nicholls, 2005) and could trigger volatile oversaturation and an eruption.

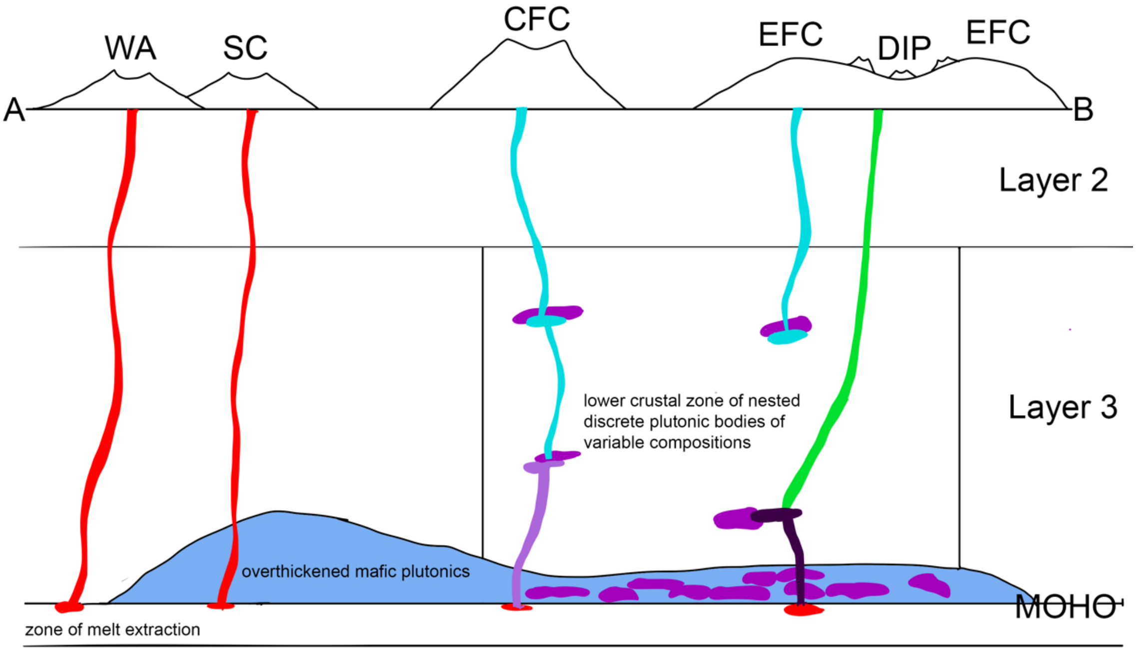

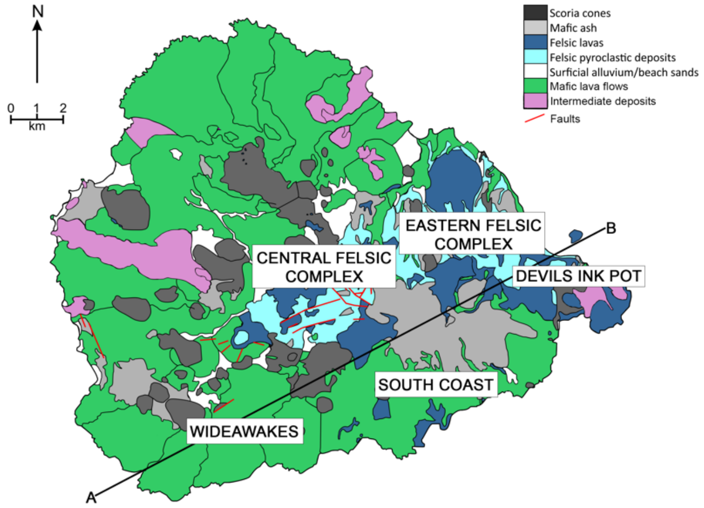

Figure 5.31: *Schematic diagram modified from Chamberlain et al., (2019), showing a cross section through the proposed magmatic plumbing system below Ascension Island. Blue and purple represent felsic magma and the plutonic bodies. Green represents the trachyandesite magma. Map shows the rough location of the cross section.*

The absence of intermediate deposits in many locations is inferred to be related to their inability to erupt (Mungall and Martin, 1995). Therefore, the scarcity of intermediate composition eruptions on Ascension island could be controlled by eruption dynamics, where the rising viscosity and rapid crystallisation through a short temperature range prevents the intermediate magma from rising (e.g., Mungall and Martin, 1995).

Volcanic eruptions have been found to be triggered by regional earthquakes (e.g., Pinatubo **(**Bautista et al., 1996**)** and Puyehue-Cordon Caulle (Lara et al., 2004)**.** Ascension Island is located within 100 km of the Mid-Atlantic Ridge is approximately 50 km from the Ascension Fracture Zone, and so regional earthquakes of magnitude 4 and higher can and have occurred (Manga and Brodsky, 2006; Chamberlain et al., 2016).

The DIP aligns with an older fissure to the north, a trachyte dome to the west and a scoria cone to the east, which suggests there is a fault system that has been reactivated through magma intrusion (e.g., Medynski et al., 2016; Witt et al., 2018). The intrusion of magma altered the compressive and decompressive stresses within the fault system (e.g., Marzochhi et al., 2002; Walter and Amelung, 2006;Gabrieli et al., 2015), causing the reactivation of a dormant system by unclogging the structures. Once these systems evolve to a critical state, any further small stress change can trigger the increase of magma pressure and cause an eruption (e.g., Walter and Amelung, 2006; Walter, 2007). However, on many occasions, earthquakes alone cannot trigger eruptions, instead they initiate other processes such as volatile exsolution (Canon-Tapier, 2014).

Velocity modelling of Ascension Island interpreted a high velocity body beneath the DIP region to be frozen magma storage regions (Evangelidis et al., 2004) however, high velocity bodies beneath rift zones in the Canary Islands have been linked to shallow level dyke intrusions (Krastel and Schmincke, 2002; Evangelidis et al., 2004). Therefore, without further investigation it cannot be completely ruled out that these bodies do not also represent shallow dyke intrusions that have allowed the fault systems to reactivate

If a seismic network was deployed on Ascension Island in the future for the purpose of volcano monitoring the following processes, timescales and features of the DIP magma transport, storage, and plumbing system could be considered**.** The relatively small melt volume and the storage depths of the magma suggests the usual monitoring techniques (e.g., Kilburn and Sammonds, 2005; Biggs and Pritchard 2017; Magee et al. 2018) used to infer the accumulation of an eruptive magma may not be able to identify a small volume accumulation of eruptible melt at depth on Ascension Island (e.g., Chamberlain et al., 2020).

5.7 Conclusions

The DIP trachyandesites are characterised by narrow ranges in plagioclase and olivine compositions that are mostly in chemical equilibrium with the host magma, and groundmass glass that is more evolved than the whole-rock composition, which suggests that the trachyandesites represent a homogenous magma. However, the pyroxenes in the magma are not in equilibrium with the host magma and are more mafic than both the olivine and whole rock composition, suggesting that they did not crystallise in the same magma and therefore must have an antecryst origin. There is limited of evidence for magma mixing (e.g., lack of variation in crystal and glass compositions), however the range in disequilibrium textures in the plagioclase and olivine crystals and the poor-fit of the liquid lines of decent from MELTs modelling (Gualda et al., 2012) shows that simple fractional crystallisation did not occur. Instead, I suggest that either the magma mixed earlier on to create a new hybrid magma, where many of the original crystals were fully or partially resorbed, or that few antecryst feldspar crystals from the felsic plutonic bodies were accumulated into a magma that was undergoing fractional crystallisation and allowed to re-equilibrate during storage, which modified the whole rock composition and lead to further disequilibrium textures in the other crystal phases

Chapter 6: Conclusions

In the following concluding chapter, I outline the principal conclusions of this thesis, outline the implications for volcanic hazards, on Ascension Island and DIP-style eruptions elsewhere, and make a series of recommendations for use of the results of this study and further work.

6.1 Synthesis of the DIP fissure eruption

At the DIP fissure magma rose through the crust as a series of dikes that propagated through faults, before localising as a sheet dikes and migrating vertically up the conduits to the surface, following the reactivation of a pre-existing feeder system on the Letterbox Peninsular. The presence of inactive areas between a number of the cones shows that the magma must have followed pre-existing routes to the surface.

As shown in the magmatic plumbing system of the island (Chamberlain et al., 2019), mafic magma ascended and then stalled, evidenced by the higher crystallinity for the lava and spatter samples, and began to fractionate due to a zone of plutonic bodies at depths of ~ 7.8 km. Antecrysts from these plutonic bodies were incorporated into the evolving DIP magma, which remained within the storage region for a period of time long enough to allow the formation of new rims in chemical equilibrium with the host magma. The incorporation of these crystals shifted the whole rock composition and led to further disequilibrium textures in crystal phases. As the magma ascended towards the surface, crystallisation of the microlites occurred under similar conditions due to degassing driven crystallisation.

The textural similarities between the eruptive products, except for the dense clasts, shows that they shared a similar storage history and therefore the changes in eruptive style, evidenced on the surface must be determined by processes happening in the shallow conduit.

Possible eruption triggers include regional earthquakes (e.g., Lara et al., 2004), a change in buoyancy due to the magma body becoming a self-mixing layer (e.g., Couch et al., 2001; Reubi et al., 2005; Bachmann and Bergantz, 2006) or the alteration of compressive and decompressive stresses within the reactivated fault system triggering the increase of magma pressure (e.g., Walter and Amelung, 2006; Walter, 2007). Phreatomagmatic activity can also not be ruled out for influencing the more explosive eruption styles.

The DIP fissure erupted predominantly as lava fountains with moderate to high intensity, and constructed small spatter cones (type 1), whilst dispersing scoria lapilli and ash away from the vents. Lava flows at 11 of the cones were syn-erupted with the lava fountaining and the complex lava flow fields show multiple lava flows were effusing at the same time. The lava and spatter textures indicate a crystal growth environment and low degrees of under cooling, often identified in lower intensity eruptions, with slightly slower ascent rates (e.g., Clarke et al., 2007; Bain et al., 2019; Preece et al., 2023; Frey et al., 2024).

Two cones (type 2) underwent more explosive activity (Fig. 3.26b), ejected ballistic bombs and lithic clasts and generated higher plumes that deposited pumice and dense clasts up to 600 m from the fissure. The high N_A and low ϕ of the dense tephra samples is indicative of nucleation dominated crystallisation and higher degrees of undercooling, which is more common in higher intensity eruptions with rapid ascent rates (e.g., Cashman and McConnell, 2005; Brugger and Hammer, 2010a; Bain et al., 2019; Preece et al., 2023). The dense clasts represent fragments of either accreted material that built up along the conduit wall, preventing the magma from reaching the surface, or a cooling body of magma that stalled due to a decrease in the magmatic flux. Combined with the distribution of the shallowest old lava lithic clasts, and the two cones being adjacent to each other, the explosive activity is linked to pressure from the ascending magma causing the plugs to break, leading to the shallow widening of the conduit at depths of no more than a few tens of meters (e.g., Reynolds et al., 2016). The lack of other lithic clast types shows that there was little erosion deeper down, therefore the conduit likely narrowed rapidly to a connected dyke at depths more than a few tens of meters.

Nine of the cones (type 3) produced paroxysmal eruptions and ejected ballistic bombs up to 600 m from the fissure. A single paroxysmal eruption through a debris fan generated a small pyroclastic flow that travelled less than 80 m from the vent at cone 1. The textures of the erupted products from these explosions also show many similarities which shows that even though the eruption styles were different (lava fountain vs explosive eruptions) all the events must have been relatively small explosions from low intensity eruptions and that there was little variation in average ascent rates. The differences between effusive and explosive activity can be linked to small changes in ascent rates and possible conduit shape dynamics.

6.2 Evolution of the DIP fissure

1. The DIP eruption was short lived, evidenced by the lack of evidence for a time break, and created a series of low angled (< 5°) cones, with small volume lava flows, scoria-rich and pumice-rich pyroclastic fall and flow deposits and ejected ballistic bombs.
2. The fissure follows a similar trend to another fissure in the area and sits above a trachyte lava flow. Therefore, the reactivation of a feeder system through movement of magma along faults cannot be ruled out.
3. The DIP fissure had three different eruption styles:
    a. Lava fountaining: moderately agglutinated to densely welded spatter deposits, scoria clast-rich fall deposits and lava flows.
    b. Explosive activity: loose to weakly agglutinated lapilli and bomb clasts, ballistic bombs, lithic clast rich talus slopes and pumice and lithic clast rich fall deposits.

    c. Paroxysmal explosions followed by lava fountaining events: deep rooted cones exposing up to 40 m of underlying country rock, ballistic bombs, moderately agglutinated to densely welded spatter deposits and in some places, small volume lava flows.

4. The fissure eruption shared similarities with basaltic fissure eruptions (e.g., spatter deposits, lava flows with low viscosity lava, and scoria-rich proximal tephra fall deposits, but had a smaller minimum total erupted volumes compared to other basaltic fissure eruptions (e.g., Iceland, Hawaii, Sicily).
5. The explosive activity is not as common in basaltic fissure eruptions and demonstrated that multiple, contrasting eruption styles could occur at a single time in close proximity.
6. The explosive activity is linked to sub-surface cooling and degassing-driven crystallisation of a magma body due to decreases in the local magmatic flux resulting in the formation of a dense plug.
7. Although minimal evidence, the increasing percentage of lithic clasts in the distal fall deposits means that water-magma interaction cannot be ruled out. However, if water content was the main cause of explosive variation, then there would be no differences in the groundmass of the DIP samples, but differences in the groundmass textures are present (e.g., Szramek et al., 2006).
8. Evidence for the dense plug can also be seen in the systematic variation and distribution of the different types of ballistic bombs clasts on both sections of the fissure. Each type of ballistic bomb represents region of a plug of semi-solidified magma within the conduit.
9. The range of eruption styles span those of basaltic and silicic eruptions and so present a wider range of volcanic hazards.

6.3 Influences on eruption style

1. The bulk eruptive products have the same composition and therefore had shared storage conditions, so the variation in eruptive styles must have been controlled by shallow magma system processes.
2. The similarity in An content and temperature show that the feldspar microlites crystallised at the same time under similar conditions due to degassing-driven crystallisation either on ascent or in the deep magma storage region.
3. The similarities in the textures of the spatter, lava, scoria, and pumice clasts show that even though the eruption styles varied from lava fountaining to more explosive explosions, all the events were on a relatively small-scale from low intensity eruptions.

4. The textures of the dense clasts favoured nucleation dominated conditions, high degrees of undercooling during faster ascent rates and degassing, leading to a high intensity eruption.

5. The higher intensity eruptions are related to erosion and shallow widening of the conduit. Accretion of material along the conduit walls formed small plugs which were destroyed as the pressure from the rising magma built up.
6. The textures of the spatter, lava, scoria, and dense clasts favoured growth dominated conditions, lower degrees of undercooling due to slower ascent rates, leading to low intensity eruptions.
7. Amphibole breakdown rims in the spatter and lava samples show that the ascent rates were slower, compared to the tephra samples in which breakdown rims were not observed.
8. The minimal differences in the textures and compositions of the DIP samples, shows that there was little variation in average ascent rates, however the differences between the effusive and explosive activity have been linked to very small changes in ascent rates.

6.4 Intermediate magma genesis:

1. MELTS modelling alone was unable to reproduce the intermediate compositions of the DIP and the more evolved compositions on the island.
2. The higher concentration of CaO, Na_2O and Al_2O_3 phases in the magma of the DIP samples compared to the modelled MELTs trends, may have resulted from the accumulation of feldspar antecrysts. However, simple accumulation calculations showed that the accumulation of more than 50% feldspars would be needed to acquire the DIP composition from basaltic Ascension Island magma. Therefore, accumulation of feldspars alone also cannot reproduce the observed composition.
3. Most of the feldspar (Type 1, 2 and 3) and olivine (Type A, B, C) crystals exhibit obvious signs of disequilibrium, but the compositions of the majority of the crystals are in apparent chemical equilibrium. However, the compositional relationships of the Type 3 crystals, where the resorbed inner rim is more calcic than the core and less calcic than the outer rim, shows that these crystals formed from the transformation of sodic to calcic plagioclase; a process that can solely represent the accumulation of more sodic feldspar into a less evolved magma.
4. The reaction rim textures in the DIP samples, particularly the T3 feldspars, show that the antecrysts have been incorporated within the storage region for a period long enough for the formation of new rims in chemical equilibrium with the host magma. The TB and TC olivines accumulated as the magma ascended, but prior to the period of stalling, and resorbed as the magma evolved. The incorporation of these antecrysts, particularly the feldspars, shifted the whole rock composition and is the reason why the composition cannot be remodelled in MELTs.
5. The T3 feldspar antecrysts were incorporated from more evolved felsic or plutonic bodies into a stalled magma body, at ~7 km depth, undergoing fractional crystallisation.

6. There are few examples where intermediate composition eruptions are studied. Island-wide studies can show closed system fractionation trends (e.g., Sete Cidades (Beier et al., 2006)), but detailed studies reveal that intermediate compositions do not always fit within the trends. This suggests intermediate magmas may commonly form through multiple processes (e.g., Legendre et al., 2005; Lanzafame et al., 2021).

6.5 Implications

The data presented in this thesis uses a detailed characterisation of the DIP eruptive products to provide interpretations of magma genesis, storage, and pathways, and ultimately to reconstruct the eruption. These insights can be used to interpret volcanic unrest if volcano monitoring, e.g., ground deformation and seismicity (Sigmundsson et al., 2022) is in place and form an eruptive scenario for Ascension Island. A hazard analysis has not been conducted as part of this study, but the data could be used to provide input parameters for modelling that could then be incorporated into volcanic hazard assessments. There are several specific findings that are significant for planning and preparation for the potential impacts of future volcanic eruptions on Ascension Island:

1. Understanding seismic unrest is important to provide insights to magma movement that may precede an eruption. Previous studies have suggested that it may be difficult to detect eruptible magma unless there is a dense seismic network installed. The combination of mid-crustal storage depth, variations in ascent rates and relatively low melt volume from the DIP fissure provide evidence that may support the interpretation of seismic signals if a seismic monitoring network is installed on Ascension Island in the future.
2. Eruptive styles associated with fissure eruptions are strongly influenced by magma ascent rates (Wilson and Head, 1981; Parfitt, 2004; Valentine and Gregg, 2008; Kósik et al., 2016) and the availability of external water (Németh and Cronin, 2011; Kósik et al., 2016). Rapid ascent rates mean little warning may be given due to rapid magma transport from the deep magma storage site (e.g., Chamberlain et al., 2020) to the point of eruption. In the absence of a seismic monitoring network, it may not be possible to detect volcanic unrest on Ascension Island. The change in eruption styles for the DIP fissure is influenced by changing ascent rates, therefore it is crucial to be able to monitor magma movement through seismic networks and ground deformation.
3. Slight variations in ascent rates, such as those that occurred during the DIP eruption, can be difficult to forecast (e.g., Cassidy et al., 2018). Even if a seismic monitoring network is in place there may be only subtle changes in monitoring parameters once an eruption is underway. Therefore, consideration of the change in volcanic hazards, for example transitions between more effusive eruptions with lava fountain and lava flows to more explosive eruptions with tephra fall deposits, weak pyroclastic flow deposits and

the ejection of ballistic bombs up to 15 m in diameter, during an eruption needs to be adding into plans for future volcanic activity on the island.

4. The DIP fissure had both effusive and explosive phases of the eruption, which resulted in a wide range of hazards, including lava flows, ballistic bomb ejecta, tephra fall, PDC's, and would likely to have been accompanied by gas and aerosol emissions. The DIP eruption could be viewed as bridging those eruptive styles typical of both basaltic and silicic eruptions and an eruption scenario based on the DIP would as a result include this range of hazards. This may make it more difficult to plan for such an eruption given the spread of eruptive vents across Ascension Island and potential for a future eruption to occur anywhere on the island.
5. The DIP eruption is a good example of shifts in eruptive activity over a short time scale. This leads to challenges in understanding the eruption from a hazard perspective. Whilst the eruption may not be long-lived, the volcanic hazards produced would have a range of impacts that may need to be considered in planning for future potential eruption scenarios on Ascension Island. Intermediate composition fissure eruptions are rarely seen or described and therefore are most likely underrepresented in the geological record for hazard assessment.
6. The abundance of ballistic clasts and lithic clasts around the cones and the tephra deposits are poorly sorted and lithic clast rich, which may indicate brief phases of limited magma-water interaction. The possible reactivation of the DIP fissure along a fault line shows that the interaction between water and magma along the fault cannot be ruled out. Phreatomagmatic activity can result in lofting of fine volcanic ash that has local impacts. The lack of preservation of fine ash in the geological record means that phreatomagmatic explosions on Ascension Island are underrepresented, and risk is potentially underestimated.
7. The definition of thresholds that anticipate the transitions between effusive and explosive eruptions is vital for improved volcano hazard assessment (Lindoo et al., 2017). For future hazard assessment the types and likelihoods of the eruption styles and hazards, including impact areas and hazard zones should be considered in order to plan effective emergency response measures and long-term plans.
8. The DIP fissure is located on a topographic high and sits on top of an older trachyte lava flow. An older fissure runs parallel to the DIP fissure, whilst an old basaltic scoria cone and trachyte dome are aligned with the DIP fissure. This shows that there is likely an established feeder system that could be reactivated under certain conditions and therefore the possibility of another eruption in this location cannot be ruled out.

6.6 Recommendations

Understanding the style, duration, magnitude and likely impacts from past eruptions provides evidence for potential hazards and impacts that may need to be considered in the event of a future eruption. Ascension Island is in an isolated location and doesn't have self-evacuation options so planning for eruption scenarios is important to reduce the risk of potential loses. Whilst the DIP eruption occurred in an unpopulated part of Ascension Island, there are volcanic vents distributed across the island and it may be possible for such an eruptive scenario to occur elsewhere onshore. The DIP eruption is a good example of shifts in eruptive activity over a short time scale, which leads to challenges in understanding the eruption from a hazard perspective. Whilst the eruption may not be long-lived, hazard footprints of the DIP eruption that can be considered for an eruption of a similar style and magnitude include:

- Fissure length ~ 1.3 km.
- Fire fountains (heights unknown, but at least 60 m based on cone depths).
- Ash dispersal to 1.5 km depending on meteorological conditions.
- Ash fall thicknesses likely to range from ~ 10 to 200 cm depending on eruption duration.
- Ballistics projecting up to 0.6 km from the axis of the eruptive fissure.
- Lava flow length up to 0.63 km (dependent on local topography for an 8.9×10^{-5} m^3 eruption volume).
- PDCs up to 0.08 km from the fissure.
- Ash sizes ranging from 64 mm (-6 φ) to 32 μm (5 φ).

If such an eruptive scenario occurred offshore the eruptive hazards may differ. Offshore eruptions are likely as only a small part of the volcanic edifice is subaerial.

I propose that detailed petrological studies are an underutilised tool in volcanic hazard assessment and emergency response and may be able to provide more of an insight into the magmatic processes and the initiation of eruptions (Re et al., 2021). Syn-eruptive petrological work demonstrated that documenting changes in the magma during ongoing eruptions is key (e.g., Pankhurst et al., 2022; Corsaro and Miraglia, 2022; Frey et al., 2023). Although the hazards associated with basaltic eruptions are well understood, the fact that the intermediate composition eruption of the DIP can present like a basaltic eruption yet project large ballistics in hazardous explosive phases highlights the need for rapid geochemical and petrological response protocols to be established within the volcanic hazard assessment (e.g., Re et al., 2021; Pankhurst et al., 2022). By knowing the initial composition of the erupting magma, the possible eruption styles and associated hazards can be identified. Using petrology and geochemistry as part of a rapid response toolkit can provide interpretations of the processes driving the eruption and the physical behaviour of the erupted products (Re et al., 2021; Pankhurst et al., 2022). It is also important in volcanic centres where there is no eruptive record, as the current eruptive products can be compared to historical eruptive products (Pankhurst et al., 2022).

Other eruptive scenarios on Ascension Island may differ from the DIP eruption (e.g., Chamberlain et al., 2016; Chamberlain et al., 2020; Winstanley, 2020; Preece et al.., 2021;

Davies et al., 2021). An eruptive scenario from the most recent eruptive centre, Sister's Peak, has been the focus of discussions with the Ascension Island Government (Vye-Brown et al. 2019). The cumulative result of this study leads me to suggest that although the DIP fissure eruption is different to other eruptions on the island, the range of hazards are similar. Therefore, if the possibility of short-term shifts in eruption styles with explosive phases lofting significant amounts of tephra are incorporated into planning for the Sister's eruption scenario, then response to an eruption similar to the DIP eruption will be covered.

6.7 Further work

As a result of my work, I have identified a number of areas that would benefit from further work, including the following.

6.7.1 Ascent rates

Textural studies can provide useful quantitative data to understand magmatic system processes and can be interlinked with direct observations and/or seismic data. However, textural studies are reliant on decompression experiments to establish crystal growth rates, residence times and ascent rates. Without decompression experiments on similar magmatic compositions, it is not possible to accurately quantify ascent rates, growth rates and nucleation rates. Decompression experiments on feldspar microlites (e.g., Szramek et al., 2006) from Ascension Island samples would provide vital data on magmatic processes on Ascension Island, as well as other similar volcanic systems.

Decompression on amphibole crystals would provide information on processes and depths of rim breakdown, and ascent rates (e.g., Szramek et al., 2006; Preece et al., 2023). Heating experiments have found clinopyroxene crystals in the rims (e.g., De Angelis et al., 2015) whilst decompression experiments produce orthopyroxene in the rims (Rutherford and Hill, 1993; Browne and Gardener, 2006).

Increasing the number of feldspar microlites studied in the deposits would identify whether there is a greater range in the An contents or the different textures. This would allow a greater understanding as to where the microlites formed and whether there were further variations in ascent rates, but also identify as the role of magma mixing. An contents can be used to calculate water concentrations and temperatures to make links between them in response to decompression processes (e.g., Bain et al., 2019).

Temperature data from feldspar microlites and CO_2 volatiles (obtained through melt inclusion studies) pressure estimates could be converted into depths of microlite formation.

Further textural work could also include:

- A study into the ballistic bomb types, to provide more detailed insights into the upper conduit processes and plug emplacement and to identify further differences or similarities between the explosive and effusive eruption styles (e.g., Bain et al., 2019).

- Vesicle size distributions and vesicle number density studies to link vesicle size and shape to ascent rates.

6.7.2 Intermediate Magma Genesis

To further understand the genesis of intermediate magma on Ascension a few recommendations are suggested:

1. To support the hypothesis that the crystals have been accumulated, I suggest expanding the datasets and collecting more chemical analyses of the different phases, in particular feldspar and olivine, to identify variations in the source magma. Trace element data could identify key processes during magma evolution.
2. The accumulated crystals are considered to be related to the felsic plutonic bodies that block ascending magma and allow them to evolve. Therefore, plutonic inclusions within the DIP deposits or in surrounding deposits, should be studied to identify any differences or similarities in crystal textures and chemical composition compared to the DIP xenocrysts.
3. Sr isotopes and O isotopes ($\delta^{18}O$) provide insights into the evolutionary processes by identifying whether the system was open or closed and could be considered in both plagioclase crystal phases and in the whole rock samples (e.g., Troll, 2002; Bellver-Baca et al., 2020). By combining the whole rock isotope data and trace element data, a multi-modelling approach, following the methods of Bellver-Baca et al., (2020) could identify whether RFC (recharge and fractional crystallisation), AFC (assimilation and fractional crystallisation), or EC-RAFC (energy constrained recharge, assimilation, and fractional crystallisation) (DePaolo, 1981; Bohrson and Spera, 2007; Freund et al., 2013; Bellver-Baca et al., 2020) had an effects on the evolution of the DIP magma.
4. Complete a similar geochemical and textural study on the deposits of other intermediate composition eruptions on the island, focusing on another eruption within the Eastern Felsic Complex and comparing it to an eruption on the north-west coast, where most eruptions have produced basaltic scoria cones and lava flows. This would improve understanding of whether the eruption location affects intermediate magma genesis.

Very few studies, especially those on ocean islands, focus purely on intermediate deposits, however a single study on Hawaii (Gansecki et al., 2019) has also shown that multiple processes can lead to intermediate magma genesis, and therefore this may be more common than once thought as not many studies. Comparative studies on islands elsewhere would help explore intermediate magma genesis on ocean island volcanoes.

This could also be done by combining MELTs modelling to look for liquid lines of descent but also through petrological and geochemical analysis, for example looking at crystal phases, their textures and their chemistry and whole rock chemistry of associated deposits.

6.7.3 Melt Inclusions

A NERC grant to study melt inclusions (MI) was awarded for the study. However due to COVID and multiple factors beyond our control, the data collection has yet to be done. The MI study will analyse volatile (H, C, F, Cl) and light lithophile trace elements (LLE: Li, Be, B) in melt inclusions and groundmass glass from the DIP and provide insights into intermediate magma genesis and the impact of degassing on eruption style. The MI compositions will be used to test the hypothesis that intermediate magmas stall in the lower crust, by calculating pressures, temperatures, and water concentrations. Combining the melt inclusion data with field and textural data, will provide further insight into how ascent affects the variability of eruption styles in a small-scale eruption and the shallow conduit region.

6.7.4 Sub-surface structures

Very little work has been done on understanding the sub-surface geometry of Ascension Island. To fully understand the links between different eruption sites further work must be completed on understanding the conduit dynamics. One way to do this could be through modelling. There are many models such as the 1D steady state model (La Spina et al., 2015), which assumes a cylindrical conduit (La Spina et al., 2019). Fissure eruptions are assumed to have more complicated plumbing systems, however past studies have used the 1D steady state model to analyse the upper 500 m of the conduit (e.g., La Spina et al., 2019). Another model to consider would be one that considers unsteady flows (e.g., Melnick and Sparks, 2002; Mason et al., 2006), due to the reasoning that initial explosive eruptions undergo more rapid decompression and fragmentation (Mason et al., 2006). The additional textural work suggested, with the addition of vesicle studies (e.g., Lautze and Houghton, 2005; Moitra et al., 2013; Pioli et al., 2017) will also help to further understand the processes that are occurring in the shallow conduit region.

Appendices 1 – Sample Log

WR – whole rock data, G – glass data, Xtl – EPMA crystal data, Pet – petrography, CSD – crystal size distribution data.

Sample No.	Locality	Grid Reference		Description	WR	G	Xtl	Pet	CSD
AI-19-007	LB4	575924	9121450	Glassy blebs in Unit 10 spatter from Crater 1a					
AI-19-008	LB4	575924	9121450	Spatter from Crater 1	X		X	X	X
AI-19-009	LB7	575933	9121600	Lithic inclusions in bomb 2 from Crater 1					
AI-19-010	LB7	575933	9121600	Glassy inclusion in bomb 2 and contact with the vein and spatter					
AI-19-011	LB7	575933	9121600	Glassy clasts in bomb 2 from Crater 1					
AI-19-012	LB7	575933	9121600	Margin to interior of bomb 2 from Crater 1					
AI-19-013	LB8	575651	9121124	Lava sample from the flow on letterbox peninsula.	X				
AI-19-018	LB4	575924	9121450	Glassy block from base of crater 1a					
AI-19-019	LB4	575924	9121450	Plutonic inclusion					
AI-19-020	LB4	575924	9121450	Plutonic inclusion within lava block					
AI-19-021	LB4	575924	9121450	Large crystal from a bomb on the crater 1 ridge					
AI-19-022	LB4	575924	9121450	Banded rhyolite with transition to glass					
AI-19-023 *CVYE-018*	LB13	576473	9121154	Block of lava/spatter from the mound on the dome					
AI-19-024 *CVYE-019*	LB14	576458	9121197	Block of lava/spatter from the top of the ridge close to dome	X				
AI-19-025 *CVYE-020*	WP 32	576427	9121266	Lava from base of the ridge	X			X	
AI-19-026 *CVYE-021*	WP 33	576508	9121239	Lava from the spiny black lava flow	X		X	X	X
AI-19-027 *CVYE-022*	WP 38	576661	9120943	Lava from the lava levee				X	

AI-19-028 *CVYE-023*	LB 16	576513	9121149	Lava block from base of delta	X		X	X	X
AI-19-029	LB17	576631	9120939	Lava block from top of delta	X				
AI-19-030 *CVYE-024*	WP 40	576761	9120979	Lava block from the flow off the sea cliffs on the peninsula	X			X	
AI-19-031 *CVYE-025*	WP 41	577614	9121243	Block of lava from the central lava on letterbox (marked on map)	X				
AI-19-032	LB 18	576472	9121029	Block of the oldest lava flow on the base	X			X	
AI-19-033 *CVYE-026*	WP 42	577099	9121272	Block of lava from the furthest flow on the peninsula	X				
AI-19-034	LB 22	577037	9121332	Lava samples from within the crater 18	X		X	X	
AI-19-039 BECCA	LB24	576563	9121982	Lava sample from the end of the flow lower lava	X			X	
AI-19-040	LB34	576329	9121823	Lower lava from C6					
AI-19-042	LB35	576043	9121491	Stretched glass (two bags)				X	
AI-19-043	LB35	576043	9121491	host lava with glassy strands					
AI-19-044	LB35	576043	9121491	host lava with glassy strands					
AI-19-045	LB35	576043	9121491	host lava with glassy strands					
AI-19-046	LB35	576043	9121491	Lava sample from the C2 flow	X			X	
AI-19-047	LB36	576167	9121549	Grey, xtl rich lithic clast				X	
AI-19-048	LB37	576167	9121549	Grey, xtl rich lithic clast					
AI-19-049	LB38	576218	9121561	Lava samples with large xtls	X			X	
AI-19-050	LB39	576411	9121515	Pink xtl rich lithic clasts - mafic blob?					
AI-19-051	LB39	576411	9121515	Grey med xtls lithic clast					
AI-19-052	LB85	576392	9121734	Pink/brown lava on path between turning circle and peninsula.				X	
AI-19-053	LB85	576392	9121734	Lava block with large crystal found on the track at entrance to DIP					

AI-19-054	LB41	576067	9121672	Lava block with large crystal					
AI-19-066	LB43	576757	9121450	Lithics from Crater 13				X	
AI-19-067	LB44	576786	9121442	Lithics from Crater 14					
AI-19-070	LB85	576392	9121734	Trachyte inlcusion in juvenille material on pre-peninsula path					
AI-19-071	LB22	577037	9121332	large xtl in juvenille material	X			X	
AI-19-072	LB22	577037	9121332	A) country rock with inlcusions, B) country rock with fresh face				X	
AI-19-073	LB85	576392	9121734	XTL rich inlusion from peninsula path					
AI-19-074	LB49	575955	9121622	Unit 1 tephra A-C					
AI-19-075	LB49	575955	9121622	Unit 2 tephra A-D					
AI-19-076	LB49	575955	9121622	Unit 3 - tephra A-D	X	X	X	X	
AI-19-077	LB49	575955	9121622	Unit 4 - tephra A-D	X	X	X	X	X
AI-19-078	LB49	575955	9121622	Unit 5 - tephra A-E					
AI-19-079	LB42	576742	9121424	Juvenille with large xtl from top of C11					
AI-19-075	LB50	576684	9121536	Spatter bomb from Unit 2					
AI-19-077	LB50	576684	9121536	Unit 1 maximum clasts					
AI-19-078	LB50	576684	9121536	Unit 3a tephra A-C					
AI-19-079	LB50	576684	9121536	Unit 3b tephra A-C					
AI-19-081	LB51	576075	9121708	Unit 3 tephra A-D					
AI-19-082	LB51	576075	9121708	Unit 2 tephra A-D					
AI-19-083	LB51	576075	9121708	Unit 1 tephra A-D					
AI-19-084	LB52	575949	9121867	Unit 1 tephra A-F					
AI-19-085	LB53	576044	9121813	Unit 1 tephra A-D					

AI-19-086	LB53	576044	9121813	Unit 2 tephra A-B					
AI-19-087	LB53	576044	9121813	Unit 3 tephra A-B					
AI-19-088	LB54	575898	9122098	Unit 1 tephra A-C					
AI-19-089	LB54	575898	9122098	Unit 2 tephra A-B					
AI-19-090	LB54	575898	9122098	Unit 3 tephra A-B					
AI-19-091	LB55	575899	9122090	Bomb from Unit 2					
AI-19-092	LB55	575899	9122090	Unit 3 tephra A-C					
AI-19-093	LB55	575899	9122090	Unit 2 tephra A-C					
AI-19-094	LB55	575899	9122090	Unit 1 tephra unsieved					
AI-19-095	LB56	575877	9121988	Unit 1 tephra unsieved					
AI-19-096	LB57	569670	9122914	Glassy bomb					
AI-19-097	LB5	575953	9121520	Juvenile material with glass patches					
AI-19-098	LB58	576011	9121487	Spatter with big black xtl (LF2)					
AI-19-099	LB58	576011	9121487	Bag of scoria from LF3 C3					
AI-19-100	LB58	576011	9121487	Vesicular rich core from a bomb					
AI-19-101	LB58	576011	9121487	Glassy rind trachyte bomb					
AI-19-102	LB58	576011	9121487	Thick glassy rind trachyte bomb					
AI-19-103	LB58	576011	9121487	Yellow trachyte substrate				X	
AI-19-104	LB58	576011	9121487	Vesicular, low density brittle looking clasts					
AI-19-105	LB58	576011	9121487	Lithics from Crater 3					
AI-19-106	LB58	576011	9121487	Dense core and agglutinated spatter from C3	X			X	
A-19-119	LB69	576339	9121425	Trachyte and mafic blebs in C8				X	
AI-19-120	LB69	576339	9121425	Tephra off crater 8 floor					

AI-19-121	LB69	576339	9121425	Dense spatter from Crater 8	X		X	X	X
AI-19-122	LB69	576339	9121425	Vesicular spatter from Crater 8					
AI-19-123	LB69	576339	9121425	Vesicular spatter from Crater 8					
AI-19-124	LB69	576339	9121425	Black, needle-like coating on spatter				X	
AI-19-125	LB70	576354	9121403	Lava block from top of spiny flow	X				
AI-19-126	LB71	576303	9121407	Lava block from top of crater 7 flow	X			X	
AI-19-127	LB72	575980	9121531	Crater 7 spatter	X		X	X	
AI-19-128	LB72	575980	9121531	Blue/grey lithic clast					
AI-19-129	LB72	575980	9121531	LF4 spatter from crater 7					
AI-19-130	LB72	575980	9121531	2 samples, have large xtls from bombs					
AI-19-131	LB72	575980	9121531	Inclusions on the spatter					
AI-19-132	LB75	576266	9121474	Red clasts from Crater 7					
AI-19-133	LB79	576156	9121512	2 samples, have large xtls from bombs					
AI-19-134	LB80	576086	9121518	Dense spatter from Crater 4	X			X	
AI-19-140	Transect 7B	576079	9121537	Bomb sample					
AI-19-141	Transect 7D (2)	576100	9121576	Bomb Sample with lithic inclusion					
AI-19-142	Transect 7D (2)	576100	9121576	Bomb Sample fresh					
AI-19-143	Transect 7D	576100	9121576	Bomb Sample					
AI-19-144	Transect 7E	576119	9121597	Bomb sample					
AI-19-145	LB79	576156	9121512	LF1 spatter from crater 5	X			X	
AI-19-146	LB79	576156	9121512	Layer 1 in the squeeze out					
AI-19-147	LB79	576156	9121512	Ripple marks on the squeeze out					
AI-19-148	LB79	576156	9121512	Layer 3 in the squeeze out	X			X	

AI-19-149	LB79	576156	9121512	LF1 spatter from crater 5 with large xtl					
AI-19-150	LB79	576156	9121512	Sample of the bomb in crater 5					
AI-19-151	LB82	576134	9121473	Speckled lithic clast				X	
AI-19-152	Transect 9	576228	9121500	Tephra off the floor near crater 7					
AI-19-153	LB83	576368	9121502	Tephra sample off floor near crater 8					
AI-19-154	LB63	576477	9121474	Crater 10 spatter	X			X	
AI-19-155	LB67	576617	9121438	Crater 11 spatter	X			X	
AI-19-156	LB68	576635	9121434	Crater 12 spatter	X			X	
AI-19-157	LB86	577041	9121361	Crater 17 spatter	X			X	
AI-19-158	LB88	576972	9121339	Plutonic inclusion from a bomb					
AI-19-159	LB91	576901	9121400	Crater 15 spatter	X			X	
AI-19-160	Transect 4B	576998	9121419	Lithic inclusion from a bomb on the peninsula					
AI-19-161	LB95	576958	9121482	Upper lava flow on peninsula	X			X	
AI-19-162	LB101	575995	9121929	Green lithic clast					
AI-19-163	LB102	575917	9121475	Inclusion clast from the beast bomb					
AI-19-164	LB103	577062	9120931	Mafic blebs on peninsula (SE) red bleb					
AI-19-165	LB103	577062	9120931	mafic blebs on peninsula (SE) black bleb					
AI-19-166	LB104	577184	9121097	Trachyte country rock					
AI-19-168	LB105	575200	9121140	Country rock from White Horse					
AI-19-169	Wig Hill 4	576079	9121057	Trachyte cauliflower bomb					
AI-19-170	Wig Hill	575960	9121229	Wig Hill scoria					
AI-19-171	LB107 (Crater 2)	575979	91212531	Banded lithic clasts				X	

AI-19-172	LB101	575995	9121929	Unit 6 tephra bag unsieved					
AI-19-173	LB101	575995	9121929	Unit 5 tephra bag unsieved					
AI-19-174	LB101	575995	9121929	Unit 4 tephra bag unsieved					
AI-19-175	LB101	575995	9121929	Unit 3 tephra A-D				X	
AI-19-176	LB101	575995	9121929	Unit 2 tephra bag unsieved					
AI-19-177	LB101	575995	9121929	Unit 1 tephra A-D	X	X	X	X	X
AI-19-178	LB100	576116	9121831	Unit 5 tephra bag unsieved					
AI-19-179	LB100	576116	9121831	Unit 4 tephra bag unsieved	X	X	X	X	X
AI-19-180	LB100	576116	9121831	Unit 3 tephra bag unsieved					
AI-19-181	LB100	576116	9121831	Unit 2 tephra bag unsieved					
AI-19-182	LB100	576116	9121831	Unit 1 tephra A-D					
AI-19-183	LB99	576111	9122105	Unit 2 tephra unsieved					
AI-19-184	LB99	576111	9122105	Unit 1 tephra A-C				X	
AI-19-185	LB99	576111	9122105	5% samples that need to be weighed					
AI-19-186	LB98	576108	9122108	Whole bag of tephra unsieved					

Appendices 2 – EPMA Data

2.1 Feldspar EPMA

C – core (Type 2), R – rim (Type 2), R-C – resorbed core (Type 1), R-R – resorbed rim (Type 1), RR – reaction rim (Type 3 (T3)), GM – groundmass, LB – normal lava bands, TB – transitional lava, DB – dark lava bands.

Sample	Type	DataSet/ Point	SiO_2	TiO_2	Al_2O_3	FeO	MnO	MgO	CaO	Na_2O	K_2O	SrO	Total
AI-19-034	C	8 / 1 .	57.92	0.06	26.38	0.40	0.01	0.05	8.81	6.48	0.36	0.11	100.58
AI-19-034	C	9 / 1 .	56.70	0.05	26.71	0.43	0.00	0.05	9.39	6.16	0.35	0.11	99.94
AI-19-008	C	1 / 1 .	57.24	0.05	27.27	0.42	0.01	0.05	9.56	5.96	0.35	0.10	101.01
AI-19-008	C	2 / 1 .	57.00	0.05	27.17	0.41	0.01	0.05	9.35	6.04	0.36	0.11	100.54
AI-19-008	C	3 / 1 .	56.73	0.05	27.29	0.42	0.00	0.05	9.51	6.21	0.34	0.11	100.71
AI-19-008	C	12 / 1 .	58.89	0.04	25.63	0.32	0.00	0.03	8.06	6.75	0.43	0.12	100.26
AI-19-008	C	13 / 1 .	58.04	0.05	25.76	0.30	-0.01	0.03	8.00	6.84	0.43	0.12	99.55
AI-19-008	C	14 / 1 .	58.96	0.05	25.51	0.30	0.00	0.03	8.07	6.90	0.43	0.12	100.36
AI-19-008	C	30 / 1 .	58.68	0.04	24.92	0.39	0.01	0.04	7.74	6.93	0.47	0.11	99.32
AI-19-008	C	31 / 1 .	58.61	0.04	25.34	0.38	0.00	0.04	7.81	6.87	0.47	0.13	99.68
AI-19-008	C	32 / 1 .	57.78	0.06	25.57	0.45	0.00	0.05	8.32	6.49	0.40	0.12	99.23
AI-19-121	C	1	55.50	0.06	27.60	0.41	0.01	0.04	9.95	5.99	0.31	0.33	100.21
AI-19-121	C	2	57.56	0.06	26.34	0.37	0.01	0.04	8.47	6.67	0.41	0.05	99.53
AI-19-121	C	3	55.94	0.06	27.29	0.40	0.00	0.02	9.57	6.06	0.30	0.15	99.33
AI-19-121	C	4	56.67	0.06	26.91	0.38	-0.01	0.06	8.98	6.26	0.37	0.12	100.24
AI-19-121	C	5	56.77	0.04	26.81	0.35	0.01	0.03	8.88	6.36	0.36	0.19	99.88
DIP-3	C	11 / 1 .	55.12	0.06	26.77	0.43	0.00	0.05	9.67	5.94	0.32	0.11	98.47
DIP-3	C	12 / 1 .	55.38	0.06	26.80	0.43	0.00	0.05	9.55	6.10	0.32	0.10	98.79
DIP-3	C	16 / 1 .	55.93	0.04	26.10	0.40	0.00	0.04	8.77	6.27	0.38	0.10	98.05
DIP-3	C	17 / 1 .	56.69	0.05	26.01	0.42	-0.01	0.04	8.71	6.43	0.38	0.10	98.83
DIP-3	C	27 / 1 .	57.89	0.03	25.30	0.37	0.01	0.04	8.03	6.83	0.42	0.11	99.02
DIP-3	C	28 / 1 .	56.87	0.04	26.30	0.40	0.01	0.05	8.74	6.37	0.37	0.12	99.26
DIP-3	C	35 / 1 .	57.58	0.05	25.69	0.38	0.00	0.04	8.19	6.74	0.45	0.12	99.22
DIP-3	C	36 / 1 .	57.56	0.05	25.01	0.39	0.01	0.05	7.74	6.85	0.48	0.13	98.26
DIP-3	C	37 / 1 .	56.80	0.11	25.99	0.80	0.02	0.16	8.75	6.43	0.59	0.10	99.75

DIP-6	C	3 / 1 .	57.88	0.07	26.32	0.55	0.01	0.06	8.42	6.60	0.42	0.12	100.45
DIP-6	C	4 / 1 .	57.93	0.08	26.44	0.57	0.01	0.06	8.36	6.66	0.44	0.13	100.68
DIP-6	C	12 / 1 .	59.47	0.03	25.35	0.39	0.01	0.04	7.37	7.25	0.48	0.09	100.48
DIP-6	C	13 / 1 .	57.73	0.04	26.37	0.39	0.00	0.04	8.55	6.78	0.38	0.09	100.37
DIP-6	C	27 / 1 .	57.64	0.06	25.58	0.59	0.00	0.05	8.19	6.60	0.42	0.14	99.27
DIP-6	C	28 / 1 .	58.14	0.07	25.91	0.58	0.01	0.06	7.95	6.79	0.46	0.14	100.11
DIP-6	C	42 / 1 .	57.36	0.04	26.53	0.40	0.01	0.04	8.80	6.53	0.35	0.11	100.17
DIP-6	C	43 / 1 .	56.81	0.03	26.43	0.38	0.01	0.04	9.05	6.50	0.34	0.10	99.70
DIP-6	C	50 / 1 .	56.31	0.05	26.68	0.42	0.01	0.05	9.34	6.23	0.33	0.10	99.53
DIP-6	C	51 / 1 .	56.09	0.06	27.14	0.44	0.00	0.05	9.53	6.13	0.33	0.11	99.87
DIP-8	C	13 / 1 .	57.06	0.06	26.14	0.38	0.00	0.04	8.69	6.39	0.35	0.15	99.26
DIP-8	C	14 / 1 .	56.84	0.05	26.32	0.39	0.00	0.05	8.87	6.17	0.33	0.16	99.18
DIP-8	C	15 / 1 .	57.29	0.05	26.49	0.40	0.00	0.04	8.97	6.28	0.33	0.16	100.01
DIP-8	C	19 / 1 .	58.52	0.03	24.80	0.33	0.01	0.03	7.61	6.92	0.52	0.10	98.87
DIP-8	C	20 / 1 .	58.89	0.04	25.31	0.36	0.00	0.03	7.59	6.99	0.51	0.11	99.82
DIP-8	C	21 / 1 .	59.01	0.04	25.04	0.36	0.00	0.03	7.54	6.85	0.53	0.12	99.51
DIP-8	C	47 / 1 .	56.47	0.05	25.95	0.41	0.01	0.04	9.11	6.12	0.32	0.15	98.63
DIP-8	C	48 / 1 .	58.68	0.04	25.07	0.38	0.00	0.04	7.54	6.92	0.43	0.14	99.25
DIP-8	C	49 / 1 .	56.21	0.06	26.78	0.43	0.00	0.05	9.28	5.86	0.33	0.17	99.17
DIP-8	C	53 / 1 .	57.76	0.05	26.26	0.37	0.01	0.04	8.61	6.27	0.39	0.16	99.92
DIP-8	C	54 / 1 .	57.51	0.05	26.36	0.37	0.00	0.04	8.62	6.44	0.38	0.15	99.92
DIP-8	C	55 / 1 .	57.60	0.05	25.91	0.39	0.01	0.04	8.39	6.60	0.39	0.16	99.54
AI-19-028	C	7 / 1 .	58.86	0.04	25.46	0.30	0.00	0.03	8.44	6.57	0.37	0.14	100.21
AI-19-028	C	8 / 1 .	58.67	0.04	25.70	0.30	0.01	0.03	8.46	6.68	0.38	0.16	100.43
AI-19-028	C	9 / 1 .	58.99	0.04	25.50	0.30	-0.01	0.03	8.09	6.83	0.39	0.14	100.30
AI-19-028	C	13 / 1 .	59.68	0.04	25.81	0.33	0.00	0.03	8.16	6.75	0.39	0.15	101.33
AI-19-028	C	14 / 1 .	60.03	0.04	25.55	0.32	0.00	0.02	7.84	6.95	0.41	0.14	101.32
AI-19-028	C	15 / 1 .	59.76	0.04	25.44	0.32	-0.01	0.03	8.12	6.66	0.40	0.14	100.89
AI-19-028	C LB	21	57.61	0.10	26.41	0.45	0.00	0.04	8.36	6.51	0.40	0.09	100.32
AI-19-028	C LB	22	57.08	0.08	26.52	0.49	-0.01	0.09	8.83	6.31	0.35	0.02	100.08
AI-19-028	C LB	23	57.09	0.07	26.24	0.45	0.00	0.04	8.61	6.38	0.40	0.02	100.13
AI-19-028	C LB	24	58.93	0.02	25.39	0.23	0.00	0.01	7.48	7.07	0.44	0.17	100.39

AI-19-028	C DB	32	56.94	0.07	26.61	0.47	0.00	0.05	8.91	6.13	0.39	0.31	99.82
AI-19-028	C DB	33	55.65	0.08	27.51	0.44	0.02	0.05	9.92	5.75	0.30	0.04	99.65
AI-19-028	C DB	40	67.59	0.01	19.71	0.25	0.00	0.01	0.50	7.96	5.01	0.22	100.16
AI-19-028	C DB	42	56.71	0.08	26.97	0.52	0.01	0.08	9.23	5.98	0.34	0.23	100.17
AI-19-026	C	1 / 1 .	57.29	0.06	26.37	0.50	0.00	0.05	9.22	6.19	0.35	0.13	100.15
AI-19-026	C	2 / 1 .	57.08	0.05	26.31	0.45	0.01	0.05	9.50	5.92	0.33	0.14	99.84
AI-19-026	C	3 / 1 .	57.79	0.06	26.50	0.45	0.00	0.05	9.29	5.96	0.38	0.12	100.61
AI-19-026	C	7 / 1 .	58.92	0.04	25.99	0.40	0.00	0.04	8.35	6.68	0.41	0.16	101.00
AI-19-026	C	8 / 1 .	57.91	0.05	26.72	0.42	0.01	0.04	9.23	6.23	0.34	0.14	101.10
AI-19-026	C	9 / 1 .	57.94	0.05	26.70	0.43	0.01	0.04	9.19	6.23	0.36	0.16	101.12
AI-19-026	C	37 / 1 .	56.93	0.06	26.96	0.39	0.00	0.05	9.72	5.88	0.30	0.13	100.41
AI-19-026	C	38 / 1 .	57.03	0.06	26.88	0.41	0.00	0.05	9.79	5.75	0.29	0.13	100.40
AI-19-026	C	39 / 1 .	56.76	0.06	26.92	0.40	0.00	0.05	9.70	5.78	0.29	0.13	100.09
AI-19-026	C	55 / 1 .	58.82	0.04	26.20	0.31	0.01	0.03	8.50	6.58	0.35	0.15	100.98
AI-19-026	C	56 / 1 .	58.45	0.05	26.22	0.31	0.00	0.03	8.63	6.52	0.35	0.14	100.71
AI-19-026	C	57 / 1 .	59.05	0.04	26.20	0.31	0.01	0.03	8.65	6.45	0.35	0.15	101.23
AI-19-026	C	6	58.52	0.05	26.01	0.33	0.00	0.00	8.06	6.75	0.49	0.21	100.43
AI-19-026	C	7	57.32	0.04	27.16	0.29	0.00	0.04	8.86	6.40	0.40	0.16	100.66
AI-19-026	C	8	58.09	0.04	26.35	0.26	0.01	0.00	8.21	6.87	0.42	0.22	100.47
AI-19-026	C	9	58.15	0.05	26.38	0.26	-0.01	0.01	8.32	6.83	0.46	0.23	100.68
AI-19-034	R	10 / 1 .	58.46	0.07	24.99	0.53	0.00	0.06	7.87	6.85	0.49	0.13	99.45
AI-19-034	R	11 / 1 .	58.67	0.04	25.01	0.33	0.00	0.03	7.57	7.08	0.46	0.12	99.31
AI-19-008	R	4 / 1 .	57.72	0.07	26.03	0.54	0.01	0.05	8.54	6.56	0.39	0.14	100.06
AI-19-008	R	5 / 1 .	59.60	0.08	25.41	0.53	-0.01	0.04	7.58	7.05	0.57	0.10	100.95
AI-19-008	R	6 / 1 .	60.84	0.09	24.78	0.57	0.00	0.05	6.77	7.26	0.72	0.11	101.18
AI-19-008	R	15 / 1 .	57.69	0.08	25.87	0.51	0.00	0.05	8.75	6.54	0.46	0.11	100.06
AI-19-008	R	16 / 1 .	56.40	0.07	26.57	0.48	0.01	0.05	9.40	6.11	0.35	0.10	99.54
AI-19-008	R	17 / 1 .	58.89	0.09	25.22	0.57	0.00	0.05	8.03	6.78	0.55	0.10	100.28
AI-19-008	R	33 / 1 .	59.67	0.09	24.41	0.62	0.01	0.05	6.79	7.16	0.64	0.08	99.54
AI-19-008	R	34 / 1 .	60.94	0.11	22.51	0.66	0.01	0.05	4.93	8.00	0.94	0.07	98.22
AI-19-008	R	35 / 1 .	63.35	0.15	21.03	0.69	0.00	0.05	3.82	8.38	1.39	0.05	98.90
AI-19-121	R	1	54.40	0.09	28.27	0.47	-0.02	0.04	10.69	5.42	0.25	0.07	99.81

AI-19-121	R	2	56.85	0.07	26.99	0.45	0.01	0.05	9.26	6.09	0.36	0.05	99.62
AI-19-121	R	3	57.85	0.06	25.95	0.38	0.00	0.04	8.01	6.95	0.43	0.12	99.05
AI-19-121	R	4	57.70	0.05	26.57	0.36	-0.01	0.03	8.50	6.70	0.40	0.20	99.96
AI-19-121	R	5	56.88	0.05	26.53	0.34	0.01	0.05	8.94	6.41	0.37	0.32	99.90
DIP-3	R	13 / 1 .	57.41	0.10	25.21	0.59	0.01	0.06	7.98	6.91	0.42	0.10	98.79
DIP-3	R	14 / 1 .	57.31	0.10	25.63	0.60	0.01	0.06	8.24	6.63	0.41	0.11	99.11
DIP-3	R	18 / 1 .	56.32	0.08	26.16	0.51	0.01	0.05	8.96	6.24	0.40	0.11	98.84
DIP-3	R	19 / 1 .	56.29	0.07	25.76	0.54	0.02	0.05	8.76	6.28	0.40	0.11	98.28
DIP-3	R	29 / 1 .	57.72	0.27	25.16	1.13	0.03	0.18	7.66	6.76	0.81	0.07	99.77
DIP-3	R	30 / 1 .	58.26	0.56	24.66	2.40	0.07	0.45	8.05	6.43	1.29	0.09	102.25
DIP-3	R	31 / 1 .	59.26	0.11	24.33	0.66	0.01	0.08	7.10	7.18	0.55	0.11	99.38
DIP-3	R	32 / 1 .	57.84	0.09	25.49	0.67	0.01	0.07	8.11	6.40	0.47	0.11	99.25
DIP-3	R	38 / 1 .	54.72	0.09	26.89	0.69	0.01	0.08	10.43	5.61	0.32	0.12	98.96
DIP-3	R	39 / 1 .	55.17	0.11	25.83	0.72	0.01	0.09	9.58	5.88	0.39	0.12	97.91
DIP-6	R	5 / 1 .	58.76	0.09	25.24	0.67	0.02	0.06	7.49	6.92	0.56	0.10	99.89
DIP-6	R	6 / 1 .	59.02	0.13	24.99	0.75	0.01	0.09	7.44	7.10	0.63	0.12	100.28
DIP-6	R	14 / 1 .	59.08	0.09	25.28	0.59	0.01	0.06	7.53	7.06	0.45	0.11	100.26
DIP-6	R	15 / 1 .	57.67	0.08	25.13	0.56	0.00	0.06	7.77	6.67	0.42	0.10	98.47
DIP-6	R	16 / 1 .	58.22	0.09	25.37	0.59	-0.01	0.06	7.74	7.02	0.44	0.12	99.65
DIP-6	R	29 / 1 .	58.15	0.10	25.38	0.77	0.01	0.06	7.27	6.93	0.54	0.12	99.32
DIP-6	R	30 / 1 .	58.78	0.09	25.25	0.67	0.01	0.06	7.66	6.86	0.56	0.15	100.09
DIP-6	R	44 / 1 .	58.52	0.08	26.02	0.58	-0.01	0.06	8.03	6.88	0.47	0.14	100.77
DIP-6	R	45 / 1 .	57.35	0.07	26.07	0.52	0.01	0.05	8.75	6.46	0.42	0.11	99.82
DIP-6	R	46 / 1 .	58.07	0.09	25.85	0.56	0.00	0.06	8.22	6.76	0.43	0.10	100.14
DIP-6	R	52 / 1 .	56.34	0.05	26.26	0.44	0.00	0.05	9.08	6.24	0.35	0.10	98.92
DIP-6	R	53 / 1 .	56.34	0.06	26.67	0.45	-0.01	0.05	9.21	6.20	0.35	0.10	99.42
DIP-8	R	16 / 1 .	57.85	0.09	25.28	0.56	0.01	0.06	7.85	6.84	0.44	0.14	99.11
DIP-8	R	17 / 1 .	57.54	0.08	25.98	0.53	0.01	0.05	8.34	6.44	0.38	0.15	99.50
DIP-8	R	18 / 1 .	56.60	0.07	25.78	0.56	-0.01	0.06	8.49	6.44	0.37	0.15	98.51
DIP-8	R	22 / 1 .	56.61	0.07	26.20	0.48	0.00	0.05	9.14	6.20	0.34	0.15	99.24
DIP-8	R	23 / 1 .	56.71	0.06	26.13	0.49	0.00	0.05	8.96	6.25	0.35	0.13	99.13
DIP-8	R	24 / 1 .	56.74	0.07	26.16	0.53	0.00	0.06	8.99	6.17	0.38	0.18	99.26

DIP-8	R	50 / 1 .	57.43	0.07	24.87	0.57	0.02	0.06	7.97	6.86	0.42	0.15	98.42
DIP-8	R	51 / 1 .	57.46	0.08	25.72	0.58	0.00	0.06	8.19	6.51	0.40	0.14	99.15
DIP-8	R	52 / 1 .	56.99	0.08	26.05	0.63	0.01	0.07	8.48	6.45	0.40	0.19	99.35
DIP-8	R	56 / 1 .	57.74	0.05	25.88	0.50	0.02	0.05	8.40	6.69	0.40	0.15	99.87
DIP-8	R	57 / 1 .	57.94	0.05	26.13	0.50	0.00	0.05	8.50	6.50	0.41	0.16	100.24
DIP-8	R	58 / 1 .	57.82	0.06	24.68	0.50	0.01	0.05	7.39	7.00	0.41	0.15	98.09
AI-19-028	R	10 / 1 .	58.13	0.06	26.34	0.46	0.01	0.05	9.08	6.16	0.34	0.14	100.77
AI-19-028	R	11 / 1 .	57.95	0.05	26.09	0.45	0.01	0.05	8.96	6.29	0.36	0.15	100.36
AI-19-028	R	12 / 1 .	58.35	0.06	26.13	0.47	0.00	0.04	8.88	6.27	0.35	0.14	100.69
AI-19-028	R	16 / 1 .	57.34	0.06	27.05	0.46	0.01	0.05	9.42	6.00	0.33	0.13	100.85
AI-19-028	R	17 / 1 .	57.84	0.06	26.79	0.47	0.01	0.05	9.64	5.93	0.33	0.13	101.24
AI-19-028	R	18 / 1 .	58.04	0.06	26.37	0.47	0.01	0.05	9.23	6.18	0.33	0.13	100.88
AI-19-028	R LB	21	56.72	0.06	26.75	0.54	0.01	0.07	8.92	6.31	0.36	0.08	100.43
AI-19-028	R LB	22	57.62	0.07	26.32	0.50	0.02	0.03	8.45	6.51	0.40	0.19	100.07
AI-19-028	R LB	24	58.02	0.05	26.12	0.29	0.00	0.01	8.00	6.80	0.41	0.07	100.03
AI-19-028	R LB	25	56.25	0.07	27.21	0.39	0.00	0.04	9.56	5.86	0.35	0.14	99.64
AI-19-028	R LB	46	58.23	0.05	26.09	0.28	0.02	0.00	7.91	6.76	0.41	0.16	99.77
AI-19-028	R DB	32	56.70	0.07	27.19	0.45	0.01	0.04	9.10	6.30	0.34	0.14	99.47
AI-19-028	R DB	33	54.35	0.08	27.12	0.45	0.02	0.02	9.98	5.54	0.31	0.19	99.77
AI-19-028	R TB	40	67.24	0.03	19.43	0.25	0.01	0.01	0.52	7.70	5.32	0.14	99.79
AI-19-028	R TB	42	56.91	0.05	26.51	0.48	0.01	0.04	9.11	6.34	0.38	-0.03	99.73
AI-19-026	R	4 / 1 .	60.24	0.40	24.00	1.57	0.03	0.14	6.81	7.42	1.11	0.07	101.78
AI-19-026	R	5 / 1 .	57.92	0.08	25.74	0.58	0.00	0.06	8.69	6.42	0.39	0.15	100.04
AI-19-026	R	6 / 1 .	59.75	0.09	24.87	0.64	0.02	0.05	7.77	6.88	0.56	0.15	100.78
AI-19-026	R	10 / 1 .	59.33	0.08	25.47	0.61	0.01	0.06	8.03	6.73	0.44	0.16	100.93
AI-19-026	R	11 / 1 .	59.37	0.05	25.73	0.42	0.01	0.03	8.15	6.96	0.40	0.15	101.28
AI-19-026	R	12 / 1 .	58.36	0.06	25.79	0.54	0.02	0.06	8.66	6.42	0.37	0.18	100.45
AI-19-026	R	40 / 1 .	59.78	0.05	25.37	0.43	0.01	0.04	7.82	6.83	0.41	0.15	100.88
AI-19-026	R	41 / 1 .	59.00	0.05	25.73	0.46	0.00	0.05	8.25	6.61	0.37	0.15	100.68
AI-19-026	R	42 / 1 .	57.24	0.07	26.76	0.52	0.01	0.05	9.58	5.95	0.38	0.15	100.70
AI-19-026	R	58 / 1 .	59.49	0.04	25.75	0.40	0.01	0.04	8.18	6.72	0.40	0.13	101.15
AI-19-026	R	59 / 1 .	61.40	0.04	24.33	0.39	0.01	0.03	6.84	7.45	0.51	0.17	101.16

AI-19-026	R	60 / 1 .	58.34	0.05	26.37	0.47	0.01	0.05	8.76	6.54	0.36	0.14	101.10
AI-19-026	R	6	57.32	0.08	27.16	0.46	0.01	0.05	9.20	6.30	0.40	0.26	101.24
AI-19-026	R	7	56.91	0.06	26.95	0.38	0.02	0.04	9.06	6.35	0.40	0.13	100.29
AI-19-026	R	8	55.75	0.06	27.00	0.36	0.02	0.06	9.68	5.97	0.34	0.13	99.37
AI-19-026	R	9	57.12	0.06	26.96	0.36	0.01	0.03	8.92	6.17	0.39	0.14	100.16
AI-19-026	R	10	57.35	0.07	26.39	0.41	0.01	0.03	8.59	6.46	0.44	0.12	99.86
AI-19-026	R	10	56.54	0.09	27.12	0.47	0.02	0.05	9.22	6.06	0.37	0.49	100.43
AI-19-034	R-C	1 / 1 .	55.94	0.05	27.53	0.47	-0.01	0.05	10.09	5.79	0.30	0.11	100.32
AI-19-034	R-C	2 / 1 .	55.80	0.04	26.87	0.45	0.01	0.06	9.88	5.85	0.32	0.11	99.38
AI-19-034	R-C	8 / 1 .	56.75	0.05	26.35	0.44	0.01	0.05	9.32	6.15	0.35	0.10	99.57
AI-19-034	R-C	9 / 1 .	56.78	0.05	26.14	0.39	0.00	0.05	9.18	6.05	0.39	0.12	99.16
AI-19-034	R-C	23 / 1 .	58.77	0.03	25.41	0.24	0.00	0.03	7.43	7.16	0.47	0.11	99.64
AI-19-034	R-C	24 / 1 .	58.96	0.04	25.70	0.25	0.01	0.02	7.77	7.04	0.46	0.12	100.38
AI-19-008	R-C	24 / 1 .	57.07	0.05	26.53	0.40	0.01	0.05	9.39	6.00	0.34	0.11	99.93
AI-19-008	R-C	25 / 1 .	57.19	0.05	26.68	0.41	0.02	0.04	9.40	6.17	0.34	0.10	100.41
AI-19-008	R-C	26 / 1 .	57.28	0.05	26.95	0.40	0.00	0.04	9.19	6.19	0.35	0.11	100.56
AI-19-008	R-C	36 / 1 .	56.90	0.06	25.72	0.41	0.00	0.04	8.62	6.44	0.42	0.11	98.72
AI-19-008	R-C	37 / 1 .	57.59	0.05	25.53	0.38	0.01	0.04	8.51	6.56	0.40	0.11	99.16
AI-19-008	R-C	38 / 1 .	56.19	0.05	26.35	0.40	0.00	0.05	9.40	6.05	0.35	0.09	98.93
AI-19-008	R-C	48 / 1 .	56.29	0.06	26.58	0.40	0.00	0.05	9.68	5.90	0.33	0.12	99.41
AI-19-008	R-C	49 / 1 .	56.35	0.06	27.38	0.41	0.01	0.05	9.75	5.87	0.31	0.10	100.27
AI-19-008	R-C	50 / 1 .	56.65	0.04	26.09	0.37	0.01	0.04	9.02	6.25	0.36	0.11	98.94
AI-19-121	R-C	10	58.47	0.05	25.73	0.32	0.00	0.00	7.90	7.03	0.44	0.26	100.03
AI-19-121	R-C	10	56.92	0.06	26.96	0.36	0.01	0.02	9.03	6.19	0.34	0.26	99.73
AI-19-121	R-C	45	57.40	0.03	26.56	0.35	0.00	0.02	8.75	6.30	0.38	0.08	100.28
AI-19-121	R-C	6	56.63	0.06	27.38	0.38	0.01	0.10	9.30	6.30	0.33	0.25	99.98
AI-19-121	R-C	7	56.42	0.06	26.93	0.40	0.01	0.03	9.06	6.14	0.36	0.19	99.31
AI-19-121	R-C	8	59.77	0.02	24.66	0.31	0.00	0.02	6.53	7.43	0.58	0.20	100.23
AI-19-121	R-C	9	55.88	0.06	27.35	0.43	0.01	0.05	9.64	6.04	0.34	0.25	99.84
DIP-8	R-C	59 / 1 .	57.40	0.04	25.55	0.41	0.00	0.04	8.32	6.44	0.38	0.15	98.72
DIP-8	R-C	60 / 1 .	57.21	0.03	26.07	0.41	0.00	0.04	8.60	6.32	0.36	0.14	99.18
DIP-8	R-C	61 / 1 .	56.54	0.05	26.61	0.43	0.01	0.04	9.24	6.08	0.33	0.14	99.47

DIP-8	R-C	65 / 1 .	57.27	0.07	25.59	0.50	0.01	0.05	8.62	6.44	0.43	0.13	99.12
AI-19-28	R-C LB	26	55.71	0.05	27.27	0.46	0.01	0.04	9.75	5.89	0.30	0.16	101.11
AI-19-28	R-C LB	27	57.89	0.05	26.05	0.38	0.01	0.04	8.12	6.67	0.43	-0.12	100.61
AI-19-28	R-C LB	29	56.82	0.06	26.96	0.39	0.00	0.03	9.04	6.08	0.37	0.23	99.89
AI-19-28	R-C LB	30	58.87	0.05	25.23	0.37	0.02	0.01	7.32	6.96	0.48	0.09	99.34
AI-19-28	R-C DB	31	57.51	0.03	26.59	0.42	0.01	-0.02	8.63	6.49	0.37	0.28	100.59
AI-19-28	R-C DB	34	44.20	0.05	21.29	0.43	0.01	0.00	9.41	5.91	0.33	0.11	100.02
AI-19-28	R-C TB	41	55.79	0.07	27.32	0.46	0.00	0.07	9.99	5.73	0.32	0.32	100.16
AI-19-28	R-C TB	43	57.91	0.06	26.16	0.28	-0.01	0.01	8.05	6.67	0.41	0.21	100.19
AI-19-026	R-C	11	57.93	0.05	25.68	0.41	0.01	0.01	8.18	6.59	0.45	0.31	99.63
AI-19-026	R-C	12	56.28	0.06	27.38	0.43	0.00	0.07	9.48	5.96	0.34	0.14	100.14
AI-19-026	R-C	13	56.00	0.05	27.27	0.45	0.01	0.01	9.51	5.92	0.35	0.18	99.73
AI-19-026	R-C	14	56.53	0.07	27.21	0.48	0.02	0.04	9.39	6.03	0.41	0.11	100.29
AI-19-026	R-C	15	55.22	0.06	28.07	0.47	0.01	0.04	10.37	5.53	0.32	0.03	100.12
AI-19-026	R-C	31	57.25	0.05	26.79	0.35	0.02	0.05	8.75	6.42	0.39	0.19	100.27
AI-19-026	R-C	32	56.11	0.08	27.76	0.43	0.01	0.08	9.71	5.71	0.34	0.00	100.23
AI-19-034	R-R	3 / 1 .	56.75	0.08	26.47	0.56	0.02	0.05	9.22	6.08	0.36	0.11	99.71
AI-19-034	R-R	4 / 1 .	57.57	0.07	25.77	0.58	0.00	0.06	8.47	6.37	0.39	0.13	99.43
AI-19-034	R-R	10 / 1 .	55.64	0.08	27.26	0.56	0.01	0.07	10.21	5.62	0.31	0.11	99.86
AI-19-034	R-R	11 / 1 .	55.89	0.07	27.75	0.48	0.01	0.06	10.05	5.71	0.29	0.10	100.40
AI-19-034	R-R	21 / 1 .	56.95	0.06	27.49	0.49	0.01	0.05	9.48	6.04	0.33	0.11	101.00
AI-19-034	R-R	22 / 1 .	56.65	0.07	27.41	0.56	0.00	0.05	9.55	5.76	0.33	0.11	100.47
AI-19-008	R-R	27 / 1 .	61.70	1.01	22.72	2.06	0.06	0.29	5.46	7.96	2.01	0.05	103.33
AI-19-008	R-R	28 / 1 .	60.41	0.13	23.71	0.55	0.00	0.05	6.11	7.54	0.86	0.07	99.43
AI-19-008	R-R	29 / 1 .	64.73	1.77	18.17	3.24	0.09	0.46	1.67	7.86	3.34	0.03	101.36
AI-19-008	R-R	39 / 1 .	56.24	0.07	26.60	0.50	0.00	0.06	9.47	6.15	0.36	0.14	99.59
AI-19-008	R-R	40 / 1 .	58.13	0.07	25.37	0.52	0.01	0.05	8.09	6.73	0.46	0.13	99.55
AI-19-008	R-R	51 / 1 .	57.13	0.05	25.56	0.45	0.00	0.05	8.83	6.47	0.38	0.11	99.04
AI-19-008	R-R	52 / 1 .	56.47	0.06	26.20	0.43	0.00	0.05	9.27	6.29	0.36	0.11	99.24
AI-19-008	R-R	53 / 1 .	56.27	0.06	26.13	0.47	0.01	0.05	9.38	6.03	0.36	0.10	98.85
AI-19-121	R-R	45	56.22	0.06	27.01	0.44	-0.01	0.03	9.57	5.88	0.30	0.25	99.47
AI-19-121	R-R	6	57.55	0.06	26.20	0.39	0.00	0.02	8.40	6.54	0.39	0.19	99.87

AI-19-121	R-R	7	56.46	0.06	26.70	0.40	0.01	-0.01	8.92	6.34	0.37	0.07	99.38
AI-19-121	R-R	10	57.70	0.06	26.32	0.39	0.03	0.01	8.25	6.61	0.42	0.11	99.58
AI-19-121	R-R	10	56.51	0.09	26.86	0.46	0.01	0.03	9.34	6.05	0.33	0.17	99.80
AI-19-121	R-R	8	56.89	0.06	26.49	0.39	-0.01	0.04	8.74	6.49	0.41	0.33	100.52
AI-19-121	R-R	9	56.85	0.06	26.37	0.44	0.01	0.01	8.91	6.43	0.37	0.03	97.90
DIP-8	R-R	68 / 1 .	58.60	0.38	24.31	1.86	0.04	0.24	7.14	7.25	1.02	0.08	100.92
DIP-8	R-R	70 / 1 .	58.66	0.36	24.66	1.71	0.06	0.26	7.01	7.16	0.90	0.10	100.87
DIP-8	R-R	62 / 1 .	57.03	0.06	26.32	0.50	0.01	0.05	8.76	6.30	0.35	0.15	99.53
DIP-8	R-R	63 / 1 .	57.06	0.07	26.47	0.52	0.00	0.05	8.91	6.14	0.35	0.14	99.71
DIP-8	R-R	64 / 1 .	56.53	0.07	26.23	0.52	0.01	0.05	8.83	6.11	0.34	0.15	98.85
AI-19-028	R-R LB	26	56.71	0.06	26.68	0.44	-0.01	0.07	9.07	6.38	0.37	0.16	100.46
AI-19-028	R-R LB	27	57.85	0.06	25.85	0.37	0.00	0.02	8.36	6.54	0.40	0.08	100.95
AI-19-028	R-R LB	28	56.08	0.06	27.58	0.39	0.02	0.04	9.85	5.87	0.29	0.03	99.58
AI-19-028	R-R LB	28	57.16	0.07	26.00	0.47	0.02	0.03	8.37	6.41	0.41	0.24	100.73
AI-19-028	R-R LB	29	56.55	0.07	27.26	0.43	0.01	0.02	9.34	6.10	0.34	0.20	99.84
AI-19-028	R-R LB	30	56.56	0.07	26.85	0.41	0.00	0.02	9.36	6.07	0.33	0.27	99.68
AI-19-028	R-R DB	31	57.74	0.07	25.88	0.37	0.00	0.02	8.02	6.60	0.42	0.14	99.82
AI-19-028	R-R DB	34	56.18	0.07	27.17	0.41	0.00	0.04	9.51	6.05	0.32	0.21	99.54
AI-19-028	R-R TB	43	59.31	0.03	25.21	0.26	0.01	0.03	7.20	7.18	0.47	0.24	100.19
AI-19-026	R-R	11	55.87	0.06	27.46	0.47	0.01	0.01	9.73	5.85	0.34	-0.01	99.81
AI-19-026	R-R	12	54.98	0.07	28.13	0.48	0.00	0.04	10.51	5.36	0.28	0.18	100.02
AI-19-026	R-R	13	58.34	0.04	26.17	0.36	0.00	0.04	8.27	6.71	0.46	0.19	100.58
AI-19-026	R-R	14	58.42	0.04	25.99	0.40	0.03	0.03	7.91	6.80	0.47	0.20	100.29
AI-19-026	R-R	15	57.94	0.03	26.03	0.46	0.01	0.03	8.23	6.72	0.45	0.16	100.09
AI-19-026	R-R	31	56.59	0.05	27.20	0.45	0.00	0.05	9.30	6.08	0.39	0.21	100.31
AI-19-026	R-R	32	57.42	0.06	26.49	0.38	0.01	0.02	8.64	6.32	0.41	0.22	99.98
AI-19-121	RR	8 / 1 .	62.38	0.20	21.79	0.82	0.02	0.03	4.16	7.85	2.08	0.04	99.38
AI-19-121	RR	9 / 1 .	58.41	0.17	25.07	0.91	0.03	0.05	7.60	6.95	0.65	0.09	99.94
AI-19-121	RR	10 / 1 .	61.69	0.24	22.72	0.93	0.01	0.11	5.15	7.65	1.44	0.05	100.00
AI-19-121	RR	12 / 1 .	61.24	0.22	22.67	0.90	0.01	0.03	5.05	7.73	1.76	0.04	99.67
AI-19-121	RR	13 / 1 .	59.86	0.19	23.67	1.25	0.03	0.19	5.85	7.66	1.07	0.06	99.82
AI-19-121	RR	15 / 1 .	61.78	0.27	22.79	0.93	0.02	0.16	4.77	7.97	1.44	0.06	100.18

AI-19-121	TYPE 3 C	11	56.39	0.07	27.56	0.31	0.00	-0.01	9.34	6.26	0.30	0.17	100.10
AI-19-121	TYPE 3 R	11	59.34	0.03	25.58	0.26	0.02	0.00	7.18	7.45	0.50	0.12	99.86
AI-19-127	RR	44 / 1 .	63.03	0.45	19.81	1.23	0.03	0.07	3.78	7.47	2.04	0.04	97.97
AI-19-127	RR	49 / 1 .	60.94	0.27	23.18	0.88	0.02	0.09	5.98	7.55	1.55	0.05	100.51
AI-19-127	RR	51 / 1 .	62.39	0.48	22.10	1.29	0.08	0.76	4.51	7.98	2.22	0.04	101.86
AI-19-127	RR	52 / 1 .	61.77	0.36	22.14	0.97	0.02	0.16	4.31	8.07	1.81	0.03	99.64
AI-19-127	RR	53 / 1 .	61.31	0.28	22.97	0.74	-0.01	0.05	5.44	7.79	1.43	0.06	100.06
AI-19-127	RR	54 / 1 .	64.45	1.29	18.17	2.97	0.10	0.30	0.86	5.47	3.42	0.01	97.03
AI-19-028	T3 RIM	28A	61.34	0.00	23.58	0.28	0.01	0.00	5.49	7.99	0.79	0.14	100.01
AI-19-026	T3 RIM	1	59.02	0.12	25.62	0.68	0.00	0.03	7.52	6.72	0.91	0.24	100.88
AI-19-026	T3 RIM	2	56.30	0.11	27.12	0.63	0.02	0.04	9.53	5.92	0.51	0.11	100.27
AI-19-026	T3 RIM	3	57.49	0.16	26.37	0.81	0.02	0.07	8.66	6.40	0.68	0.12	100.79
AI-19-028	T3 RIM	4	56.01	0.11	27.46	0.75	0.00	0.01	9.84	5.85	0.42	0.25	100.70
AI-19-028	T3 SIEVE	28B	60.34	0.89	19.81	3.64	0.17	0.70	5.22	6.37	2.41	0.14	99.74
AI-19-026	T3 SIEVE	1	58.94	0.20	24.74	1.00	0.04	0.12	7.37	6.65	1.12	0.03	100.20
AI-19-026	T3 SIEVE	2	61.16	0.84	19.87	3.88	0.15	0.68	4.86	6.38	2.68	0.09	100.59
AI-19-026	T3 SIEVE	3	61.43	0.27	22.64	1.57	0.07	0.27	5.39	7.22	2.07	0.08	101.01
AI-19-028	T3 INNER RIM	28C	57.81	0.04	25.83	0.28	0.01	0.01	7.99	6.85	0.39	0.14	100.25
AI-19-026	T3 INNER RIM	1	64.10	0.02	22.29	0.18	0.00	0.00	3.50	9.19	1.35	0.13	100.77
AI-19-026	T3 INNER RIM	2	61.44	0.02	23.98	0.26	0.03	0.04	5.49	8.09	0.76	0.13	100.24
AI-19-026	T3 INNER RIM	3	63.01	0.07	21.47	1.44	0.05	0.14	4.58	7.22	2.22	0.20	100.41
AI-19-028	T3 CORE	28D	62.48	0.01	22.82	0.18	-0.01	0.02	4.23	8.57	0.88	0.34	100.26
AI-19-026	T3 CORE	1	64.72	0.01	21.88	0.21	0.00	0.01	2.92	9.32	1.65	0.06	100.78
AI-19-026	T3 CORE	2	60.17	0.04	24.78	0.24	0.02	0.00	6.59	7.64	0.62	0.06	100.15
AI-19-026	T3 CORE	3	64.29	0.03	21.92	0.21	-0.01	-0.02	3.14	8.94	1.71	0.30	100.52
AI-19-026	T3 CORE	4	58.05	0.07	26.17	0.44	0.00	0.01	8.28	6.77	0.47	0.05	100.32
AI-19-026	T3 POINTS	5	67.63	0.01	19.52	0.50	0.00	0.01	0.80	8.51	4.57	-0.02	101.53
AI-19-026	T3 POINTS	5	68.53	0.06	18.23	1.20	0.02	-0.02	0.69	8.05	4.68	0.00	101.44
AI-19-026	T3 POINTS	5	68.44	0.04	18.27	0.95	-0.01	0.00	0.37	8.10	5.41	0.02	101.59
AI-19-034	GM	14 / 1 .	59.57	0.12	24.60	0.65	0.00	0.06	7.31	7.05	0.69	0.08	100.13
AI-19-034	GM	15 / 1 .	59.68	0.11	24.48	0.69	0.01	0.05	6.82	7.10	0.80	0.10	99.85
AI-19-034	GM	5 / 1 .	58.19	0.12	24.43	0.70	0.02	0.06	7.69	6.82	0.59	0.09	98.69

AI-19-034	GM	6 / 1 .	58.42	0.13	24.75	0.78	0.02	0.06	7.74	6.88	0.72	0.09	99.58
AI-19-034	GM	17 / 1 .	59.13	0.11	24.66	0.63	0.01	0.05	7.62	6.94	0.57	0.09	99.82
AI-19-034	GM	20 / 1 .	58.40	0.12	25.03	0.72	0.01	0.06	7.83	6.91	0.56	0.09	99.72
AI-19-008	GM	1 / 1 .	58.25	0.13	25.10	0.67	0.01	0.05	7.57	7.00	0.71	0.07	99.56
AI-19-008	GM	2 / 1 .	57.55	0.10	25.32	0.68	0.00	0.07	8.08	6.62	0.55	0.11	99.09
AI-19-008	GM	3 / 1 .	60.85	0.25	21.73	0.95	0.03	0.08	4.78	7.81	1.25	0.03	97.77
AI-19-008	GM	4 / 1 .	58.96	0.12	24.47	0.79	0.01	0.06	6.82	7.14	0.69	0.08	99.13
AI-19-008	GM	5 / 1 .	58.67	0.13	24.34	0.79	0.02	0.05	6.98	7.21	0.68	0.11	98.98
AI-19-008	GM	6 / 1 .	58.56	0.12	24.68	0.78	0.02	0.11	7.24	7.13	0.78	0.07	99.50
AI-19-008	GM	31 / 1 .	58.59	0.08	24.87	0.65	0.00	0.06	7.62	6.95	0.53	0.12	99.47
AI-19-008	GM	32 / 1 .	58.64	0.11	24.79	0.64	0.01	0.06	7.40	7.16	0.55	0.13	99.49
AI-19-008	GM	34 / 1 .	58.18	0.15	25.80	0.79	0.01	0.08	8.11	6.68	0.56	0.11	100.46
AI-19-008	GM	35 / 1 .	58.33	0.10	25.48	0.72	0.01	0.05	7.83	6.89	0.61	0.10	100.13
AI-19-121	GM	12	56.22	0.07	27.21	0.47	0.01	0.03	9.40	5.92	0.31	0.08	99.82
AI-19-121	GM	13	58.70	0.12	25.44	0.54	0.00	0.04	7.64	6.87	0.48	0.21	99.98
AI-19-121	GM	14	57.46	0.08	26.28	0.53	-0.01	0.06	8.62	6.55	0.37	0.18	81.81
AI-19-121	GM	15	57.20	0.06	26.55	0.45	0.00	0.05	8.69	6.41	0.35	-0.03	100.17
AI-19-121	GM	16	57.97	0.09	25.86	0.66	0.00	0.04	8.27	6.63	0.46	0.07	100.04
AI-19-121	GM	17	58.35	0.06	26.10	0.35	0.01	0.00	7.81	6.80	0.47	0.13	100.47
AI-19-121	GM	18	58.03	0.11	25.63	0.60	0.01	0.10	7.73	7.14	0.56	-0.13	100.37
AI-19-121	GM	19	57.75	0.10	25.65	0.58	0.03	0.00	7.97	6.75	0.51	0.02	101.08
AI-19-121	GM	20	56.68	0.06	25.60	0.40	0.00	0.02	7.65	6.86	0.39	0.29	100.04
AI-19-121	GM	21	59.03	0.13	25.02	0.60	0.01	0.02	7.10	6.94	0.78	0.31	100.12
DIP-3	GM	20 / 1 .	57.92	0.16	24.12	0.80	0.00	0.07	7.12	7.06	0.70	0.08	98.03
DIP-3	GM	23 / 1 .	57.58	0.15	25.80	0.86	0.02	0.10	8.40	6.38	0.45	0.12	99.84
DIP-3	GM	25 / 1 .	57.48	0.13	25.48	0.74	0.02	0.08	8.42	6.49	0.45	0.10	99.40
DIP-3	GM	46 / 1 .	59.36	0.15	24.71	0.78	0.01	0.07	7.24	7.11	0.60	0.10	100.15
DIP-6	GM	56 / 1 .	58.13	0.10	25.42	0.68	0.00	0.07	7.96	6.71	0.49	0.10	99.65
DIP-6	GM	8 / 1 .	58.32	0.08	25.55	0.58	0.01	0.05	8.23	6.78	0.47	0.13	100.21
DIP-6	GM	47 / 1 .	58.35	0.13	25.47	0.85	0.02	0.09	7.79	6.80	0.53	0.11	100.12
DIP-6	GM	48 / 1 .	58.16	0.10	25.52	0.70	0.01	0.06	7.84	7.10	0.54	0.08	100.11
DIP-8	GM	1 / 1 .	58.05	0.09	25.07	0.78	0.02	0.06	7.64	6.97	0.47	0.17	99.32

DIP-8	GM	3 / 1 .	58.56	0.10	24.83	0.65	0.01	0.05	7.36	6.97	0.51	0.16	99.19
DIP-8	GM	8 / 1 .	57.85	0.10	25.10	0.66	0.01	0.06	7.82	6.86	0.48	0.16	99.10
DIP-8	GM	9 / 1 .	56.76	0.11	25.50	0.71	0.00	0.07	8.00	6.45	0.49	0.16	98.24
DIP-8	GM	13 / 1 .	58.33	0.11	24.46	0.74	0.02	0.06	7.40	6.99	0.52	0.16	98.79
DIP-8	GM	14 / 1 .	57.40	0.08	25.78	0.73	0.00	0.06	8.39	6.71	0.44	0.18	99.76
DIP-8	GM	15 / 1 .	57.44	0.10	26.11	0.71	0.00	0.06	8.41	6.50	0.40	0.16	99.89
DIP-8	GM	18 / 1 .	57.61	0.08	25.12	0.63	0.01	0.06	7.77	6.78	0.46	0.19	98.70
DIP-8	GM	19 / 1 .	57.92	0.10	25.23	0.67	0.03	0.05	8.04	6.84	0.47	0.15	99.49
DIP-8	GM	24 / 1 .	56.96	0.08	26.04	0.66	0.01	0.07	9.01	6.41	0.37	0.17	99.79
DIP-8	GM	28 / 1 .	57.37	0.06	25.29	0.45	0.01	0.04	8.33	6.72	0.42	0.14	98.82
DIP-8	GM	33 / 1 .	56.75	0.08	25.83	0.67	0.01	0.07	8.60	6.54	0.40	0.18	99.15
DIP-8	GM	34 / 1 .	58.71	0.09	25.12	0.62	0.01	0.06	7.65	6.90	0.45	0.13	99.74
AI-19-028	GM	1 / 1 .	59.72	0.11	24.45	0.69	0.01	0.04	6.70	7.07	0.64	0.10	99.54
AI-19-028	GM	2 / 1 .	60.13	0.23	22.92	1.13	0.03	0.09	6.37	7.26	1.18	0.09	99.43
AI-19-028	GM	6 / 1 .	59.55	0.10	24.87	0.72	0.01	0.05	7.34	6.98	0.57	0.11	100.29
AI-19-028	GM	8 / 1 .	58.00	0.09	24.92	0.62	0.01	0.06	7.67	6.73	0.48	0.15	98.74
AI-19-028	GM LB	11	57.66	0.10	26.09	0.56	-0.01	0.01	8.47	6.48	0.39	0.26	100.02
AI-19-028	GM LB	12	56.53	0.08	26.38	0.60	0.02	0.03	9.06	6.11	0.42	0.16	99.38
AI-19-028	GM LB	13	55.45	0.12	27.44	0.55	0.02	0.01	10.01	5.78	0.29	0.22	99.91
AI-19-028	GM LB	14	57.41	0.10	26.00	0.62	0.01	0.03	8.36	6.65	0.42	0.20	99.80
AI-19-028	GM LB	15	56.09	0.07	26.93	0.46	0.01	0.07	9.55	5.85	0.32	0.11	99.46
AI-19-028	GM LB	16	57.43	0.08	25.97	0.57	0.02	0.06	8.48	6.62	0.42	0.16	99.80
AI-19-028	GM LB	17	58.71	0.10	24.83	0.63	0.00	0.05	7.36	7.09	0.66	0.11	99.53
AI-19-028	GM LB	18	58.37	0.12	25.50	0.58	0.02	0.04	7.68	6.87	0.53	0.26	99.97
AI-19-028	GM LB	19	57.24	0.07	26.66	0.55	0.00	0.00	8.80	6.31	0.39	0.16	100.19
AI-19-028	GM LB	20	57.95	0.09	26.02	0.56	0.00	0.05	8.25	6.73	0.44	0.23	100.32
AI-19-028	GM DB	1	58.57	0.10	25.45	0.60	0.02	-0.01	7.68	6.77	0.49	0.21	99.89
AI-19-028	GM DB	10	58.11	0.07	25.71	0.54	0.01	0.07	7.95	6.83	0.43	0.18	99.69
AI-19-028	GM DB	2	57.08	0.10	26.19	0.57	0.01	0.04	8.69	6.40	0.43	0.25	99.94
AI-19-028	GM DB	3	57.53	0.12	25.99	0.60	0.01	0.06	8.39	6.55	0.44	0.10	99.10
AI-19-028	GM DB	4	58.62	0.09	25.02	0.56	0.02	0.06	7.05	7.04	0.53	0.12	99.03
AI-19-028	GM DB	5	57.03	0.09	26.03	0.53	0.00	0.02	8.50	6.30	0.42	0.16	99.93

AI-19-028	GM DB	6	57.29	0.08	26.25	0.52	0.01	0.04	8.59	6.58	0.41	0.18	99.37
AI-19-028	GM DB	7	56.67	0.11	26.17	0.65	0.03	0.10	8.55	6.49	0.41	0.32	99.95
AI-19-028	GM DB	8	58.94	0.10	25.08	0.67	0.01	0.05	7.17	7.07	0.56	0.27	99.47
AI-19-028	GM DB	9	57.67	0.08	25.60	0.59	0.02	0.07	8.01	6.72	0.44	0.06	99.79
AI-19-028	GM TB	35	67.00	0.03	19.48	0.28	0.01	-0.09	0.58	7.99	4.92	0.19	99.63
AI-19-028	GM TB	36	66.43	0.05	19.88	0.30	0.01	0.00	1.03	7.91	4.35	0.22	100.01
AI-19-028	GM TB	37	56.67	0.09	27.04	0.53	0.02	0.04	9.42	6.19	0.35	0.25	100.48
AI-19-028	GM TB	38	58.42	0.07	25.62	0.47	0.02	0.00	7.74	6.83	0.48	0.32	100.70
AI-19-028	GM TB	39	57.44	0.10	26.17	0.57	0.01	0.01	8.39	6.42	0.42	0.30	100.10
AI-19-026	GM	1 / 1 .	61.13	0.13	24.40	0.84	0.01	0.04	7.10	6.99	0.91	0.11	101.66
AI-19-026	GM	2 / 1 .	63.41	0.12	23.68	0.75	0.01	0.04	5.80	7.76	1.06	0.09	102.71
AI-19-026	GM	3 / 1 .	61.63	0.11	24.89	0.93	0.00	0.04	6.93	7.30	0.88	0.10	102.82
AI-19-026	GM	4 / 1 .	66.03	0.66	18.60	4.51	0.14	0.54	2.08	7.54	1.81	0.05	101.97
AI-19-026	GM	5 / 1 .	59.55	0.08	25.53	0.64	0.02	0.05	7.99	6.73	0.57	0.15	101.32
AI-19-026	GM	6 / 1 .	60.76	0.33	24.65	1.41	0.03	0.14	7.01	7.25	1.25	0.10	102.92
AI-19-026	GM	7 / 1 .	60.81	0.10	25.04	0.61	0.02	0.05	7.61	6.93	0.67	0.12	101.95
AI-19-026	GM	16	58.18	0.23	25.02	1.04	0.02	0.07	7.92	6.48	0.82	0.09	99.86
AI-19-026	GM	17	58.12	0.11	26.17	0.59	0.01	-0.03	8.24	6.43	0.56	0.21	100.41
AI-19-026	GM	18	58.10	0.10	26.16	0.59	0.02	0.00	8.13	6.68	0.50	0.19	100.46
AI-19-026	GM	20	59.16	0.16	24.68	0.75	0.02	0.05	6.98	7.06	0.90	0.25	100.02
AI-19-026	GM	21	58.66	0.09	25.23	0.63	0.02	0.00	7.55	6.89	0.59	0.00	99.66
AI-19-026	GM	22	57.82	0.09	25.95	0.55	0.01	0.04	8.32	6.51	0.49	0.06	99.84
AI-19-026	GM	23	58.09	0.09	25.96	0.66	0.00	0.05	8.14	6.57	0.50	0.12	100.16
AI-19-026	GM	19	57.54	0.10	25.36	0.55	0.03	0.04	8.73	6.76	0.52	0.17	99.79
AI-19-026	GM	24	58.10	0.24	25.10	1.16	0.02	0.06	7.33	6.61	0.90	0.19	99.70
AI-19-026	GM	25	56.12	0.08	27.06	0.58	0.00	0.02	9.50	5.94	0.34	0.21	99.84
AI-19-026	GM	26	57.05	0.08	26.31	0.61	0.01	-0.02	8.65	6.39	0.44	0.33	99.85
AI-19-026	GM	27	58.49	0.09	25.74	0.66	0.02	0.04	7.84	6.71	0.64	0.22	100.43
AI-19-026	GM	28	58.07	0.11	25.98	0.66	0.02	0.07	8.17	6.47	0.49	0.20	100.25
AI-19-026	GM	29	57.01	0.10	26.34	0.58	-0.01	0.05	8.78	6.03	0.44	0.22	99.54
AI-19-026	GM	30	57.80	0.10	26.42	0.66	0.02	0.07	8.42	6.54	0.49	0.15	100.67

2.2 Olivine EPMA

C – core (Type A), R – rim (Type A), TB – type B, TC – Type C, GM – groundmass.

Sample	Type	Data Set/ Point	SiO_2	TiO_2	Al_2O_3	FeO	MnO	MgO	CaO	Cr_2O_3	P_2O_5	NiO	Total
AI-19-034	GM	12 / 1 .	34.99	0.06	0.02	36.14	1.44	26.00	0.38	0.00	0.14	0.00	99.18
AI-19-034	GM	13/1	34.24	0.12	0.05	35.20	1.30	26.40	1.11	0.01	2.31	0.01	100.75
AI-19-034	GM	18 / 1 .	35.04	0.11	0.11	37.50	1.51	23.80	0.63	0.00	0.33	-0.01	99.03
AI-19-034	GM	19 / 1 .	35.23	0.06	0.02	34.82	1.33	27.42	0.26	0.00	0.18	0.01	99.34
AI-19-008	GM	33 / 1 .	34.57	0.06	0.02	39.43	1.71	23.70	0.26	0.00	0.25	0.01	100.01
AI-19-008	GM	36 / 1 .	35.40	0.05	0.02	34.02	1.30	28.66	0.23	0.01	0.21	0.00	99.89
AI-19-008	GM	37 / 1 .	35.50	0.06	0.02	34.83	1.39	27.21	0.30	0.00	0.18	-0.01	99.48
AI-19-008	Grain	30 / 1 .	35.63	0.05	0.02	33.82	1.27	28.87	0.43	0.01	0.27	0.00	100.36
AI-19-008	C	18 / 1 .	36.72	0.05	0.02	31.74	1.09	30.76	0.17	0.00	0.04	0.01	100.58
AI-19-008	C	19 / 1 .	36.31	0.04	0.02	31.80	1.07	30.49	0.18	0.01	0.04	-0.01	99.95
AI-19-008	C	20 / 1 .	36.50	0.04	0.01	32.39	1.09	30.62	0.17	0.00	0.03	-0.01	100.84
AI-19-008	R	21 / 1 .	36.13	0.03	0.02	31.94	1.09	30.92	0.17	0.00	0.01	-0.01	100.31
AI-19-008	R	22 / 1 .	36.38	0.03	0.04	31.97	1.08	30.62	0.18	0.00	0.02	-0.01	100.32
AI-19-008	R	23 / 1 .	36.28	0.03	0.02	31.79	1.10	30.78	0.18	0.00	0.02	0.01	100.20
AI-19-121	C	18 / 1 .	36.41	0.05	0.02	31.77	1.09	30.65	0.18	0.00	0.03	0.01	100.20
AI-19-121	C	19 / 1 .	36.50	0.04	0.01	32.24	1.09	30.45	0.17	-0.01	0.03	0.01	100.55
AI-19-121	C	20 / 1 .	36.31	0.05	0.02	31.68	1.07	30.81	0.17	0.01	0.03	0.00	100.15
AI-19-121	C	25 / 1 .	36.54	0.03	0.01	31.99	1.06	30.91	0.18	-0.01	0.03	-0.01	100.72
AI-19-121	C	26 / 1 .	36.19	0.03	0.01	31.58	1.08	30.98	0.18	-0.01	0.02	-0.01	100.05
AI-19-121	R	21 / 1 .	35.96	0.04	0.02	34.85	1.19	28.46	0.20	-0.01	0.03	0.00	100.74
AI-19-121	R	22 / 1 .	36.35	0.03	0.01	32.08	1.13	30.38	0.91	0.00	0.98	-0.01	101.86
AI-19-121	R	23 / 1 .	36.25	0.03	0.02	31.37	1.08	30.61	0.21	-0.01	0.04	0.00	99.59
AI-19-121	R	24 / 1 .	35.86	0.03	0.02	31.77	1.10	30.76	0.19	0.00	0.04	-0.02	99.75
AI-19-121	R	27 / 1 .	35.61	0.05	0.04	36.58	1.43	26.08	0.27	-0.01	0.12	0.00	100.17
AI-19-121	R	28 / 1 .	35.30	0.04	0.02	35.43	1.34	26.70	0.21	0.00	0.08	-0.01	99.11
AI-19-121	R	29 / 1 .	35.07	0.05	0.01	36.45	1.41	25.99	0.23	0.00	0.10	0.00	99.31
DIP-3	GM	21 / 1 .	35.98		0.03	29.25	0.93	31.92	0.26				98.39
DIP-3	GM	22 / 1 .	36.39		0.05	30.71	1.02	30.48	0.27				98.97
DIP-3	GM	26 / 1 .	35.58		0.01	34.47	1.33	28.27	0.26				99.96
DIP-3	GM	33 / 1 .	36.57		0.03	29.22	0.90	32.40	0.22				99.36
DIP-3	GM	34 / 1 .	35.92		0.02	30.67	0.98	31.32	0.29				99.24
DIP-3	GM	45 / 1 .	36.55	0.19	0.03	28.62	0.86	33.98	0.24	0.00			100.49
DIP-3	GM	47 / 1 .	35.51	0.05	0.03	32.43	1.15	29.61	0.28	0.00			99.09
DIP-3	GM	48 / 1 .	36.11	0.06	0.04	28.65	0.86	33.24	0.47	0.00			99.48
DIP-3	GM	49 / 1 .	36.03	0.06	0.04	28.95	0.91	33.62	0.53	-0.01			100.17
DIP-3	GM	57 / 1 .	36.34	0.06	0.03	29.16	0.93	31.96	0.22	0.01			98.71
DIP-3	GM	58 / 1 .	36.40	0.11	0.18	32.00	1.13	28.46	0.34	-0.01			98.75
DIP-3	GM	1	36.94	0.04	0.04	27.12	0.89	31.66	1.93	0.01		0.01	98.64
DIP-3	GM	2	37.63	0.13	0.65	28.35	0.95	29.48	0.74	0.00		0.01	97.94
DIP-3	R	2	36.87	0.04	-0.01	31.07	1.13	30.10	0.18	-0.01		0.00	99.37
DIP-3	R	3	37.29	0.05	0.00	29.34	0.99	31.57	0.18	0.00		-0.01	99.40
DIP-3	R	4	37.52	0.03	0.00	27.81	0.85	33.27	0.27	0.00		0.00	99.75
DIP-3	R	5	37.62	0.03	0.01	27.83	0.84	32.97	0.19	-0.01		-0.01	99.48

DIP-3	C	2	36.74	0.04	-0.01	31.05	1.14	30.08	0.18	-0.01		-0.01	99.21
DIP-3	C	3	37.44	0.04	0.00	29.47	1.00	31.68	0.18	0.00		-0.01	99.79
DIP-3	C	4	37.39	0.03	0.00	27.91	0.85	32.88	0.18	-0.01		0.00	99.23
DIP-3	C	5	37.09	0.05	0.01	27.98	0.85	32.99	0.18	0.00		-0.01	99.13
DIP-6	GM	40 / 1 .	35.88	0.05	0.03	31.83	1.13	30.74	0.22	0.00			99.92
DIP-6	GM	10 / 1 .	35.72	0.05	0.07	33.40	1.28	28.38	0.28	0.00			99.23
DIP-8	C	1 / 1 .	36.51	0.03	0.02	31.62	1.11	30.90	0.19	-0.01	0.04	0.00	100.41
DIP-8	C	2 / 1 .	36.22	0.03	0.02	31.90	1.09	30.94	0.18	0.00	0.07	0.00	100.46
DIP-8	C	3 / 1 .	36.82	0.03	0.07	31.75	1.12	30.98	0.27	0.00	0.09	0.01	101.15
DIP-8	C	7 / 1 .	36.33	0.03	0.01	31.47	1.08	30.96	0.17	0.00	0.05	0.00	100.11
DIP-8	C	8 / 1 .	36.64	0.05	0.51	32.24	1.05	30.83	0.42	0.00	0.20	0.00	101.95
DIP-8	C	9 / 1 .	36.65	0.02	0.02	31.43	1.09	31.03	0.18	0.00	0.05	-0.01	100.47
DIP-8	C	37 / 1 .	36.56	0.06	0.02	31.77	1.09	31.00	0.16	0.00	0.03	0.01	100.70
DIP-8	C	38 / 1 .	36.38	0.05	0.02	32.12	1.10	31.18	0.16	0.00	0.03	0.01	101.06
DIP-8	C	39 / 1 .	36.61	0.05	0.02	31.97	1.11	31.15	0.16	0.01	0.02	0.01	101.10
DIP-8	R	4 / 1 .	36.05	0.04	0.02	31.72	1.10	30.93	0.31	0.00	0.03	0.00	100.21
DIP-8	R	5 / 1 .	36.81	0.03	0.02	31.55	1.11	30.82	0.22	0.00	0.04	0.00	100.60
DIP-8	R	6 / 1 .	36.91	0.04	0.02	32.08	1.09	30.70	0.20	0.00	0.02	0.00	101.06
DIP-8	R	10 / 1 .	37.01	0.03	0.02	30.97	1.12	30.66	0.19	-0.01	0.02	0.01	100.04
DIP-8	R	11 / 1 .	36.67	0.03	0.02	31.32	1.09	30.62	0.19	-0.01	0.03	-0.01	99.95
DIP-8	R	12 / 1 .	36.90	0.04	0.02	31.47	1.09	30.73	0.19	-0.01	0.03	0.00	100.45
DIP-8	R	40 / 1 .	36.22	0.03	0.02	31.95	1.08	31.10	0.18	0.00	0.03	0.00	100.59
DIP-8	R	41 / 1 .	36.44	0.02	0.02	31.86	1.09	31.24	0.17	0.01	0.04	0.00	100.88
DIP-8	R	42 / 1 .	36.62	0.03	0.02	31.79	1.07	31.39	0.17	0.01	0.05	0.01	101.14
DIP-8	GM	2 / 1 .	35.92	0.06	0.04	31.38	1.14	30.29	0.29	0.01	0.28	-0.01	99.38
DIP-8	GM	4 / 1 .	35.85	0.08	0.03	31.82	1.17	30.34	0.24	-0.01	0.13	0.00	99.64
DIP-8	GM	5 / 1 .	35.53	0.06	0.03	31.54	1.13	30.68	0.22	0.00	0.24	0.00	99.43
DIP-8	GM	10 / 1 .	36.08	0.10	0.44	32.38	1.22	29.06	0.35	0.00	0.14	0.00	99.78
DIP-8	GM	16 / 1 .	36.41	0.08	0.08	33.67	1.34	27.64	0.26	0.00	0.12	0.01	99.61
DIP-8	GM	17 / 1 .	35.42	0.06	0.03	31.19	1.16	29.33	0.52	0.01	0.30	0.01	98.03
DIP-8	GM	20 / 1 .	35.95	0.05	0.03	31.52	1.18	30.03	0.24	-0.01	0.22	0.01	99.21
DIP-8	GM	21 / 1 .	36.57	0.06	0.03	31.51	1.15	30.56	0.23	0.00	0.21	-0.01	100.31
DIP-8	GM	27 / 1 .	36.13	0.08	0.05	31.70	1.13	30.94	0.26	0.00	0.09	0.01	100.38
DIP-8	GM	30 / 1 .	35.41	0.06	0.03	31.86	1.19	30.19	0.23	0.00	0.15	-0.01	99.13
DIP-8	GM	31 / 1 .	36.35	0.06	0.03	31.63	1.16	30.61	0.22	0.00	0.23	0.01	100.29
DIP-8	GM	36 / 1 .	36.01	0.05	0.03	31.89	1.11	30.46	0.21	0.00	0.21	0.01	99.99
AI-19-028	C	1 / 1 .	36.40	0.04	0.01	31.98	1.10	31.13	0.17	-0.01	0.03	-0.01	100.86
AI-19-028	C	2 / 1 .	35.91	0.04	0.01	31.56	1.11	31.14	0.17	0.01	0.04	0.00	99.99
AI-19-028	C	3 / 1 .	35.85	0.04	0.01	32.49	1.09	31.20	0.17	0.00	0.03	0.00	100.88
AI-19-028	C	25 / 1 .	36.69	0.02	0.01	29.53	0.90	33.08	0.17	0.00	0.06	0.00	100.46
AI-19-028	C	26 / 1 .	36.30	0.02	0.02	29.76	0.91	33.19	0.17	-0.01	0.07	0.00	100.43
AI-19-028	C	27 / 1 .	36.89	0.06	0.38	30.00	0.88	33.06	0.29	0.00	0.06	0.00	101.62
AI-19-028	C	19 / 1 .	36.79	0.06	0.02	30.18	0.94	32.20	0.18	0.00		0.00	100.36
AI-19-028	C	20 / 1 .	36.98	0.08	0.02	29.98	0.92	32.08	0.15	-0.01		0.00	100.19
AI-19-028	C	21 / 1 .	36.91	0.06	0.02	30.45	0.93	32.20	0.19	0.00		0.00	100.76
AI-19-028	R	4 / 1 .	35.76	0.04	0.02	31.99	1.10	31.12	0.18	0.00	0.08	0.00	100.29
AI-19-028	R	5 / 1 .	36.19	0.04	0.01	31.77	1.08	31.01	0.19	0.01	0.04	-0.01	100.32

AI-19-028	R	6 / 1 .	35.47	0.05	0.04	32.31	1.19	29.76	0.24	0.00	0.17	-0.01	99.23
AI-19-028	R	28 / 1 .	36.53	0.03	0.01	29.53	0.92	32.64	0.19	0.00	0.03	0.01	99.89
AI-19-028	R	29 / 1 .	36.50	0.03	0.01	29.49	0.92	32.92	0.19	0.00	0.05	0.00	100.11
AI-19-028	R	30 / 1 .	36.39	0.03	0.02	29.59	0.93	32.88	0.20	0.00	0.04	0.00	100.06
AI-19-028	R	22 / 1 .	36.12	0.04	0.02	31.62	1.11	30.12	0.17	0.00		0.01	99.23
AI-19-028	R	23 / 1 .	36.47	0.03	0.02	30.21	0.94	31.68	0.19	0.00		0.00	99.56
AI-19-028	R	24 / 1 .	36.86	0.03	0.01	30.10	0.96	31.85	0.17	0.00		0.00	99.99
AI-19-028	GM	4 / 1 .	34.31	0.10	0.03	31.94	1.64	29.47	0.26	0.00	0.27	0.00	98.02
AI-19-028	GM	5 / 1 .	35.80	0.06	0.03	32.85	1.55	28.86	0.27	0.00	0.25	-0.01	99.67
AI-19-028	GM	7 / 1 .	35.01	0.08	0.05	33.78	1.45	28.43	0.26	0.00	0.20	0.00	99.26
AI-19-028	GM	9 / 1 .	35.88	0.13	0.64	32.76	1.58	28.45	0.38	-0.01	0.16	0.00	99.98
AI-19-028	GM	3 / 1 .	36.48	0.21	0.15	31.91	1.49	29.76	0.28	0.00		0.01	100.32
AI-19-026	GM	14 / 1 .	34.93	0.07	0.02	37.52	1.67	24.58	0.34	-0.01	0.24	0.00	99.36
AI-19-026	GM	15 / 1 .	34.97	0.07	0.02	37.70	1.67	24.72	0.42	0.00	0.26	0.00	99.84
AI-19-026	GM	21 / 1 .	36.04	0.05	0.02	35.96	1.50	26.81	0.25	0.00	0.06	0.01	100.71
AI-19-026	GM	27 / 1 .	35.15	0.08	0.02	37.82	1.66	24.57	0.39	-0.01	0.21	0.00	99.90
AI-19-026	GM	10 / 1 .	34.67	0.09	0.04	37.25	1.66	24.97	0.35	0.00		0.00	99.06
AI-19-026	GM	11 / 1 .	34.70	0.07	0.02	38.05	1.68	24.07	0.35	0.00		0.00	98.94
AI-19-026	GM	12 / 1 .	34.84	0.05	0.02	38.23	1.65	24.42	0.29	0.00		0.01	99.55
AI-19-026	C	16 / 1 .	36.25	0.05	0.02	32.39	1.19	29.59	0.19	0.00	0.05	-0.01	99.73
AI-19-026	C	17 / 1 .	35.72	0.05	0.01	32.99	1.22	29.35	0.18	0.00	0.07	0.00	99.60
AI-19-026	C	31 / 1 .	35.54	0.27	0.03	33.41	1.20	29.70	0.20	0.00	0.02	0.00	100.36
AI-19-026	C	32 / 1 .	36.08	0.07	0.02	33.35	1.15	29.50	0.19	0.00	0.01	0.00	100.38
AI-19-026	C	33 / 1 .	36.23	0.07	0.02	32.46	1.12	30.75	0.17	0.00	0.01	0.00	100.84
AI-19-026	C	43 / 1 .	35.88	0.02	0.03	31.71	1.02	31.05	0.16	0.00		-0.01	99.85
AI-19-026	C	44 / 1 .	35.82	0.02	0.03	32.20	1.02	31.49	0.17	0.00		-0.01	100.73
AI-19-026	C	45 / 1 .	35.74	0.02	0.03	32.19	1.03	30.48	0.16	0.00		0.00	99.67
AI-19-026	R	34 / 1 .	35.17	0.08	0.02	36.70	1.51	26.48	0.26	0.00	0.08	0.00	100.29
AI-19-026	R	35 / 1 .	35.44	0.05	0.02	35.13	1.41	27.56	0.22	0.00	0.05	0.01	99.89
AI-19-026	R	36 / 1 .	35.53	0.04	0.02	34.64	1.35	28.43	0.21	-0.01	0.02	-0.01	100.22
AI-19-026	R	46 / 1 .	34.21	0.03	0.02	42.71	2.01	21.40	0.21	0.00		-0.01	100.56
AI-19-026	R	47 / 1 .	34.78	0.04	0.03	40.00	1.75	22.99	0.28	0.00		0.00	99.89
AI-19-026	R	48 / 1 .	34.41	0.05	0.03	40.10	1.78	23.03	0.26	0.00		-0.01	99.65
AI-19-026	R	18 / 1 .	35.30	0.08	0.08	37.05	1.59	25.32	0.56	-0.01	0.25	0.00	100.22
AI-19-026	R	19 / 1 .	34.79	0.12	0.02	38.04	1.58	25.57	0.29	0.00	0.14	-0.01	100.53
AI-19-026	TC C	1	33.94	0.11	-0.02	44.62	2.35	18.48	0.17	0.00		-0.02	99.63
AI-19-026	TC C	6	36.14	0.06	-0.01	31.58	1.15	29.92	0.18	0.00		-0.01	99.00
AI-19-026	C	5	36.41	0.04	-0.01	31.63	1.16	30.12	0.18	-0.01		-0.01	99.51
AI-19-026	C	7	36.61	0.03	0.00	30.16	1.03	31.46	0.17	0.01		-0.01	99.47
AI-19-026	C	8	36.18	0.02	0.00	31.02	1.12	30.48	0.18	0.00		0.01	99.00
AI-19-026	C	8	36.18	0.02	0.00	31.02	1.11	30.40	0.18	0.00		-0.02	98.90
AI-19-026	C	9	35.96	0.03	-0.01	31.03	1.12	30.48	0.18	-0.01		0.00	98.79
AI-19-026	C	14	36.30	0.03	-0.02	31.28	1.12	30.74	0.19	0.00		-0.01	99.64
AI-19-026	C	16	36.40	0.03	0.00	31.31	1.16	30.20	0.18	0.00		0.00	99.26
AI-19-026	TC R	1	34.23	0.16	-0.01	43.14	2.27	19.65	0.21	0.00		0.00	99.65
AI-19-026	TC R	6	36.16	0.04	-0.01	31.71	1.18	29.87	0.17	-0.01		-0.01	99.11
AI-19-026	R	5	36.39	0.03	0.00	31.92	1.19	29.79	0.17	-0.01		0.00	99.47

AI-19-026	R	7	36.51	0.03	0.00	30.09	1.02	31.57	0.20	0.01		-0.01	99.42
AI-19-026	R	8	36.45	0.03	0.00	30.79	1.12	30.48	0.18	0.01		-0.01	99.04
AI-19-026	R	9	36.38	0.03	0.01	31.21	1.12	30.45	0.17	0.00		0.00	99.36
AI-19-026	R	14	36.61	0.05	0.00	31.38	1.10	30.80	0.16	-0.01		0.00	100.12
AI-19-026	R	16	36.57	0.02	0.00	31.33	1.12	30.19	0.18	0.01		0.00	99.40
AI-19-026	C	2	35.21	0.05	0.02	35.00	1.53	26.21	0.29	-0.01		0.01	98.30
AI-19-026	TB	10	36.66	0.03	-0.01	31.40	1.13	30.05	0.18	-0.01		-0.01	99.43
AI-19-026	TB	11A	36.00	0.06	-0.01	32.59	1.23	29.10	0.18	0.00		-0.01	99.14
AI-19-026	TB	11B	35.82	0.05	0.00	32.74	1.25	29.19	0.18	-0.01		-0.02	99.19
AI-19-026	TB	12A	36.57	0.04	0.00	31.42	1.15	30.46	0.17	0.00		0.01	99.82
AI-19-026	TB	12B	36.43	0.06	-0.01	31.27	1.15	29.91	0.32	-0.01		-0.01	99.11
AI-19-026	TB	13A	36.34	0.03	0.00	31.31	1.12	30.04	0.18	0.01		-0.01	99.03
AI-19-026	TB	13B	36.32	0.05	-0.01	31.32	1.15	30.05	0.18	0.00		0.00	99.05
AI-19-026	TB	17A	36.87	0.05	0.00	31.41	1.16	30.22	0.18	0.01		0.02	99.90
AI-19-026	TB	17B	36.48	0.04	0.00	31.19	1.14	30.26	0.21	0.01		-0.01	99.31
AI-19-026	GM	1	35.53	0.05	0.00	36.29	1.66	25.11	0.29	0.00		0.00	98.92
AI-19-026	GM	2	35.86	0.03	0.00	34.88	1.48	26.85	0.21	0.00		-0.01	99.30
AI-19-026	GM	4	35.28	0.05	-0.01	35.78	1.63	25.57	0.35	0.01		0.00	98.66
AI-19-026	GM	5	35.94	0.04	-0.02	34.87	1.51	26.55	0.22	0.00		-0.01	99.10
AI-19-026	GM	6	35.32	0.09	0.07	36.57	1.70	24.08	0.98	0.00		-0.02	98.78
AI-19-026	GM	1	36.94	0.04	0.04	27.12	0.89	31.66	1.93	0.01		0.01	98.64

2.3 Pyroxene EPMA

C – core, R – rim, GM – groundmass.

Sample	Type	Data Set/ Point	SiO_2	TiO_2	Al_2O_2	FeO	MnO	MgO	CaO	Na_2O	K_2O	Cr_2O_3	Total
AI-19-034	C	16 / 1 .	51.56	0.53	1.46	11.56	0.77	14.66	18.80	0.37	0.00	0.00	99.72
AI-19-034	C	17 / 1 .	50.35	0.81	2.78	10.95	0.65	13.68	19.59	0.50	0.00	0.00	99.30
AI-19-034	C	20 / 1 .	51.37	0.65	2.02	10.39	0.68	15.10	19.03	0.45	0.00	0.00	99.70
AI-19-034	C	21 / 1 .	51.36	0.63	1.97	10.32	0.67	15.11	19.01	0.47	0.00	0.00	99.54
AI-19-034	C	12 / 1 .	50.85	0.79	2.32	9.78	0.51	14.43	20.34	0.47	0.00	-0.01	99.48
AI-19-034	C	13 / 1 .	50.90	0.80	2.42	9.72	0.54	14.49	20.08	0.45	0.00	-0.01	99.40
AI-19-034	R	14 / 1 .	50.72	0.88	2.57	9.43	0.52	14.28	20.39	0.52	0.02	0.00	99.33
AI-19-034	R	15 / 1 .	49.99	0.86	2.48	9.35	0.52	14.33	20.45	0.47	0.02	0.01	98.48
AI-19-034	R	16 / 1 .	51.04	0.88	2.49	9.39	0.51	14.39	20.55	0.49	0.01	0.01	99.75
AI-19-034	R	18 / 1 .	51.31	0.62	1.75	10.09	0.64	14.86	19.41	0.41	0.01	0.01	99.10
AI-19-034	R	19 / 1 .	51.90	0.65	1.85	9.58	0.59	14.76	19.83	0.44	0.01	-0.01	99.59
AI-19-034	R	22 / 1 .	51.74	0.71	2.10	9.48	0.59	14.95	19.76	0.46	0.03	0.00	99.82
AI-19-034	R	23 / 1 .	50.38	0.80	2.37	9.43	0.55	14.21	19.94	0.48	0.02	0.00	98.18
AI-19-034	GM	7 / 1 .	51.20	0.56	1.60	10.74	0.69	14.99	18.93	0.40	0.00	0.00	99.12
AI-19-034	GM	25 / 1 .	51.53	0.57	1.83	10.62	0.71	14.58	19.07	0.45	0.00	-0.01	99.36
AI-19-008	C	7 / 1 .	50.84	0.87	2.71	11.14	0.71	13.47	19.77	0.50	0.00	0.00	100.03
AI-19-008	C	8 / 1 .	50.15	0.85	2.69	11.08	0.67	13.55	19.68	0.47	0.00	0.00	99.12
AI-19-008	C	42 / 1 .	50.30	0.52	1.76	15.88	1.01	10.46	19.53	0.46	0.00	0.00	99.92
AI-19-008	C	43 / 1 .	50.21	0.52	1.76	15.58	1.03	10.37	19.64	0.48	0.00	0.01	99.60
AI-19-008	C	44 / 1 .	50.45	0.53	1.77	15.66	1.00	10.46	19.71	0.47	0.00	0.00	100.06
AI-19-008	R	9 / 1 .	51.19	0.85	2.53	9.42	0.54	14.24	20.58	0.51	0.02	0.00	99.88
AI-19-008	R	10 / 1 .	50.85	0.85	2.50	9.36	0.57	14.43	20.69	0.48	0.02	0.00	99.74
AI-19-008	R	45 / 1 .	50.23	0.87	2.52	9.41	0.54	14.37	20.09	0.52	0.01	0.01	98.57
AI-19-008	R	46 / 1 .	50.66	0.69	1.94	9.21	0.56	14.82	20.19	0.44	0.00	-0.01	98.51
AI-19-008	R	47 / 1 .	51.16	0.74	2.07	9.43	0.54	14.58	20.24	0.50	0.00	0.01	99.26
AI-19-008	GM	11 / 1 .	50.84	0.72	2.15	10.63	0.63	14.08	19.94	0.52	0.01	0.00	99.51
AI-19-127	C	55 / 1 .	49.79	1.02	2.95	10.84	0.65	13.90	19.49	0.53	0.00	0.00	99.15
AI-19-127	C	56 / 1 .	49.56	1.04	2.62	11.36	0.76	13.65	19.02	0.53	0.00	0.01	98.55
AI-19-127	C	57 / 1 .	51.94	0.55	1.53	11.78	0.81	14.92	17.87	0.40	0.00	0.00	99.80
AI-19-127	C	60 / 1 .	51.66	0.55	1.57	10.90	0.73	15.19	18.49	0.43	0.00	0.00	99.51
AI-19-127	R	58 / 1 .	51.62	0.70	1.95	9.80	0.61	14.65	19.78	0.47	0.03	0.00	99.61
AI-19-127	R	59 / 1 .	50.98	0.76	2.21	9.28	0.53	14.58	20.45	0.47	0.01	0.00	99.27
AI-19-127	R	61 / 1 .	50.38	1.09	3.07	9.90	0.55	13.88	20.13	0.46	0.01	-0.01	99.45
AI-19-127	R	62 / 1 .	50.01	1.06	2.97	10.01	0.56	14.05	20.06	0.50	0.01	0.00	99.23
DIP-3	C	1	50.16	0.61	1.68	10.03	0.70	14.51	19.82	0.39	0.00	-0.01	97.88
DIP-3	C	2	51.20	0.62	1.59	10.37	0.71	14.88	19.10	0.41	0.00	0.00	98.88
DIP-3	C	3	49.90	0.81	2.43	11.16	0.73	13.23	19.74	0.46	0.00	0.00	98.47
DIP-3	C	4	49.40	1.30	3.40	8.61	0.37	14.29	20.72	0.53	0.00	-0.01	98.60

DIP-3	C	6	49.78	0.94	2.69	10.29	0.69	13.69	19.97	0.53	0.00	0.01	98.57
DIP-3	C	7	49.69	0.91	2.66	10.95	0.70	13.50	19.49	0.49	0.00	0.00	98.40
DIP-3	R	1	50.81	0.65	1.67	9.80	0.65	15.01	19.38	0.41	0.00	0.00	98.38
DIP-3	R	3	50.92	0.55	1.49	10.96	0.79	14.51	18.95	0.38	0.00	0.00	98.55
DIP-3	R	4	48.16	1.73	4.21	9.31	0.43	13.68	20.22	0.58	0.00	0.00	98.33
DIP-3	R	6	49.46	1.17	3.07	8.46	0.42	14.44	20.41	0.52	0.00	0.00	97.95
DIP-3	R	7	48.27	1.39	4.16	9.85	0.48	13.86	19.38	0.58	0.00	-0.01	97.97
DIP-3	POINT A	5	50.79	0.71	1.85	9.31	0.60	14.87	19.99	0.42	0.01	-0.01	98.53
DIP-3	POINT B	5	50.37	0.78	2.19	9.20	0.56	14.51	20.20	0.48	0.00	0.00	98.29
DIP-3	POINT A	8	50.16	0.97	2.69	10.27	0.63	13.77	19.96	0.48	0.00	0.00	98.94
DIP-3	POINT B	8	49.19	1.08	3.10	10.14	0.59	13.38	20.23	0.53	0.01	-0.01	98.22
DIP-3	POINT A	9	48.76	1.17	3.31	10.79	0.67	13.22	19.59	0.52	0.00	0.00	98.02
DIP-3	POINT B	9	49.18	0.98	2.91	9.90	0.59	13.74	20.11	0.54	0.00	0.00	97.95
DIP-3	POINT	10	48.92	1.27	3.41	8.68	0.37	14.38	20.26	0.52	0.01	0.01	97.82
DIP-3	POINT A	15	50.19	0.86	2.33	10.29	0.63	14.06	19.94	0.47	0.00	0.00	98.77
DIP-3	POINT B	15	49.87	0.95	2.56	10.40	0.66	14.06	19.49	0.47	0.01	0.01	98.47
DIP-6	C	31 / 1 .	50.11	0.99	3.04	11.63	0.74	13.42	18.86	0.54	0.00	0.00	99.33
DIP-6	C	32 / 1 .	50.21	1.05	3.00	11.27	0.70	13.70	19.26	0.54	0.00	0.00	99.73
DIP-6	C	35 / 1 .	50.61	0.89	2.84	10.44	0.62	13.50	20.28	0.52	0.00	-0.01	99.70
DIP-6	C	36 / 1 .	50.58	0.88	2.83	10.64	0.61	13.59	20.17	0.47	0.00	0.00	99.77
DIP-6	C	18 / 1 .	50.28	1.22	3.64	10.81	0.57	14.38	18.86	0.50	0.00	0.00	100.26
DIP-6	C	19 / 1 .	48.86	1.69	4.42	10.53	0.54	13.56	19.68	0.60	0.00	0.01	99.90
DIP-6	C	23 / 1 .	50.35	1.09	3.10	10.57	0.62	14.02	19.27	0.48	0.01	0.00	99.50
DIP-6	C	24 / 1 .	50.02	1.06	3.12	10.75	0.64	14.06	19.33	0.50	0.00	0.00	99.49
DIP-6	R	33 / 1 .	50.31	1.03	2.88	9.72	0.54	14.06	20.43	0.46	0.02	0.01	99.46
DIP-6	R	34 / 1 .	50.64	1.07	3.10	9.83	0.53	13.92	20.32	0.49	0.02	0.00	99.91
DIP-6	R	37 / 1 .	50.70	0.95	2.81	9.84	0.58	14.11	20.05	0.49	0.01	0.00	99.53
DIP-6	R	38 / 1 .	50.05	0.96	2.83	9.92	0.57	13.95	19.99	0.50	0.01	0.00	98.78
DIP-6	R	39 / 1 .	50.66	0.96	2.85	10.04	0.57	14.13	20.27	0.47	0.01	-0.01	99.95
DIP-6	R	21 / 1 .	49.93	1.18	3.06	11.34	0.58	14.21	19.03	0.54	0.01	0.00	99.89
DIP-6	R	22 / 1 .	50.67	1.30	3.40	10.19	0.57	14.45	19.93	0.54	0.01	0.00	101.05
DIP-6	R	25 / 1 .	51.20	0.85	2.42	9.43	0.56	14.45	20.26	0.45	0.03	0.00	99.63
DIP-6	R	26 / 1 .	51.33	0.72	2.15	9.60	0.60	15.07	19.96	0.44	0.08	-0.01	99.93
DIP-8	C	31 / 1 .	51.68	0.83	2.31	9.21	0.44	15.37	19.38	0.45	0.00	0.00	99.66
DIP-8	C	32 / 1 .	51.02	0.86	2.48	8.64	0.46	15.10	19.59	0.45	0.00	0.00	98.60
DIP-8	C	33 / 1 .	50.26	0.97	2.65	9.65	0.42	14.55	19.56	0.53	0.00	0.00	98.58
DIP-8	C	43 / 1 .	50.28	1.47	4.00	9.84	0.49	13.92	19.09	0.55	0.00	0.00	99.65
DIP-8	C	44 / 1 .	50.61	1.06	3.01	9.83	0.48	14.45	19.58	0.54	0.01	0.00	99.57
DIP-8	C	71 / 1 .	51.38	0.56	1.64	11.06	0.65	13.64	19.69	0.47	0.00	-0.01	99.08
DIP-8	C	72 / 1 .	51.23	0.52	1.65	11.46	0.73	13.16	20.09	0.48	0.00	0.00	99.32
DIP-8	C	73 / 1 .	51.42	0.48	1.45	12.43	0.77	12.55	19.91	0.46	0.00	0.00	99.48
DIP-8	C	22 / 1 .	51.63	0.67	1.84	9.90	0.64	14.73	19.63	0.48	0.01	0.00	99.54
DIP-8	R	34 / 1 .	50.56	0.97	2.77	9.76	0.55	14.19	19.70	0.49	0.01	0.00	98.99
DIP-8	R	35 / 1 .	50.44	1.00	2.82	9.56	0.54	14.25	19.62	0.50	0.01	0.00	98.74

DIP-8	R	36 / 1 .	50.83	1.02	2.91	9.80	0.57	14.24	19.29	0.57	0.01	0.00	99.23
DIP-8	R	45 / 1 .	50.45	1.20	3.95	10.30	0.57	14.07	19.37	0.44	0.18	0.00	100.52
DIP-8	R	46 / 1 .	51.50	0.93	3.44	9.77	0.55	14.42	19.72	0.52	0.04	0.00	100.88
DIP-8	R	74 / 1 .	51.14	0.89	2.64	9.57	0.54	14.50	20.03	0.53	0.02	0.00	99.88
DIP-8	R	75 / 1 .	51.26	0.84	2.47	9.47	0.54	14.59	19.80	0.47	0.01	0.00	99.47
DIP-8	R	76 / 1 .	51.03	0.89	2.57	9.52	0.52	14.51	19.96	0.49	0.02	-0.01	99.49
DIP-8	R	23 / 1 .	50.86	0.97	2.75	9.53	0.55	14.28	20.07	0.52	0.01	0.00	99.52
AI-19-026	C	13 / 1 .	51.69	0.54	1.45	11.49	0.77	14.43	18.87	0.37	0.00	-0.01	99.59
AI-19-026	C	14 / 1 .	51.38	0.54	1.52	10.87	0.74	14.39	19.14	0.43	0.00	0.00	99.02
AI-19-026	C	15 / 1 .	51.76	0.54	1.48	10.99	0.73	14.49	18.85	0.38	0.00	-0.01	99.19
AI-19-026	C	19 / 1 .	49.21	1.39	3.79	11.17	0.64	12.92	19.19	0.54	0.00	0.00	98.85
AI-19-026	C	20 / 1 .	49.35	1.18	3.39	11.32	0.66	13.07	19.44	0.56	0.00	-0.01	98.95
AI-19-026	C	21 / 1 .	48.91	1.30	3.91	11.58	0.63	13.08	19.00	0.62	0.00	0.00	99.02
AI-19-026	C	49 / 1 .	51.01	0.73	2.22	11.13	0.63	13.48	19.49	0.47	0.00	0.00	99.14
AI-19-026	C	50 / 1 .	51.14	0.81	2.47	11.15	0.65	13.51	19.53	0.43	0.00	0.00	99.68
AI-19-026	C	51 / 1 .	50.64	0.86	2.60	10.92	0.60	13.33	20.08	0.46	0.00	0.00	99.48
AI-19-026	R	16 / 1 .	50.86	0.87	2.47	9.33	0.52	14.37	20.04	0.50	0.01	0.00	98.98
AI-19-026	R	17 / 1 .	50.60	0.91	2.56	9.64	0.52	14.24	19.82	0.51	0.01	0.00	98.82
AI-19-026	R	18 / 1 .	50.30	1.12	2.74	10.06	0.57	14.19	19.32	0.51	0.01	0.00	98.83
AI-19-026	R	22 / 1 .	51.04	0.95	2.73	9.42	0.55	14.33	19.71	0.47	0.02	0.00	99.22
AI-19-026	R	23 / 1 .	50.59	1.06	3.04	9.82	0.56	13.91	19.66	0.53	0.01	0.00	99.19
AI-19-026	R	24 / 1 .	50.56	0.88	2.57	9.46	0.54	14.22	19.95	0.43	0.01	-0.01	98.62
AI-19-026	R	52 / 1 .	50.80	0.98	2.77	9.79	0.55	14.10	19.62	0.53	0.02	0.00	99.16
AI-19-026	R	53 / 1 .	50.61	0.93	2.65	9.62	0.54	14.18	19.42	0.48	0.02	0.01	98.45
AI-19-026	R	54 / 1 .	50.72	0.97	2.76	9.68	0.55	14.07	19.88	0.48	0.02	0.00	99.13
AI-19-026	R	1	49.57	0.96	2.64	10.76	0.68	13.73	19.29	0.48	0.00	0.00	98.10
AI-19-026	R	2	49.39	1.09	3.09	9.90	0.57	14.03	19.36	0.50	0.00	-0.01	97.94
AI-19-026	R	4	48.83	1.56	4.02	9.54	0.46	13.94	19.83	0.52	0.00	0.00	98.71
AI-19-026	R	5	48.07	1.41	3.72	9.73	0.50	13.86	19.66	0.56	0.00	0.01	97.54
AI-19-026	R	10	49.19	1.01	2.77	10.25	0.64	13.95	19.49	0.49	0.00	0.00	97.79
AI-19-026	C	1	50.64	0.62	1.51	10.45	0.71	15.03	18.57	0.43	0.00	0.01	97.98
AI-19-026	C	2	50.95	0.61	1.51	10.56	0.72	14.53	19.29	0.35	0.00	0.01	98.53
AI-19-026	C	4	47.90	1.52	3.84	9.55	0.46	13.71	20.06	0.52	0.00	0.00	97.56
AI-19-026	C	5	48.23	1.45	3.64	9.50	0.50	13.87	19.99	0.54	0.00	-0.02	97.69
AI-19-026	C	10	48.55	1.25	3.23	10.66	0.64	13.58	19.29	0.51	0.00	0.00	97.71
AI-19-026	POINT A	3	50.76	0.71	1.80	9.44	0.59	14.87	19.81	0.41	0.00	-0.01	98.38
AI-19-026	POINT B	3	51.18	0.66	1.61	10.02	0.67	15.07	19.17	0.35	0.00	-0.01	98.70
AI-19-026	POINT	6	50.67	0.72	1.79	9.63	0.62	14.91	19.69	0.43	0.00	-0.01	98.46
AI-19-026	POINT	7	50.85	0.69	1.82	9.29	0.58	14.88	19.98	0.42	0.01	-0.01	98.52
AI-19-026	POINT A	8	49.36	0.93	2.61	10.66	0.67	13.93	19.15	0.49	0.00	-0.01	97.80
AI-19-026	POINT A	9	49.65	1.11	2.88	10.23	0.56	14.96	18.25	0.43	0.01	0.00	98.08

2.4 Amphibole EPMA

C – core, R – rim.

Sample	Type	Data Set/ Point	SiO_2	TiO_2	Al_2O_2	FeO	MnO	MgO	CaO	Na_2O	K_2O	Cr_2O_3	Cl	F	Total
AI-19-034	C	4 / 1 .	43.05	3.78	10.34	14.74	0.48	12.39	11.03	2.92	0.69	0.01	0.05	0.26	99.73
AI-19-034	C	5 / 1 .	42.63	3.73	10.30	14.90	0.48	12.22	10.91	2.87	0.69	0.00	0.06	0.27	99.05
AI-19-034	C	26 / 1 .	41.79	4.32	10.48	16.38	0.47	10.94	10.94	2.87	0.67	0.00	0.04	0.21	99.12
AI-19-034	C	27 / 1 .	42.11	4.37	10.68	16.57	0.48	10.88	10.95	2.78	0.68	0.00	0.04	0.20	99.74
AI-19-034	R	6 / 1 .	42.23	3.79	10.32	15.79	0.51	11.68	10.83	2.91	0.71	-0.01	0.06	0.25	99.08
AI-19-034	R	7 / 1 .	42.15	3.78	10.27	15.61	0.50	11.76	10.77	2.73	0.72	0.00	0.07	0.22	98.58
AI-19-034	R	28 / 1 .	41.68	4.36	10.71	15.99	0.45	11.08	10.86	2.78	0.67	-0.01	0.04	0.20	98.83
AI-19-034	R	29 / 1 .	41.57	4.44	10.72	16.30	0.45	11.24	10.99	2.81	0.68	-0.01	0.04	0.19	99.44
AI-19-121	C	1 / 1 .	42.32	4.46	10.68	14.87	0.41	11.96	10.99	2.89	0.63	0.00	0.04	0.17	99.41
AI-19-121	C	2 / 1 .	41.60	4.47	10.65	14.97	0.40	12.03	11.03	2.89	0.64	0.01	0.04	0.17	98.90
AI-19-121	C	3 / 1 .	41.98	4.46	10.64	14.98	0.39	11.99	10.93	2.86	0.63	0.00	0.04	0.17	99.06
AI-19-121	R	4 / 1 .	41.99	4.42	10.64	14.81	0.39	12.11	10.96	2.89	0.66	0.01	0.04	0.17	99.08
AI-19-121	R	5 / 1 .	41.85	4.46	10.69	14.68	0.39	12.00	10.98	2.88	0.63	0.00	0.04	0.18	98.80
AI-19-121	R	6 / 1 .	41.57	4.44	10.63	14.76	0.40	12.10	11.04	2.88	0.63	0.00	0.04	0.16	98.65
AI-19-127	C	35 / 1 .	41.84	4.32	10.60	17.00	0.50	10.71	10.81	2.83	0.68	0.00	0.05	0.16	99.49
AI-19-127	C	36 / 1 .	41.61	4.22	10.64	17.92	0.55	10.21	11.04	2.86	0.67	-0.01	0.05	0.16	99.93
AI-19-127	C	37 / 1 .	41.58	4.79	10.76	13.07	0.34	13.07	11.10	2.89	0.64	-0.01	0.03	0.20	98.47
AI-19-127	C	38 / 1 .	41.85	4.78	10.79	13.20	0.34	12.99	11.22	2.95	0.64	0.00	0.03	0.18	98.98
AI-19-127	C	63 / 1 .	43.49	3.89	10.31	14.70	0.46	12.62	10.92	2.97	0.68	0.00	0.05	0.24	100.34
AI-19-127	C	64 / 1 .	42.22	3.97	10.43	14.67	0.45	12.63	10.72	2.93	0.67	0.00	0.05	0.21	98.93
AI-19-127	C	65 / 1 .	42.60	4.01	10.38	14.46	0.45	12.80	10.92	2.90	0.67	0.00	0.05	0.21	99.44
AI-19-127	G	47 / 1 .	41.55	4.30	10.56	16.20	0.47	11.28	11.00	2.94	0.68	0.00	0.05	0.18	99.19
AI-19-127	R	39 / 1 .	41.26	4.25	10.35	17.82	0.53	10.34	10.97	2.78	0.66	0.00	0.05	0.15	99.16
AI-19-127	R	40 / 1 .	48.92	3.95	14.47	12.12	0.38	6.90	7.45	5.24	0.92	0.00	0.03	0.09	100.47
AI-19-127	R	41 / 1 .	42.38	4.77	11.05	13.04	0.34	13.01	11.29	2.87	0.65	0.00	0.04	0.19	99.63
AI-19-127	R	42 / 1 .	41.90	4.27	10.46	17.51	0.52	10.45	10.93	2.96	0.68	0.00	0.05	0.15	99.86
AI-19-127	R	66 / 1 .	42.49	3.60	10.21	15.86	0.51	11.85	10.69	2.97	0.71	-0.01	0.06	0.23	99.18
AI-19-127	R	67 / 1 .	42.32	3.60	10.25	15.95	0.54	11.98	10.75	2.93	0.71	0.00	0.06	0.24	99.32
AI-19-127	R	68 / 1 .	43.25	3.55	9.92	15.99	0.54	11.89	10.65	3.07	0.71	0.00	0.06	0.23	99.84
AI-19-127	R	69 / 1 .	43.38	3.55	9.95	15.99	0.54	11.67	10.54	2.96	0.70	0.00	0.06	0.20	99.56
DIP-8	C	25 / 1 .	40.76	4.29	10.17	16.45	0.51	10.80	10.23	2.83	0.64	0.00	0.04	0.38	97.10
DIP-8	C	26 / 1 .	41.23	4.30	10.18	16.58	0.50	10.73	10.36	2.90	0.63	0.00	0.04	0.37	97.82
DIP-8	C	27 / 1 .	40.92	3.93	10.32	17.29	0.52	10.65	10.28	2.89	0.61	0.00	0.04	0.39	97.85
DIP-8	R	28 / 1 .	41.69	4.17	10.11	17.26	0.52	10.31	10.28	2.76	0.67	-0.01	0.05	0.39	98.21
DIP-8	R	29 / 1 .	41.21	4.12	10.03	17.44	0.51	10.30	10.34	2.77	0.67	0.00	0.04	0.35	97.78
DIP-8	R	30 / 1 .	41.15	4.11	10.06	17.49	0.53	10.19	10.31	2.75	0.67	0.00	0.04	0.36	97.66

AI-19-026	C	9 / 1 .	40.54	4.29	10.41	17.46	0.56	9.67	10.63	2.91	0.67	0.00	0.04	0.36	97.53
AI-19-026	C	22 / 1 .	41.90	4.60	10.48	13.13	0.38	12.69	10.96	2.81	0.65	0.01	0.04	0.43	98.06
AI-19-026	C	25 / 1 .	41.65	4.58	10.16	12.78	0.37	12.88	10.72	2.84	0.60	-0.01	0.03	0.46	97.07
AI-19-026	C	26 / 1 .	41.46	4.69	10.35	13.42	0.38	12.77	10.71	2.96	0.61	0.00	0.03	0.47	97.87
AI-19-026	C	27 / 1 .	41.98	4.57	10.13	13.10	0.38	12.81	10.72	2.83	0.60	0.01	0.04	0.46	97.63
AI-19-026	R	28 / 1 .	41.72	4.45	10.41	14.03	0.41	12.34	10.67	2.77	0.62	0.00	0.03	0.44	97.91
AI-19-026	R	29 / 1 .	42.38	4.43	10.09	13.33	0.39	12.47	10.71	2.90	0.63	0.01	0.04	0.44	97.82
AI-19-026	R	30 / 1 .	41.75	4.40	10.21	13.70	0.42	12.45	10.58	2.79	0.63	0.00	0.04	0.45	97.41

2.4 Glass EPMA

Sample	Data Set/ Point	SiO_2	TiO_2	Al_2O_2	FeO	MnO	MgO	CaO	Na_2O	K_2O	Cr_2O_3	Cl	F	P_2O_5	SO_2	Total
DIP-3	6 / 1 .	60.60	1.84	14.90	7.17	0.27	1.57	3.63	5.71	3.44	0.01	0.18	0.10	0.73	0.01	100.17
DIP-3	7 / 1 .	59.89	1.89	14.92	7.70	0.27	1.66	3.75	5.77	3.57	-0.01	0.19	0.10	0.72	0.01	100.42
DIP-3	8 / 1 .	59.83	1.91	14.72	7.40	0.27	1.69	3.67	5.91	3.51	0.01	0.19	0.11	0.72	0.01	99.95
DIP-3	9 / 1 .	59.58	1.80	14.71	7.54	0.26	1.59	3.36	5.63	3.52	-0.01	0.19	0.11	0.60	0.01	98.89
DIP-3	15 / 1 .	61.04	1.67	15.15	6.89	0.27	1.57	3.14	5.87	3.77	0.01	0.20	0.09	0.55	0.01	100.22
DIP-3	42 / 1 .	59.19	1.93	14.91	7.96	0.28	1.79	3.76	5.74	3.63	-0.01	0.17	0.10	0.72	0.01	100.17
DIP-3	43 / 1 .	59.65	1.88	14.98	6.84	0.26	1.71	3.81	6.08	3.19	0.00	0.16	0.08	0.72	0.01	99.37
DIP-3	44 / 1 .	58.94	1.95	15.10	7.60	0.27	1.74	3.90	5.71	3.47	0.00	0.18	0.10	0.75	0.01	99.74
DIP-6	1 / 1 .	61.44	1.25	16.21	6.07	0.23	1.49	3.18	6.05	3.41	0.00	0.19	0.08	0.44	0.00	100.05
DIP-6	2 / 1 .	61.78	1.28	16.56	5.77	0.24	1.38	3.32	6.00	3.26	0.01	0.18	0.09	0.45	0.00	100.31
DIP-6	7 / 1 .	61.82	1.28	16.18	6.10	0.24	1.42	3.19	5.95	3.34	0.00	0.19	0.08	0.44	0.00	100.23
DIP-6	9 / 1 .	62.46	1.30	16.17	6.24	0.24	1.34	3.02	5.96	3.23	0.00	0.20	0.08	0.46	0.01	100.70
DIP-6	11 / 1 .	61.66	1.31	15.93	6.06	0.26	1.32	2.94	6.37	3.29	0.00	0.20	0.09	0.43	0.01	99.87
DIP-6	54 / 1 .	61.64	1.33	15.91	6.15	0.25	1.25	2.98	5.85	3.40	0.00	0.21	0.09	0.42	0.00	99.49
DIP-6	55 / 1 .	61.39	1.29	15.84	6.13	0.26	1.37	3.03	6.08	3.52	0.01	0.19	0.07	0.43	0.00	99.61
DIP-8	6 / 1 .	61.01	1.13	17.01	5.99	0.25	1.19	2.60	6.31	4.09	0.00	0.21	0.22	0.42		100.41
DIP-8	7 / 1 .	62.35	1.49	14.88	6.32	0.26	1.33	2.42	5.95	4.13	0.00	0.16	0.22	0.52		100.04
DIP-8	11 / 1 .	61.94	1.55	14.96	6.40	0.30	1.34	2.52	5.78	4.05	0.00	0.22	0.26	0.56		99.87
DIP-8	12 / 1 .	62.13	1.52	15.05	5.86	0.23	1.09	2.29	5.79	4.19	0.00	0.14	0.23	0.53		99.05
DIP-8	25 / 1 .	61.92	1.34	15.67	6.33	0.26	1.40	2.82	6.04	3.71	0.00	0.20	0.22	0.49		100.41
DIP-8	26 / 1 .	62.43	1.34	15.40	6.42	0.25	1.47	2.76	6.11	3.61	0.00	0.19	0.22	0.46		100.67
DIP-8	29 / 1 .	61.40	1.37	16.02	6.23	0.27	1.37	2.98	5.95	3.60	0.00	0.21	0.22	0.49		100.11
DIP-8	32 / 1 .	62.46	1.36	16.05	6.33	0.26	1.44	2.93	6.20	3.57	0.00	0.20	0.21	0.49		101.51
DIP-8	35 / 1 .	61.44	1.38	15.72	6.21	0.27	1.42	2.79	6.01	3.72	0.01	0.21	0.24	0.51		99.91

Appendices 3 – Crystal Size Distribution (CSD) Data

Classic CSD – AI-19-008 (Spatter)

Mid Inter (um)	ln(pop den)	ln(min PD)	ln(max PD)	Cry Num	vol%
662	-25.61	#NAME?	-24.92	2.29E-09	5.711
417	-23.1	-23.71	-22.73	1.78E-08	11.17
263	-21.17	-21.49	-20.92	7.79E-08	12.26
166.2	-19.2	-19.37	-19.04	3.52E-07	13.93
104.9	-17.67	-17.8	-17.55	1.03E-06	10.2
66.2	-15.81	-15.89	-15.74	4.15E-06	10.35
41.7	-14.35	-14.41	-14.29	1.13E-05	7.074
26.3	-13.39	-13.46	-13.34	1.85E-05	2.907
16.62	-12.66	-12.73	-12.6	0.0000242	0.957
10.49	-12.43	-12.53	-12.33	0.0000194	0.192
6.62	-14.28	-15.81	-13.7	1.92E-06	0.004
4.17					
2.63					
1.662					
1.049					
0.662					

Classic CSD – AI-19-121 (Spatter)

Mid Inter (um)	ln(pop den)	ln(min PD)	ln(max PD)	Cry Num	vol%
403	-23.89	-24.32	-23.58	7.84E-09	4.567
254	-22.46	-22.79	-22.21	2.07E-08	3.025
160.3	-20.7	-20.91	-20.53	7.53E-08	2.766
101.1	-18.92	-19.04	-18.8	2.84E-07	2.619
63.8	-17.49	-17.59	-17.4	7.44E-07	1.724
40.3	-16.31	-16.4	-16.23	1.53E-06	0.891
25.4	-15.53	-15.63	-15.45	2.10E-06	0.307
16.03	-15.01	-15.14	-14.9	2.23E-06	0.082
10.11	-15.63	-16.02	-15.35	7.59E-07	0.007
6.38					
4.03					
2.54					
1.603					

Classic CSD – AI-19-026 (Normal Lava)

Mid Inter (um)	ln(pop den)	ln(min PD)	ln(max PD)	Cry Num	vol%
474	-24.79	#NAME?	-24.1	3.72E-09	5.133
299	-21.8	-22.25	-21.5	4.67E-08	16.17
189	-20.23	-20.53	-19.99	1.43E-07	12.42
119.1	-19.07	-19.34	-18.86	2.86E-07	6.25
75.1	-17.15	-17.3	-17.02	1.23E-06	6.761
47.4	-15.27	-15.36	-15.18	5.11E-06	7.038
29.9	-13.94	-14.02	-13.87	1.21E-05	4.19
18.9	-13.08	-13.16	-13.01	1.81E-05	1.573
11.91	-12.34	-12.43	-12.26	0.000024	0.523
7.51	-11.55	-11.65	-11.46	0.0000333	0.182
4.74	-12.16	-12.45	-11.93	1.15E-05	0.015
2.99					
1.89					
1.191					
0.751					
0.474					

Classic CSD – AI-19-028 (Normal Lava)

Mid Inter (um)	ln(pop den)	ln(min PD)	ln(max PD)	Cry Num	vol%
603	-25.15	#NAME?	-24.46	3.31E-09	5.631
380	-22.86	-23.58	-22.45	2.06E-08	8.801
240	-20.33	-20.59	-20.13	1.63E-07	17.55
151.4	-19.01	-19.22	-18.84	3.87E-07	10.43
95.5	-17.07	-17.19	-16.97	1.69E-06	11.46
60.3	-15.31	-15.39	-15.24	6.23E-06	10.61
38	-13.61	-13.66	-13.56	2.15E-05	9.198
24	-12.49	-12.54	-12.44	4.16E-05	4.469
15.14	-11.59	-11.64	-11.55	0.0000642	1.734
9.55	-10.8	-10.85	-10.74	0.0000902	0.611
6.03	-10.12	-10.19	-10.07	1.11E-04	0.189
3.8	-11.02	-11.25	-10.84	2.86E-05	0.012
2.4					
1.514					
0.955					
0.603					

Classic CSD – AI-19-028 (Dark Lava Bands)

Mid Inter (um)	ln(pop den)	ln(min PD)	ln(max PD)	Cry Num	vol%
589	-25.22	-26.08	-24.77	3.01E-09	4.629
372	-22.47	-22.73	-22.26	2.99E-08	11.54
234	-21.06	-21.27	-20.89	7.71E-08	7.474
147.9	-19.2	-19.32	-19.09	3.12E-07	7.597
93.3	-16.98	-17.04	-16.92	1.82E-06	11.15
58.9	-15.15	-15.19	-15.11	7.17E-06	11.01
37.2	-14.07	-14.11	-14.03	1.33E-05	5.127
23.4	-14.2	-14.27	-14.13	7.37E-06	0.714
14.79					
9.33					
5.89					

Classic CSD – DIP-3 (Scoria clasts)

Mid Inter (um)	ln(pop den)	ln(min PD)	ln(max PD)	Cry Num	vol%
286	-24.37	-25.07	-23.97	3.42E-09	0.639
180	-22.14	-22.45	-21.91	2.01E-08	0.942
113.7	-20.06	-20.22	-19.93	1.01E-07	1.193
71.8	-18.14	-18.23	-18.05	4.40E-07	1.3
45.3	-16.41	-16.48	-16.36	1.55E-06	1.153
28.6	-14.85	-14.89	-14.8	4.69E-06	0.876
18	-13.59	-13.63	-13.56	1.04E-05	0.487
11.37	-12.65	-12.69	-12.62	1.67E-05	0.197
7.18	-12.02	-12.06	-11.97	0.00002	0.059
4.53	-11.84	-11.91	-11.77	0.0000151	0.011
2.86	-13.49	-14.11	-13.11	1.83E-06	0
1.8					
1.137					
0.718					
0.453					

Classic CSD – DIP-5 (Pumice clasts)

Mid Inter (um)	ln(pop den)	ln(min PD)	ln(max PD)	Cry Num	vol%
510	-26.2	-27.43	-25.67	9.82E-10	1.275
322	-23.79	-24.21	-23.5	6.89E-09	2.247
203	-21.36	-21.53	-21.21	4.97E-08	4.07
128.2	-20.31	-20.48	-20.17	8.93E-08	1.837
80.9	-18.68	-18.79	-18.58	2.87E-07	1.485
51	-17	-17.08	-16.93	9.73E-07	1.264
32.2	-15.66	-15.72	-15.6	2.35E-06	0.766
20.3	-14.55	-14.61	-14.5	4.50E-06	0.368
12.82	-13.48	-13.53	-13.43	8.27E-06	0.17
8.09	-13.07	-13.14	-13	7.85E-06	0.04
5.1	-13.71	-13.92	-13.53	2.62E-06	0.003
3.22					
2.03					
1.282					
0.809					
0.51					

Classic CSD – DIP-8 (Dense Clasts)

Mid Inter (um)	ln(pop den)	ln(min PD)	ln(max PD)	Cry Num	vol%
180	-22.32	#NAME?	-21.62	1.69E-08	0.792
113.7	-19.46	-19.93	-19.13	1.86E-07	2.193
71.8	-17.79	-18.1	-17.56	6.20E-07	1.836
45.3	-15.72	-15.89	-15.59	3.09E-06	2.297
28.6	-14.09	-14.2	-13.99	1.00E-05	1.87
18	-12.29	-12.36	-12.22	3.83E-05	1.798
11.37	-10.94	-11	-10.89	9.28E-05	1.093
7.18	-9.71	-9.76	-9.67	2.00E-04	0.591
4.53	-9.06	-9.11	-9	0.000243	0.18
2.86	-9	-9.1	-8.92	0.000162	0.03
1.8	-9.36	-9.61	-9.16	7.15E-05	0.003
1.137	-8.42	-8.64	-8.24	1.15E-04	0.001
0.453	-6.58	-6.75	-6.44	0.000289	0

References

- Abbey S. , 1975. The search for "Best Values" - A study of three Canadian rocks. Geostandards Newsletter 5, 13-26.
- Allen, S.R., 2004. Complex spatter-and pumice-rich pyroclastic deposits from an andesitic caldera-forming eruption: the Siwi pyroclastic sequence, Tanna, Vanuatu. *Bulletin of Volcanology*, *67*(1), pp.27-41.
- Alparone, S., Andronico, D., Lodato, L. and Sgroi, T., 2003. Relationship between tremor and volcanic activity during the Southeast Crater eruption on Mount Etna in early 2000. *Journal of Geophysical Research: Solid Earth*, *108*(B5).
- Ammon, K., Dunai, T.J., Stuart, F.M., Meriaux, A.S. and Gayer, E., 2009. Cosmogenic 3He exposure ages and geochemistry of basalts from Ascension Island, Atlantic Ocean. *Quaternary Geochronology*, *4*(6), pp.525-532.
- Anderson, A.T., 1976. Magma mixing: petrological process and volcanological tool. *Journal of Volcanology and Geothermal Research*, *1*(1), pp.3-33.
- Anderson, A.T., 1984. Probable relations between plagioclase zoning and magma dynamics, Fuego Volcano, Guatemala. *American Mineralogist*, *69*(7-8), pp.660-676.
- Andronico, D., Cristaldi, A. and Scollo, S., 2008. The 4–5 September 2007 lava fountain at south-east crater of Mt Etna, Italy. *Journal of Volcanology and Geothermal Research*, *173*(3-4), pp.325-328.
- Arzilli, F., Agostini, C., Landi, P., Fortunati, A., Mancini, L. and Carroll, M.R., 2015. Plagioclase nucleation and growth kinetics in a hydrous basaltic melt by decompression experiments. *Contributions to Mineralogy and Petrology*, *170*, pp.1-16.
- Arzilli, F., La Spina, G., Burton, M.R., Polacci, M., Le Gall, N., Hartley, M.E., Di Genova, D., Cai, B., Vo, N.T., Bamber, E.C. and Nonni, S., 2019. Magma fragmentation in highly explosive basaltic eruptions induced by rapid crystallization. *Nature Geoscience*, *12*(12), pp.1023-1028.
- Bachmann, O., Dungan, M.A. and Lipman, P.W., 2002. The Fish Canyon magma body, San Juan volcanic field, Colorado: rejuvenation and eruption of an upper-crustal batholith. *Journal of Petrology*, *43*(8), pp.1469-1503.
- Bacon, C.R. and Lowenstern, J.B., 2005. Late Pleistocene granodiorite source for recycled zircon and phenocrysts in rhyodacite lava at Crater Lake, Oregon. *Earth and Planetary Science Letters*, *233*(3-4), pp.277-293.

- Bain, A.A., Calder, E.S., Cortés, J.A., Cortés, G.P. and Loughlin, S.C., 2019. Textural and geochemical constraints on andesitic plug emplacement prior to the 2004–2010 vulcanian explosions at Galeras volcano, Colombia. *Bulletin of volcanology*, *81*(1), pp.1-25.
- Bain, A.A., Calder, E.S., Cortés, J.A., Cortés, G.P. and Loughlin, S.C., 2019. Textural and geochemical constraints on andesitic plug emplacement prior to the 2004–2010 vulcanian explosions at Galeras volcano, Colombia. *Bulletin of Volcanology*, *81*, pp.1-25.
- Bain, A.A., Calder, E.S., Cortés, J.A., Cortés, G.P.J. and Loughlin, S.C., 2018. Eruption dynamics of cyclic vulcanian explosions from Galeras volcano, Colombia. *NERC Scientific Facilities and Technology Ion Microprobe Facility*, p.3.
- Baker, I., 1968. Intermediate oceanic volcanic rocks and the 'Daly gap'. *Earth and Planetary Science Letters*, *4*(2), pp.103-106.
- Bamber, E.C., Arzilli, F., Polacci, M., Hartley, M.E., Fellowes, J., Di Genova, D., Chavarría, D., Saballos, J.A. and Burton, M.R., 2020. Pre-and syn-eruptive conditions of a basaltic Plinian eruption at Masaya Volcano, Nicaragua: the Masaya Triple Layer (2.1 ka). *Journal of Volcanology and Geothermal Research*, *392*, p.106761.
- Bamber, E.C., La Spina, G., Arzilli, F., de'Michieli Vitturi, M., Polacci, M., Hartley, M.E., Petrelli, M., Fellowes, J. and Burton, M., 2022. Basaltic Plinian eruptions at Las Sierras-Masaya volcano driven by cool storage of crystal-rich magmas. *Communications Earth & Environment*, *3*(1), p.253.
- Barberi, F., Cioni, R., Rosi, M., Santacroce, R., Sbrana, A. and Vecci, R., 1989. Magmatic and phreatomagmatic phases in explosive eruptions of Vesuvius as deduced by grain-size and component analysis of the pyroclastic deposits. *Journal of Volcanology and Geothermal Research*, *38*(3-4), pp.287-307.
- Bautista, B.C., Bautista, M.L.P., Stein, R.S., Barcelona, E.S., Punongbayan, R.S., Laguerta, E.P., Rasdas, A.R., Ambubuyog, G., Amin, E.Q. and Newhall, C.G., 1996. Relationship of regional and local structures to Mount Pinatubo activity. *Fire and mud: eruptions and lahars of Mount Pinatubo, Philippines*, pp.351-370.
- Befus, K.S. and Andrews, B.J., 2018. Crystal nucleation and growth produced by continuous decompression of Pinatubo magma. *Contributions to Mineralogy and Petrology*, *173*, pp.1-20.
- Beier, C., Haase, K.M. and Hansteen, T.H., 2006. Magma evolution of the Sete Cidades volcano, São Miguel, Azores. *Journal of Petrology*, *47*(7), pp.1375-1411.

- Bellver-Baca, M.T., Chiaradia, M., Beate, B., Beguelin, P., Deriaz, B., Mendez-Chazarra, N. and Villagómez, D., 2020. Geochemical evolution of the Quaternary Chachimbiro Volcanic Complex (frontal volcanic arc of Ecuador). *Lithos*, *356*, p.105237.
- Belousov, A. and Belousova, M., 2001. Eruptive process, effects and deposits of the 1996 and the ancient basaltic phreatomagmatic eruptions in Karymskoye lake, Kamchatka, Russia. *Volcaniclastic sedimentation in lacustrine settings*, pp.35-60.
- Belousov, A., Belousova, M., Auer, A., Walter, T.R. and Kotenko, T., 2021. Mechanism of the historical and the ongoing Vulcanian eruptions of Ebeko volcano, Northern Kuriles. *Bulletin of Volcanology*, *83*, pp.1-24.
- Belousov, A., Belousova, M., Edwards, B., Volynets, A. and Melnikov, D., 2015. Overview of the precursors and dynamics of the 2012–13 basaltic fissure eruption of Tolbachik Volcano, Kamchatka, Russia. *Journal of Volcanology and Geothermal Research*, *307*, pp.22-37.
- Benage, M.C., Dufek, J., Degruyter, W., Geist, D., Harpp, K. and Rader, E., 2014. Tying textures of breadcrust bombs to their transport regime and cooling history. *Journal of Volcanology and Geothermal Research*, *274*, pp.92-107.
- Bertagnini, A. and Landi, P., 1996. The Secche di Lazzaro pyroclastics of Stromboli volcano: a phreatomagmatic eruption related to the Sciara del Fuoco sector collapse. *Bulletin of Volcanology*, *58*, pp.239-245.
- Biggs, J. and Pritchard, M.E., 2017. Global volcano monitoring: What does it mean when volcanoes deform?. *Elements*, *13*(1), pp.17-22.
- Bindeman, I.N., Deegan, F.M., Troll, V.R., Thordarson, T., Höskuldsson, Á., Moreland, W.M., Zorn, E.U., Shevchenko, A.V. and Walter, T.R., 2022. Diverse mantle components with invariant oxygen isotopes in the 2021 Fagradalsfjall eruption, Iceland. *Nature Communications*, *13*(1), p.3737.
- Blackburn, E.A., Wilson, L. and Sparks, R.J., 1976. Mechanisms and dynamics of strombolian activity. *Journal of the Geological Society*, *132*(4), pp.429-440.
- Blake, S., 2000. Comment on" Cooling and crystallization of lava in open channels, and the transition of pahoehoe lava to'a'a". *Bulletin of volcanology*, *62*, pp.362-364.

- Blake, S., 2000. Comment on" Cooling and crystallization of lava in open channels, and the transition of pahoehoe lava to'a'a". *Bulletin of volcanology*, *62*, pp.362-364.

- Blundy, J., Cashman, K. and Humphreys, M., 2006. Magma heating by decompression-driven crystallization beneath andesite volcanoes. *Nature*, *443*(7107), pp.76-80.

- Bohrson, W.A. and Reid, M.R., 1997. Genesis of silicic peralkaline volcanic rocks in an ocean island setting by crustal melting and open-system processes: Socorro Island, Mexico. *Journal of Petrology*, *38*(9), pp.1137-1166.
- Bohrson, W.A. and Spera, F.J., 2007. Energy-Constrained Recharge, Assimilation, and Fractional Crystallization (EC-RAχFC): A Visual Basic computer code for calculating trace element and isotope variations of open-system magmatic systems. *Geochemistry, Geophysics, Geosystems*, *8*(11).
- Bonaccorso, A. and Calvari, S., 2017. A new approach to investigate an eruptive paroxysmal sequence using camera and strainmeter networks: Lessons from the 3–5 December 2015 activity at Etna volcano. *Earth and Planetary Science Letters*, *475*, pp.231-241.
- Bonadonna, C., Pistolesi, M., Biass, S., Voloschina, M., Romero, J., Coppola, D., Folch, A., D'Auria, L., Martin-Lorenzo, A., Dominguez, L. and Pastore, C., 2022. Physical Characterization of Long-Lasting Hybrid Eruptions: The 2021 Tajogaite Eruption of Cumbre Vieja (La Palma, Canary Islands). *Journal of Geophysical Research: Solid Earth*, *127*(11), p.e2022JB025302.
- Bonnefoi, C.C., Provost, A. and Albarede, F., 1995. The'Daly gap'as a magmatic catastrophe. *Nature*, *378*(6554), pp.270-272.
- Branney, M.J., Kokelaar, B.P. and McConnell, B.J., 1992. The Bad Step Tuff: a lava-like rheomorphic ignimbrite in a calc-alkaline piecemeal caldera, English Lake District. *Bulletin of Volcanology*, *54*, pp.187-199.
- Breard, E.C.P., Lube, G., Cronin, S.J., Fitzgerald, R., Kennedy, B., Scheu, B., Montanaro, C., White, J.D.L., Tost, M., Procter, J.N. and Moebis, A., 2014. Using the spatial distribution and lithology of ballistic blocks to interpret eruption sequence and dynamics: August 6 2012 Upper Te Maari eruption, New Zealand. *Journal of Volcanology and Geothermal Research*, *286*, pp.373-386.
- Brown, R.J., Blake, S., Thordarson, T. and Self, S., 2014. Pyroclastic edifices record vigorous lava fountains during the emplacement of a flood basalt flow field, Roza Member, Columbia River Basalt Province, USA. *Bulletin*, *126*(7-8), pp.875-891.
- Browne, B. and Szramek, L., 2015. Rates of magma ascent and storage. In *The encyclopedia of volcanoes* (pp. 203-214). Academic Press.
- Browne, B.L. and Gardner, J.E., 2006. The influence of magma ascent path on the texture, mineralogy, and formation of hornblende reaction rims. *Earth and Planetary Science Letters*, *246*(3-4), pp.161-176.

- Brozena, J.M., 1986. Temporal and spatial variability of seafloor spreading processes in the northern South Atlantic. *Journal of Geophysical Research: Solid Earth*, *91*(B1), pp.497-510.
- Brugger, C.R. and Hammer, J.E., 2010a. Crystallization kinetics in continuous decompression experiments: implications for interpreting natural magma ascent processes. *Journal of Petrology*, *51*(9), pp.1941-1965.
- Brugger, C.R. and Hammer, J.E., 2010b. Crystal size distribution analysis of plagioclase in experimentally decompressed hydrous rhyodacite magma. *Earth and Planetary Science Letters*, *300*(3-4), pp.246-254.
- Burchardt, S., Tanner, D.C., Troll, V.R., Krumbholz, M. and Gustafsson, L.E., 2011. Three-dimensional geometry of concentric intrusive sheet swarms in the Geitafell and the Dyrfjöll volcanoes, eastern Iceland. *Geochemistry, Geophysics, Geosystems*, *12*(7).
- Burchardt, S., Walter, T.R. and Tuffen, H., 2018. Growth of a volcanic edifice through plumbing system processes—Volcanic rift zones, magmatic sheet-intrusion swarms and long-lived conduits. In *Volcanic and igneous plumbing systems*(pp. 89-112). Elsevier.
- Burgisser, A. and Bergantz, G.W., 2011. A rapid mechanism to remobilize and homogenize highly crystalline magma bodies. *Nature*, *471*(7337), pp.212-215.
- Burgisser, A. and Degruyter, W., 2015. Magma ascent and degassing at shallow levels. *The encyclopedia of volcanoes*, pp.225-236.
- Burgisser, A., Poussineau, S., Arbaret, L., Druitt, T.H., Giachetti, T. and Bourdier, J.L., 2010. Pre-explosive conduit conditions of the 1997 Vulcanian explosions at Soufrière Hills Volcano, Montserrat: I. Pressure and vesicularity distributions. *Journal of Volcanology and Geothermal Research*, *194*(1-3), pp.27-41.
- Burton, M.R., Mader, H.M. and Polacci, M., 2007. The role of gas percolation in quiescent degassing of persistently active basaltic volcanoes. *Earth and Planetary Science Letters*, *264*(1-2), pp.46-60.
- C Vye-Brown, RJ Brown, J Crummy, S Engwell, SC Loughlin 2019. _Volcanic history and future hazards affecting Ascension Island. *British Geological Survey Open File Report*, OR/19/026
- Cabrera, A.P. and Caffe, P.J., 2009. The Cerro Morado Andesites: Volcanic history and eruptive styles of a mafic volcanic field from northern Puna, Argentina. *Journal of South American Earth Sciences*, *28*(2), pp.113-131.
- Calder, E.S., Lavallée, Y., Kendrick, J.E. and Bernstein, M., 2015. Lava dome eruptions. In *The encyclopedia of volcanoes*(pp. 343-362). Academic Press.

- Calvari, S., Bonaccorso, A. and Ganci, G., 2021. Anatomy of a Paroxysmal Lava Fountain at Etna Volcano: The Case of the 12 March 2021, Episode. *Remote Sensing*, *13*(15), p.3052.
- Calvari, S., Cannavò, F., Bonaccorso, A., Spampinato, L. and Pellegrino, A.G., 2018. Paroxysmal explosions, lava fountains and ash plumes at Etna Volcano: Eruptive processes and hazard implications. *Frontiers in Earth Science*, *6*, p.107.
- Capaccioni, B. and Cuccoli, F., 2005. Spatter and welded air fall deposits generated by fire-fountaining eruptions: cooling of pyroclasts during transport and deposition. *Journal of volcanology and geothermal research*, *145*(3-4), pp.263-280.
- Carey, R.J., Houghton, B.F. and Thordarson, T., 2008a. Contrasting styles of welding observed in the proximal Askja 1875 eruption deposits II: local welding. *Journal of Volcanology and Geothermal Research*, *171*(1-2), pp.20-44.
- Carey, R.J., Houghton, B.F. and Thordarson, T., 2008b. Contrasting styles of welding observed in the proximal Askja 1875 eruption deposits I: Regional welding. *Journal of Volcanology and Geothermal Research*, *171*(1-2), pp.1-19.
- Caricchi, L. and Blundy, J., 2015. The temporal evolution of chemical and physical properties of magmatic systems. *Geological Society, London, Special Publications*, *422*(1), pp.1-15.
- Carracedo, J.C., Troll, V.R., Day, J.M., Geiger, H., Aulinas, M., Soler, V., Deegan, F.M., Perez-Torrado, F.J., Gisbert, G., Gazel, E. and Rodriguez-Gonzalez, A., 2022. The 2021 eruption of the Cumbre Vieja Volcanic Ridge on La Palma, Canary Islands. *Geology Today*, *38*(3), pp.94-107.
- Cas, R. and Wright, J., 1987. *Volcanic successions modern and ancient: A geological approach to processes, products and successions*. Springer Science & Business Media.
- Cas, R.A., Wolff, J.A., Martí, J., Olin, P.H., Edgar, C.J., Pittari, A. and Simmons, J.M., 2022. Tenerife, a complex end member of basaltic oceanic island volcanoes, with explosive polygenetic phonolitic calderas, and phonolitic-basaltic stratovolcanoes. *Earth-Science Reviews*, *230*, p.103990.
- Cas, R.A.F., Wright, J.V., Cas, R.A.F. and Wright, J.V., 1988. Three types of pyroclastic deposits and their eruption: an introduction. *Volcanic Successions Modern and Ancient: A geological approach to processes, products and successions*, pp.92-126.
- Cashman, K. and Blundy, J., 2000. Degassing and crystallization of ascending andesite and dacite. *Philosophical Transactions of the Royal Society of London. Series A: Mathematical, Physical and Engineering Sciences*, *358*(1770), pp.1487-1513.

- Cashman, K.V. and McConnell, S.M., 2005. Multiple levels of magma storage during the 1980 summer eruptions of Mount St. Helens, WA. *Bulletin of Volcanology*, *68*, pp.57-75.
- Cashman, K.V. and Scheu, B., 2015. Magmatic fragmentation. In *The encyclopedia of volcanoes* (pp. 459-471). Academic Press.
- Cashman, K.V. and Sparks, R.S.J., 2013. How volcanoes work: A 25 year perspective. *Bulletin*, *125*(5-6), pp.664-690.
- Cashman, K.V., 1992. Groundmass crystallization of Mount St. Helens dacite, 1980–1986: a tool for interpreting shallow magmatic processes. *Contributions to Mineralogy and Petrology*, *109*(4), pp.431-449.
- Cashman, K.V., 1993. Relationship between plagioclase crystallization and cooling rate in basaltic melts. *Contributions to Mineralogy and Petrology*, *113*(1), pp.126-142.
- Cashman, K.V., 2020. Crystal size distribution (CSD) analysis of volcanic samples: advances and challenges. *Frontiers in earth science*, *8*, p.291.
- Cassidy, M., Cole, P.D., Hicks, K.E., Varley, N.R., Peters, N. and Lerner, A.H., 2015. Rapid and slow: Varying magma ascent rates as a mechanism for Vulcanian explosions. *Earth and Planetary Science Letters*, *420*, pp.73-84.
- Cassidy, M., Manga, M., Cashman, K. and Bachmann, O., 2018. Controls on explosive-effusive volcanic eruption styles. *Nature communications*, *9*(1), p.2839.
- Chamberlain, K.J., Barclay, J., Preece, K., Brown, R. and McIntosh, I., 2020. Deep and disturbed: conditions for formation and eruption of a mingled rhyolite at Ascension Island, South Atlantic. *Volcanica*, *3*(1), pp.139-153.
- Chamberlain, K.J., Barclay, J., Preece, K., Brown, R.J. and Davidson, J.P., 2016. Origin and evolution of silicic magmas at ocean islands: Perspectives from a zoned fall deposit on Ascension Island, South Atlantic. *Journal of Volcanology and Geothermal Research*, *327*, pp.349-360.
- Chamberlain, K.J., Barclay, J., Preece, K.J., Brown, R.J. and Davidson, J.P., 2019. Lower crustal heterogeneity and fractional crystallization control evolution of small-volume magma batches at ocean island volcanoes (Ascension Island, South Atlantic). *Journal of Petrology*, *60*(8), pp.1489-1522.
- Chaput, M., Famin, V. and Michon, L., 2014. Deformation of basaltic shield volcanoes under cointrusive stress permutations. *Journal of Geophysical Research: Solid Earth*, *119*(1), pp.274-301.

- Cioni, R. and Pistolesi, M., 2014. Reply to the Comment by Delmelle et al.(2013) on" Scavenging of sulfur, halogens and trace metals by volcanic ash: The 2010 Eyjafjallajokull eruption" by Bagnato et al.(2013). *GEOCHIMICA ET COSMOCHIMICA ACTA*, *127*, pp.385-389.
- Cioni, R., Bertagnini, A., Santacroce, R. and Andronico, D., 2008. Explosive activity and eruption scenarios at Somma-Vesuvius (Italy): towards a new classification scheme. *Journal of Volcanology and Geothermal Research*, *178*(3), pp.331-346.
- Clague, D.A. and Dixon, J.E., 2000. Extrinsic controls on the evolution of Hawaiian ocean island volcanoes. *Geochemistry, Geophysics, Geosystems*, *1*(4).
- Clarke, A.B., 2013. Unsteady explosive activity: Vulcanian eruptions. *Modeling volcanic processes. The physics and mathematics of volcanism*, pp.129-152.
- Clarke, A.B., Ongaro, T.E. and Belousov, A., 2015. Vulcanian eruptions. In *The encyclopedia of volcanoes* (pp. 505-518). Academic Press.
- Clarke, A.B., Stephens, S., Teasdale, R., Sparks, R.S.J. and Diller, K., 2007. Petrologic constraints on the decompression history of magma prior to Vulcanian explosions at the Soufrière Hills volcano, Montserrat. *Journal of Volcanology and Geothermal Research*, *161*(4), pp.261-274.
- Clarke, H., Troll, V.R. and Carracedo, J.C., 2009. Phreatomagmatic to strombolian eruptive activity of basaltic cinder cones: Montana Los Erales, Tenerife, Canary Islands. *Journal of Volcanology and Geothermal Research*, *180*(2-4), pp.225-245.
- Conte, A.M., Perinelli, C. and Trigila, R., 2006. Cooling kinetics experiments on different Stromboli lavas: Effects on crystal morphologies and phases composition. *Journal of Volcanology and Geothermal Research*, *155*(3-4), pp.179-200.
- Corsaro, R.A. and Miraglia, L., 2022. Near real-time petrologic monitoring on volcanic glass to infer magmatic processes during the February–April 2021 paroxysms of the South-East Crater, Etna. *Frontiers in Earth Science*, *10*, p.828026.
- Couch, S., Harford, C.L., Sparks, R.S.J. and Carroll, M.R., 2003. Experimental constraints on the conditions of formation of highly calcic plagioclase microlites at the Soufrire Hills Volcano, Montserrat. *Journal of Petrology*, *44*(8), pp.1455-1475.
- D'Mello, N.G., Zellmer, G.F., Negrini, M., Kereszturi, G., Procter, J., Stewart, R., Prior, D., Usuki, M. and Iizuka, Y., 2021. Deciphering magma storage and ascent processes of Taranaki, New Zealand, from the complexity of amphibole breakdown textures. *Lithos*, *398*, p.106264.

- D'Mello, N.G., Zellmer, G.F., Negrini, M., Kereszturi, G., Procter, J., Stewart, R., Prior, D., Usuki, M. and Iizuka, Y., 2021. Deciphering magma storage and ascent processes of Taranaki, New Zealand, from the complexity of amphibole breakdown textures. *Lithos*, *398*, p.106264.
- D'Oriano, C., Bertagnini, A., Cioni, R. and Pompilio, M., 2014. Identifying recycled ash in basaltic eruptions. *Scientific reports*, *4*(1), p.5851.
- Daly, R. (1925). The Geology of Ascension Island. *Proceedings of the American Academy of Arts and Sciences, 60*(1), pp 3-80.
- Davies, B.V., Brown, R.J., Barclay, J., Scarrow, J.H. and Herd, R.A., 2021. Rapid eruptive transitions from low to high intensity explosions and effusive activity: insights from textural analysis of a small-volume trachytic eruption, Ascension Island, South Atlantic. *Bulletin of Volcanology*, *83*, pp.1-40.
- De Angelis, S.H., Larsen, J., Coombs, M., Dunn, A. and Hayden, L., 2015. Amphibole reaction rims as a record of pre-eruptive magmatic heating: an experimental approach. *Earth and Planetary Science Letters*, *426*, pp.235-245.
- Deer, W.A., Howie, R.A. and Zussman, J., 2013. *An introduction to the rock-forming minerals*. Mineralogical Society of Great Britain and Ireland.
- DePaolo, D.J., 1981. Trace element and isotopic effects of combined wallrock assimilation and fractional crystallization. *Earth and planetary science letters*, *53*(2), pp.189-202.
- Déruelle, B., Ngounouno, I. and Demaiffe, D., 2007. The ‘Cameroon Hot Line’(CHL): a unique example of active alkaline intraplate structure in both oceanic and continental lithospheres. *Comptes Rendus Geoscience*, *339*(9), pp.589-600.

- Déruelle, B., Ngounouno, I. and Demaiffe, D., 2007. The ‘Cameroon Hot Line’(CHL): a unique example of active alkaline intraplate structure in both oceanic and continental lithospheres. *Comptes Rendus Geoscience*, *339*(9), pp.589-600.

- Devine, J.D., Rutherford, M.J. and Gardner, J.E., 1998. Petrologic determination of ascent rates for the 1995–1997 Soufriere Hills Volcano andesitic magma. *Geophysical Research Letters*, *25*(19), pp.3673-3676.
- Di Roberto, A., Bertagnini, A., Pompilio, M. and Bisson, M., 2014. Pyroclastic density currents at Stromboli volcano (Aeolian Islands, Italy): a case study of the 1930 eruption. *Bulletin of volcanology*, *76*(6), pp.1-14.
- Di Traglia, F., Cimarelli, C., de Rita, D.O.N.A.T.E.L.L.A. and Torrente, D.G., 2009. Changing eruptive styles in basaltic explosive volcanism: examples from Croscat complex scoria cone,

Garrotxa Volcanic Field (NE Iberian Peninsula). *Journal of Volcanology and Geothermal Research*, *180*(2-4), pp.89-109.

- Dieterich, J.H., 1988. Growth and persistence of Hawaiian volcanic rift zones. *Journal of Geophysical Research: Solid Earth*, *93*(B5), pp.4258-4270.
- Diller, K., Clarke, A.B., Voight, B. and Neri, A., 2006. Mechanisms of conduit plug formation: Implications for vulcanian explosions. *Geophysical Research Letters*, *33*(20).
- Dominguez, L., Pioli, L., Bonadonna, C., Connor, C.B., Andronico, D., Harris, A.J.L. and Ripepe, M., 2016. Quantifying unsteadiness and dynamics of pulsatory volcanic activity. *Earth and planetary science letters*, *444*, pp.160-168.
- Druitt, T.H., Young, S.R., Baptie, B., Bonadonna, C., Calder, E.S., Clarke, A.B., Cole, P.D., Harford, C.L., Herd, R.A., Luckett, R. and Ryan, G., 2002. Episodes of cyclic Vulcanian explosive activity with fountain collapse at Soufrière Hills Volcano, Montserrat.
- Dufek, J. and Bachmann, O., 2010. Quantum magmatism: Magmatic compositional gaps generated by melt-crystal dynamics. *Geology*, *38*(8), pp.687-690.
- Edwards, B., Belousov, A., Belousova, M., Volynets, A., Melnikov, D., Chirkov, S., Senyukov, S., Gordeev, E., Muraviev, Y., Izbekov, P. and Demianchuk, Y., 2013. Another “Great Tolbachik” Eruption?. *Eos, Transactions American Geophysical Union*, *94*(21), pp.189-191.
- Eibl, E.P., Thordarson, T., Höskuldsson, Á., Gudnason, E.Á., Dietrich, T., Hersir, G.P. and Ágústsdóttir, T., 2022. Evolving Shallow-conduit Container Affects the Lava Fountaining during the 2021 Fagradalsfjall Eruption, Iceland.
- Evangelidis, C.P., Minshull, T.A. and Henstock, T.J., 2004. Three-dimensional crustal structure of Ascension Island from active source seismic tomography. *Geophysical Journal International*, *159*(1), pp.311-325.
- Eychenne, J., Le Pennec, J.L., Troncoso, L., Gouhier, M. and Nedelec, J.M., 2012. Causes and consequences of bimodal grain-size distribution of tephra fall deposited during the August 2006 Tungurahua eruption (Ecuador). *Bulletin of Volcanology*, *74*, pp.187-205.
- Faneros, G. and Arnold, F., 2003, September. Geomorphology of Two Seamounts Offshore Ascension Island, South Atlantic Ocean. In *Oceans 2003. Celebrating the Past... Teaming Toward the Future (IEEE Cat. No. 03CH37492)* (Vol. 1, pp. 39-49). IEEE.
- Fedotov, S.A., Chirkov, A.M., Gusev, N.A., Kovalev, G.N. and Slezin, Y.B., 1980. The large fissure eruption in the region of Plosky Tolbachik volcano in Kamchatka, 1975–1976. *Bulletin Volcanologique*, *43*(1), pp.47-60.

- Ferla, P. and Meli, C., 2006. Evidence of magma mixing in the 'Daly Gap'of alkaline suites: a case study from the enclaves of Pantelleria (Italy). *Journal of Petrology*, *47*(8), pp.1467-1507.
- Fisher, R.V., Schmincke, H.U., Fisher, R.V. and Schmincke, H.U., 1984. Alteration of volcanic glass. *Pyroclastic rocks*, pp.312-345.
- Fiske, R.S., Rose, T.R., Swanson, D.A., Champion, D.E. and McGeehin, J.P., 2009. Kulanaokuaiki Tephra (ca. AD 400–1000): Newly recognized evidence for highly explosive eruptions at Kīlauea Volcano, Hawai 'i. *Geological Society of America Bulletin*, *121*(5-6), pp.712-728.
- Flood, S.H. and Knapp, W.J., 1968. Structural characteristics of liquid mixtures of feldspar and silica. *Journal of the American Ceramic Society*, *51*(5), pp.259-263.
- Formenti, Y., Druitt, T.H. and Kelfoun, K., 2003. Characterisation of the 1997 Vulcanian explosions of Soufrière Hills Volcano, Montserrat, by video analysis. *Bulletin of Volcanology*, *65*, pp.587-605.
- Foster, A., 2020. *An Insight into the Origin of Fluidal Obsidian Pyroclasts from a Basaltic Fissure Eruption, Ascension Island, South Atlantic* (Masters by Research dissertation, Durham University).
- Freise, M., Holtz, F., Koepke, J., Scoates, J. and Leyrit, H., 2003. Experimental constraints on the storage conditions of phonolites from the Kerguelen Archipelago. *Contributions to Mineralogy and Petrology*, *145*, pp.659-672.
- Freund, S., Beier, C., Krumm, S. and Haase, K.M., 2013. Oxygen isotope evidence for the formation of andesitic–dacitic magmas from the fast-spreading Pacific–Antarctic Rise by assimilation–fractional crystallisation. *Chemical Geology*, *347*, pp.271-283.
- Freundt, A. and Schmincke, H.U., 1995. Petrogenesis of rhyolite-trachyte-basalt composite ignimbrite P1, Gran Canada, Canary Islands. *Journal of Geophysical Research: Solid Earth*, *100*(B1), pp.455-474.
- Frey, H.M., Manon, M.R., Barclay, J., Davies, B.V., Walters, S.A., Cole, P.D., Christopher, T.E. and Joseph, E.P., 2024. Petrology of the explosive deposits from the April 2021 eruption of La Soufrière volcano, St Vincent: a time-series analysis of microlites. *Geological Society, London, Special Publications*, *539*(1), pp.SP539-2022.
- Gabellini, P., Cioni, R., Geshi, N., Pistolesi, M., Miwa, T., Lacanna, G. and Ripepe, M., 2022. Eruptive dynamics and fragmentation mechanisms during cyclic Vulcanian activity at Sakurajima

volcano (Japan): Insights from ash texture analysis. *Journal of Volcanology and Geothermal Research*, *428*, p.107582.

- Gabrieli, A., Wilson, L. and Lane, S., 2015. Volcano–tectonic interactions as triggers of volcanic eruptions. *Proceedings of the Geologists' Association*, *126*(6), pp.675-682
- Gansecki, C., Lee, R.L., Shea, T., Lundblad, S.P., Hon, K. and Parcheta, C., 2019. The tangled tale of Kīlauea’s 2018 eruption as told by geochemical monitoring. *Science*, *366*(6470), p.eaaz0147.
- Gardner, J.E., Rutherford, M., Carey, S. and Sigurdsson, H., 1995. Experimental constraints on pre-eruptive water contents and changing magma storage prior to explosive eruptions of Mount St Helens volcano. *Bulletin of Volcanology*, *57*, pp.1-17.
- Gaunt, H.E., Burgisser, A., Mothes, P.A., Browning, J., Meredith, P.G., Criollo, E. and Bernard, B., 2020. Triggering of the powerful 14 july 2013 vulcanian explosion at tungurahua volcano, Ecuador. *Journal of Volcanology and Geothermal Research*, *392*, p.106762.

- Gaunt, H.E., Burgisser, A., Mothes, P.A., Browning, J., Meredith, P.G., Criollo, E. and Bernard, B., 2020. Triggering of the powerful 14 july 2013 vulcanian explosion at tungurahua volcano, Ecuador. *Journal of Volcanology and Geothermal Research*, *392*, p.106762.

- Geist, D., Howard, K.A. and Larson, P., 1995. The generation of oceanic rhyolites by crystal fractionation: the basalt-rhyolite association at Volcán Alcedo, Galápagos Archipelago. *Journal of Petrology*, *36*(4), pp.965-982.
- Gevrek, A.İ. and Kazanci, N., 2000. A Pleistocene, pyroclastic-poor maar from central Anatolia, Turkey: influence of a local fault on a phreatomagmatic eruption. *Journal of Volcanology and Geothermal Research*, *95*(1-4), pp.309-317.
- Giordano, D., Russell, J.K. and Dingwell, D.B., 2008. Viscosity of magmatic liquids: a model. *Earth and Planetary Science Letters*, *271*(1-4), pp.123-134.
- Gonnermann, H.M., Manga, M. and Fagents, S.A., 2013. Dynamics of magma ascent in the volcanic conduit. *Modeling volcanic processes: The physics and mathematics of volcanism*, pp.55-84.
- Gregg, T.K., 2017. Patterns and processes: Subaerial lava flow morphologies: A review. *Journal of Volcanology and Geothermal Research*, *342*, pp.3-12.

- Gregg, T.K., 2017. Patterns and processes: Subaerial lava flow morphologies: A review. *Journal of Volcanology and Geothermal Research*, *342*, pp.3-12.

- Grogan, S.E. and Reavy, R.J., 2002. Disequilibrium textures in the Leinster Granite Complex, SE Ireland: evidence for acid-acid magma mixing. *Mineralogical Magazine*, *66*(6), pp.929-939.
- Grove, T.L., Kinzler, R.J. and Bryan, W.B., 1992. Fractionation of mid-ocean ridge basalt (MORB). *Washington DC American geophysical union geophysical monograph series*, *71*, pp.281-310.
- Gualda, G.A., Ghiorso, M.S., Lemons, R.V. and Carley, T.L., 2012. Rhyolite-MELTS: a modified calibration of MELTS optimized for silica-rich, fluid-bearing magmatic systems. *Journal of Petrology*, *53*(5), pp.875-890.
- Guest, J.E., Kilburn, C.R.J., Pinkerton, H. and Duncan, A.M., 1987. The evolution of lava flow-fields: observations of the 1981 and 1983 eruptions of Mount Etna, Sicily. *Bulletin of Volcanology*, *49*, pp.527-540.
- Guilbaud, M.N., Self, S., Thordarson, T. and Blake, S., 2005. Morphology, surface structures, and emplacement of lavas produced by Laki, AD 1783–1784. *Geological Society of America Special Papers*, *396*, pp.81-102.
- Haase, K.M., Stroncik, N.A., Hékinian, R. and Stoffers, P., 2005. Nb-depleted andesites from the Pacific-Antarctic Rise as analogs for early continental crust. *Geology*, *33*(12), pp.921-924.
- Hammer, J.E. and Rutherford, M.J., 2002. An experimental study of the kinetics of decompression-induced crystallization in silicic melt. *Journal of Geophysical Research: Solid Earth*, *107*(B1), pp.ECV-8.
- Hammer, J.E., Cashman, K.V. and Voight, B., 2000. Magmatic processes revealed by textural and compositional trends in Merapi dome lavas. *Journal of Volcanology and Geothermal Research*, *100*(1-4), pp.165-192.
- Hammer, J.E., Cashman, K.V., Hoblitt, R.P. and Newman, S., 1999. Degassing and microlite crystallization during pre-climactic events of the 1991 eruption of Mt. Pinatubo, Philippines. *Bulletin of Volcanology*, *60*, pp.355-380.
- Harris, A.J. and Rowland, S.K., 2015. Lava flows and rheology. In *The encyclopedia of volcanoes* (pp. 321-342). Academic Press.
- Harris, A.J., Favalli, M., Mazzarini, F. and Hamilton, C.W., 2009. Construction dynamics of a lava channel. *Bulletin of Volcanology*, *71*, pp.459-474.
- Harris, A.J., Rowland, S.K., Villeneuve, N. and Thordarson, T., 2017. Pāhoehoe,‘a ‘ā, and block lava: an illustrated history of the nomenclature. *Bulletin of Volcanology*, *79*, pp.1-34.

- Harris, C., 1983. The petrology of lavas and associated plutonic inclusions of Ascension Island. *Journal of Petrology*, *24*(4), pp.424-470.
- Head III, J.W. and Wilson, L., 1987. Lava fountain heights at Pu'u'O'o, Kilauea, Hawaii: Indicators of amount and variations of exsolved magma volatiles. *Journal of Geophysical Research: Solid Earth*, *92*(B13), pp.13715-13719.
- Head III, J.W. and Wilson, L., 1989. Basaltic pyroclastic eruptions: influence of gas-release patterns and volume fluxes on fountain structure, and the formation of cinder cones, spatter cones, rootless flows, lava ponds and lava flows. *Journal of Volcanology and Geothermal Research*, *37*(3-4), pp.261-271.
- Heiken, G. and Wohletz, K., 1987. Tephra deposits associated with silicic domes and lava flows. *Geol Soc Am Spec Pap*, *212*, pp.55-76.
- Helz, R.T., 1976. Phase relations of basalts in their melting ranges at P H_2O= 5 kb. Part II. Melt compositions. *Journal of Petrology*, *17*(2), pp.139-193.
- Henry, C.D., Price, J.G., Parker, D.F. and Wolff, J.A., 1989. Mid-Tertiary silicic alkalic magmatism of Trans-Pecos Texas: rheomorphic tuffs and extensive silicic lavas. *Field excursions to volcanic terranes in the western United States*, *1*, pp.231-274.
- Herd, R.A., Edmonds, M. and Bass, V.A., 2005. Catastrophic lava dome failure at Soufrière Hills volcano, Montserrat, 12–13 July 2003. *Journal of Volcanology and Geothermal Research*, *148*(3-4), pp.234-252.

- Herd, R.A., Edmonds, M. and Bass, V.A., 2005. Catastrophic lava dome failure at Soufrière Hills volcano, Montserrat, 12–13 July 2003. *Journal of Volcanology and Geothermal Research*, *148*(3-4), pp.234-252.

- Hibbard, M.J., 1981. The magma mixing origin of mantled feldspars. *Contributions to Mineralogy and Petrology*, *76*(2), pp.158-170.
- Hicks, A., Barclay, J., Mark, D.F. and Loughlin, S., 2012. Tristan da Cunha: constraining eruptive behavior using the 40Ar/39Ar dating technique. *Geology*, *40*(8), pp.723-726.
- Higgins, M.D., 1994. Determination of crystal morphology and size from bulk measurements on thin sections: numerical modelling. *American Mineralogist*, *79*, pp.113-119.
- Higgins, M.D., 1996. Crystal size distributions and other quantitative textural measurements in lavas and tuff from Egmont volcano (Mt. Taranaki), New Zealand. *Bulletin of Volcanology*, *58*, pp.194-204.

- Higgins, M.D., 2002. Closure in crystal size distributions (CSD), verification of CSD calculations, and the significance of CSD fans. *American Mineralogist*, *87*(1), pp.171-175.
- Higgins, M.D., 2006. Verification of ideal semi-logarithmic, lognormal or fractal crystal size distributions from 2D datasets. *Journal of Volcanology and Geothermal Research*, *154*(1-2), pp.8-16.
- Hoblitt, R.P. and Harmon, R.S., 1993. Bimodal density distribution of cryptodome dacite from the 1980 eruption of Mount St. Helens, Washington. *Bulletin of Volcanology*, *55*, pp.421-437.
- Hoblitt, R.P., Crandell, D.R. and Mullineaux, D.R., 1980. Mount St. Helens eruptive behavior during the past 1,500 yr. *Geology*, *8*(11), pp.555-559.
- Hoernle, K., Hauff, F., Kokfelt, T.F., Haase, K., Garbe-Schönberg, D. and Werner, R., 2011. On- and off-axis chemical heterogeneities along the South Atlantic Mid-Ocean-Ridge (5–11° S): shallow or deep recycling of ocean crust and/or intraplate volcanism?. *Earth and Planetary Science Letters*, *306*(1-2), pp.86-97.
- Houghton, B. and Carey, R.J., 2015. Pyroclastic fall deposits. In *The encyclopedia of volcanoes* (pp. 599-616). Academic Press.
- Houghton, B., White, J.D. and Van Eaton, A.R., 2015. Phreatomagmatic and related eruption styles. In *The Encyclopedia of Volcanoes* (pp. 537-552). Academic Press.
- Houghton, B.F. and Gonnermann, H.M., 2008. Basaltic explosive volcanism: constraints from deposits and models. *Geochemistry*, *68*(2), pp.117-140.
- Houghton, B.F. and Hackett, W.R., 1984. Strombolian and phreatomagmatic deposits of Ohakune Craters, Ruapehu, New Zealand: a complex interaction between external water and rising basaltic magma. *Journal of volcanology and geothermal research*, *21*(3-4), pp.207-231.
- Houghton, B.F. and Schmincke, H.U., 1986. Mixed deposits of simultaneous strombolian and phreatomagmatic volcanism: Rothenberg volcano, east Eifel volcanic field. *Journal of volcanology and geothermal research*, *30*(1-2), pp.117-130.
- Houghton, B.F. and Schmincke, H.U., 1989. Rothenberg scoria cone, East Eifel: a complex Strombolian and phreatomagmatic volcano. *Bulletin of Volcanology*, *52*, pp.28-48.
- Houghton, B.F. and Wilson, C.J.N., 1989. A vesicularity index for pyroclastic deposits. *Bulletin of volcanology*, *51*(6), pp.451-462.
- Houghton, B.F., Taddeucci, J., Andronico, D., Gonnermann, H.M., Pistolesi, M., Patrick, M.R., Orr, T.R., Swanson, D.A., Edmonds, M., Gaudin, D. and Carey, R.J., 2016. Stronger or longer: Discriminating between Hawaiian and Strombolian eruption styles. *Geology*, *44*(2), pp.163-166.

- Houghton, Bruce F., Caroline M. Tisdale, Edward W. Llewellin, Jacopo Taddeucci, Tim R. Orr, Brett H. Walker, and Matthew R. Patrick. "The birth of a Hawaiian fissure eruption." *Journal of Geophysical Research: Solid Earth* 126, no. 1 (2021): e2020JB020903.
- Hulme, G., 1974. The interpretation of lava flow morphology. *Geophysical Journal International*, *39*(2), pp.361-383.
- Huppert, H.E. and Sparks, R.S.J., 1988. The generation of granitic magmas by intrusion of basalt into continental crust. *Journal of Petrology*, *29*(3), pp.599-624.
- Isgett, S.J., Houghton, B.F., Fagents, S.A., Biass, S., Burgisser, A. and Arbaret, L., 2017. Eruptive and shallow conduit dynamics during Vulcanian explosions: insights from the Episode IV block field of the 1912 eruption of Novarupta, Alaska. *Bulletin of Volcanology*, *79*(8), pp.1-18.
- Jarosewich, E., Nelen, J.A. and Norberg, J.A., 1980. Reference samples for electron microprobe analysis. *Geostandards Newsletter*, *4*(1), pp.43-47.
- Jeffery, A.J. and Gertisser, R., 2018. Peralkaline felsic magmatism of the Atlantic Islands. *Frontiers in Earth Science*, *6*, p.145.
- Jicha, B.R., Singer, B.S. and Valentine, M.J., 2013. 40Ar/39Ar geochronology of subaerial Ascension Island and a re-evaluation of the temporal progression of basaltic to rhyolitic volcanism. *Journal of Petrology*, *54*(12), pp.2581-2596.
- Jutzeler, M., White, J.D., Proussevitch, A.A. and Gordee, S.M., 2016. Vesiculation and fragmentation history in a submarine scoria cone-forming eruption, an example from Nishiizu (Izu Peninsula, Japan). *Bulletin of Volcanology*, *78*, pp.1-25.
- Kar, A., Weaver, B., Davidson, J. and Colucci, M., 1998. Origin of differentiated volcanic and plutonic rocks from Ascension Island, South Atlantic Ocean. *Journal of Petrology*, *39*(5), pp.1009-1024.
- Kearns, S., no year. Labradorite. Bristol. Sr by ICP-MS. Block LPL-03. Oxide and Elemental Composition
- Keiding, J.K. and Sigmarsson, O., 2012. Geothermobarometry of the 2010 Eyjafjallajökull eruption: New constraints on Icelandic magma plumbing systems. *Journal of Geophysical Research: Solid Earth*, *117*(B9).
- Kent, A.J., 2014. Preferential eruption of andesitic magmas: Implications for volcanic magma fluxes at convergent margins. *Geological Society, London, Special Publications*, *385*(1), pp.257-280.

- Kent, A.J., 2014. Preferential eruption of andesitic magmas: Implications for volcanic magma fluxes at convergent margins. *Geological Society, London, Special Publications*, *385*(1), pp.257-280.
- Kilburn, C., 1990. Surfaces of aa flow-fields on Mount Etna, Sicily: morphology, rheology, crystallization and scaling phenomena. *Lava flows and domes: emplacement mechanisms and hazard implications*, pp.129-156.
- Kilburn, C.R. and Sammonds, P.R., 2005. Maximum warning times for imminent volcanic eruptions. *Geophysical Research Letters*, *32*(24).
- Kilgour, G.N., Saunders, K.E., Blundy, J.D., Cashman, K.V., Scott, B.J. and Miller, C.A., 2014. Timescales of magmatic processes at Ruapehu volcano from diffusion chronometry and their comparison to monitoring data. *Journal of Volcanology and Geothermal Research*, *288*, pp.62-75.
- Kimura, J.I., Tateno, M. and Osaka, I., 2005. Geology and geochemistry of Karasugasen lava dome, Daisen–Hiruzen volcano group, southwest Japan. *Island Arc*, *14*(2), pp.115-136.
- Kirkpatrick, R.J., 1977. Nucleation and growth of plagioclase, Makaopuhi and Alae lava lakes, Kilauea Volcano, Hawaii. *Geological Society of America Bulletin*, *88*(1), pp.78-84.
- Klingelhöfer, F., Minshull, T.A., Blackman, D.K., Harben, P. and Childers, V., 2001. Crustal structure of Ascension Island from wide-angle seismic data: implications for the formation of near-ridge volcanic islands. *Earth and Planetary Science Letters*, *190*(1-2), pp.41-56.
- Klügel, A., Longpré, M.A., García-Cañada, L. and Stix, J., 2015. Deep intrusions, lateral magma transport and related uplift at ocean island volcanoes. *Earth and Planetary Science Letters*, *431*, pp.140-149.
- Kósik, S., Németh, K., Kereszturi, G., Procter, J.N., Zellmer, G.F. and Geshi, N., 2016. Phreatomagmatic and water-influenced Strombolian eruptions of a small-volume parasitic cone complex on the southern ringplain of Mt. Ruapehu, New Zealand: facies architecture and eruption mechanisms of the Ohakune Volcanic Complex controlled by an unstable fissure eruption. *Journal of Volcanology and Geothermal Research*, *327*, pp.99-115.
- Krastel, S. and Schmincke, H.U., 2002. Crustal structure of northern Gran Canaria, Canary Islands, deduced from active seismic tomography. *Journal of Volcanology and Geothermal Research*, *115*(1-2), pp.153-177.

- Kubanek, J., Richardson, J.A., Charbonnier, S.J. and Connor, L.J., 2015. Lava flow mapping and volume calculations for the 2012–2013 Tolbachik, Kamchatka, fissure eruption using bistatic TanDEM-X InSAR. *Bulletin of Volcanology*, *77*, pp.1-13.
- La Spina, G., Arzilli, F., Llewellin, E.W., Burton, M.R., Clarke, A.B., Vitturi, M.D.M., Polacci, M., Hartley, M.E., Di Genova, D. and Mader, H.M., 2021. Explosivity of basaltic lava fountains is controlled by magma rheology, ascent rate and outgassing. *Earth and Planetary Science Letters*, *553*, p.116658.
- La Spina, G., Burton, M., de'Michieli Vitturi, M. and Arzilli, F., 2016. Role of syn-eruptive plagioclase disequilibrium crystallization in basaltic magma ascent dynamics. *Nature communications*, *7*(1), p.13402.
- La Spina, G., Clarke, A.B., Vitturi, M.D.M., Burton, M., Allison, C.M., Roggensack, K. and Alfano, F., 2019. Conduit dynamics of highly explosive basaltic eruptions: The 1085 CE Sunset Crater sub-Plinian events. *Journal of Volcanology and Geothermal Research*, *387*, p.106658.
- Lakroud, K., Remmal, T., El Amrani, I., Mountaj, S., El Kamel, F., de Vries, B.V.W., Boivin, P., Balcone-Boissard, H., Makhoukhi, S. and Soufi, M., 2019. Monogenetic Strombolian Activity at Aguelmane Sidi Ali Volcano (Middle Atlas Volcanic Province, Morocco). *Geographical Bulletin*, *60*(2).
- Landi, P., Métrich, N., Bertagnini, A. and Rosi, M., 2004. Dynamics of magma mixing and degassing recorded in plagioclase at Stromboli (Aeolian Archipelago, Italy). *Contributions to Mineralogy and Petrology*, *147*, pp.213-227.
- Lanzafame, G., Casetta, F., Giacomoni, P.P., Coltorti, M. and Ferlito, C., 2021. The Rare Trachyandesitic Lavas at Mount Etna: A Case Study to Investigate Eruptive Process and Propose a New Interpretation for Magma Genesis. *Minerals*, *11*(3), p.333.
- Lara, L.E., Moreno H., 2008. Tuff cones and maars along the Liquiñe-Ofqui Fault Zone (Southern Andes, Chile): tectonic controls for phreatomagmatic eruptions? IAVCEI – CVS – IAS 3IMC Conference Abstract.
- Lara, L.E., Naranjo, J.A. and Moreno, H., 2004. Rhyodacitic fissure eruption in Southern Andes (Cordón Caulle; 40.5 S) after the 1960 (Mw: 9.5) Chilean earthquake: a structural interpretation. *Journal of Volcanology and Geothermal Research*, *138*(1-2), pp.127-138.
- Lautze, N.C. and Houghton, B.F., 2005. Physical mingling of magma and complex eruption dynamics in the shallow conduit at Stromboli volcano, Italy. *Geology*, *33*(5), pp.425-428.

- Le Roex, A.P., Cliff, R.A. and Adair, B.J.I., 1990. Tristan da Cunha, South Atlantic: geochemistry and petrogenesis of a basanite-phonolite lava series. *Journal of Petrology*, *31*(4), pp.779-812.
- Legendre, C., Maury, R.C., Savanier, D., Cotten, J., Chauvel, C., Hémond, C., Bollinger, C., Guille, G., Blais, S. and Rossi, P., 2005. The origin of intermediate and evolved lavas in the Marquesas archipelago: an example from Nuku Hiva island (French Polynesia). *Journal of Volcanology and Geothermal Research*, *143*(4), pp.293-317.
- Lindoo, A., Larsen, J.F., Cashman, K.V. and Oppenheimer, J., 2017. Crystal controls on permeability development and degassing in basaltic andesite magma. *Geology*, *45*(9), pp.831-834.
- Liu, E.J., Cashman, K.V., Rust, A.C. and Höskuldsson, A., 2017. Contrasting mechanisms of magma fragmentation during coeval magmatic and hydromagmatic activity: the Hverfjall Fires fissure eruption, Iceland. *Bulletin of Volcanology*, *79*(10), p.68.
- Loewen, M.W., Dietterich, H.R., Graham, N. and Izbekov, P., 2021. Evolution in eruptive style of the 2018 eruption of Veniaminof volcano, Alaska, reflected in groundmass textures and remote sensing. *Bulletin of Volcanology*, *83*(11), p.72.
- Lofgren, G., 1974. An experimental study of plagioclase crystal morphology; isothermal crystallization. *American journal of Science*, *274*(3), pp.243-273.
- Longpré, M.A., Klügel, A., Diehl, A. and Stix, J., 2014. Mixing in mantle magma reservoirs prior to and during the 2011–2012 eruption at El Hierro, Canary Islands. *Geology*, *42*(4), pp.315-318.
- Lormand, C., Zellmer, G.F., Kilgour, G.N., Németh, K., Palmer, A.S., Sakamoto, N., Yurimoto, H., Kuritani, T., Iizuka, Y. and Moebis, A., 2020. Slow ascent of unusually hot intermediate magmas triggering Strombolian to sub-Plinian eruptions. *Journal of Petrology*, *61*(10), p.egaa077.
- Macdonald, G.A., 1953. Pahoehoe, aa, and block lava. *American Journal of Science*, *251*(3), pp.169-191.
- Macdonald, R., Belkin, H.E., Fitton, J.G., Rogers, N.W., Nejbert, K., Tindle, A.G. and Marshall, A.S., 2008. The roles of fractional crystallization, magma mixing, crystal mush remobilization and volatile–melt interactions in the genesis of a young basalt–peralkaline rhyolite suite, the Greater Olkaria Volcanic Complex, Kenya Rift Valley. *Journal of Petrology*, *49*(8), pp.1515-1547.
- Magee, C., Stevenson, C.T., Ebmeier, S.K., Keir, D., Hammond, J.O., Gottsmann, J.H., Whaler, K.A., Schofield, N., Jackson, C.A., Petronis, M.S. and O'driscoll, B., 2018. Magma plumbing systems: a geophysical perspective. *Journal of Petrology*, *59*(6), pp.1217-1251.

- Magee, C., Stevenson, C.T., Ebmeier, S.K., Keir, D., Hammond, J.O., Gottsmann, J.H., Whaler, K.A., Schofield, N., Jackson, C.A., Petronis, M.S. and O'driscoll, B., 2018. Magma plumbing systems: a geophysical perspective. *Journal of Petrology*, *59*(6), pp.1217-1251.
- Magnall, N., James, M.R., Tuffen, H. and Vye-Brown, C., 2017. Emplacing a cooling-limited rhyolite lava flow: similarities with basaltic lava flows. *Frontiers in Earth Science*, *5*, p.44.
- Manga, M. and Brodsky, E., 2006. Seismic triggering of eruptions in the far field: Volcanoes and geysers. *Annu. Rev. Earth Planet. Sci*, *34*(1), pp.263-291.
- Mangler, M.F., Humphreys, M.C., Wadsworth, F.B., Iveson, A.A. and Higgins, M.D., 2022. Variation of plagioclase shape with size in intermediate magmas: a window into incipient plagioclase crystallisation. *Contributions to Mineralogy and Petrology*, *177*(6), p.64.
- Marsh, B.D., 1988. Crystal size distribution (CSD) in rocks and the kinetics and dynamics of crystallization: I. Theory. *Contributions to Mineralogy and Petrology*, *99*, pp.277-291.
- Martel, C. and Schmidt, B.C., 2003. Decompression experiments as an insight into ascent rates of silicic magmas. *Contributions to Mineralogy and Petrology*, *144*(4), pp.397-415.
- Martin, E. and Sigmarsson, O., 2007. Crustal thermal state and origin of silicic magma in Iceland: the case of Torfajökull, Ljósufjöll and Snæfellsjökull volcanoes. *Contributions to Mineralogy and Petrology*, *153*, pp.593-605.
- Marzocchi, W., Casarotti, E. and Piersanti, A., 2002. Modeling the stress variations induced by great earthquakes on the largest volcanic eruptions of the 20th century. *Journal of Geophysical Research: Solid Earth*, *107*(B11), pp.ESE-13.
- Mason, R.M., Starostin, A.B., Melnik, O.E. and Sparks, R.S.J., 2006. From Vulcanian explosions to sustained explosive eruptions: the role of diffusive mass transfer in conduit flow dynamics. *Journal of volcanology and geothermal research*, *153*(1-2), pp.148-165.
- Matthews, S.J., Sparks, R.S.J. and Gardeweg, M.C., 1999. The Piedras Grandes–Soncor eruptions, Lascar volcano, Chile; evolution of a zoned magma chamber in the central Andean upper crust. *Journal of Petrology*, *40*(12), pp.1891-1919.
- McDonough, W.F. and Sun, S.S., 1995. The composition of the Earth. *Chemical geology*, *120*(3-4), pp.223-253.
- Meade, F.C., Troll, V.R., Ellam, R.M., Freda, C., Font, L., Donaldson, C.H. and Klonowska, I., 2014. Bimodal magmatism produced by progressively inhibited crustal assimilation. *Nature communications*, *5*(1), p.4199.

- Medynski, S., Pik, R., Burnard, P., Dumont, S., Grandin, R., Williams, A., Blard, P.H., Schimmelpfennig, I., Vye-Brown, C., France, L. and Ayalew, D., 2016. Magmatic cycles pace tectonic and morphological expression of rifting (Afar depression, Ethiopia). *Earth and Planetary Science Letters*, *446*, pp.77-88.
- Melnik, O. and Sparks, R.S.J., 2002. Modelling of conduit flow dynamics during explosive activity at Soufrière Hills Volcano, Montserrat. *Geological Society, London, Memoirs*, *21*(1), pp.307-317.
- Melson, W.G. and Saenz, R., 1973. Volume, energy and cyclicity of eruptions of Arenal Volcano, Costa Rica. *Bulletin Volcanologique*, *37*, pp.416-437.
- Mercalli, G. and Silvestri, O., 1891. Le eruzioni dell'Isola di Vulcano incominciate il 3 agosto 1888 e terminate il 22 marzo 1890, relazione scientifica. *Ann Ufficio Centrale Metereol Geodin Ital*, *10*, pp.1-213.
- Michon, L., Ferrazzini, V., Di Muro, A., Villeneuve, N. and Famin, V., 2015. Rift zones and magma plumbing system of Piton de la Fournaise volcano: How do they differ from Hawaii and Etna? *Journal of Volcanology and Geothermal Research*, *303*, pp.112-129.
- Minshull, T.A., Ishizuka, O. and Garcia-Castellanos, D., 2010. Long-term growth and subsidence of Ascension Island: Constraints on the rheology of young oceanic lithosphere. *Geophysical Research Letters*, *37*(23).
- Miwa, T., Geshi, N. and Shinohara, H., 2013. Temporal variation in volcanic ash texture during a vulcanian eruption at the Sakurajima volcano, Japan. *Journal of volcanology and geothermal research*, *260*, pp.80-89.
- Miwa, T., Toramaru, A. and Iguchi, M., 2009. Correlations of volcanic ash texture with explosion earthquakes from vulcanian eruptions at Sakurajima volcano, Japan. *Journal of Volcanology and Geothermal Research*, *184*(3-4), pp.473-486.
- Mock, A. and Jerram, D.A., 2005. Crystal size distributions (CSD) in three dimensions: insights from the 3D reconstruction of a highly porphyritic rhyolite. *Journal of Petrology*, *46*(8), pp.1525-1541.
- Moitra, P., Gonnermann, H.M., Houghton, B.F. and Giachetti, T., 2013. Relating vesicle shapes in pyroclasts to eruption styles. *Bulletin of volcanology*, *75*(2), p.691.
- Moitra, P., Gonnermann, H.M., Houghton, B.F. and Tiwary, C.S., 2018. Fragmentation and Plinian eruption of crystallizing basaltic magma. *Earth and Planetary Science Letters*, *500*, pp.97-104.

- Morgan, D.J. and Jerram, D.A., 2006. On estimating crystal shape for crystal size distribution analysis. *Journal of Volcanology and Geothermal Research*, *154*(1-2), pp.1-7.
- Morrissey M.M., and Mastin L.G., 2000. Vulcanian eruptions. In *The encyclopedia of volcanoes* (pp. 463-475). Academic Press.
- Moschini, P., Mollo, S., Pontesilli, A., Nazzari, M., Petrone, C.M., Fanara, S., Vona, A., Gaeta, M., Romano, C. and Scarlato, P., 2023. A review of plagioclase growth rate and compositional evolution in mafic alkaline magmas: Guidelines for thermometry, hygrometry, and timescales of magma dynamics at Stromboli and Mt. Etna. *Earth-Science Reviews*, p.104399.
- Mungall, J.E. and Martin, R.F., 1995. Petrogenesis of basalt-comendite and basalt-pantellerite suites, Terceira, Azores, and some implications for the origin of ocean-island rhyolites. *Contributions to Mineralogy and Petrology*, *119*(1), pp.43-55.
- Nairn, I.A. and Self, S., 1978. Explosive eruptions and pyroclastic avalanches from Ngauruhoe in February 1975. *Journal of volcanology and geothermal research*, *3*(1-2), pp.39-60.
- Nakada, S., Zaennudin, A., Yoshimoto, M., Maeno, F., Suzuki, Y., Hokanishi, N., Sasaki, H., Iguchi, M., Ohkura, T., Gunawan, H. and Triastuty, H., 2019. Growth process of the lava dome/flow complex at Sinabung Volcano during 2013–2016. *Journal of Volcanology and Geothermal Research*, *382*, pp.120-136.
- Namiki, A., Patrick, M.R., Manga, M. and Houghton, B.F., 2021. Brittle fragmentation by rapid gas separation in a Hawaiian fountain. *Nature Geoscience*, *14*(4), pp.242-247.
- Naranjo, J.A. and Lara, L.E., 2004. August-September 2003 small vulcanian eruption at the Nevados de Chillán Volcanic Complex (36° 50'S), Southern Andes (Chile). *Revista geológica de Chile*, *31*(2), pp.359-366.
- Naranjo, J.A., Sparks, R.S.J., Stasiuk, M.V., Moreno, H. and Ablay, G.J., 1992. Morphological, structural and textural variations in the 1988–1990 andesite lava of Lonquimay Volcano, Chile. *Geological Magazine*, *129*(6), pp.657-678.
- Neave, D.A. and Putirka, K.D., 2017. A new clinopyroxene-liquid barometer, and implications for magma storage pressures under Icelandic rift zones. *American Mineralogist*, *102*(4), pp.777-794.
- Németh, K. and Cronin, S.J., 2011. Drivers of explosivity and elevated hazard in basaltic fissure eruptions: the 1913 eruption of Ambrym Volcano, Vanuatu (SW-Pacific). *Journal of volcanology and geothermal research*, *201*(1-4), pp.194-209.

- Németh, K., Martin, U. and Harangi, S., 2001. Miocene phreatomagmatic volcanism at Tihany (Pannonian Basin, Hungary). *Journal of Volcanology and Geothermal Research*, *111*(1-4), pp.111-135.
- Newhall, C.G. and Self, S., 1982. The volcanic explosivity index (VEI) an estimate of explosive magnitude for historical volcanism. *Journal of Geophysical Research: Oceans*, *87*(C2), pp.1231-1238.
- Nicholis, M.G. and Rutherford, M.J., 2004. Experimental constraints on magma ascent rate for the Crater Flat volcanic zone hawaiite. *Geology*, *32*(6), pp.489-492.
- Nielson, D.L. and Sibbett, B.S., 1996. Geology of Ascension Island, South Atlantic Ocean. *Geothermics*, *25*(4-5), pp.427-448.
- Nielson, D.L. and Stiger, S.G., 1996. Drilling and evaluation of Ascension# 1, a geothermal exploration well on Ascension Island, South Atlantic Ocean. *Geothermics*, *25*(4-5), pp.543-560.
- Niu, Y., Wilson, M., Humphreys, E.R. and O'Hara, M.J., 2011. The origin of intra-plate ocean island basalts (OIB): the lid effect and its geodynamic implications. *Journal of Petrology*, *52*(7-8), pp.1443-1468.
- Nixon, G.T., 1988. Petrology of the younger andesites and dacites of Iztaccihuatl volcano, Mexico: I. Disequilibrium phenocryst assemblages as indicators of magma chamber processes. *Journal of petrology*, *29*(2), pp.213-264.
- Okumura, S., 2011. The H2O content of andesitic magmas from three volcanoes in Japan, inferred from the infrared analysis of clinopyroxene. *European Journal of Mineralogy*, *23*(5), pp.771-778.
- Osman, S., Thomas, M., Crummy, J. and Carver, S., 2022. Investigation of geomechanical properties of tephra relevant to roof loading for application in vulnerability analyses. *Journal of Applied Volcanology*, *11*(1), pp.1-17.
- Pal, T., Mitra, S.K., Sengupta, S., Katari, A., Bandopadhyay, P.C. and Bhattacharya, A.K., 2007. Dacite–andesites of Narcondam volcano in the Andaman Sea—an imprint of magma mixing in the inner arc of the Andaman–Java subduction system. *Journal of Volcanology and Geothermal Research*, *168*(1-4), pp.93-113.
- Pallister, J.S., Trusdell, F.A., Brownfield, I.K., Siems, D.F., Budahn, J.R. and Sutley, S.F., 2005. The 2003 phreatomagmatic eruptions of Anatahan volcano—textural and petrologic features of deposits at an emergent island volcano. *Journal of Volcanology and Geothermal Research*, *146*(1-3), pp.208-225.

- Pan, R., Hou, T., Wang, X., Encarnación, J. and Botcharnikov, R., 2022. Multiple magma storage regions and open system processes revealed by chemistry and textures of the Datong tholeiitic lavas, North China Craton. *Journal of Petrology*, *63*(5), p.p 034.
- Pankhurst, M.J., Scarrow, J.H., Barbee, O.A., Hickey, J., Coldwell, B.C., Rollinson, G.K., Rodríguez-Losada, J.A., Lorenzo, A.M., Rodríguez, F., Hernández, W. and Fernández, D.C., 2022. Rapid response petrology for the opening eruptive phase of the 2021 Cumbre Vieja eruption, La Palma, Canary Islands. *Volcanica*, *5*(1), pp.1-10.
- Parcheta, C.E., Houghton, B.F. and Swanson, D.A., 2012. Hawaiian fissure fountains 1: decoding deposits—episode 1 of the 1969–1974 Mauna Ulu eruption. *Bulletin of Volcanology*, *74*(7), pp.1729-1743.
- Parcheta, C.E., Houghton, B.F. and Swanson, D.A., 2013. Contrasting patterns of vesiculation in low, intermediate, and high Hawaiian fountains: a case study of the 1969 Mauna Ulu eruption. *Journal of Volcanology and Geothermal Research*, *255*, pp.79-89.
- Parfitt, E.A. and Wilson, L., 1995. Explosive volcanic eruptions—IX. The transition between Hawaiian-style lava fountaining and Strombolian explosive activity. *Geophysical Journal International*, *121*(1), pp.226-232.
- Parfitt, E.A., 2004. A discussion of the mechanisms of explosive basaltic eruptions. *Journal of Volcanology and Geothermal Research*, *134*(1-2), pp.77-107.
- Paris, R., Ramalho, R.S., Madeira, J., Ávila, S., May, S.M., Rixhon, G., Engel, M., Brückner, H., Herzog, M., Schukraft, G. and Perez-Torrado, F.J., 2018. Mega-tsunami conglomerates and flank collapses of ocean island volcanoes. *Marine Geology*, *395*, pp.168-187.
- Paulick, H., Münker, C. and Schuth, S., 2010. The influence of small-scale mantle heterogeneities on Mid-Ocean Ridge volcanism: evidence from the southern Mid-Atlantic Ridge (7 30′ S to 11 30′ S) and Ascension Island. *Earth and Planetary Science Letters*, *296*(3-4), pp.299-310.
- Pedersen, G.B., Belart, J.M., Óskarsson, B.V., Gudmundsson, M.T., Gies, N., Högnadóttir, T., Hjartardóttir, Á.R., Pinel, V., Berthier, E., Dürig, T. and Reynolds, H.I., 2022. Volume, effusion rate, and lava transport during the 2021 Fagradalsfjall eruption: Results from near real-time photogrammetric monitoring. *Geophysical Research Letters*, *49*(13), p.e2021GL097125.
- Pedersen, G.B.M., Höskuldsson, A., Dürig, T., Thordarson, T., Jonsdottir, I., Riishuus, M.S., Óskarsson, B.V., Dumont, S., Magnússon, E., Gudmundsson, M.T. and Sigmundsson, F., 2017.

Lava field evolution and emplacement dynamics of the 2014–2015 basaltic fissure eruption at Holuhraun, Iceland. *Journal of Volcanology and Geothermal Research*, *340*, pp.155-169.

- Peltonen, P.E.T.R.I., 1990. Metamorphic olivine in picritic metavolcanics from southern Finland. *Bulletin of the Geological Society of Finland*, *62*(2), pp.99-114.
- Perugini, D., Poli, G., Christofides, G. and Eleftheriadis, G., 2003. Magma mixing in the Sithonia Plutonic Complex, Greece: evidence from mafic microgranular enclaves. *Mineralogy and Petrology*, *78*, pp.173-200.
- Peterson, D.W., 1979. Significance of the flattening of pumice fragments in ash-flow tuffs.
- Pimentel, A., Self, S., Pacheco, J.M., Jeffery, A.J. and Gertisser, R., 2021. Eruption style, emplacement dynamics and geometry of peralkaline ignimbrites: Insights from the Lajes-Angra ignimbrite formation, Terceira Island, Azores. *Frontiers in Earth Science*, *9*, p.673686.
- Pinkerton, H. and Sparks, R.S.J., 1976. The 1975 sub-terminal lavas, Mount Etna: a case history of the formation of a compound lava field. *Journal of Volcanology and Geothermal Research*, *1*(2), pp.167-182.
- Pioli, L. and Harris, A.J., 2019. Real-time geophysical monitoring of particle size distribution during volcanic explosions at Stromboli volcano (Italy). *Frontiers in Earth Science*, *7*, p.52.
- Pioli, L., Azzopardi, B.J. and Cashman, K.V., 2009. Controls on the explosivity of scoria cone eruptions: Magma segregation at conduit junctions. *Journal of volcanology and geothermal research*, *186*, pp.407-415.
- Pioli, L., Azzopardi, B.J., Bonadonna, C., Brunet, M. and Kurokawa, A.K., 2017. Outgassing and eruption of basaltic magmas: The effect of conduit geometry. *Geology*, *45*(8), pp.759-762.
- Pioli, L., Erlund, E., Johnson, E., Cashman, K., Wallace, P., Rosi, M. and Granados, H.D., 2008. Explosive dynamics of violent Strombolian eruptions: the eruption of Parícutin Volcano 1943–1952 (Mexico). *Earth and planetary science letters*, *271*(1-4), pp.359-368.
- Polacci, M., Corsaro, R.A. and Andronico, D., 2006. Coupled textural and compositional characterization of basaltic scoria: Insights into the transition from Strombolian to fire fountain activity at Mount Etna, Italy. *Geology*, *34*(3), pp.201-204.
- Polacci, M., Papale, P. and Rosi, M., 2001. Textural heterogeneities in pumices from the climactic eruption of Mount Pinatubo, 15 June 1991, and implications for magma ascent dynamics. *Bulletin of Volcanology*, *63*, pp.83-97.

- Pompilio, M., Bertagnini, A., Del Carlo, P. and Di Roberto, A., 2017. Magma dynamics within a basaltic conduit revealed by textural and compositional features of erupted ash: the December 2015 Mt. Etna paroxysms. *Scientific Reports*, *7*(1), p.4805.
- Pontesilli, A., Brenna, M., Mollo, S., Masotta, M., Nazzari, M., Le Roux, P. and Scarlato, P., 2022. Trachyte-phonolite transition at Dunedin Volcano: Fingerprints of magma plumbing system maturity and mush evolution. *Lithos*, *408*, p.106545.
- Potts P.J., Webb P.C., Watson J.S., Govindaraju K. 1994. Report on Whin Sill dolerite WS-E from England and Pitscurrie microgabbro PM-S from Scotland: Assessment by one hundred and four international laboratories". Geostandards Newsletter 18 (2), 211-300.
- Preece, K., Barclay, J., Brown, R.J., Chamberlain, K.J. and Mark, D.F., 2021. Explosive felsic eruptions on ocean islands: a case study from Ascension Island (South Atlantic). *Journal of Volcanology and Geothermal Research*, *416*, p.107284.
- Preece, K., Barclay, J., Gertisser, R. and Herd, R.A., 2013. Textural and micro-petrological variations in the eruptive products of the 2006 dome-forming eruption of Merapi volcano, Indonesia: implications for sub-surface processes. *Journal of Volcanology and Geothermal Research*, *261*, pp.98-120.
- Preece, K., Gertisser, R., Barclay, J., Charbonnier, S.J., Komorowski, J.C. and Herd, R.A., 2016. Transitions between explosive and effusive phases during the cataclysmic 2010 eruption of Merapi volcano, Java, Indonesia. *Bulletin of Volcanology*, *78*, pp.1-16.
- Preece, K., Mark, D.F., Barclay, J., Cohen, B.E., Chamberlain, K.J., Jowitt, C., Vye-Brown, C., Brown, R.J. and Hamilton, S., 2018. Bridging the gap: 40Ar/39Ar dating of volcanic eruptions from the ‘Age of Discovery’. *Geology*, *46*(12), pp.1035-1038.
- Preece, K., van der Zwan, F., Hammer, J. and Gertisser, R., 2023. A textural perspective on the magmatic system and eruptive behaviour of Merapi volcano. In *Merapi Volcano: Geology, Eruptive Activity, and Monitoring of a High-Risk Volcano* (pp. 265-289). Cham: Springer International Publishing.
- Putirka, K., 2016. Amphibole thermometers and barometers for igneous systems and some implications for eruption mechanisms of felsic magmas at arc volcanoes. *American Mineralogist*, *101*(4), pp.841-858.
- Putirka, K.D., 2005. Igneous thermometers and barometers based on plagioclase+ liquid equilibria: Tests of some existing models and new calibrations. *American Mineralogist*, *90*(2-3), pp.336-346.

- Putirka, K.D., Perfit, M., Ryerson, F.J. and Jackson, M.G., 2007. Ambient and excess mantle temperatures, olivine thermometry, and active vs. passive upwelling. *Chemical Geology*, *241*(3-4), pp.177-206.
- Quane, S.L. and Russell, J.K., 2005. Ranking welding intensity in pyroclastic deposits. *Bulletin of Volcanology*, *67*(2), pp.129-143.
- Quane, S.L. and Russell, J.K., 2005. Welding: insights from high-temperature analogue experiments. *Journal of Volcanology and Geothermal Research*, *142*(1-2), pp.67-87.
- Rader, E. and Geist, D., 2015. Eruption conditions of spatter deposits. *Journal of Volcanology and Geothermal Research*, *304*, pp.287-293.
- Rader, E., Kobs Nawotniak, S. and Heldmann, J., 2018. Variability of spatter morphology in pyroclastic deposits in southern Idaho, as correlated to thermal conditions and eruptive environment. *Earth and Space Science*, *5*(10), pp.592-603.
- Ray, D., Rajan, S., Ravindra, R. and Jana, A., 2011. Microtextural and mineral chemical analyses of andesite–dacite from Barren and Narcondam islands: Evidences for magma mixing and petrological implications. *Journal of earth system science*, *120*, pp.145-155.
- Re, G., Corsaro, R.A., D'Oriano, C. and Pompilio, M., 2021. Petrological monitoring of active volcanoes: A review of existing procedures to achieve best practices and operative protocols during eruptions. *Journal of Volcanology and Geothermal Research*, *419*, p.107365.
- Reubi, O. and Nicholls, I.A., 2004. Magmatic evolution at Batur volcanic field, Bali, Indonesia: petrological evidence for polybaric fractional crystallization and implications for caldera-forming eruptions. *Journal of Volcanology and Geothermal Research*, *138*(3-4), pp.345-369.
- Reubi, O. and Nicholls, I.A., 2005. Structure and dynamics of a silicic magmatic system associated with caldera-forming eruptions at Batur volcanic field, Bali, Indonesia. *Journal of Petrology*, *46*(7), pp.1367-1391.
- Reubi, O., Nicholls, I.A. and Kamenetsky, V.S., 2003. Early mixing and mingling in the evolution of basaltic magmas: evidence from phenocryst assemblages, Slamet Volcano, Java, Indonesia. *Journal of Volcanology and Geothermal Research*, *119*(1-4), pp.255-274.
- Reynolds, P., Brown, R.J., Thordarson, T. and Llewellin, E.W., 2016. The architecture and shallow conduits of Laki-type pyroclastic cones: insights into a basaltic fissure eruption. *Bulletin of Volcanology*, *78*(5), pp.1-18.
- Ridolfi, F., 2021. Amp-TB2: an updated model for calcic amphibole thermobarometry. *Minerals*, *11*(3), p.324.

- Riedel, C., Ernst, G.G.J. and Riley, M., 2003. Controls on the growth and geometry of pyroclastic constructs. *Journal of Volcanology and Geothermal Research*, *127*(1-2), pp.121-152.
- Riker, J.M., Cashman, K.V., Kauahikaua, J.P. and Montierth, C.M., 2009. The length of channelized lava flows: Insight from the 1859 eruption of Mauna Loa Volcano, Hawai ‘i. *Journal of Volcanology and Geothermal Research*, *183*(3-4), pp.139-156.
- Ripepe, M., Lacanna, G., Pistolesi, M., Silengo, M.C., Aiuppa, A., Laiolo, M., Massimetti, F., Innocenti, L., Della Schiava, M., Bitetto, M. and La Monica, F.P., 2021. Ground deformation reveals the scale-invariant conduit dynamics driving explosive basaltic eruptions. *Nature Communications*, *12*(1), p.1683.

- Ripepe, M., Lacanna, G., Pistolesi, M., Silengo, M.C., Aiuppa, A., Laiolo, M., Massimetti, F., Innocenti, L., Della Schiava, M., Bitetto, M. and La Monica, F.P., 2021. Ground deformation reveals the scale-invariant conduit dynamics driving explosive basaltic eruptions. *Nature Communications*, *12*(1), p.1683.

- Roeder, P.L. and Emslie, R., 1970. Olivine-liquid equilibrium. *Contributions to mineralogy and petrology*, *29*(4), pp.275-289.
- Romano, C., Giordano, D., Papale, P., Mincione, V., Dingwell, D.B. and Rosi, M., 2003. The dry and hydrous viscosities of alkaline melts from Vesuvius and Phlegrean Fields. *Chemical Geology*, *202*(1-2), pp.23-38.
- Romero, J.E., Aguilera, F., Delgado, F., Guzmán, D., Van Eaton, A.R., Luengo, N., Caro, J., Bustillos, J., Guevara, A., Holbik, S. and Tormey, D., 2020. Combining ash analyses with remote sensing to identify juvenile magma involvement and fragmentation mechanisms during the 2018/19 small eruption of Peteroa volcano (Southern Andes). *Journal of Volcanology and Geothermal Research*, *402*, p.106984.
- Romero, J.E., Burton, M., Cáceres, F., Taddeucci, J., Civico, R., Ricci, T., Pankhurst, M.J., Hernández, P.A., Bonadonna, C., Llewellin, E.W. and Pistolesi, M., 2022. The initial phase of the 2021 Cumbre Vieja ridge eruption (Canary Islands): Products and dynamics controlling edifice growth and collapse. *Journal of Volcanology and Geothermal Research*, *431*, p.107642.
- Rondet, M., Martel, C. and Bourdier, J.L., 2019. The intermediate step in fractionation trends of mildly alkaline volcanic suites: An experimental insight from the Pavin trachyandesite (Massif Central, France). *Comptes Rendus Geoscience*, *351*(8), pp.525-539.
- Ross, H.P., Nielson, D.L. and Green, D.J., 1996. Aeromagnetic survey and interpretation, Ascension Island, South Atlantic Ocean. *Geothermics*, *25*(4-5), pp.471-488.

- Ross, P.S., Dürig, T., Comida, P.P., Lefebvre, N., White, J.D., Andronico, D., Thivet, S., Eychenne, J. and Gurioli, L., 2022. Standardized analysis of juvenile pyroclasts in comparative studies of primary magma fragmentation; 1. Overview and workflow. *Bulletin of volcanology*, *84*, pp.1-29.
- Royet, J.P., 1991. Stereology: a method for analyzing images. *Progress in neurobiology*, *37*(5), pp.433-474.
- Russell, J.K. and Quane, S.L., 2005. Rheology of welding: inversion of field constraints. *Journal of Volcanology and Geothermal Research*, *142*(1-2), pp.173-191.
- Rutherford, M.J. and Hill, P.M., 1993. Magma ascent rates from amphibole breakdown: an experimental study applied to the 1980–1986 Mount St. Helens eruptions. *Journal of Geophysical Research: Solid Earth*, *98*(B11), pp.19667-19685.

- Rutherford, M.J. and Hill, P.M., 1993. Magma ascent rates from amphibole breakdown: an experimental study applied to the 1980–1986 Mount St. Helens eruptions. *Journal of Geophysical Research: Solid Earth*, *98*(B11), pp.19667-19685.

- Rutherford, M.J., 2008. Magma ascent rates. *Reviews in Mineralogy and Geochemistry*, *69*(1), pp.241-271.
- Sánchez, M.C., Sarrionandia, F., Arostegui, J., Eguiluz, L. and Ibarguchi, J.G., 2012. The transition of spatter to lava-like body in lava fountain deposits: features and examples from the Cabezo Segura volcano (Calatrava, Spain). *Journal of Volcanology and Geothermal Research*, *227*, pp.1-14.

- Sánchez, M.C., Sarrionandia, F., Arostegui, J., Eguiluz, L. and Ibarguchi, J.G., 2012. The transition of spatter to lava-like body in lava fountain deposits: features and examples from the Cabezo Segura volcano (Calatrava, Spain). *Journal of Volcanology and Geothermal Research*, *227*, pp.1-14.

- Scandone, R. and Malone, S.D., 1985. Magma supply, magma discharge and readjustment of the feeding system of Mount St. Helens during 1980. *Journal of Volcanology and Geothermal Research*, *23*(3-4), pp.239-262.
- Schilling, J.G., Thompson, G., Kingsley, R. and Humphris, S., 1985. Hotspot—migrating ridge interaction in the South Atlantic. *Nature*, *313*(5999), p.187
- Self, S., Sparks, R.S.J., Booth, B. and Walker, G.P.L., 1974. The 1973 Heimaey strombolian scoria deposit, Iceland. *Geological Magazine*, *111*(6), pp.539-548.

- Self, S., Thordarson, T. and Keszthelyi, L., 1997. Emplacement of continental flood basalt lava flows. *Geophysical Monograph-American Geophysical Union*, *100*, pp.381-410.
- Sharp, W.D. and Renne, P.R., 2005. The 40Ar/39Ar dating of core recovered by the Hawaii Scientific Drilling Project (phase 2), Hilo, Hawaii. *Geochemistry, Geophysics, Geosystems*, *6*(4).
- Shaw, C.S. and Dingwell, D.B., 2008. Experimental peridotite–melt reaction at one atmosphere: a textural and chemical study. *Contributions to Mineralogy and Petrology*, *155*, pp.199-214.
- Shea, T. and Hammer, J.E., 2013. Kinetics of cooling-and decompression-induced crystallization in hydrous mafic-intermediate magmas. *Journal of Volcanology and Geothermal research*, *260*, pp.127-145.
- Shea, T. and Owen, J., 2016. Discovery of a trachyte ignimbrite sequence at Hualālai, Hawaii. *Bulletin of Volcanology*, *78*, pp.1-8.
- Sheridan, M.F. and Ragan, D.M., 1975. Compaction of ash-flow tuffs.
- Sheridan, M.F. and Wohletz, K.H., 1983. Hydrovolcanism: basic considerations and review. *Journal of Volcanology and Geothermal Research*, *17*(1-4), pp.1-29.

- Sheridan, M.F. and Wohletz, K.H., 1983. Hydrovolcanism: basic considerations and review. *Journal of Volcanology and Geothermal Research*, *17*(1-4), pp.1-29.

- Sigmarsson, O., Condomines, M., Grönvold, K. and Thordarson, T., 1991. Extreme magma homogeneity in the 1783–84 Lakagigar eruption: origin of a large volume of evolved basalt in Iceland. *Geophysical Research Letters*, *18*(12), pp.2229-2232.
- Sigmundsson, F., Parks, M., Hooper, A., Geirsson, H., Vogfjörd, K.S., Drouin, V., Ófeigsson, B.G., Hreinsdóttir, S., Hjaltadóttir, S., Jónsdóttir, K. and Einarsson, P., 2022. Deformation and seismicity decline before the 2021 Fagradalsfjall eruption. *Nature*, *609*(7927), pp.523-528.
- Smith, R.L. and Bailey, R.A., 1966. *The Bandelier Tuff: a study of ash-flow eruption cycles from zoned magma chambers*. Francesco Giannini.
- Smith, R.L., 1960. *Zones and zonal variations in welded ash flows* (No. 354-F, pp. 149-159). US Geological Survey.
- Snee, E., Degruyter, W., Bonadonna, C., Scollo, S., Rossi, E. and Freret-Lorgeril, V., 2021. A model for buoyant tephra plumes coupled to lava fountains with an application to the 29th of August 2011 paroxysmal eruption at Mount Etna, Italy. *Journal of Geophysical Research: Solid Earth*, *126*(12).

- Son, M., Kim, J.S., Jung, S., Ki, J.S., Kim, M.C. and Sohn, Y.K., 2012. Tectonically controlled vent migration during maar–diatreme formation: An example from a Miocene half-graben basin in SE Korea. *Journal of Volcanology and Geothermal Research*, *223*, pp.29-46.
- Sparks, R.S.J., 1978. The dynamics of bubble formation and growth in magmas: a review and analysis. *Journal of Volcanology and Geothermal Research*, *3*(1-2), pp.1-37.
- Sparks, R.S.J., 1997. Causes and consequences of pressurisation in lava dome eruptions. *Earth and Planetary Science Letters*, *150*(3-4), pp.177-189.
- Sparks, R.S.J., Wright J.V., 1979. Welded air-fall tufts. Ash-flow Tufts, Geol. Soc. Amer. Spec. Paper, vol. 190 pp. 155-166.
- Sparks, R.S.J., Young, S.R., Barclay, J., Calder, E.S., Cole, P., Darroux, B., Davies, M.A., Druitt, T.H., Harford, C., Herd, R. and James, M., 1998. Magma production and growth of the lava dome of the Soufriere Hills Volcano, Montserrat, West Indies: November 1995 to December 1997. *Geophysical Research Letters*, *25*(18), pp.3421-3424.

- Sparks, R.S.J., Young, S.R., Barclay, J., Calder, E.S., Cole, P., Darroux, B., Davies, M.A., Druitt, T.H., Harford, C., Herd, R. and James, M., 1998. Magma production and growth of the lava dome of the Soufriere Hills Volcano, Montserrat, West Indies: November 1995 to December 1997. *Geophysical Research Letters*, *25*(18), pp.3421-3424.

- Stix, J., Torres, R.C., Narváez, L., Raigosa, J.A., Gómez, D. and Castonguay, R., 1997. A model of vulcanian eruptions at Galeras volcano, Colombia. *Journal of Volcanology and Geothermal Research*, *77*(1-4), pp.285-303.
- Stovall, W.K., Houghton, B.F., Gonnermann, H., Fagents, S.A. and Swanson, D.A., 2011. Eruption dynamics of Hawaiian-style fountains: the case study of episode 1 of the Kīlauea Iki 1959 eruption. *Bulletin of Volcanology*, *73*, pp.511-529.
- Streck, M.J. and Grunder, A.L., 1995. Crystallization and welding variations in a widespread ignimbrite sheet; the Rattlesnake Tuff, eastern Oregon, USA. *Bulletin of Volcanology*, *57*, pp.151-169.
- Sumner, J.M. and Wolff, J., 2003. Petrogenesis of mixed-magma, high-grade, peralkaline ignimbrite 'TL'(Gran Canaria): diverse styles of mixing in a replenished, zoned magma chamber. *Journal of Volcanology and Geothermal Research*, *126*(1-2), pp.109-126.
- Sumner, J.M., 1998. Formation of clastogenic lava flows during fissure eruption and scoria cone collapse: the 1986 eruption of Izu-Oshima Volcano, eastern Japan. *Bulletin of Volcanology*, *60*, pp.195-212.

- Sumner, J.M., Blake, S., Matela, R.J. and Wolff, J.A., 2005. Spatter. *Journal of Volcanology and Geothermal Research*, *142*(1-2), pp.49-65.
- Szramek, L., Gardner, J.E. and Larsen, J., 2006. Degassing and microlite crystallization of basaltic andesite magma erupting at Arenal Volcano, Costa Rica. *Journal of Volcanology and Geothermal Research*, *157*(1-3), pp.182-201.
- Taddeucci, J., Edmonds, M., Houghton, B., James, M.R. and Vergniolle, S., 2015. Hawaiian and Strombolian eruptions. In *The encyclopedia of volcanoes* (pp. 485-503). Academic Press.
- Taddeucci, J., Pompilio, M. and Scarlato, P., 2004. Conduit processes during the July–August 2001 explosive activity of Mt. Etna (Italy): inferences from glass chemistry and crystal size distribution of ash particles. *Journal of Volcanology and Geothermal Research*, *137*(1-3), pp.33-54.
- Tamura, Y., Yuhara, M., Ishii, T., Irino, N. and Shukuno, H., 2003. Andesites and dacites from Daisen volcano, Japan: partial-to-total remelting of an andesite magma body. *Journal of Petrology*, *44*(12), pp.2243-2260.
- Tegner, C., Cawthorn, R.G. and Kruger, F.J., 2006. Cyclicity in the Main and Upper Zones of the Bushveld Complex, South Africa: crystallization from a zoned magma sheet. *Journal of Petrology*, *47*(11), pp.2257-2279.
- Tepley Iii, F.J., Davidson, J.P. and Clynne, M.A., 1999. Magmatic interactions as recorded in plagioclase phenocrysts of Chaos Crags, Lassen Volcanic Center, California. *Journal of Petrology*, *40*(5), pp.787-806.
- TEPLEY III, F.J., Davidson, J.P., Tilling, R.I. and Arth, J.G., 2000. Magma mixing, recharge and eruption histories recorded in plagioclase phenocrysts from El Chichon Volcano, Mexico. *Journal of Petrology*, *41*(9), pp.1397-1411.
- Tepp, G., Ebinger, C.J., Ruiz, M. and Belachew, M., 2014. Imaging rapidly deforming ocean island volcanoes in the western Galápagos archipelago, Ecuador. *Journal of Geophysical Research: Solid Earth*, *119*(1), pp.442-463.
- Thiele, S.T., Cruden, A.R., Zhang, X., Micklethwaite, S. and Matchan, E.L., 2021. Reactivation of magma pathways: Insights from field observations, geochronology, geomechanical tests, and numerical models. *Journal of Geophysical Research: Solid Earth*, *126*(5), p.e2020JB021477.
- Thivet, S., Gurioli, L., Di Muro, A., Derrien, A., Ferrazzini, V., Gouhier, M., Coppola, D., Galle, B. and Arellano, S., 2020. Evidences of plug pressurization enhancing magma fragmentation during

the September 2016 basaltic eruption at Piton de la Fournaise (La Réunion Island, France). *Geochemistry, Geophysics, Geosystems*, *21*(2), p.e2019GC008611.

- Thomas, R.M.E. and Sparks, R.S.J., 1992. Cooling of tephra during fallout from eruption columns. *Bulletin of Volcanology*, *54*(7), pp.542-55
- Thordarson, T. and Larsen, G., 2007. Volcanism in Iceland in historical time: Volcano types, eruption styles and eruptive history. *Journal of Geodynamics*, *43*(1), pp.118-152.
- Tibaldi, A., 2015. Structure of volcano plumbing systems: A review of multi-parametric effects. *Journal of Volcanology and Geothermal Research*, *298*, pp.85-135.
- Tibaldi, A., Bonali, F.L., Pasquaré, F.A., Rust, D., Cavallo, A. and D'urso, A., 2013. Structure of regional dykes and local cone sheets in the Midhyrna-Lysuskard area, Snaefellsnes Peninsula (NW Iceland). *Bulletin of volcanology*, *75*, pp.1-16.
- Troll, V.R. and Schmincke, H.U., 2002. Magma mixing and crustal recycling recorded in ternary feldspar from compositionally zoned peralkaline ignimbrite 'A', Gran Canaria, Canary Islands. *Journal of Petrology*, *43*(2), pp.243-270.
- Turbeville, B.N., 1992. Tephra fountaining, rheomorphism, and spatter flow during emplacement of the Pitigliano Tuffs, Latera caldera, Italy. *Journal of volcanology and geothermal research*, *53*(1-4), pp.309-327.

- Turbeville, B.N., 1992. Tephra fountaining, rheomorphism, and spatter flow during emplacement of the Pitigliano Tuffs, Latera caldera, Italy. *Journal of volcanology and geothermal research*, *53*(1-4), pp.309-327.

- Umino, S. and Horio, A., 1998. Multistage magma mixing revealed in phenocryst zoning of the Yunokuchi Pumice Akagi Volcano, Japan. *Journal of Petrology*, *39*(1), pp.101-124.
- Valentine, G.A. and Gregg, T.K.P., 2008. Continental basaltic volcanoes—processes and problems. *Journal of Volcanology and Geothermal Research*, *177*(4), pp.857-873.
- Valentine, G.A. and Krogh, K.E., 2006. Emplacement of shallow dikes and sills beneath a small basaltic volcanic center–The role of pre-existing structure (Paiute Ridge, southern Nevada, USA). *Earth and Planetary Science Letters*, *246*(3-4), pp.217-230.
- Vergniolle, S. and Jaupart, C., 1986. Separated two-phase flow and basaltic eruptions. *Journal of Geophysical Research: Solid Earth*, *91*(B12), pp.12842-12860.
- Viccaro, M., Cannata, A., Cannavò, F., De Rosa, R., Giuffrida, M., Nicotra, E., Petrelli, M. and Sacco, G., 2021. Shallow conduit dynamics fuel the unexpected paroxysms of Stromboli volcano during the summer 2019. *Scientific Reports*, *11*(1), p.266.

- Vitturi, M.D.M., Clarke, A.B., Neri, A. and Voight, B., 2008. Effects of conduit geometry on magma ascent dynamics in dome-forming eruptions. *Earth and Planetary Science Letters*, *272*(3-4), pp.567-578.
- Volynets, A.O., Edwards, B.R., Melnikov, D., Yakushev, A. and Griboedova, I., 2015. Monitoring of the volcanic rock compositions during the 2012–2013 fissure eruption at Tolbachik volcano, Kamchatka. *Journal of Volcanology and Geothermal Research*, *307*, pp.120-132.
- Walker, G.P., 1973. Explosive volcanic eruptions—a new classification scheme. *Geologische Rundschau*, *62*, pp.431-446.
- Walker, G.P., 1991. Structure, and origin by injection of lava under surface crust, of tumuli,“lava rises”,“lava-rise pits”, and “lava-inflation clefts” in Hawaii. *Bulletin of Volcanology*, *53*, pp.546-558.
- Walker, G.P.L. and Croasdale, R., 1971. Characteristics of some basaltic pyroclastics. *Bulletin volcanologique*, *35*, pp.303-317.
- Walker, G.P.L., 1969. The breaking of magma. *Geological Magazine*, *106*(2), pp.166-173.
- Walker, G.P.L., 1971. Compound and simple lava flows and flood basalts. *Bulletin Volcanologique*, *35*, pp.579-590.
- Walker, G.P.L., 1973. Mount Etna and the 1971 eruption-lengths of lava flows. *Philosophical Transactions of the Royal Society of London. Series A, Mathematical and Physical Sciences*, *274*(1238), pp.107-118.
- Walker, G.P.L., 1982. Eruptions of andesitic volcanoes.
- Wallace, P.J., 2005. Volatiles in subduction zone magmas: concentrations and fluxes based on melt inclusion and volcanic gas data. *Journal of volcanology and Geothermal Research*, *140*(1-3), pp.217-240.
- Walter, T.R. and Amelung, F., 2006. Volcano-earthquake interaction at Mauna Loa volcano, Hawaii. *Journal of Geophysical Research: Solid Earth*, *111*(B5).
- Walter, T.R., 2007. How a tectonic earthquake may wake up volcanoes: Stress transfer during the 1996 earthquake–eruption sequence at the Karymsky Volcanic Group, Kamchatka. *Earth and Planetary Science Letters*, *264*(3-4), pp.347-359.
- Wark, D.A. and Stimac, J.A., 1992. Origin of mantle (rapakivi) feldspars: Experimental evidence of a dissolution-and diffusion-controlled mechanism. *Contributions to Mineralogy and Petrology*, *111*(3), pp.345-361.

- Waters, L.E. and Lange, R.A., 2015. An updated calibration of the plagioclase-liquid hygrometer-thermometer applicable to basalts through rhyolites. *American mineralogist*, *100*(10), pp.2172-2184.
- Waters, L.E., Andrews, B.J. and Frey, H.M., 2021. Daly gaps at south sister, Oregon, USA, generated via partial melting. *Contributions to Mineralogy and Petrology*, *176*(7), p.52.
- Weaver, B., Kar, A., Davidson, J. and Colucci, M., 1996. Geochemical characteristics of volcanic rocks from Ascension Island, south Atlantic Ocean. *Geothermics*, *25*(4-5), pp.449-470.
- Webster, J.D. and Rebbert, C.R., 2001. The geochemical signature of fluid-saturated magma determined from silicate melt inclusions in Ascension Island granite xenoliths. *Geochimica et Cosmochimica Acta*, *65*(1), pp.123-136.
- White, J.D. and Schmincke, H.U., 1999. Phreatomagmatic eruptive and depositional processes during the 1949 eruption on La Palma (Canary Islands). *Journal of Volcanology and Geothermal Research*, *94*(1-4), pp.283-304.
- White, W.M., Tapia, M.D. and Schilling, J.G., 1979. The petrology and geochemistry of the Azores Islands. *Contributions to Mineralogy and Petrology*, *69*, pp.201-213.
- Wilson S.A. , 1997. The collection, preparation and testing of USGS reference material BCR-2, Columbia River Basalt. U.S. Geological Survey Open-File Report.
- Wilson, C.J. and Hildreth, W., 2003. Assembling an ignimbrite: Mechanical and thermal building blocks in the Bishop Tuff, California. *The Journal of Geology*, *111*(6), pp.653-670.
- Wilson, L. and Head III, J.W., 1981. Ascent and eruption of basaltic magma on the Earth and Moon. *Journal of Geophysical Research: Solid Earth*, *86*(B4), pp.2971-3001.
- Winstanley, R., 2020. *A preliminary investigation into the growth of the Sisters scoria cone complex, Ascension Island* (Masters by Research dissertation, Durham University).
- Witt, T., Walter, T.R., Müller, D., Guðmundsson, M.T. and Schöpa, A., 2018. The relationship between lava fountaining and vent morphology for the 2014–2015 Holuhraun eruption, Iceland, analyzed by video monitoring and topographic mapping. *Frontiers in Earth Science*, *6*, p.235.
- Wolfe, E.W., Neal, C.A., Banks, N.G., Duggan, T.J. and Wolfe, E., 1988. Geologic observations and chronology of eruptive events, in the Pu'u'O'o eruption of Kilauea volcano, episodes 1–20, January 3, 1983 to June 8, 1984. *US Geological Survey Professional Papers*, *1463*, pp.471-508.
- Wood, C.A., 1980. Morphometric evolution of cinder cones. *Journal of Volcanology and Geothermal Research*, *7*(3-4), pp.387-413.

- Wright, H.M., Cashman, K.V., Rosi, M. and Cioni, R., 2007. Breadcrust bombs as indicators of Vulcanian eruption dynamics at Guagua Pichincha volcano, Ecuador. *Bulletin of Volcanology*, *69*, pp.281-300.
- Wyers, G.P. and Barton, M., 1986. Petrology and evolution of transitional alkaline—sub alkaline lavas from Patmos, Dodecanesos, Greece: evidence for fractional crystallization, magma mixing and assimilation. *Contributions to Mineralogy and Petrology*, *93*(3), pp.297-311.

- Wyers, G.P. and Barton, M., 1986. Petrology and evolution of transitional alkaline—sub alkaline lavas from Patmos, Dodecanesos, Greece: evidence for fractional crystallization, magma mixing and assimilation. *Contributions to Mineralogy and Petrology*, *93*(3), pp.297-311.

- Xing, C.M., Wang, C.Y. and Tan, W., 2017. Disequilibrium growth of olivine in mafic magmas revealed by phosphorus zoning patterns of olivine from mafic–ultramafic intrusions. *Earth and Planetary Science Letters*, *479*, pp.108-119.
- Yamagishi, H. and Feebrey, C., 1994. Ballistic ejecta from the 1988–1989 andesitic Vulcanian eruptions of Tokachidake volcano, Japan: morphological features and genesis. *Journal of volcanology and geothermal research*, *59*(4), pp.269-278.
- Zhang, Y., Xu, Z., Zhu, M. and Wang, H., 2007. Silicate melt properties and volcanic eruptions. *Reviews of Geophysics*, *45*(4).
- Zieg, M.J. and Marsh, B.D., 2002. Crystal size distributions and scaling laws in the quantification of igneous textures. *Journal of Petrology*, *43*(1), pp.85-101.
- Zimanowski, B., Büttner, R., Lorenz, V. and Häfele, H.G., 1997. Fragmentation of basaltic melt in the course of explosive volcanism. *Journal of Geophysical Research: Solid Earth*, *102*(B1), pp.803-814.
- Zobin, V.M., Carrasco-Núñez, G. and Vargas-Gutiérrez, V.R., 2016. Field and seismic evaluation of the block-and-ash flows emplaced from eruption columns of the 2005 Vulcanian explosions at Volcán de Colima, Mexico. *Bulletin of volcanology*, *78*, pp.1-9.